Using Positron Emission Particle Tracking (PEPT) to investigate the motion of granular media in a laboratory-scale tumbling mill

Angus James Morrison

Dissertation presented for the degree of Master of Science
in the Department of Physics
University of Cape Town

May 2012

Plagiarism declaration

I know the meaning of Plagiarism and declare that all of the work in the document, save for that which is properly acknowledged, is my own.

Angus James Morrison

Abstract

Positron emission particle tracking is a Lagrangian, single particle tracking technique in which the trajectory of a representative tracer particle is triangulated from the decay products of the positron-emitting radioisotope with which it is labelled. Although the trajectories of a tracer particle moving in a bulk of similar particles can be of interest, it is often more informative to employ the ergodic assumption and to thus convert trajectory data in the Lagrangian reference frame of the tracer particle into a fixed Eulerian reference frame. This has, in the past, been done by dividing 3D space into voxels and assigning a location probability density to each voxel based on the number of times that triangulated tracer particle locations fall into it- a process called simple binning.

A major outcome of my work has been to develop an alternative probability density based on the cumulative time spent by the tracer particle in a given voxel. This method is called residence time binning, and the resultant probability distribution- which I argue is proportional to, among other things, the mass and solidicity distributions of the tracer particle- the residence time distribution (RTD). In this work I propose, implement and test the residence time binning method, and show that it significantly outperforms the simple binning method in all situations.

A second thrust of my work has been to develop a suite of general analysis routines for positron emission particle tracking (PEPT) data, based on the RTD. This suite contains routines for the triangulation, optimisation and pre-processing of PEPT data, as well as for obtaining residence time probability and time-averaged kinematic distributions in 3D space, and for aggregating and visualising the results. I have also extended this general set of routines for the special case of cylindrical symmetry through the addition of routines for the further pre-processing of RTDs, as well as for the calculation of angular measures about an arbitrary axis in space.

Finally, I further extended this set of routines for application to tumbling mills. My tumbling mill analysis includes the identification of charge features and regions, and the isolation of charge in each region so-defined for further analysis. These features, particularly the shape of the bulk free and equilibrium surfaces, the angular position of the centre of circulation (CoC) of the charge, and the position of its impact toe allow me to characterise the behaviour of the charge under a range of conditions. This characterisation, together with the shear rate distributions and power draughts that I also calculate, allow me to speak meaningfully about the evolution of grinding regions in tumbling mills- information that could be used to construct charge motion and grinding models to inform the use of tumbling mills in industry.

In this work, I apply these analysis routines to a small subset of the experiments performed by the UCT Centre for Minerals Research (CMR) on laboratory-scale tumbling mills, and in so-doing elucidate the behaviour of charge in its different regions- and the evolution of such behaviour with mill operating parameters- and discuss the implications of these to grinding efficacy in tumbling mills.

Acknowledgements

I'd like to thank my supervisors, Dr Indresan Govender and Dr Aubrey Mainza, who recruited me into the CMR in 2007, and whose faith in me has not wavered- at least not dramatically- since then.

I'd particularly like to thank Indresan who has given me space to explore my own (often tangential) ideas, time to write general case code in the face of competing deadlines, and the guidance I needed to realise what was important and achievable (and, importantly, what wasn't).

I'd like to thank Aubrey and my 'grandsupervisor'[1], Prof. Malcolm Powell, for helping me to make the connection between my work and industrial tumbling mills, and for introducing me into the world of minerals processing.

I'd like, too, to thank the CMR, for all of their support- financial and practical- during my project. I'd particularly like to thank Lawrence Bbosa with whom I have worked closely over the last few years, and with whom I spent over a month in Birmingham collecting data. I'd also like to thank André van de Westhuizen, with whom I have also worked closely, and who was an important part of the CMR team whose data I have analysed here.

At the University of Birmingham's Positron Imaging Centre, I'd like to thank Prof. David Parker and Dr Tom Leadbeater for their help and support as I learnt the PEPT technique. Tom, particularly, has been very patient in answering my hardware-related questions, and in going beyond the call of duty to track down both our raw data from the early days, and an antiquated tape drive with which to read it.

For personal financial support during this work, I'd like to thank UCT's Minerals to Metals Initiative and, in particular, the SARChI Chair in Minerals Beneficiation, Prof. Jean-Paul Franzidis.

I'd like to thank, also, Prof. Andy Buffler for a good deal of advice and moral support over the years, as well as for useful discussions on a range of technical topics.

On a personal note, I'd like to mention my officemates, Mike Malahe and Angus Comrie, who made these years manageable through Futurama-, Wikipedia game-[2] and cricket-based initiatives, my brother, Graham, who offered advice and perspective well beyond his tender years, my parade of more-or-less respectible digsmates, particularly Squeaky, Arno and Hannah, and my mates, Long Graham, Johndog, Gorgeous, Just Duncan and the Munter (in order of height), for unremitting distraction and commiseration over the years.

[1] My supervisors' PhD supervisor.

[2] `http://en.wikipedia.org/wiki/Wikiracing`

Contents

List of Figures

List of Tables

Part I

Background

http://www.sciencecartoonsplus.com

Chapter 1

Introduction

1.1 My aims and objectives

I have had two aims in performing the research that I present in this dissertation. The first has been to develop as complete as possible a set of analysis routines that can be applied to positron emission particle tracking (PEPT) data in general, and to the study of tumbling mills in particular, and the second has been to use these to test some of the assumptions made about the motion of granular media inside such tumbling mills.

PEPT is a Lagrangian, single particle tracking technique in which the trajectory of a representative tracer particle is triangulated from the decay products of the positron-emitting radioisotope with which it is labelled. Although the trajectories of a tracer particle moving in a bulk of similar particles can be of interest, it is often more informative to employ the ergodic assumption and to thus convert trajectory data in the Lagrangian reference frame of the tracer particle into a fixed Eulerian reference frame. This has, in the past, been done by dividing 3D space into voxels and assigning a location probability density and average kinematics to each voxel based on the number of times that triangulated tracer particle locations fall into it- a process called binning. The central aim of my work has been to develop an alternative probability density based on the cumulative time spent by the tracer particle in a given voxel, and a system of more representative, time-averaged kinematic distributions. I call this new method residence time binning, and the new probability distribution- which I argue is proportional to, among other things, the mass and solidicity distributions of the tracer particle- the residence time distribution (RTD).

Around this centrepiece, it was my intention to build a suite of integrated analysis routines that can be applied to general PEPT data. These routines were to span the full range of a PEPT experiment- from the management of raw data; the optimal triangulation of this data; the obtaining, plotting and interrogation of kinematics from trajectory data; the residence time binning of the trajectory data in 3D to produce both a RTD, and a range of basic kinematic distributions from which more complex distributions could be built; the projection of these distributions onto arbitrary planes; and the sectioning of these distributions by planes, cylinders and spheres; to the visualisation of the results and aggregate results of all of these operations. It was my hope that these routines could provide a basic toolkit for the analysis of PEPT data in the general case.

My next aim was to build on these routines to develop a specialised toolkit for the analysis of data in a cylindrical reference frame about an arbitrary line in space. This meant augmenting the above routines with additional ones to calculate angular, radial, tangential and transverse kinematics about this arbitrary line, and introducing additional binning techniques based on angular and

radial grids.

Having done all of this, it was my plan to test these toolkits on experiments performed on laboratory-scale tumbling mills. In fact, it was my intention to demonstrate the data-handling and batch-processing capabilities of these toolkits by analysing *all* of the PEPT experiments performed by the UCT Centre for Minerals Research (CMR) on tumbling mills since 2006.

In order to make these analyses useful, however, I have had to further specialise my general cylindrical symmetry routines for application to tumbling mills. This meant developing a range of charge analysis routines specific to tumbling mills, including routines for obtaining charge features and regions; routines for obtaining power draw estimations; and routines for obtaining shear rate distributions in the charge[1]. It became an additional aim of my work to develop and test these routines and, having done so, to apply them to the interrogation of the motion of granular media in a laboratory-scale tumbling mill.

1.2 A very brief motivation for the study of charge motion in laboratory-scale tumbling mills

Tumbling mills are ubiquitous comminution devices, used in processes as disparate as the manufacture of pigments and of cement. They have been used in minerals processing since at least the 1870s, and continue to be the workhorses of comminution in this context, yet they remain only poorly understand.

Tumbling mills remain a significant cost driver in the mineral processing circuit, in terms of their electricity, lifter and liner and- in the case of ball, run of mine (RoM) and semi-autogenous mills- grinding media consumption. All of these factors, as well as grinding efficacy, are related to the motion of the charge within the mill.

While many successful empirical models of the tumbling mill exist, these are all so-called 'black box' models built on inferences and assumptions, and the fitting of model parameters to external measurements made on a large number of real mills. The research program of which this project is a part is the first realistic attempt to quantify the motion of granular media in rotating drums with a focus on mineral processing applications.

1.3 An outline of this dissertation

This dissertation is divided into four parts- Background, Experiment and Analysis, Results and Conclusions, and Appendices.

The first part of this dissertation, which contains this chapter, also contains my two literature review chapters- Chapters 2 and 3. Chapter 2 contains a history of PEPT, a detailed description of the PEPT technique, and a description of the apparatus necessary to perform a PEPT experiment. Chapter 3 provides the bulk of the motivation for my investigation of tumbling mills. It contains a survey of the understanding of granular material motion in rotating drums, a description of the use of rotating drums- tumbling mills- in the mining industry, and a review of the minerals processing literature on charge motion in tumbling mills.

The second part of this dissertation contains only two chapters- the experiment and analysis chapters. Chapter 4 is the experiment chapter. It contains a description of the laboratory-scale

[1] As a means of measuring abrasion and attrition grinding efficacy.

tumbling mills used in this work, a summary of the experiments performed on them[2], and a description of the optimisation and pre-processing procedures through which I put all of these experiments[3].

Chapter 5, the analysis chapter, is the most important of this dissertation. It is in this chapter[4] that I develop the mathematical and philosophical underpinnings of the PEPT technique in order to justify my introduction of the residence time binning technique. It is also in this chapter that I derive the general PEPT toolkit that I mention in the preceeding section, as well as those for the special cases of cylindrical symmetry and tumbling mills. It is particularly important to read this chapter with Appendix I, in which I compare the residence time binning method to the simple binning method, and test the limits of the precision and accuracy of both.

The third part of this dissertation contains my application of the routines described in Chapter 5 to the investigation of charge behaviour in tumbling mills. In Chapter 6 I present a basic analysis of PEPT data, both in the Lagrangian and in the Eulerian reference frames.

In Chapter 7 I present a more complete analysis, also of monosize data. In this chapter I demonstrate the charge feature and regions routines I describe in Chapter 5, as well as the power draw and radial measures also described therein. I use the results thus obtained to discuss the evolution of modes of charge motion with speed, to categorise the types of motion that occur in different charge regions, and to thus to clarify some long-held assumptions about the motion of charge in tumbling mills.

I also use the results obtained in Chapter 7, particularly those relating to shear rates in the charge, to discuss grinding regions in a tumbling mill; a discussion carried on in my conclusions chapter- Chapter 8.

In my conclusions chapter, I summarise the work done for this dissertation, and devote some time to further work that could be done with the rest of the data listed in Appendix D; experiments that I have triangulated, pre-processed and residence time binned up to the general case- experiments ripe for further meta analysis. In this chapter, too, I identify what I think are gaps in our experimental program so far, and opportunities for further work towards the understanding of granular flow in tumbling mills and rotating drums.

The final part of this dissertation contains my appendices- technical or supporting material that, if included in the body, would detract from the readability of the text.

[2]For the full list, see Appendix D.
[3]Detailed and demonstrated in Appendix E.
[4]And the appendices to which it refers.

1.4 Academic output arising from this work

The following is a list of peer-reviewed journal articles, conference talks and posters, workshop presentations, and seminars that I have given based on the work presented in this dissertation.

Peer-reviewed journals

[1] TS Volkwyn, A Buffler, I Govender, J-P Franzidis, **AJ Morrison**, A Odo, NP van der Meulen and C Vermeulen, *Studies of the effect of tracer activity on time-averaged positron emission particle tracking measurements on tumbling mills at PEPT Cape Town*, Minerals Engineering, **2011**, *24*, 261-266.

Conference proceedings

[1] I Govender, **AJ Morrison**, AN Mainza, A van der Westhuizen, J-P Franzidis and MS Powell, *Using Positron Emission Particle Tracking (PEPT) to investigate industrial systems*, XXV International Mineral Processing Congress(IMPC) Proceedings, **2010**, 2843-2853.

[2] **AJ Morrison**, I Govender and AN Mainza, *Time-averaged kinematics in tumbling mills using positron emission particle tracking*, Minerals Engineering International Comminution Conference, **2010**.

Conference presentations

[1] **AJ Morrison**, I Govender and AN Mainza, *Towards grinding regions in tumbling mills. Contributions from PEPT*, Minerals Engineering International Comminution Conference, Cape Town, South Africa, 17-20 April **2012**.

[2] I Govender, **AJ Morrison**, AN Mainza, A van der Westhuizen, J-P Franzidis and MS Powell, *Using Positron Emission Particle Tracking (PEPT) to investigate industrial systems*, XXV International Mineral Processing Congress(IMPC), Brisbane, Australia, 6-10 September **2010**.

[3] **AJ Morrison**, I Govender and AN Mainza, *Using Positron Emission Particle Tracking (PEPT) to investigate the charge dynamics inside a laboratory scale tumbling mill*, South African Institute of Mining and Metallurgy (SAIMM) Minerals Processing Conference, Cape Town, South Africa, 5-6 August **2010**.

[4] **AJ Morrison**, I Govender and AN Mainza, *Time-averaged kinematics inside tumbling mills using positron emission particle tracking (PEPT)*, Minerals Engineering International Comminution Conference, Cape Town, South Africa, 13-16 April **2010**.

[5] **AJ Morrison**, I Govender and AN Mainza, *Using positron emission particle tracking to investigate industrial systems*, 53rd Annual Conference of the South African Institute of Physics (SAIP), Polokwane, South Africa, 8-11 July **2008**.

Workshop presentations

[1] **AJ Morrison** and I Govender, *The analysis of PEPT data*, International Comminution Researchers' Association (ICRA) Workshop, Franschoek, South Africa, 10-12 April **2010**.

[2] **AJ Morrison**, LS Bbosa, J Newling and N Fowkes, *Positron emission particle tracking*, 7$^{\text{th}}$ Mathematics in Industry Study Group (MISG), African Institute for Mathematical Sciences, Muizenberg, South Africa, 11-15 January **2010**.

Seminar presentations

[1] **AJ Morrison**, I Govender and AN Mainza, *Towards grinding regions in tumbling mills. Contributions from PEPT*, Centre for Mineral Research Seminar Series, University of Cape Town, 4 May **2012**.

[2] **AJ Morrison**, I Govender and AN Mainza, *Granular flow modelling in rotating drums: Development and validation using PEPT*, Centre for Mineral Research Seminar Series, University of Cape Town, 14 March **2011**.

[3] **AJ Morrison**, I Govender and AN Mainza, *Using biplanar x-ray imaging and positron emission particle tracking (PEPT) to validate the discrete element method (DEM) for tumbling mills*, 3$^{\text{rd}}$ Annual Minerals to Metals Research Day, Cape Town, South Africa, 20 October **2010**.

[4] **AJ Morrison**, I Govender and AN Mainza, *Using biplanar x-ray imaging and positron emission particle tracking (PEPT) to validate the discrete element method (DEM) for tumbling mills*, 9$^{\text{th}}$ Annual Centre for Minerals Research Student Research Day, Cape Town, South Africa, 19 October **2010**.

[5] **AJ Morrison**, I Govender and AN Mainza, *Using biplanar x-ray imaging and positron emission particle tracking (PEPT) to validate the discrete element method (DEM) for tumbling mills*, 2$^{\text{nd}}$ Annual Minerals to Metals Research Day, Cape Town, South Africa, 5 October **2009**.

[6] **AJ Morrison**, I Govender and AN Mainza, *Using positron emission particle tracking (PEPT) to investigate charge motion in a tumbling mill*, 8$^{\text{th}}$ Annual Centre for Minerals Research Student Research Day, Cape Town, South Africa, 3 September **2009**.

[7] **AJ Morrison**, *The physics of positron emission particle tracking (PEPT)*, The Minerals to Metals Winter Seminar Series, Cape Town, 13 August **2008**.

Conference posters

[1] **AJ Morrison**, I Govender and AN Mainza, *Using biplanar x-ray imaging and positron emission particle tracking (PEPT) to investigate industrial systems*, South African Institute of Mining and Metallurgy (SAIMM) Minerals Processing Conference, Cape Town, South Africa, 6-7 August **2009**.

Chapter 2

Positron emission particle tracking

2.1 Positron emission and annihilation

Positrons- the antiparticles of electrons- are emitted in the $\beta+$ decay of proton-heavy nuclei, by the reaction

$$ {}^{A}_{Z}X \rightarrow {}^{A}_{Z-1}Y + e^{+} + \nu_e + energy. \tag{2.1} $$

The inclusion of the *energy* term in equation 2.1 is to denote the fact that the decay of a proton into a neutron can only occur when the proton is in a bound state[1].

Equation 2.1 is a statement of Enrico Fermi's 1930 suggestion that the continuous energy distribution of electrons ejected from the decay of neutron-heavy nuclei is due to the fact that an electrically-neutral and massless neutrino, ν, is ejected at the same time. In fact, what Fermi had called a neutrino was what is now called an electron anti-neutrino, $\bar{\nu}_e$, which not only carries away some of the momentum and energy of the parent nucleus in the decay, but also conserves the lepton number of the system. Since the positron is the antiparticle of the electron, it has a lepton number of -1- the same as that of the $\bar{\nu}_e$- and its creation must be balanced by the emission of a neutrino, ν_e, of lepton number 1- the same as that of an electron.

The shape of the continuous kinetic energy distribution, $N(T_l)$ of an emitted lepton- electron or positron- can be modelled, after [Krane, 1988], as

$$ N(T_l) = \frac{C}{c^5}\left(T_l^2 + 2T_l m_l c^2\right)^{\frac{1}{2}}(Q - T_l)^2\left(T_l + m_l c^2\right)F(Z', T_l)\left|M_{fi}\right|^2 S(T_l, T_\nu) \tag{2.2} $$

where C is an empirically-determined constant.

The term $F(Z', T_l)$ is the Fermi function, which accounts for the Coulomb interaction between the emitted lepton and the nucleus. It depends on both the atomic number of the daughter nucleus, Z' and the kinetic energy of the emitted lepton, T_l. $|M_{fi}|^2$ sets the strength of interaction between initial and final states, and $S(T_l, T_\nu)$ is a shape factor which corrects for forbidden decay channels.

The rest of the terms in equation 2.2 are statistical ones. They depend on the kinetic energy and mass of the emitted lepton, as well as the Q value of the reaction. The Q value of a reaction is the amount of energy released by the reaction. From equation 2.2, it can be seen that the Q value of the reaction is also the maximum kinetic energy T_l with which the lepton can be emitted. It is approximately the difference in energy between the rest masses of the parent nucleus, M_P and of

[1] Or at least has so far only been observed to decay in the nucleus.

the daughter nucleus M_D and products

$$Q \cong (M_P - M_D - m_l - m_\nu)\, c^2 \tag{2.3}$$

neglecting binding energy and cross terms.

Figure 2.1, taken from [Levin and Hoffman, 1999], shows a emitted positron energy spectra for a range of radionuclides.

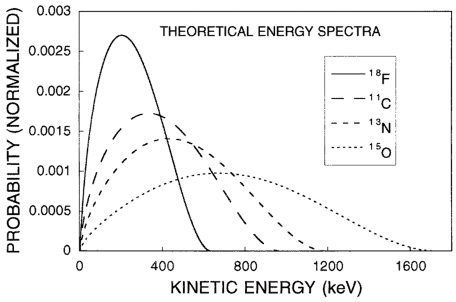

Figure 2.1: Emitted positron energy spectra for various radioisotopes, taken from Levin and Hoffman.

For certain radioactive isotopes, such as ^{22}Na, some of the Q value of the reaction can be retained by its daughter nucleus after positron emission. The daughter nucleus, ^{22}Ne in the case of ^{22}Na, decays from its excited state to its ground state by the emission of an associated gamma ray of the energy of the excited state.

A positron- emitted with some energy in a positron decay- interacts with the medium through which it moves mainly in two ways. While it has sufficient energy, it collides inelastically with other charged particles in the medium- predominantly electrons- dissipating its energy and thus slowing down. This process is called *thermalisation* because it proceeds until the positrons have about the same energy as do its neighbouring particles due to their thermal motion. Once the positron has slowed down to this extent, it is captured by an electron to form a short-lived exotic atom called positronium.

Positronium, Ps, is a short-lived bound state of a positron and an electron. In structure it is similar to a hydrogen, but with a smaller reduced mass. Unlike a hydrogen atom, however, it is extremely unstable and decays by the electromagnetic interaction into two or more gamma rays.

Positronium is an atom, and therefore has zero net charge. Annihilation of the electron-positron pair into gamma rays ensures that this zero net charge is conserved. In order to conserve linear momentum, at least two gamma rays must be created in the annihilation event, and to conserve energy the total energy of the positronium before annihilation[2], must be shared between the gamma rays thus produced.

Since spin angular momentum must also be conserved, and the spin of a photon is always 1, the number of gamma rays produced in the decay of positronium depends on its spin state. Positronium comes in two spin states- a singlet[3] called *para-Positronium* (p-PS), and a triplet state[4] called *ortho-Positronium* (o-PS). To conserve spin angular momentum, the singlet state can only decay into an even number of gamma rays, and the triplet can only decay into an odd number. In fact, it turns out that the branching ratios between the production of two and four gamma rays in the annihilation of p-Ps, and that between three and five gamma rays in the annihilation of o-Ps are both $\sim 10^{-6}$, making two or three gamma ray events overwhelmingly more likely.

[2] $m_e^2c^2 + T_{ps}$
[3] Antiparallel spins resulting in $S = 0, M_S = 0$.
[4] Parallel spins resulting in $S = 1, M_S = -1, 0, 1$.

The average lifetime of p-Ps is $0.124ns$, and that of o-Ps is $138ns$. Assuming it is equally likely that a captured positron has spin parallel or antiparallel to that of the capturing electron, and given that the spin conversion rate from o-Ps to p-Ps is about 4 times that of p-Ps to o-Ps, this difference in lifetime means that there will be many more p-Ps than o-Ps available for decay per positron emission event, and thus two gamma ray annihilations are the most likely fate of a positron created in $\beta+$ decay.

In two gamma ray annihilation events, the energy of the parent p-Ps is shared equally between them.

Recall that the relativistic energy of a photon is given by

$$E = \sqrt{m_\gamma^2 c^4 + p^2 c^2} = pc \tag{2.4}$$

because a photon has no rest mass. Assuming that the p-Ps is at rest, this equipartition of energy can be written as

$$\sqrt{4m_e^2 c^4 + p_{Ps}^2 c^2} = 2m_e c^2 = p_1 c + p_2 c = 2pc = 2E_\gamma \tag{2.5}$$

Thus both gamma rays have the rest mass energy of an electron- $511keV$ and, similarly, the same momentum $p = m_e c$.

The foregone assumes that the p-Ps has zero linear momentum. In order to conserve linear momentum in the decay, the combined linear momentum of the two gamma rays produced must be that of the centre of mass of the parent p-Ps. Since the positron must have thermalised in the medium before being captured, and since electrons in the medium are effectively at rest, the centre of mass of a positronium atom formed in this way is usually considered to be at rest. Actually, it is more correctly in thermal equilibrium with the medium.

Assuming, for simplicity of argument, that the medium is a monatomic ideal gas at some temperature T, then its kinetic energy, T_{Ps}, in terms of its momentum, p, is

$$T_{Ps} = \frac{p_{Ps}^2}{4m_e} = \frac{3}{2}kT \tag{2.6}$$

where k is Boltzmann's constant. Thus the magnitude of the average instantaneous momentum of a positronium atom at temperature T is

$$p_{Ps} = \sqrt{6m_e kT} \tag{2.7}$$

Inserting this estimate into equation 2.5 hardly changes the energy of the two gammas[5], but has an effect on their momentum.

Suppose that the p-Ps momentum given in equation 2.6 is two-dimensional and at some small angle θ to the horizontal. Suppose too that the magnitude of the linear momentum of both gamma rays produced remains $m_e c$, and that one of these momenta is entirely horizontal. Then the conservation of momentum can be written as

$$\begin{aligned} p_x: \; p_{Ps}\cos\theta &= m_e c\,(1-\cos\phi) \\ p_y: \; p_{Ps}\sin\theta &= m_e c \sin\phi \end{aligned} \tag{2.8}$$

Using the estimate for p-Ps momentum given in equation 2.6, and the conservation of momentum above, an estimate for the angle of deviation from colinearity between the two gamma rays can be

[5]Because of the factor of c^2 in the rest mass.

given as

$$\begin{aligned} \phi &= \arcsin\left(\sqrt{\frac{6kT}{m_e c^2}}\sin\theta\right) \\ &\approx \arcsin\left(10^{-5}T^{\frac{1}{2}}\sin\theta\right) \\ &\approx \arcsin\left(10^{-5}T^{\frac{1}{2}}\right) \end{aligned} \tag{2.9}$$

as $\theta \to \frac{\pi}{2}$.

Using this admittedly-rough series of approximations, the angle of deviation from colinear of the two gammas can be estimated as $\phi < 2 \times 10^{-5} radians$ at the boiling point of water. Thus it is fair to consider the gamma rays produced in the decay of p-Ps to be back-to-back even in the laboratory frame.

2.2 Nuclear imaging

2.2.1 A brief history of medical and physiological nuclear imaging

The Hungarian chemist, George de Hevesy, first proposed the use of radioactive isotopes for studying biological systems in the early 1920s. In 1923 he labelled a lead salt with radioactive ^{212}Pb and measured its uptake by plants. He did this by placing several plants in the salt solution, removing and burning them at intervals, and measuring the radioactivity in the resulting ash with a Geiger counter. The applicability of this approach was limited by the fact that those biologically-active elements that had naturally-occurring radioactive isotopes where generally toxic to animals, and could thus only really be used on plants. de Hevesy was eventually awarded the Nobel Prize in Chemistry in 1943

> *for his work on the use of isotopes as tracers in the study of chemical processes.*

In 1934, Irène Joliot-Curie and Frédéric Joliot discovered that radioisotopes could be artificially produced by bombarding certain stable isotopes with alpha particles[6][Curie and Joliot, 1934]. This opened the door for the production of a range of non-toxic, biologically-active radioisotopes to be produced and used for medical and physiological imaging[7]. In 1935, Joliot and Joliot-Curie jointly won the Nobel Prize in Chemistry

> *in recognition for their synthesis of new radioactive elements.*

At the same time that Joliot and Joliot-Curie were performing the work that led to their discovery of artificial radioactivity, Ernest Lawrence and his group at the University of California at Berkeley had been routinely, albeit unknowingly, creating artificial radioisotopes with the cyclotron that Lawrence had invented in 1930. Once Joliot and Joliot-Curie's discovery was announced, however, they[8] quickly realised that they could produce large quantities of such radioisotopes. This made Berkeley so much a hub for early nuclear medicine that Lawrence's group named their 1938 cyclotron a 'medical cyclotron'. Lawrence earned the 1939 Nobel Prize in Physics

> *for the invention and development of the cyclotron and for results obtained with it, especially with regard to artificial radioactive elements.*

[6] $^{4}_{2}He$
[7] Of course, among many, many other uses of artificial radioactivity.
[8] After overcoming, no doubt, their disappointment.

From the early 1940s the field of nuclear imaging began to establish itself. At first, it proceeded by the use of a hand-held Geiger counter to measure the concentration of radioactivity in the body. Taking measurements in a systematic pattern allowed a rough picture of the distribution of the tracer to be built up. In 1950 Benedict Cassen at the University of California at Los Angeles automated this process, producing a 'gamma scanner'. He also replaced Geiger-Müller tubes with the newly-developed $NaI(Tl)$ scintillation crystals[Cassen et al., 1950].

In 1952, Hal Anger at UC Berkeley coupled these scintillation crystals with photomultiplier tubes, creating the first electronic gamma camera. By 1957[Anger, 1957], he had developed a method of detecting gamma rays that allowed for electronic pre-processing, amplification and energy-discrimination. Many researchers used these capabilities, along with the concept of collimation[9], to develop direct-sensitive gamma cameras. Anger himself said of this development

> 'The motion of tracers in plants and animals, *as well as industrial processes*, could be studied in this way.'

emphasise mine, [Anger, 1957].

At around the same time, researchers were beginning to appreciate the possibility of using the highly-correlated decay products of a positron emission to improve the direction-sensitivity of gamma cameras. In 1963, Anger produced a version of his electronic gamma camera to take advantage of the colinearity of the gamma rays produced in positron annihilation[Anger, 1963]. This was followed in 1966 by a similar device produced at the Brookhaven National Laboratory. The development of such devices made it possible to drastically improve the reconstruction of the distribution of radioisotopes in a subject. The field of tomography was thereby developed by [Kuhl and Edwards, 1968], [Phelps et al., 1975], [Ter-Pogossian et al., 1975] and others in the early 1970s.

The synthesis of flourine-18 deoxyglucose[10] (^{18}F-FDG) by [Reivich et al., 1979], coupled with all of the advances discussed above, led to the birth of the now mainstream medical imaging technique, positron emission tomography (PET)[11].

2.2.2 Industrial positrons- from PET to PEPT

Despite Anger's 1957 comment about the potential use of positrons to study industrial processes, this was not actually done until [Hawkesworth et al., 1986] used PET to study the distribution of radiolabelled lubricating oil in an aircraft engine and gearbox.

Hawkesworth *et al.* were members of the School of Physics at the University of Birmingham. They had recently come into possession of one of two PET cameras built at the Rutherford Appleton Laboratory in Oxfordshire, England. The second was used for medical research at the Royal Marsden Hospital in Sutton, England.

Following the success of early PET experiments on industrial and geophysical flows, [Bemrose et al., 1988] suggested the possibility of tracking a single, radiolabelled tracer particle in a system of interest. This idea was implemented by [Parker et al., 1993], and the resulting technique called positron emission particle tracking (PEPT).

The PEPT technique will be the subject of the rest of this chapter.

[9] The use of shielding to restrict the angles at which gamma rays can enter the detector.
[10] A radiolabelled version of an extremely important metabolic molecule.
[11] Much of this overview was based on [Wagner, 1998] and reading around it.

2.3 The PEPT technique

Positron emission particle tracking (PEPT) is an extension of the medical nuclear imaging technique PET to the tracking of a single particle in a bulk. It uses the same equipment as PET- a gamma camera or PET scanner- and takes advantage of the same radioactive decay mode- $\beta+$ decay or positron emission[12]- as does PET.

However, whereas PET produces a radiation density distribution by integrating a large number of detections over time, PEPT takes advantage of the *a priori* knowledge that the system of interest contains only one radiolabelled tracer particle to drasticly reduce the number of detections required.

In particular, detecting the two back-to-back γ-rays produced in a $\beta+$ decay allows a line of response (LoR) along which the decay must have occurred to be defined. The density of LoRs intersecting a region in space is proportional to the concentration of the radioisotope in that region, allowing a density distribution to be built up- the basis of the PET technique.

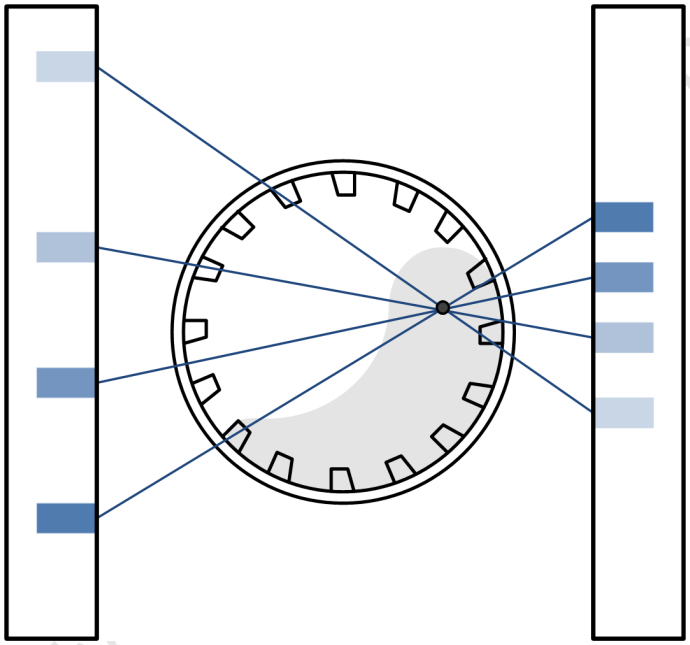

Figure 2.2: The PEPT technique: Triangulation of the position of a radiolabelled tracer particle.

In PEPT, however, we know *a priori* that only a single radioactive tracer particle is in the field of view of the PET scanner, and so the location of this tracer particle can be triangulated from the LoRs as shown in Figure 2.2.

In PET, detected LoRs are integrated into *sinograms*[13], which are then inverted to recover the underlying radiation density distribution using algorithms such as *filtered back projection*, the *inverse Radon transform*, and a range of iterative algorithms[14]. In order to obtain sufficient statistics to be able to perform accurate image reconstruction, PET requires that LoRs be collected for at least a few minutes for 2D reconstruction, and up to an hour for 3D reconstruction. PET is thus not suitable for dynamic imaging except in a limited sense. [Bemrose et al., 1988], for instance, collected data in list mode[15] and then reconstructed the radiation density for successively larger subsets of the total dataset to track the movement of the leading surface of radioactive fluid through porous rock- a semi-dynamic study of a slow-moving medium.

[12] See equation 2.1.
[13] A form of Radon transform.
[14] Much more on this in [Bailey et al., 2005].
[15] That is, recorded the end points of the LoRs rather than immediately combining them into sinograms.

In the PEPT case, however, only two or three LoRs are necessary per location[16]. Since many, many LoRs are detected per second- up to 50000 events per second on the camera used for this work[Parker et al., 2002]- either an arbitrarily accurate triangulation of the tracer particle's position can be obtained as described below, or, more usefully, the motion of the tracer particle can be recovered.

Thus the key advantage of PEPT over PET for the study of industrial systems is that PEPT can be used to obtain the detailed kinematics of the tracer particle in the bulk.

The key advantage of PET over PEPT, on the other hand, is that PET provides a system-wide view of tracer concentration, one which can only be obtained from PEPT if the system fulfils the ergodic hypothesis[17].

2.3.1 Lines of response

The overview of PEPT and PET given above assumes that all LoRs, since they are defined by the detected endpoints of two back-to-back γ-rays, pass through the radioactive tracer particle. In reality, this is not the case- some of the LoRs are so-called spurious events. Those LoRs that are not spurious are called true events.

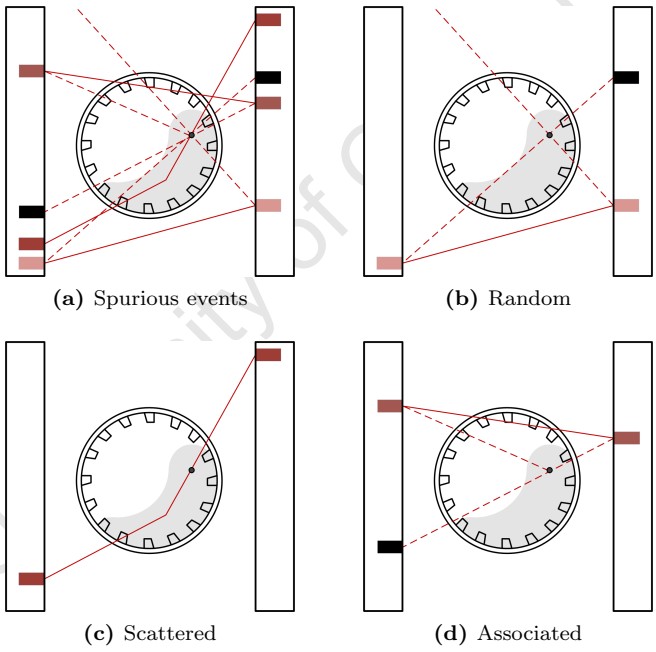

(a) Spurious events **(b)** Random **(c)** Scattered **(d)** Associated

Figure 2.3: Examples of the three main categories of spurious detections, combined (top left) and separately.

There are several types of spurious event, as shown in Figure 2.3.

Figure 2.3b shows a random event. Such an event occurs when the endpoints of two different LoRs are detected and erroneously assumed to define a third, random LoR. A random event can occur for a number of different reasons.

The first is a consequence of the limited field of view of the gamma camera[18], or, more correctly,

[16] At least in principle, more on this in a moment.
[17] More on this in Section 5.3.1.
[18] In these illustrations, a parallel-plate configuration gamma camera is depicted because the one used in this work was of such a configuration. However, gamma cameras can also come in ring or exotic configurations. The above solid angle-based argument applies in general, though.

the solid angle into which a γ-ray can be emitted and still be detected by the camera[19]. If one γ-ray from a true event is emitted into the solid angle of receptivity of the camera and the other not, then the detected event is available to form half of a random event.

The second source of random events has to do with the hardware definition of a coincident event. [Leadbeater, 2009] contains a description of the coincidence gate method; the method by which a pair of detected events is determined to be in coincidence or not. The coincidence gate method operates by using an event that occurs in one detector to open a coincidence 'gate'. If another event occurs in a second detector while the gate is still open[20], these two events are considered to be in coincidence. A large field of view camera will consist of many more than just two detectors. Thus if an event in detector A opens a gate during which no event is registered in detector B, it may still be the case that one would be registered in detectors C, D and so on. Thus, once a gate has been opened, all of the detectors that are candidates for coincidences[21] must be polled in some appropriate order. Due to the stochastic nature of radioactive decay, it is possible that another decay may have occurred in the period of the gate being open, one of whose gammas has been registered in a detector that is polled before the true one, leading to a random event. This could also happen if the true detector is damaged for some reason.

Random coincidences, clearly depend on the geometry of the gamma cameras in use, and on the position of the tracer particle in the field of view of the camera. For instance, when a tracer is very close to one plate of a parallel-plate camera the near plate has a large solid angle of receptivity, but the far plate has a smaller one. Since the γ-rays produced in positron emission are back-to-back, the total solid angle of receptivity of the whole camera is determined by the smaller of the two. A similar argument could be made about tracers close to the edge of the field of view.

Figure 2.3c shows a scattered event. These arise because the γ-rays emitted in a positron decay interact with the material through which they pass. For $511keV$ γ-rays of the sort created in positron annihilation, the dominant interaction with matter is inelastic or Compton scattering. Compton scattering is the interaction between a photon moving in a medium and a bound electron in that medium. The angle by which the photon is scattered gives rise to scattered events.

The amount of scattering that occurs in a given experiment depends on the attenuating environment that each half of a true LoR must traverse before it is detected.

Clearly the amount of material that the photon travels through affects this attenuating environment- for a given material, the more of it that a photon must pass through, the more likely it is to have interacted with the material in doing so. This is a factor of both the absolute amount of material in the field of view, and of the position of the tracer in that material. The effect of the position of the tracer particle in the attenuating material is further exacerbated when it is asymmetrically embedded in the material so that one half of the true LoR must pass through more material than the other. As was the case for the solid angle of receptivity of the detectors, the less-favourable halfspace into which the γ-ray is emitted determines the effective environment.

The composition of the attenuating material also has an important effect on the attenuating environment- γ-rays of a given energy are more likely to interact or interact more strongly with some materials than with others. The various cross-sections[22] of γ-rays of various energies with a large range of materials are available from the Physical Measurement Library of the American

[19] More on this in a moment.

[20] $12ns$ for the camera used in this work.

[21] That is, there is no point checking for coincidences in adjacent detectors, since a LoR could not possible extend from one to the other. In the case of a parallel-plate gamma camera, a gate opened in one of the plates can only have a coincidence from the other.

[22] A measure of the likeliness of interaction.

National Institute of Standards and Technology (NIST)[23].

The likelihood of interaction of a photon of given energy with a given material per unit thickness of that material is usually given in terms of either a mean free path or half-value layer (HVL), or of a linear attenuation coefficient. The mean free path of a photon in a given material is the average distance it can travel through that material before interacting in a way which will change either its energy or momentum. HVL of a material is the thickness which reduces the intensity of a beam of photons of given energy passing through it by half. That is, the thickness of material through which a beam of photons of given energy can pass before half of its constituents have interacted in the material. The linear attenuation coefficient of a material for photons of a given energy is a measure of how quickly a beam of such photons is absorbed, scattered or deviated from its original properties[24].

The following table, based on [Berger and Hubbell, 1987], shows some indicative linear attenuation coefficients, $\boldsymbol{\mu}$, and half-value layers for $511keV$ photons

Material	**Density** $/g.cm^{-3}$	$\boldsymbol{\mu}$ $/cm^{-1}$	**HVL** $/mm$
Water	1.00	0.095	72.9
Glass	2.23	0.194	35.7
Concrete	2.35	0.209	33.2
Stainless steel	8.00	0.816	8.5
Lead	11.35	1.750	4.0

Table 2.1: Some linear attenuation coefficients and half-value layers for $511keV$ photons in various materials.

Table 2.1 shows that the density of a material is usually a good indicator of how attenuating it will be, at least to γ-rays and at least at this energy. It also shows how short are the HVLs through which only 50% of $511keV\gamma$-rays can pass without being scattered.

Luckily, however, Compton scattering is inelastic, and the energy lost in the interaction depends on the angle through which the photon is scattered. The increase in the wavelength of the photon is given by Compton's formula[25]

$$\Delta\lambda = \frac{h}{m_e c}\left(1 - \cos\theta\right) \tag{2.10}$$

where θ is the scattering angle. Thus the energy lost by the photon in the interaction can be calculated from

$$E = \frac{hc}{\lambda} \tag{2.11}$$

γ-rays that have been scattered by some threshold angle can thus be excluded from the accepted LoRs by gating the detectors on the energy of the detected event. This excludes many of the worst scattered events.

Figure 2.3d shows an associated event. An associated event can occur when an associated γ-ray- one that is produced by the radioisotope as part of its decay process, unrelated to its positron emission- is detected as an endpoint of a LoR. This might occur in an isotope such as ^{22}Na which not only emits a positron, but also an associated γ-ray of energy $1.27MeV$[26]. This source of

[23] Available from `http://www.nist.gov/pml/data/xcom/`

[24] A linear attenuation coefficient of $1cm^{-1}$ means that the intensity of the beam of photons is reduced by a factor of $\frac{1}{e}$, or about 38%, after traversing $1cm$ of the material, and a linear attenuation coefficient of $0cm^{-1}$ means that it is not at all attenuated by the material.

[25] In 1923, Arthur Compton explained the increase in wavelength when X-rays scatter from matter by treating photons as particles and applying the conservation of energy and momentum to the collision between a massless photon and a stationary electron.

[26] When ^{22}Na decays by positron emission, it leaves its daughter nucleus, ^{22}Ne, in an excited state. It is the decay of this excited daughter back to ground state that results in the emission of a $1274keV\gamma$-ray.

spurious events can be eliminated by choosing a radioisotope that does not have an associated γ-ray[27], or, even more easily, by gating the detectors on energy as is done to exclude the worst scattered events.

The result of having spurious as well as true event in a dataset is that the real state of affairs resembles Figure 2.2 less than it does Figure 2.4.

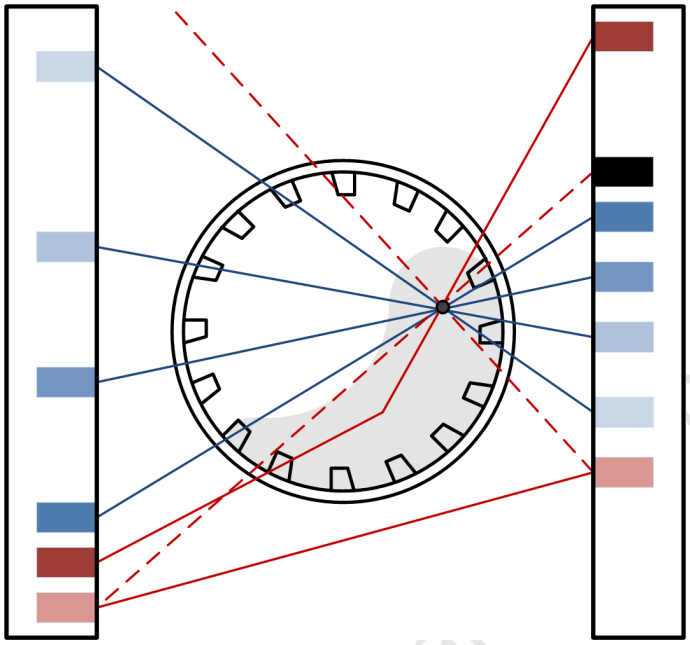

Figure 2.4: An 2D illustration of a realistic dataset consisting of both true and spurious events.

2.3.2 Triangulation

Although the latter two sources of spurious events mentioned above- scattered events and associated events- can be minimised, they can't be eliminated, and neither can any of the many sources of random events. The solution to this problem is, following [Parker et al., 1993], to employ an iterative triangulation scheme.

If only true LoRs were detected, as in Figure 2.2, then they would all cross at a single point, and the triangulation of a particle's position would merely consist of finding that point. Because of the spurious LoRs mentioned above[28], this is not the case, and it is more meaningful to define a centroid[29] of all of the LoRs.

Figure 2.5 shows such a centroid. It is the point of minimum distance to all three of the lines shown in Figure 2.5, and is obtainable in the following way.

It is possible to write down equations for an arbitrary point, p_i, on each of the lines in Figure 2.5 in terms of the endpoints, p_{i1} and p_i2, from which the lines are defined, thus

$$\begin{aligned} \underline{p}_1 &= \underline{p}_{11} + \lambda_1 \left(\underline{p}_{12} - \underline{p}_{11} \right) \\ \underline{p}_2 &= \underline{p}_{21} + \lambda_2 \left(\underline{p}_{22} - \underline{p}_{21} \right) \\ \underline{p}_3 &= \underline{p}_{31} + \lambda_3 \left(\underline{p}_{32} - \underline{p}_{31} \right) \end{aligned} \tag{2.12}$$

[27] Such as ^{18}F.

[28] And also because of the finite volume of the tracer particle to which I will return in considering sources of uncertainty.

[29] Similar but not identical to the idea of a geometric centroid of a uniform body.

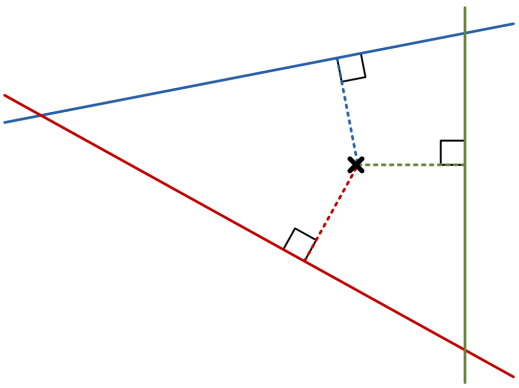

Figure 2.5: An 2D illustration of the centroid of 3 lines.

Since the shortest distance between some point, p_0, and a line is perpendicular to the line, the point of nearest approach to that point, p_0, along that line obeys

$$\left(\underline{p}_0 - \underline{p}_i\right) \cdot \left(\underline{p}_{i2} - \underline{p}_{i1}\right) = 0 \tag{2.13}$$

which implies that the point of nearest approach is some distance λ_i along the line in the direction given by $\underline{p}_{i2} - \underline{p}_{i1}$ from the point p_{i1}, such that

$$\lambda_i = \frac{\left(\underline{p}_0 - \underline{p}_{i1}\right) \cdot \left(\underline{p}_{i2} - \underline{p}_{i1}\right)}{\left(\underline{p}_{i2} - \underline{p}_{i1}\right) \cdot \left(\underline{p}_{i2} - \underline{p}_{i1}\right)} \tag{2.14}$$

The distance between some point, p_0, and a line in the form of equation 2.12 is given by

$$\begin{aligned} d_i &= \left|\underline{p}_0 - \underline{p}_i\right| \\ &= \left|\underline{p}_0 - \underline{p}_{i1} + \lambda_1 \left(\underline{p}_{i2} - \underline{p}_{i1}\right)\right| \\ &= \sqrt{\left(\lambda_i - 1\right)^2 |\underline{p}_{i1}|^2 - 2\lambda_i \left(\lambda_i - 1\right) \underline{p}_{i1} \cdot \underline{p}_{i2} + 2\left(\lambda_i - 1\right) \underline{p}_{i1} \cdot \underline{p}_{i3} + \lambda_i^2 |\underline{p}_{i2}|^2 - 2\lambda_i \underline{p}_{i2} \cdot \underline{p}_{i3} + |\underline{p}_{i3}|^2} \end{aligned} \tag{2.15}$$

The point that minimises the distance between all of the lines and that point minimises the distance $D(x, y, z) = \Sigma_{i=1}^{3} d_i(x, y, z)$, and thus satisfies the following conditions:

$$\frac{\delta D}{\delta x} = 0 \qquad \frac{\delta D}{\delta y} = 0 \qquad \frac{\delta D}{\delta z} = 0 \tag{2.16}$$

The point, p_0 that minimises the total distance D for the general case of N LoRs can be solved for numerically following [Parker et al., 1993]. The mean deviation of the N lines from the minimum distance point is then given by

$$\sigma = \frac{D(x, y, z)}{N} = \frac{\Sigma_{i=1}^{N} d_i}{N} \tag{2.17}$$

which is interpreted as the uncertainty in the triangulation, [Fan et al., 2006b].

This uncertainty can be decreased by decreasing N, the number of LoRs used in the triangulation, in such a way that the result is not to increase the remaining d_is. The obvious way to do this is to remove those LoRs corresponding to the largest d_i for a given centroid, recalculate the centroid and repeat the process until some condition is met. This procedure is called iterative triangulation.

Figure 2.6 shows the iterative calculation of the centroid of some illustrative LoRs. As the LoRs whose d_is are largest (the red ones in the diagram) are excluded, the uncertainty in the triangulation

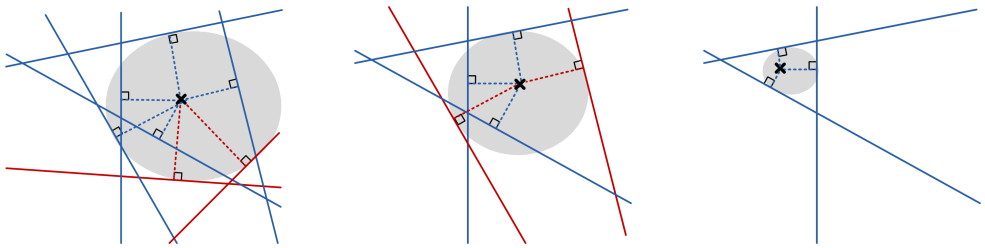

Figure 2.6: An 2D illustration of the iterative triangulation procedure in which more and more spurious events are rejected at each iteration (left to right).

(visualised as a grey cloud in the diagram) shrinks. [Parker et al., 1993] use the uncertainty in the triangulation as well as the number of LoRs remaining after iterations as the stopping conditions for their iterative triangulation routine[30].

Since spurious events are assumed to be uniformly distributed in space, but true ones clustered around the tracer particle, it should be possible to triangulate the position of such a tracer with arbitrary accuracy given enough iterations.

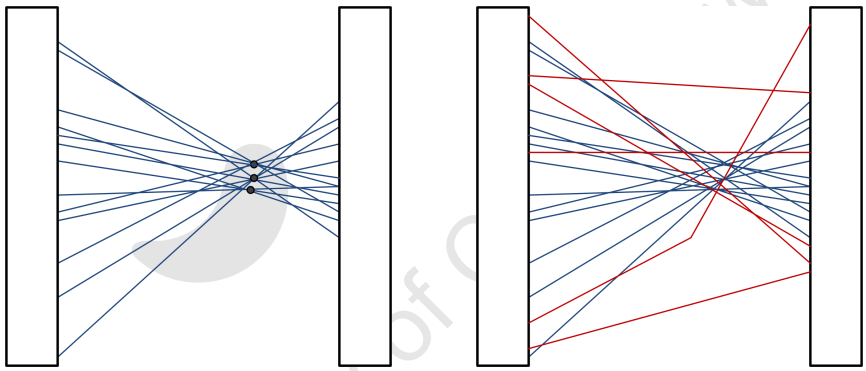

(a) True events from a moving tracer **(b)** All events from a moving tracer

Figure 2.7: Schematics of the true (left) and combined (right) lines of response from a moving tracer particle.

While this is the case for a stationary particle- whose true LoRs look like Figure 2.2, and whose combined LoRs look like Figure 2.4- it is not for the case of a moving particle. Figure 2.7a shows the smearing out of the focal point of detected LoRs from a moving tracer particle, and Figure 2.7b shows the complete set of detected LoRs including spurious ones.

From Figure 2.7b it is clear that it is not as straightforward to identify (by sight) true events from a moving tracer as it was from a stationary one. It is similarly less easy to do so using the iterative triangulation routine here described. In fact, in order to do so, one must approximate the stationary particle case.

In order to track a moving particle's motion, the total number of detected LoRs are divided into 'slices' of events collected over a sufficiently short time during which the tracer particle is effectively stationary. For the rest of this discussion, the number of LoRs in each of these slices will be labelled as N_{events}. No matter how short the time spanned by the N_{events}, there will always be some smearing of the centroid due to the motion of the particle; more for faster moving particles and less for slower moving ones. The motion of a tracer particle thus introduces unavoidable uncertainty into the triangulation procedure.

Accepting this limitation, however, it is clear that the position of a tracer particle can be iteratively

[30] More on this in Section 2.3.3.

triangulated for each successive slice to obtain the trajectory of the tracked particle. Since each pair of coincident events are recorded with their time of detection, t_i, a time can be associated with each triangulation, given by the average time at which all of the LoRs used in that triangulation were detected,

$$t_{loc} = \frac{\Sigma_{i=1}^{N_{events}} t_i}{N_{events}} \tag{2.18}$$

2.3.3 Optimisation of triangulation parameters

From the above discussion it is clear that the iterative triangulation scheme adopted for PEPT requires two sets of parameters to be set *a priori*- the stopping conditions, and the number of events per slice, N_{events}, over which moving tracer particles are effectively stationary.

As already mentioned, the two stopping conditions employed by [Parker et al., 1993][31] are the uncertainty in the location and the fraction of the original number of LoRs that are used in the final iteration. This fraction is a measure of the fraction of detected events that were likely spurious[32]. This depends on a number of factors, such as the attenuating environment of the system of interest, the geometry of the gamma camera, and the motion of the tracer.

Since the dominant factors affecting the fraction of LoRs that are defined by true events- that is, by the detection of γ-rays that have not interacted in such a way as to change their energy or momentum- are independent of the motion of the tracer particle, it is possible to calibrate the optimum fraction, f_{opt}, to retain in the triangulation before performing the experiment.

[Parker et al., 1993] do exactly this by placing a stationary radiolabelled tracer particle at various points in the field of view of their camera. They perform a series of iterative triangulations to obtain a spread of locations about a point in space. Histogramming these locations in 3D space reveals this spread to be Gaussian in shape, and the standard deviation in the mean in each direction- $\hat{x}$, $\hat{y}$ and $\hat{z}$- are interpreted as measures of the precision of the location. Graphing these standard deviations as a function of the fraction of LoRs retained in the final triangulation reveals a minimum corresponding to the f_{opt} for a particle in that position[33].

[Parker et al., 1993] found not only an f_{opt}, but also that the minimum standard deviation- interpreted as uncertainty in location- is higher for ^{22}Na, which has an associated γ-ray, than for ^{18}F, which doesn't.

In the course of my work, I have found that the value of f_{opt} further depends on the activity of the tracer particle, the time resolution of the gamma camera, and- importantly- on the attenuating environment of the system of interest[34].

As well as the calibration experiments described here, it has also been suggested by my group[35] that f_{opt} could be determined by Monte Carlo modelling of each system of interest- an interesting, but time-consuming proposal, and one that has not yet been followed up.

The starting number of events, N_{events}, used for each location depends much more on the motion of the tracer particle than does the f_{opt}. In particular, the number of events in a slice should be small enough that the tracer particle has not moved too far, but large enough that the optimal fraction of remaining LoRs, $f_{opt}N_{events}$, is large enough for a meaningful triangulation to take place. This condition can be captured by extending, after [Chou, 2007], the expression for the

[31] See also [Parker et al., 1997], [Parker et al., 2002] and [Yang et al., 2007].
[32] Or effectively spurious for moving tracers.
[33] Compare this to the point spread function which is used as a measure of the sensitivity of gamma cameras.
[34] See Appendix E.
[35] See `http://www.pept.uct.ac.za/`

precision of a location, given by [Fan et al., 2006b]

$$\Delta \approx \frac{\sigma}{\sqrt{f_{opt} N_{events}}} \tag{2.19}$$

to account for the rate at which detections are made, R, the speed of the tracer particle, v, and the time interval, dt, over which the N_{events} are recorded, thus

$$\frac{\sigma}{\sqrt{f_{opt} R dt}} \approx v dt \tag{2.20}$$

which yields, since $N = Rdt$, an estimate for the optimal N_{events} for a given data rate, R, and particle motion, v

$$N^{\frac{3}{2}} \approx \frac{\sigma R}{v\sqrt{f_{opt}}} \tag{2.21}$$

The stochastic nature of radioactive decay, however, means that it is impossible to predict the number of decays that will occur in a *specific* time interval[36]. Even if some representative number, such as the data rate, R, above, can be agreed upon, the variable behaviour of the tracer particle in any moderately interesting system make it impossible to accurately predict how far it will have moved in such a time interval. Thus, the optimum number of events in a slice is impossible to determine analytically.

Without a pre-existing expectation of the motion of the tracer particle in the system being studied, it is impossible to evaluate how good or bad a result was produced by triangulation with a given set of triangulation parameters. It is, however, with a sufficiently detailed pre-existing expectation of the particle's motion; which would make such a system uninteresting to study.

'Toy' or contrived experiments- in which the tracer particle moves along a well-known trajectory in a system that otherwise resembles the one of interest as closely as possible- can be used, though, as a tool to optimise the triangulation of the real system. This approach is used in Appendix E, which contains the optimisation procedure performed on a representative set of experiments.

2.3.4 Sources of uncertainty in a PEPT experiment

In the preceding sections I have mentioned many sources of uncertainty for a PEPT experiment. In this subsection I will categorise these and introduce a few more.

The first category I will mention here are uncertainties due to the physics of positron emission. As described in Section 2.1, a proton-heavy nucleus can decay by the emission of a positron and electron antineutrino. Depending on the radioisotope, the daughter nuclei thus produced may or may not be in an excited state. If the daughter is excited, its decay to ground state is a source of associated γ-rays, the detection of which contribute to the error in the triangulation of the tracer particle.

The positron itself thermalises in the medium before being captured by an electron to form a short-lived positronium atom. In the process of thermalising, the positron may excite orbital electrons in the medium- another source of associated γ-rays. The atom of positronium formed by the positron and an electron in the medium predominantly decays into two or three γ-rays, depending on its spin state- the third γ-ray is a third source of associated γ-rays.

In Section 2.1 I illustrated how colinear are the back-to-back γ-rays produced in the annihilation of

[36] Of course, the activity of a radioactive source is a measure of how many decays occur on average in *any* time interval.

Isotope	**Q-value** /MeV	Mean range /mm
^{18}F	0.64	0.6
^{22}Na	1.00	1.1
^{68}Ga	1.90	2.9

Table 2.2: Q values for positron decay for some common PET isotopes, and the maximum range of the positrons emitted in water.

para-positronium even at high temperatures. However, I neglected the case of a moving particle in which the positronium is embedded, giving it some non-zero momentum and thus a small angular deviation. Following the procedure in Section 2.1, the angular deviation from colinearity, ϕ, can be estimated for the decay of a positronium atom embedded in a particle moving at speed v thus

$$\phi = \arcsin\left(\frac{2v\sin\theta}{c}\right) \approx \arcsin\left(10^{-8}v\right) \tag{2.22}$$

which is, even for very fast-moving tracers, of the order of $10^{-7} radians$ and so again negligible.

The most important physics-based source of error for a PEPT experiment, however, is the range of the emitted positron in the medium. As discussed in Section 2.1, the distance travelled by a thermalising positron depends on its energy and on the density of the medium through which it travels[37]. The energy of a positron emitted in $\beta+$ decay is described empirically by the formula given in equation 2.2 and visualised in Figure 2.1. The maximum emission energy, and thus the maximum travelling distance, can be calculated from the Q value of the decay. Table 2.2 gives some typical Q values for three common PET radioisotopes, and the mean range of their emitted positrons in water.

The second category of sources of uncertainty are those arising from the nature of the system being studied. This includes its attenuating environment as well as the motion of the system. The attenuating environment of the system effects the likelihood of the γ-rays produced in the annihilation of positronium reaching the detectors undeviated. This has been dealt with extensively in Section 2.3.1. The system under study could also be a source of associated γ-rays. For instance, naturally-occuring ^{40}K[38] has an 11.2% branching ratio to $\beta+$ decay.

The motion of the system can lead to a dynamically-varying attenuating environment, making it hard to optimise triangulation parameters. It can also effect the tracer particle by increasing the chances of leaching or chipping off radioactive material. Its biggest effect, though is on the distribution of detected LoRs in space. The uncertainties thus introduced are more-closely related to the third category of sources of error- those due to the assumptions of the triangulation routine.

The iterative triangulation routine introduced by Parker *et al* has been successfully used for both single-, [Parker et al., 1993], and multiple-particle tracking, [Yang et al., 2007], for nearly two decades. For its application, however, it is necessary to assume that the tracer particle is a point source of radiation. In fact, depending on how the radioisotope is attached to the tracer particle, it is either a lob-sided radiation distribution or a shell of radioactive material adsorbed onto the surface of something else. The effectively non-point-like nature of the tracer particle is exacerbated by the movement of the tracer particle, as already discussed. Due to the statistical nature of the iterative triangulation routine, it is possible- in principle and given enough LoRs- to locate the tracer particle to arbitrary precision. It may be, though, that beyond some characteristic length scale of the tracer particle, potentially increased to take into account motion, this precision is meaningless.

[37] In so far as density is correlated with the Z number of the material.
[38] Found in granite, guano and bananas, for instance.

A second assumption necessary for the application of the iterative triangulation routine is that γ-rays are emitted uniformly into all space. The assertion that true and undeviated γ-rays originate at the tracer particle- as do, unfortunately, associated γ-rays- while scattered ones are uniformly distributed in space, provides the rationale for iteratively removing the farthest lying LoRs from the centroid calculation. While this uniform distribution assumption is a good one in principle, it may not hold for parallel-plate gamma cameras, or for gamma cameras with variable acceptances. This could introduce location uncertainties dependent on the position of the tracer particle in the field of view of the gamma camera[39].

The equipment used is, of course, a very important source of uncertainties. In a PET experiment, the quantum efficiency of the detectors, their deadtime and resolution are the most important determinants of reconstruction accuracy. The first two of these limit the total number of coincidences that can be detected per unit time. Since spurious events in a PET reconstruction are dealt with by averaging them out, the total number of events recorded effectively determines the accuracy of the result. This is less important for a PEPT experiment, since far fewer LoRs can be used to triangulate a tracer particle's position. More important for PEPT is the resolution of the camera.

A gamma camera actually has three types of resolution- time, energy and spatial. The time resolution of a gamma camera determines how short a gate can be set for the coincidence circuit. The greater the time resolution, the smaller the coincidence gate and the more random and associated event will be excluded. The energy resolution of a gamma camera is how well the energy deposited by a γ-ray incident on a detector can be determined. The better the deposited energy can be determined, the smaller can be set the energy window[40], and thus the more scattered and associated event can be excluded.

The time and energy resolution of a gamma camera improve the quality of the data recorded. Excluded detected events on the basis of their arrival time and deposited energy is the equivalent of performing the iterations of the triangulation routine to remove spurious events.

The spatial resolution of a gamma camera has a very direct effect on the uncertainty in a location. The triangulation routine mentioned in Section 2.3.2 relies on LoRs which are defined by their endpoints- coincidences recorded in the detectors. The finite spatial resolution of a gamma camera means that these endpoints are no longer points, but rather circles in which the γ-ray could actually have been incident. This means that even an arbitrarily precise triangulation based on these LoRs is actually a region.

In practice, even the circular region of acceptance mentioned above is not representative because even events that do not fall in the dead regions between detector elements are usually assigned the coordinates of the centre of the nearest element. This leads to a discrete sampling[41]. Further, the resolution across the camera may not be uniform because of malfunctioning elements, dead regions between detectors, and the unpredictable ageing of the scintillation material. These non-uniform responses further mitigate against the assumption of spatial uniformity of detected LoRs, further limiting location precision.

Gamma cameras do not consist only of detectors- they also include a fair amount of pre-processing electronics which are effected by temperature fluctuations, liable to malfunction and susceptible to calibration errors. Many gamma cameras also contain a radioactive calibration source, which can be a source of associated events and, depending on the activity of this and the sources used in experiments, contain materials that can become active themselves.

[39] From this discussion it is clear that category three sources of uncertainty- those to do with the triangulation routine- might be better described as limits to precision.

[40] Photons which deposit lower or higher energies than those that define the window are not recorded.

[41] Visible in a plot of raw LoRs.

The fifth and last category of sources of uncertainty that I will consider here are those arising from the radiolabelling of the tracer particle. I have already mentioned the effect of the finite extent of the radiation distribution on a tracer, and of the presence or absence of associated γ-rays in its decay spectrum, on the achievable precision of its triangulation. Here I will mention the effect of the level of radioactivity on a tracer particle.

A high activity tracer is one in which many decays occur per unit time. This has an effect on the absolute number of events that can be realistically collected in an experiment. Whereas PEPT does not require all that many LoRs to perform a triangulation, the statistical nature of the triangulation routine means that the greater the number of events included in the triangulation, the greater the precision of the result[42]. While there may be no real benefit to having many more than a few dozen events for the location of a stationary particle, clearly for a moving particle, the more and the more frequent are the detected events, the shorter can be made the time interval over which a slice of events is collected. This can have an important effect on the location accuracy of a moving tracer.

As well as a limit to the activity that can be put on a particular tracer, there is a limit to the number of events that can be detected by the camera- too many and it saturates, introducing a new source of uncertainty.

Most of these uncertainties can be minimised by increasing the number of LoRs and of iterations used in the triangulation routine. Some are systematic, and some can only be modelled. While some of the uncertainty can be accounted for in analysis, many of these sources of uncertainty must just be borne in mind.

2.4 Apparatus

2.4.1 The PEPT camera

The gamma camera used in this work was the one belonging to the Positron Imaging Centre[43] at the University of Birmingham in England. It is an ADAC Forte PET camera modified to operate in list mode- that is, to produce output in the form of LoRs rather than sinograms or medical reconstructions[44].

It is a parallel-plate camera whose detectors are of a variable separation- between $250mm$ and $800mm$. Each detector consists of a single, $590\times470mm^2$ crystal of $NaI(Tl)$ scintillator of thickness $16mm$ optically-coupled to an array of 55 photomultipliers. Each of these is connected to its own ADC, which feeds into one of two pre-processing cards- one for each array of photomultipliers. Signals from both of these cards are sent to a coincidence modules, and coincident events are recorded sequentially for future processing.

Figure 2.8 is a picture of the Birmingham camera, and Table 2.3 contains its most important specifications according to [Parker et al., 2002], [Parker et al., 2008] and [Leadbeater, 2009].

2.4.2 Activation

Of course, for a PEPT experiment to be possible, a tracer particle must be made radioactive. This can be done in a number of ways, but the most common way is to put a substance containing

[42] With all of the caveats already mentioned.
[43] See `http://www.np.ph.bham.ac.uk/pic/forte`
[44] For more on this, see [Sadrmomtaz et al., 2007].

Figure 2.8: Birmingham's ADAC Forte PET scanner.

Configuration Field of view	Parallel-plate $250 - 800 \times 590 \times 470 mm^3$
Quantum efficiency	23%
Spatial resolution	$6 - 8mm$
Time resolution Dead time per detection Effective coincidence rate	$12ns$ $170ns$ $100kEs^{-1}$

Table 2.3: Specifications of the ADAC Forte PET scanner at the Birmingham Positron Imaging Centre.

elemental oxygen into the target of a ^3He cyclotron beam to convert naturally occurring ^{16}O into positron-emitting ^{18}F by the reactions

$$^{16}O(^3_2He, p)^{18}F$$

or, equivalently,

$$^{16}O(^3_2He, n)^{18}Ne \rightarrow^{18} F$$

A tracer particle can then be labelled with radioactive ^{18}F in one of two ways. If the particle is large enough[45] and contains sufficient ^{16}O, it can be directly activated in the beam of a cyclotron. At Birmingham this is done using a $33MeV ^3_2He$ beam produced in their in-house SCANDITRONIX MC40 medical cyclotron.

If the required tracer particle is either too small or does not contain ^{16}O, it may be possible to activate H_2O so that contains ^{18}F ions, and absorb these onto the surface of the tracer particle. This is easily done for a range of anion exchange resins, which come in a range of sizes and densities. In other cases, however, this can only be achieved by surface modification, as per [Fan et al., 2006a] and [Fan et al., 2009], if at all.

Much more can be found on the radiolabelling of tracer particles for PEPT in [Fan et al., 2006b].

[45] To present a large enough target, and also so that it does not melt under bombardment by ^3_2He ions.

2.5 Summary

In this chapter I have offered an overview of the radioactive process of positron emission. I have quickly surveyed the history of nuclear imaging with a focus on the development of the PEPT technique. I then described the PEPT technique in some detail from the radiolabelling of tracer particles and the conduction of a PEPT experiment to the triangulation step at which tracer trajectories are recovered. In doing so I mentioned the need for and process of optimisation of the triangulation parameters, and drew attention to sources of uncertainty in the triangulation of PEPT data. In Chapter 3 I will describe the type of system- tumbling mills- that I will use this technique to investigate.

References

[Anger, 1957] Anger, H. (1957). A new instrument for mapping gamma ray emitters. *University of California Radiation Laboratory*, 3653:xxx–xxx.

[Anger, 1963] Anger, H. (1963). Positron scintillation camera. *Nuclear Medicine*, 4:326–330.

[Bailey et al., 2005] Bailey, D. L., Townsend, D. W., Valk, P. E., and Maisey, M. N., editors (2005). *Positron Emission Tomography*. Springer-Verlag London Ltd.

[Bemrose et al., 1988] Bemrose, C., Fowles, P., Hawkesworth, M., and O'Dwyer, M. (1988). Application of positron emission tomography to particulate flow measurement in chemical engineering processes. *Nuclear Instruments and Methods in Physics Research A*, 273:874–880. Unread.

[Berger and Hubbell, 1987] Berger, M. and Hubbell, J. (1987). Xcom: Photon cross sections database. Technical report, National Institute of Standards and Technology.

[Cassen et al., 1950] Cassen, B., Curtis, L., and Reed, C. (1950). A sensitive directional gamma-ray detector. *Nucleonics*, 2:78–81.

[Chou, 2007] Chou, C.-W. (2007). Application of pept to track a single labelled red blood cell in vitro. Master's thesis, University of Birmingham.

[Curie and Joliot, 1934] Curie, I. and Joliot, F. (1934). Artificial production of a new kind of radioactive element. *Nature*, 133:201.

[Fan et al., 2006a] Fan, X., Parker, D., and Smith, M. (2006a). Enhancing 18f uptake in a single particle for positron emission particle tracking through modification of solid surface chemistry. *Nuclear Instruments and Methods in Physics Research A*, 558:542546.

[Fan et al., 2006b] Fan, X., Parker, D., and Smith, M. (2006b). Labelling a single particle for positron emission particle tracking using direct activation and ion-exchange techniques. *Nuclear Instruments and Methods in Physics Research A*, 562:345350.

[Fan et al., 2009] Fan, X., Waters, K. E., Rowson, N. A., and Parker, D. J. (2009). Modification of ilmenite surface chemistry for enhancing surfactants adsorption and bubble attachment. *Journal of Colloid and Interface Science*, 329:167172.

[Hawkesworth et al., 1986] Hawkesworth, M., O'Dwyer, M., Walker, J., Fowles, P., Heritage, J., Stewart, P., Witcomb, R., Bateman, J., Connolly, J., and Stephenson., R. (1986). A positron camera for industrial application. *Nuclear Instruments and Methods in Physics Research A*, 253:145–157.

[Krane, 1988] Krane, K. S. (1988). *Introductory Nuclear Physics*. Wiley.

[Kuhl and Edwards, 1968] Kuhl, D. and Edwards, R. (1968). Reorganizing data from transverse section scans using digital processing. *Radiology*, 91:975–983.

[Leadbeater, 2009] Leadbeater, T. W. (2009). *The Development of Positron Imaging Systems for Applications in Industrial Process Tomography*. PhD thesis, University of Birmingham.

[Levin and Hoffman, 1999] Levin, C. S. and Hoffman, E. J. (1999). Calculation of positron range and its effect on the fundamental limit of positron emission tomography system spatial resolution. *Phys. Med. Biol.*, 44:781–799.

[Parker et al., 1993] Parker, D., Broadbent, C., Fowles, P., Hawkesworth, M., and McNeil, P. (1993). Positron emission particle tracking - a technique for studying flow within engineering equipment. *Nuclear Instruments and Methods in Physics Research A*, 326:592. Unread.

[Parker et al., 2002] Parker, D., Forster, R., Fowles, P., and Takhar, P. (2002). Positron emission particle trackingusingthe new birmingham positron camera. *Nuclear Instruments and Methods in Physics Research A*, 477:540545.

[Parker et al., 2008] Parker, D., Leadbeater, T., Fan, X., Hausard, M., Ingram, A., and Yang, Z. (2008). Positron imaging techniques for process engineering: recent developments at birmingham. *Measurement Science and Technology*, 19:xxx–xxx.

[Parker et al., 1997] Parker, D. J., Allen, D., Benton, D., Fowles, P., McNeil, P., Tan, M., and Beynona, T. (1997). Developments in particle tracking using the birmingham positron camera. *Nuclear Instruments and Methods in Physics Research A*, 392:421–426.

[Phelps et al., 1975] Phelps, M., Hoffman, E., and Mullani, M. (1975). Application of annihilation coincidence detection to transaxial reconstruction tomography. *Journal of Nuclear Medecine*, 16:210–224.

[Reivich et al., 1979] Reivich, M., Kuhl, D., and Wolf, A. (1979). The [18f]fluoro-deoxyglucose method for the measurement of local cerebral glucose utilization in man. *Circulation Research*, 44:127–137.

[Sadrmomtaz et al., 2007] Sadrmomtaz, A., Parker, D., and Byars, L. (2007). Modification of a medical pet scanner for pept studies. *Nuclear Instruments and Methods in Physics Research A*, 573:9194.

[Ter-Pogossian et al., 1975] Ter-Pogossian, M., Phelps, M., and Hoffman, E. (1975). A positron-emission transaxial tomograph for nuclear imaging (pett). *Radiology*, 114:89–98.

[Wagner, 1998] Wagner, H. N. (1998). A brief history of positron emission tomography (pet). *Seminars in Nuclear Medicine*, Vol XXVIII, No 3:213–220.

[Yang et al., 2007] Yang, Z., Fryer, P., Bakalis, S., Fan, X., Parker, D., and Seville, J. (2007). An improved algorithm for tracking multiple, freely moving particles in a positron emission particle tracking system. *Nuclear Instruments and Methods in Physics Research A*, 577:585594.

Chapter 3

Tumbling mills

3.1 Industrial use of rotating drums

3.1.1 Rotating drums in granular materials handling

Rotating drums are used extensively in the processing of powders and of granular materials. In their simplest form they consist of a cylindrical shell rotated at a constant angular velocity about its axis. After a few revolutions, the granular material contained in the drum- often called the load or charge- is said to have reached steady state. However, this is only true to a limited extent. In particular, if there is no net flow of charge into or out of the drum and the angular velocity and constitution of that charge is such that no breakage occurs, then the power drawn to maintain the constant angular velocity of the shell approaches a steady state value and the *shape*[1] of the charge remains effectively constant. The charge inside a rotating drum, however, is in dynamic rather than static equilibrium, so although the charge as a bulk can be said to be in steady state under these conditions, this is not the case for its constituents.

As a grain-filled drum rotates, grains are raised until they reach a turning point, called the shoulder of the charge, where they either roll down the surface of the rising charge[2], or are projected into flight depending on their speed and position in the drum. At the bottom of the dynamic granular heap, the grains reach another turning point, called the toe of the charge, where they are re-inducted into the rising charge. Since this toe region is the confluence of three streams of charge- the charge that has rolled down the dynamic heap, the charge that has been projected into flight and landed in the toe region, and the charge that has been projected onto the shell and carried by it down into the toe region- it is a chaotic one. As a result, a rotating drum is, in the long term, a perfect mixer of similar[3] grains. This property is exploited in the use of rotating drums to mix pharmaceutical powders and the ingredients of foodstuffs, and to ensure uniform heating of grains in rotary kilns, for instance.

A granular flow consists (at least to a first approximation) of layers flowing over each other. Friction forces between such layers give rise to shear stress that dissipate energy as heat or through the abrasion of the grains in the layers. If the granular material is sufficiently dilated, grains can also collide inelastically, dissipating energy as heat or through the plastic deformation or fracture of

[1] The shape of the charge is normally thought of in terms of the so-called S-shape of its free surface, often indirectly in terms of the shoulder and toe of the charge- the points where the charge departs from and regains contact with the shell respectively, and of its centre of circulation (CoC). More on this in Sections 3.2.2 and 5.5.

[2] That portion of the charge that is being carried upwards by either direct or indirect contact with the inner surface of the drum.

[3] See Section 3.3.6 for a discussion of non-uniform grains.

the colliding grains. Thus a granular flow quickly dissipates energy through friction and collision forces between its constituents and must be sustained by a driving force. The motion of rotating drums results in a continuously circulating granular flow. The power drawn by the drum to keep it at a constant angular velocity is therefore directly related to the energy dissipated by the charge, some of which has gone into reducing the size of its constituent grains. This property of rotated granular flows is exploited in the use of rotating drums, generally called in this context tumbling mills, for the size reduction of powders and granular materials in the food, the pharmaceutical and, of particular interest to us, the mineral processing industries.

3.2 Granular flow in rotating drums

3.2.1 Experimental investigation of granular flow in rotating drums

Various experimental techniques have been used to study the motion of granular material in rotating drums, predominantly in the context of rotary kilns and of tumbling mills. These techniques can be divided into two categories- visual and radiological.

The visual experiments generally consist of a laboratory-scale rotating drum fitted with a transparent end window through which the dynamic granular bed is observed. The dynamic bed is then either filmed to obtain a dynamic picture of the motion of the charge[4], or photographed. Because of its simplicity, the end-window approach was the first approach adopted, and remains in use. It was adopted by, for instance [Rogovin and Herbst, 1989], [Santomaso et al., 2003] and [Tordesillas and Arber, 2005].

The photographs produced by end-window filming are used to measure the position of charge features of the sort that will be discussed here, and variants can be used to estimate the speed of tracer particles in the bed. The first, and simpler, method of obtaining particle speeds from end-window filming is so-called streak photography. In streak photography, long-exposure still photographs are taken of a charge containing visually-differentiated tracer particles. The length of the streaks produced over the time of the exposure give an average speed of the tracer particle. This method is employed by, for instance, [Morell, 1992] and [Cleary et al., 2003]. The second method is the well-developed technique of particle image velocimetry (PIV), which involves comparing the positions of tracer particles in sequences of high-speed photographs. [Jain et al., 2002] used this technique.

The obvious drawback of end-window techniques is that they are limited to what can be seen through the side of the mill. This makes it impossible to control for obfuscating end effects that may not be representative of the motion of the bulk of the charge. To overcome this, [Powell and Nurick, 1996b] used biplanar[5] x-ray imaging of a rotating drum to obtain, by the density-dependent transmission of x-rays through matter, a better representation of the shape of the dynamic bed in the mill. [Govender et al., 2001] extended this technique to single-particle tracking of a more-attenuating particle in a bulk of similar particles as a means of obtaining a more representative velocity of the tracer particle in the bulk. This is the first example of a radiological experimental technique applied to tumbling mills.

[Powell and Nurick, 1996b] also used a positron emission tomography (PET)-like method of building up the density distribution of a gamma-emitting isotope over a short time to obtain streaks of

[4] From whence observations such as the the fact that the positions of the shoulder of the charge and its CoC vary stochastically even at steady state.

[5] In the axial and transverse directions.

activity that were indicative of the bed shape and related to streamline velocities as in the case of streak photography.

[Nakagawa et al., 1993] performed an interesting study of the motion of mustard seeds in a rotary kiln using nuclear magnetic resonance imaging (NMRI), which is still much cited today.

Positron emission particle tracking[6] has also been applied to the study of bed motion in tumbling mills by groups at the University of Birmingham, for instance [Ding et al., 2001a], [Ding et al., 2001b] [Ding et al., 2002], [Lim et al., 2003], [Ingram et al., 2005], and others; and at the University of Cape Town, for instance [Buffler et al., 2011], [Govender et al., 2011b], [Kallon et al., 2011], [Govender et al., 2011a], [Sichalwe et al., 2011], [Bbosa et al., 2011] and others. The further application of positron emission particle tracking (PEPT) to the study of charge motion in tumbling mills will be the subject of this dissertation.

A final 'experimental' technique worthy of mention here is, in fact, a computational one- the discrete element method (DEM). The DEM is a simply-stated computational technique for modelling the behaviour of a system of discrete particles by summing all of the contact and body forces acting on each particle, and integrating the resultant acceleration to obtain the velocities and displacements of each particle at each time step. It has been applied, notably, to the study of granular motion in tumbling mills by Rajamani[Mishra and Rajamani, 1994] and Cleary[Cleary, 1998][Cleary, 2001], and has since become a useful and mainstream tool.

3.2.2 The motion of granular media in rotating drums

In this section I will offer some definitions of the operating variables for a rotating drum, give a brief overview of the behaviour of the bed material in a rotating drum, and describe the regions into which these behaviours can be divided.

Operating variables: fill level and rotational speed

When a rotating drum partially-filled with granular material is at rest, the material forms a layer in the lowest segment of the drum that can accommodate it. The surface of the granular pile in a stationary drum is as straight a chord as is consistent with the packing of granular material, and the volume of the area subtended by this segment. For most applications, and certainly in this work, fill level or load fraction is defined as this volume as a fraction of the total volume of the drum. Of course, the volume of granular material in the drum is related to the packing density of the material[7], but this is not taken into account when quoting the fill or load of the drum.

As well as the volume of material inside a rotating drum, the other key operating variable for such systems is the rotational speed at which they are operated. This could be expressed in terms of the rotational speed of the drum itself, in revolutions per minute (rpm) or rotational frequency (Hz) and so on, but in keeping with the scalable measure of load, a non-dimensional operating speed is employed. In fact, two different measures are used- the Froude number and as a fraction of the critical speed of the drum.

[6] The subject of Chapter 2.

[7] For spheres, Gauss showed that the maximum possible packing fraction is $\frac{\pi}{3\sqrt{2}}$. This is often called the close- or thickest regular packing of spheres, and has a coordination number of 12- any given sphere is in contact with 12 others. The thinnest regular packing of spheres, with a coordination number of 6, is given by $\pi\sqrt{2}\left(\sqrt{3}-\frac{3}{2}\right)^3$. The most useful packing fraction for this sort of application, however, is the so-called poured random packing, which has been determined experimentally to be between 0.6 and 0.68.

The Froude number is a ratio of characteristic velocity and length used in fluid mechanics to non-dimensionalise flow speed. A similar number has been used to enable the scale-up of granular flow experiments in rotating drums. Two competing Froude numbers have been proposed for this application.

[Elperin and Vikhansky, 2000] defined the Froude number for rotating drums as:

$$Fr = \omega\sqrt{\frac{R}{g}} \tag{3.1}$$

and [Mellmann, 2001], [Ding et al., 2002] and others define it as

$$Fr = \frac{\omega^2 R}{g} \tag{3.2}$$

In this work, I will employ the definition given in equation 3.2.

The critical speed of a rotating drum is the rotational speed at which the outermost layer of granular material begins to centrifuge- to stick to and rotate with the drum. It is defined, in revolutions per second, by [Rose and Sullivan, 1957] as:

$$N_c = \frac{1}{2\pi}\sqrt{\frac{2g}{D-2r}} \tag{3.3}$$

where D is the inner diameter of the rotating drum, and r is the radius of a grain in the bed. Since in industrial use- and in the mining industry in particular- $r << D$, the critical speed of a tumbling mill is usually approximated (in rpm) as:

$$N_c \approx \frac{42.3}{\sqrt{D}} \tag{3.4}$$

Although equation 3.4 is an imperfect approximation, and although the critical speed of a rotating drum has been shown to be more complicated than that shown in equation 3.3, for instance by [Watanabe, 1999], I have employed the definition in equation 3.4 for ease of comparison with industry and industrial data.

Bed regions in a rotating drum

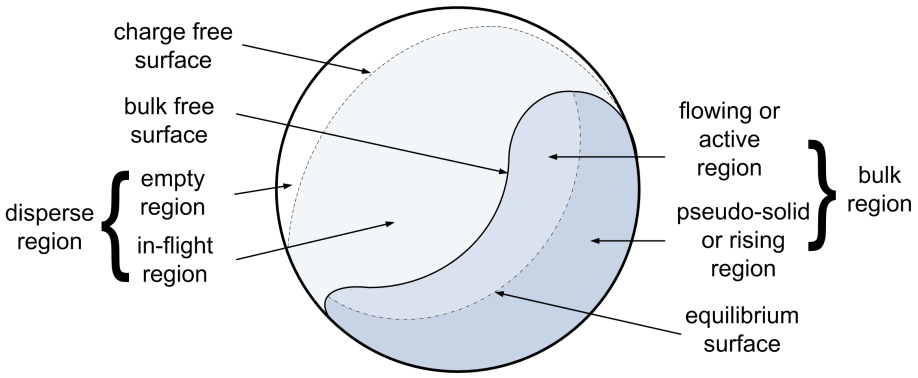

Figure 3.1: A schematic of the dynamic bed in a typical rotating drum, showing the three flow regions bounded by the equilibrium and bulk and charge free surfaces.

Figure 3.1 shows a schematic of the motion of granular material in a rotating cylinder operated

in cascading mode[8]. It is divided by a free surface into two main regions- the bulk and disperse regions, each further subdivided into two more.

The rising region

The bulk region consists of the dense, kidney-shaped body of the dynamic bed, which- at low rotational speeds[9]- may comprise the entirety of the bed. It is divided into two further regions- the rising region and the flowing or active region. These have been identified and variously named by a range of researchers. Here I use the names that I give them in Section 5.5.2.

In the rising region, material in contact with the drum experiences a frictional interaction, causing it to rise with the rotating drum. The frictional force on an element of the bed is proportional to the normal force exerted by the surface of the drum on that element. The two main contributors to the normal force on an element are the component of the weight acting through that element[10], and the centrifugal force due to the rotation of the bed[11].

A single particle in a rotating drum would be raised by the frictional force in the direction of rotation of the drum until the component of its weight tangent to the drum exceeds the static friction it experiences due to the normal force just mentioned. It would then slide back down to the bottom of the drum and repeat the process. How high such a particle would get before sliding down again would depend on the weight of the particle and on the coefficient of limiting friction between it and the drum. Increasing either the friction or the effective friction[12] between particles and the drum is what allows different modes of granular motion to develop[13].

However, elements of the bed in a rotating drum cannot simply be considered to be in isolation [Powell and Nurick, 1996a]. The interactions between elements go beyond increasing the effective weight of an element in contact with the shell, they can effect the maximum height achieved by such an element in the following way. Consider a layer of bed elements lining the drum and in contact with each other. When an element has reached the point at which the tangential component of its weight equals the limiting friction it experiences in contact with the drum, so that it is at the point of rolling back down, the element directly below it has not yet. The first element is thus propped up by the second, which may reduce the height that could be achieved by the second element slightly, but it too is propped up by the one below it and so on. The component of weight perpendicular to the drum increases for each element down the drum, increasing its carrying capacity and enabling it, given a sufficient coefficient of friction, to support those above it. This effect is compounded when the effect of allowing elements to slide back down the rising layer is permitted. Since the slope of the rising layer decreases towards the bottom of the drum, the component of the acceleration of an element sliding back towards the bottom of the drum similarly decreases, leading to an increasing thickness of the bulk region lower down[14], and thus a greater normal force. Thus a dynamic bed may reach a greater maximum height in a rotating drum than would be expected from single particle considerations.

The rising region of the bed is the most dense in the dynamic bed. So dense, in fact, that it can be considered to consist of concentric layers, with very little mixing between them, i.e. $\vec{v} - \vec{v}_t \approx 0$.

[8] See Section 3.2.3.

[9] See below.

[10] Maximum at the lowest point of the drum where the normal to the drum is vertical, and zero above the horizontal where weight and the normal to the drum are perpendicular.

[11] Here the centrifugal force is the inertial force that must be overcome to keep an element of the bed in circular motion of the curvature of the drum.

[12] Lifter bars raise the effective friction between the charge and the shell by trapping one or more layers of charge next to the shell. See Section 3.3.3 for more.

[13] See Section 3.2.3.

[14] This effect is counter-acted by the induction of material back into the rising region- more on this later

This approximation holds, though, only in the thickest part of the rising region and begins to break down at the turning points at which material enters and leaves this region. Segregation and density distributions within the bed can also introduce mixing regions that are usually neglected.

Because of its density, the rising region has been called the solid or pseudo-solid region. This led to the persistent and persistently-refuted assumption that the material moving in this region moves in rigid body-like layers, that is with a shear rate $\frac{d\vec{v}}{dr} = 1$. Researchers such as [Morell, 1992], [Boateng and Barr, 1996], [Powell and Nurick, 1996c] and others have shown that the shear rate in the rising region, although constant, is greater than 1, indicating slippage between layers even when there is none between the bed and the drum.

The turning points at which material enters and leaves the rising region depend on the radial position of the layer in which they occur. At smaller radii, the contribution to the normal force due to the centrifugal force decreases, as does the depth of the layer in the bulk, reducing the maximum frictional force that that layer can experience. These two factors decrease the height of the equilibrium point at which the material is no longer raised by friction. The reduction of the frictional force in a smaller radius layer reduces the pushing capacity of that layer, and the slippage between layers reduces the inertia of the material once it reaches the equilibrium point, both reducing the height above the equilibrium point that the material can rise to. Thus lower radii layers reach the shoulder of their motion sooner than higher radii ones, reducing the thickness of the rising region above the equilibrium point.

The reduced height reached by lower radius layers reduces the gravitation potential that such layers have at the shoulder of their motion. This reduces the energy that they can dissipate as they flow down the face of the bed (either of the rising material for the first falling layer, or of other falling layers), so they come to rest and re-enter the rising region sooner. The point of re-entry into the rising region of the bed is called the toe of the bed.

The top, and thus lowest radius[15] layer of material turns around at the lowest shoulder, slows down almost immediately, and re-enters the rising region. The layer immediately below it rises at minimum[16] a layer thickness higher than this because it must flow over the layer above it. This is true for each subsequent layer. Similarly, each subsequent falling layer can only re-enter the rising region at minimum a layer thickness lower than the layer below it. The effect of the foregone is to thicken the rising region around the CoC[17] of the bed.

The surface that contains all of the turning points of each layer- both leaving and re-entering the rising region is called the equilibrium surface. The equilibrium surface is a locus of points of zero transverse velocity, and divides the bulk region into the rising and active regions. The thickening of the rising region mentioned above is what gives rise to the elliptical projection of the equilibrium surface[18].

The flowing region

Once an element of granular material has reached its turning point, called the shoulder of the bed, it begins to slide back down the rising material. It has entered the flowing or active region.

A single particle that has reached the shoulder of its motion does so having had its gravitational potential energy increased by the action of the drum. If the rotational speed of the drum is low

[15] For loads less than 50%.

[16] It could of course, rise more than a layer thickness higher than the layer above it. cf layers thrown into the in-flight region.

[17] More later.

[18] A claim that will be substantiated in the results.

enough, it remains in contact with the drum as it passes its equilibrium point[19] and, after having converted its remaining kinetic into potential energy, it will come to rest in contact with the drum[20], and slide back down along the drum. As it slides back down the drum it dissipates energy by a kinetic frictional interaction with the drum, and may not reach the bottom of the drum again before being dragged back up by it. If the particle is not isolated, and rather slides back down a layer of rising charge, it then dissipates energy through friction between it and the rising layer.

As an element of the bed slides down either the drum or the rising layers of material, it experiences a shallower and shallower slope[21] and hence a greater and greater frictional force and a smaller and smaller component of its gravitational acceleration.

Consider the element sliding down the surface of a rotating drum shown in Figure 3.2. In this

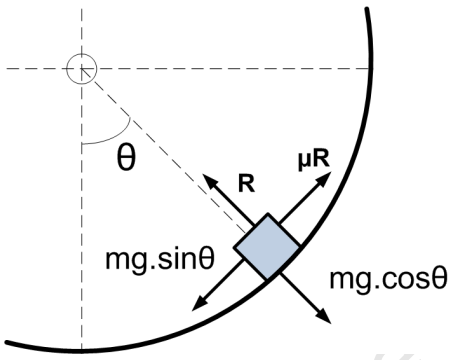

Figure 3.2: A bed element sliding down the surface of a rotating drum.

reference frame the net force acting on the element as a function of angular position θ is

$$F_{res} = mg\,(\sin\theta - \mu\cos\theta) \tag{3.5}$$

At $\theta = \arctan\mu$, the critical angle or angle of repose of the bed, the resultant force, F_{res}, on the element is zero. As the element slides down the surface of the drum, its angular position $\theta \to 0$ from above. Since $\lim_{\theta\to 0}\cos\theta = 1$ and $\lim_{\theta\to 0}\sin\theta = 0$, below the angle of repose the element decelerates. This leads to a build-up of material around the angle of repose[22], which contributes to the characteristic bean shape of the granular pile in a rotating drum.

As it flows down the decreasing slope of granular material below it, the material in the active region slows down until it comes momentarily to rest. It is then re-inducted into the rising region of the bed, by the action of friction, for another circulation. The point at which an element comes to rest depends on the frictional force it experiences and the angle of the slope formed by the material below it as discussed in the preceding section.

Unlike the densely-packed rising region of the bulk, however, the granular bed in the active region is capable of dilation. How much the bed dilates in a particular region depends on the effective weight of material, how fast it is moving, and the degrees of freedom available to it[23]. By these considerations it is clear that material less deep in the bed or higher up in the drum- where the normal component of its effective weight is smaller- is more likely to dilate than material more deeply embedded and lower down in the dynamic bed. This dilation of the material higher up in

[19]The point at which the frictional force it experiences is no longer enough to counteract the gravitational force it experiences.

[20]If it does not remain in contact with the drum, it enters the in-flight region of the bed.

[21]Due to the curvature of the drum.

[22]And thus around the CoC as will be shown in Section 3.2.4.

[23]Related to the amount of material in which that region is embedded, which also effects the effective weight of material in that region.

the drum, together with the deceleration that the flowing material experiences below the angle of repose of the material, contributes to the S-shape of the dynamic bed at higher rotational speeds.

The lowering of the density of the flowing layer due to dilation also leads to lower shear rates in the active region[24], for this reason[25] the bed motion in the rising region is termed shear-driven, while that in the active region is termed gravity-driven.

Since each subsequent layer in the active region moves more quickly than the one below it- in contrast with the rising region in which the converse is true- the dilation of the bed increases with increasing distance from the equilibrium surface, compounding the effect of lower kinetic frictional force with decreasing depth from the surface of the bed to further reduce the shear rates in the active region.

It is important to note, however, that although the bed motion in the active region is gravity-driven, it is still extremely shear-influenced. For layers further and further from the equilibrium surface, however, this influence gets less and less, as does the density of the bed.

The disperse region

Eventually, at sufficiently large distances from the equilibrium surface, the bed becomes so dilute that individual particles are not consistently in contact with each other, and the dominant interaction between them becomes collisions rather than shear.

This transition happens gradually as each subsequent layer of falling material becomes more and more dilated, and there is no clear transition between these two regimes. In the transition zone, however, the density of the bed drops off rapidly, and it is possible to unambiguously identify the transition zone, if not a transition surface. This surface, which occurs at some density threshold, is called the bulk free surface. It divides the bulk region of the dynamic granular bed from the in-flight region.

The in-flight region of the bed consists of a truly gravity-driven flow of material projected into free-fall from the shoulder region of the bed. The volume of material in the in-flight region effects, clearly, the volume in the bulk region- the more there is in flight, the less is available to constitute the bulk. Reducing the material in the bulk reduces the thickness of both the rising and the active regions of the bed. It reduces the thickness of the rising region by reducing the maximum static friction in the bulk, increasing the shear rate between layers, and it reduces the active region by conservation of mass. By reducing the maximum static friction in the bulk, increasing the fraction of the material in-flight also reduces the maximum shoulder height of the bed. These two effects can negatively-impact grinding efficacy and heat transfer in the bed.

Material that is projected from the shoulder of the bed into the in-flight region rejoins the bed lower down in the drum. Because of the variety of projection speeds, positions and angles of the in-flight material- depending from whence in the rising region it is drawn- the point at which this stream rejoins the body of the bed can range from some way down the topmost layer of material in the active region to directly onto the inner surface of the drum.

A single particle projected into flight from the shoulder of the bed would follow a parabolic trajectory. However, there is some interaction between particles in flight, leading to a spreading out of the expected trajectories.

Coming into contact with the bulk of the bed diverts the in-flight charge from its parabolic trajectory- it generally bounces off or slips down the bulk free surface depending on its incid-

[24]Making it a less important abrasion and attrition breakage region that the rising region. See Section 3.3.4.
[25]And the other, obvious reason.

ent angle and on the local angle of the bulk free surface at the point of impact. This effects the thickness of the transition zone between the bulk and disperse regions of the bed, and- if the mass flux of material impacting the bulk free surface is sufficient- have an effect on the effective weight of material in the bulk.

Increased effective weight can lead to a thicker rising region and to greater shear rates in the active region, further thickening the rising region around the CoC. These effects further contribute to flattening[26] of the equilibrium surface.

Increased effective weight can also suppress bed dilation. Since in-flight material is both more likely to impact the bed lower down in the shell, and moving more quickly when it does[27], this effect is most pronounced in the lower portion of the bulk region of the bed- further contributing to the S-shape of the bulk free surface.

The in-flight stream of the dynamic bed provides an additional route for material to re-enter the rising region in a less laminar way. Material that rejoins the bulk from the in-flight region, because of its incident speed and angle, is unlikely to be inducted smoothly into one of the flowing layers. Much more likely is for it to enter a chaotic mixing region called the toe region. It does this either by joining a stream of material flowing down the surface of the bed, or directly if it impacts low enough in the drum. Material is inducted into the bulk of the bed from this region by the frictional interaction between it and the drum.

The toe region

The toe region of a rotating drum is an important mixing region. The influx of high-energy particles in the toe region fluidises the material there. That is, not only do incoming particles rebound from the bed and from the drum in this region, but they impart energy to material in the bulk, causing them to jostle around too. Material in the toe region is dragged by the friction between it and the drum, or between it and layers of material being dragged by the drum back into the rising region of the bed. The jostling of the material in the toe region of a rotating drum ensures that it is well-mixed material that is so re-inducted, but can also increase the abrasive wear experienced by the drum in this region.

The extent of the toe region can have a small effect on the thickness of the active and rising regions of the bed. Its biggest effect on the shape of the bed here, though, is to increase the thickness of the transition zone between its bulk and disperse regions.

The impact toe is the point of farthest impact of in-flight material either with the bed or with the drum. A very high impact toe is indistinguishable from a very dilated upper region of the bed, exaggerating the S-shape of the bulk free surface. A very low one- one in which the in-flight stream strikes the inner surface of the drum can have the opposite effect. By removing material from the active region, it can lead to a concave bulk free surface.

3.2.3 Modes of granular bed motion in rotating drums

Depending on the shape of the bulk free surface of a granular bed in a rotating drum, on the fraction of its material in the in-flight region, and on the behaviour of material in its bulk region, a number of categories of bed motion have been defined. The categories of motion shown in Figure 3.3 are based on the definitions of [Boateng and Barr, 1996], [Mellmann, 2001] and [Ding et al., 2002].

[26] Increasing the aspect ratio of the ellipse arc length that represents the equilibrium surface.
[27] Since $v = \sqrt{2g\Delta h}$ by conservation of energy.

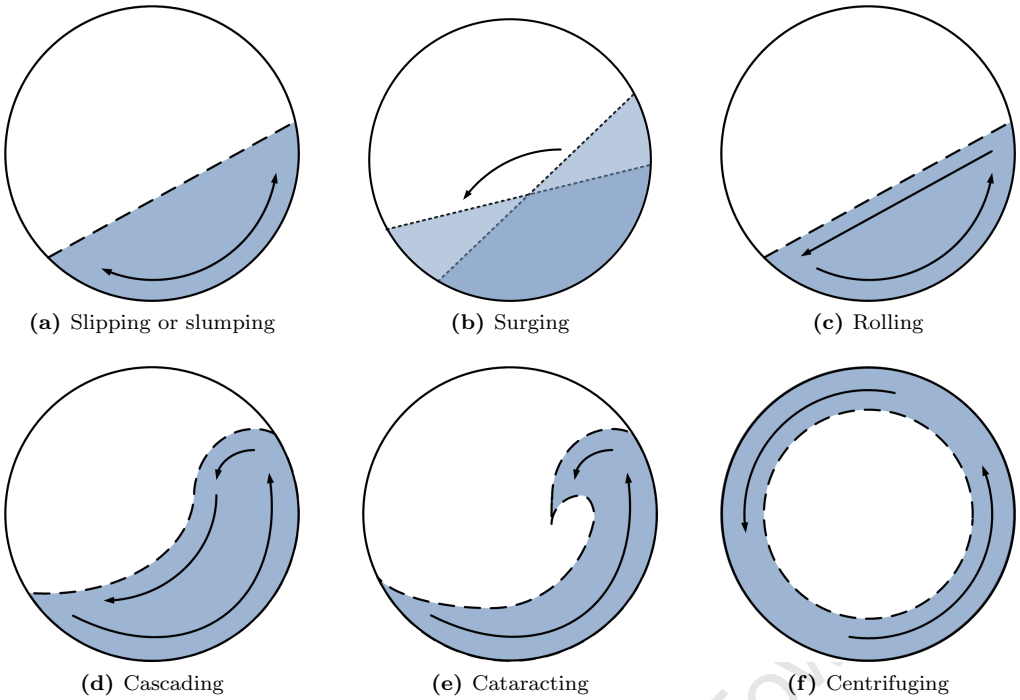

Figure 3.3: Six categories of granular bed motion in a rotating drum in order of increasing rotational speed (or wall friction), left to right and top to bottom.

Figure 3.3a shows the least energetic mode of bed motion in a rotating drum- slipping. Slipping occurs when the frictional force between particles in the bed and the surface of the drum is sufficiently large to be able to raise the bed some distance, but not so large that the top layer of material begins to roll down the rest of it. The bed reaches the maximum height to which it can lift and either remains there with the drum rotating beneath it or slumps down to a lower level[28]. The bed consists only of a rising region with a zero shear rate- it acts like a non-rotating solid body.

Figure 3.3b shows the surging motion of a granular bed. Surging occurs when the frictional force acting on the bed is enough to carry it above its angle of repose, but not to cause its top layer to roll down its face. The bed thus rises to its maximum height and then the material above its angle of repose (the upper pale triangle in the diagram) rolls down that part of the bed that is at the angle of repose. Once all of this non-equilibrium material has reached an equilibrium position (the lower pale triangle in the diagram), the process repeats itself in surges.

Both slipping (or slumping) and surging can only occur if the inner surface of the drum is cylindrical. If not, then a layer of material would be trapped near the surface of the drum, and rolling would occur.

Figure 3.3c shows a bed undergoing a rolling motion. As is the case for surging motion, the frictional force, both directly and through the pushing of lower material, is enough to raise the bed to above its angle of repose. In the rolling case, however, material reaching this high point has enough momentum to be projected slightly away from the drum, allowing at least one layer of material to enter the active region of the bed. A granular bed is in rolling mode if it has at least one layer flowing down its face, and thus an equilibrium surface dividing it into a rising and active region. A rolling mode bed thus has a CoC that is not the centre of the drum.

Once the material entering the active region of the bed begins moving fast enough that material

[28]Such motion is called slumping.

in its upper part begins to dilate, the bed has entered cascading motion. Cascading motion is thus distinguished from rolling motion by the S-shape of the bulk free surface of the bed, itself only possible once the active region has increased beyond a certain thickness.

Once the speed of the material entering the falling region of the bed has increased beyond some threshold, some of this material begins to enter the in-flight region of the bed. As more and more material enters the in-flight region, less and less enters the active region, and the S-shape of the bulk free surface becomes less and less pronounced. Once the bulk free surface has become a concave shape, the bed has entered cataracting motion, as shown in Figure 3.3e.

As the rotational speed of the drum, and thus of the material in the outermost layer of the granular bed, increases, so does the highest point reached by the material- termed the head of the bed. Eventually, the head of the bed coincides with the highest point in the drum, and a layer of material begins to centrifuge. The rotational speed at which the outermost layer of material begins to centrifuge is called the critical speed. Once more than, say, 25% of the material in the drum is centrifuging, the bed is said to be in centrifuging motion, as shown in Figure 3.3f. This is an undesirable mode since the shear rate in the centrifuging material is again zero, and no mixing or grinding occurs in it.

Different modes of bed motion are desirable for different industrial applications, depending on whether mixing, heat dispersion, chemical reactions, or comminution, for instance, is desired. In this work I focus on tumbling mills, whose use is in the comminution of granular material. The most important modes for this application are cascading and cataracting.

3.2.4 Characterising the motion of granular media in rotating drums

In this section I will discuss some of the features of the dynamic bed that I have used in my discussion of its motion and modes of motion. In Section 5.5.3 I will re-define all of these features to make them rigorous and unambiguous. Here I present the definitions offered in the literature to facilitate my discussion of the drivers of charge motion in Section 3.3.6.

These features are most explicitly defined in the minerals processing literature, but occur also in the literature of granular flows, powder handling, and rotary kilns; often under various names. For this reason I adopt the nomenclature of [Powell and McBride, 2004] with clarifications as per my definitions in Section 5.5.3. Appendix A contains a transcription of Powell and McBride's extensive set of definitions.

The shape of the granular pile in a rotating drum- the bulk free surface

The shape of a granular pile in a rotating drum is the most obvious charge feature, and one that is relied on in the definitions of the modes of bed motion in devices consisting of rotating cylinders, as in [Boateng and Barr, 1996], [Mellmann, 2001] and [Ding et al., 2002], for instance.

The shape of the bed is determined by its bulk free surface- the surface that divides its bulk region from its disperse region, as defined in Section 3.2.2 and again in 5.5.3. Figure 3.4 shows an example of the S-shaped bulk free surface of a dynamic bed undergoing cascading motion in a rotating drum.

The shape of the bulk free surface and, in particular, its evolution from a straight line to an S-shape to a concave shape have been investigated extensively by researchers such as [Henein et al., 1983], [Boateng and Barr, 1997], [Ding et al., 2001b], [Mellmann, 2001], [Ding et al., 2002] and

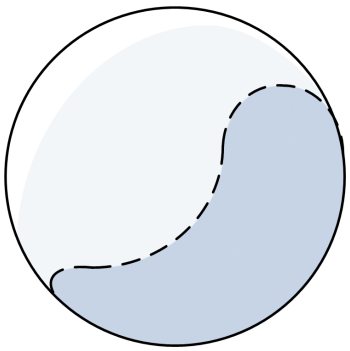

Figure 3.4: A schematic of the dynamic bed in a rotating drum, showing the shape of its bulk free surface.

[Santomaso et al., 2003], who have all been interested in the transitions between different modes of bed motion.

The main factor that gives rise to the S-shape of the bulk free surface is the inter-particle friction in the bed, and that between the bed and the drum[Zik et al., 1994],[Taberlet et al., 2006]. [Taberlet et al., 2006] has shown, too, that the friction between the bed and the end-plates of the drum plays a big role in lowering the rotational speed at which the S-shape develops.

The shape of the bed is an important feature, not only in characterising the rolling mode of the bed, but also for use in modelling the motion of granular material in the bed. Models have been proposed by, among others, [Zik et al., 1994], [Tordesillas and Arber, 2005] and- building on and extending the work of Zik *et al.*- [Taberlet et al., 2006].

In chemical engineering and industry-related literature, however, it is more usual just to approximate the shape of the bed, rather than to model it. Figure 3.4 shows the shape of a typical bed undergoing cascading motion, and Figure 3.5 shows various approximations to it.

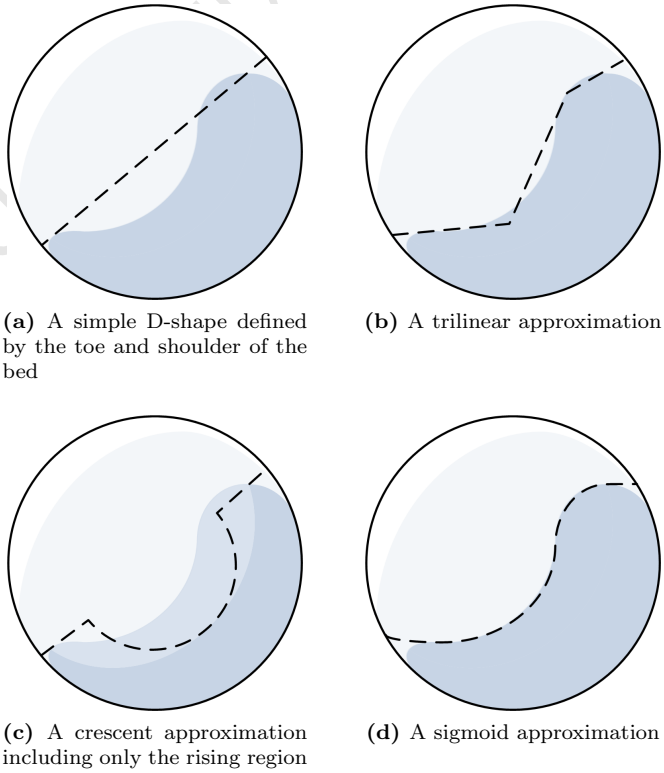

(a) A simple D-shape defined by the toe and shoulder of the bed

(b) A trilinear approximation

(c) A crescent approximation including only the rising region

(d) A sigmoid approximation

Figure 3.5: Four approximations to the bed shape.

Figure 3.5a shows the simplest approximation that can be made to the shape of the dynamic bed in a rotating drum- the so-called D-shape approximation. The surface of the bed consists of a chord defined by a line joining its toe and shoulder. This approximation is a common one in the simplest implementation of the torque-arm approach to power draw calculation[29] as in [Hogg et al., 1972], for an early example. Whereas it might approximate the shape of a bed undergoing slipping, surging, or even rolling motion, it clearly breaks down when- as in this schematic- the shape of the charge takes on a pronounced S- or concave shape.

In extending the torque-arm-based power model, [Dong and Moys, 2003] approximates the bulk free surface- which they call the 'free rolling surface'- by approximating it with a trilinear model, after the work of [Dury et al., 1998], and as shown in Figure 3.5b. Figure 3.6 shows the types

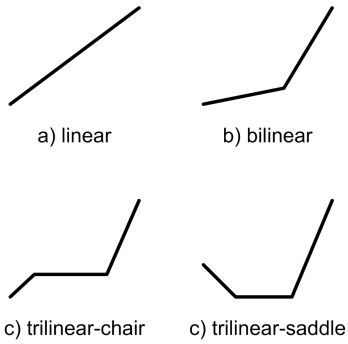

Figure 3.6: Dong and Moys' trilinear approximation to the 'rolling free surface'.

of free surface that can be modelled with the trilinear model as proposed by Dong and Moys. Figure 3.5b shows an important fifth permutation not mentioned by them. Following the D-shape approximation, Dong and Moys' trilinear model has as its endpoints the toe and shoulder of the bed, and thus each variation can be defined by specifying two points (in addition to the positions of the toe and shoulder). For instance, if the two points coincide, the result is either a linear or bilinear approximation, depending on their position.

Figure 3.5c shows the approximation to the shape of the bed proposed and employed by [Morell, 1992] in the development of his seminal power draw model. In his work, Morrell includes only the rising region of the bed in his approximation, but a crescent model of this sort could be used to approximate the shape of a cataracting bed reasonably closely.

The final approximation considered here is a sigmoid one. It is the most realistic approximation to the shape of a dynamic bed that can be made with simply-defined curves. It consists of an odd function, such as a logistic or Gompertz curve fitted to the bulk free surface. It is employed by, for instance, [Santomaso et al., 2003] and implicitly by [Powell and McBride, 2004] and [Govender and Powell, 2006].

For my own work I use a generalised logistic function of the form

$$y(x) = a + \frac{b-a}{\left(1 + c\exp^{-d(x-f)}\right)^{g}} \tag{3.6}$$

where a and b are the lower and upper asymptotes[30], d is the effective slope of the curve, f is the point at which the maximum slope occurs, and $0 < g < 1$ determines near which asymptote the maximum slope occurs.

The biggest drawback of using a sigmoid curve to model the bulk free surface of a dynamic bed is the limitations on the curvature that such simple functions permit. For instance, although the

[29] See Section 3.3.5
[30] Related to the toe and shoulder.

logistic function given in equation 3.6 is assymetric about its point of inflection, as required, the slope above its point of inflection is still related to that below it. Since there is some thickness to the transition layer between the bulk and disperse regions, equation 3.6 usually approximates the shape of the bulk free surface fairly well, but can begin to deviate for different modes, especially in the middle part of the curve. For this reason, perhaps a multi-domain approximation would be appropriate, but adopting such an approach increases the complexity of the approximation[31] without adding any new information.

A particular area in which all sigmoid approximations fail is in the toe and shoulder regions in which there is an additional curvature as the material moves between the rising and descending layers, and vice versa. [Powell and McBride, 2004] seem to accept this limitation implicitly and incorporate it explicitly into their definition of the bulk toe[32].

The shape of the rising region- the equilibrium surface

The equilibrium surface is the surface that divides the rising and descending regions of the bed. Because of shear in the material, each subsequent layer in the rising region above the layer of material in contact with the drum moves at a lower and lower angular speed, and each subsequent layer above the equilibrium surface in the active region moves at a higher and higher angular speed about the CoC of the rotating bed. The equilibrium surface, since it is the interface between the rising and active regions is a locus of points of zero velocity tangent to radial lines passing through the CoC.

The equilibrium surface can be roughly identified in end-window filming and streak photography experiments, and can be unambiguously identified- according to the criteria mentioned in [Powell and McBride, 2004], or that proposed by me in Section 5.5.2- from data obtained from DEM or a Lagrangian particle tracking technique such as biplanar x-ray imaging[33] or PEPT.

In particular, horizontal and vertical equilibrium surfaces can be constructed as the loci of points of zero horizontal or vertical bed velocity. The horizontal equilibrium surface thus separates the bed into left- and right-going regions, and the vertical equilibrium surface separates it into vertically-rising and falling regions. These two equilibrium surfaces intersect at a stationary point, called the CoC. The equilibrium surface of the bed consists of the vertical equilibrium surfaces above the CoC and the horizontal equilibrium surface below it[Powell and McBride, 2004].

The centre of circulation (CoC) of the rotating media

The centre of circulation (CoC) of a rotating granular bed is the point about which all of the material circulates. It lies along the equilibrium surface of the bed, and is the intersection between the surfaces of zero horizontal and vertical velocity- it is thus a stationary point in the bed. As such it can easily be identified from streak photographs or any of the Lagrangian techniques mentioned in Section 3.2.1.

The CoC is an important feature of a rotating granular bed because it gives an easily-obtained indication of the position of the bulk region of the bed. Taking advantage of this fact, and using biplanar x-ray imaging, [Govender and Powell, 2006] obtained a correlation between the position of the CoC and the centre of mass (CoM) of the charge in a tumbling mill to build a power draw model based on the CoC, for instance.

[31] By, for instance introducing an additional smoothness constraint at the domain boundaries.
[32] What I call the re-entry toe to remove this implicit approximation.
[33] See [Govender et al., 2001].

The importance of the CoC in characterising bed motion is compounded by the fact that it must be derived from surfaces of zero horizontal and vertical bed velocities, which means that it is a measure of both the position and, indirectly, of the motion of the material in the bed. For these reasons, [Cleary, 1998] and [McBride et al., 2004] used the position of the CoC as a comparator in the validation of DEM simulations of tumbling mills.

The extent of the bed- toes, shoulders and heads

The last bed features that I will consider now are the turning points of the material in the bed.

The toe of the bed is the lower turning point of the bed's motion. It is, however, not a well-defined point. In the preceding discussion, I have referred to the toe of the motion of each layer of the bed- effectively tracing out the lower half of the equilibrium surface. However, the toe is usually reserved for just the lowest turning point of the outermost layer of material. Even within this definition there is some ambiguity- the toe is sometimes considered to be the turning point of the bulk[34][Morell, 1992], the point at which the material re-enters the rising region, or the point of intersection of a line drawn from the turning point of the outermost layer of material and the drum[Powell and McBride, 2004]. [Powell and McBride, 2004] also defines an impact toe, which is the point of contact of the outermost layer of in-flight material with the drum. In Section 5.5.3 I unambiguously define a series of toes.

The shoulder of the bed is the higher turning point of the motion of the bulk of the material. The head of the bed is the turning point of the motion of the in-flight bed material. The two coincide up to modest cataracting motion of the bed. Sometimes the point of departure of the rising material from the wall of the drum is called the shoulder[35], and the upper turning point of the outermost layer of material the head. This can introduce an ambiguity when there is in-flight material.

More important for some applications than the position of the toe and head of the bed is the distance between the two. The length of the arc running from the toe to the shoulder of the bed determines the total contact area between the drum and the bed- important in rotary kilns in which heat is applied to the outside of the drum. The vertical distance between the toe and head is sometimes called the *rise* of the bed. It determines how much potential energy is imparted to material leaving the rising region of the bed and entering the disperse region, and thus how much energy is available for breakage through collisions in the toe region of the drum.

3.3 Tumbling mills- rotating drums in the mining industry

Tumbling mills are an example of the use of rotating drums in mineral processing. They are used in the final step of comminution, that is, in the final size reduction of mineral-bearing ores in order to liberate these minerals.

In this section I will describe tumbling mills and their use in the mining industry, and explain the choices we made for their experimental investigation by PEPT. In doing this, I have relied heavily on Barry Wills' *Mineral Processing Technology*[Wills, 2001] and on the The Julius Kruttschnitt Mineral Research Centre (JKMRC)'s so-called blue book[Napier-Munn et al., 2005].

[34] What I call the bulk toe in Section 5.5.3.
[35] In Section 5.5.3, I define a departure shoulder to remove this ambiguity.

3.3.1 Comminution

Comminution, the size reduction of ores, is often called milling. It consists of up to three steps- blasting, crushing and grinding. Only the machines used in the final stage- grinding- however, are referred to as mills.

The first step in the comminution of mineral-bearing ores is blasting- the use of explosives to dislodge and break up, or at least to loosen for removal by drilling, the rock containing the ore of interest[36] to facilitate its transport to the surface for further treatment and concentration. The coarse particles produced by blasting are called the run of mine (RoM) ore.

The second step in comminution is usually crushing- the process in which the RoM ore produced in blasting is coarsely reduced in size by its compression against or impact with rigid surfaces. A variety of crushing devices exist, which all have in common a fixed anvil, roll or jaw against which to crush the ore. Crushing is normally a dry, multi-stage process with a small reduction ratio at each stage. Alternatively, the second stage of comminution could consist of one or more run of mine ball mills. These are tumbling mills whose charge consists only of the RoM ore. Such a mill is said to be an autogenous mill because it contains only charge and no grinding media, although the term autogenous mill is usually reserved for a grinding mill.

The third step in comminution is grinding. Grinding is the final stage in the size reduction of mineral-bearing ore before it is sent for concentration. A wide range of mills are used, depending on the size distribution, competence and constitution of the feed ore, and on the required size distribution of the product. Grinding mills fall into two broad categories- stirred mills and tumbling mills.

Stirred mills consist of a stationary shell containing a more or less complicated system of rotors that circulate a charge consisting of ore and grinding media. The cylindrical shell can either be vertically-aligned as in the pin mill or horizontally-aligned as in the IsaMill^{TM}. They are usually operated at high charge densities, and so the grinding mechanism is dominated by the shearing of particles[37]. As such, stirred mills are usually used for fine grinding applications.

Tumbling mills consist of a horizontally-aligned cylindrical shell which rotates about its axis causing its charge to circulate by the friction between it and the lining of the shell. There are various designs and operating modes for tumbling mills, which will be considered in the following subsections.

Of course, there are many other grinding and comminution devices than the ones mentioned here, but in this work I will focus only on tumbling mills.

3.3.2 Types of tumbling mill

Tumbling mills are classified according to the composition of their charge. Charge can either be *autogenous* if it consists only of the ore to be ground (and, perhaps, some slurry), or it can be *semi-autogenous* if it contains also grinding aids, called grinding media.

Autogenous mills

Autogenous mills can be used either as primary or run of mine ball mills to reduce coarse, RoM ore to a size amenable to further grinding, or as a secondary or grinding mill.

[36] Usually while underground.
[37] More later in Section 3.3.4.

As a primary milling stage, the feed supplied to an autogenous mill usually consists of the uncrushed RoM ore produced by the mine. Sometimes, however, the ratio of the top and bulk sizes of the RoM ore is not large enough for the top size to act as a grinding aid. In such a case, the RoM ore can be pre-screened and all but the top size sent to a crusher before the feed is reconstituted to fix this. Alternatively, larger competent or pre-conditioned 'pebbles' can be added to the feed. In both of these cases, the autogenous mill can then be termed a pebble mill. This is almost always done for a secondary autogenous mill.

Autogenous mills have several advantages over the conventional semi-autogenous mill. The first is that the grinding media that must be added to semi-autogenous mills are a major expense in mineral beneficiation, an expense which is obviously eliminated in the case of autogenous mills. The second is that, since the grinding media often make up the bulk of the charge at least by mass, autogenous mills often do not require the same design strength as semi-autogenous mills, and can thus be made either more cheaply, or bigger. Finally, mills are often used as chemical reactors to facilitate downstream concentration, and grinding media are either extremely reactive, as is the case for steel balls, or prohibitively expensive, as is the case for ceramic alternatives.

There are two main disadvantages of autogenous mills over semi-autogenous mills. Since the density of steel, the most common material from which grinding media are made, is between 2 and 5 times that of a typical ore, the specific energy of a steel ball at a given speed is much greater than that of a similar ore particle at a similar speed. Thus autogenous mills have been known to draw more power for the same grinding rate, using both energy less efficiently, and potentially wearing liners more quickly. This effect, however, is highly dependent on the feed.

Steel is also typically much harder than ore and thus takes much longer to wear down, so not only is the mass of the charge dominated by the grinding media, but it is also stabilised by it. That is, a semi-autogenous mill containing steel grinding media effectively contains a permanent charge independent of the feed[38]. The load of autogenous mills, on the other hand, depends very strongly on its feed, and measures such as the power drawn by the mill must be actively monitored and the feed rate actively adjusted to avoid shock-loading of other circuit elements, such as belts and bins, or grinding out downstream units[39].

Autogenous mills come in various sizes, but, because the density of their grinding media is the same as that of the rest of the charge they are impractical for smaller mills in which high speeds are not achievable. The aspect ratio of a mill is defined as the ratio between the diameter and length of the mill. Since the residence time of the charge in an autogenous mill is not very long, and since autogenous grinding media often require large impact speeds, high aspect ratios[40] are common for autogenous mills, particularly in North America. In South Africa, lower aspect ratios are more common, and in Australia it depends on the industry.

Semi-autogenous mills

All other tumbling mills are semi-autogenous. However, the name is usually reserved for autogenous mills whose charge has been slightly augmented with the addition of around 5% by volume of steel balls. Semi-autogenous mills are used for grinding rather than primary milling.

Semi-autogenous mills are usually of low or square aspect ratios.

[38] Of course, worn balls that discharge from the mill must be replaced, but this is done at comparatively infrequent intervals.

[39] A particular worry for high-pressure grinding rolls.

[40] Mills with aspect ratios of about $1.5 - 3$ are often called 'pancake' mills.

Ball mills

In general, for a semi-autogenous mill to qualify as a ball mill, it need only consist of a rotating drum containing spherical grinding media. However, in mineral processing, a ball mill must also have an aspect ratio of between 1 and 1.5. Low aspect ratio ball mills, that is those whose lengths are more than 1.5 times their diameters, are called tube mills.

Tube and ball mills differ from so-called semi-autogenous mills only in the proportion of the charge made up by steel balls- between 65% and 80% by volume. In effect, the charge in a rotating ball mill consists of a dilated bed of steel balls whose interstices are filled with a (potentially fairly coarse) slurry. Thus the balls dominate both the power drawn by the mill[41], and its grinding efficiency.

The high relative density of steel balls make them particularly suited to impact breakage[42], quickly reducing the size of coarse particles, that would otherwise be reduced by the much slower abrasion process[43]. The large surface area of balls also makes them an effective vehicle of attrition breakage.

However, the particle-particle and particle-grinding media interactions in tumbling mills are all stochastic, which means that the likelihood (controlling for different cross-sectional areas) of a fine particle being impacted by a ball is the same as that for a coarse particle, and the likelihood of a coarse particle being trapped between two balls is the same as that of a fine particle. Thus although ball mills are capable, given enough time, of grinding to any degree of fineness, they always produce a wide product size distribution.

Over-grinding, a significant problem in terms of slimes production and energy inefficiency, can be minimised by effective transport of sufficiently fine particles out of the mill. This is a function of the feed rate, discharge rate[44], and the dynamic porous bed presented by the moving charge. Slurry transport is a significant determinant of grinding efficiency, but one that will not be considered here. Instead, I will limit myself to the effect that slurry has on charge motion and not *vice versa*.

Size segregation of the charge might also be useful in ensuring that large particles, which would benefit most from impact breakage, are more likely to end up in the toe of the charge, and small particles, that would benefit most from abrasion and attrition are more likely to be in high shear regions of the charge. This level of control, however, is extremely unlikely to be practicable on any realistic tumbling mill system.

As already mentioned above, the hardness of steel means that the balls in a ball mill grind down very slowly compared to the feed. However, they do grind down, and must be replaced periodically. This results in a size distribution of worn balls, whose top size is continually replenished, and whose bottom size is continually discharged from the mill. This size distribution increases the packing density of the grinding media, and can also lead to its size segregation

It may turn out to be more feasible to control the size segregation of grinding media than of the rest of the charge, and grinding media size segregation may turn out to affect grinding efficiency in an intuitive way. Impact breakage relies on specific energies of particles in inelastic collisions, and so is aided by larger particles, but only if they can build up speed by leaving the dense charge. Attrition of ore particles between balls depends both on the shear rates and the surface area available- itself dependent on the density of the grinding media. Thus it may seem that a scenario in which large media segregate to the less dense periphery of the circulating charge, and small media to the more

[41] Which is closely related to the mass of the load.
[42] Which I will define in Section 3.3.4.
[43] Again, to be defined in Section 3.3.4.
[44] Dependent on the design of the discharge, see Section 3.3.3.

dense centre might improve grinding efficiency, but there are more factors to be considered in Section 3.3.4.

On the other hand, high charge density can lead to excessive grinding media wear, and unfavourable segregation could lead to lifter and liner wear, as well as to dead regions and low shear rates. I will also consider this further in Section 3.3.4.

Ball mills are capable of grinding a wide range of feed sizes, making them an extremely important and versatile piece of equipment in a comminution circuit. Unfortunately, however, the vast majority of the energy supplied to a tumbling mill in general and a ball mill in particular, does not go into the useful comminution of ore. As much as 90% of it goes into the generation of heat and sound through sub-breakage energy particle-media collisions and elastic media-media interactions. The latter effect particular besets ball mills with their high media fraction. A better understanding of the motion of charge and of grinding media in a ball mill could help to reduce this inefficient use of energy.

Notwithstanding, ball mills are one of the most effective all-purpose grinding devices from very small, laboratory-scale applications to enormous mining equipment.

Rods, cones and other grinding media

Rod mills, semi-autogenous tumbling mills whose grinding media consists of rods of roughly the length of the mill, used to be a common device in comminution circuits.

Some experiments have been performed with grinding media of various shapes, with little difference in the grinding efficiency between these shapes and the conventional steel ball. Other work has shown that shape has an effect on granular motion, especially with regard to segregation. This effect will not be considered in this work.

3.3.3 The anatomy of a tumbling mill

At its simplest, a tumbling mill consists merely of a charge-filled, horizontally-aligned cylinder rotated about its axis. What distinguishes a tumbling mill from other uses of rotating drums[45] is its mode of operation. Since tumbling mills are used to comminute their contents, they are operated such that the motion of their contents is much more aggressive than for other, generally mixing-related, uses of rotating drums.

As a result of the comminution of charge inside a tumbling mill, the individual constituents of its charge evolve in size (and relative density and composition). This means that the dynamic charge in a tumbling mill is not in steady state even in the limited sense that I defined in Section 3.1. This is true, though, only for those tumbling mills whose charge is neither added to nor taken from during its operation. Such mills are called *batch* mills, or said to be operated in *batch mode*. It is possible, and in fact common practice, however, to continuously replenish the charge in the mill at one end, and remove ground-down charge from the other, to maintain a pseudo-steady state of charge size distribution.

Tumbling mills must thus be modified to facilitate the necessary aggressive charge motion, and to allow ground-down charge to be efficiently removed and fresh feed to be supplied to the mill. Figure 3.7 shows a schematic of a typical mineral processing tumbling mill, whose features I will further discuss in the following subsections.

[45] As discussed in Section 3.2.

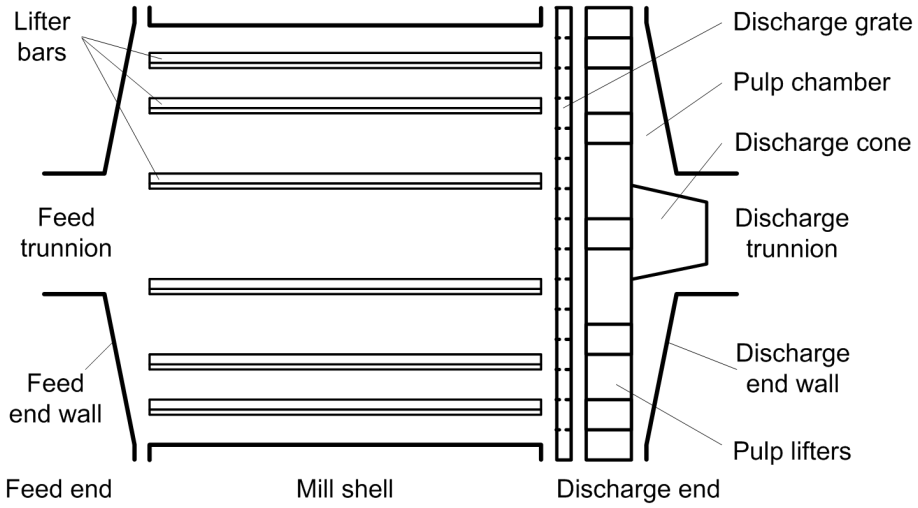

Figure 3.7: A schematic of a typical tumbling mill

Liners and lifters

This aggressive charge motion I mention in Section 3.2.3 and above can be achieved either by increasing the speed at which the drum is rotated, or by increasing the friction between the charge and the inside surface of the drum.

Merely increasing the rotational speed of the drum, though, has several drawbacks. The first is that it generally takes more energy than expected to do so, even discounting the effect of raising the charge higher in the drum, because of inefficiency loses in bearings, gearboxes and so on. The second is that without increasing the friction between the charge and the drum, it is possible that slipping or surging of the charge could occur rather than the required aggressive charge motion.

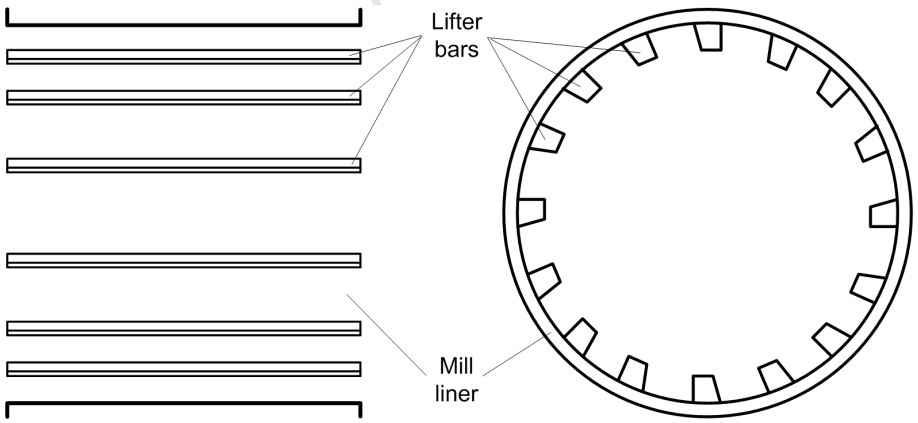

Figure 3.8: A schematic of the body of a typical tumbling mill showing a simple lifter configuration.

For these reasons, tumbling mills are equipped with lifter bars, whose role is to raise charge with the moving shell.

Figure 3.8 shows a simple lifter configuration inside a mill shell. In this configuration, the lifters are all of the same height, base width and lifter face angle or *chamfer*; and are evenly distributed around the circumference of the mill shell. These lifters are simple bars which do not vary along their length, and which are aligned axially with the mill shell. A good deal of more complicated lifter designs and configurations are used in industry. Wills gives a good overview of some of the more common of these[Wills, 2001].

Lifters can be thought of as raising the effective friction between the charge and the inner surface

of the mill shell. In fact, sufficiently many sufficiently large lifters trap a layer of charge against the shell, enforcing a non-slip boundary condition between the charge and the shell[46].

This layer is formed when charge in the toe region is inducted into the dense bulk region of the moving charge by the action of the lifters as mentioned in Section 3.2. Since a charge element in contact with a lifter pushes along charge elements in contact with it, which push along those in contact with them and so on, and since the resultant layer is held in place by the weight of charge above it, lifters have thus increased the effective friction between the charge and the shell as claimed.

Lifters thus raise the point, mentioned also in Section 3.2, at which a layer of charge is no longer held against the mill shell and thus begins to fall. Furthermore, charge in the outermost layers of the bulk region have their point of departure from the shell further delayed by the 'lifting' action from whence lifters get their name. The combination of these two effects is what allows lifters to increase the 'aggression' of the charge motion without having to increase the mill speed.

Despite increasing the friction between the charge and the mill shell to the point of the outer layer being effectively non-slip, some slippage remains even in the rising bulk region, contributing to the abrasive wear of the mill shell. In the shoulder and toe regions of the moving charge, even more slippage occurs as the charge enters or leaves the bulk region. This is particularly true in the chaotic, mixing toe region. The resultant wear on the mill shell is exacerbated by the stream of *in-flight* charge created by the effect of the lifters on the outermost layers of charge, some of which may directly impact on the shell rather than on other charge in the toe region. To combat this, mills are fitted with sacrificial mill liners which can be replaced at the same time as worn down lifter bars. A variety of mill liner designs are used in industry, as documented by [Napier-Munn et al., 2005].

Feed and discharge

As already mentioned, the size distribution of the charge inside a tumbling mill evolves over time under the comminuting self-action of the charge itself and of the grinding media.

For some small-scale applications, tumbling mills are operated in batch mode- that is, a sealed mill is rotated until its charge is judged to have reached the required fineness. This is generally acceptable for a small volume of broadly uniform charge. For large volumes of more heterogeneous charge, it is much more efficient to operate a tumbling mill in continuous mode- that is, feeding in fresh charge and removing sufficiently fine product while the mill is in operation. This obviates the time wasted emptying and filling the mill in batches, and mitigates the wear and tear associated with stopping and starting of the particularly large mills.

In order for a mill to be successfully operated in continuous mode, it must have an effective size classification system to remove sufficiently fine product from the mill before it is over-ground[47]. Although some industrial mills use gravity feeding of sized discharge slots on the periphery of the mill as a classification and discharge system, the majority use a fluid- air, water or slurry- to set up a pressure gradient from the feed to the discharge ends of the mill and either an internal or external classification system to select charge for discharge.

Examples of discharge modes are given in the 'Blue Book' [Napier-Munn et al., 2005]. I will restrict my discussion to a particular configuration of internal classifier- the pulp chamber.

[46] The use of grid liners, mill shell liners consisting of hollow grids into which charge can become lodged, is another method of enforcing this no slip boundary condition. More on mill liners later.

[47] Over-grinding- grinding beyond the point at which the useful values are liberated- is not only a waste of energy, but can also have deleterious effects on downstream processes. cf. slime production.

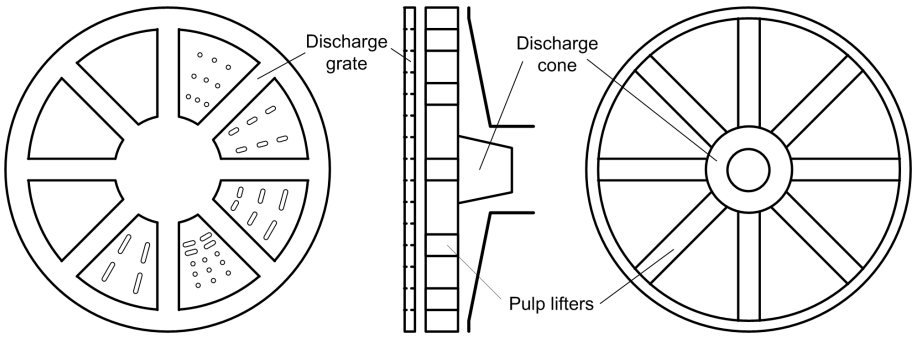

Figure 3.9: A schematic of a typical pulp chamber showing some examples of possible discharge grates (left), a simple pulp lifter system (right), and their relation to the discharge cone (centre).

Figure 3.7 in Section 3.3.3 shows a schematic of a continuous mode tumbling mill with a pulp chamber discharge system. Fresh feed is introduced into the mill through the feed trunnion and sufficiently fine product is removed through the discharge trunnion. Feed that is introduced through the feed trunnion enters the mill under the influence of gravity, but in order to be discharged, fines must be actively moved and then funnelled into the discharge trunnion. This is done in the pulp chamber.

Figure 3.9 shows a schematic of the pulp chamber. The pulp chamber is separated from the body of the mill by a discharge grate. At its simplest, a discharge grate consists of metal plate perforated with circular holes, elongated slots, or a combination of the two, designed to allow sufficiently fine product to enter the pulp chamber for discharge. The leftmost diagram in Figure 3.9 shows some possible configurations of the discharge grate. The fraction of the area of the discharge grate occupied by these holes or slots is called the open area. The position[48] of the holes in the discharge grate, and the open area strongly determines the transport efficiency and likelihood of pooling of the slurry. See for instance [Wills, 2001].

Inside the pulp chamber are pulp lifters. Unlike the lifter bars in the body of the mill[49], pulp lifters extend all the way to the centre of the pulp chamber, and resemble the wheels of a paddle steamer or of a water-powered flour mill. Their job is to raise the pulp which collects in the bottom of the pulp chamber where it enters through the discharge grate and to pour it onto the discharge cone[50], which deflects it into the discharge trunnion.

End walls

I have mentioned already the variation in aspect ratio between different types of tumbling mills[51]. I will not go further into this beyond saying that for structural reasons, low aspect ratio mills usually have so-called conical end walls- that is, their end faces are sloped as in Figure 3.7. These end walls are often fitted with ribs or lifters not unlike those in the pulp chamber. These end wall lifters can significantly change the flow of charge in tumbling mills by, for instance, introducing a re-circulation stream or otherwise complicating the end wall effects.

3.3.4 Grinding mechanisms

The comminution of charge in a tumbling mill occurs by three mechanisms- abrasion, attrition, and impact breakage.

[48] Generally near the mill shell to take advantage of the draining of slurry through the charge.
[49] See Section 3.3.3.
[50] See Figure 3.9.
[51] See Section 3.3.2.

All three of these breakage processes are probabilistic- the likelihood of a particle breaking under the compressive forces of impact, or the shear forces of abrasion or attrition obeys an underlying probability distribution. This probability distribution depends on the material properties of the particles- on their composition, their structure, distributions of cracks or crystal defects in each grain, surface roughness, the hardness or malleability of the material and so on.

Furthermore, in a tumbling mill, whether a particle experiences a particular breakage interaction is also probabilistic- it depends on where in the mill the particle is[52], and on the chaotic behaviour of all of the other particles. This exacerbating factor is why stirred mills generally produce narrower product size distributions than tumbling mills.

Abrasion and attrition

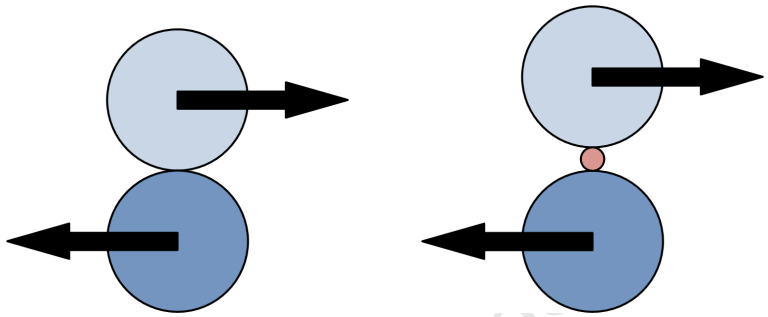

(a) Two particles undergoing abrasion

(b) A small particle undergoing attrition between two larger particles

Figure 3.10: Examples of particles undergoing abrasion (left) and attrition (right).

Abrasion and attrition are surface shear processes. They occur when there is relative motion between particles in a direction perpendicular to the normals to their point of contact. Figure 3.10 shows schematically such relative motion between particles. Figure 3.10 also shows the difference between abrasion (Figure 3.10a), which is between two similar particles, and attrition (Figure 3.10b), which occurs when a small particle is sheared between two larger ones.

Both abrasion and attrition occur when frictional particles rub against each other. Whilst in contact, the friction between the surfaces of the particles resists the relative motion of the two particles. In overcoming this frictional interaction, small pieces of the particles are removed from the surfaces of the interacting particles, grinding them down. These, then, are comparatively slow grinding mechanisms that preferentially produce fine products.

Since abrasion and attrition are surface processes, their grinding rate and efficacy depend on the surface properties of the particles involved, in particular hardness and roughness, but also shape. The shape (and also size) of the particles plays a role because it affects how much surface contact is possible. This is also affected by the packing density of particles- more densely packed particles are obviously more susceptible to abrasion and attrition since they have more surface contacts. The nature of these contacts are also significant, since the frictional force is proportional to the normal force between particles. For this reason, not only tightly-packed, but also heavier particles or particles deeper in the granular pile experience greater frictional shear forces and thus abrasion and attrition grinding. Finally, since abrasion and attrition are shear-driven processes, their efficacy depends on the relative velocity between particles or layers of particles- a densely packed parcel of rough, brittle particles will still not undergo abrasion or attrition if it moves as a solid body.

[52] More on this in Section 3.3.4.

Impact breakage

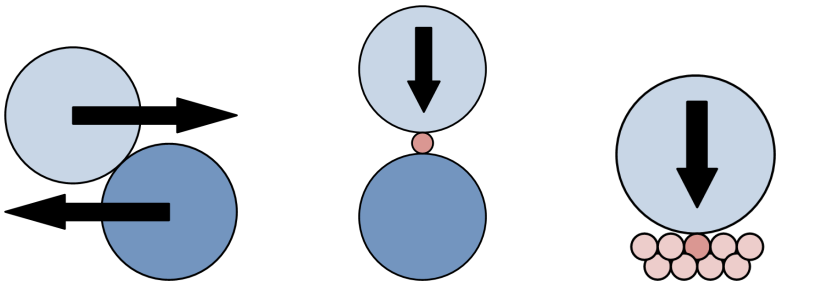

(a) Two colliding particles- candidates for impact breakage

(b) A smaller particle trapped between an incoming particle and either a stationary or moving anvil particle

(c) An incoming particle colliding with a packed bed of particles

Figure 3.11: Examples of three different kinds of impact breakage- collision (left), anvil (centre) and packed bed impacts (left).

There are several types of interaction that can lead to impact breakage- particle-particle collisions, hammer and anvil interactions, and packed bed impacts. These are shown in Figure 3.11. What they all have in common are the relatively short duration of interaction[53], and a compressive force component of that interaction.

Impact breakage is dominated by compressive forces- forces normal to the plane of contact between the interacting particles which force these particles to reduce in size. To understand the breakage effect of compressive forces, it is helpful to consider their effect on crystals. Compressing a crystalline solid causes the bonds between its constituent bases to shorten in a coaxial direction, increasing the stored elastic energy of the solid. For a small enough applied force, this compression can be elastic- the solid springs back to its normal size when the force is removed. Above this threshold force, however, the bases of the crystal could realign- creating or taking advantage of crystal defects such as dislocations, inclusions and voids- causing a permanent deformation. If the applied force is either greater than this or applied sufficiently sharply, it can become energetically preferable for the crystal to cleave into two or more pieces- also usually along defects. This is the breakage mechanism of compressive forces.

Ore particles, for instance, are generally polycrystalline solids, which introduces the possibility of defects such as grain boundaries, cracks and comparatively brittle constituents along which to break.

Figure 3.11a shows a collision, an example of a two-body impact breakage event in which both particles are equally likely (given a similar make-up, and controlling for size and specific energies) to break. Figures 3.11b and 3.11c, however, show many-body impact breakage events. Figure 3.11b shows a so-called 'hammer and anvil' event in which a larger (or higher specific energy) particle is incident on another which cannot rebound from the collision because it is in contact with a relatively immovable 'anvil'. This anvil could be another larger particle, a piece of geometry[54], or a densely packed bed of other particles. In this last special case, the impact is called a 'packed bed' one and is shown in Figure 3.11c.

Impact breakage is not restricted to that induced by compressive forces, however, shear forces can also play a role. In the impact shown in Figure 3.11a, there is both a normal and a shear

[53] cf. abrasion and attrition in which the interacting particles are in contact with each other for some time.
[54] Such as a lifter or the shell.

component to the resultant stress in the particles. This combination of shear and normal stress makes a type of breakage called 'chipping' possible. Chipping is when a single large piece of one of the impacting particles breaks off. It is most likely in inhomogeneous, irregularly-shaped particles. Once particles have reached a roughly spherical shape, consist of a roughly homogeneous material, and no longer contain easily broken cracks and grain boundaries, they constitute a 'conditioned' charge.

Impact breakage depends on two factors- the specific energy of interactions, and their frequencies. High specific energy- faster moving or heavier- particles are more likely to exceed the breakage energy threshold beneath which particles either deform or rebound elastically after impact, and (probabilistically) the more interactions a particle undergoes, the more likely it is to break. Thus, unlike in the case of breakage by abrasion or attrition, impact breakage occurs most effectively for larger particles in dilute areas of the charge in which they can build up speed.

Other breakage modes

The nature of charge motion in tumbling mills makes breakage by other modes less important. In particular, the dynamic motion of the charge makes failure under load unlikely, and the nature of the charge itself makes it difficult to imagine tensile stresses contributing significantly to breakage. It is important to concede, however, that charge bahaviour inside a tumbling mill is chaotic, and so other breakage modes can not be written off entirely.

Grinding regions in a tumbling mill

From earlier discussions of charge motion in tumbling mills[55], and of the dominant breakage mechanisms in a tumbling mill, some inferences about grinding regions in tumbling mills can be made.

With reference to Figure 3.1 and to the discussion in Section 3.2.2, three charge regions can be identified- the pseudo-solid rising region below the equilibrium surface, the flowing active region between the equilibrium surface and the bulk free surface, and the in-flight region between the bulk and charge free surfaces. The rising and active regions together are called the bulk region[56].

The charge is at its most dense in the bulk region, and within the bulk region, in the rising region. Of course, emergent properties such as size segregation and probabilistic density fluctuations mean that there are regions even within the bulk which are more or less dense, but, broadly, this is true.

In the rising region, the charge is raised by the action of the lifters and of friction between the shell and the outermost layer of charge, transmitted by inter-layer friction within the charge. It has been shown[57], however, that the motion of the charge in the rising region is not that of a solid body- there is a shear rate within it.

In the active region, charge flows in layers over the equilibrium surface under the action of gravity. The speed of the mill shell and the action of the lifters determine only how high the departure shoulder of the bulk charge is. The maximum height, or *lift*, reached by the bulk charge affects the motion of the charge in the active region by affecting its potential energy available to be converted into kinetic energy, although most is dissipated through frictional interactions between particles. Thus the speed of the charge in the active region is likely less than that in the rising region. The charge in the active region is also less dense than in the rising region because the flowing charge is free to dilate as it flows. This dilation also increases the maximum radial distance between the

[55] See Section 3.2.2.
[56] for my unambiguous redefinitions, see Sections 5.5.2 and 5.5.3.
[57] For instance in [Napier-Munn et al., 2005] and references therein, and by me later.

CoC of the charge and the outermost layer of charge in the active region, reducing the shear rate[58] in this region.

The increased thickness of the active region compared to the rising region is reduced by the fact that some of the charge in the rising region enters the in-flight region. However, the combined effect of the reduced shear rate and lower absolute speeds in the active region make the rising region the site of the highest breakage rate by abrasion and attrition.

The in-flight region of the charge is the most dilute, which means that it is the least suited to breakage by abrasion and attrition, but also that the least energy is dissipated in this region. Since particles enter the in-flight region by the lifters raising them above the departure shoulder to the head of the charge, particles in this region also have the highest potential energy and thus specific energy for impact breakage. Unfortunately, this energy is only realised on collisions which occur in the toe region of the charge, once per circulation. Luckily, both the specific energy of particles in the in-flight region, and their circulation rate[59] are increased by increasing the mill speed and decreasing the face angle of the lifters.

The toe region of the charge merits special mention. It is usually thought of as the site of mixing in a rotating drum. However, it is also the region in which the in-flight stream of the charge rejoins the bulk of the charge and thus where most of the high-energy impact breakage events occur. The chaotic motion of the charge in the toe region also means that a fair amount of abrasion and attrition, as well as secondary, lower-energy impacts[60] may occur in this region. A large toe region could thus contribute to the desired grind, but it has the disadvantage of being the major contributor to liner wear.

3.3.5 Power drawn by tumbling mills

The power drawn by a tumbling mill is a useful proxy for what's going on inside it, if only because power draw is one of the few things that can be measured without stopping the mill.

Power draw is used as an indicator of mill load, and thus as a variable to control feed rates. A sudden drop in power draw can be an indication that centrifuging of the charge has occurred, and spikes and troughs[61] are a signature of surging and slipping of the charge, all undesirable operation modes. Most importantly, however, the power drawn by the mill is related to grinding efficacy by correlation with required product size distributions[62].

These and other uses of the power drawn by a tumbling mill have been discussed in more detail in Sections 3.1 and 3.3.2. In this section I will consider some of the models that have been proposed to predict the power drawn by tumbling mills.

The power drawn by a tumbling mill is interpreted in three main ways. It can be considered to be the work done by the mill per unit time against the torque exerted on its shell by its charge, as the work done per unit time in imparting gravitational potential and kinetic energy to that charge, and as the energy dissipated in collisions between particles in the charge.[63]

[58] $\frac{dv}{dr}$ for flowing layers.

[59] More on circulation rates in Section 5.5.5 and the results.

[60] Which produce roughly the same product size distribution as do abrasion and attrition, according to [Leung, 1987]

[61] Beyond the spikes that occur every time a lifter enters the bulk charge.

[62] See [Bond, 1961] and many subsequent works not considered here.

[63] Note though, that the fist two of these interpretations do not explicitly include the energy lost in the charge through inelastic collisions and frictional interactions, without which no grinding would occur in tumbling mills. For this reason, I'd expect any power draw model to underpredict the power drawn by a tumbling mill. That the models I will consider here do not do so significantly might be for one of two reasons. The first is that they are all based on experiments performed on laboratory-scale tumbling mills containing either conditioned charge or glass beads, which do not undergo comminution; although even laboratory-scale mills heat up, indicated some dissipated energy.

The first interpretation of the power draw- as work done against applied torque per unit time was first adopted on pragmatic grounds. It is certainly true that work must be done to overcome the retarding torque applied to the mill by the charge or, equivalently, the torque applied to the charge by the mill causing it to move up in the direction of the mill's rotation. The torques[64] applied to the mill by each charge element in a given time slice can be obtained from DEM simulations, and it has been found by [Cleary, 1998] and [El-Rahman et al., 2001] that the sum of these matches measured mill power fairly well.

However, the strength of the torque interpretation of power is that it can be simplified into the earliest and most intuitive power draw model- the torque-arm approximation. The torque-arm approximation adopts the interpretation of the power draw as the work done per unit time in raising and maintaining the charge in its non-equilibrium position up the side of the mill.

[Bbosa et al., 2011] apply the torque-arm approximation by dividing the charge in the mill into volume elements (dV_i) and using the radial (r_i) and angular (θ_i) positions , mass $\rho_i dV_i$ and angular velocity ω_i of each of these elements to calculate their contribution to the required power as

$$P_i = \rho_i dV_i g r_i \cos\theta_i \omega_i \tag{3.7}$$

and thus the total power drawn by the charge as

$$P_{tot} = \Sigma_i \rho_i dV_i g r_i \cos\theta_i \omega_i \tag{3.8}$$

[Bbosa et al., 2011] are only capable of doing this because they used PEPT to obtain the detailed kinematics of the charge. If this is not available, for instance in end-window experiments, coarser approximations must be employed.

Several researchers, such as [Harris et al., 1985], [Powell and Nurick, 1996a], [Dong and Moys, 2003] and [Govender and Powell, 2006], have used the position of the centre of mass of the charge to define the torque-arm, simplifying the equations above. In general, they do this by determining the positions of the toe, shoulder and, sometimes, CoC of the charge by end-window experiments[65] and using these to guide their approximation of the shape of what they assume to be a charge of uniform density. In Section 3.2.4 I mention some of these approximations to the charge shape.

A long-standing and, I think, unresolved consideration for the centre of mass-based torque-arm approach is how much of the charge to include in the calculation. [Morell, 1992] has included only the rising region, [Harris et al., 1985] includes only the bulk region, and [Powell and Nurick, 1996a], [Dong and Moys, 2003] and [Govender and Powell, 2006] include all of the charge. Whereas Morrell justifies his approximation by claiming that the active region is small in mass, close to the centre of the mill, and effectively stationary[66], and [Harris et al., 1985] theirs by pointing out that only the bulk region is in contact with the shell, [Powell and Nurick, 1996a] and [Govender and Powell, 2006] appeal only to how well their approach works. [Dong and Moys, 2003] attempt to rationalise the agreement obtained by including all of the charge in their calculation by observing that in-flight charge impacting on the shell exerts more than its weight's worth of torque and that the additional effect is taken into account by considering the energy in the in-flight region.

Although a historically successful approach, [Bbosa et al., 2011] show that the centre of mass-based torque-arm approach is, unsurprisingly, a less good one than their 'torque-per-bin' approach.

The second is that they are often based on experimental fits that could implicitly account for such lost energy.

[64] Which can, actually, be both retarding and driving torques depending on incident angle.

[65] Except for [Govender and Powell, 2006] who uses detailed kinematics from biplanar x-ray imaging to obtain correlations between the easily-identifiable CoC of a charge and its centre of mass and then uses these correlations in the same way.

[66] All big stretches.

The second interpretation of the power drawn by the charge- as the gravitational potential and kinetic energy imparted to the charge by the mill- is the one adopted by Morrell to produce his seminal power draw model[Morell, 1992]. To do this, Morrell used streak photographs to obtain the positions of the toe, shoulder and CoC of the charge as well as the tangential velocity of layers at various radial distances from the centre of the mill. He fitted functions of mill speed and load to variations in the positions of these features and to the shear rates in layers in the rising region, and used these to write down a form for the rate of transfer of gravitational potential and kinetic energy to the charge by the mill. I have worked through his model in Appendix B.

The final interpretation of the power drawn by a tumbling mill is as the energy dissipated by the charge in collisions. I think that it is clear that this could not be a complete interpretation, since work must clearly be done to maintain the charge in its state of motion. However, I believe that coupling this contribution to the power draw with that of the motion, could make up the underprediction that I hypothesised for purely motion-based models.

The drawback with any approach based on the energy dissipated in the charge is that there is no way to measure this dissipation directly. Such detailed information is likely only available from DEM simulations. [Cleary, 1998] points out, however, that interactions in DEM are governed by contact models which may not approximate the true situation as well as necessary. This is an area of active research.

3.3.6 The drivers of granular flow in tumbling mills

The steady state properties of the bulk charge- the power drawn by the charge, the position of the CoC and the shape of the free surface of the charge- depend at least on the angular velocity of the drum, the amount of charge in the drum, the geometry and material properties of the shell, and on properties of the grains making up the charge. The angular velocity and filling of the drum affect the shape of the charge in intuitive ways, as do the properties of the shell, but the effect of the composition of the charge on these features is more complicated.

In particular, the non-regularity of composition of the granular material in a rotating drum results in segregation of the charge by size, shape, density, and so on. In this work, however, every attempt has been made to isolate and control for these effects. I will thus confine my discussion to the effects of rotational speed and mill load on the charge behaviour.

The variation in charge shape with mill rotational speed

[Boateng and Barr, 1996], [Mellmann, 2001] and [Ding et al., 2002] all agree on the evolution of the bulk free surface of the charge with rotational speed. It begins as a straight line at the angle of repose of the material, slowly begins to develop an S-shape with increasing speed[Rajchenbach, 1990], which erodes into a concave shape as more and more charge is flung into the in-flight region and less enters the active region. Finally, once the mill has reached critical speed, charge begins to centrifuge, with the layer of centrifuging charge increasing with further increases in rotational speed[Cleary, 1998].

The variation in charge shape with mill load

The effect of increasing the load in a tumbling mill (at the same rotational speed) is to flatten its bulk free surface; to delay the onset of each new rolling mode[67].

[67] See Section 3.2.3.

It is constructive to consider the evolution of the shape of the charge with decreasing load, here following [Cleary, 1998].

As the load decreases at constant speed, the bulk free surface becomes less and less S-shaped as less and less material is available to enter the active region[68]. The bulk region thus becomes thinner and thinner.

The variation in the charge features with rotational speed

As the rotational speed of a mill increases, the height of its shoulder increases, dragging with it the CoC and CoM of the charge. At the same time, the toe of the charge moves down. It does so less quickly than the shoulder moves up, though, leading to a stretching out of the charge[Cleary, 1998].

This thinning of the bulk region of the charge is exacerbated by the larger proportion of the charge entering the in-flight region at higher speed. This leads to an increasing radial position of the CoC of the charge, but a decreasing radial position of the CoM[Govender and Powell, 2006]. [Dong and Moys, 2003] call this the 'upward and inward' motion of the CoM with increasing speed.

The variation in the charge features with mill load

Decreasing mill load increases the radial positions of the CoC and CoM of the charge- pushes them out towards the shell- and increases their angular positions as discussed above.

The stretching out of the bulk region with decreasing load, also discussed above, is due to the angular position of the shoulder rising more quickly than the toe falls.

The variation in shear rates with mill load and rotational speed

The thinning of the bulk region with increasing speed or decreasing load has an effect on the shear rates in the charge.

Recall that the outermost layer of the charge in contact with the mill shell moves at the tangential velocity of the mill, and that the layer of charge along the equilibrium surface has zero tangential velocity. Recall too that the shear rate is given by $\dot{\gamma} = \frac{d\vec{v}_t}{dr}$. Since the difference in velocities between the outermost layer and that of the equilibrium surface remains the same, while the distance over which it changes has reduced, the shear rate in the rising region must increase with increased mill speed or decreased mill load.

Since the shoulder of the charge moves downward only slowly with decreasing load, the velocity of material in the outermost flowing layer of the active region also decreases fairly slowly, allowing a similar increased shear rate argument to be made. This is complicated, however, by charge dilation and the complete fluidisation of the descending charge at some threshold.

The variation in power draw with mill load and rotational speed

[Bbosa et al., 2011] found an increase in the power drawn by a mill with increasing rotational speed. This trend is borne out by the results of, for instance, [Lidell and Moys, 1988], [Cleary, 1998], [Dong and Moys, 2003] and [Govender and Powell, 2006], who all saw an additional feature.

[68] At very low loads there is no active region as all descending charge enters the in-flight region.

All of these researchers found that the power drawn by a tumbling mill increases with increasing speed up to a maximum[69], and then drops off. [Cleary, 1998] showed that this was due to an increasing torque on the shell due to impacts, which gradually become shielded by the layers of charge that have either centrifuged or impacted higher up in the mill and then rolled down to the toe.

[Cleary, 1998] also explained this drop in terms of the CoM-based torque-arm approximation; *viz* that as more and more charge enters the cataracting regime, the charge becomes less asymmetric and thus requires a smaller torque to maintain its position.

Increasing the mill load generally increases the power drawn by the mill by increasing the mass of material that must be moved. This effect can be dealt with by considering the specific power draw- the power draw per unit mass of charge. Doing so allows one to isolate the effect of rolling mode on the power draw. Whereas the power drawn by a charge of increasing mass increases towards the maximum for a completely-filled mill, the specific power draw shows the same peaking phenomenon as does the power drawn by increasingly fast rotation.

The structure of the power curves are more complicated than presented here, and are used in the design and optimisation of mills, and in the optimisation of their operation. I will not consider this further.

3.4 Summary

In this chapter I have conducted a critical review of the existing literature on the motion of granular material in rotating drums, especially with application to the minerals processing industry. For the sake of focus, I have not dealt with the extremely important topics of segregation of the granular material in the axial transport of material through the drum. This is because in this work I will focus on the transaxial motion of charge in batch mode tumbling mills, and will try to control for effects other than those due to the operating conditions of the mills. In Chapter 4 I will describe the laboratory-scale tumbling mills that I have used for this work.

[69] Variously between 70% and 85% of critical speed.

References

[Bbosa et al., 2011] Bbosa, L., Govender, I., Mainza, A., and Powell, M. (2011). Power draw estimations in experimental tumbling mills using pept. *Minerals Engineering*, 24:319–324.

[Boateng and Barr, 1996] Boateng, A. and Barr, P. (1996). Modelling of particle mixing and segregation in the transverse plane of a rotary kiln. *Chemical Engineering Science*, 51:4167–4181.

[Boateng and Barr, 1997] Boateng, A. and Barr, P. (1997). Granular flow behaviour in the transverse plane of a partially filled rotating cylinder. *Journal of Fluid Mechanics*, 330:233–249.

[Bond, 1961] Bond, F. (1961). Crushing and grinding calculations part i and ii. *British Chemical Engineering*, 6(6):xxx.

[Buffler et al., 2011] Buffler, A., Govender, I., Cilliers, J., Parker, D., Franzidis, J.-P., Mainza, A., Newman, R., Powell, M., and van der Westhuizen, A. (2011). Pept cape town: a new positron emission particle tracking facility at ithemba labs. *Minerals Engineering*, 24:261–266.

[Cleary, 1998] Cleary, P. (1998). Predicting charge motion, power draw, segregation, wear and particle breakage in ball mills using discrete element methods. *Minerals Engineering*, 11:1061–1080.

[Cleary, 2001] Cleary, P. (2001). Charge behaviour and power consumption in ball mills: Sensitivity to mill operating conditions, liner geometry and charge composition. *International Journal of Mineral Processing*, 63:79–114.

[Cleary et al., 2003] Cleary, P. W., Morrison, R., and Morrell, S. (2003). Comparison of dem and experiment for a scale model sag mill. *International Journal of Mineral Processing*, 68:129–165.

[Ding et al., 2002] Ding, Y., Forster, R., Seville, J., and Parker, D. (2002). Granular motion in rotating drums: bed turnover time and slumpingrolling transition. *Powder Technology*, 124:18 27.

[Ding et al., 2001a] Ding, Y. L., Forster, R. N., Seville, J. P. K., and Parker, D. J. (2001a). Scaling relationships for rotating drums. *Chemical Engineering Science*, 56:37373750.

[Ding et al., 2001b] Ding, Y. L., Seville, J. P. K., Forster, R., and Parker, D. J. (2001b). Solids motion in rolling mode rotating drums operated at low to medium rotational speeds. *Chemical Engineering Science*, 56:1769–1780.

[Dong and Moys, 2003] Dong, H. and Moys, M. (2003). Load behavior and mill power. *International Journal of Mineral Processing*, 69:11–28.

[Dury et al., 1998] Dury, C., Ristow, G., Moss, J., and Nakagawa, M. (1998). Boundary effects on the angle of repose in rotating cylinders. *Physical Review E*, 57(4):4491–4497.

[El-Rahman et al., 2001] El-Rahman, M. A., Mishra, B., and Rajamani, R. (2001). Industrial tumbling mill power prediction using the discrete element method. *Minerals Engineering*, 14:1321–1328.

[Elperin and Vikhansky, 2000] Elperin, T. and Vikhansky, A. (2000). Granular flow in a three-dimensional rotating cylinder. *Physical Review E*, 62(3):4446–4449.

[Govender et al., 2011a] Govender, I., Mangesana, N., Mainza, A., and Franzidis, J.-P. (2011a). Measurement of shear rates in a laboratory tumbling mill. *Minerals Engineering*, 24:225–229.

[Govender and Powell, 2006] Govender, I. and Powell, M. (2006). An empirical power model derived from 3d particle tracking experiments. *Minerals Engineering*, 19:1005–1012.

[Govender et al., 2001] Govender, I., Powell, M., and Nurick, G. (2001). 3d particle tracking: A rigorous technique for verifying dem. *Minerals Engineering*, 14(10):1329–1340.

[Govender et al., 2011b] Govender, I., Tupper, G., and Mainza, A. (2011b). Towards a mechanistic model for slurry transport in tumbling mills. *Minerals Engineering*, 24:230–235.

[Harris et al., 1985] Harris, C., Schnock, E., and Arbiter, N. (1985). Grinding mill power consumption. *Mineral Processing and Extractive Metallurgy Review*, 1:297–345.

[Henein et al., 1983] Henein, H., Brimacombe, J., and Watson, A. (1983). Experimental study of transverse bed motion in rotary kilns. *Metallurgical and materials transactions B*, 14(2):191–205.

[Hogg et al., 1972] Hogg, R., , and Fuerstenau, D. (1972). Power relationships for tumbling mills. *Transaction of SME/AIME*, 252:418–423.

[Ingram et al., 2005] Ingram, A., Seville, J., Parker, D., Fan, X., and Forster, R. (2005). Axial and radial dispersion in rolling mode rotating drums. *Powder Technology*, 158:76–91.

[Jain et al., 2002] Jain, N., Ottino, J., and Lueptow, R. (2002). An experimental study of the flowing granular layer in a rotating tumbler. *Physics of fluids*, 14:572–582.

[Kallon et al., 2011] Kallon, D., Govender, I., and Mainza, A. (2011). Circulation rate modelling of charge using positron emission particle tracking. *Minerals Engineering*, 24:282–289.

[Leung, 1987] Leung, K. (1987). *An energy-based, ore-specific model for autogeneous and semi-autogeneous grinding*. PhD thesis, University of Queensland.

[Lidell and Moys, 1988] Lidell, K. and Moys, M. (1988). The effects of mill speed and filling on the behaviour of the load in a rotary grinding mill. *Journal of the South African Institute of Mining and Metallurgy*, 88:49–57.

[Lim et al., 2003] Lim, S.-Y., Davidson, J., Forster, R., Parker, D., Scott, D., and Seville, J. (2003). Avalanching of granular material in a horizontal slowly rotating cylinder: Pept studies. *Powder Technology*, 138:25–30.

[McBride et al., 2004] McBride, A., Govender, I., Powell, M., and Cloete, T. (2004). Contributions to the experimental validation of the discrete element method applied to tumbling mills. *Engineering Computations*, 21:119–136.

[Mellmann, 2001] Mellmann, J. (2001). The transvers motion of solids in rotating cylinders- forms of motion and transition behaviour. *Powder Technology*, 118:251–270.

[Mishra and Rajamani, 1994] Mishra, B. and Rajamani, R. (1994). Simulation of charge motion in ball mills: Part 1. experimental verifications. *International Journal of Mineral Processing*, 40:171–186.

[Morell, 1992] Morell, S. (1992). Prediction of grinding-mill power. *Transactions of the Institution of Mining and Metallurgy Section C: Mineral Processing Extraction and Metallurgy*, 101:C25–C32.

[Nakagawa et al., 1993] Nakagawa, M., Altobelli, S., Caprihan, A., Fukushima, E., and Jeong, E. (1993). Non-invasive measurements of granular flows by magnetic resonance imaging. *Experiments in Fluids*, 16(1):54–60.

[Napier-Munn et al., 2005] Napier-Munn, T., Morrell, S., Morrison, R., and Kojovic, T. (2005). *Mineral Comminution Circuits*. The Julis Kruttscnitt Mineral Research Centre.

[Powell and McBride, 2004] Powell, M. and McBride, A. (2004). A three-dimensional analysis of media motion and grinding regions in mills. *Minerals Engineering*, 17:1099–1109.

[Powell and Nurick, 1996a] Powell, M. and Nurick, G. (1996a). A study of charge motion in rotary mills part 1- extension of the theory. *Minerals Engineering*, 9:259–268.

[Powell and Nurick, 1996b] Powell, M. and Nurick, G. (1996b). A study of charge motion in rotary mills part 2- experimental work. *Minerals Engineering*, 9:343–350.

[Powell and Nurick, 1996c] Powell, M. and Nurick, G. (1996c). A study of charge motion in rotary mills part 3- analysis of results. *Minerals Engineering*, 9:399–418.

[Rajchenbach, 1990] Rajchenbach, J. (1990). Flow in powders: From discrete avalanches to continuous regime. *Physical Review Letters*, 65(18):2221–2224.

[Rogovin and Herbst, 1989] Rogovin, Z. and Herbst, J. (1989). Charge motion in a semi-autogeneous grinding mill. *Minerals and Metallurgical Processing*, 6:18–23.

[Rose and Sullivan, 1957] Rose, H. and Sullivan, R. (1957). *A treatise on the Internal Mechanics of Ball, Tube and Rod mills*. Constable, London.

[Santomaso et al., 2003] Santomaso, A., Ding, Y., Lickiss, J., and York, D. (2003). Investigation of the granular behaviour in a rotating drum operated over a wide range of rotational speed. *Transactions of the Institute of Chemical Engineers*, 81:936–945.

[Sichalwe et al., 2011] Sichalwe, K., Govender, I., and Mainza, A. (2011). Characterising porosity of multi-component mixtures in rotary mills. *Minerals Engineering*, 24:276–281.

[Taberlet et al., 2006] Taberlet, N., Richard, P., and hinch, E. J. (2006). S shape of a granular pile in a rotating drum. *Physical Review E*, 73:050301–1–4.

[Tordesillas and Arber, 2005] Tordesillas, A. and Arber, D. (2005). Capturing the s in segregation: A simple model of flowing granular mixtures in rotating drums. *International Journal of Mathematical Education in Science and Technology*, 36(8):861–877.

[Watanabe, 1999] Watanabe, H. (1999). Critical rotation speed for ball-milling. *Powder Technology*, 104:95–99.

[Wills, 2001] Wills, B. A. (2001). *Mineral Processing Technology*. Butterworth Heinemann, 6 edition.

[Zik et al., 1994] Zik, O., Levine, D., Lipson, S., Shtrikman, S., and Stavans, J. (1994). Rotationally induced segregation of granular materials. *Physical Review Letters*, 73(5):644–647.

Part II

Experiment and Analysis

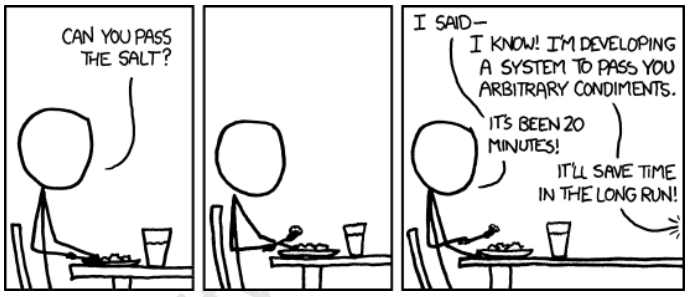

www.xkcd.com

Chapter 4

Experiment

Figure 3.7 shows a schematic of the sort of full-scale tumbling mill used in the mining industry. In this work, I use three laboratory-scale mills of various levels of realism to approximate such a mill.

4.1 The $140mm$ mill

The first of these laboratory scale mill is the simplest. It is a basic square mill- its internal diameter is the same as its internal length- of $140mm$ diameter. Figure 4.1a shows the mill in its frame, and Figure 4.1b shows the inside of the mill and, in particular, its nylon lifter bars.

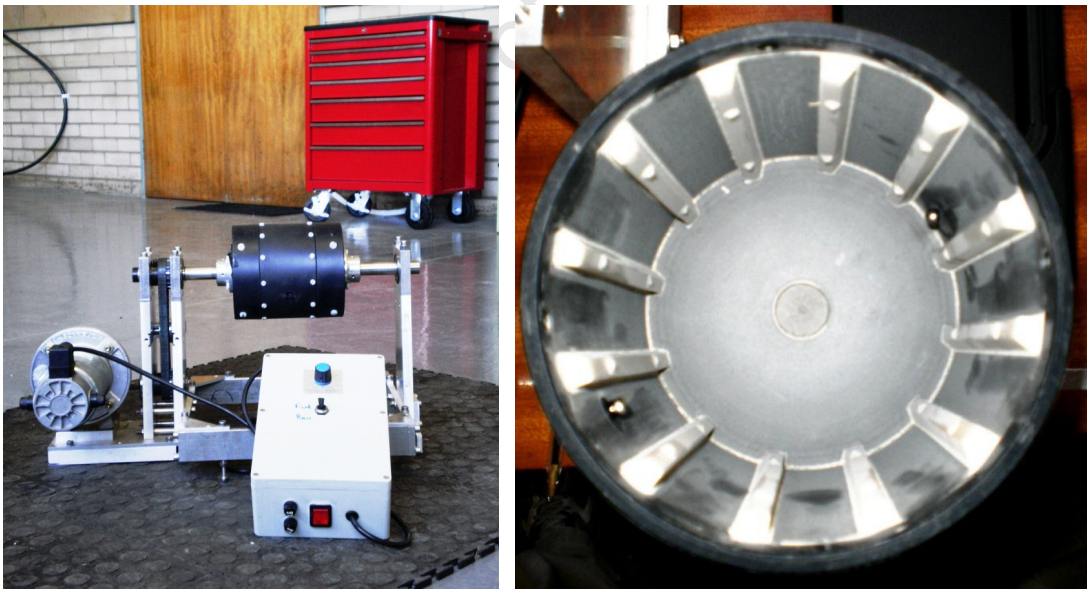

(a) The 'x-ray' mill. **(b)** Inside the mill

Figure 4.1: Two views of the $140mm$ mill- with its motor and motor controller (left), and of its lifters and end-wall (right).

The mill is made of a cylindrical central body to which smooth caps are bolted on each end- see Figure 4.1a. Both the body and the caps are made of high-density polyethylene (HDPE). In Figure 4.1b one smooth- or very nearly smooth- end-face of the mill is visible.

The central body of has been fitted with 12 nylon lifter bars as shown also in Figure 4.1b. Figure 4.2 shows a profile of one of the lifter bars. In this work, chamfered lifters of uniform cross section

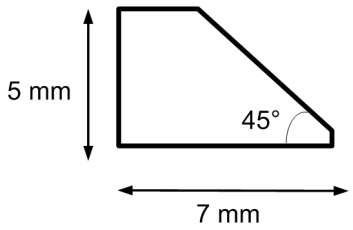

Figure 4.2: A profile of the lifter bars used in the 140mm mill.

are used. Such lifters can be described in terms of a base length, a height and a chamfer or lifter face angle. In this case, these are 7mm, 5mm and 45° respectively.

The lifter bars are removable, as can be seen in Figure 4.1b, so that they can be interchanged with others of different heights, face angles and so on. However, this was not done in this work.

Figure 4.1a shows the 140mm mill in its frame. On the left is its motor- a 90W electric motor fitted with 40 : 1 reduction gearbox. In the foreground of Figure 4.1a is the motor controller box which allows the speed and direction of the motor's rotation to be controlled.

The 140mm mill is often called the 'x-ray mill' because it was designed for use in biplanar x-ray imaging experiments. To be so used, the mill had to be of a certain maximum size, it had to be made of a non-attenuating material, and its body had to be at some distance from the motor assembly. This is why the mill is not directly but rather belt-driven. The frame, drive system and removable mill, however, turn out to be a versatile piece of equipment for conducting other positron emission particle tracking (PEPT) experiments.

4.2 The 300mm mills

The 300mm mills are a good deal more realistic than the 140mm one. They are roughly square mills of diameter 300mm, made from HDPE with nylon lifter bars. Unlike the batch 140mm mill, however, they are designed for material to flow through them in continuous mode.

As such they have inlet and outlet (or feed and discharge) trunnions, discharge grates and pulp chamber.

The 'old' 300mm mill was the first used for PEPT experiments, including the early scoping experiments with real charge and slurry. The 'new' 300mm was designed as an improvement on the 'old' one, with- among other things- a different discharge grate and transparent end-windows for better visibility of the tumbling charge.

4.2.1 The 'old' 300mm mill

Figure 4.3 shows the 'old' 300mm mill in profile, with the feed end on the left and the discharge end on the right. In the figure, the bolts that hold its interchangeable lifters in place have been coated with silicon to make the mill water-tight. Figure 4.7 is a schematic of the 'old' 300mm mill based not on technical drawings of the mill, but on my measurements of it. Technical drawings of both 300mm mills are given in Appendix C. Although the 'old' 300mm mill is a roughly square mill, the internal length of its main chamber is actually only 270mm. The remainder of its length is taken up by its pulp chamber. Figure 4.4a is a view of the inside of the 'old' 300mm mill showing its aluminium lifters and its discharge grate. Figure 4.5 shows a selection of the lifters of different heights and face angles that can be fitted to the 'old' mill. The discharge grate visible in Figure

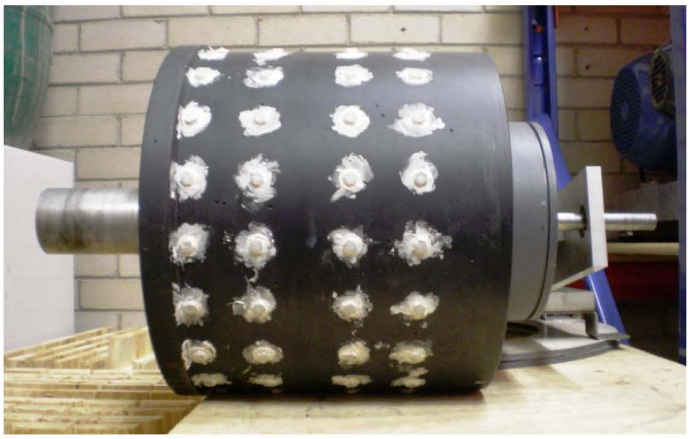

Figure 4.3: A profile of the old 300mm mill.

(a) Discharge grate. **(b)** Pulp lifters. **(c)** Discharge cone.

Figure 4.4: The pulp chamber of the old 300mm mill, showing its discharge grate (left), pulp lifters (centre), and discharge cone (right).

4.4 divides the main chamber of the 'old' 300mm mill from its pulp chamber. Figure 4.4 shows the an effectively exploded view of this pulp chamber. Figure 4.4b shows the nylon pulp lifters that funnel slurry and pulp towards the discharge cone shown in Figure 4.4c.

The discharge grate visible from either side in Figures 4.4a and 4.4b consists of a HDPE plate through which are drilled 3mm diameter holes. These holes are arranged as shown in Figure 4.6a. In particular, Figure 4.6a shows a segment between two pulp lifters. The holes in the discharge grate are arranged in concentric rings about the discharge cone. The inner four rings are relatively widely spaced- four rows of four holes between each two pulp lifters- and the outer four more closely spaced- four rows of 11 holes between each two pulp lifters. The open area of the discharge grate was varied in these experiments by blocking some or all of the holes with masking tape.

Figure 4.5: A selection of lifters for the 300mm mills.

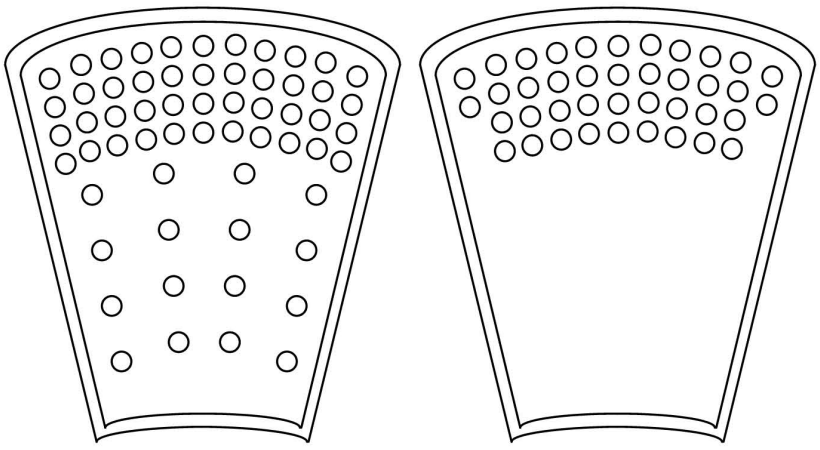

(a) Old 300mm mill **(b)** New 300mm mill

Figure 4.6: Examples of the discharge grates of the old (left) and new (right) 300mm mills.

4.2.2 The 'new' 300mm mill

Figure 4.8 is a schematic of the 'new' 300mm mill, and Figure 4.9 is a photograph of it in profile, with its feed end on the left and its discharge end on the right. An access hatch- one of the most useful improvements in the 'new' from the 'old' 300mm mill- is visible in this figure.

Figure 4.10 shows another important improvement in the 'new' 300mm mill- large perspex end-windows, which make it possible to watch the motion of the tumbling charge while the mill is in motion- see Figure 4.11.

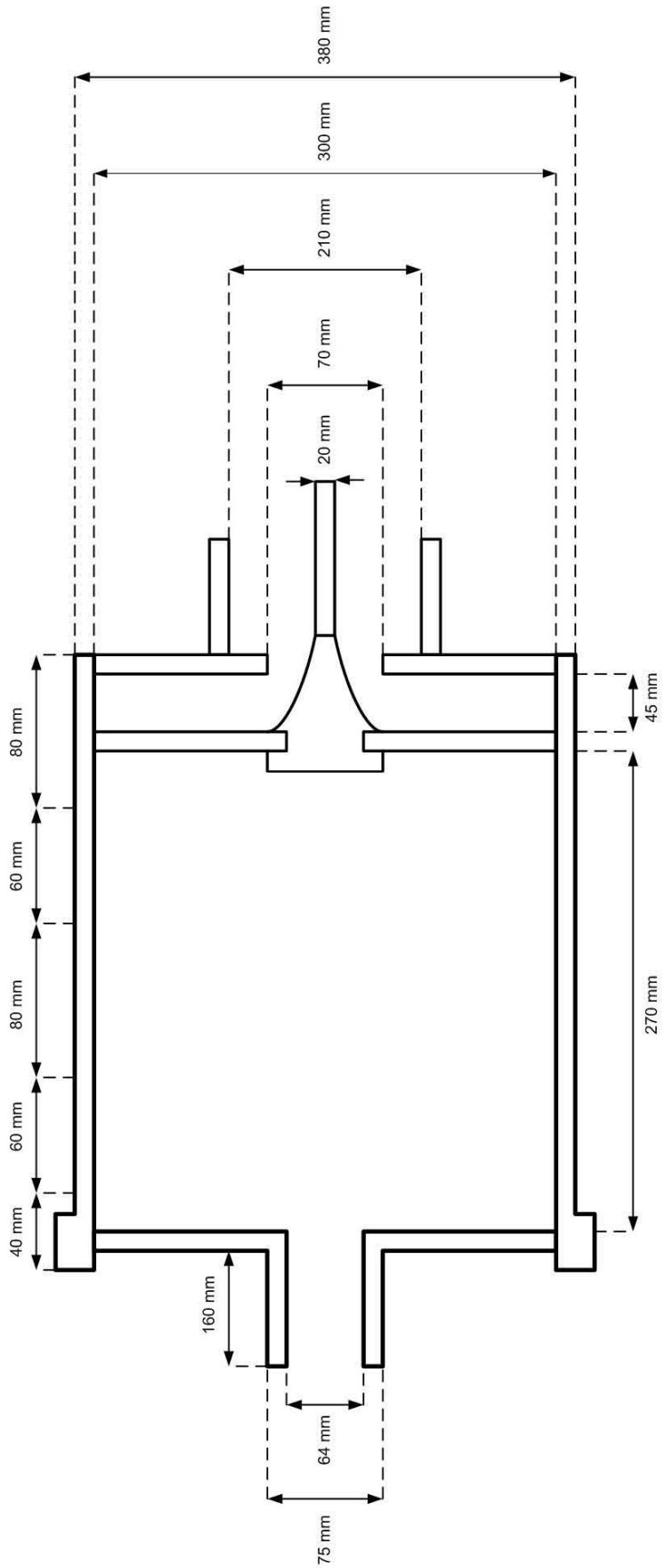

Figure 4.7: A schematic of the old 300mm mill with dimensions.

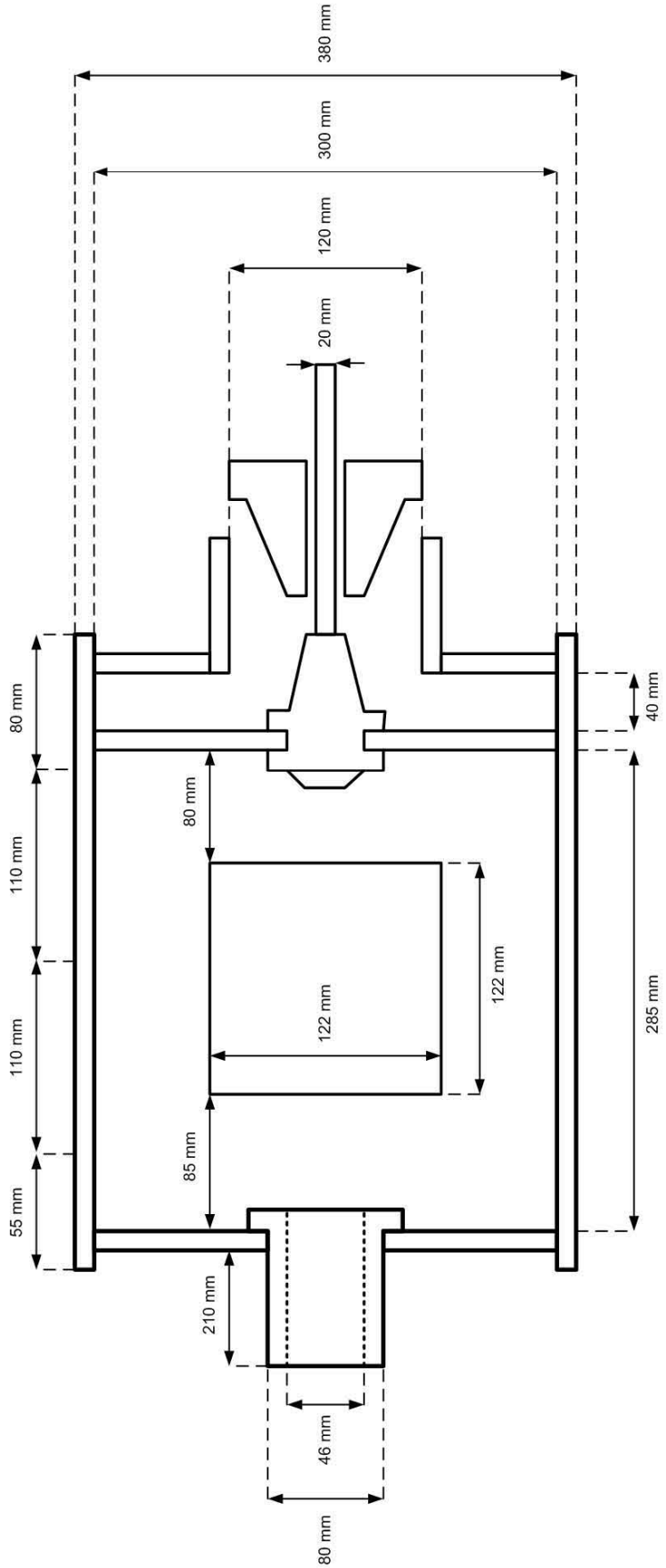

Figure 4.8: A schematic of the new 300mm mill with dimensions.

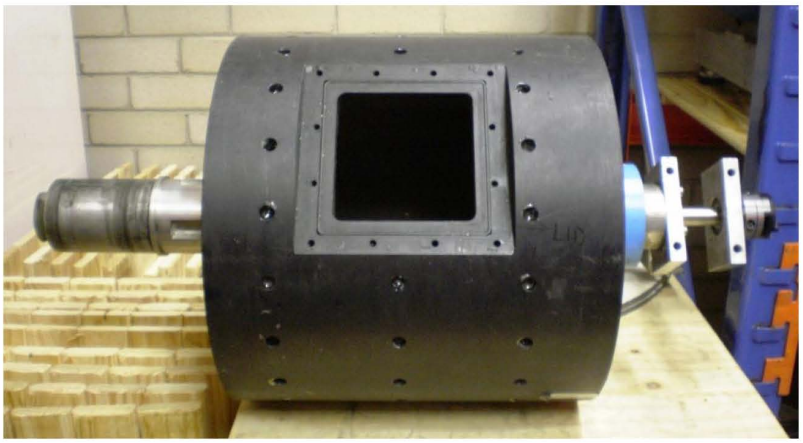

Figure 4.9: A profile of the new 300mm mill.

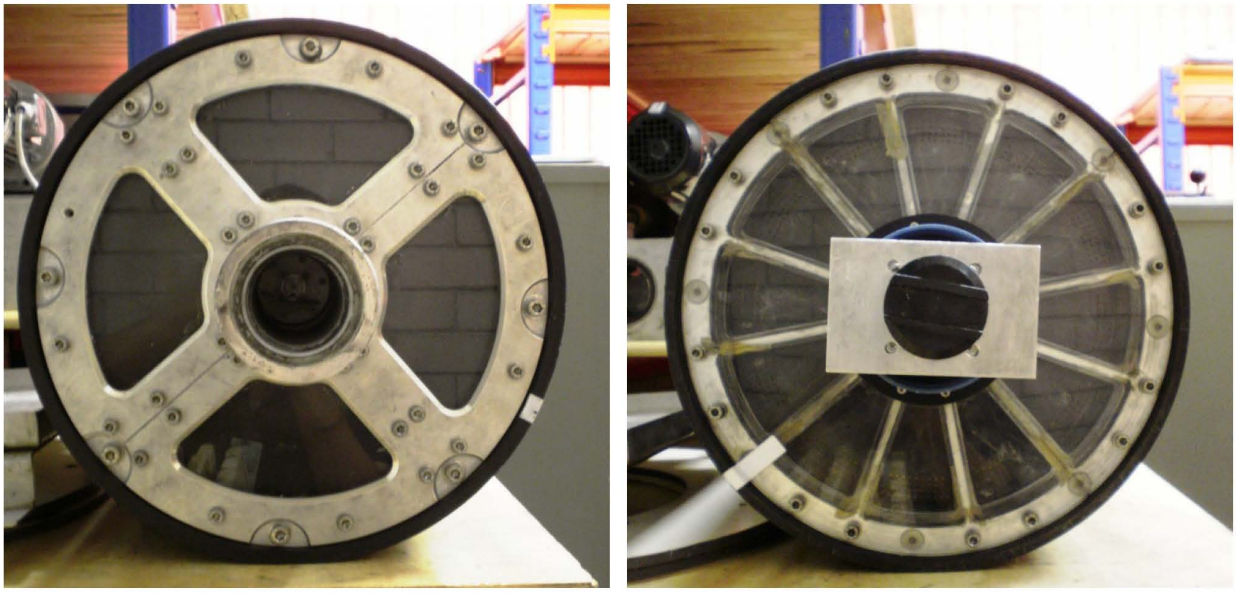

(a) Feed end. **(b)** Discharge end.

Figure 4.10: The feed (left) and discharge (right) ends of the new 300mm mill.

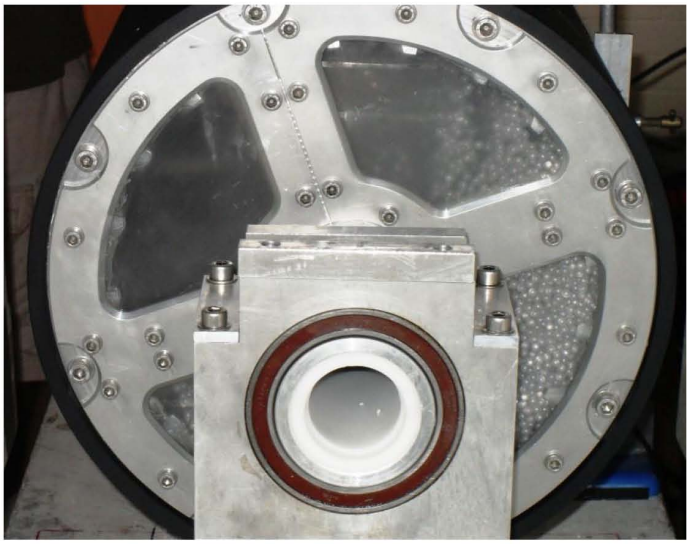

Figure 4.11: A charge of glass beads seen tumbling through the end-windows of the new 300mm mill.

In Figures 4.8 and 4.12b, the 'new' 300mm mill's much more elaborate discharge cone and pulp lifter system is visible. Also visible on the discharge trunnion is a strip of reflective tape used, with an optical tachometer, to determine the mill's rotational speed. Its discharge grate, however, is

(a) Discharge grate. **(b)** Discharge cone.

Figure 4.12: The discharge grate (left) and discharge cone (right) of the new 300mm mill.

much less elaborate than that of the 'old' 300mm mill, consisting only of four rows of holes around the edge of the mill shell, as seen in Figure 4.6b.

4.2.3 Mill motors and power draw

Figure 4.13a shows the 'old' 300mm mill in the field of view of a PEPT camera. Extending out from the mill towards the point of view of the photographer is its drive chain, culminating in its large, blue motor and gearbox. Between the mill and the motor is a torque sensor- shown in Figure 4.13b- from which the power drawn by the rotating mill is obtained. Figure 4.14 shows a more side-on view of the 'new' 300mm mill in the field of view of the PEPT camera. Visible in this figure are not only the mill, motor and torque sensor, but also the logging computer to which the torque sensor is connected during a run.

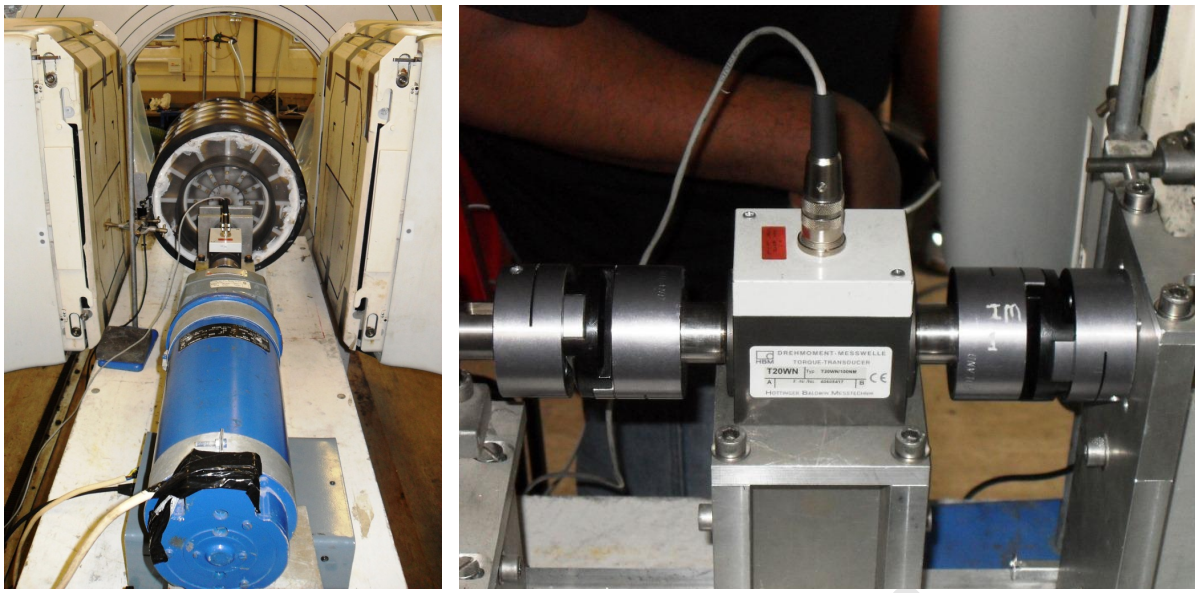

(a) Motor assembly **(b)** The torque sensor.

Figure 4.13: The drive of the old 300mm mill, showing its motor, gearbox and driveshaft (left), and the inline torque sensor (right).

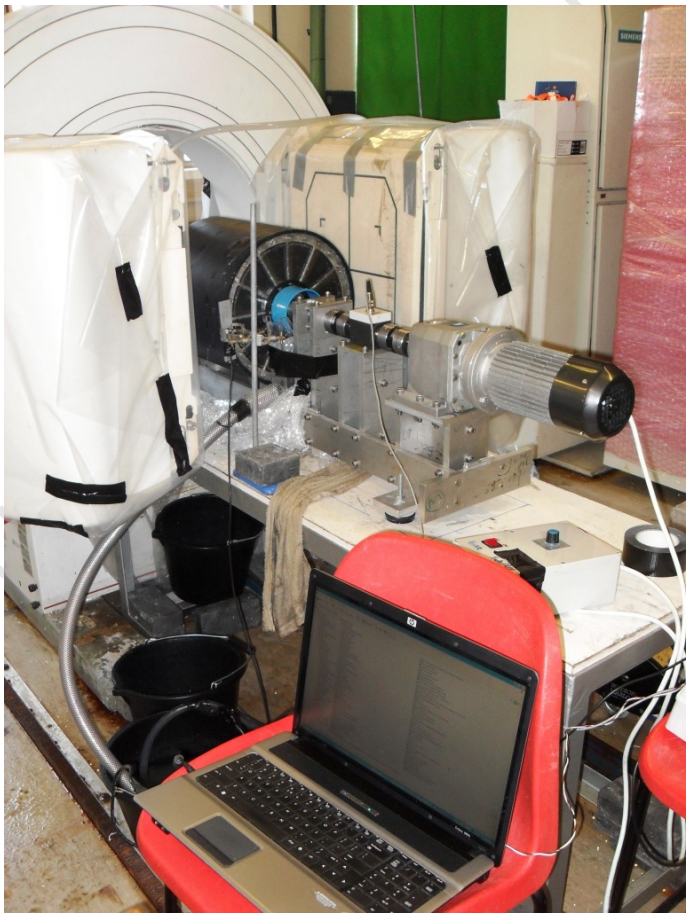

Figure 4.14: The drive of the new 300mm mill showing the torque sensor and analysis computer.

(a) The dry charge. **(b)** The wet charge.

Figure 4.15: A charge of conditioned bluestone, dry (left) and in a slurry (right).

4.3 The charge

4.3.1 Materials

Three charge materials are used in this work- glass and plastic beads, and bluestone.

In the least realistic of the tumbling mills used here- the $140mm$ mill- only charges of plastic, glass or plastic and glass beads were used.

In the $300mm$ mills, however, not only glass beads, but also a real charge of conditioned bluestone was used. Further, these charges were run dry, with water, and with platinum slurries of various solids fractions. Figure 4.15 shows the bluestone charge in the 'old' $300mm$ mill, both dry and before a run- Figure 4.15a- and with platinum slurry, as seen through the feed trunnion - Figure 4.15b.

The glass charge used in this work was made up of laboratory standard, high sphericity beads. Glass beads were chosen for their uniformity in shape, density and material properties; in an effort to drastically simplify the system under study. Although it was the intention to investigate only the motion and not the grinding of charge in these simplified experiments, it turned out that at aggressive speeds and loads some grinding could not be avoided- see Figure 4.16.

4.3.2 Distributions

The first charge ever investigated by PEPT was the bluestone one. It was constituted according to the industrially-based Rosin-Rammler size distribution shown in Figure 4.17. Subsequent glass and plastic charges[1] were constituted according to this same distribution.

In addition to the Rosin-Rammler distribution shown in Figure 4.17, monosize and binary size distributions were also investigated.

[1]For all three mills.

Figure 4.16: Glass beads ground by the new $300mm$ mill.

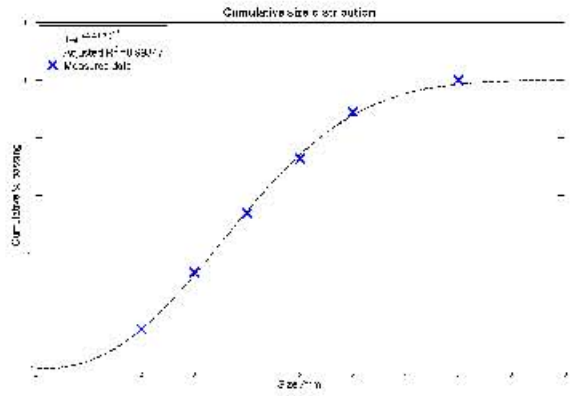

Figure 4.17: The cumulative Rosin-Rammler size distribution used in this work.

4.3.3 Load fraction

The load fraction in a tumbling mill is the volume of the mill occupied by the charge it contains, calculated from its fill level. That is, the quoted load does not take into account the packing fraction, and thus bulk density, of the charge. It is constituted for each experiment in the following way.

Consider a cylinder of diameter D and length L. Its volume is then

$$V_{cylinder} = \frac{1}{4}\pi D^2 L \tag{4.1}$$

Let f be the load fraction of the mill, and η be the packing density of the charge. Then the volume taken up by the charge is

$$V_{charge} = \frac{f\eta}{4}\pi D^2 L \tag{4.2}$$

Suppose that the charge consists of a potentially continuous distribution of sizes $g(d)$, where d is some representative diameter of the particles that constitute the charge. Then the volume of charge of some size-class, d, is just

$$V_d = g(d)V_{charge} = \frac{g(d)f\eta}{4}\pi D^2 L \tag{4.3}$$

This allows the mass contribution of a particular size class to be calculated as

$$m_d = \rho_d g(d)V_{charge} = \frac{\rho_d g(d)f\eta}{4}\pi D^2 L \tag{4.4}$$

assuming that all particles in that size-class are of the same density. If not, a more complex distribution, which is a function of both size and density, $g'(d, \rho_i)$ can be used

$$m_{d,\rho_i} = \rho_i g(d, \rho_i)V_{charge} = \frac{\rho_i g(d, \rho_i)f\eta}{4}\pi D^2 L \tag{4.5}$$

and so on for more and more complicated combinations of particle properties.

Calculating the contributions of classes of particles by mass is a useful way of constituting the charge in practice. However, sometimes- such as when performing a discrete element method (DEM) simulation- it is helpful to calculate the number of each size class. This can be done by assuming spherical particles of volume

$$V_{particle} = \frac{1}{6}\pi d^3 \tag{4.6}$$

then the volume contribution of each size class is

$$V_d = g(d)V_{charge} = NV_{particle} \tag{4.7}$$

where N is the number of particles in size class d, given by

$$\begin{aligned} N &= \frac{g(d)V_{charge}}{V_{particle}} \\ &= \frac{3}{2}g(d)f\eta\frac{d^2 L}{d^3} \end{aligned} \tag{4.8}$$

4.4 Experiments conducted

A summary of the experiments conducted for each mill are given in Tables 4.1, 4.2 and 4.3.

A comprehensive record of the experiments conducted by trip, mill, charge material and distribution, and so on, is given in Appendix D.

Table 4.4 contains a summary of the experiments actually analysed for this work- only the dry ones.

Table 4.1: A summary of the experiments performed on the 140 mm-diameter 'x-ray' mill.

Fill			Load	Speeds	Tracer		Duration
Distribution	**Material**	$^{d}/_{mm}$	**/%**	**/% v_{crit}**	**Mat.**	$^{d}/_{mm}$	
Rosin-Rammler	glass	2:6,8	12.5:12.5:50.0	40:10:110	glass	2:6,8	short
			37.5	70		2	medium
			50	65:10:85		8	short
binary	glass/plastic	3,5	10:10:40	40:10:110	plastic	3,5	short
			20:10:40	60:10:90	glass	3,5	
binary	plastic	3,5	20:10:40	60:10:90	plastic	3,5	short
			30	60:10:80			long

Table 4.2: A summary of the experiments performed on the 'old' 300 mm mill.

Lifter		Fill				Load	Speeds	Tracer		Dur.
$\theta/^{\circ}$	$^{h}/_{mm}$	**Distr.**	**fl.**	**Mat.**	$^{d}/_{mm}$	**/%**	**/% v_{crit}**	**Mat.**	$^{d}/_{mm}$	
60	19	R-R	dry	stone	2-8	24.64	65,75,80	stone	6x2	short
90							65,75:5:95			
60, 90						30:5:40				
90						23.6	90,95		5	
60, 90						15, 35, 40	65,75:5:95		2	
90	5		30%			40	55,65:5:100		1	
							75,85	Cu		
			dry	glass	2-8	12.5:12.5:50	60,70,75,80,90	glass	2-8	
						31.25				
						12.5	85		5	
						37.5	40, 50, 100, 120		2	
						43.5	60,70,75,80,90			
						50	30:10:50,100,120		6, 8	
60						31.25	60,75		2-8	long
		mono			3		60,75		3	
					5		50,60,75		5	

Table 4.3: A summary of the experiments performed on the 'new' 300 mm mill.

Fill				Load	Speeds	Tracer		Dur.
Distr.	**Fluid**	**Mat.**	$^{d}/_{mm}$	**/%**	**/% v_{crit}**	**Mat.**	$^{d}/_{mm}$	
mono	dry	glass	3	31.25	60, 75	glass	3.0	long
			5		31, 60, 75		5.0	
	wet		3		75	glass	3.0	
			5		75	resin	0.5	
					31, 50, 60, 75	glass	5.0	
	20:10:40% conc		5		60, 75	glass	5.0	
	20% conc				75	resin	0.5	
	20:10:40% conc				60, 75	stone	1.0	

Table 4.4: A summary of the experiments performed with a 'dry' charge.

Mill	Lifter /	Lifter h/mm	Fill Distr.	Fill Mat.	Fill d /mm	Load /%	Speeds /%	Tracer Mat.	Tracer d /mm	Dur.
X-ray	45	5	Rosin-Rammler	glass	2:6,8	12.5:12.5:50.0	40:10:110	glass	2:6,8	short
						37.5	70		2	medium
						50	65:10:85		8	short
			binary	glass/plastic	3,5	10:10:40	40:10:110	plastic	3,5	short
						20:10:40	60:10:90	glass	3,5	
			binary	plastic	3,5	20:10:40	60:10:90	plastic	3,5	short
						30	60:10:80			long
New 300 mm	60	5	mono	glass	3	31.25	60, 75	glass	3	long
					5		31, 60, 75		5	
Old 300 mm	60	19	Rosin-Rammler	stone	2-8	24.64	65, 75, 80	stone	6x2	short
	90						65, 75:5:95			
	60, 90					30:5:40				
	90					23.6	90, 95		5	
	60,90					15, 35, 40	65,75:5:95		2	
	90	5		glass	2-8	12.5:12.5:50	60,70,75,80,90	glass	2-8	
						31.25				
						12.5	85		5	
						37.5	40, 50, 100, 120		2	
						43.5	60,70,75,80,90			
						50	30:10:50,100,120		6, 8	
	60		mono		3	31.25	60,75		3	long
					5		50,60,75		5	

4.5 Preprocessing the PEPT data

The experiments listed in Tables 4.1, 4.2 and 4.3 were all triangulated according to the procedure given in Section 2.3.2, optimised according to the procedure illustrated in Appendix E. The results were then preprocessed according to the procedures given in Appendix F, and analysed as described in Chapter 5.

4.6 Summary

In this chapter I have described in detail the laboratory-scale tumbling mills that I have investigated using the PEPT technique described in Chapter 2. I have described the efforts made to approximate some of the more important features of tumbling mills- as mentioned in Chapter 3- in these laboratory-scale mills, and the steps taken to constitute a charge representative of an industrial one. I finished by summarising the experiments performed with each of theses mills and the preprocessing applied to the resulting data. In Chapter 5 I will describe the analysis routines that I apply to the Lagrangian particle tracking data thus obtained.

References

Chapter 5

Analysis

5.1 Lagrangian particle tracking techniques

Single particle tracking techniques such as positron emission particle tracking (PEPT), biplanar x-ray imaging and particle image velocimetry (PIV) are often called *Lagrangian* particle tracking techniques. This is in analogy with the Lagrangian reference frame of fluid mechanics in which the flow field of a fluid is specified in terms of the behaviour of moving parcels, or pseudoparticles, of fluid over time. Lagrangian particle tracking techniques are thus so-called because they build up the trajectories of single particles moving in some continua. The alternative case, in which the flow field of a fluid is specified in terms of the behaviour of that fluid at fixed spatial reference points, is called the Eulerian reference frame. The Eulerian approach is often said to be concerned with the overall behaviour of a system and the Lagrangian with that of its constituent elements.[1]

5.1.1 Kinematics from Lagrangian particle tracking techniques

The particle trajectories obtained from Lagrangian particle tracking techniques consist of a series of particle locations at given times, $\vec{s}(t) = (\vec{x}(t), \vec{y}(t), \vec{z}(t))$. This data can be used to obtain the instantaneous kinematics of the tracked particle along its trajectory. In cases where the particle's trajectory is sampled at fixed (and sufficiently small) time intervals Δt, its velocity and acceleration at those times can be calculated using simple finite difference methods. If, however, the time intervals Δt_i between locations are either not uniform or not sufficiently small, then the data must first be interpolated before the particle's velocities and accelerations can be obtained.

There are two ways that one might use the interpolated data to obtain the particle's kinematics. Both require the explicit calculation of an interpolating function. The first, and more computationally-expensive way is to evaluate the interpolating polynomials at more frequent, fixed time intervals and then to use an appropriate finite difference method. The second way is to consider the interpolating polynomial an explicit function of the trajectory in terms of time and to then differentiate this function symbolically. In Section 5.3 I explain why I have chosen the latter method.

[1] This distinction is often illustrated by considering Lagrange to be floating down a river in some sort of boat, while Euler watches serenely from the bank. Of course, to build up a complete flow field of the river, several Lagranges would have to compare notes on their separate trips down the river, or several Eulers would have to observe different points along the river. If the river is flowing steadily and hardly changes over time, Lagrange could do this on his own by floating down the river several times, or Euler could do it on his own by sequentially observing the river from different points along its bank. In principle, these two approaches are equivalent, although they have different strengths and weaknesses in practice.

5.2 Interpolation

To simplify the binning algorithm, I have chosen to use polynomials to interpolate the trajectories obtained from Lagrangian particle tracking techniques such as PEPT. These trajectories are of the form $\vec{s}(t) = (\vec{x}(t), \vec{y}(t), \vec{z}(t))$. Since the co-ordinates of the particle in sequential locations vary independently in each dimension, and since the interpolation error is related to the order of the interpolating polynomial (as explained in Section G.1.2 below), it is prudent to interpolate each dimension separately and with as low a degree polynomial as will adequately capture the time variation of that co-ordinate. For ease of implementation, I have chosen to use Lagrangian [2] polynomials as interpolants. By the Fundamental Theorem of Algebra, however, for any set of data points (s_i, t_i) the interpolating polynomial of the least degree is unique, and so this choice is only as good as any other.

In Appendix G I define the interpolating polynomial, give a proof of its uniqueness, and derive an expression for the interpolation error.

5.2.1 Lagrange polynomials

Lagrange polynomials are a convenient form[3] of interpolant for data in which the independent variable, t_i in this case, is non-degenerate. The interpolating polynomial in Lagrange form, $L(t)$, can be written as a linear combination of Lagrange basis polynomials

$$l_i(t) = \prod_{j=0,\ j\neq i}^{n} \frac{t - t_j}{t_i - t_j} = \frac{t - t_0}{t_i - t_0} \cdots \frac{t - t_n}{t_i - t_n} \tag{5.1}$$

such that, in our case,

$$\vec{s}(t) = L_n(t) = \sum_{i=1}^{n} s_i l_i(t) \tag{5.2}$$

5.2.2 Kinematics from interpolated data

An *nth* order polynomial is differentiable $(n-1)$ times. Thus, if we express a tracked particle's location as a polynomial in time, it is possible to obtain by differentiation its velocity and acceleration at all times. So far in this discussion it has been assumed that the particle is located, as it is in PEPT, in Cartesian co-ordinates. If so, it is trivial to convert these to cylindrical or spherical co-ordinates, for instance, and the particle's rectilinear into curvilinear kinematics.

5.2.3 Implementation

To minimise the error and to mitigate oscillatory artefacts like the Runge phenomenon[4], it is important to choose as low order an interpolant as will adequately reproduce the variation in the dataset. For most applications of Lagrangian particle tracking, and certainly for the PEPT and biplanar x-ray imaging cases, the trajectory sampling frequency will be sufficiently high that the tracked particle will have moved only a very short distance between locations. Over extremely short distances, any movement will be approximately linear.

[2] Unrelated to *Lagrangian* particle tracking. Unrelated, even, to Lagrange- Lagrange polynomials were discovered by Euler. They are also unrelated to Eulerian tracking.

[3] As shown in Section G.1.1, there is only actually one possible interpolating polynomial of least degree, which can be written in various *forms*.

[4] See Appendix G.1.2.

If we believe, as I do, that the tracked particle in such cases only moves a very short distance between locations, then using a 2^{nd} or 3^{rd} order interpolation polynomial should capture most of the variation in the particle's location without introducing too much error. Of course, this remains an approximation to the tracked particle's true path, but in chaotic regions of particle motion especially, some smoothing is inevitable and the best we can hope for is to minimise its effect.

It is worth recalling, however, that this interpolation is done independently for each dimension and that even a 2^{nd} order parametric equation can yield some fairly interesting paths when combined with two other 2^{nd} order parametric equations in orthogonal dimensions.

Explicit forms

In this work I have implemented 2^{nd} and 3^{rd}order versions of Lagrange interpolation. In Appendix G.2 I provide explicit forms of these in terms of sample points t_i.

5.3 Binning: Lagrangian particle tracking and the Eulerian reference frame

The Lagrangian approach to particle tracking, based on the trajectory of a tracked particle, is an important and powerful way of investigating the dynamics and kinematics of a system. However, it can often be much more informative to obtain an overall picture of the motion of all of the particles in the system- to adopt the Eulerian reference frame. The key distinction between the two is that in the Lagrangian reference frame the flow field is sampled along the trajectories of tracer particles, whereas in the Eulerian reference frame it is sampled at fixed points in space. Given sufficiently many Lagrangian experiments performed on an ergodic system (See Section 5.3.1), it is possible to aggregated the recovered trajectories and sample them at fixed points in space to obtain a flow field in the Eulerian reference frame[5].

If the system of interest is in, or is sufficiently close to, steady state then it should be possible to obtain such a picture by combining (in some way) sufficient repetitions of a Lagrangian experiment as to completely sample[6] every microstate of that system's phase space. If the system of interest is both steady-state and periodic, however, then a single, sufficiently long experiment could[7] meet this requirement. Systems must at least meet the steady-state condition to be said to be *ergodic*.

5.3.1 The ergodic assumption and the ergodic hypothesis

A dynamical system is ergodic if, simply put and for our purposes[8], its time-averaged behaviour is the same as its ensemble-averaged behaviour. This is the ergodic assumption.

The ergodic hypothesis is that over a sufficiently long time, the time spent by a particle in some region of the phase space of microstates corresponding to a fixed macrostate of a system is propor-

[5]In principle, given a flow field in the Eulerian reference frame, one can recover a series of Lagrangian-like trajectories through the flow field. However, there is some asymmetry here because given enough Lagrangian experiments, an Eulerian description can be recovered, but only *possible* or more or less *probable* Lagrangian trajectories can be recovered from an Eulerian flow field, no matter how precise.

[6]That is, enough experiments to allow the tracked particle to attain every allowed combination of position, momentum, and so on.

[7]See Section 5.3.1

[8]As opposed to, for instance, the definition employed by economists for whom the ergodic assumption is closer to an inductive assumption- that past and present macroeconomic events can be used to predict future macroeconomic events. The definition offered here is a simplification of the mathematical definition of ergodicity. We also employ the *ergodic hypothesis* of statistical physics.

tional to the volume of that region of the phase space. That is, since the likelihood of a particle being in some microstate at a given time is proportional, and often assumed identical, to the likelihood of it being in that state at all, over a sufficiently long time a tracked particle will visit all possible combinations of position, momentum and so on with the probability of that microstate's instantiation.

Thus by repeating a steady state experiment often enough, or by allowing a periodic steady state experiment to run for long enough, for even the most unlikely microstates to be attained, and by keeping track of the frequency of occurrence of each of these microstates, one can not only build up the instantaneous distribution of microstates, but also their probability.

Of course, exactly how long a periodic experiment need be run for or how many repetitions of a non-periodic experiment are representative, depends on the exact nature of the system under study. Since a particle will visit a microstate with the probability of that microstate existing, systems with dominant orbits in phase space will require longer studies or more repetitions to ensure that the weakly represented phase states are sampled. In fact, even periodic systems with very dominant, locked-in orbits, might require several distinct repetitions to fully characterise these orbits.

In general, there is no way to determine *a priori* how many experiments need be performed for how long to sample the entire phase space- for very asymmetric phase spaces, it may be practically impossible to do so- and so a pragmatic cut-off must be decided on. It may be possible, however, to measure some bulk property of the system that is also calculable from the accumulated trajectories in Eulerian form[9], and to use the convergence of the measured and calculated values as a guide. For my system of interest, the tumbling mill, I use the convergence of the measured and calculated power drawn by the mill as an ergodic criteria (See Section 5.5.4).

5.3.2 The representative particle

One of the key assumptions made in converting Lagrangian data into Eulerian form is that the tracked particle is *representative* of all particles of its class in the system. What constitutes a distinct particle class in a system of interest depends on the drivers of motion in that system, but could include the size and shape of the particles, their density and their surface properties. If a tracked particle is representative of its class, then we can employ the ergodic assumption to interpret the time-averaged behaviour of that particle as the instantaneous ensemble average of particles of its class. Thus a complete picture of the flow field of a multicomponent flow can be built up by tracking representative particles of each class of particles in the system.

5.3.3 Binning

Consider the illustrative trajectory shown in Figure 5.1a. It consists of a series of sample points along a path in 2D space, shown here as a dashed line. From these positions and their associated times, the kinematics of the tracked particle can be obtained as outlined in Section 5.1, resulting in a *Lagrangian* description of the flow field *along that path.* In order to recast this information as an *Eulerian* description of the flow field of the system, the kinematics of the particle must be sampled in all space, rather than just along the particle's trajectory. Pragmatically, and to minimise the effect of statistical fluctuations in stochastic systems, this is achieved by sampling the particle's kinematics in some small region of space, rather than at a point. The procedure of discretising space into sample volumes is called binning, and the sample volumes, or voxels, are often called bins. Figure 5.1b shows a 2D grid of bins superimposed on the trajectory of Figure 5.1a. For the

[9]That is, system-wide rather than on a particle-by-particle basis.

rest of this discussion, I will consider the case of 2D binning, but in general this procedure can be applied in 3D.

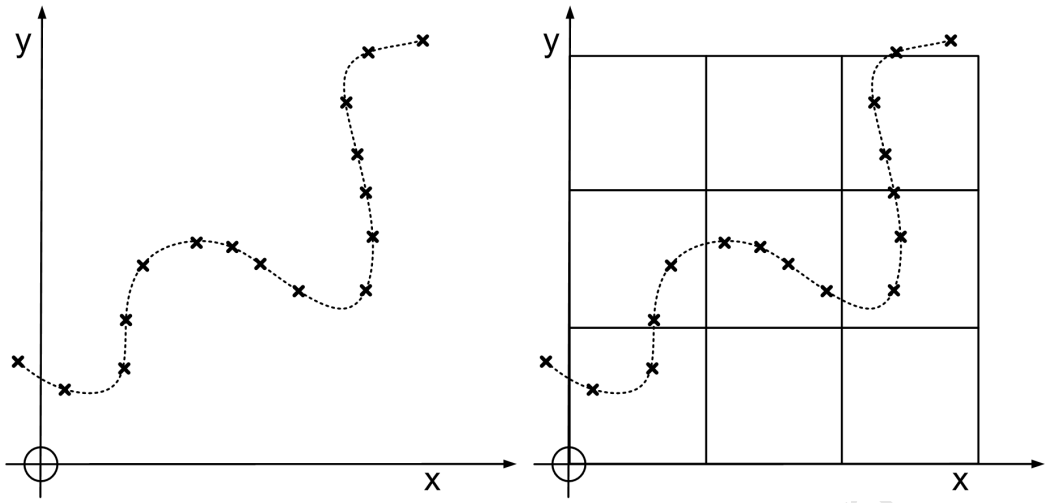

(a) 2D trajectory **(b)** Superimposed grid

Figure 5.1: An illustrative trajectory in 2D space without (left) and with (right) a binning grid superimposed.

Once a grid of bins has been superimposed on the region of interest, the next step in binning Lagrangian data is to assign sample points (such as those shown in Figure 5.1) to the bins that they fall within. Since each sample point has a time, position, velocity, acceleration, and so on associated with it, by assigning a sample point to a bin, you assign each of these attributes to the bin.

The probability distribution

Assigning sample points to bins is the first step in recovering the flow field of the system of interest in the Eulerian form, but it also serves another purpose. By the ergodic hypothesis, the time spent by a particle in some microstate is proportional to the likelihood of that microstate's existence (see Section 5.3.1). Thus, the time spent by a particle in some region of space (in a steady state system) is proportional to its likelihood of being there at any given moment. This, together with the representative particle assumption (see Section 5.3.2) means that the time spent by a tracked particle in a given bin, normalised to the total duration of the experiment, can be interpreted as the probability that a particle of that class will be found in that bin at any given instant. The distribution of normalised times spent in each bin is called the probability distribution, and can be calculated in a number of ways.

The choice of binning method for the probability distribution will have implications for the way in which kinematic distributions are calculated. I will consider the simplest binning method, and then the more complicated residence time distribution (RTD) method.

5.3.4 Simple binning

By simple binning I mean the procedure of assigning sample points to the bins in which they fall. This is, of course, the most intuitive binning method and, in certain cases, can be the least computationally expensive. However, simple binning is only valid under certain conditions, namely, when the sample points are uniformly, and sufficiently frequently, distributed in time.

Simple binning is an approximation to the probability distribution based on the ergodic hypothesis (see Section 5.3.1). Its basic rationale is that the time spent in each bin is proportional to the arclength of its trajectory contained in that bin, which is in turn proportional to the number of sample points contained in that bin.

Consider the particle trajectory shown in Figure 5.1. Assume that the sample points shown are uniformly distributed in time. Then the simple binning procedure can be illustrated as in Figure 5.2. Here I have labelled the horizontal bins with letters, and the vertical bins with numbers, so that the bottom left bin of each grid can be referred to as bin 1C[10], for instance.

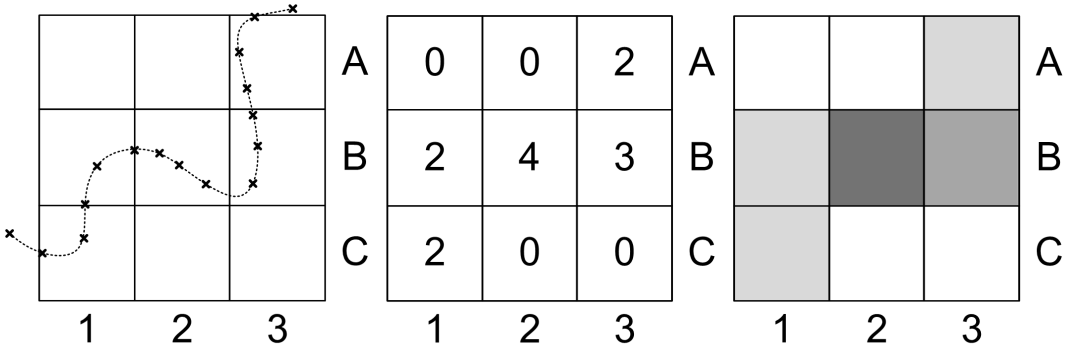

(a) Binned trajectory **(b)** Simple bin counts **(c)** Simple bin count visualisation

Figure 5.2: The simple binning procedure: gridding the space (left), counting sample points (centre), and visualising the probability density distribution (right).

Figure 5.2 shows the steps taken in the simple binning procedure. In Figure 5.2a the region of interest is divided into bins, as discussed in Section 5.3.3. Then the number of sample points that fall into each bin are tallied and assigned as the weighting for that bin, as shown in Figure 5.2b. Since the density distribution of sample points is interpreted as the residence time distribution of the tracked particle, this is, by the ergodic hypothesis, proportional to the particle's probability distribution once normalised by the total number of sample points in the entire region of interest. Such a probability distribution can be more easily and qualitatively visualised in the form shown in Figure 5.2c, where darker colours represent higher probabilities of the particle being found in that bin at any instant.

An obvious shortcoming of binning as a way of converting data from a Lagrangian reference frame into an Eulerian reference frame is that it is inevitable that some of the fine detail of the tracked particle's trajectory must necessarily be lost in the aggregating procedure[11]. This effect is clear in this example, assuming that the dashed line in Figure 5.2a is the true trajectory of the tracked particle.

This washing out of detail is due to the large spatial volume over which the residence time is aggregated: all the points lying in the range of a given bin[12] are counted as being at the centre point of that bin. This also means that the resulting location error is at least half of the bin side length in each dimension. It would seem, then, that both this unavoidable smoothing and the location error can be minimised by increasing the resolution of the superimposed grid.

Figure 5.3 shows the same, simple binning procedure as applied in Figure 5.2, applied to the same data but with a higher-resolution grid. This higher-resolution grid is only twice as fine as that in

[10] This is almost the complete converse of the chess convention, due mainly to poor planning.

[11] This is the source of the asymmetry in converting between the two reference frames mentioned in an earlier footnote.

[12] In this case, the left and lower boundaries of the each bin are included in its count, and the right and upper boundaries therefore excluded.

Figure 5.2, and yet it results in a much more detailed (if not necessarily more accurate) residence time distribution. It is tempting to assume that increasing the resolution of the grid to an arbitrary extent would increase the accuracy of the Eulerian data to a similar extent but, as I will show a bit later, it is not possible to do this beyond some optimum resolution determined by the trajectory's sampling frequency.

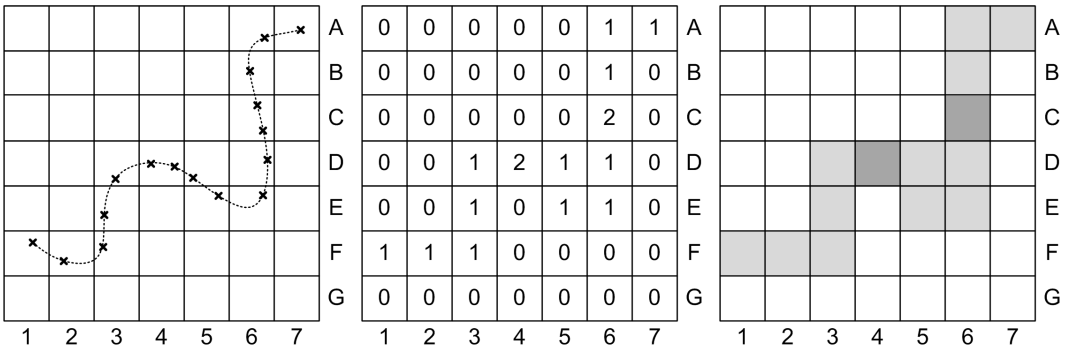

(a) Fine gridded trajectory **(b)** Simple bin counts **(c)** Simple bin count visualisation

Figure 5.3: The simple binning procedure applied to a higher-resolution grid: gridding the space (left), counting sample points (centre), and visualising the probability density distribution (right).

In the preceding examples, the data was assumed to be sampled at uniform time steps, and has so far been sampled sufficiently frequently as to provide meaningful data at the resolutions discussed. Such conditions might hold for sufficiently high-frequency biplanar x-ray imaging data, for instance, but not for data obtained from techniques such as PEPT, which rely on stochastic underlying processes. In the general case of non-uniformly or insufficiently frequently sampled data, it will be necessary to *interpolate* and re-sample the data, incurring the same computational expense as for residence time binning, which will be discussed (and motivated) in Section 5.3.5, and thus removing the primary advantage of simple binning.

Consider again the trajectory shown in Figure 5.2a, but this time, let the data be sampled at non-uniform time intervals. As discussed, non-time-uniform data must be re-sampled at fixed time intervals in order for the ergodic hypothesis to hold. Figure 5.4 shows the particle's trajectory (the dashed line) sampled at fixed time intervals and binned in the simple way.

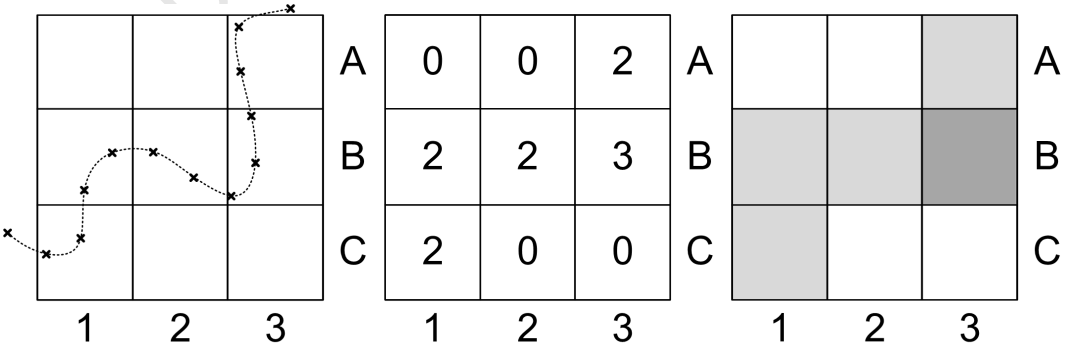

(a) Re-sampled trajectory **(b)** Simple bin counts **(c)** Simple bin count visualisation

Figure 5.4: The simple binning procedure for non-time-uniform data: re-sampling the trajectory in gridded the space (left), counting sample points (centre), and visualising the probability density distribution (right).

The re-sampling frequency employed in Figure 5.4 is high enough to capture the entire trajectory of the tracked particle more or less representatively. However, increasing the resolution of the

grid to lessen the washing out effect and to minimise the location error discussed above, results in Figures 5.5a to 5.5c. On the face of it, Figure 5.5c might seem to be more representative than Figure 5.4c, but its re-sampling frequency leads to a misleading RTD. In particular, although the particle's trajectory passes through bin 5D in Figure 5.5a, the trajectory is not sampled in that bin, and so its contribution does not appear in the residence time distribution. Also, there is a smoothing effect if the sampling frequency is particularly low, which artificially recovers a roughly even particle residence time (and thus location probability) along its trajectory[13].

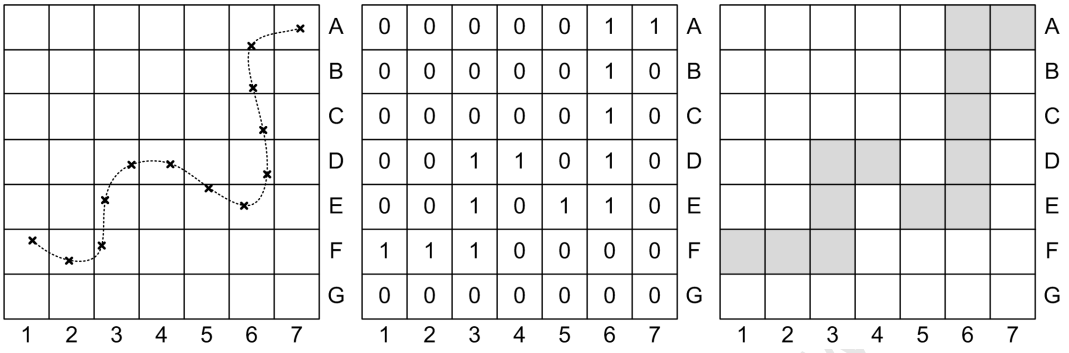

(a) Low frequency re-sampled trajectory

(b) Simple bin counts

(c) Simple bin count visualisation

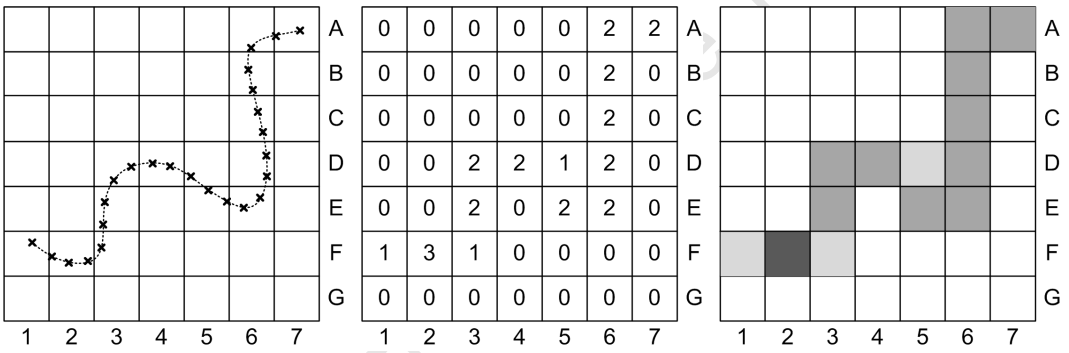

(d) High-frequency re-sampled trajectory

(e) Simple bin counts

(f) Simple bin count visualisation

Figure 5.5: The simple binning procedure for non-time-uniform data: re-sampling the trajectory in a high-resolution grid (left), counting sample points (centre), and visualising the probability density distribution (right), shown for a low (upper row) and a high (lower row) frequency re-sampling rates.

Figures 5.5d to 5.5f show the same trajectory in the same grid, re-sampled at a higher frequency, which shortens the minimum path length that will be represented in the RTD. The effect on the residence time distribution in this case is to include the contribution to bin 5D missed before, and to re-weight the residence time along the particle's trajectory in a more representative way.

Unfortunately, even once the computational expense of interpolating the sample points has been incurred, evaluating the interpolant at N sample points goes, at best, like $\mathcal{O}(N)$, and thus doubling the sampling frequency may improve the accuracy of the resultant RTD, but only at the expense of *at least* doubling the computational cost of binning the data. I will return to this balance between the accuracy and cost of simple binning in Section 5.3.5.

[13]This is, of course, illustrative, qualitative data, but this effect will be evident in the testing of the routines in Section 5.5.

Eulerian flow fields in the simple binning case

Our original motivation for binning the data obtained from Lagrangian particle tracking techniques was to recover an overall view of the motion of particles in the system. The first step towards doing this was to find some way of assigning kinematic values to spatial sampling points in the Eulerian reference frame. The most intuitive approach to this was what I have called simple binning, which has been the subject of the last few sections. In performing this assignment, we have also been able to invoke the ergodic hypothesis to interpret the RTD as a probability distribution, see Section 5.3.6. We now return to the task at hand.

Recall that the data obtained from Lagrangian particle tracking experiments is in the form of a series of tracked particle positions and associated times, and that this data can be further used to obtain the kinematics of the particle at those times (see Section 5.1.1). Thus associated with each time is not only a particle location, but also the particle's velocity and acceleration, and any other quantity that can be derived from the Lagrangian trajectory data, augmented perhaps, with knowledge of the system under study. Figure 5.6 shows another illustrative trajectory with velocities and accelerations calculated from the interpolant associated with each sample point.

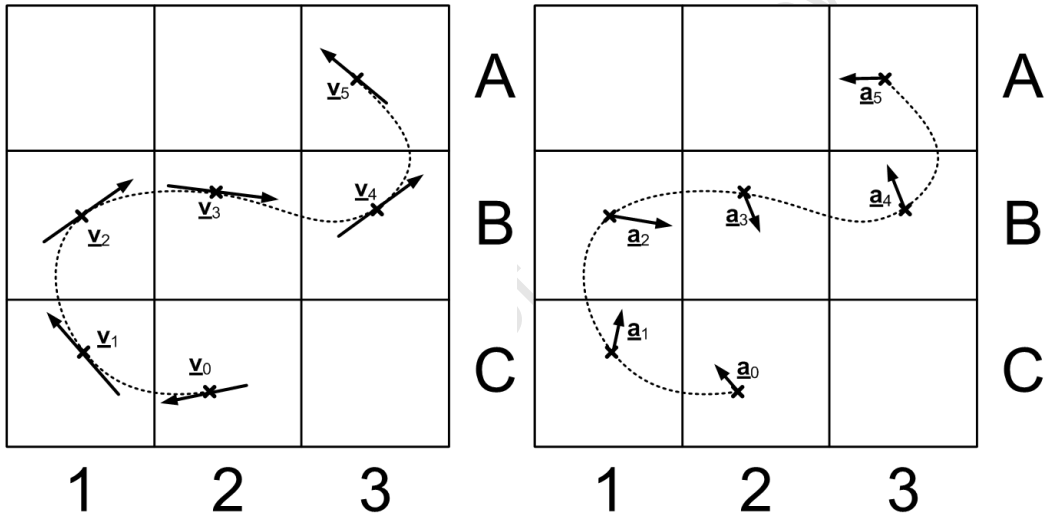

(a) Calculated velocities **(b)** Calculated accelerations

Figure 5.6: At each sample point in the tracked particle's interpolated trajectory, its instantaneous velocity (left) and acceleration (right) can be calculated.

Recall further that in order to limit the order of the interpolating function and to restrict the operation to a bivariate one, this interpolation is performed for each dimension separately. Thus the calculation of the particle's kinematics can be performed in each dimension separately, resulting in a *vector* flow field, as shown in Figure 5.7.

The Eulerian vector flow field of a tracked particle can thus be built up by aggregating its kinematic information in the bins in which its location falls at each time. In the case of simply binned data, a simple average of the kinematic data in each bin can be performed. The kinematics of a tracked particle binned in this way are susceptible to the same sampling bias as is the RTD thus obtained. Bin 2B in Figure 5.8, in particular, shows an example in which the average velocity of a tracked particle may be completely misrepresented due to this sampling bias.

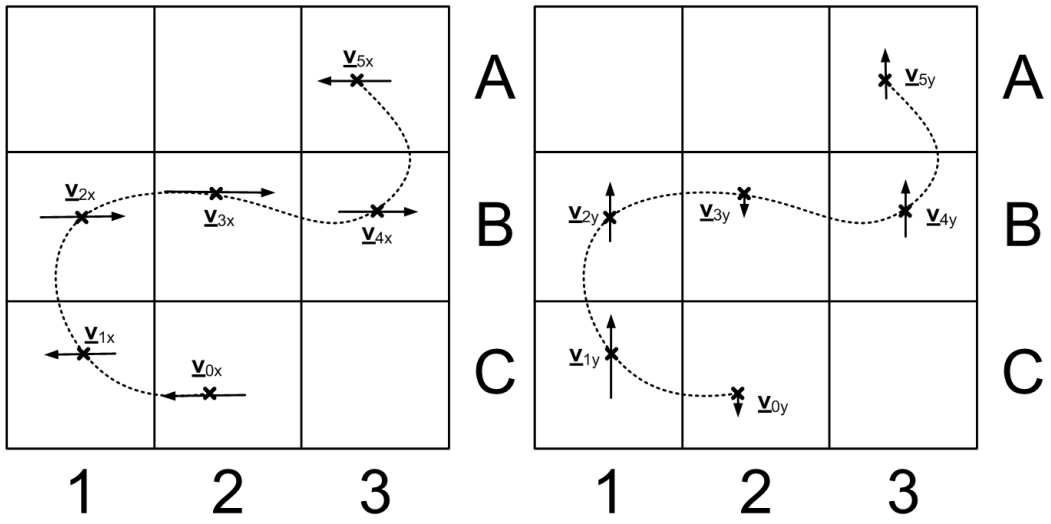

(a) Calculated x-velocities **(b)** Calculated y-velocities

Figure 5.7: At each sample point in the tracked particle's interpolated trajectory, its instantaneous velocity can be calculated in the $\hat{x}$ (left), the $\hat{y}$ (right) and the $\hat{z}$ directions (not shown) separately.

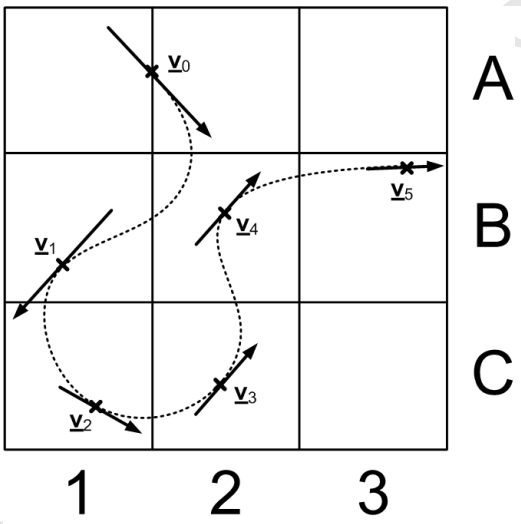

Figure 5.8: An example of a situation in which the simple average of a particle's velocity evaluated only at sample points, might misrepresent that velocity in a given bin. In this case, in bin 2B.

Binning error estimation in the simple binning case

In the simple binning case, the representative particle's RTD is based on the number of sample points that fall in each bin. No error estimate in the probability distribution is thus possible. However, since a simple average of the kinematic data is calculated for each bin, a standard deviation of these values can be similarly calculated and interpreted as an error[14].

In practice, this means accumulating both the kinematic quantities and their squares in separate grids, since

$$\sigma_x = \sqrt{\bar{x^2} - \bar{x}^2} \tag{5.3}$$

where $\bar{x}$ is the mean of variable x and $\bar{x^2}$ is the mean of the squares of variable x.

[14]Some caution is required here. Some researchers interpret the standard deviation in binned kinematic quantities differently. A prime example is the absolute magnitude of the standard deviation in a particle's velocity, which is interpreted as a granular temperature in analogy with thermodynamics. I'm not sure whether I can endorse this idea in the case of highly-dissipative granular flows.

5.3.5 Residence time binning

In the last few sections, I drew attention to the sampling bias that may be introduced into even uniformly re-sampled Lagrangian data when binned more finely than the sample rate will support. In this section, I propose an alternative- residence time binning.

As is the case with simple binning, the residence time binning method is based on the ergodic hypothesis[15]. In the residence time case, however, an attempt is made to calculate the time spent by a tracked particle in each bin based on the particle's trajectory rather than to simply infer it from the density of sample points in those bins.

Consider again the now-familiar trajectory shown in Figure 5.1, and assume that the sample points are non-uniform in time[16]. The residence time binning method, applied to this data, could be illustrated as in Figure 5.9.

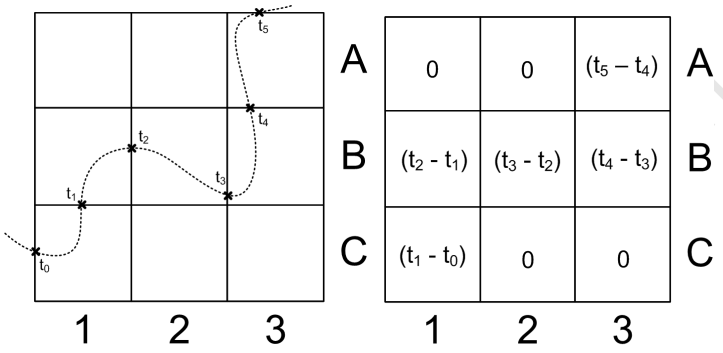

(a) Binned trajectory sampled at bin crossings

(b) Residence times

Figure 5.9: The residence time binning procedure: calculating bin boundary crossing times (left) and thus bin residence times (right).

In the residence time binning method, the interpolated trajectory (shown as a dashed line in Figure 5.9a) is only re-sampled at its points of entry and exit into each bin[17]. In the case of simple binning the aim of re-sampling the trajectory was to ensure that the sampling was uniform in time- we chose evenly-distributed sampling times and evaluated the interpolant to obtain the particle's position at those times. In the residence time binning case, however, we know the points at which to re-sample the trajectory and need only calculate the times at which these points are reached by each interpolant, labelled t_i in the figure. The time spent by the particle in a given bin, termed the particle's *residence time* in that bin, is then just the time interval $\Delta t_i = t_{exit} - t_{entry}|_i$, as shown in Figure 5.9b. These residence times can be normalised to the total time that the particle was tracked for to obtain the probability distribution as per the ergodic hypothesis.

Implementation

Of course, we don't know the exact points of entry and exit of each interpolating polynomial into each bin. Recall, however, that for pragmatic reasons[18], the particle's trajectory is interpolated in each dimension separately. Since we know the coordinates of the boundaries of each bin, we know the only possible coordinates of entry and exit into each bin in 1D. For each interpolant, we can

[15] In fact, both the simple and this less simple method could both be properly termed residence time binning, but I choose not to do so in an effort to highlight the explicitly estimated, rather than inferred, residence times used in the less simple case.

[16] So that the trajectory must be interpolated (see Section 5.2) and re-sampled, even to be simply binned subsequently.

[17] A bit further on, I'll discuss the performance implications of this compared to the simple binning case.

[18] See Section 5.2.3.

evaluate the inverse form of the Lagrangian interpolating polynomial, given in Equation G.8, to yield the times at which these boundaries are crossed by each interpolant. I say *each* interpolant because, to minimise the interpolating error and oscillatory artefacts such as Runge's phenomenon, a new Nth-degree polynomial must be used to interpolate each new set of (over-lapping) $N+1$ points. These $N+1$ points correspond to some time interval over which the interpolating function is valid. This time interval thus provides a range of allowable time solutions to Equation G.8 for each such interpolating function. This procedure can be performed over the same $N+1$ points for each dimension to produce a series of 1D bin boundary crossing times.

Handling and interpreting these crossing times is best explained with reference to a 2D example, although a full 3D solution is implemented for this work as given in Appendix H.

Consider again the trajectory shown in Figure 5.9a. The times at which the trajectory crosses each bin boundary are labelled t_i in the figure. Let the leftmost horizontal bin boundaries be labelled by their column numbers: 1, 2, 3 and so on; and the bottommost vertical bin boundaries be labelled by their row letters: A, B, C and so on. The residence time binning procedure is as follows.

Starting with the $\hat{x}$-direction as defined in Figure 5.1, the trajectory crosses horizontal bin boundaries 1, 2 and 3 at times t_0, t_2 and t_3. In the $\hat{y}$-direction, the same trajectory crosses vertical bin boundaries C, B and A at times t_1, t_4 and t_5. The crossing times can be represented in a table as follows, where a zero entry in the horizontal boundary column means that no horizontal boundary was crossed at that time, and similarly for the vertical boundary column.

Crossing time	Column	Row
t_0	1	0
t_1	0	C
t_2	2	0
t_3	3	0
t_4	0	B
t_5	0	A

(a) Bin boundary crossing times

Residence time	Row	Column
$t_1 - t_0$	1	D
$t_2 - t_1$	1	C
$t_3 - t_2$	2	C
$t_4 - t_3$	3	C
$t_5 - t_4$	3	B

(b) Bin index residence times

Table 5.1: Handling crossing times in the residence time binning procedure

Except in the special case[19] of a crossing at a vertex (not shown here), the particle will stay in the same column when crossing a vertical boundary and in the same row when crossing a horizontal one. Replacing zero entries in the index columns of Table 5.1a with their preceding entries and subtracting the preceding crossing time from the second and subsequent entries results in the residence times and corresponding bin indices shown in Table 5.1b. Remember in reading this table that, here, bin 1C is labelled with indices 1 and D, bin 3A is labelled with indices 3 and B, and so on.

Notice that there is one fewer row in Table 5.1b than in Table 5.1a, and that the first row of Table 5.1b was not produced by replacing a zero entry with the preceding entry in the same column as suggested. This is because the end points of the trajectory must be treated differently from other crossing points. In particular, the bin containing the start point of the interpolated trajectory must be added to the beginning of Table 5.1a, and that containing the end point must added to the end of Table 5.1a. As a result, the first row in Table 5.1a would not contain a zero in either the Row or the Column entry, which might otherwise be a problem when replacing the zero entry in the second row as detailed above. Also, the last and second-last entries in Table 5.1a would be the same, removing any compunction about removing the last row in the table when performing the residence time calculation. Finally, in this example, the trajectory would start in the unlabelled

[19] Treatment of this and other more technical special cases can be found in comments in my code.

bin before 1C, and end in the unlabelled bin above A3. In general, the interpolating function will be defined over an interval that does not start and end on a bin boundary. Treating the start and endpoints of the interpolated trajectory in this way, would take this into account in a natural way.

The fact that, in this example and also in my implementation, bins are labelled by the co-ordinates of their bottom left corner means that the foregone explanation of residence time binning applies only to particles crossing bin boundaries from the left to the right, or from the bottom to the top of the grid. Particles crossing in the opposite sense will start out in the bin labelled by the crossed boundary. This can easily be dealt with, however, by simply decrementing repeated entries in each column before replacing zero entries with the preceding entries in the same column.

Eulerian flow fields in the residence time binning case

In the simple binning procedure, a kinematic quantity (such as a component of the particle's velocity or acceleration) is associated with each sample point in the particle's trajectory and assigned to the bin in which that sample point falls in order to build up its Eulerian vector flow field. In the residence time binning procedure, the particle's trajectory is not sampled in the same way. Rather, the times at which the particle enters and then leaves each bin are obtained from the inverse of the Lagrangian interpolating polynomial. Thus for each bin we have an interpolating polynomial as a function of time and the time limits of the particle's trajectory in each bin. This information allows a more sophisticated bin average of the particle's kinematic quantities to be calculated.

All of the kinematic quantities that I will invoke in the rest of this chapter can be calculated from combinations of the particle's position, velocity and acceleration. Space and time averages of all of these quantities can thus be obtained from the particle's RTD, and binned averages of the components of its velocity and acceleration.

In the simple binning case, a simple average of the particle's sufficiently frequently sampled velocity is assumed to approximate the time average velocity of a particle of that class[20] in each bin. In the residence time binning case, however, a time-average of the particle's velocity *on each pass* can be determined (for each dimension) from a continuous time-average of the Lagrangian interpolating polynomial given in equation G.7 over the time interval obtained in the residence time binning procedure.

A tracer particle's continuous time-averaged x-velocity, for instance, for a transit j through a given bin is given by

$$\begin{aligned}
\bar{v}_{x,j} &= \frac{\int_{t_i}^{t_f} \frac{dx(t)}{dt} dt}{\int_{t_i}^{t_f} dt} \\
&= \frac{\int_{t_i}^{t_f} \frac{d(p_x t^2 - q_x t + r_x)}{dt} dt}{t_f - t_i} \\
&= \frac{\int_{t_i}^{t_f} 2p_x t - q_x dt}{\Delta t_j} \\
&= \frac{p_x(t_f^2 - t_i^2) - q_x(t_f - t_i)}{\Delta t_j} \\
&= \frac{x(t_f) - x(t_i)}{t_f - t_i}
\end{aligned} \tag{5.4}$$

[20] By the ergodic hypothesis.

Its time-weighted average x-velocity for each of its N passes through a given bin can be calculated as follows:

$$\begin{aligned} \bar{v}_x &= \frac{\sum_{j=1}^{N} \Delta t_j \bar{v}_{x,j}}{T} \\ &= \frac{\sum_{j=1}^{N} \Delta t_j \{x_j(t_f) - x_j(t_i)\}}{\Delta t_j T} \\ &= \frac{\sum_{j=1}^{N} \{x_j(t_f) - x_j(t_i)\}}{T} \end{aligned} \tag{5.5}$$

where T is the total time over which the particle was tracked. The time-weighted average of a tracked particle's continuously time-averaged velocity in a given bin is thus very simply given as the sum of the differences between the particle's velocities upon entering and then leaving that bin, divided by the total time over which it was tracked.

A similar procedure for the particle's continuous time-averaged x-acceleration yields an even neater result, *viz*

$$\begin{aligned} \bar{a}_{x,j} &= \frac{\int_{t_i}^{t_f} \frac{d^2x(t)}{dt^2} dt}{\int_{t_i}^{t_f} dt} \\ &= \frac{\int_{t_i}^{t_f} \frac{d^2(p_x t^2 - q_x t + r_x)}{dt^2} dt}{t_f - t_i} \\ &= \frac{\int_{t_i}^{t_f} 2p_x dt}{\Delta t_j} \\ &= \frac{2p_x(t_f - t_i)}{\Delta t_j} \\ &= \frac{2p_x \Delta t_j}{\Delta t_j} \\ &= 2p_x \end{aligned} \tag{5.6}$$

$$\tag{5.7}$$

and thus a time-weighted average of

$$\begin{aligned} \bar{a}_x &= \frac{\sum_{j=1}^{N} \Delta t_j \bar{a}_{x,j}}{T} \\ &= \frac{2\sum_{j=1}^{N} \Delta t_j p_{x,j}}{T} \end{aligned} \tag{5.8}$$

Binning error estimation in the residence binning case

In the simple binning case the representative particle's RTD was based on the number of sample points in a given bin and, therefore, no error estimate in the probability distribution was possible. In the residence time binning case, however, the representative particle's RTD is based on the time that particle spends in each bin on each pass. An error estimate in the probability distribution of particles of the class represented can thus be obtained from the standard deviation in the time spent in each bin on each pass.

The error in the probability distribution of kinematic quantities can be estimated from the standard deviation of the contributions to each bin, as outlined in Section 5.3.4.

Simple versus time-weighted binning

Both simple binning and residence time binning result in approximations to the true RTD of particles of the class represented by the tracer particle (see Section 5.3.2). The choice between them boils down to which of the two produces the best such approximation, *ceteris paribus*. Of course, some pragmatic balance must be struck between the accuracy of the result and the secondary consideration of the computational expense of achieving this accuracy.

Some tests using artificial data are given in Appendix I. They show the accuracy of the residence time binning procedure for known, non-uniformly sampled trajectories, and that the simple binning procedure can be made to match, but not surpass, this accuracy[21].

It is not generally possible to optimise the sample rate for simple binning, as done in Appendix I, and so the only way to ensure that a simply-binned RTD is at most as good as a residence time-binned one is to sample at very high frequencies. As the resolution of the bins increases, so the sampling frequency must similarly increase to keep up, driving up the computational expense of binning the data.

Since, in the residence time binning procedure, the particle's interpolated trajectory is sampled at fixed spatial positions- the bin boundaries- rather than at fixed times, the resultant RTDs and Eulerian flow fields scale perfectly with the number of bins, drastically reducing the computational expense of obtaining high-resolution Eulerian flow fields, and ensuring that the washing out effect from which simple binning suffers does not affect residence time binning.

5.3.6 Probability distributions

So far I have discussed the residence time distribution (RTD) and the Eulerian vector flow fields of velocity and acceleration. I have claimed that all kinematic quantities of interest can be derived from these, and I will go on to do this for the special case of cylindrical symmetry in Section 5.4, and for the application of all of this to tumbling mills in Section 5.5. First, though, I will mention some interpretations of the RTD in general, all of which can be termed probability distributions.

Mass and density distributions

By the ergodic hypothesis[22], the RTD of a tracked particle is proportional to the likelihood of that particle being in a given spatial region. We generally know the properties of the tracked particle since it is to be chosen as a representative of a given class of particles. Thus the RTD of the tracked particle in a granular material consisting of only similar particles can be interpreted as being proportional to the mass distribution in the system[23]. In fact, I interpret the total mass of all of the particles in the system multiplied by the normalised RTD of the tracked particle as being *exactly* the mass distribution in the system[24].

[21] Of course, since both procedures rely on the same approximating interpolating polynomial, this is unsurprising.
[22] See Section 5.3.1
[23] This assumption actually breaks down when, for instance, a particle is trapped in a low-density region for a long time. Then the fact that a particle spends a long time in that region does not mean that that region is, necessarily, a high mass or density region. This is assumed, however, to be a fairly low frequency occurrence.
[24] This and the other assumptions mentioned here are tested in Appendix I using the measured and calculated power drawn by my laboratory scale mill. See Section 5.5.4.

If the system consists of several classes of particles, then by the ergodic hypothesis again, it is possible to combine all of their contributions to the total mass distribution by weighted average of these contributions[25].

Once the total mass distribution has been calculated, then a density distribution can easily be obtained from it since each bin is of a known volume. The density distribution in the system is, however, generally less useful than the solidicity or porosity distributions mentioned below.

Porosity and solidicity distributions

Solidicity is the fraction of a given volume that is filled. Porosity is its compliment- the fraction of empty space per unit volume. Since we know the volume of the tracer particle, and thus the total volume of all of the particles of the class it represents, a volume distribution is calculable in the same way as a mass distribution. That is, the total volume of each class of particles, V_i multiplied by their corresponding normalised 3D RTD, $R_{xyz,i}$, can be combined to yield a total volume distribution, V_{xyz}. This total volume distribution divided by the volume of a single bin v_{bin} is the solidicity distribution, S_{xyz} given by:

$$\begin{aligned} S_{xyz} &= \frac{V_{xyz}}{v_{bin}} \\ &= \frac{\sum_i V_i R_{xyz,i}}{v_{bin}} \end{aligned} \tag{5.9}$$

Usually the porosity, which gives a measure of how much open space there is for other particles or fluid etc. to travel through in the packed bed, is of more use. It is just the compliment of the solidicity, *viz*

$$P_{xyz} = 1 - S_{xyz} \tag{5.10}$$

5.3.7 Selecting regions of interest

Often it is useful to be able to select only regions of interest to bin, either to exclude uninteresting regions such as circulating pipes etc. or to focus on areas that are amenable to particular analyses. Sometimes this can be done by choosing the limits of the binned space appropriately, perhaps with some rotation of the triangulated data in space first. In other situations this may not be possible.

In this work, I use three primitives to exclude unwanted locations- planes, cylinders and spheres. Choosing the limits of the binned space is a special case of excluding points that fall in the half-spaces defined by the positive and negative axes and passing through the upper and lower limits in these dimensions, respectively. Once binning has been performed for the region of interest thus defined, further bins can be excluded based on their position relative to a combination of the primitives and the RTD re-normalised.

An infinite plane divides space into two half-spaces, one extending into the direction defined by the plane's normal and the other into the direction defined by its anti-normal. An infinite plane can

[25]This procedure is also possible for contributions to the overall vector flow fields etc., but I do not do this in my work because I feel that the result can be misleading.

be defined by three points, say p_1, p_2 and p_3, which define two lines, $\vec{r}_1 = \vec{p}_2 - \vec{p}_1$ and $\vec{r}_2 = \vec{p}_2 - \vec{p}_3$, for instance. The normal to the plane defined by these two lines might be given by

$$\hat{n} = \frac{\vec{r}_1 \times \vec{r}_2}{|\vec{r}_1 \times \vec{r}_2|} \tag{5.11}$$

and thus the plane given by

$$\hat{n} \cdot \vec{x}_0 - \hat{n} \cdot \vec{p}_1 = 0 \tag{5.12}$$

The distance between the plane thus defined and a point $\vec{x}_0$ is

$$D = \hat{n} \cdot \vec{x}_0 - \hat{n} \cdot \vec{p}_1 \tag{5.13}$$

If the perpendicular distance, D, between the plane and the point $\vec{x}_0$ is positive definite, then the point lies either on the plane (if the distance $D = 0$) or in the half-space defined by its normal $\hat{n}$. This provides a condition to decide whether to exclude the contribution to the RTD from a particular bin or not. Of course, care must be taken to ensure that the order of points p_i results in a normal to the plane in the required sense.

An infinitely long cylinder divides space into two regions- that inside the cylinder, and that outside it. An infinitely long cylinder can be defined by its radius, R, and its axis. Its axis is an infinite line, and so can be defined by two points, p_1 and p_2. The perpendicular distance between a point, x_0, and a line was given in Section 5.4. If that distance is greater than the radius of the cylinder, then the point lies outside the cylinder and *vice versa*. For completeness, this condition can be written as:

$$R > \frac{|(\vec{x}_0 - \vec{p}_1) \times (\vec{x}_0 - \vec{p}_2)|}{|\vec{p}_2 - \vec{p}_1|} \tag{5.14}$$

The third primitive is the simplest. A sphere can be defined in terms of a centre point, O, and a radius, R. If the distance from a point x_0 to the centre of the sphere is greater than the radius of the sphere, then that point lies outside the sphere, and *vice versa*. For completeness, this condition can be written as:

$$R > |(\vec{x}_0 - \vec{O})| \tag{5.15}$$

A fair amount of space can be excluded using combinations of these primitives.

Dealing with the tracer moving into and out of the field of view

Since the residence time binning procedure involves fitting an interpolating polynomial to locations in each dimension, it has the capacity to produce very biased data at the limits of this field of view if the tracer particle leaves and re-enters it at some later time. This can only occur if the particle actually goes out of the field of view of the camera, not merely the field of view of the binned space. This is because my implementation fits interpolating polynomials to the underlying data even if it falls outside the binned space.

The only way to overcome the, sometimes catastrophic, error introduced by the tracer moving into and out of the field of view of the camera is to divide the experiment into subexperiments *ex post*

facto consisting of intervals during which the particle was in the field of view. These subexperiments can then be recombined into a single experiment by invoking the ergodic hypothesis and performing a weighted-average as was done for the mass and porosity distributions above.

In my implementation, this is done by histogramming the time intervals between particle locations and starting a new subexperiment between points whose time difference is more than three standard deviations greater than the mean time. This does not deal with situations in which the particle quickly leaves and then re-enters the field of view, but the error introduced in such a case would be small, and could be excluded by restricting the region of interest as above.

Projections and sections

Sometimes it may be interesting to consider a projection of the binned data onto the xy-, xz-, zy- or some arbitrary plane. This is easily achieved for planes orthogonal to one axis, by summing bins along that axis. For instance, a projection of some binned measure M_{xyz} onto the xy-plane would be achieved by summing along the z axis, *viz* $M_{xy} = \sum_i M_{xyi}$.

Projection onto an arbitrary plane is achieved by defining the plane by its normal as given in equation 5.11 and then rotating the data until this normal is orthogonal to one of the xy-, xz- or zy-planes.

Sections of the data can be obtained by selecting the region of interest with two plane primitives as discussed above, and then performing a projection of the selected data.

Radial binning

Another special binning technique that will have particular significance in the following Section 5.4 is radial binning. In this procedure, binned data is re-binned based on the perpendicular distance of the centre of the bin from a line in 3D space calculated from a version of equation 5.14. This is particularly useful for not only vertically-aligned funnels, silos and fluidised beds, but also inclined but cylindrically symmetric systems such as pipes, chutes and hydrocyclones.

5.4 The special case of cylindrical symmetry

Many systems of interest to industry are cylindrically symmetric; from pipes and silos to stirred tanks and tumbling mills, my system of interest. In some cases, such as that of pipes or silos, this cylindrical symmetry is motivated by ease of manufacture or by material stress considerations. Their cylindrical shape, however, still has implications for the transport of material through them. In other, perhaps more interesting if equally important, cases the cylindrical shape of the system is specifically chosen to affect the motion of material in that system. This second class of cylindrically symmetric equipment might be subdivided into two further classes- stirred systems and agitated systems. The motivation in both of these cases is to drive material periodically.

5.4.1 Stirred and agitated cylindrical systems

Stirred systems- such as bladed mixers, stirred tanks and stirred mills- consist of stationary cylindrical shells whose contents are circulated by the, generally, rotational motion of an impeller. The axes of such systems can either be vertically-aligned, as is the case in certain bladed mixers and stirred tanks, or horizontally-aligned, as is the case in some stirred mills such as the IsaMill$^{\text{TM}}$.

Assuming that the stationary vessel is perfectly smooth and cylindrically symmetric, the motion of material in a vertically-aligned stirred vessel is likely also to be cylindrically symmetric. That is, the motion of the tracer particle should be independent of its angular position, for a given radial and axial position. This makes it possible to improve the probability distribution statistics by performing the radial binning procedure discussed in Section 5.3.7. For these purposes, gas- or pressure-fluidised beds can also be considered to be vertically-aligned stirred systems. The materials inside horizontally-aligned stirred systems, such as plough shear mixers, hammer mills and IsaMills$^{\text{TM}}$, experience a non-axial body force due to gravity, and so can not exhibit cylindrically symmetric motion. In such cases, the statistics of the system's probability distributions can be improved by projecting the binned data transaxially as explained in Section 5.3.7.

Agitated systems could be either rocked or rotated. Rocked systems, like rocking drum mixers or elliptically-driven vibro-fluidised beds, can be fairly difficult to analyse, at least in the Lagrangian reference frame of the system, unless the driving function is well-known. Even then, the interpretation of the results can be fairly complex because body forces like gravity may not be constant in the Lagrangian reference frame of the system. Vertically-aligned and vertically-agitated systems, like 1D pulsed vibro-fluidised beds, at least, should show a cylindrical symmetry of motion similar to that of vertically-aligned stirred systems and can thus be similarly radially binned.

Rotated systems, such tumbling mills or rotary kilns, dryers, mixers, reaction vessels and classifiers, all rely on the motion of the vessel to induce motion in its contained material. All of the systems that I mention here rotate about a horizontally-aligned axis because it is this type of system in which I am particularly interested. Such systems, much like horizontally-aligned stirred vessels, do not display cylindrically symmetric charge motion and so are not candidates for radial binning. There are rotated systems, however, such as vertical drum classifiers, which can be candidates for radial binning, and others, such as planetary mills, which present similar difficulties in analysis and interpretation as do most rocked systems.

5.4.2 Angular kinematics

If a system is at least cylindrically symmetric, well-behaved in its Lagrangian reference frame, and exhibits motion that can reasonably be interpreted as circulating about some axis, it then makes sense to consider the angular kinematics of that system. As I claimed in Section 5.3.5, it is possible to obtain the angular kinematics of a system from its RTD and binned velocity and acceleration fields, once one has defined a cylindrical reference frame.

The cylindrical reference frame

In order to do this, one must define an axis about which the reference frame is cylindrically symmetric, and zero points for the z- and θ-axes. The radial, $\hat{r}$-, direction in the resultant reference frame is perpendicular to the unit vector in the direction of the line, the $\hat{z}$-direction is parallel to the unit vector in the direction of the line, and the $\hat{\theta}$ direction revolves about this unit vector in the sense given by the right-hand rule.

In my implementation, zero points for the z- and θ-axes are defined by an additional off-axis point. The perpendicular line joining this point and the axis of cylindrical symmetry defines the zero of the θ-axis, and the intersection point of the two lines defines the zero point of the z-axis.

The point of intersection, p_0, between the axis of cylindrical symmetry, defined by the points p_1 and p_2, and the perpendicular line from a point in space p_3 can be calculated as follows.

As noted elsewhere[26], the line joining the point p_3 and the point of nearest approach to it lying on the axis of the cylinder, is perpendicular to the axis of the cylinder. Thus

$$(\vec{p}_3 - \vec{p}_0) \cdot (\vec{p}_2 - \vec{p}_1) = 0 \tag{5.16}$$

The point of nearest approach, p_0 lies on the line defined by p_1 and p_2, so it satisfies the point-direction equation of the line

$$\vec{p}_0 = \vec{p}_1 + \lambda(\vec{p}_2 - \vec{p}_1) \tag{5.17}$$

where λ is the scalar distance of p_0 from p_1 along the line joining p_1 and p_2. Using equality 5.17 in equation 5.16, and solving for the scalar distance yields

$$\lambda = \frac{(\vec{p}_3 - \vec{p}_2) \cdot (\vec{p}_2 - \vec{p}_1)}{|\vec{p}_2 - \vec{p}_1|^2} \tag{5.18}$$

which can be inserted into equation 5.17 to obtain the coordinates of the point of intersection. The line defined by the points p_3 and p_0 is, in my implementation, the zero of the θ-axis, and the point of intersection, $p_0 = (x_0, y_0, z_0)$ is at the zero of the cylindrical reference frame.

This approach can also be used to find the point on the axis of the cylindrical reference frame, p_4, nearest to a given bin. The scalar distance along the line from the zero point to p_4 is that bin's z-coordinate, and can be used to find its vector z position, $\vec{z}$. The perpendicular distance of the bin from the cylindrical axis is that bin's r-coordinate and the dot product of the normals of the lines defined by the specified off-axis point, the bin location and their points of closest approach respectively, is that bin's θ-coordinate. The perpendicular line defined by the bin location, $b = (x_b, y_b, z_b)$ and its point of nearest approach to the cylinder axis also provides a vector radial position, $\vec{r}$, and thus also a radial unit vector $\hat{r} = \frac{\vec{r}}{|\vec{r}|}$. The bin's vector θ position can be obtained from its θ-coordinate already mentioned, and the unit vector $\hat{\theta}$, given below

$$\hat{\theta} = \frac{((\vec{p}_3 - \vec{p}_0) + \langle 0, 0, z_0 \rangle) \times (\vec{b} - \vec{p}_4)}{|((\vec{p}_3 - \vec{p}_0) + \langle 0, 0, z_0 \rangle) \times (\vec{b} - \vec{p}_4)|} \tag{5.19}$$

This general case requires unit vectors to be recalculated for each bin- a computationally-expensive undertaking. If the axis of the cylindrical reference frame is already aligned with the z-axis of the Eulerian reference frame of the system, then the coordinates of each bin in the cylindrical reference frame can be written in terms of their location in Cartesian space, and of the zero of the cylindrical reference $\vec{p}_0 = \langle x_0, y_0, z_0 \rangle$, as follows:

$$\vec{b} = \begin{pmatrix} x_0 + r\cos\theta \\ y_0 + r\sin\theta \\ z_0 + z \end{pmatrix} \tag{5.20}$$

where

$$\begin{aligned} r &= \sqrt{x^2 + y^2} \\ \theta &= \arctan(\frac{y}{x}) \end{aligned} \tag{5.21}$$

[26] See Section 4.5.

and thus the unit vectors of the cylindrical reference frame as:

$$\begin{aligned}
\hat{r} &= \frac{\frac{\delta\vec{b}}{\delta r}}{|\frac{\delta\vec{b}}{\delta r}|} = \langle \cos\theta, \sin\theta, 0 \rangle \\
\hat{\theta} &= \frac{\frac{\delta\vec{b}}{\delta\theta}}{|\frac{\delta\vec{b}}{\delta\theta}|} = \langle -\sin\theta, \cos\theta, 0 \rangle \\
\hat{z} &= \frac{\frac{\delta\vec{b}}{\delta z}}{|\frac{\delta\vec{b}}{\delta z}|} = \langle 0, 0, 1 \rangle
\end{aligned} \tag{5.22}$$

In my application, I rotate non-perfectly aligned systems to take advantage of this simplification[27].

Angular measures

With such unit vectors, it is possible to project each kinematic quantity $\vec{k}$ in Cartesian coordinates into radial, angular and axial directions using the dot product. For this work I include also a tangential projection, as shown below (with the other projections for completeness)

$$\begin{aligned}
\vec{k}_r &= \vec{k} \cdot \hat{r} \\
\vec{k}_t &= \vec{k} - \vec{k} \cdot \hat{r} \\
\vec{k}_\theta &= \vec{k} \cdot \hat{\theta} \\
\vec{k}_z &= \vec{k} \cdot \hat{z}
\end{aligned} \tag{5.23}$$

(5.24)

These components in the cylindrical reference frame make possible the calculation, and binning, of a range of angular measures such as the angular velocity and acceleration of the tracer particle, since

$$\begin{aligned}
\vec{\omega} &= \frac{\vec{r} \times \vec{v}_t}{|\vec{r}|^2} \\
\vec{\alpha} &= \frac{\vec{r} \times \vec{a}_t}{|\vec{r}|^2}
\end{aligned} \tag{5.25}$$

and hence more complicated measures such as angular momentum

$$\begin{aligned}
\vec{L} &= \vec{r} \times \vec{p} \\
&= I\vec{\omega}
\end{aligned} \tag{5.26}$$

and torque

$$\begin{aligned}
\vec{\tau} &= \vec{r} \times \vec{F} \\
&= I\vec{\alpha}
\end{aligned} \tag{5.27}$$

where m is the mass of the tracer particle, and I its *moment of inertia* about the axis of rotation

$$I = m|\vec{r}|^2 \tag{5.28}$$

assuming that it is not revolving itself, and so on. Many more examples will be given from Chapter 6 onwards.

[27] See Section 5.5.1.

5.4.3 Cylindrical binning

So far I have explained the procedure for translating data from a Lagrangian particle tracking experiment into the Eulerian reference frame of the system of interest using binning in general and residence time binning in particular. In Section 5.4.2 above, I showed that it is possible to to obtain the radial and angular positions of a bin in Cartesian space relative to an axis defined by two points along it. Thus each bin in Cartesian space can be assigned a location in cylindrical space. This makes it possible to re-bin already residence time binned[28] data in the cylindrical reference frame.

I have implemented two types of cylindrical binning in this work- radial binning, and polar binning.

Radial binning

Radial binning is the allocating of each bin in Cartesian space to its location in a space defined by it's $\hat{z}$ and $\hat{r}$ coordinates, as defined in Section 5.4.2.

I do this by dividing the rz space into a specified number of bins and assigning to each rz bin, the time-weighted average values contained by the residence time bins whose $\hat{r}$ and $\hat{z}$ fall in that bin. This is an implementation of the simple binning procedure[29] in which the effect of increasing the sampling frequency by interpolation[30] is obtained by increasing the resolution of the RTD.

Radial binning is particularly useful in cylindrically symmetric systems with little or no angular dependence, such as vertically aligned fluidised beds or flotation columns.

Polar binning

Polar binning is the allocating of each bin in Cartesian space to its location in a space defined by it's $\hat{\theta}$ and $\hat{r}$ coordinates, as defined in Section 5.4.2. It is performed in exactly the same way as radial binning, with the same considerations.

Polar binned data makes explicit regularities in the binned data that show radial or angular dependence, but little variation along the axis of the cylinder. I use polar binning later as a step towards obtaining certain charge features[31], and to investigate the limits of rigid-body and other behaviours in angular ranges[32].

5.4.4 Radial bin selection

In Section 5.3.7 I alluded to the usefulness, on occasion, of sectioning and projecting binned data. In the case of cylindrically-symmetric data, a natural projection is in the axial plane- which could also be done in axial sections- and a useful section is the radial one.

I have implemented two radial bin selection routines for 2D projections- one takes a specified number of evenly spaced radial slices through a given centre in the 2D grid, and the other takes a single slice at a specified angle. The latter routine is useful in calculating shear rates in Section 5.5.6 below. Both of these routines are based on producing a mask- an array of the same size as the projected grid containing 1s in elements whose coordinates fall along the required slice, and 0s

[28] See Section 5.3.5.
[29] See Section 5.3.4.
[30] See Section 5.2.
[31] See Section 5.5.2.
[32] See Chapters 6 and 7.

elsewhere- which can be used as a multiplicative factor to select radial slices from the projections of a range of binned kinematics for plotting in easy to interpret 2D graphs.

In the case of radially binned data[33], the radial position of the sample point is unambiguous, but in the full 2π projection, radii with non-zero projections onto the negative x-axis are labelled as negative, and those with non-zero projections onto the positive x-axis as positive. Angular positions are measured from 0 to $\frac{\pi}{2}$ radians anticlockwise from the positive x-axis, and from 0 to $-\frac{\pi}{2}$ radians in the clockwise direction.

5.5 Application-tumbling mills

The horizontally-aligned rotated systems that I have mentioned in Section 5.4 fall into two broad categories- mixing and segregating systems, with the tumbling mill a complicated combination of the two[34].

Mixing systems, such as rotary kilns, dryers, mixers and reaction vessels, are cylindrically symmetric systems whose operation rely on the material inside them being continuously circulated through as much of the volume of the system as possible. In the case of rotary kilns, and of rotary dryers and reaction vessels, this is to expose as much of the circulating material to as much as possible of the heat applied to the surface of the vessel or reactant[35] pumped through it, respectively. In the case of rotary mixers, it is simply to produce as uniformly mixed a product as possible.

Segregating systems, such as rotary classifiers, are the exact opposite. They rely on the segregation of their constituent particles into preferred orbits by size, shape, density and so on. An example of a vertically-aligned rotary classifier is the familiar centrifuge- a device used to separate materials by density, and an example of a horizontally-aligned one is the trommel- a device used in the mining industry to separate material by size.

As discussed in Chapter 3, a tumbling mill-a rotating cylinder containing granular material of various sizes, shapes and densities- can also experience segregation. Tumbling mills are, after all, the same machines in principle as both rotary mixers and trommels. The grinding efficacy of tumbling mills can be enhanced if oversize particles are segregated into grinding regions, and undersize particles into transport regions. Industrial tumbling mills are fed oversize rocks at one end and discharge undersize product on the other. This fresh feed must be efficiently mixed into the body of the charge for grinding. Thus a tension exists between the mixing and segregating modes of the tumbling mill.

Segregation and mixing efficacy are driven by the motion of the charge in the tumbling mill, as is the proportion of the mill's power partitioned into each of the grinding mechanisms. In Chapters 6 and 7, all of the binning techniques mentioned so far, as well as the special cases mentioned below, will be used to elucidate the motion of charge in tumbling mills.

5.5.1 Pre-processing

The tumbling mill is, of course, a system with cylindrical symmetry. As mentioned in Section 5.4.2, the calculation of angular kinematics in such a system can be greatly simplified if its axis of cylindrical symmetry is aligned with one of the axes in the Eulerian reference frame of the system.

[33] See Section 5.3.7.
[34] Of course, mixing and segregation are far from exclusive to cylindrically symmetric systems.
[35] Chemical in the case of reacting vessel or hot, dry air in the case of rotary dryer.

In practice, it is not always possible to ensure that the system being studied is perfectly aligned with one of the axes of the reference frame. This can be dealt with by using marker points to define the Lagrangian reference frame of the system and then rotating the data until this Lagrangian reference frame is correctly aligned. In the case of tumbling mills, this is particularly easy.

Since a tumbling mill rotates about its axis of cylindrical symmetry, a tracer particle attached to a known point on the surface of its shell will trace out a circle in space. Such a circle in 3D space can be expressed in terms of its radius, centre and two angles of orientation, as derived below. These parameters can be used to translate and rotate the Lagrangian reference frame of the mill so that its axis of cylindrical symmetry aligns with the z-axis of the Eulerian reference frame of the system. In this implementation, these parameters are based on either 3 or 4 fitted circles, depending on the size of the mill. The procedure I have followed in doing this is given in Appendix F.

Once the mill has been centred and aligned in the Eulerian reference frame of the system, it is possible to take advantage of the simplifications mentioned in Section 5.4.2 when treating it as an instance of the special case of cylindrical symmetry [36].

5.5.2 Charge regions

Tumbling mills have been workhorses in the minerals processing industry for over a century[37], and as such have been studied in some detail in so far as has been possible with existing non-invasive techniques.

One, particularly fruitful, approach has been to observe the motion of the charge inside tumbling mills through a transparent end wall[38]. This has enabled researchers to investigate the two-dimensional features of the moving charge in the transverse section of the mill.

Qualitatively, the motion of the charge in a tumbling mill takes on a distinctive S-shape[39]. The form of this S, from an almost flat surface to a very pronounced curve as shown in Figure 5.10, depends on the speed at which the mill shell is being rotated, the volume of charge in the mill, and the geometry of the mill liner[40].

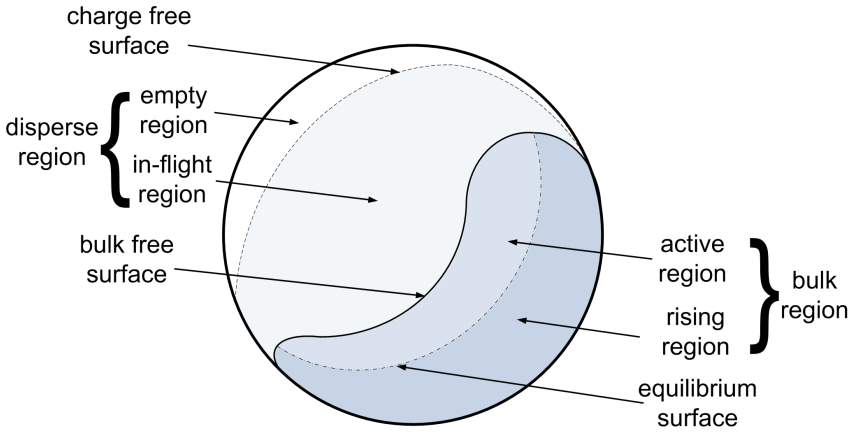

Figure 5.10: A schematic of the transverse section of a tumbling mill showing the distinct regions of the charge in motion.

[36] See Section 5.4.
[37] See Chapter 3.
[38] See Chapter 3.
[39] See Chapter 3.
[40] See Chapters 6 and 7.

This characteristic S-shape is the shape of the surface, called the bulk free surface, that divides the dense bulk region of the charge moving as a granular body and the dilute disperse region of the charge in free fall above it. In this section I offer procedures for obtaining this, and the other surfaces that divide the moving charge into distinct regions, quantitatively.

Edge detection and free surfaces

The bulk free surface of the charge in a tumbling mill can easily be identified, for instance, by eye from a streak image taken through a transparent end-window or, in the case of PEPT data, from a cylindrically-binned[41] transverse projection of the RTD of a tracked particle of the charge[42].

Computationally, the easiest way to obtain the bulk free surface is by using the image analysis procedure of edge detection. Edge detection is a well-established technique supported by a large body of literature spanning several decades. At its crux is the realisation that an edge in an image[43] generally occurs at a line of maximum change in intensity. The essence of edge detection is thus just the calculus of variations.

Unfortunately, intensity gradients along an edge do not generally show the steps or discontinuities necessary to unambiguously identify that edge, and certainly not all the way along the edge. A good deal of filtering, thresholding and multi-step processing must be done in order to robustly obtain these edges, especially in a case such as ours in which the edge is required to form a closed loop.

In this work, I use a so-called *Laplacian of a Gaussian* smoothing filter followed by a closed-loop *Canny*[Canny, 1986] edge detection routine to obtain the bulk free surface of the charge.

Due to the chaotic motion of the charge in the toe region, and the halo of charge of intermediate density between the bulk region and disperse region, there is still some uncertainty in what constitutes the actual bulk free surface of the charge. I use as a threshold the minimum porosity in which a particle of the size being considered would not be in contact with any other.

The requirement that the detected edge should form a closed loop (with the shell), delineating the bulk region of the charge is a stringent one. It turns out that the edge detection routines are much more stable for concave shapes. For this reason, I use the polar binning procedure described in Section 5.4.3 to obtain concave polar shapes for the charge as shown in Figure 5.12.

A polar bin is, of course, periodic in its angular coordinate. Figure 5.12 consists of two such plots- Figure 5.11a shows the charge centred in the angular direction on the angular position of the centre of circulation (CoC)[44], and Figure 5.11b shows the same charge centred on the angular position between the *departure shoulder* and *re-entry toe*[45].

Both Figures 5.11a and 5.11b show concave shapes that bound, in the case of Figure 5.11a, the bulk region of the charge and, in the case of Figure 5.11b, the empty region of the charge. These, excluding the straight vertical line of the mill shell, are the bulk free surface and charge free surface respectively.

The shape of these two free surfaces are strongly determined by the operating parameters of the tumbling mill, and can be used to characterise the motion of the charge, as described in Chapter 3.

[41] See Section 5.4.
[42] See Section 5.3.5.
[43] An image, such as that produced by the binning procedure, consists of a 2D array of pixel values.
[44] See Section 5.5.3.
[45] See Section 5.5.3.

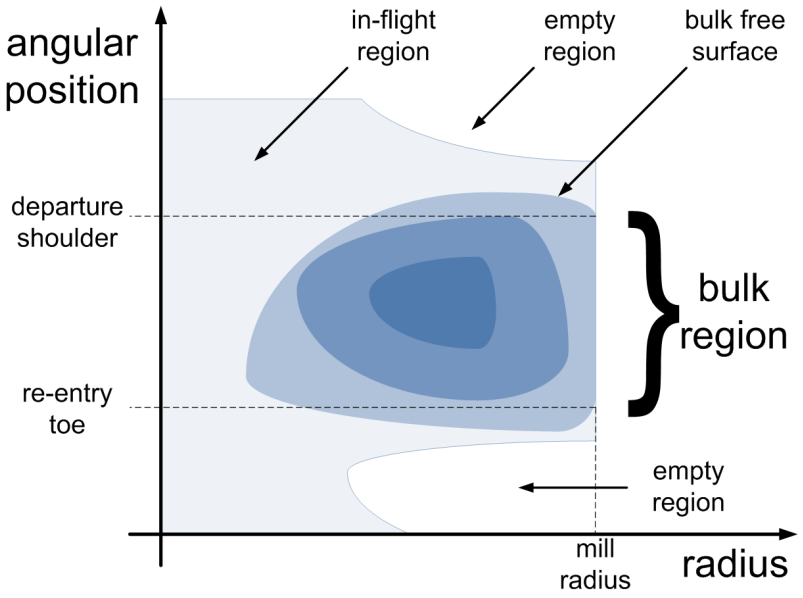

(a) Polar bin plot of the bulk region of the charge

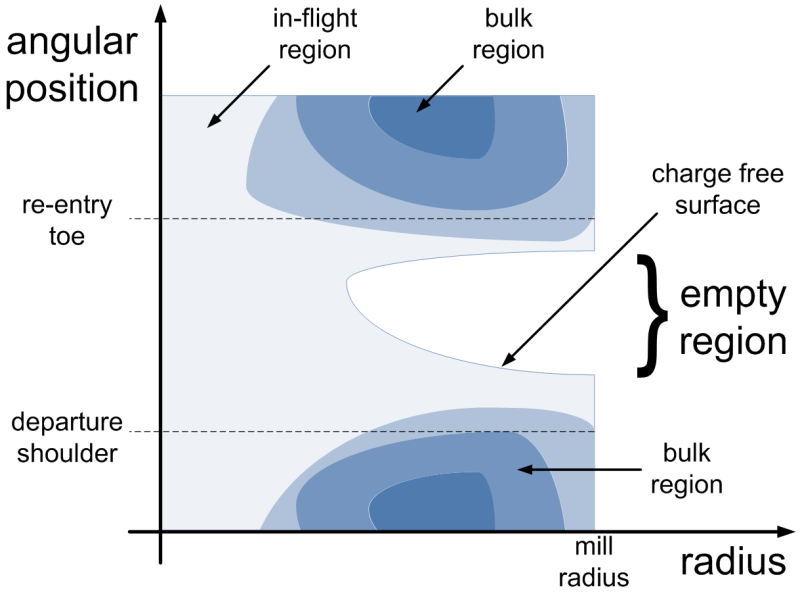

(b) Polar bin plot of the disperse region of the charge

Figure 5.11: Two schematics of a polar bin plot of a typical tumbling mill experiment, focussing on the bulk region (above) and the disperse region (below).

The equilibrium surface

The region of the charge below in the bulk free surface is called the bulk region. It consists of granular charge of sufficient density that its constituents are in contact with each other at all times. The bulk region is made up of two distinct regions- the rising region and the active region.

The rising region of the charge, as the name suggests, is that portion of the charge that is moving upwards through contact with either the mill shell or other rising charge. As I discuss in Chapters 6 and 7, charge in this region displays quasi-rigid body motion about the centre of the mill[46].

The active region of the charge consists of material flowing down over the rising charge under the influence of gravity. It is sufficiently dilute to be able to flow in a fluid-like, albeit high dissipative, way, but not so dilute that any of its constituents are in free fall at any time. It includes a layer of

[46]With some complications involving the CoC.

charge, called the transition layer, in which the density of the bulk region drops off very sharply to that of the in-flight region of the charge, and also the chaotic toe region in which charge from the in-flight region impacts with and remixes into the active region proper.

The surface that separates the active region from the rising region is called the equilibrium surface. It is obtainable from the binned velocity distribution in the transverse section of the mill by recognising that charge on either side of it are moving in opposite directions. The equilibrium surface is the interface between these two regions at which, as is obvious through continuity considerations, the velocity of the charge must be zero.

Data obtained from *Lagrangian* particle tracking techniques takes the form of locations and their associated times, from which can be obtained velocities at each location and time in each dimension separately[47]. Velocities in the components of the transverse section can be residence time-binned to yield two velocity distributions, as shown schematically in Figures 5.12a and 5.12b. The intersection of these two surfaces is called the CoC[48]. Figure 5.12c shows the equilibrium surface, which consists of the the vertical free surface above the *centre of circulation*, and the horizontal free surface below it.

5.5.3 Charge features

One of the most complete discussions of the 2D features of the moving charge inside a tumbling mill was given by Powell and Nurick using streak images taken through the transparent end wall of a laboratory-scale mill[Powell and Nurick, 1996a, Powell and Nurick, 1996b, Powell and Nurick, 1996c]. In later work, using the discrete element method (DEM), Powell and McBride produced a more complete and mathematically refined set of these definitions [Powell and McBride, 2004]. In this work I further extend the number and mathematical rigour of these definitions to take advantage of the detailed information available from PEPT.

Figure 5.13 shows a schematic of the features of the moving charge that I will define below. In order to do so, I will appeal to the definitions of the charge regions that I have developed in Section 5.5.2 above, and draw heavily on the work of Powell *et al.*

The centres of circulation and of mass

The centre of circulation (CoC) of the moving charge is usually thought of as the point about which the charge rotates in a transverse section of the mill. However, it is actually a curve broadly parallel to the axis of the mill, and so should perhaps be called the axis of circulation. Once end effects have been dealt with, however, it is strictly parallel to the axis of the mill[49], and so can be approximated as a point in the transverse plane.

In general, the CoC of the dynamic charge in a tumbling mill does not coincide with the centre of the mill[50]. If it is the point about which the charge rotates, it must be in the bulk region, since the bulk region consists of rising charge- the rising region- and falling charge- the active region. In fact, it is the point of intersection between the horizontal and vertical free surfaces defined in Section 5.5.2[51], and can thus be unambiguously determined as a step in obtaining the equilibrium

[47] See Section 5.1.1.
[48] See Section 5.5.3.
[49] Within stochastic variations.
[50] Except when the mill is either very full, or moving so fast that the charge is centrifuging. See Chapter 3.
[51] This makes intuitive sense because the point about which charge rotates must itself be stationary. The vertical equilibrium surface joins points with zero velocity in the vertical direction, and the horizontal one joins points of zero velocity in the horizontal direction. Their intersection thus is a point with zero vertical and horizontal velocities- a stationary point.

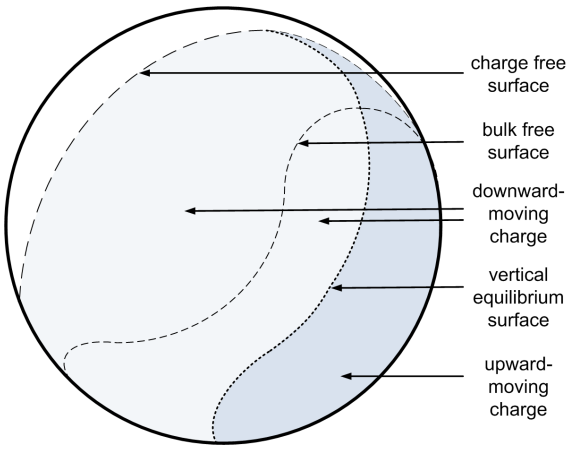

(a) A binned vertical velocity distribution showing the vertical equilibrium surface that divides the upward- and downward-moving charge.

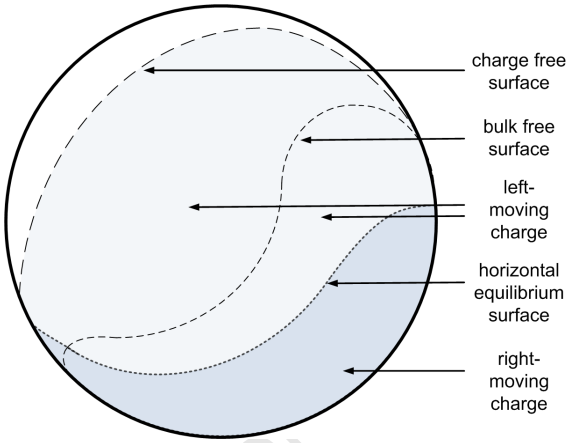

(b) A binned horizontal velocity distribution showing the horizontal equilibrium surface that divides the left- and right-moving charge.

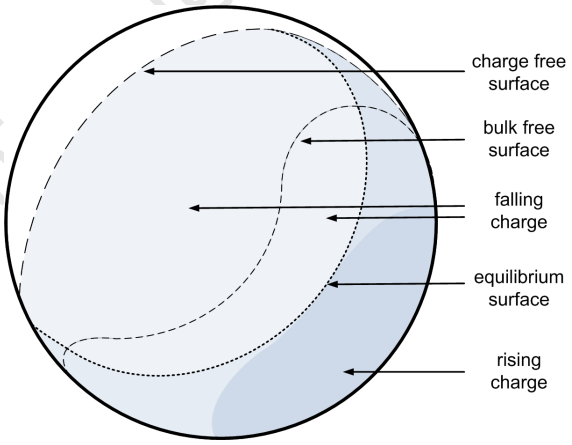

(c) A superposition of the binned horizontal and vertical velocity distributions showing the equilibrium surface that divides the rising and falling charge.

Figure 5.12: Schematics of the transverse section of a tumbling mill showing the vertical equilibrium (top), horizontal (middle), and combined (bottom) equilibrium surfaces.

surface[52]. The angular position of the CoC is often quoted as the dynamic angle of repose of the moving charge.

The centre of mass (CoM) of the charge also does not, in general, coincide with the centre of the

[52]See Figure 5.12c.

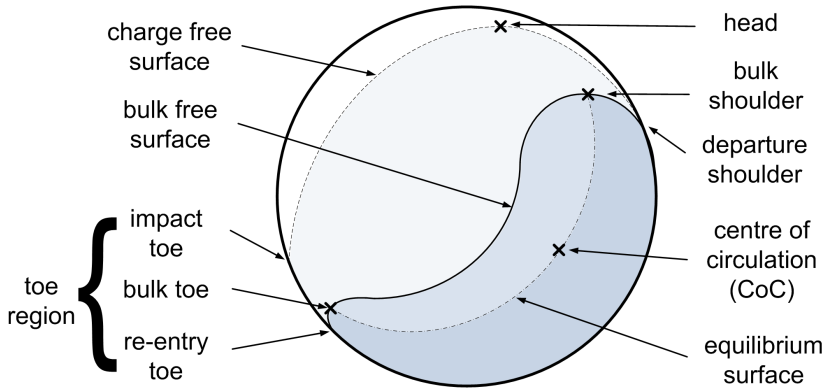

Figure 5.13: A schematic of the transverse section of a tumbling mill showing the features of the charge in motion.

mill[53], and neither does it generally coincide with the CoC of the charge. The CoM of a body made up of identical particles[54] is easily obtainable from the *Lagrangian* location data, or from the *Eulerian* binned data as

$$\vec{r}_{CoM} = \frac{\Sigma_i^N m \cdot \vec{r}_i}{\Sigma_i^N m} = \frac{m\Sigma_i^N \vec{r}_i}{m \cdot N} = \frac{1}{N}\Sigma_i^N \vec{r}_i \tag{5.29}$$

The CoM of a body made up of a range of different particle types is the mass-weighted average of the CoMs of each of the different particle types calculated separately. A similar argument can be made for the CoC of such a body.

Head, shoulders and toes

Although the bulk free surface of the charge is, as I will show in Chapters 6 and 7, a good indicator of the type of motion occuring in a tumbling mill, it is often more convenient to compare different regimes by comparing so-called scalar indicators. Powell and McBride define four of these- the head, shoulder, bulk toe and impact toe of the charge.

I retain Powell and McBride's definition of the head- the highest point attained by the outermost layer of in-flight charge. This is obtainable by searching for the highest bin occupied in each vertical row of bins- that is, the largest y-component for each band of x-components- and then fitting a quadratic[55] smoothing function to the resultant points. The head of the charge is the turning point of this quadratic function.

Powell and McBride define the shoulder of the charge as the '[u]ppermost point at which material leaves the mill shell'. I redefine this point as the departure shoulder of the charge. The departure shoulder can be obtained by one of two methods, both involving a polar bin plot[56] of the RTD of the charge. The first method is just to apply an averaging filter to the polar bin plot to fill in stochastically empty bins in the in-flight region and then extracting the range of empty $r = r_{mill}$ bins. The beginning and end of this range corresponds to the angular positions of the departure shoulder and impact toe respectively. My impact toe is the one defined by Powell and McBride as the '[h]ighest point at which cataracting material strikes the mill shell'.

[53] Except in the same circumstances as for the CoC.
[54] Given by the locations of the tracer particle by the ergodic hypothesis.
[55] Since the in-flight charge is, of course, in free fall.
[56] See Section 5.4.3.

Powell and McBride elsewhere in the same paper define the impact toe as '[t]he *region* where cataracting charge impacts on the mill shell', emphasis mine. I call the region between the impact toe and a re-entry toe the toe region. I define the re-entry toe as the intersection between the mill shell and the bulk free surface of the charge. At high mill speeds or severe lifter angles, charge may be carried by the lifters out of the bulk region to the departure shoulder as defined above. In this case, I define an addition bulk departure shoulder as the intersection of the mill shell and the bulk free surface.

Finally, Powell and McBride define a bulk toe as '[t]he intersection of the equilibrium surface with the mill shell, when all direct impact events are excluded'. I define the bulk shoulder and bulk toe as the upper and lower intersections between the bulk free surface and the equilibrium surface.

Not all of these charge features are defined for all types of charge motion. In particular, there are two important limiting cases- slow- and fast-moving mill shells, complicated by mill liner geometries and mill loads.

In the case of a slowly rotated mill (exacerbated by shallow or no lifters, and large mill loads), there may be no charge in the in-flight region- the disperse region may consist entirely of the empty region. In such a case, the head of the charge would coincide with its bulk shoulder, its departure shoulder would coincide with its bulk departure shoulder, and its impact toe would correspond with its re-entry toe. The term impact toe would thus be slightly misleading, and the toe region would not exist.

In the case of the quickly rotated mill (exacerbated by severe lifters and small mill loads), the in-flight charge may fill the disperse region of the mill, which would then coincide with, nonsensically, the toe region. The departure shoulder and re-entry toe would be undefined, as would be the equilibrium surface, the free surfaces, and thus the bulk toe and shoulder. In such a case, the CoC and CoM would approach and even coincide with the centre of the mill.

These considerations are dealt with as special cases in my implementation.

5.5.4 Power draw and ergodicity

In Section 5.3.1 I asserted that there was no way to know *a priori* whether a system would obey the ergodic assumption or, if it did, how long it would take for it to fulfil the ergodic hypothesis. For this work, I use the power drawn by the charge as a test of ergodicity.

The power drawn by a tumbling mill can be measured non-invasively at its drive end. This fact, together with correlations between power drawn and grinding efficacy, has made mill power draw an important diagnostic and control variable on the plant[57]. The power drawn by the laboratory scale mills used in this work was measured as described in Chapter 4.

At steady state, the power drawn by a tumbling mill is roughly constant[58]. This is especially true in the case of a batch mill of conditioned charge[59]. The fact that the charge reaches steady state is demonstrated by the measured mill power[60]. The power drawn by a tumbling mill can, for comparison, be calculated from the *Lagrangian* trajectory of a representative tracer particle, as long as the ergodic assumption holds.

[57] See Section 3.

[58] There are variations in the power draw due to the action of the lifters, surging of the charge, and statistical fluctuations.

[59] Charge that has already been milled so that only hard and unlikely to break particles remain.

[60] See Chapters 6 and 7.

Bbosa *et al.*[Bbosa et al., 2011] introduce two methods of calculating the power draw from data produced by the PEPT technique- the CoM approach, and the torque per bin approach.

The CoM approach to calculation the power drawn by a tumbling mill is also often called the torque arm approach. In this approach, the charge is modelled as a single particle of the same mass as the charge in the position of its CoM[61]. This point mass experiences a gravitational torque about the centre of the mill[62], and is considered to rotate about the centre of the mill with the same angular frequency as the mill shell. This yields an estimate of the power drawn given by

$$P_{CoM} = \tau \cdot \omega = MgR_{CoM} \cos\theta_{CoM} \omega_{shell} \tag{5.30}$$

Although in [Bbosa et al., 2011] Bbosa *et al.* take the angular frequency of the charge condensed to it CoM to be that of the mill shell, some discussion has taken place about replacing it with the circulation rate or bed turnover rate of the charge. For completeness, I have implemented this version too, based on the circulation rate calculations I mention in Section 5.5.5.

The second approach of Bbosa *et al.* is the torque per bin approach one. In this case, each bin in the RTD is taken to exert a torque about the central axis of the tumbling mill, and to rotate about the centre of the mill with its own angular frequency. The resultant power draughts are then summed for all N bins as

$$P_{bin} = \frac{Mg}{\Sigma_i^N t_i} \Sigma_i^N t_i r_i \cos\theta_i \omega_i \tag{5.31}$$

Bbosa *et al.* consider the centre of the mill to be the point about which each bin rotates. Using the procedures I have developed for the special case of cylindrical symmetry discussed in Section 5.4.3 above, I have implemented a version of the torque per bin approach in which the bins rotate about the CoC of the charge.

Finally, Bbosa *et al.* include all of the charge in their analyses, but using bin selection by the regions I have defined in Section 5.5.2, I can consider the contribution to the total power draw from different regions[63].

In Chapters 6 and 7, I compare all of the foregone power draw calculations and use the most applicable to bound the ergodic assumption and verify the ergodic hypothesis for tumbling mills.

5.5.5 Circulation rate

The circulation rate of the charge in a tumbling mill is often called its bed turnover rate because it is a measure of how often, on average, the charge circulates about the CoC. Of course, since the charge is not a rigid body[64], layers at increasing radial distance from the CoC will circulate at different rates.

In my implementation, I use the pre-processing procedures developed in Section 5.5.1 to rotate the charge in 3D space in such a way that the centre of the mill is aligned with the $\hat{z}$-axis of the Eulerian reference frame of the field of view, and the surface passing through the $\hat{z}$-axis and the axis of circulation is in the xy-plane. This surface is the one through which all of the circulating charge

[61] Hence the name.
[62] Again, hence the name.
[63] See Chapters 6 and 7.
[64] See Chapters 6 and 7, and consider the requirement for the conservation of mass given that the rising charge forms a thinner and thus slower layer than the falling charge.

must eventually pass. Thus every second zero-crossing in the interpolated function of position in either the $\hat{x}$ or $\hat{y}$ direction[65] marks the beginning of a new orbital period of variable length.

Histogramming these periods results in a distribution of orbital times, which can be fit with an appropriate distribution[66] to obtain an estimate of the mean and range of orbital periods of the tracked particle. The inverse of this mean period is the mean orbital frequency of the particle, interpreted as the circulation rate of the charge.

5.5.6 Radial measures

In Section 5.4.4 I explained the procedure I have implemented for selected radial bins through a given centre in a 2D projection of a, generally cylindrically symmetric, RTD.

This procedure is a useful one in the case of tumbling mills, which, as well as being an important piece of mining machinery, are also an exemplar of a class of gravity and shear-driven granular systems. Radial bin selection allows the *Lagrangian* particle trajectory data visualised in the Eulerian reference frame by binning to be converted into a series of functions of r and θ; as functions in the natural reference frame of the system. The potential applications of such functions for granular flow modelling are powerful indeed.

To return to the more specific case of the tumbling mill, however, the most important application of radial bin selection is in the calculation of shear rates, which have implications for grinding efficacy[67].

Shear rates

The shear rate of a material is related to its shear stress tensor by a constitutive law. The shear stress tensor is a component of the total stress tensor, which can be related to power dissipation and grinding efficacy in tumbling mills. As well as this practical application of the shear rate, the constitutive laws that relate shear stress and shear rate are an active research area in granular flow, and are thus of intrinsic value.

The motion of charge in a tumbling mill can be modelled as that of layers concentric with the CoC. In fact, since in a batch mill there is assumed to be little or no movement in the axial direction, this motion reduces to a relative movement in only one direction in the cylindrical reference frame- the $\hat{\theta}$-direction.

This assumption is not, of course, strictly true, but it is a useful simplification. Given this concentric layer assumption, the shear rate in a tumbling mill can be written in cylindrical coordinates as

$$\dot{\gamma} = r\frac{d}{dr}\left(\frac{v_{\theta(r)}}{r}\right) \tag{5.32}$$

where r is the radial position of the bin, and $\theta(r)$ is the functional form of the velocity associated with that bin projected in the $\hat{\theta}$-direction, as calculated in Section 5.4.2.

[65] as appropriate
[66] Such as a normal or Gaussian distribution.
[67] See Chapter 3.

5.6 Summary

In this chapter I have discussed the analysis routines that I have applied to the experimental data described in Chapter 4. I have introduced and justified the assumptions that must be made to convert data in the Lagrangian reference frame into the more easily interpreted Eulerian reference frame, and developed techniques to present this Eulerian data in illuminating ways. I have presented these techniques in the general case, in the special case of cylindrical symmetry and as applied to tumbling mills. In Chapters 6 and 7 I will present the results of these analyses.

References

[Bbosa et al., 2011] Bbosa, L., Govender, I., Mainza, A., and Powell, M. (2011). Power draw estimations in experimental tumbling mills using pept. *Minerals Engineering*, 24:319–324.

[Canny, 1986] Canny, J. (1986). A computational approach to edge detection. *IEEE Transactions on Pattern Analysis and Machine Intelligence*, PAMI-8:679–698.

[Powell and McBride, 2004] Powell, M. and McBride, A. (2004). A three-dimensional analysis of media motion and grinding regions in mills. *Minerals Engineering*, 17:1099–1109.

[Powell and Nurick, 1996a] Powell, M. and Nurick, G. (1996a). A study of charge motion in rotary mills part 1- extension of the theory. *Minerals Engineering*, 9:259–268.

[Powell and Nurick, 1996b] Powell, M. and Nurick, G. (1996b). A study of charge motion in rotary mills part 2- experimental work. *Minerals Engineering*, 9:343–350.

[Powell and Nurick, 1996c] Powell, M. and Nurick, G. (1996c). A study of charge motion in rotary mills part 3- analysis of results. *Minerals Engineering*, 9:399–418.

Part III

Results and conclusions

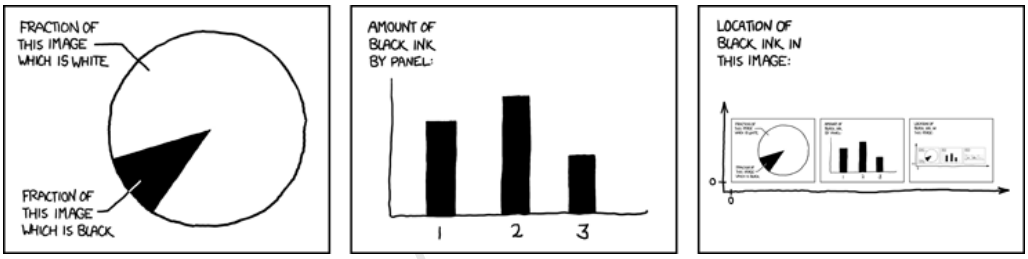

www.xkcd.com

Chapter 6

A basic analysis

In this, the first of my results chapters, I will present a basic set of analyses of the trajectory data obtainable from PEPT. In order to do so, I will consider two experiments. Both were performed on the 'old' 300mm diameter tumbling mill[1], filled to 31.25% of its volume[2] with a monosize charge of 3mm diameter glass beads.

6.1 Tracer particle locations

6.1.1 3D tracer locations

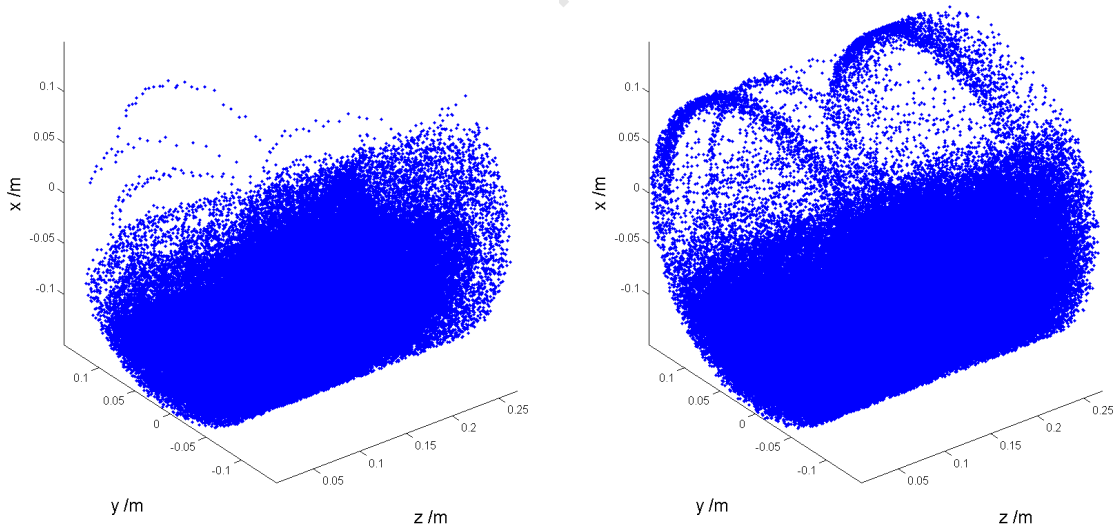

(a) 60%*ofcriticalspeed.* **(b)** 75%*ofcriticalspeed.*

Figure 6.1: Combined 3D plots of all of the triangulated locations of a 3mm tracer particle in the 'old' 300mm mill filled to 31.25% and rotated at 60% (left) and 75% (right) of its critical speed.

The first of these experiments is of the 'old' 300mm mill rotated at 60% of its critical speed, and the second at 75% of its critical speed. The complete set of tracer particle locations triangulated from data collected over these two hour-long experiments are shown in Figures 6.1a and 6.1b.

The plots shown in Figure 6.1 are dense and difficult to interpret. Perhaps the only point of interest

[1] See Section 1.
[2] See Section 4.3.3.

is that it appears that particles had begun centrifuging even at 75% of the mill's critical speed. Of course, this could be due to the particle getting stuck in a lifter, or coated with some contaminant, or even charged with static electricity- all impossible to tell *a posteri*.

6.1.2 Variations in the tracer location with time

The data obtained from a PEPT experiment takes the form of trajectories; of sets of locations of the form (t_i, x_i, y_i, z_i). Rather than plotting all of the locations in 3D space, it can be of interest to plot the variation of each component of the tracer particle's motion as a function of time.

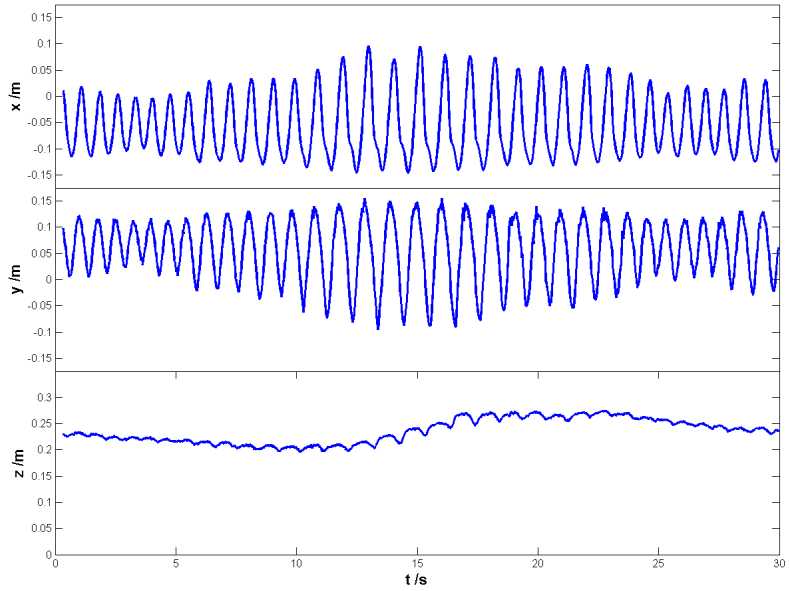

(a) 60% of critical speed.

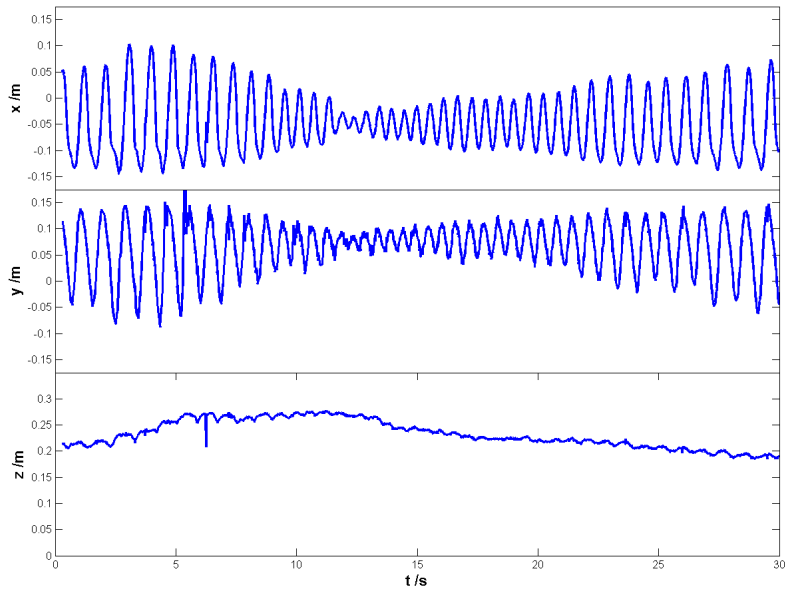

(b) 75% of critical speed.

Figure 6.2: The variation of the $\hat{x}$ (top), $\hat{y}$ (middle), and $\hat{z}$ (bottom in each subplot) coordinates of a $3mm$ tracer particle in the 'old' $300mm$ mill filled to 31.25% and rotated at 60% (top subplot) and 75% (bottom subplot) of its critical speed, for the first $30s$ of each experiment.

Figure 6.2 shows the variation of the tracer particle's $\hat{x}$, $\hat{y}$ and $\hat{z}$ coordinates over the first $30s$ of

each of the experiments mentioned above. Here the $\hat{x}$ and $\hat{y}$ directions are transaxial; they define the plane of circulation of the charge. Thus the variation of the $\hat{x}$ and $\hat{y}$ coordinates are sinusoidal. The variation of the $\hat{z}$ coordinate- the axial direction- is comparatively small over the length of the $30s$ intervals shown in Figure 6.2.

Figure 6.3 shows the variations of each of the coordinates for the full hour of the 60% of critical experiment. In the lowest frame of this figure it can be seen that the $\hat{z}$-coordinate of the tracer particle's position varies stochastically, but that it does traverse the full length of the $270mm$ internal length mill, satisfying the minimum condition for the application of the ergodic hypothesis[3].

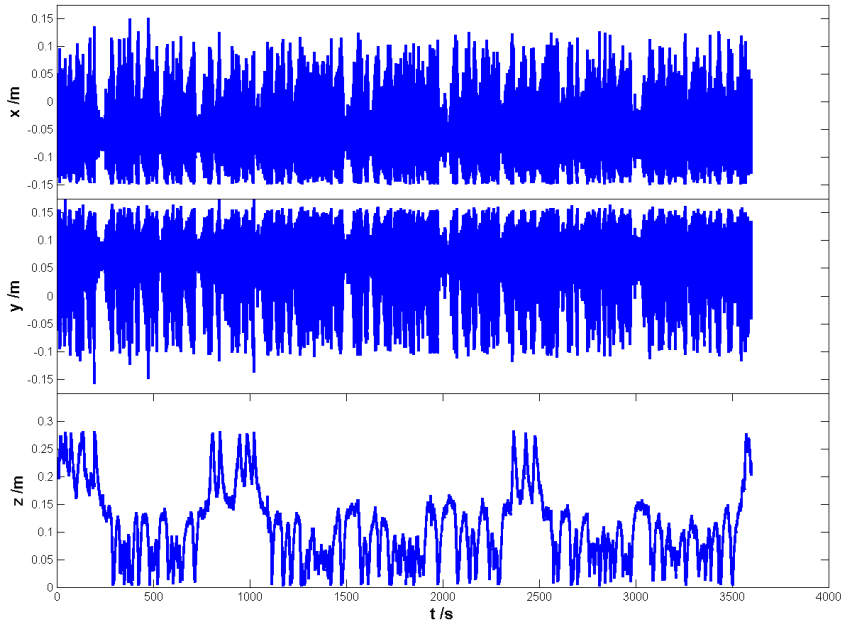

Figure 6.3: The variation of the $\hat{x}$ (top), $\hat{y}$ (middle), and $\hat{z}$ (bottom) coordinates of a $3mm$ tracer particle in the 'old' $300mm$ mill filled to 31.25% and rotated at 60% of its critical speed, for a full, hour-long experiment.

The stochastic behaviour of the tracer particle in the $\hat{z}$-direction is because there is no preferential pressure in the axial direction. This is because the mill is horizontal, there is no feed or discharge of the material in the mill- the mill is in 'batch' mode- and there is no fluid pressure. Thus the tracer particle is, in some sense, diffusing along the length of the mill during the experiment.

Since all of the experiments I will discuss in these results are of *batch* mills, I feel justified in treating the motion of the charge in these mills as effectively 2D, or at least as dominated by its 2D transverse motion. For this reason I will, from now on, consider only the transaxial plane of the mills under study.

6.1.3 Transaxial projections

Figure 6.4 shows 2D transaxial projections of the tracer particle locations shown in Figure 6.1. Here the shape of the charge, at least, is a good deal clearer than it was in the full 3D plot. In each of these 2D projections are visible the S-shape of the free surface of the charge, the fluidised material in the shoulder, and the developing cataracting stream. In Figure 6.4b is also more clearly visible the centrifuging charge already mentioned.

[3]See Section 5.3.1.

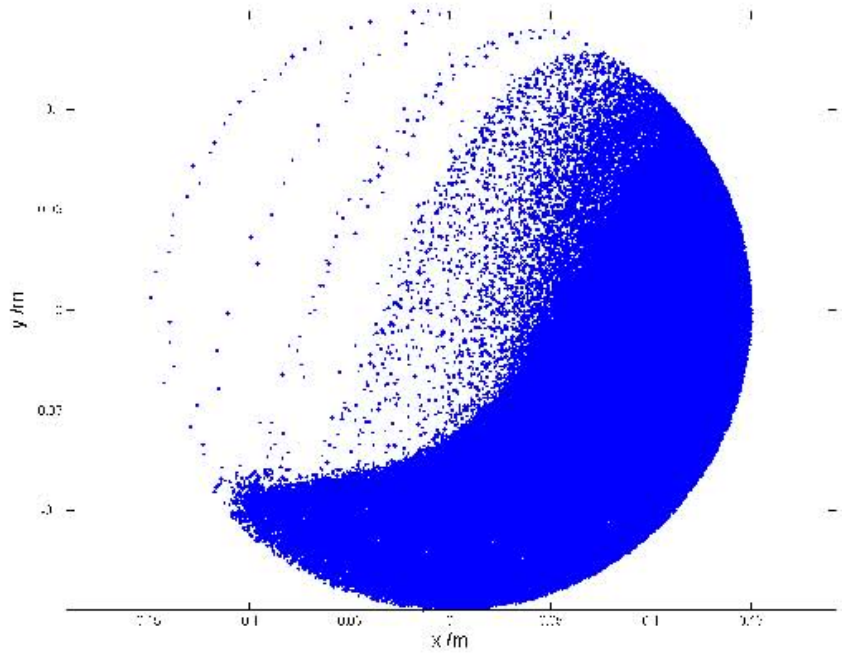

(a) $60\% of critical speed.$

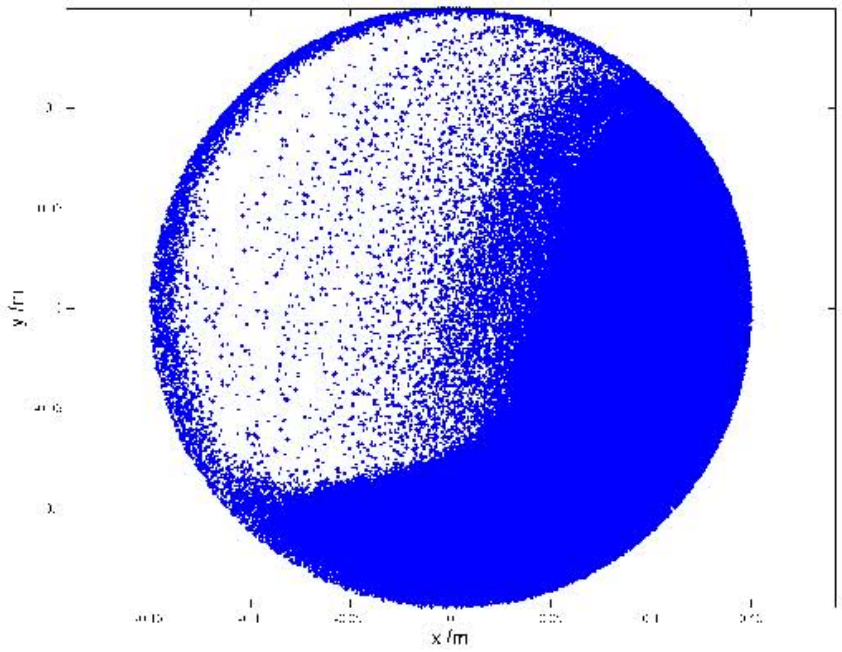

(b) $75\% of critical speed.$

Figure 6.4: Transaxial projections of all of the triangulated locations of a $3mm$ tracer particle in the 'old' $300mm$ mill filled to 31.25% and rotated at 60% (top) and 75% (bottom) of its critical speed.

6.1.4 Residence time distributions

Although it is of interest to consider the variations in the coordinates of the tracer particle, and the point-cloud of locations in two- or three-dimensional space, the real power of PEPT data comes in converting it from the Lagrangian reference frame to the Eulerian reference frame by residence time binning[4]. Figure 6.5 shows the RTDs of the $3mm$ tracer particle in each of the two experiments under consideration here[5].

[4]See secion 5.3.5.

[5]See Appendix I for a discussion of the optimal bin size to use.

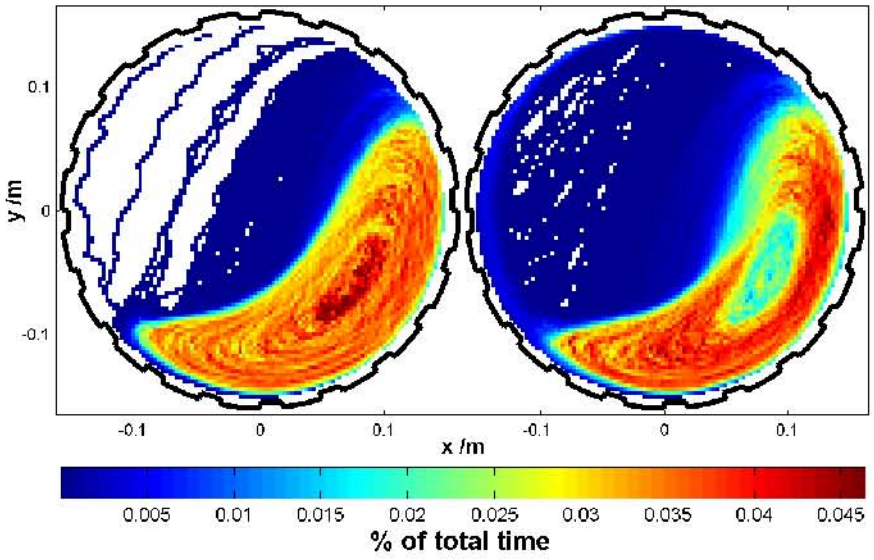

Figure 6.5: The residence time distributions of a $3mm$ tracer particle in the 'old' $300mm$ mill filled to 31.25% and rotated at 60% (left) and 75% (right) of its critical speed.

The RTD is related to the mass distribution of the class of particles represented by the tracer particle by a factor of the total mass of that class[6], and to its solidicity[7] by a factor of its total volume divided by the volume of one of the bins into which the distribution is divided. Thus, in the case of a charge of identical beads, the RTD of a tracer particle can be interpreted[8] as a density distribution of the total charge in the tumbling mill.

The left-hand subplot of Figure 6.5 shows the RTD of the $3mm$ tracer particle in the 'old' $300mm$ mill rotated at 60% of its critical speed. In this subplot, the S-shape of the charge is clearly delineated by the thin transition layer between the high residence time- and thus high density- orange region and the low residence time- and thus low density- blue region. This transition layer is more blurred in the higher speed case than in the lower, particularly in the shoulder region where significant fluidisation- shown as turquoise- is evident.

This fluidisation is easier to accept when the RTD is cast as a solidicity. Figure 6.6 shows the solidicity- or packing fraction- of the charge as a fraction of the maximum packing fraction of spheres- $\frac{\pi}{\sqrt{18}}$. From this figure it is clear that much of the bulk region[9] of the charge is between 0.7 and 0.9 the density of close-packed spheres, but that there is a significant low density region- about 0.4 the density of close-packed spheres- around the CoC of the charge. The converse is true of the 60% of critical case, as can be inferred from Figure 6.5.

Also evident from Figure 6.5 is the increasing S-shape of the bulk free surface of the charge, and the increasing volume of cataracting charge with increasing speed. Because of the comparative density of the bulk region of the charge, however, the size and shape of the cascading stream is not very obvious in these plots.

Figure 6.7 shows the standard deviation in the time spent by the tracer particle in each bin on each pass. A low standard deviation in a given bin means that the tracer particle spent roughly the same amount of time in that bin on each pass. Such behaviour would be characteristic of dense, pseudo-solid body motion, which locks particles into a restricted range of motion.

[6] See Section 5.3.6.
[7] Or, inversely, to its porosity.
[8] By adopting the ergodic assumption.
[9] See Section 5.5.2.

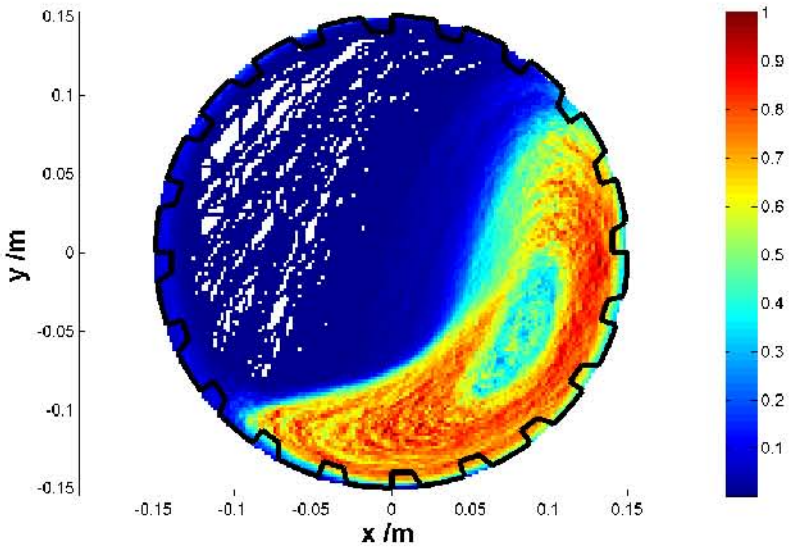

Figure 6.6: The solidicity of the $3mm$ charge in the 'old' $300mm$ mill filled to 31.25% and rotated at 75% of its critical speed.

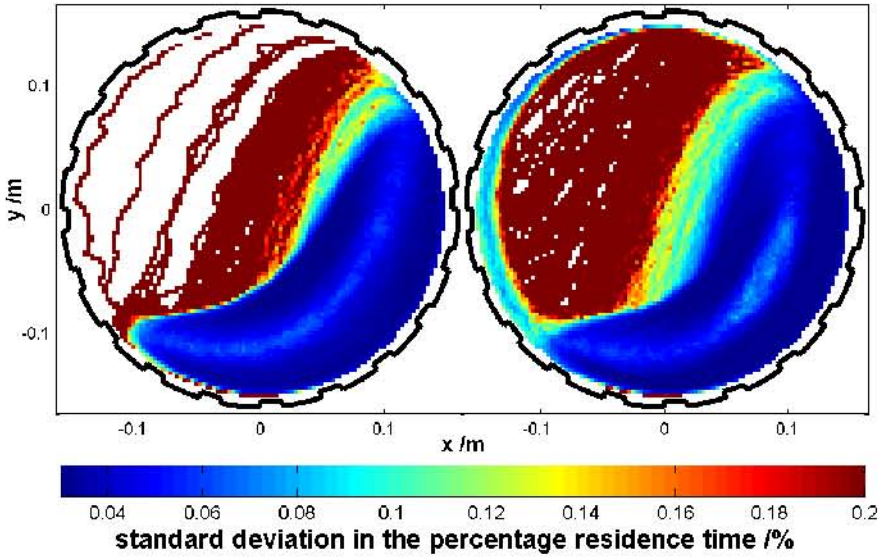

Figure 6.7: Standard deviations in the residence time distributions of a $3mm$ tracer particle in the 'old' $300mm$ mill filled to 31.25% and rotated at 60% (left) and 75% (right) of its critical speed.

Conversely, a high standard deviation in a given bin means that the tracer particle spent a variable amount of time in that bin on each pass. This could be due to the dilution of the region through which the tracer particle is moving- a loosely-packed region offers more opportunity for the particle to jostle around, resulting in both a wider range of speeds and in more complex motion.

More complex motion can lead to a larger standard deviation in a given bin in the following way. Consider the contrived particle trajectories shown in Figure 6.8. Suppose that the three passes shown in Figure 6.8a are, at least in bins $B1-3$, are arclengths of a rigid body rotation of frequency ω. In the first- and simplest- case, that of bin $B2$, the arclengths and curvatures of each of the passes are roughly the same, and so the time spent in bin $B2$ by the tracer particle on each path are roughly the same too. In the case of bin $B1$, however, the situation is slightly different- the paths are of different lengths of $s_i = R_i\theta$, with tangential speeds $v_i = \omega R_i$. Thus the time spent in

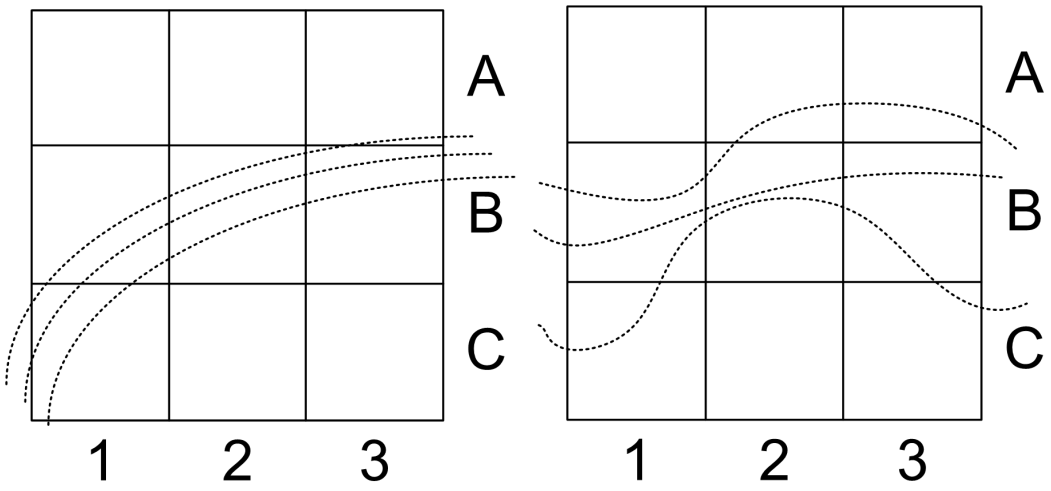

(a) Smooth trajectories. **(b)** Complex trajectories

Figure 6.8: Simplified examples of smooth (left) and complex (right) tracer particle trajectories.

the bin at each pass is $t_i \approx \frac{\theta}{\omega} = \bar{t}$, for small enough bin sizes[10]. These are examples of the simple particle motions that can occur when the particles are 'locked' in dense particle flows.

Now suppose that the particles in Figure 6.8a are not moving in a rigid body rotation, but rather have independent speeds on each pass- only possible if the layers are not in constant contact with each other. Such a situation might arise in the dilute in-flight region in which particles follow parabolic trajectories but are not, in general, in contact with each other in-flight. Variations in particle speed even in nearly-parallel layers are possible in the in-flight region because particles are ejected from the shoulder at higher speeds and steeper angles of projection the further they are from the equilibrium surface. This is what gives rise to the large variations in residence time in the in-flight region.

The cascading regions of the charge are much more visible in Figure 6.7 than they were in Figure 6.5. This is because the cascading region is a lot more dilute than the bulk region, but not much more dense than the in-flight region. It is sufficiently more dense, though, that there is significantly more inter-particle interaction in the cascading region than in the in-flight one. Thus the standard deviations in the residence time in the dilute, multi-speed in-flight region are significantly higher than in the comparatively correlated cascading region.

Even in the dense bulk region of the charge, though, there is some variation in the standard deviation of residence times. In particular, more complex motion contributes to the marginally-higher standard deviations along the equilibrium surface of the charge and in its toe region.

Along the equilibrium surface, particles sliding or rolling down the slope created by the rising charge slow down by the action of friction. When they have come to rest with respect to the flowing layer directly below them, they begin to move up with that layer also under the action of friction- they re-enter the rising region. This re-entry is stochastic, and the particle may jostle around for a moment before being inducted into the rising region, fractionally increasing the range of residence times that such a particle can have along the equilibrium surface.

Also contributing to the increased range of residence times of the tracer particle along the equilibrium surface is the much greater curvature of the particle's motion in this region. Figure 6.8b shows a range of passes of a tracer particle through a region of space. Unlike in the case of Figure 6.8a, these trajectories are uncorrelated, so that there is no simple speed relation that, if it held,

[10] And thus roughly constant θ.

would imply that the tracer particle spent similar times in a given bin on each pass. In fact, it would be an unlikely coincidence if they did. The difference in the arclength in each bin is most pronounced when the difference in curvature between each pass is most pronounced- for instance between the upper two and lower passes in bin $B1$ and between the lower two and upper passes in bin $B2$. Since the turning point of each subsequent flowing layer in the active region must turn around the one below it, each subsequent turning path in the region of the equilibrium surface is of a higher curvature than the last.

This effect is even more pronounced in regions of chaotic charge motion, such as in the toe region of the charge in which particles bounce around before being re-inducted into the rising region. This random bouncing of incoming charge from the cascading and cataracting streams leads to both a larger range of speeds- and thus residence times in each bin- as well as more complex motion.

Eventually, the charge settles down into a fluidised region of roughly the density of the cascading charge. In the 60% of critical speed case, this manifests as a slightly thickened transition layer between the disperse and bulk regions. In the 75% of critical speed case, however, there is a clear pool of fluidised material waiting to be re-inducted into the rising region of the charge. Again, this is much clearer in Figure 6.7 than Figure 6.5. In Figure 6.7, too, can be seen that it takes some time before the newly-inducted charge has been settles down to rotate with the shell. This is visible as the lifter-thin arc of relatively high residence time variability in the lower part of the rising region of the charge.

6.2 Kinematic quantities

6.2.1 Variations in the tracer kinematics with time

The variations in tracer particle location shown in Figure 6.2 can be differentiated numerically to obtain the velocities shown in Figure 6.9 and accelerations shown in Figure 6.10[11].

As expected from the knowledge that the xy-plane is the plane of rotation of the charge and that the mill is operated in batch mode, there is very little variation in the particles' small $\hat{z}$-velocities, and the variations in their $\hat{x}$- and $\hat{y}$-velocities is sinusoidal.

The harmonics in the tracer particles' motion are more pronounced in their velocities, and even more pronounced in their accelerations as their amplitudes are increased by factors of their higher and higher frequencies. This leads to the jagged shape of the variations in these kinematic quantities.

The tracer particles' accelerations are again sinusoidal in the xy-plane and small and stochastic in the $\hat{z}$-direction. The effect of gravity in the $\hat{y}$-direction is to increase the magnitudes of the particles' accelerations in this direction.

[11] See Section 5.2.

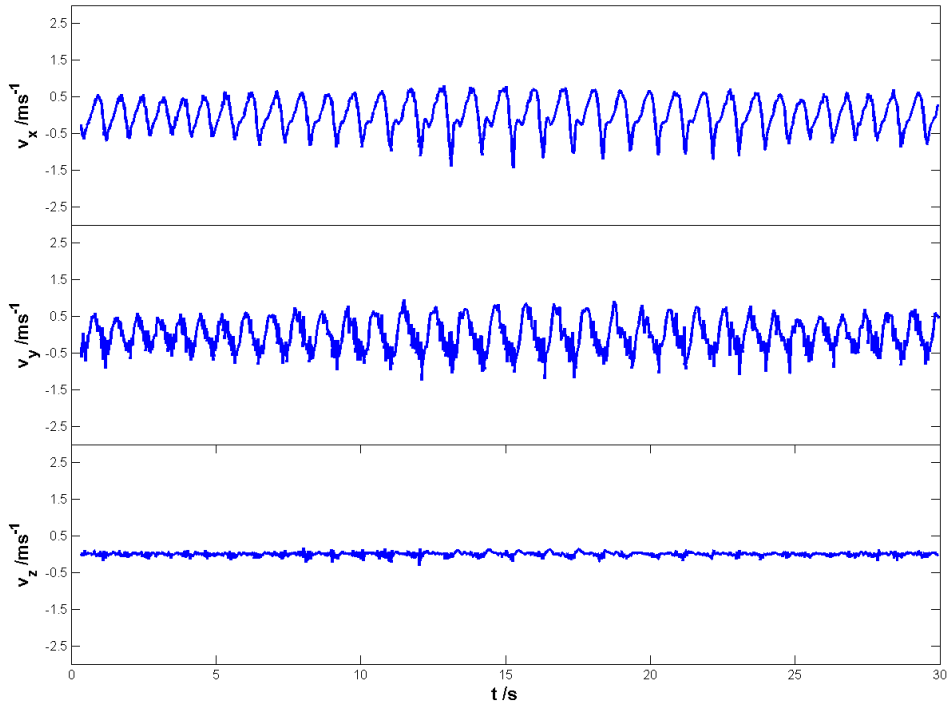

(a) 60% of critical speed.

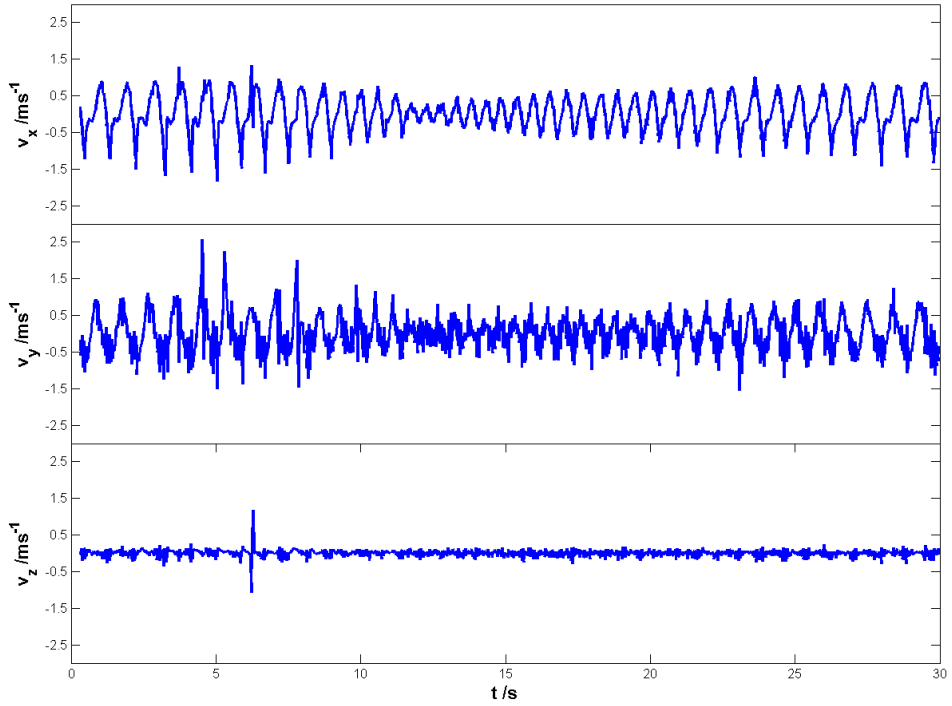

(b) 75% of critical speed.

Figure 6.9: The variation of the $\hat{x}$ (top), $\hat{y}$ (middle), and $\hat{z}$ (bottom of each subplot) velocity of a $3mm$ tracer particle in the 'old' $300mm$ mill filled to 31.25% and rotated at 60% (top) and 75% (bottom) of its critical speed.

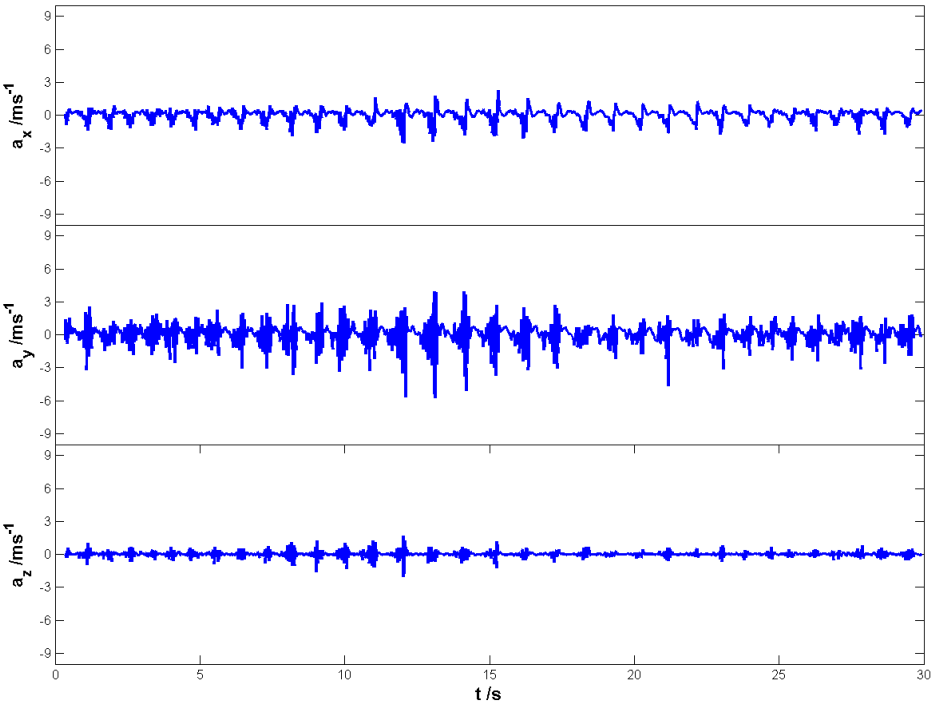

(a) 60% of critical speed.

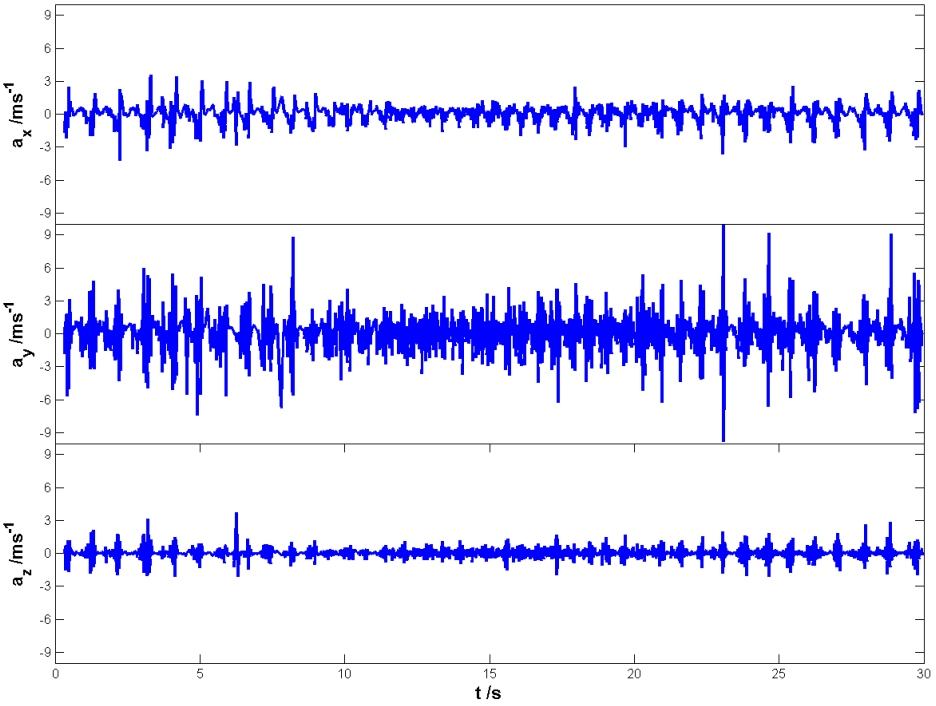

(b) 75% of critical speed.

Figure 6.10: The variation of the $\hat{x}$ (top), $\hat{y}$ (middle), and $\hat{z}$ (bottom of each subplot) acceleration of a $3mm$ tracer particle in the 'old' $300mm$ mill filled to 31.25% and rotated at 60% (top) and 75% (bottom) of its critical speed.

6.2.2 Binned kinematics

Velocity

As was the case for the variation of the tracer particle's location over time, it is more interesting to consider its kinematic quantities in the Eulerian reference frame than in the Lagrangian reference frame by residence time binning the data shown in Figures 6.9 and 6.10.

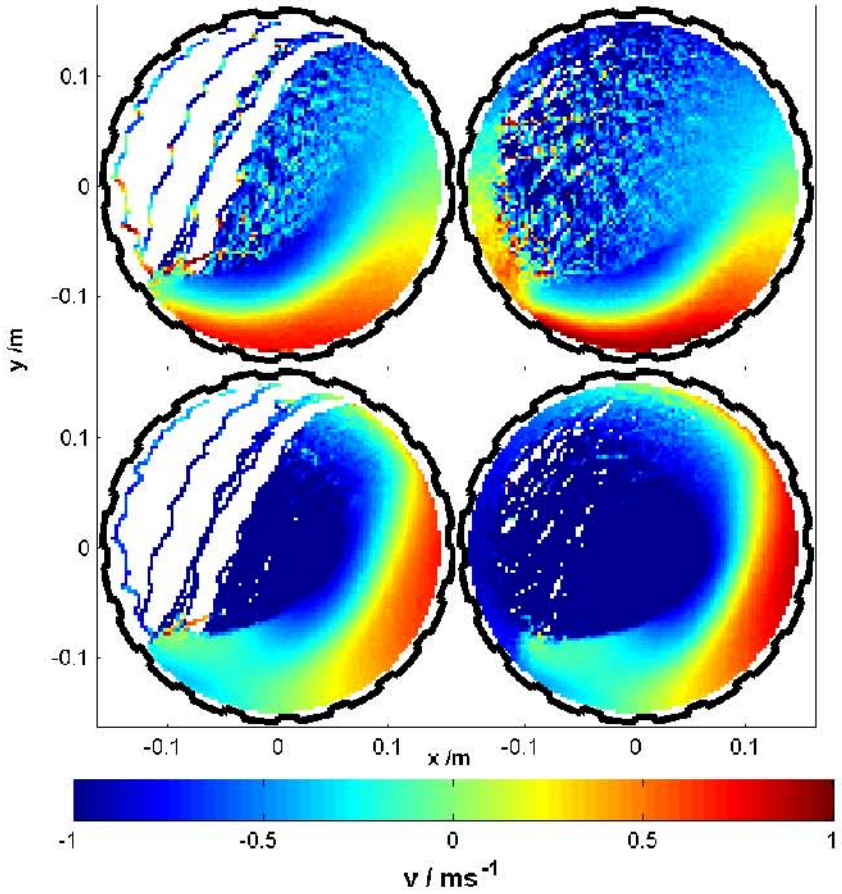

Figure 6.11: Time-weighted $\hat{x}$- (top) and $\hat{y}$-velocity (bottom) distributions of a $3mm$ tracer particle in the 'old' $300mm$ mill filled to 31.25% and rotated at 60% (left) and 75% (right) of its critical speed.

Figure 6.11 shows the residence time-weighted binned[12] velocity of the tracer particle in the $\hat{x}$- (top) and $\hat{y}$-directions for the mill rotated at 60% (left) and 75% of its critical speed.

In the upper plots in Figure 6.11- those of the $\hat{x}$-velocity distributions- there is a clear rightward-moving region in the lower part of the bulk region of the charge and left-ward region in the upper part. In the case of the mill rotated at 75% of its critical speed, especially, it is clear that there is a gradient from maximum rightward velocity (burgundy in the plot) at the very bottom of the mill, approaching (through red, orange and yellow regions) a zero $\hat{x}$-velocity region (light green) and then entering more and more negative (turquoise to light blue to dark blue) $\hat{x}$-velocity regions.

A similar trend is visible in the $\hat{y}$-velocities, with graded rising charge on the right and falling charge on the left. The line of zero velocity that divides the rising and falling charge is actually the equilibrium surface, which will be discussed further in Chapter 7. It is more obvious in the plots of speed shown in Figure 6.12.

The standard deviations in the time-weighted velocity distributions of Figure 6.11 are shown in Figure 6.13. The same trends as were visible in the tracer particles' velocities are visible in the

[12] See Section 5.3.5.

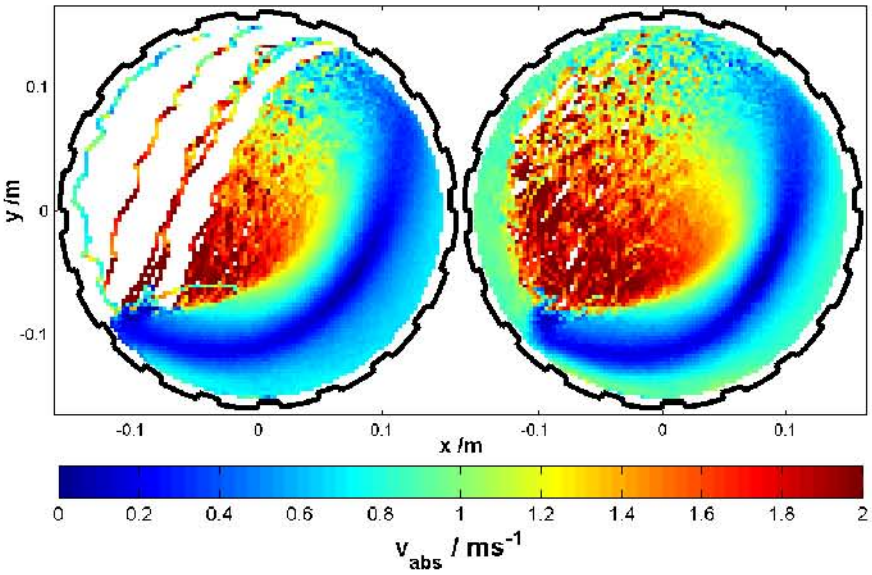

Figure 6.12: The time-weighted speed distribution of a $3mm$ tracer particle in the 'old' $300mm$ mill filled to 31.25% and rotated at 60% (left) and 75% (right) of its critical speed.

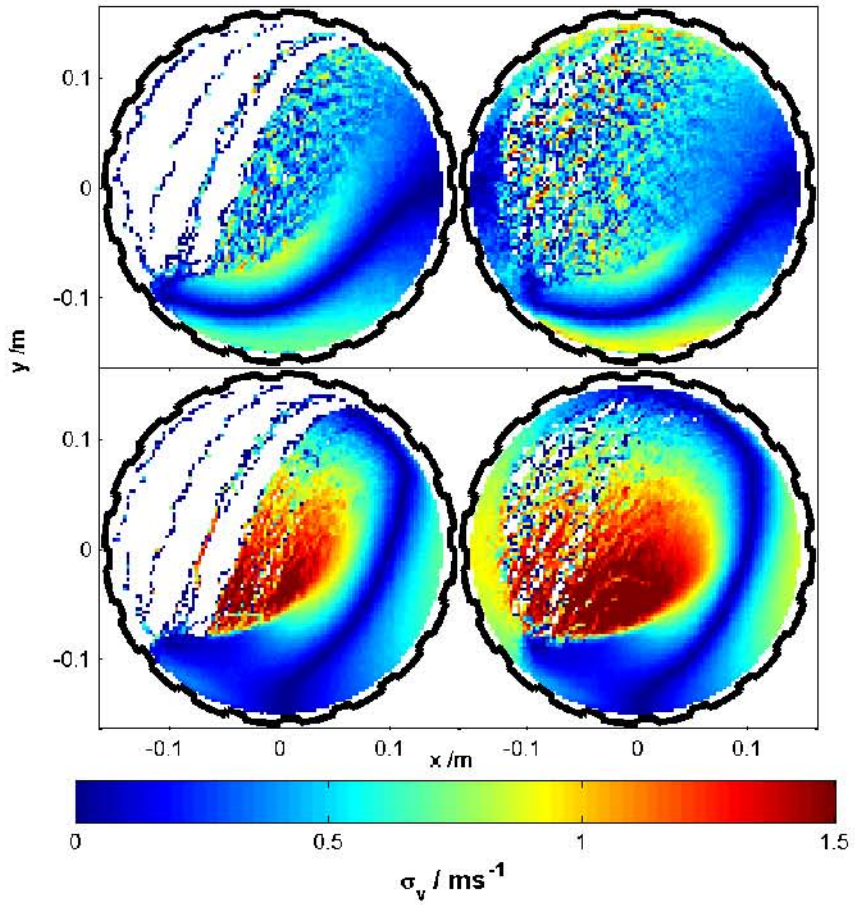

Figure 6.13: Standard deviation in the time-weighted $\hat{x}$- (top) and $\hat{y}$-velocity (bottom) distributions of a $3mm$ tracer particle in the 'old' $300mm$ mill filled to 31.25% and rotated at 60% (left) and 75% (right) of its critical speed.

standard deviations of these velocities, but with exaggerated gradients. As a result, the horizontal and vertical equilibrium surfaces are visible in both of these as dark blue lines.

The standard deviation in the absolute velocities are shown in Figure 6.14. Here the difference between the standard deviation in and the mean absolute velocities shown in Figure 6.12 are even

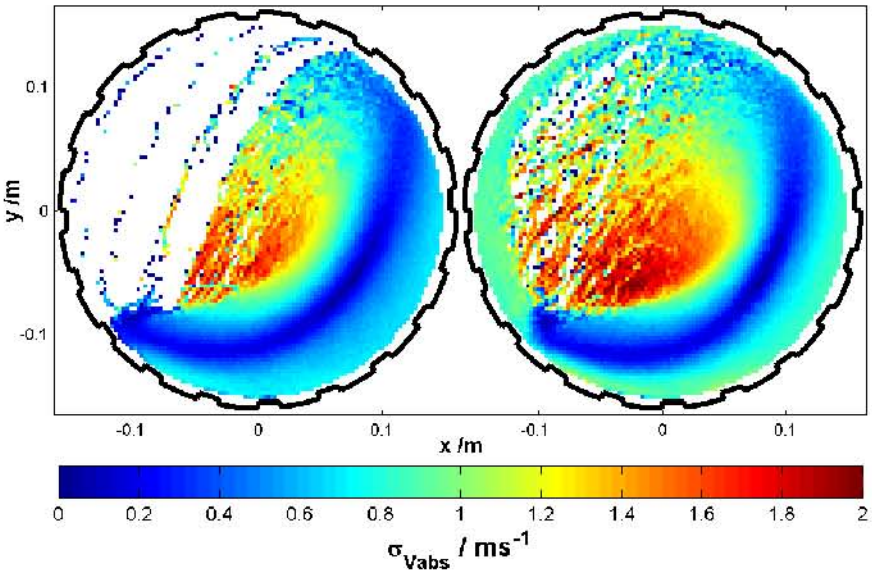

Figure 6.14: Standard deviation in the time-weighted speed distribution of a $3mm$ tracer particle in the 'old' $300mm$ mill filled to 31.25% and rotated at 60% (left) and 75% (right) of its critical speed.

less pronounced.

This standard deviation in the speed has been interpreted as a *granular temperature* in analogy with the kinetic theory of heat. Figure 6.14 suggests that there is little information to be had from this interpretation not available from merely considering the speed distributions themselves.

The granular temperature interpretation of the standard deviation of speed suggests that there is a 'cool' region around the CoC of the charge, that the 'hottest' region is the impact toe, and that faster rotating charge has a larger and 'hotter' high granular temperature region. All of these observations can be simply re-cast in terms of the particles' motion- there is a slow-moving dead region around the CoC, and the fastest-moving charge is in the dilute and unimpeded in-flight region in which the charge has attained a higher maximum height and has less opportunity to dissipate energy through friction.

Figure 6.15 contains a selection of projected velocity distributions- in the transverse plane, tangent to a radial line through the centre of the mill, and along this radial line. That all of these circular projections are similar in shape, if not magnitude, to the speed distributions shown in Figure 6.12 goes some way to proving that the motion of the charge is dominated by circulation in the transverse plane. A similar conclusion could be reached from the standard deviations in these velocity projections, as shown in Figure 6.16.

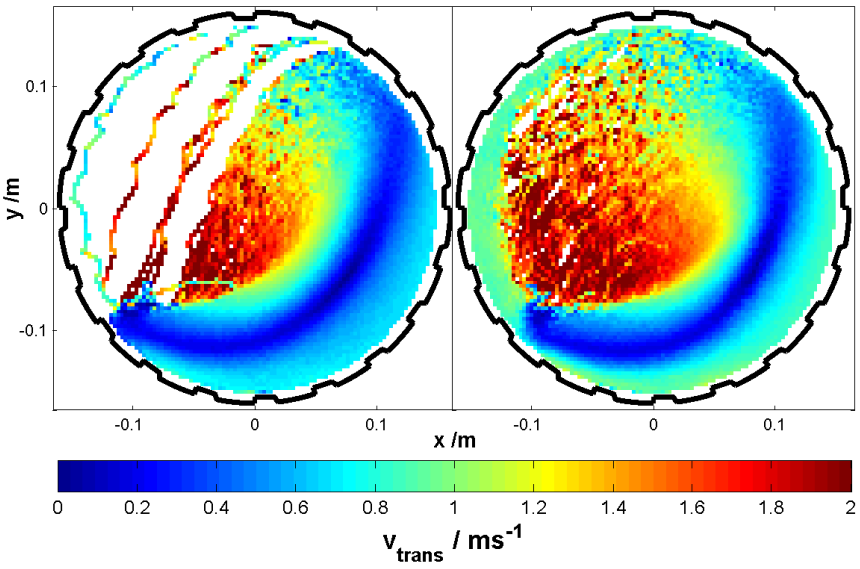

(a) Transverse velocity.

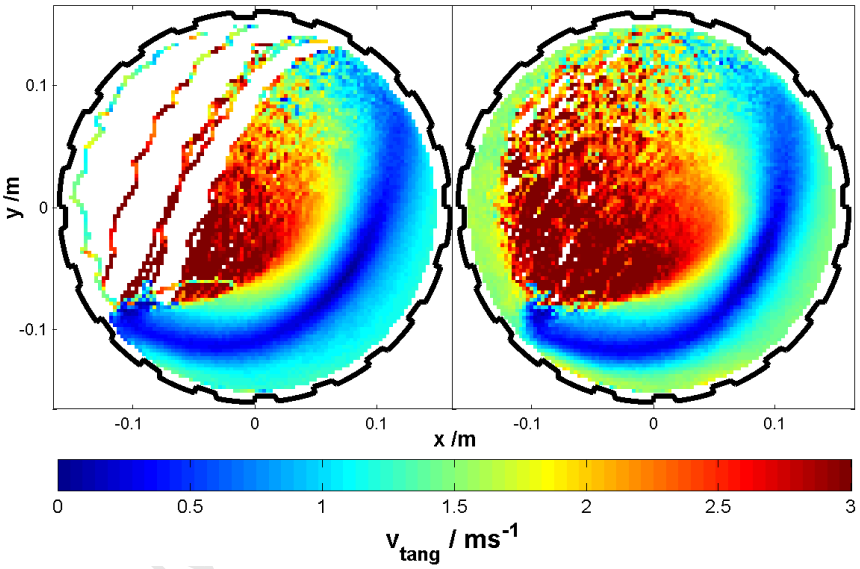

(b) Tangential velocity.

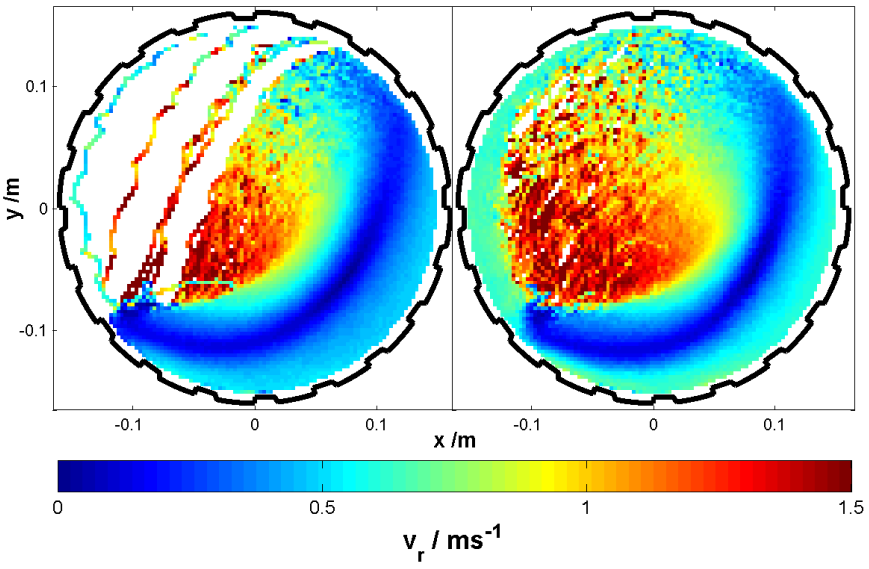

(c) Radial velocity.

Figure 6.15: A selection of time-weighted velocity distributions of a 3*mm* tracer particle in the 'old' 300*mm* mill filled to 31.25% and rotated at 60% (left) and 75% (right) of its critical speed.

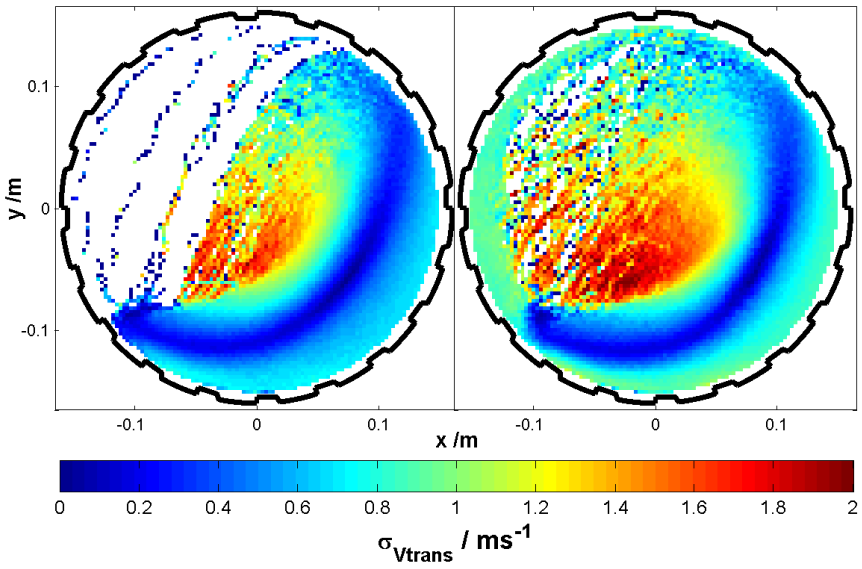

(a) Transverse velocity.

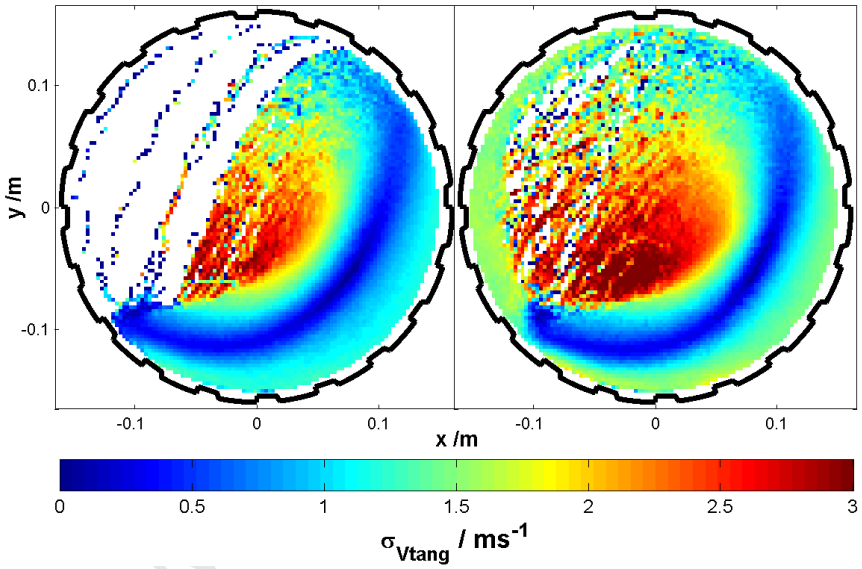

(b) Tangential velocity.

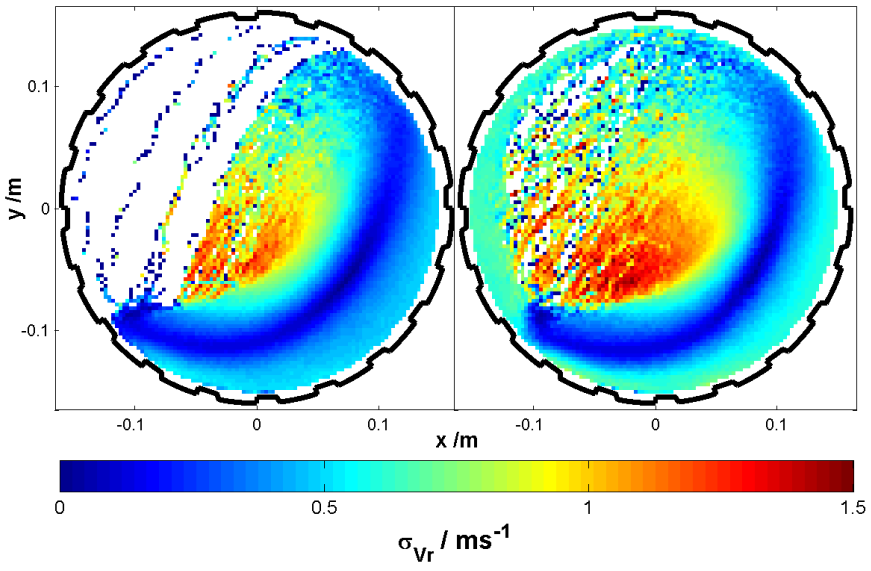

(c) Radial velocity.

Figure 6.16: A selection of standard deviations in the time-weighted velocity distributions of a $3mm$ tracer particle in the 'old' $300mm$ mill filled to 31.25% and rotated at 60% (left) and 75% (right) of its critical speed.

Acceleration

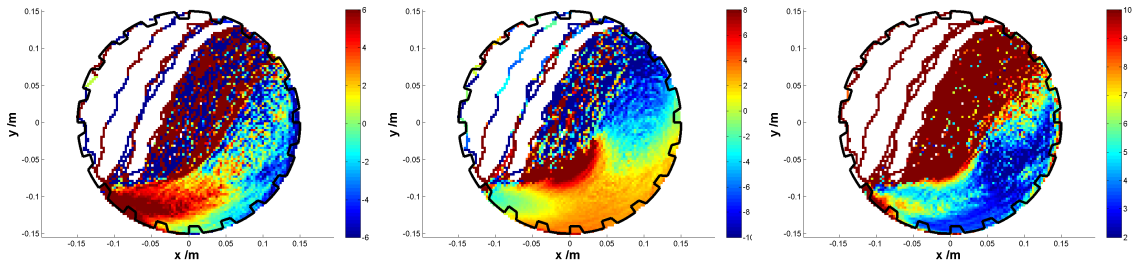

(a) $\hat{x}$-acceleration. **(b)** $\hat{y}$-acceleration. **(c)** Transverse acceleration.

Figure 6.17: The time-weighted $\hat{x}$- (left), $\hat{y}$- (centre), and transverse (right) acceleration distribution of a $3mm$ tracer particle in the 'old' $300mm$ mill filled to 31.25% and rotated at 60% of its critical speed.

Figure 6.17 shows the $\hat{x}$-, $\hat{y}$- and transverse accelerations of the tracer particle in the mill rotated at 60% of its critical speed.

As expected, the $\hat{x}$-acceleration in Figure 6.17a shows a strong positive acceleration in the toe region where the charge is being turned from left-moving to right-moving, and a slightly less strong negative acceleration in the shoulder region in which the opposite is happening.

Figure 6.17b shows a positive $\hat{y}$-acceleration in the lower part of the rising region in which charge is being accelerated upward before being decelerated near the shoulder, and finally projected into free-fall beyond the departure shoulder.

There is some chaotic acceleration in the in-flight region as unconstrained particles collide elastically, but the most interesting feature of these plots is the large positive $\hat{y}$-acceleration in the impact toe- in this case on the lower free surface of the charge- as particles come to an abrupt stop (or bounce back up off the charge). This region, and the size of this region, can have an important role to play in determining the amount of impact breakage occurring in the mill.

Figure 6.17c shows the transverse acceleration of the tracer particle in the mill. As well as the features discussed above, there is a clear centripetal wedge in which particles are rotating in a pseudo-rigid body way about the CoC of the charge. This will be investigated further in Chapters 6 and 7.

6.3 Discussion

In this chapter I performed a basic PEPT analysis of a mono-sized charge of glass beads rotated at two different speeds. By considering the point-cloud of triangulated tracer particle locations, and the variation of each location coordinate over time, I highlighted the limitations of simple Lagrangian particle tracking, and thus motivated the residence time binning technique.

I used this technique to obtain RTDs of the tracer particles in the mill. I had previously interpreted the RTD as being proportional to measures such as the mass, density, porosity, solidicity and probability distributions, and thus was able to use these RTDs to discuss the shape of the charge with particular reference to the S-shape of its bulk free surface.

I also presented and interpreted the standard deviation in the RTD as a complimentary measure of the density of the charge and of the speed and complexity of motion. I showed how the RTD and its standard deviation could be used together to consider the cascading and toe regions of the charge and to shed light on the behaviour of layers of charge at the equilibrium surface.

I went on to discuss time-weighted velocity distributions in each of the transverse directions, in the transverse plane, as an absolute magnitude and in a range of circular projections. From these I was able to identify pseudo-solid body like behaviour and- importantly for the next chapter- the horizontal, vertical and combined equilibrium surfaces.

By comparing circular projections- in the transverse, tangential and radial directions- with the speed of the charge, I was able to conclude that its motion is dominated by the circulatory motion.

I briefly discussed the interpretation of the standard deviation in the time-weighted velocity distributions as a granular temperature, but showed that such an interpretation offered no additional explanatory power. In fact, it has no explanatory power at all beyond the comparison of a dense granular flow with an oversimplified kinetic theory of gases analogy.

Finally, I considered the time-weighted acceleration distributions in each of the transverse directions and as a transverse magnitude. From these I identified all of the expected high-acceleration regions at the turning points, as well as a solid-body-like wedge of centripetal acceleration in the rising region centred at the CoC of the charge. Interestingly, I also found a high $\hat{y}$-acceleration region in the impact toe, which could effect impact grinding efficacy in the mill.

In Chapter 7 I will make more rigorous my observations about the shape of the charge.

Chapter 7

A more complete analysis

In this second results chapter, I perform a more detailed analysis of three more experiments performed on the 'old' 300mm diameter tumbling mill[1], filled to 31.25% of its volume[2], this time with a monosize charge of 5mm diameter glass beads.

7.1 Charge features and regions

In this section I demonstrate the dynamic charge characterisation routines described in Sections 5.5.2 and 5.5.3.

7.1.1 The shape of the charge

Figure 7.1 shows the RTDs of the three experiments considered in this chapter- the 'old' 300mm mill rotated at 50%, 60% and 75% of its critical speed.

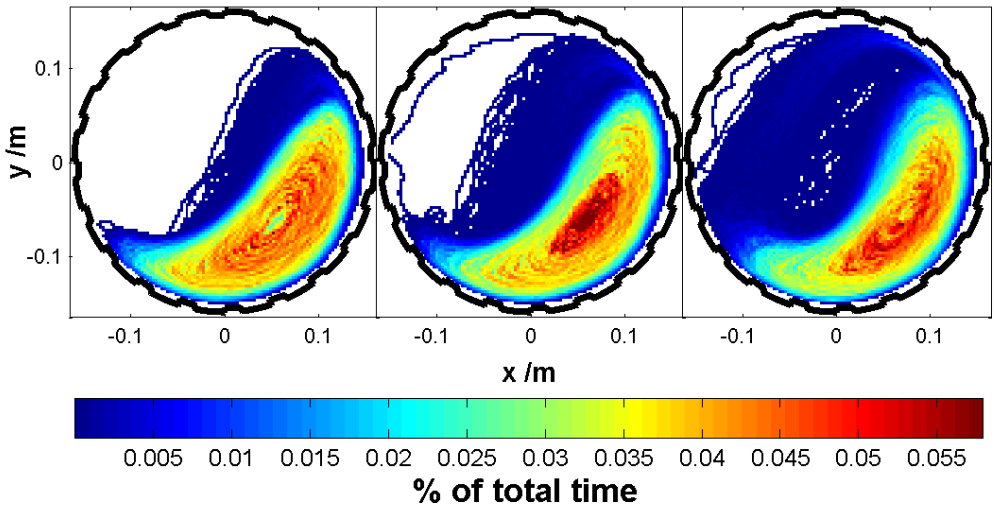

Figure 7.1: The residence time distributions of a 5mm tracer particle in the 'old' 300mm mill filled to 31.25% and rotated at 50% (left), 60% (middle) and 75% (right) of its critical speed.

[1]See section .
[2]See Section 4.3.3.

Qualitatively, there are several differences between the shape of the charge at each mill speed. The first, and most obvious, is the amount of charge in the in-flight region of the mill- the dilute (blue) region above the main body of the charge. The second is the shape of the bulk free surface, which becomes more and more sigmoid at increasing speed[3], and the third is the local structure of the RTD in the bulk. This last feature- the local structure- will not be discussed here, but the first two will.

The bulk free surface

In order to quantify the amount of charge in the in-flight region, and to make rigorous the discussion of the shape of the charge, it is necessary to unambiguously identify the bulk free surface. This is easily done by eye, because of the density difference between the bulk and in-flight regions, suggesting computational edge-detection as a strategy. However, for the reasons given in Section 5.5.2, this is best done with the RTD not in the form shown in Figure 7.1, but rather re-binned as described in Section 5.4.3- that is in polar rather than Cartesian co-ordinates.

Figure 7.2 shows the same RTDs as are shown in Figure 7.1 but with the bins re-organised in terms of their angular and radial positions[4]. In these plots, the bulk region is bounded by an almost entirely concave curve[5] surrounded by the dilute (blue) in-flight region. Since the angular co-ordinates on the y-axis of the plots in Figure 7.2 are periodic, these plots could be modified so that the white empty regions form similarly concave shapes. By careful choice of intensity threshold[6] and angular normalisation, either the bulk free surface or charge free surface can be obtained from polar bin plots of the sort shown in Figure 7.2.

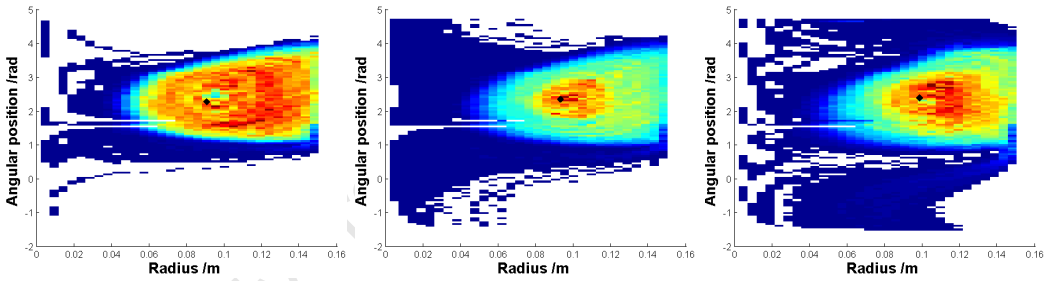

Figure 7.2: The residence time distributions of a $5mm$ tracer particle in the 'old' $300mm$ mill filled to 31.25% and rotated at 50% (left), 60% (middle) and 75% (right) of its critical speed, re-binned in a polar reference frame.

Figure 7.3 shows the bulk free surfaces of the three experiments under consideration superimposed on their RTDs. The top row of plots in Figure 7.3 show these bulk free surfaces as obtained from the edge detection, smoothed and interpolated with cubic splines, and the bottom row shows logistic functions of the form

$$y(x) = \frac{a}{1 + be^{-rx}} + d \tag{7.1}$$

fitted to this data.

It is important to note that these logistics do not represent a model of the bulk free surface, and were merely chosen for their sigmoid shape. They do, however, conform very well to the smoothed free surface obtained from the edge-detection routine, especially at low rotational speeds at which the transition layer is relatively thin.

[3]Also, the transition layer becomes thicker with increasing speed.
[4]This is a simplification- see Section 5.4.3.
[5]Except for the straight line defining the inner radius of the mill shell.
[6]See Section 5.4.3.

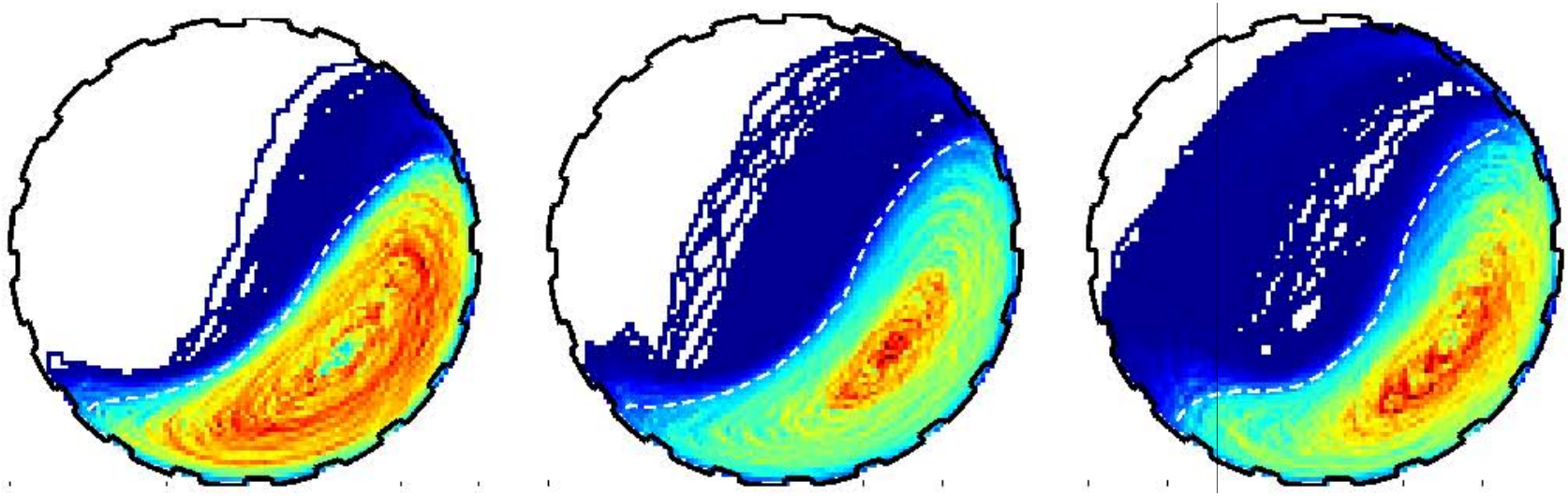

(a) Edge-detected bulk free surface

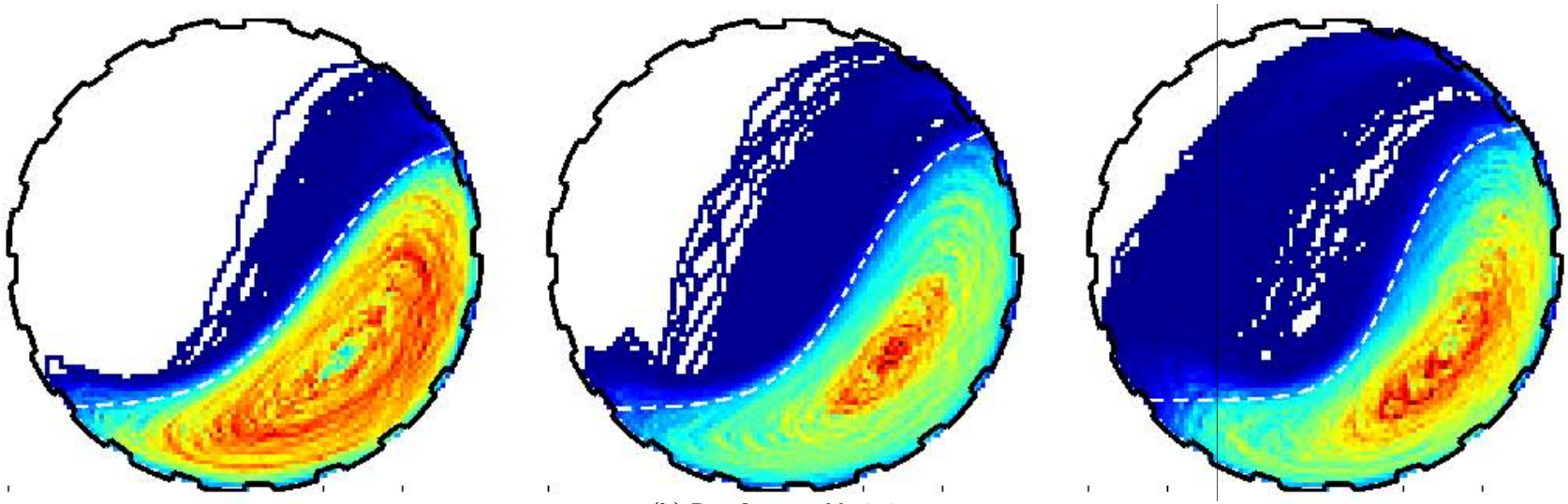

(b) Best fit general logistics

Figure 7.3: Edge-detected equilibrium surfaces (top) and general logistic approximations to them (bottom) for the motion of a $5mm$ tracer particle in the 'old' $300mm$ mill filled to 31.25% and rotated at 50% (left), 50% (middle) and 75% (right) of its critical speed.

This sensitivity to the thickness of the transition layer is evident not only from the less-good fit at high rotational speeds, but also in the toe region. Notwithstanding, it is clearly possible to obtain a good approximation of the bulk free surface in this way.

The bulk free surface obtained by edge detection divides the charge into the bulk and disperse regions. It can thus be used to divide the charge into these two regions for further analysis. For instance, the CoM of the entire charge and of its bulk region for different mill speeds are given in Table 7.1.

Mill speed / $\%v_{crit}$	**Full charge** θ / °	**r /m**	**Bulk charge** θ / °	**r /m**
50	-30.2	0.080	-46.7	0.084
60	-28.7	0.079	-43.9	0.085
75	-27.1	0.074	-42.2	0.085

(a) Centres of mass

Mill speed / $\%v_{crit}$	**In-flight mass fraction**	**Occupied fraction**
50	0.040	0.445
60	0.052	0.554
75	0.078	0.697

(b) Measures of mass distribution

Table 7.1: Angular and radial positions of the centre of mass of the bulk and full charge, the fraction of charge in-flight, and the fraction of the mill volume occupied by charge for various mill speeds.

From Table 7.1a it can be seen that the CoM of the entire charge moves upwards and inwards with increasing mill speed, while that of the bulk region moves upwards, but stays roughly at the same radial distance from the centre of the mill. This difference is because the large increase in the volume of the mill 'occupied' by charge- from $\backsim$ 45% to $\backsim$ 70%- is due to only a very small mass fraction- $\backsim$ 4% of the total mass of the charge, as shown in Table 7.1b. The bulk region of the charge rises, but thins rather than thickening radially with increasing speed- unlike the total charge.

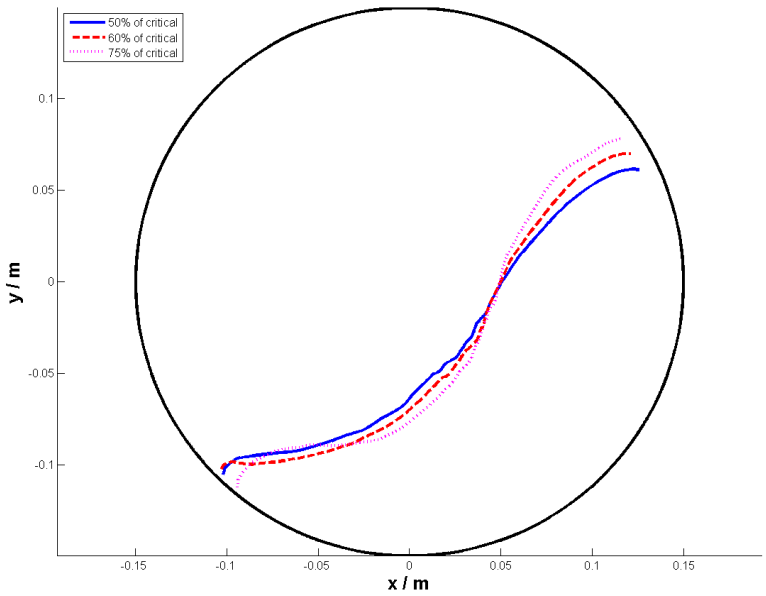

Figure 7.4: The edge-detected bulk free surfaces of the motion of a $5mm$ tracer particle in the 'old' $300mm$ mill filled to 31.25% and rotated at 50%, 60% and 75% of its critical speed.

Figure 7.4 shows the edge-detected, smoothed bulk free surfaces of the charge rotated at 50%, 60% and 75% of the critical speed of the mill, all on the same plot. From this, the increased S-shape of the bulk free surface- but only very marginal radial thinning of the bulk region- with increasing mill speed begins to emerge, though the range of speeds is not that wide here. Also from this figure, the rising shoulder and lowering toe of the charge appears.

The departure shoulder, head and impact and re-entry toes

In particular, the departure shoulder is defined as the point at which the trajectory of the outermost layer of charge begins to deviate from circular motion with the mill shell, and the re-entry toe as the point at which it rejoins this circular motion[7]. These points are obtainable as the points of intersection between the bulk free surface and the mill shell, or as the points at which the outermost edge of the charge begins to curve in Figure 7.2. Because of the ambiguity in the shoulder and toe regions in Figure 7.3, I use the latter approach here.

Mill speed / $\%v_{crit}$	**Departure shoulder** θ / °	**Re-entry toe** θ / °	**Impact toe** θ / °
50	19.7	-132.0	-150.4
60	22.1	-132.4	-148.5
75	27.3	-129.4	-164.1

Table 7.2: Angular positions of the departure shoulders, and impact and re-entry toes of the motion of a $5mm$ tracer particle in the 'old' $300mm$ mill filled to 31.25% and rotated at 50%, 60% and 75% of its critical speed.

Table 7.2 shows the variation of the angular positions of the departure shoulder and impact and re-entry toes of this charge at various mill speeds. From this table, as well as from Figure 7.4, it is clear that there really isn't much variation between the limits of the bulk region of the charge- defined by the positions of the departure shoulder and re-entry toe- over these speeds. Of course, the departure shoulder of the charge rises, and its re-entry toe falls (less markedly) with increasing mill speed, but the big difference is in the impact toe. In fact- despite the values given in Table 7.2, which are the angular positions of the highest point of impact from the active rather than in-flight region- the impact toes of the charge rotated at 50% and 60% of critical speed are actually on the surface of the charge. This could have implications for the shape of the charge[8] and- more practically- on grinding efficacy.

The maximum height reached by the charge- its head or *lift*- also has an effect on the grinding efficacy of a tumbling mill thus operated by determining the amount of potential energy available for impacts in the toe region. Table 7.3 shows the maximum heights achieved by the charge for each mill speed, normalised to the maximum possible height- the mill diameter.

Mill speed / $\%v_{crit}$	**Lift / mill diameter**
50	0.904
60	0.942
75	0.971

Table 7.3: Lift- the maximum height reached by a $5mm$ tracer particle in the 'old' $300mm$ mill filled to 31.25% and rotated at 50%, 60% and 75% of its critical speed.

[7]Both in Section 5.5.3.

[8]Even beyond mass conservation considerations.

7.1.2 The motion of the charge

I return now to characterising the charge motion. In the preceding subsection I considered the shape of the charge. I did this by obtaining the bulk and charge free surfaces and considering their shape and intersections with the mill shell- yielding the departure shoulder, head, impact toe and re-entry toe of the charge. I also discussed the CoM of both the full charge and that of the bulk region, separated from the disperse region by the bulk free surface.

I now turn to characterising the motion of the charge. Figure 7.5 shows the $\hat{x}$- and $\hat{y}$-velocity distributions of the $5mm$ monosize charge rotated at 50%, 60% and 75% of the mill's critical speed.

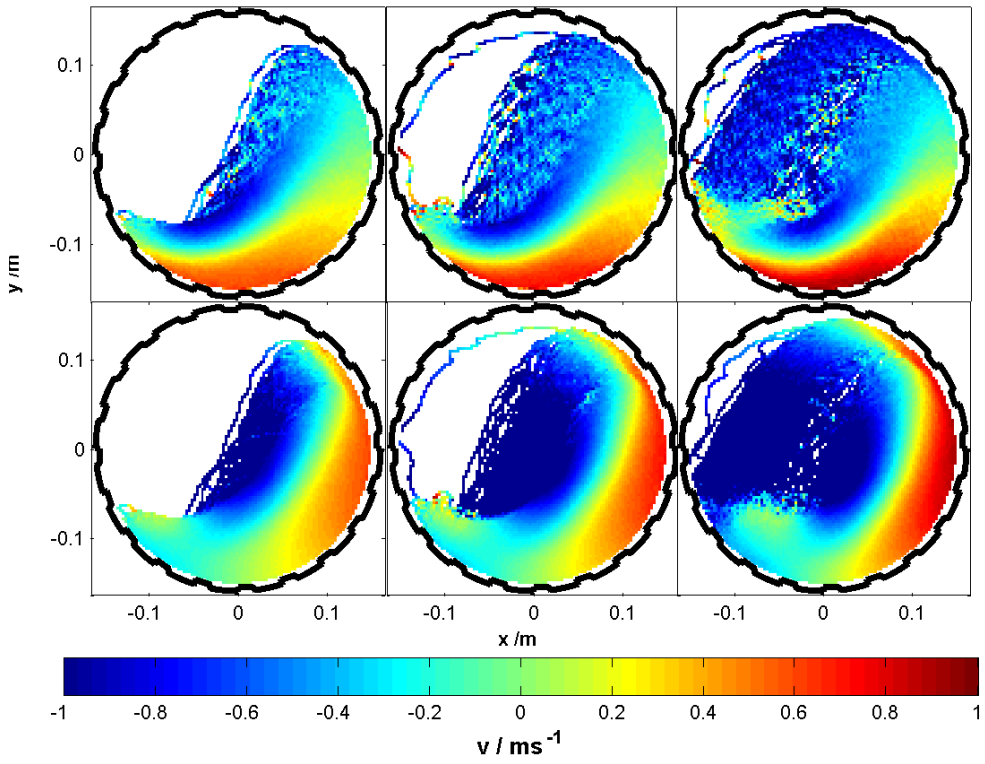

Figure 7.5: Time-weighted $\hat{x}$- (top) and $\hat{y}$-velocity (bottom) distributions of a $3mm$ tracer particle in the 'old' $300mm$ mill filled to 31.25% and rotated at 50% (left), 60% (middle) and 75% (right) of its critical speed.

The equilibrium surface

The plots in Figure 7.5 clearly show that each distributions are divided into two regions. In the case of the $\hat{x}$-velocity, these are regions of left- and right-going charge, and in the case of the $\hat{y}$-velocity, these are regions of rising and falling charge. As seen in Figure 7.1, the charge is densely-packed in a region containing both rising and falling (and left- and right-going) material. Since nearest the shell, charge is moving with the shell, and nearest the bulk free surface it is moving in the opposite direction, and since between these two points, the charge is densely-packed, there must be a more or less smooth velocity gradient between them passing through zero. The points of zero velocity are called equilibrium points. There are equilibrium points corresponding to each component that can be taken of the velocity- horizontal, vertical, radial, and so on.

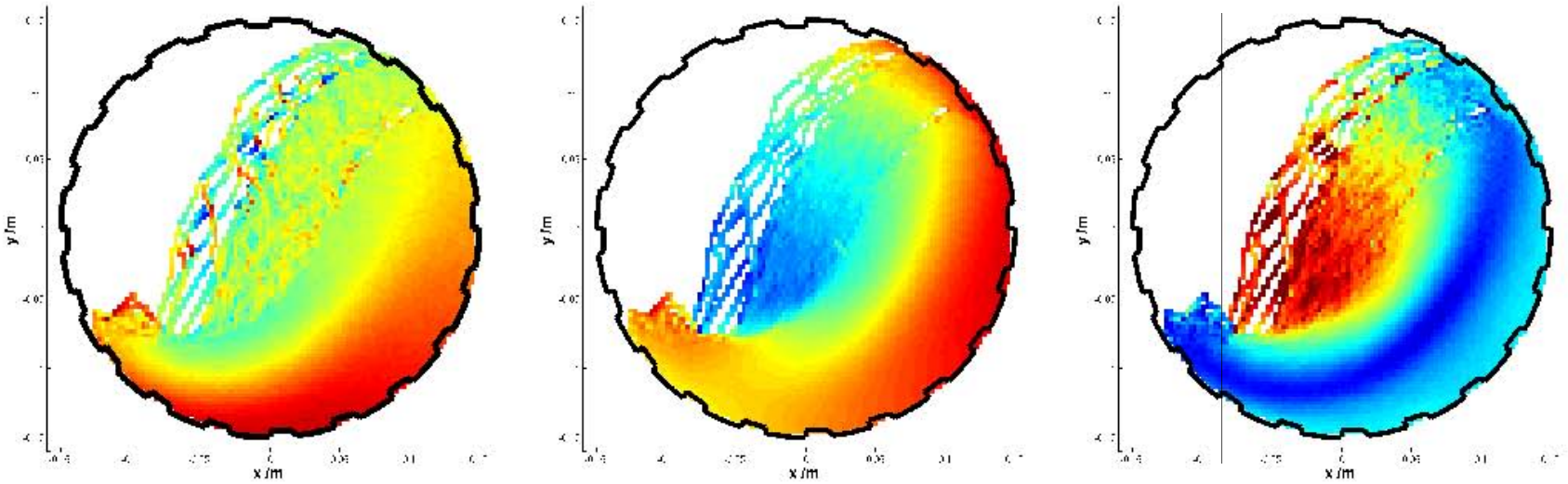

(a) $\hat{x}$- (left), $\hat{y}$- (middle) and transverse (right) velocity distributions.

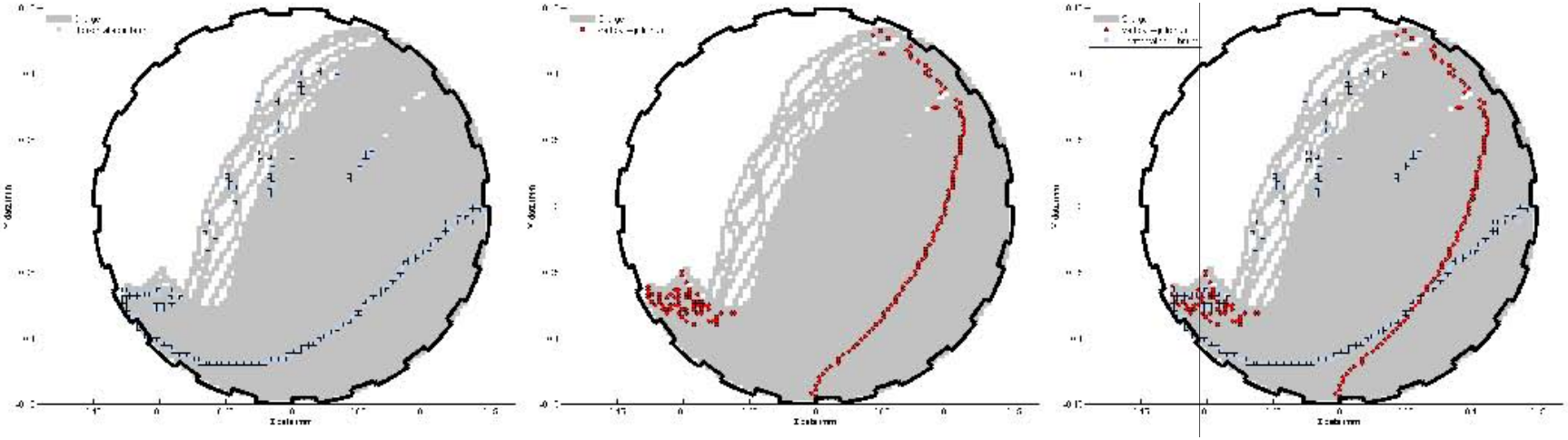

(b) The horizontal (left), vertical (middle) and combined (right) equilibrium points.

Figure 7.6: Time-weighted velocity distributions (top) and the flow equilibrium points (bottom) of the motion of a $3mm$ tracer particle in the 'old' $300mm$ mill filled to 31.25% and rotated at 60% of its critical speed.

The top row of Figure 7.6 shows the $\hat{x}$-, $\hat{y}$- and transverse velocity distributions of the $5mm$ tracer particle in the mill rotated at 60% of its critical speed. Immediately below the $\hat{x}$-, $\hat{y}$-velocity distributions are plots of horizontal and vertical equilibrium points. These equilibrium points define equilibrium surfaces that extend the length of the mill.

As already mentioned in Section 6.2.2, the transverse velocity distribution contains a line of zero velocity called the equilibrium surface[9], visible in Figure 7.6 as a curved blue band. The combined upper part of the vertical and lower part of the horizontal equilibrium surfaces, also shown in Figure 7.6, constitute this equilibrium surface[10].

It turns out, as shown in Figure 7.7, that the equilibrium surface conforms remarkably well to an elliptical arc, but- as with the logistic form of the bulk free surface- this elliptical form is not a model and was chosen merely because of its shape.

[9] See also Section 5.5.2.

[10] Of course, not all equilibrium points are part of the equilibrium surfaces- there are many in the dilute in-flight region and the chaotic toe region that are coincidental- but that all of those in the bulk region are.

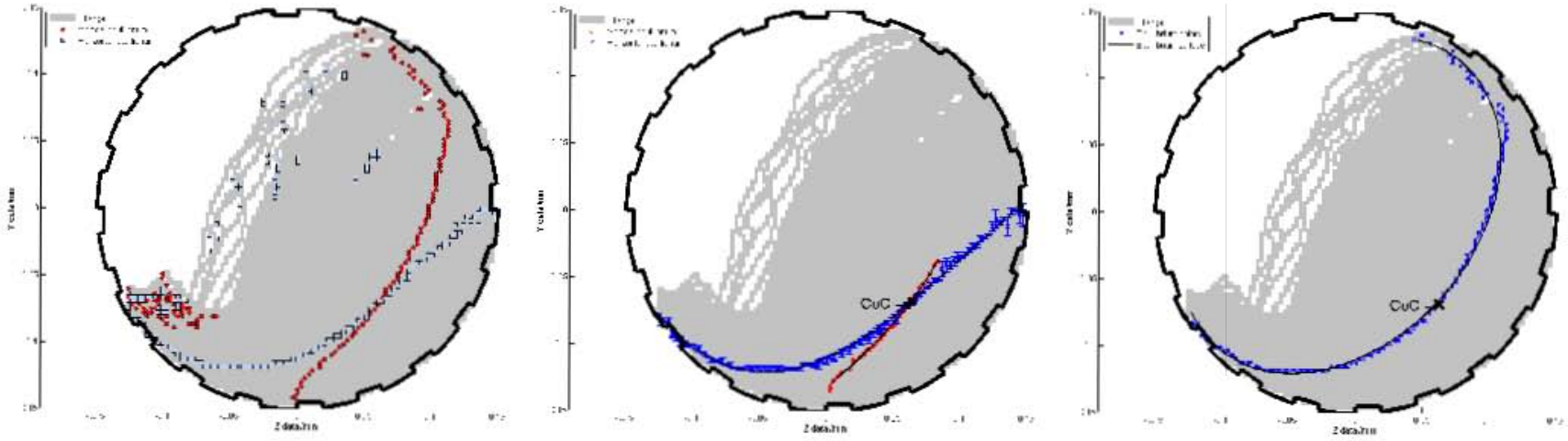

Figure 7.7: The flow equilibrium points (left), their point of intersection (middle), and the equilibrium surface of the motion of a $5mm$ tracer particle in the 'old' $300mm$ mill filled to 31.25% and rotated at 60% of its critical speed.

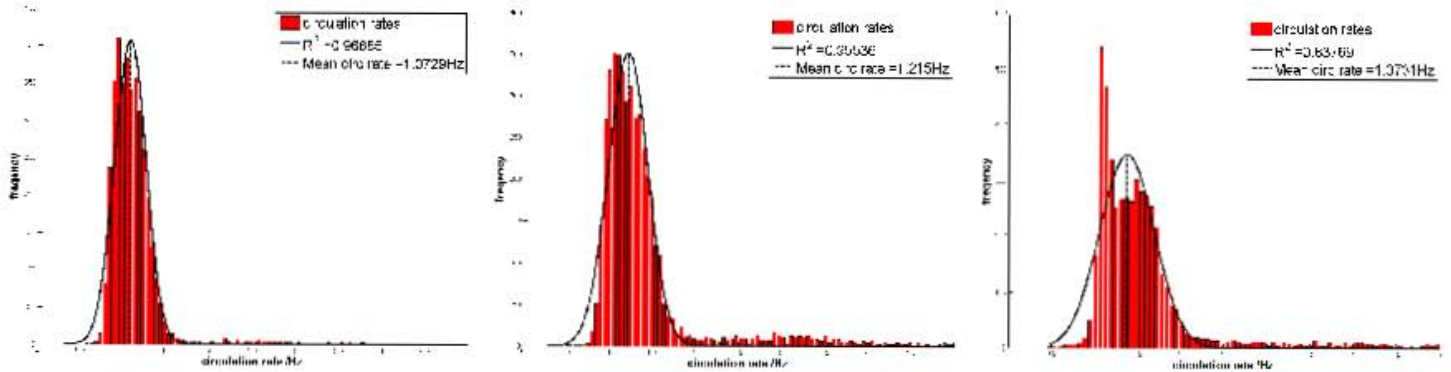

Figure 7.8: Circulation rates about the CoC of $5mm$ monosize charge in the old' $300mm$ mill filled to 31.25% and rotated at 50% (left), 60% (middle) and 75% (right) of its critical speed.

The centre of circulation

The point of intersection of these two surfaces[11] has both zero horizontal and zero vertical velocity- it is a stationary point in the charge. It is called the CoC of the charge, and is the point- at least in the transaxial projection- about which all of the charge revolves. Figure 7.7 shows the two sets of equilibrium points, the procedure used to obtain the CoC from them, and the equilibrium surface as the vertical free surface above the CoC and the horizontal one below it.

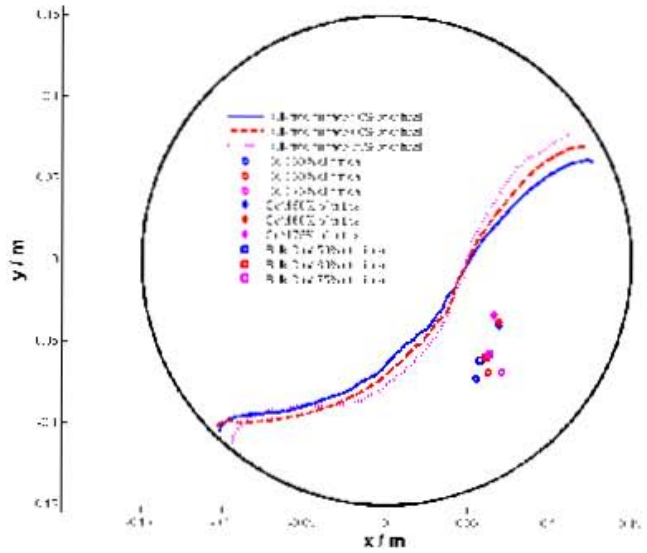

Figure 7.9: A summary of the features of a charge of $5mm$ tracer particles in the 'old' $300mm$ mill filled to 31.25% and rotated at 50%, 60% and 75% of its critical speed.

The CoC is a particularly important point in the charge because it is a measure of not just the position of the bulk charge, but also of its motion. Figure 7.9 shows the positions of the CoCs as well as the CoMs of the bulk and full charge in the 'old' $300mm$ mill operated at a range of speeds. From this figure, it is clear that the CoC is less affected by the development of a disperse region than is the CoM- it is much closer to the CoM of the bulk of the charge than to that of the whole charge.

Since it is a stationary point in the charge, and must lie on the equilibrium surface, it is more sensitive to the flattening of the rising region of the charge against the mill shell at high speeds, leading to a larger spread of positions than the CoMs of even just the bulk of the charge.

Finally, since all of the charge in the mill circulates about the CoC, mass flux must be conserved along any line passing through it. This makes such lines through the CoC preferential sampling cuts in the mill[12].

Circulation rates

Figure 7.8 shows histograms of the circulation rates of tracer particles about the CoC, calculated as per Section 5.5.5. These histograms are shown with best-fit Gaussians superimposed. It is clear from these plots that the distribution of circulation rates in the charge are not normal- they are skewed towards low frequencies. However, Gaussians are a reasonable first approximation[13].

[11] Actually, of course, a line of intersection.
[12] By convention, we consider the line passing through both the CoC and the centre of the mill.
[13] With adjusted $R^2 > 0.95$ for the lower speeds.

Mill speed / $\%v_{crit}$	Mill speed / Hz	Calculated circulation rate Mean / Hz	Std dev / Hz	Normalised circulation rate Mean / Hz	Std dev / Hz
50	0.644	1.122	0.259	1.743	0.402
60	0.772	1.213	0.321	1.571	0.416
75	0.965	1.373	0.447	1.422	0.463

Table 7.4: A comparison of the mill rotational and charge circulation rates, absolute and normalised to the mill rotational frequency.

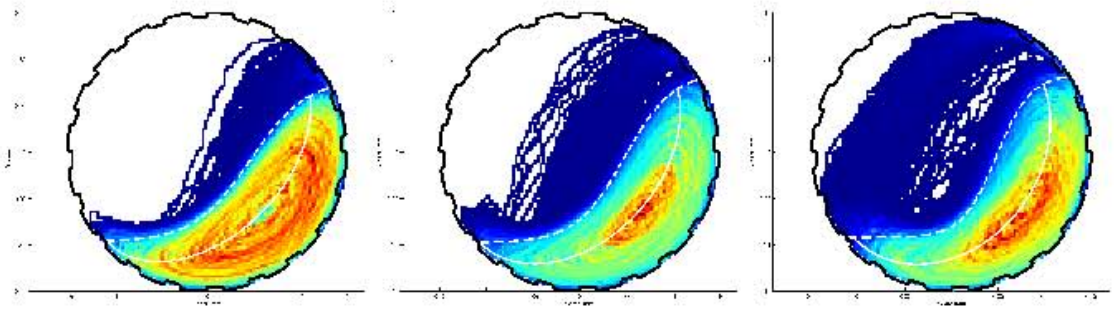

Figure 7.10: General logistic and elliptic approximations to the bulk free and equilibrium surfaces respectively for a the motion of a $5mm$ tracer particle in the 'old' $300mm$ mill filled to 31.25% and rotated at 50% (left), 60% (middle) and 75% (right) of its critical speed.

Table 7.4 shows a comparison of the circulation rates calculated in this way and the mill rotational frequencies. From this table, it is clear that the ubiquitous assumption that the charge circulates once per mill revolution is patently false. Since a particle in the outermost layer of the charge moves up with the mill shell, it reaches the departure shoulder with the same speed as the mill shell. From the departure shoulder, however, it has a shorter distance to travel down the face of the charge- or in the outermost layer of the disperse region- than it would if it were affixed to the shell, but with the same starting speed. Furthermore, the falling particle is accelerated by gravity while one affixed to the constantly-rotating mill shell is not. Thus the falling particle reaches the toe region much sooner than would one affixed to the mill shell. This effect is most pronounced at low mill speeds at which the disperse region is least developed, and disappears when the charge begins centrifuging.

The charge, though, does not behave like a rigid body, even in its bulk region. For this reason, the histogram of circulation rates of the tracer particle over an experiment is not a single, sharp peak. The thickness of the peak is a measure of the number of possible rotation rates that can exist in the charge- an indirect measure of the shear rates in the charge[14].

The rising and active regions

Returning to the equilibrium surface, Figure 7.10 shows logistic bulk free surfaces and elliptical equilibrium surfaces superimposed on the RTDs of the three experiments under consideration. Just as the bulk free surface divided the charge into the bulk and disperse regions, the equilibrium surface divides the bulk region into rising region and the active region[15].

The relative thicknesses of these two regions can be discussed in terms of their radial thicknesses along the line passing through both the CoC and the centre of the mill. Table 7.5 shows these relative thicknesses for the experiments under consideration. Whereas the absolute thicknesses of the two regions change only very slowly, they do so in opposite directions. This is what makes

[14]Not directly linked to grinding efficacy, because no account is taken of the density in the shear regions.
[15]See Section 5.5.2.

Mill speed / $\%v_{crit}$	Active region \m	Rising region \m	Relative thickness
50	0.046	0.059	0.771
60	0.045	0.057	0.799
75	0.051	0.052	0.989

Table 7.5: Relative thicknesses of the rising and active regions of the charge inside the 'old' 300mm mill filled to 31.25% and rotated at 50%, 60% and 75% of its critical speed.

the CoM of even just the bulk of the charge a poor indicator of the actual shape of the charge, and the CoC a better one. However, this ratio of thicknesses turns out to be a useful indicator of the mode of charge motion[16]. In particular, both the thinning of the rising region captured in the movement of the CoC outwards with increasing mill speed, and the increased S-shape of the bulk free surface are reflected in this ratio.

The bulk shoulder and toe

The intersections between the equilibrium and bulk free surfaces provide two additional charge features- the bulk shoulder and toe.

The re-entry toe and departure shoulder mark the beginning and end of a special type of motion-circular motion with the mill shell- and the impact toe marks the end of the motion of charge in free fall. The bulk shoulder and toe do not mark the beginning or end of any type of motion, but rather turning points in the motion of the bed. They are like the head in this respect, which marks a turning point in the free fall motion of charge in the in-flight region.

The equilibrium surface joins all of the turning points in the motion of the charge. Its intersection with the charge free surface is the head of the charge, and its intersections with the bulk free surface are the bulk shoulder and toe of the charge. These can be identified in Figure 7.10, and are given in Table 7.6.

Mill speed	Bulk shoulder		Bulk toe	
/ $\%v_{crit}$	θ / °	r /m	θ / °	r /m
50	28.7	0.127	-134.5	0.141
60	32.2	0.126	-133.9	0.142
75	36.3	0.124	-138.0	0.135

Table 7.6: Angular and radial positions of the bulk shoulder and toe of the charge in the 'old' 300mm mill rotated at various rotational speeds.

There is some uncertainty in the locations of the bulk shoulder and toe, arising from the increased thickness of the transition layer in the shoulder and toe regions. However, Table 7.6 can be read in conjunction with Figure 7.10 to deal with this uncertainty.

The first thing to note is that the position of the bulk toe hardly moves as the mill speed increases from 50% to 60% of its critical speed and then moves down the shell and towards the centre of the mill. This corresponds with the movement of the *true* impact toe from the surface of the charge onto the mill shell, resulting in a much more chaotic toe region.

The angular position of the bulk shoulder follows the same trends as does the departure shoulder-rising with the rising charge. What is not captured by the trends in the departure shoulder is the increased curvature of the equilibrium surface. This is captured, though, in the increasing radial distance between the location of the CoM and CoC, as shown in Figure 7.11.

[16] See Chapter 3.

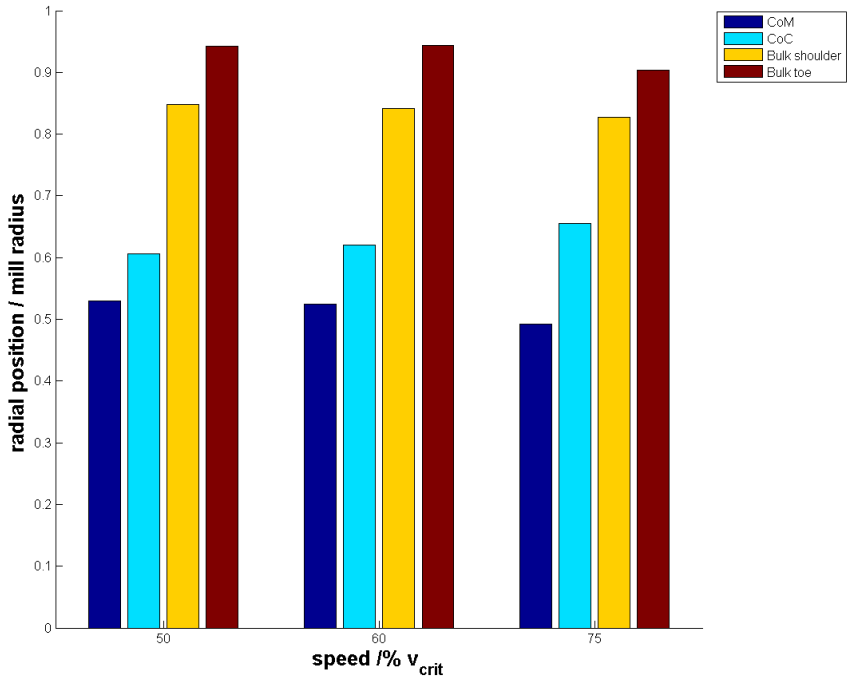

Figure 7.11: Radial positions of the centres of mass and circulation and of the bulk shoulder and toe as a function of mill speed.

7.1.3 A summary of charge features

The significance of various ratios and measures, of the shapes of the equilibrium and bulk free surfaces and so on, have been discussed above. Figure 7.12 shows a summary of the angular positions of all of the charge features mentioned in the preceding sections.

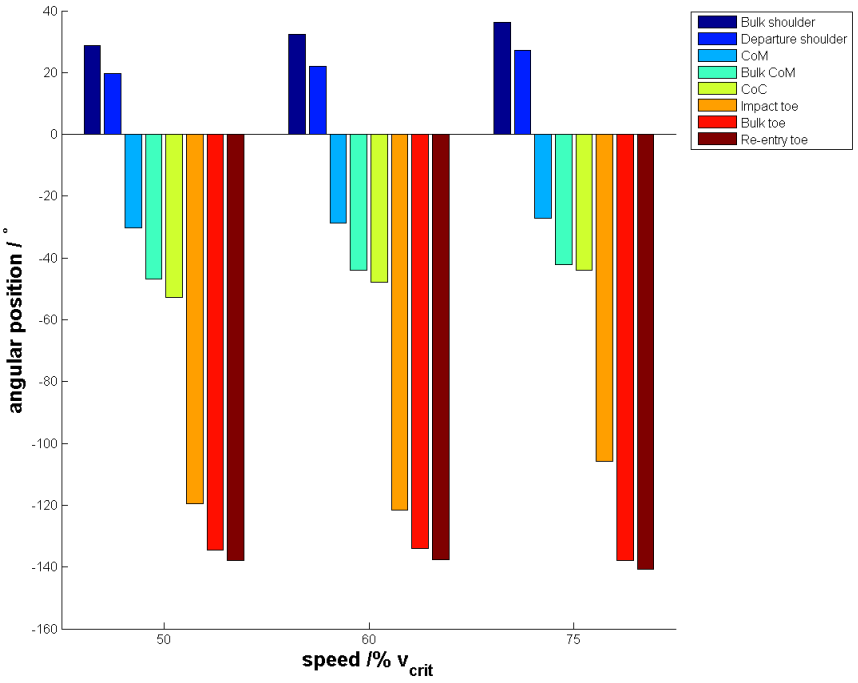

Figure 7.12: Angular positions of various charge features as a function of mill speed.

From this figure, however, it is clear that there is not all that much variation of the charge features over the speeds considered here[17]. What, then, are their use?

Charge features can be used both to characterise and to *summarise* the shape and motion of charge inside tumbling mills. Point-like features such as the CoC, shoulders and toes can be used as inputs into models of tumbling mills, and surface-like features can be used to validate such models.

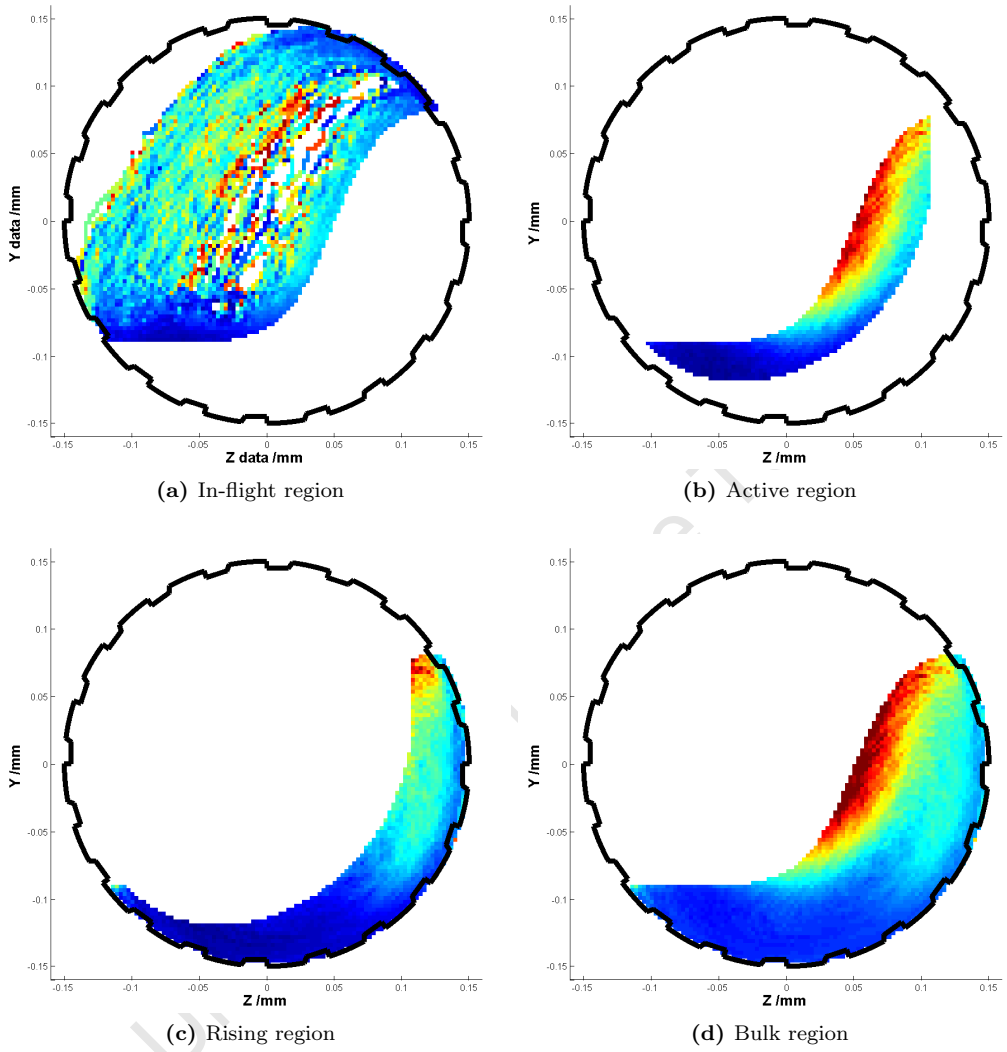

(a) In-flight region **(b)** Active region

(c) Rising region **(d)** Bulk region

Figure 7.13: The transverse acceleration distribution of the motion of a $5mm$ tracer particle in the 'old' $300mm$ mill filled to 31.25% and rotated at 60% of its critical speed, divided into various charge regions.

Surface-like features can also be used to divide the charge up into regions, as has been done for the transverse acceleration in Figure 7.13. Doing so has allowed the range of colours used to be tailored for the range of transverse accelerations in each region, allowing the the centripetal acceleration about the CoC to emerge more clearly.

Figure 7.14 shows the proportion of the charge in each region of the mill, by the fraction of the total mass of the charge in each region, and by the volume of the mill it occupies. Table 7.7 shows the same information numerically.

From this data, it is clear that- for the range of speeds considered here- the mass of charge in the in-flight region increases with increasing speed, marginally more at the expense of the mass of

[17]That they do not change much here does not mean that they do not change much over the full range of operating conditions.

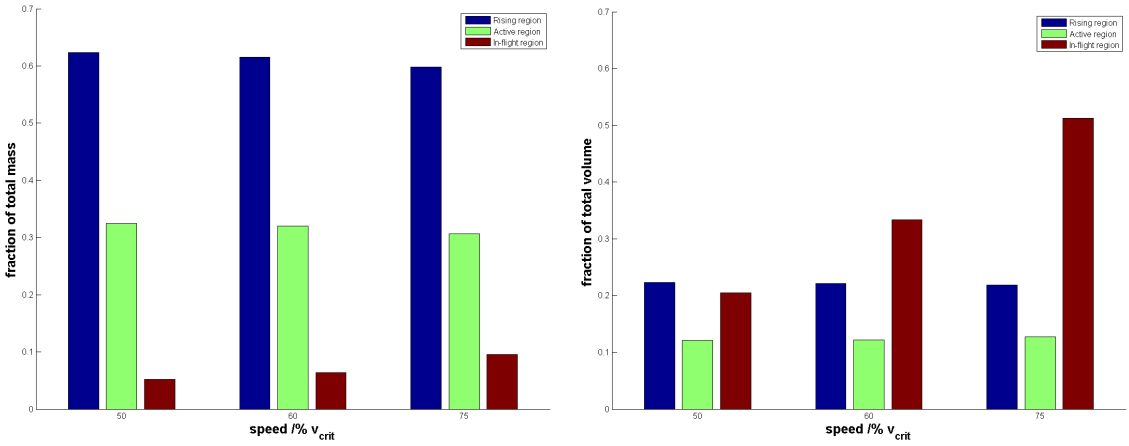

(a) Mass fraction **(b)** Volume fraction

Figure 7.14: The proportions of the charge in the in-flight, active and rising regions, by mass fraction (left), and mill volume (right).

Mill speed / $\%v_{crit}$	Share by mass of the charge			Share by volume of the mill		
	In-flight	Active	Rising	In-flight	Active	Rising
50	0.052	0.323	0.620	0.205	0.121	0.223
60	0.064	0.318	0.612	0.333	0.122	0.221
75	0.095	0.304	0.594	0.513	0.127	0.219

Table 7.7: The proportion of the charge in the rising, active and in-flight regions, by mass and by the volume of the mill occupied

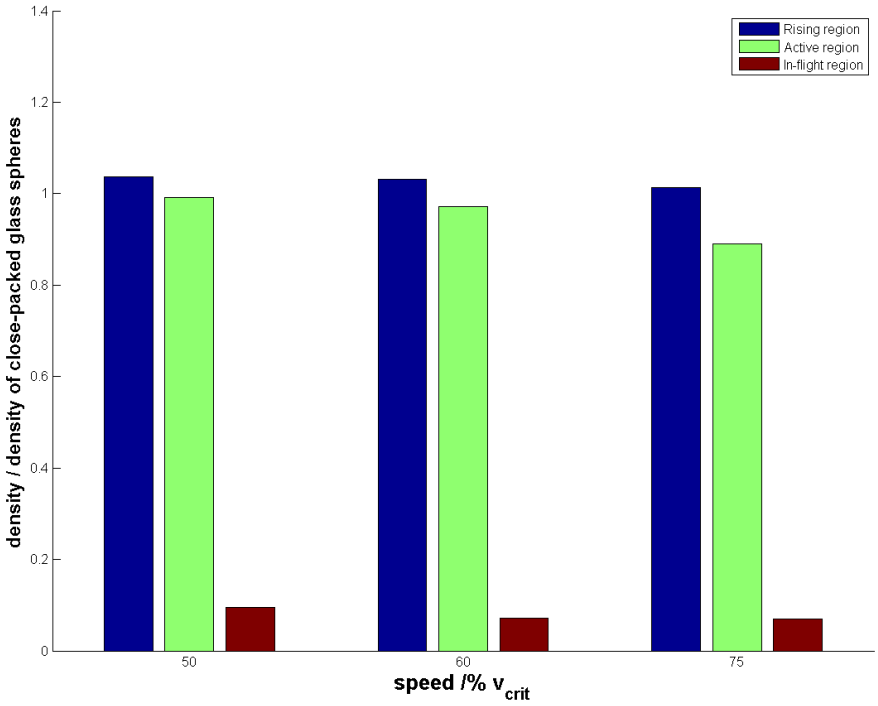

Figure 7.15: The density of the charge in the in-flight, active and rising regions, normalised to the density of tightly-packed glass spheres.

charge in the rising than in the active regions[18]. At the same time, the volume of the mill occupied by the charge in the in-flight and active regions increases- the in-flight region quickly as more and more charge enters this region, and the active region more slowly as its charge dilates- while the volume of the mill occupied by the charge in the rising region decreases. These changes lead to

[18]Particularly at high mill speeds.

the small drop in bulk density of the charge in the rising and in-flight regions, and larger drop in the dilating active region, as shown in Figure 7.15[19].

In the following section I will, as an example, use charge features and regions to investigate the power drawn by a tumbling mill.

7.2 Power draw

In Section 3.3.5 I introduced and motivated the idea of power draw as a proxy for the shape and motion of the charge in a tumbling mill, and one that can be measured externally, in real systems, and in such a way as not to interfere with that motion.

Mill speed / $\%v_{crit}$	**Measured power** **P / W**	ΔP **/ W**
50	19.69	0.44
60	23.74	0.61
75	29.83	1.11

Table 7.8: The power drawn by the 'old' 300mm mill filled to 31.25% of its volume with a monosize charge of 5mm beads, and rotated at 50%, 60% and 75% of its critical speed.

In Section 4.2.3, I described the apparatus used to measure the power drawn by the laboratory-scale tumbling mills used in this work. The measured power drawn by the 'old' 300mm for the experiments under consideration in this chapter are given in Table 7.8.

The idea of the power draw as a proxy for charge motion stems from two different interpretations of the power draw. The first is the interpretation of the power drawn by a tumbling mill as the work done in rotating the mill against the action of the retarding torque applied by the charge. The second is as the energy required, per unit time, to raise the charge to its steady-state position in the mill, and to there rotate it at its steady-state turnover- or circulation- rate. Both of these interpretations depend on the shape, position and motion of the charge in the mill, but they differ, philosophically in at least one important way.

Considering the torque applied by the charge on the mill shell implies a contact force, whereas considering the mechanical energy of the charge does not. This has compounded a long-running ambiguity in the modelling of the power drawn by tumbling mills- how much of the charge to include in the calculation. So far, this has only been 'resolved' by considering how close to measured the model comes excluding more or less of the charge. I argue that if one is to apply the first interpretation in a logically consistent manner, then only the bulk region of the charge should be included. Although it is not possible to settle the matter with PEPT data, I will adopt the above assertion in this presentation.

In Sections 3.3.5 and 5.5.4, I describe some of the torque-based models used to estimate the power draw from experimental data. In the following subsections I will implement these and compare the results, for the 'old' 300mm mill filled to 31.25% of its volume with a monosize charge of 5mm glass beads, and rotated at 50%, 60% and 75% of its critical speed.

[19]That the charge appears to be more dense in the rising region than tightly-packed spheres could be due to the untested assumption that the glass is of density $2700kg \cdot m^{-3}$. The peak density here is $2797kg \cdot m^{-3}$.

7.2.1 Models based on the CoM of the charge

The earliest, and simplest, power draw model is the so-called torque arm approach. This is the procedure of considering all of the weight of the charge to be acting through its CoM. Then, the power drawn in rotating the mill against this torque is

$$P_{CoM} = mgr_{CoM} \cos\theta_{CoM} \cdot \omega_{mill} \tag{7.2}$$

Mill speed / $\%v_{crit}$	**Mill speed** $rad \cdot s^{-1}$	**CoM power**	
		full / W	**bulk / W**
50	4.044	26.501	22.080
60	4.852	31.871	28.170
75	6.066	37.873	36.202

Table 7.9: Power draw estimates using the centre of mass torque arm about the centre of the mill.

Using the angular and radial positions given in Table 7.1a yields the power draw estimates given in Table 7.9. These are a good deal higher than the measured power draw, which is unphysical. Of course, we can't expect such a crude model to accurately predict the power drawn, but- since energy must be lost in the bearings, dissipated in inter-particle interactions, and so on- we'd expect a valid model to under- not over-predict. Including only the bulk region in the calculation of the CoM lessens but does not eliminate this effect.

A modification that has been proposed to the CoM torque arm approach is to use the circulation rate of the charge, rather than the angular velocity of the mill. As shown in Section 7.1.2, the circulation rates of the charge are, in general, higher than the angular velocity of the mill, so using these values would *increase* the unphysical over-prediction problem. This is in addition to the logical inconsistency of using the circulation rate of the charge and the torque exerted *by* the charge on the mill shell.

Mill spd / $\%v_{crit}$	**Circ rate**		**Torque arm**		**Full CoM**		**Bulk CoM**	
	mean /Hz	**std** /Hz	**full /m**	**bulk /m**	P /W	ΔP /W	P /W	ΔP /W
50	7.048	1.625	0.014	0.003	9.019	2.079	1.670	0.385
60	7.622	2.019	0.006	0.001	4.696	1.244	0.939	0.249
75	8.627	2.809	0.005	0.007	4.089	1.331	6.133	1.997

Table 7.10: Power draw estimates using the centre of mass torque arm about the centre of circulation of the charge.

This logical inconsistently can be dealt with by replacing the position of the CoM of the charge with respect to the centre of the mill, with that with respect to the CoC of the charge. This yields the power estimates given in Table 7.10. Here, though, the fact that the CoCs and CoMs, especially the bulk CoMs, of the charge are so close together[20] means that the torque arms defined by the distance between them are very short. Thus the power draw is badly under-predicted with this method- it seems inconceivable that so much energy could be lost by the mill per second[21]. Also, the movement of the CoM from the left to the right hand side of the CoC results in the strange dip in the power draw at 60% of critical speed.

[20] See Figure 7.9.

[21] For instance, given a charge of $5mm$ diameter glass beads of mass $\backsim$ 9.662 kg and specific heat capacity $c_p = 0.84Jg^{-1}K^{-1}$, the energy lost per second at 50% of critical speed would raise the temperature of the charge by a very noticeable $\Delta T = \frac{mc_p\Delta t}{\Delta P} \approx 5°\text{C}$ over the course of an hour-long experiment.

7.2.2 Models based on binning the charge

A better way to shift the focus from the motion of the mill shell to the motion of the charge is to consider the torque per bin approach. In this approach, the total power drawn by the charge is interpreted as the sum of the power that would be drawn by each volume element to maintain its motion against the gravitational torque it experiences about some point[22]. Thus equation 7.2 would become

$$P = \Sigma_i^N \Sigma_j^N P_{ij} = \Sigma_i^N \Sigma_j^N m_{ij} g r_{ij} \cos\theta_{ij} \cdot \omega_{ij} \tag{7.3}$$

where the indices i and j refer to bins in the transverse projection, and the angular speed, ω, of the charge can be calculated about the centre of the mill, or the CoC of the charge.

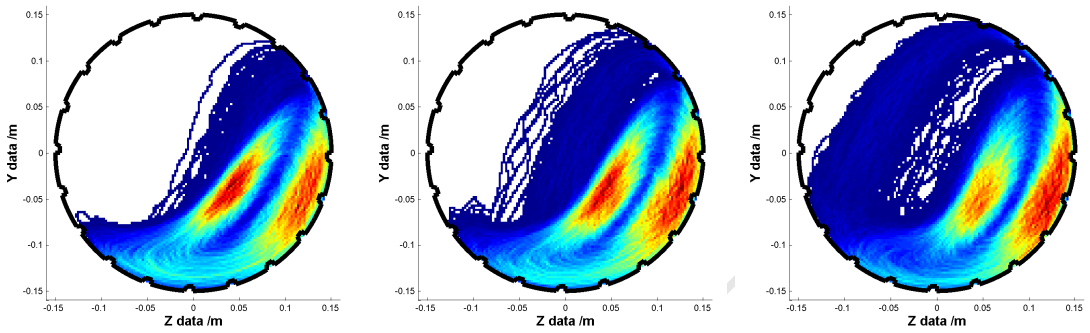

Figure 7.16: Power draw distributions of a $5mm$ tracer particle in the 'old' $300mm$ mill filled to 31.25% and rotated at 50% (left), 60% (middle) and 75% (right) of its critical speed.

Figure 7.16 shows power draw distributions calculated as per equation 7.3, with the angular speed of the charge calculated about the centre of the mill. In these plots, it is clear that despite the high particle speeds in the in-flight region, most power is drawn in the bulk region of the charge.

Considering Figure 7.16 in conjunction with Figures 7.1 and 7.5 makes it clear that it is those regions whose density and tangential speed are greatest that contribute the most to the power draw, and- considering equation 7.3- that this effect is further exaggerated for those regions at the largest horizontal distance from the point about which the angular speed of the bins is calculated[23].

In fact, since the magnitude of the angular speed is used in equation 7.3, the power draw distributions obtained for circulation about the centre of the mill and about the CoC are qualitatively similar. Since, though, the horizontal distances between the CoC and elements in the bulk of the charge are much shorter than in the case of the angular speed about the centre of the mill, it might be expected that the predicted power draw in the former case would be much lower than in the later. However, since $\omega = \frac{v_t}{r}$, this reduction in horizontal distance- $x = r\cos\theta$- is partially compensated for by a resultant increase in the angular speed- $\omega' = \frac{v'_t}{r'}$. Thus it turns out that the torque per bin about the CoC produces only a slightly lower power prediction than does the torque per bin about the centre of the mill.

Mill spd	Full about $\bigoplus$		Bulk about $\bigoplus$		Full about CoC		Bulk about CoC	
/ $\%v_{crit}$	P /W	ΔP /W	P /W	ΔP /W	P /W	ΔP /W	P /W	ΔP /W
50	22.184	0.022	20.022	0.021	21.732	0.021	19.589	0.020
60	25.623	0.023	22.948	0.022	25.166	0.023	22.485	0.022
75	30.502	0.024	26.092	0.023	30.049	0.024	23.765	0.023

Table 7.11: Torque per bin power draw estimates using the centre of the mill ($\bigoplus$) and CoC of the charge as the points about which the charge rotates.

[22] See Section 5.5.4.
[23] The centre of the mill in Figure 7.16.

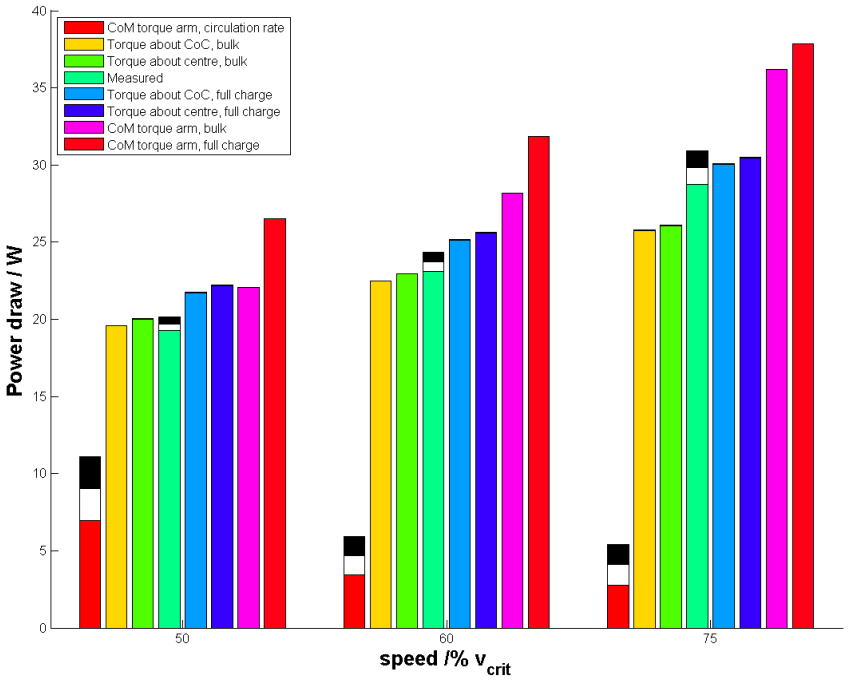

Figure 7.17: The power drawn by a monosize charge of $5mm$ tracer particles in the 'old' $300mm$ mill filled to 31.25% and rotated at 50%, 60% and 75% of its critical speed, calculated using a range of power draw models.

Table 7.11 shows the power draw calculated by summing the contributions from each bin in distributions such as those shown in Figure 7.16, with the torque and angular speed of the tracer particle calculated about the CoC and centre of the mill.

7.2.3 A summary of power draw calculations

Figure 7.17 shows the power draw for the 'old' $300mm$ diameter mill rotated at 50%, 60% and 75% of its critical speed, calculated with the power draw models mentioned in the preceding subsections. Here the black and white parts of the bars represent the regions of uncertainty, such that the coloured bars end at $\bar{P} - \Delta P$, the white ones at $\bar{P}$ and the black ones at $\bar{P} + \Delta P$. Thus it is clear that only the measured power draw and that calculated from the CoM torque arm approximation using the circulation rate of the charge have significant uncertainties.

As already mentioned above, it is unphysical to predict a larger than measured power draw- an under-prediction can be explained in terms of losses in bearings, inelastic collisions, frictional dissipation, and so on, but an over-prediction can only be explained by an *additional* source of energy for the charge. In these glass bead-based experiments, at least, there are no chemical reactions occurring in the charge, and the mill is driven only by the shaft from which the measured torque- and thus power- is obtained. Models that significantly over-predict the power draw can, thus, be excluded.

In Figure 7.17, the simple CoM torque arm approximations significantly over-predict the power and can thus be discarded. Using the simple CoM torque arm approximation and the circulation rate of the charge significantly under-predicts the power draw, and can thus also be discarded- albeit with less conviction.

In Figure 7.17, too, the torque per bin approach about both the CoC and the centre of the mill less-

significantly over-predict the top end of the measured power draw for low mill rotational speeds. At high rotational speeds, we expect the power calculated from tracer particle kinematics to more significantly under-predict the measured power draw because more inelastic collisions between particles and between particles and the mill shell should lead to a larger proportion of supplied energy lost in ways that are not measurable by PEPT. Here, though, the torque per bin approach yields power draws that are comparable to the measured power and greater than the lower bound of the measured power. This leaves, as a viable model, only the torque per bin approach excluding charge in the in-flight region.

All of the models presented here employed 'the overcoming gravitational torque' interpretation of power draw. Thus, since the retarding torque can only be communicated to the shell by direct contact, including only the bulk region of the charge makes intuitive sense. I will not, however, interrogate this further here- I consider power draw only as a proof of ergodicity[24], and as an example of the use of charge features in modelling the behaviour of charge in tumbling mills.

7.3 Radial measures

7.3.1 Polar binning

I now turn my attention to the interrogation of charge behaviour by radially re-sampling distributions such as those shown in Figures 7.1 and 7.5.

In Section 7.1.1 I made use of polar binning, as defined in Section 5.4.3, to facilitate the edge-detection of the bulk free surface of the charge. Although a useful intermediate step, it is difficult to interpret polar bin plots such as those shown in Figure 7.18.

In the rest of this section I will instead consider the procedure of radial bin selection, as described in Section 5.4.4.

[24]See Appendix I.

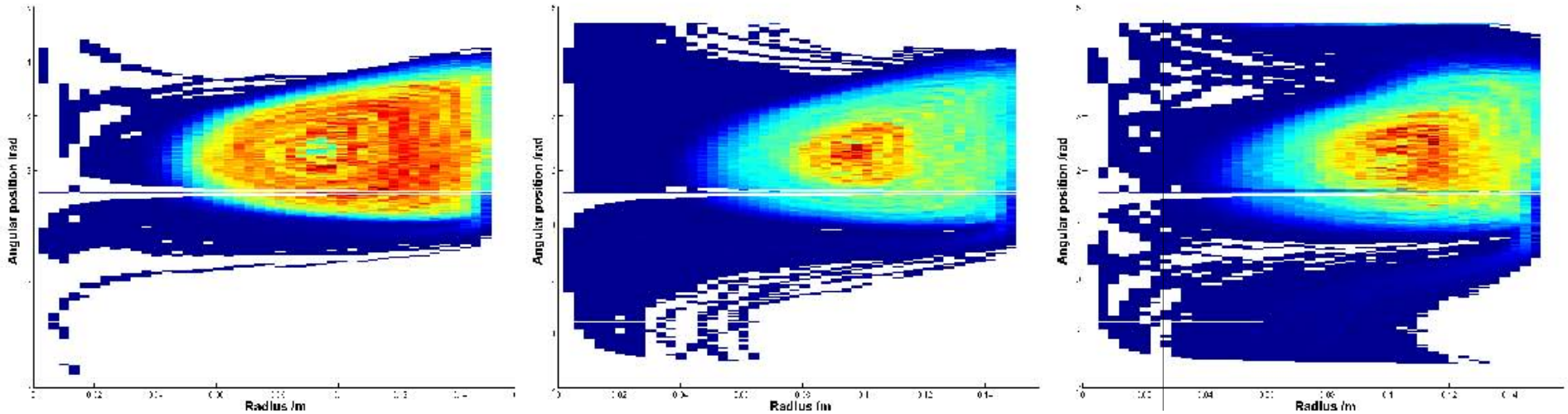

(a) Mass

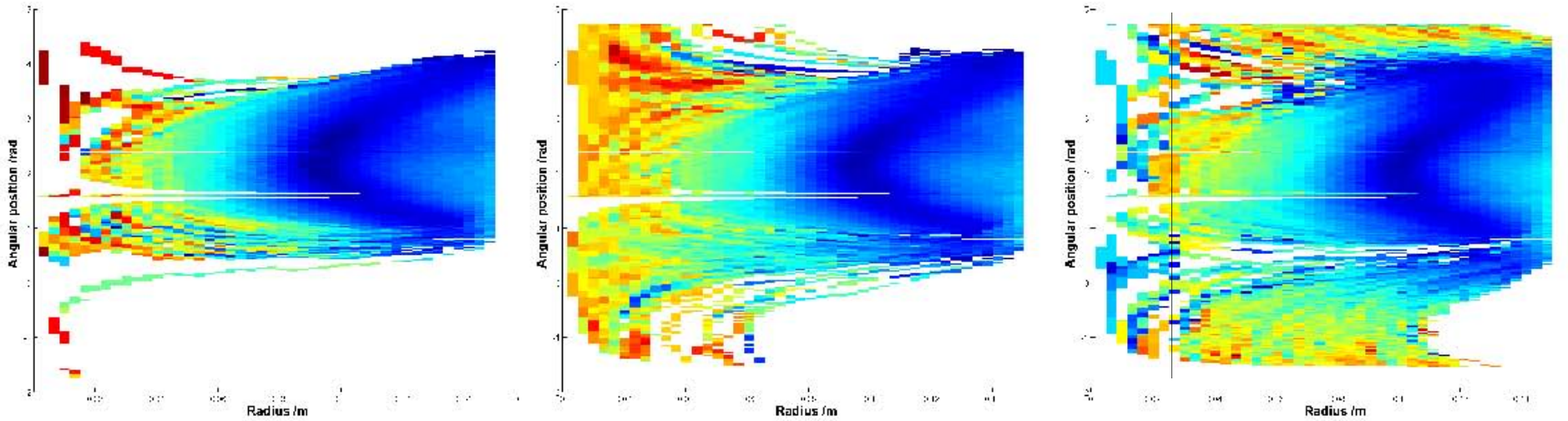

(b) Transverse velocity

Figure 7.18: Polar binned mass (top) and transverse velocity (bottom) distributions of the motion of a $5mm$ tracer particle in the 'old' $300mm$ mill filled to 31.25% and rotated at 50% (left), 60% (middle) and 75% (right) of its critical speed.

7.3.2 Radial bin selection

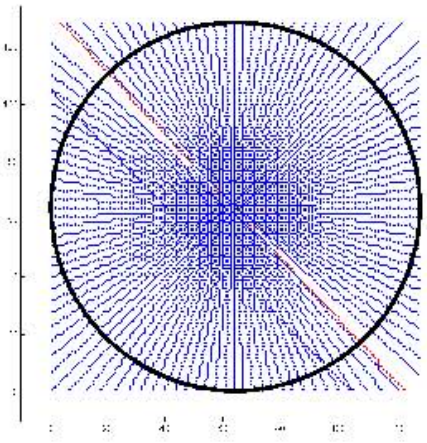

Figure 7.19: A plot of the bin indices of a 128×128 grid divided into $90 + 1$ radial slices, where the red slice passes through the CoC of a given charge.

Figure 7.19 shows a plot of the bin indices of a 128×128 grid divided into $90 + 1$ radial slices- 90 'evenly' spread slices and 1 slice through the CoC. The radial slices shown in Figure 7.19 are not perfectly evenly spaced in the 2π radians of the circle. For practical reasons, the circle is dived by the lines $y = x$ and $y = -x$ into four quadrants, each divided into $\frac{N}{4}$ slices, where $N = 90$ in this case. Furthermore, the discrete nature of the grid means that the radial bins selected do not fall on a perfectly straight line. For large enough grid sizes, however, this effect is not large.

In subsequent figures I have adopted the following conventions: the angular position of a bin is measured clockwise from the positive $\hat{x}$-axis, and its radial position is positive if it falls on the right of the $\hat{y}$-axis, and negative otherwise. Also, the angular positions of the radial slices run between $-\frac{\pi}{2}$ and $\frac{\pi}{2}$ because it is measured between the positive $\hat{x}$-axis and the positive half of its radial slice. Thus, the slice along the line $y = x$ would be labelled as being at an angle of $\frac{\pi}{4}$ radians, and the line $y = -x$ would be labelled as being at an angle of $-\frac{\pi}{4}$ radians. In this formulation, the radial slices at angles $-\frac{\pi}{2}$ and $\frac{\pi}{2}$ radians are, in fact, the same slice.

Figure 7.19 shows radial slices through the centre of the mill, but slices can also be taken through any specified point- usually the CoC of the charge. In such a case, the origin of the reference frame is moved to this point and the preceding definitions still hold.

Figure 7.20 shows the values of the mass distribution and of the transverse velocity distribution re-sampled along several radial slices, for the 'old' $300mm$ rotated at 50%, 60% and 75% of its critical speed. As well as the sample points, cubic-splines are fitted to mildly-smoothed versions of these points, and plotted as an aid to the visualisation of trends in the data.

The top row of Figure 7.20 shows radial slices through the mass distributions of each of these experiments in steps of 30°. By the convention mentioned above, most of the mass is at positive radial locations. Since neither the equilibrium surface nor the bulk free surface are at constant radial positions for all angles, these curves are somewhat difficult to interpret. What can be seen, however, is that the mass density of the charge increases from the in-flight region, more or less uniformly until it reaches a noisy maximum region in the bulk. It then decreases towards some non-zero minimum at the shell. This minimum is roughly constant when the bulk of the charge is in contact with the shell, but rapidly drops off after the shoulder of the charge[25].

It is interesting to note that as the rotational speed of the mill increases, the radial mass distribu-

[25] Above an angular position of 30° in these examples.

tions in the bulk of the charge become narrower and more pointed, and do so over a much smaller angular range than at low speeds. This reflects the flattening and stretching of the bulk region of the charge that occurs at higher speeds.

The bottom row of Figure 7.20 shows radial slices through the transverse velocity distributions of the same three experiments. Although these plots show transverse velocity magnitudes, these magnitudes are plotted as positive when their $\hat{y}$-components are positive- when the tracer particle is moving upwards- and negative otherwise. This results in a more or less straight line in the radial velocity distribution running from maximum positive transverse velocity at the mill shell to a maximum negative at the bulk free surface. In fact, though, this 'maximum' negative transverse velocity is only the maximum for the bulk region of the charge. The radial velocity distributions in the in-flight region are extremely chaotic, especially for high mill speeds, and make analysis of this region difficult.

The insights gained from Figure 7.20 are hard to unpack because, among other reasons, the radial positions of the equilibrium and bulk free surfaces are different for each angular location[26]. This makes it difficult to interpret plots that are already crowded despite sampling at intervals of only $\frac{\pi}{6}$ radians.

Figure 7.21 show the same data as does Figure 7.20, but only sampled along a radial line through the centre of the mill and through the CoC[27]. The plot areas in Figure 7.21 are divided into the in-flight, active and rising regions, as well as into that region occupied by the lifters.

The top row of Figure 7.21 shows the radial mass distributions of the charge at each of the three mill speeds. Here, the difference in the shape of the three distributions is much clearer. Consider Figure 7.1, in which there appears to be a low density core around the CoC of an otherwise fairly uniform bulk region for the case of the mill rotated at 50% of its critical speed. This feature is clearly visible in Figure 7.21. On the other hand, Figure 7.1 shows a much larger density gradient tending towards a high-density core about the CoC- again clearly visible in Figure 7.21. Also visible in Figure 7.21 is the mass density drop in the lifter region, easily explicable by the fact that the lifters themselves take up volume.

The effect of lifters on the tangential speed of the tracer particle can also be seen in Figure 7.21. More interesting, however, are the functional forms of the tangential velocity distributions in the rising and active regions.

[26]Note, for instance the curved shape of the equilibrium surface in Figure 7.18, which would appear as a vertical line if the equilibrium surface were at a constant radial distance from the centre of the mill.

[27]Since the CoC is a special point, and since the mass flux through any radial line through the CoC must be conserved, it is hoped that such a radial slice would be a representative one.

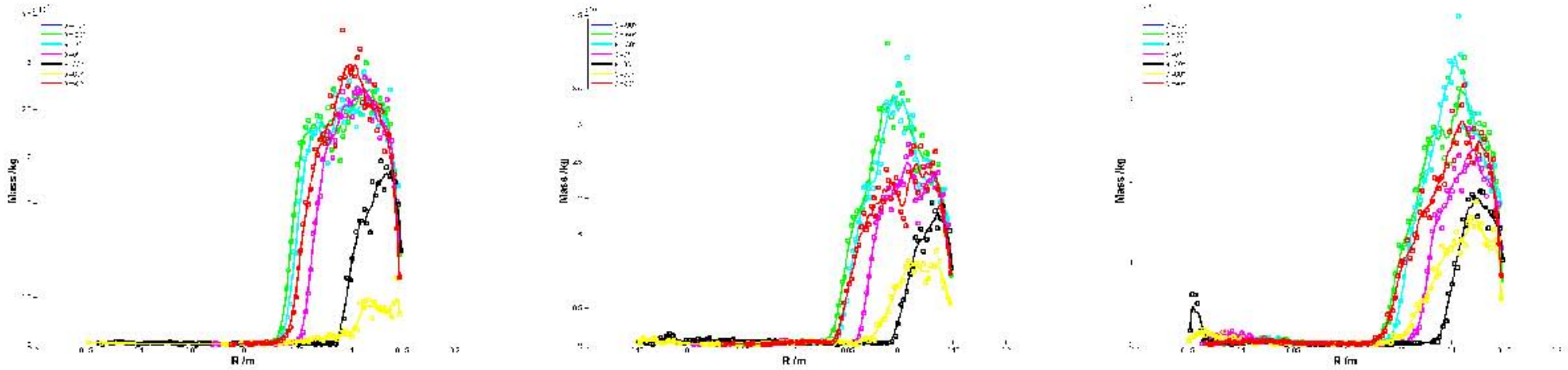

(a) Radially sampled masses

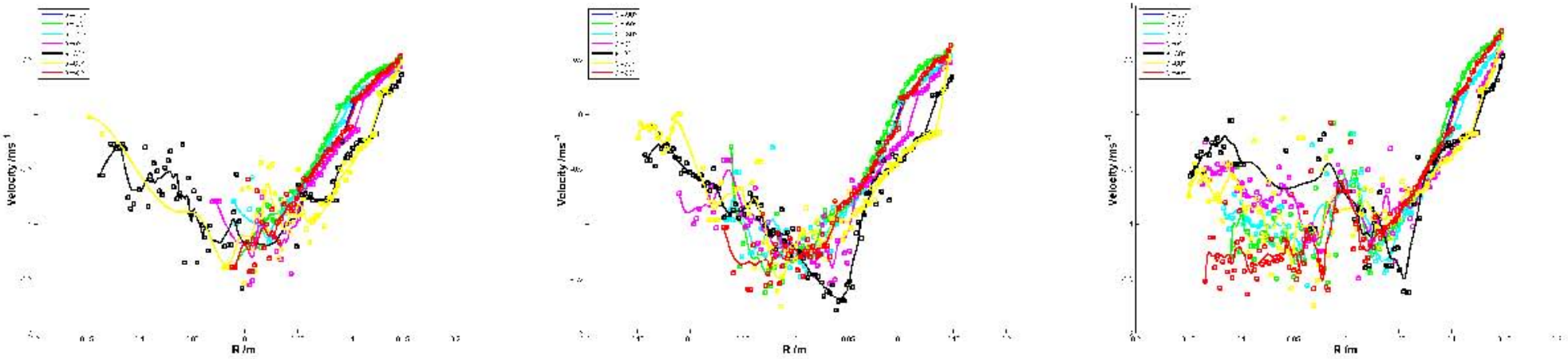

(b) Radially sampled transverse velocities

Figure 7.20: Radial samples of the mass (top) and transverse velocities (bottom) distributions of the motion of a $5mm$ tracer particle in the 'old' $300mm$ mill filled to 31.25% and rotated at 50% (left), 60% (middle) and 75% (right) of its critical speed.

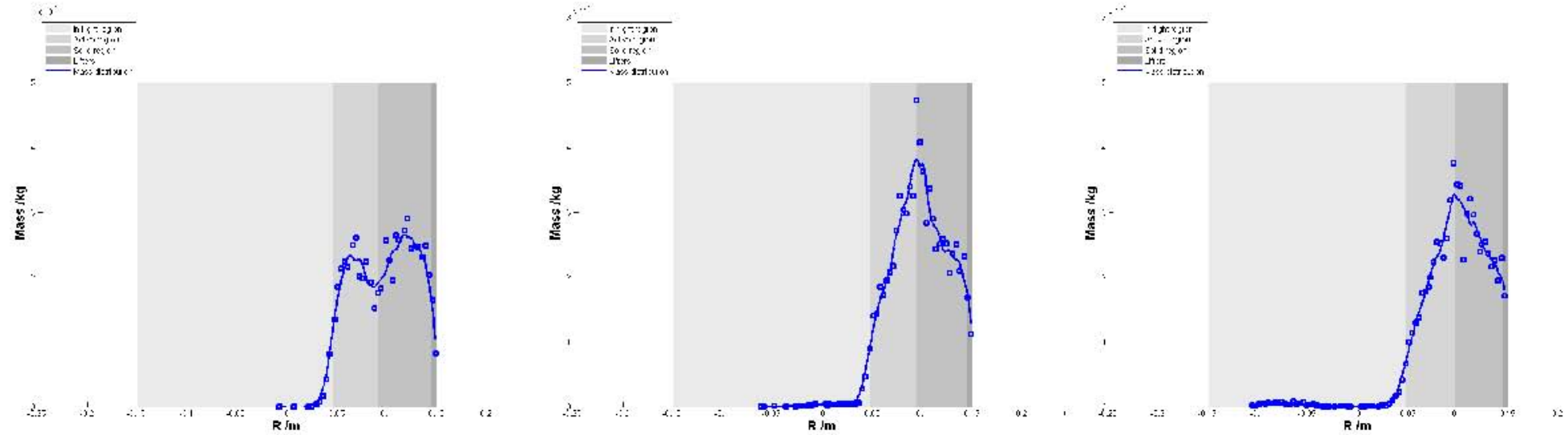

(a) Radially sampled masses through the CoC

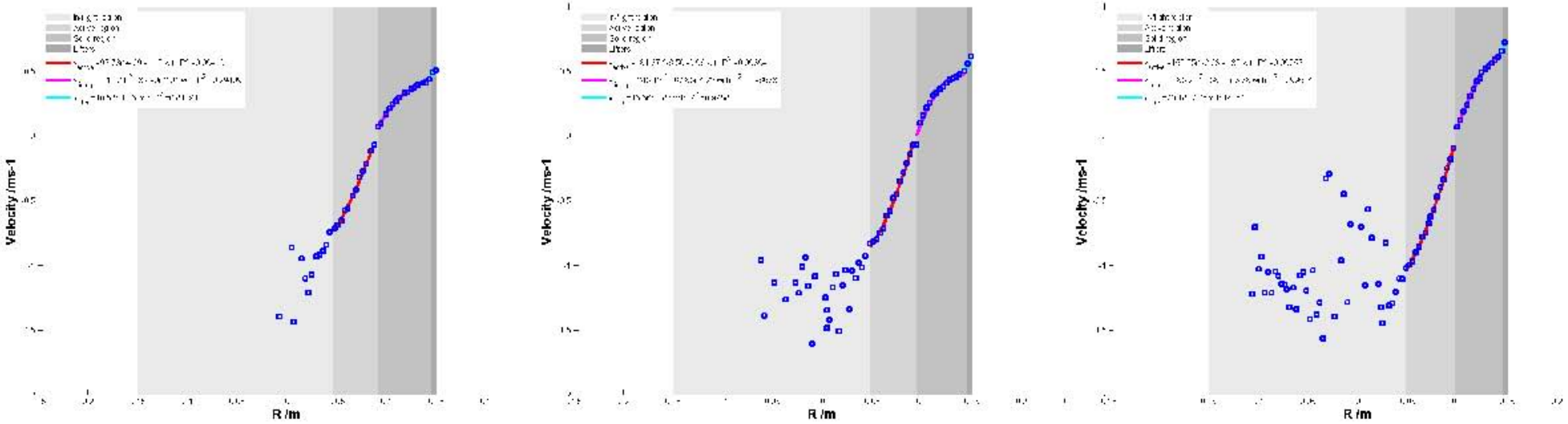

(b) Radially sampled transverse velocities through the CoC

Figure 7.21: Radial samples through the CoC of the mass (top) and transverse velocities (bottom) distributions of the motion of a $5mm$ tracer particle in the 'old' $300mm$ mill filled to 31.25% and rotated at 50% (left), 60% (middle) and 75% (right) of its critical speed.

7.3.3 Shear rates

The magnitude of the tangential velocity decreases quadratically from the shell to the CoC and then increases quadratically from the CoC to the bulk free surface. Thereafter, in the in-flight region of the charge, however, the tangential velocity of the material does not follow so clear a trend, especially at high mill speeds.

Figure 7.21 shows quadratic functions fitted to the tangential velocities of the charge rotated at 50%, 60% and 75% of the critical speed of the mill, sampled along lines through their CoCs. In all cases, these best-fit quadratics have adjusted $R^2 > 0.99$. In Figure 7.21, too, are lines of best fit to the last sample point before the lifters and those in the lifter region.

If the tangential velocities in Figure 7.21 conformed to straight lines whose gradients were just the angular frequency of the mill shell, this would justify some of the more naive assumptions about the linear velocity profile in the charge. That this is not the case implies a shear rate, and that the velocity profiles are not linear implies a varying shear rate in the charge. Since shear rate is just $\dot{\gamma} = \frac{\delta v}{\delta r}$, the portions of the the quadratic curves in Figure 7.21 with the largest magnitude gradient experience the greatest shear rate. At all three mill speeds considered here, the charge experiences the greatest shear rate close to the equilibrium surface[28].

Mill speed / $\%v_{crit}$	**Radial limits /m** **Active region**	**Rising region**	**Lifter region**
50	$0.045 \leqslant r < 0.091$	$0.091 \leqslant r < 0.145$	$0.145 \leqslant r < 0.15$
60	$0.048 \leqslant r < 0.093$	$0.093 \leqslant r < 0.145$	$0.145 \leqslant r < 0.15$
75	$0.047 \leqslant r < 0.097$	$0.097 \leqslant r < 0.145$	$0.145 \leqslant r < 0.15$
	Velocity (/ms^{-1}) as a function of radial position		
50	$92.78r^2 + 4.29r - 1.15$	$-111.20r^2 + 32.90r - 2.01$	$10.58r - 1.06$
60	$181.40r^2 - 6.51r - 0.96$	$-245.10r^2 + 67.85r - 4.22$	$16.66r - 1.87$
75	$152.70r^2 - 2.03r - 1.30$	$-185.90r^2 + 58.15r - 3.88$	$20.18r - 2.25$
	Shear rate (/s^{-1}) as a function of radial position		
50	$185.56r + 4.29$	$-222.40r + 32.90$	10.58
60	$362.80r - 6.51$	$-490.20r + 67.85$	16.66
75	$305.40r - 2.03$	$-371.80r + 58.15$	20.18

Table 7.12: The radial limits (top) of each charge region, their velocity (middle) and shear rates (bottom) as a function of radial position for each mill rotational speed.

Table 7.12 contains the tangential velocity and shear rate functions in the lifter, rising and active

[28]Or, equivalently in this case, close to the CoC.

regions of the charge at each mill speed. These are visualised in Figure 7.22.

From Figure 7.21, it is clear that the tangential velocity function has a greater curvature in the rising region than it does in the active region. This is captured in Table 7.12 as a larger (magnitude) second derivative in the rising than in the active region, and in Figure 7.22 as a larger range of shear rates.

This greater rate of change of shear rate in the rising region is because the charge in this region moves entirely under the action of the mill shell, which is transmitted to each layer by the one immediately below it. Each subsequent layer, however, slips slightly with respect to the one below it, to an extent depending on the frictional force between the layers. Since this frictional force is dependent on the normal force between the layers, which is itself dependent on the weight of charge acting on the upper of the two layers, it becomes smaller and smaller- thus allowing more and more slippage- for each subsequent layer. Thus at a sufficient depth, the charge is effectively locked in a pseudo-solid body motion- it would have a horizontal line velocity function in Figure 7.21. As the depth of the layer in the charge decreases, it experiences less and less of a normal force, and thus becomes more and more mobile with respect to the layer below it- a greater and greater magnitude gradient in Figure 7.21. As the magnitude of the tangential velocity of the charge decreases towards its equilibrium surface, its shear rate increases to some maximum.

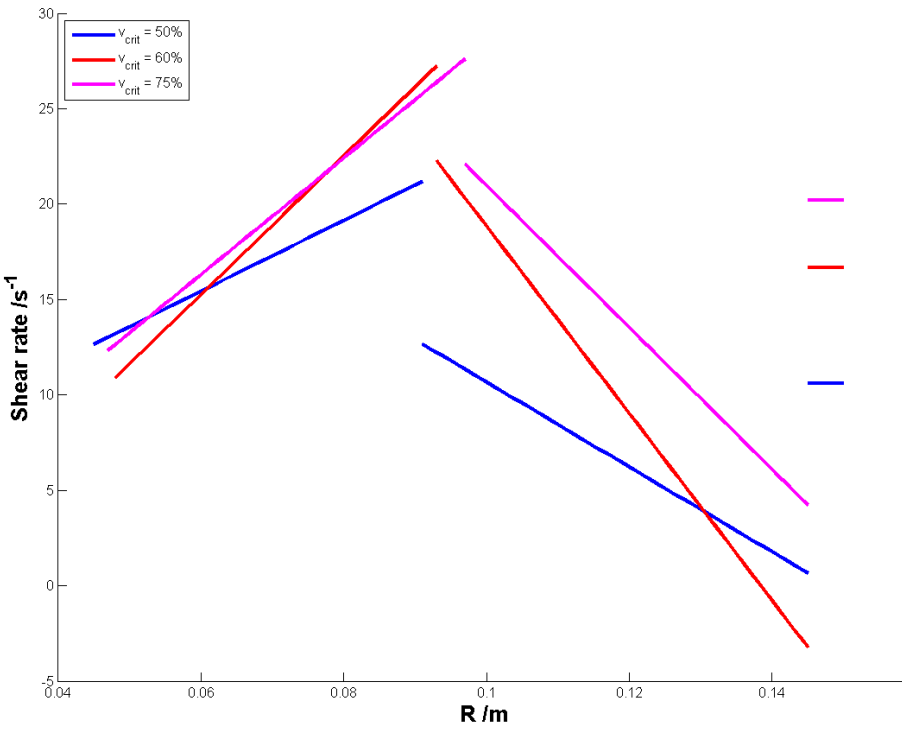

Figure 7.22: Shear rates in the bulk of a monosize charge of 5mm glass beads in the 'old' 300mm mill rotated at various speeds.

Above the equilibrium surface, the charge is no longer moving upwards under the influence of the mill shell, and has begun to flow down the face of the charge under the influence of gravity. This gravitational acceleration of the falling charge leads to greater charge speeds in active region, which result in a larger shear rate between the first layer of the active region and the equilibrium surface than between the last layer of the rising region and the equilibrium surface.

Furthermore, the outermost layers of charge in the active region are free to dilate, an effect which penetrates to some depth in the active region, reducing the normal force between its layers. For this reason, the rate of change of the shear rate in the active region is less than in the rising region-

its tangential velocity as a function of radial position is less curved than that in the rising region. In fact, this reduction in normal force due both to depth and dilation- coupled with the fact that outer layers of the charge, by virtue of their position in the mill, enter the active region with a larger initial speed and greater gravitational potential energy than do inner layers- leads to higher shear rates in the active than in the rising region in general, particularly for inner layers of the active region.

7.3.4 Shear rate binning

The preceding discussion has applied only to a single radial slice through the CoC- that through the centre of the mill as well. This is a radial line that passes through the body of the charge, and is assumed to be representative of the bulk, but it does not take into account the behaviour of the charge in the complicated shoulder and toe regions, for example.

In order to gain an overview of the shear environment in a tumbling mill, it is useful to consider a shear rate distribution. Unlike all other distributions presented in this work, however, the shear rate distribution is not directly calculable at the time of binning because the shear rate must be calculated along radial lines. It is calculable, however, after the fact using the bin selection technique visualised in Figure 7.19 and described in Section 5.4.4.

The first step in producing the shear rate distribution is to obtain the tangential speed of the charge in the mill. If the charge in the mill moved in concentric layers with the mill shell, this would be unambiguous, and the shear rate would just be the the difference in tangential speed between layers divided by the thickness of each layer. If this were the case, too, there'd be no radial component to the velocity of the charge. Unfortunately, this is not the case, and the reality is a bit more complicated.

The radial component of the velocity is a measure of how much mixing occurs between layers. The first column of Figure 7.23 shows radial velocity distributions of the charge at each rotational speed considered here. From this, it is clear that the assumption that the charge moves in immiscible layers is a poor one- the turning action of the charge about its CoC, the induction of charge in the toe region, and the thickening of the rising region as the charge moves up in the mill all cause a good deal of mixing between layers.

Even obtaining the radial velocity about the CoC of the charge- as is done in Figure 7.24- does not remove all feature from its distribution for the same reasons as above, and because much of the charge in the rising region does actually move concentrically with the shell.

The last column of Figure 7.23 shows the magnitude of the tangential velocity of the charge about the centre of the mill. In these plots, it is clear that the tangential velocity of the charge about the centre of the mill is greatest in a band parallel to the line through both the CoC and the centre of the mill, and least along those parts of the equilibrium surfaces considered in Section 7.1.2 below and to the right of the CoC- those parts that do not constitute the equilibrium surface.

A similar, high tangential speed band is visible in that calculated about the CoC of the charge, as shown in the last column of Figure 7.24. Here, though, both the horizontal and the vertical equilibrium surfaces are visible in their entirety as minimum tangential velocity surfaces, and the high tangential velocity regions in the shoulder and toe regions of the charge are more visible than they were in Figure 7.23.

From the radial velocity distributions in Figures 7.23 and 7.24 we can conclude that neither the tangential velocity about the centre of the mill, nor that about the CoC capture the motion of all

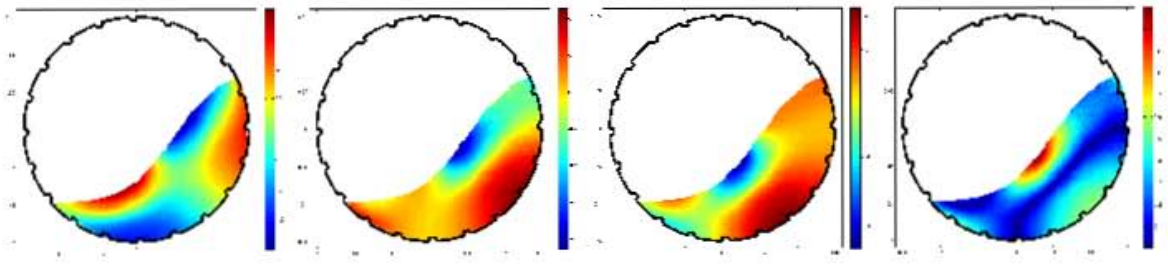

(a) $50\%v_{crit}$

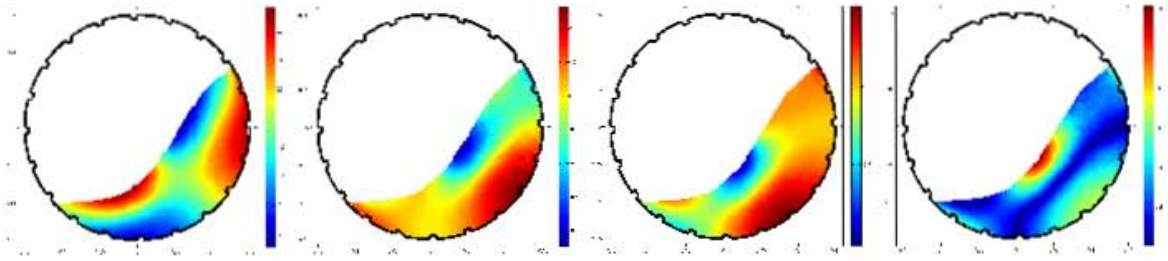

(b) $60\%v_{crit}$

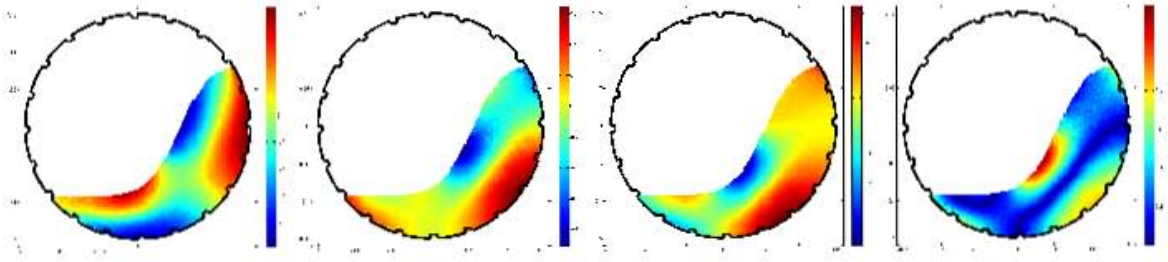

(c) $75\%v_{crit}$

Figure 7.23: The radial (left), and $\hat{x}$- (left middle) and $\hat{y}$-components (right middle) and magnitude (right) of the tangential velocity of the charge about the centre of the mill.

of the charge. However, we can say that they do a fair job in the band passing through the centre of the mill and the CoC of the charge, and to a lesser extent in the toe region. Further, we can say that the tangential velocity about the centre of the mill does a fair job for more of the band through the mill centre and the CoC of the charge than does that through the CoC. It is useful, then, to consider both of these sets of distributions, with the foregone caveats in mind.

The next step to obtaining shear rate distributions is to sample the tangential velocity distributions discussed above along radial lines passing through either the centre of the mill or the CoC of the charge as appropriate. The shear rate in each bin is then the difference between the tangential velocity in a bin and that in the adjacent bin along such a radial slice, divided by the radial separation between these two bins.

Figure 7.25 shows the shear rate distributions of the charge rotated at 50%, 60% and 75% of the critical speed of the mill. As expected, the shear rates in the charge are greatest in the band passing through both the centre of the mill and the CoC of the charge. Furthermore, as expected from Figure 7.21 and Table 7.12, the shear rates are greatest in the active region of the charge. This is particularly evident for the shear rate distributions calculated about the CoC of the charge, which capture more of the shear rates in the turning part of the charge motion.

From this consideration of shear rates, it seems that the active region has lived up to its name as the most important site for abrasion and attrition breakage- which are both linked to shear rates- and that the toe region, both above and below the equilibrium surface, is an equally important high-shear region.

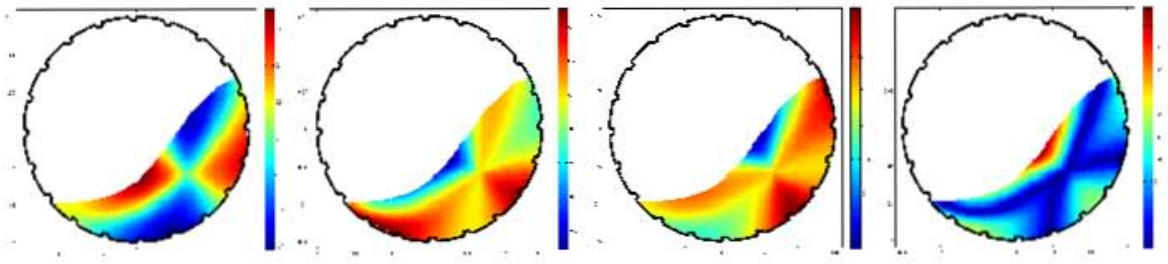

(a) $50\%v_{crit}$

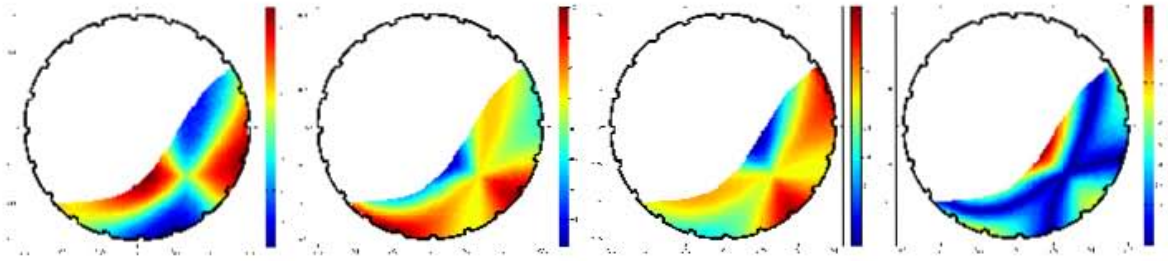

(b) $60\%v_{crit}$

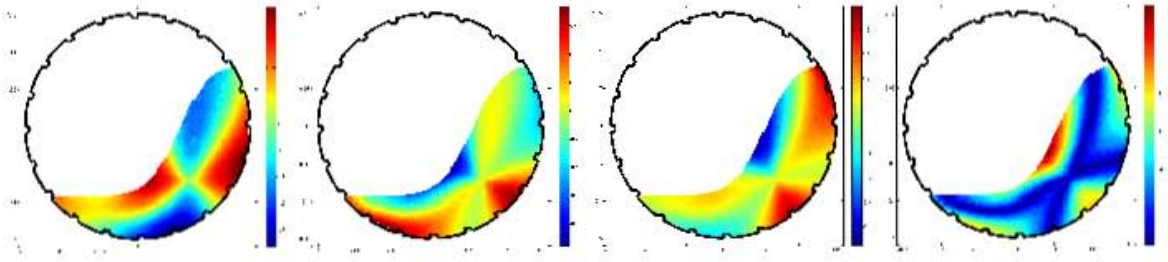

(c) $75\%v_{crit}$

Figure 7.24: The radial (left), and $\hat{x}$- (left middle) and $\hat{y}$-components (right middle) and magnitude (right) of the tangential velocity of the charge about its centre of circulation.

Since the toe region is also the impact site of charge leaving the in-flight region, this makes the toe region a doubly important breakage and grinding region.

7.4 Discussion

In this chapter I presented a more complete analysis of the data obtained from a PEPT experiment performed on a monosize charge in the 'old' $300mm$ diameter mill, rotated at three different speeds. I did this by building on the basic analysis presented in Chapter 6.

In the first part of this chapter, I demonstrated the use of charge features[29] as a means of making rigorous the trends in the shape and motion of the charge discussed qualitatively in Chapter 6, and of dividing the charge into regions of distinct charge motions.

In particular, I showed how the bulk free surface of the charge becomes more and more S-shaped at increasing mill speeds, and that as it does, its departure shoulder moves up the shell faster than its re-entry toe moves down it, causing a flattening of the charge against the mill shell. I showed that more and more charge enters the in-flight region and attains a higher head at increasing mill speeds, and that its impact toe moves along the face of the charge and begins to impact directly with the shell at the highest speeds.

I, further, showed that the equilibrium surface becomes more and more curved at increasing mill

[29] As defined in Section 5.5.3.

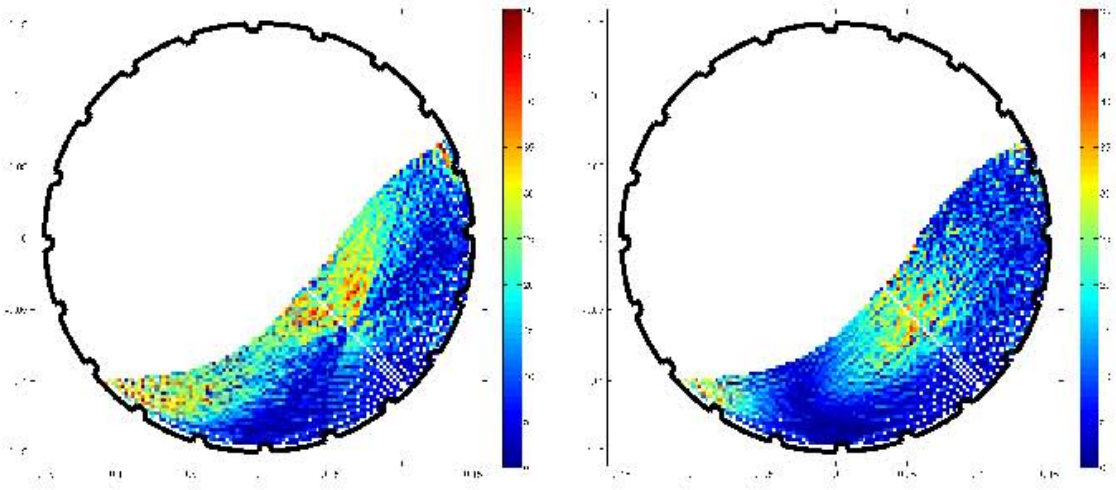

(a) $50\%v_{crit}$

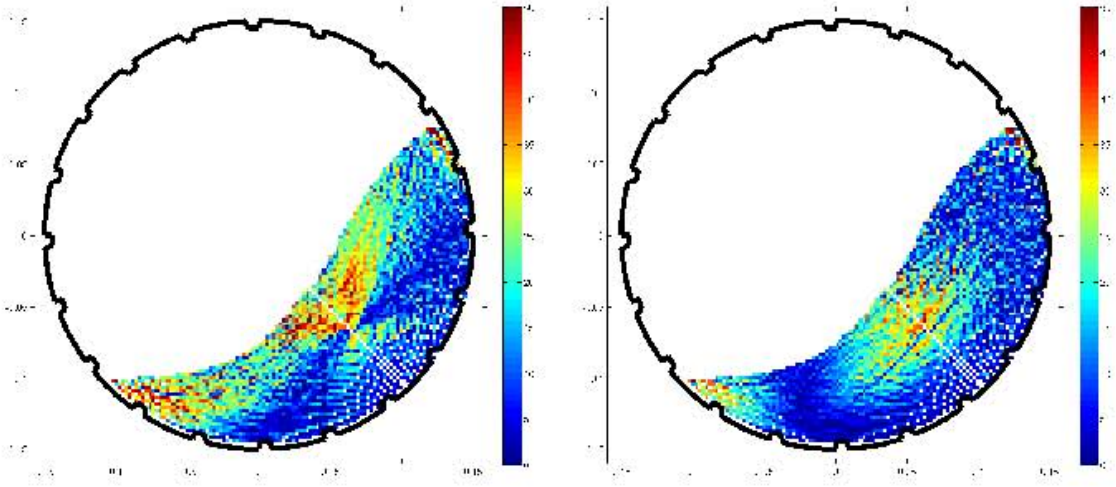

(b) $60\%v_{crit}$

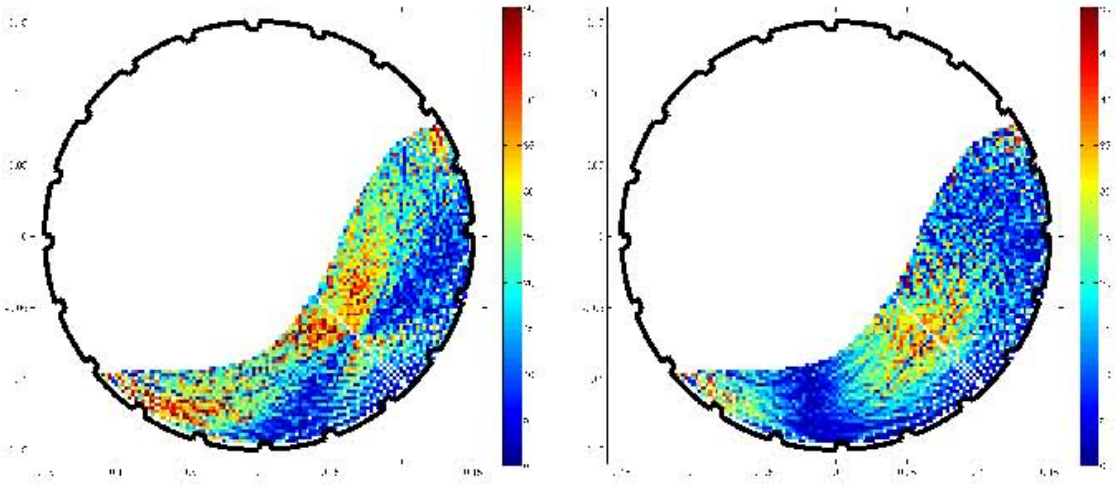

(c) $75\%v_{crit}$

Figure 7.25: Shear rate distributions calculated about the CoC (left) and centre of the mill (right).

speeds, even as the charge in the active region dilates, leading to a convergence in the thicknesses of the active and rising regions; a convergence that reverses itself at even higher speeds as the active region disappears in favour of the in-flight region.

Finally, in the first part of the chapter, I demonstrated that the CoC- since it is derived from the zero points of the velocity of the charge; from the equilibrium surfaces- is an indicator of both the position and motion of the charge, sensitive to both the rising and the flattening of the charge in the shell, but not to the increasing volume fraction of the in-flight region as is the CoM. I also used the CoC as a centre about which to calculate circulation rates, angular speeds, and so on, and used the example of power draw modelling to illustrate all of the foregone uses of charge features and regions.

In the second part of this chapter, I introduced the idea of radial bin selection for re-sampling RTDs and kinematic distributions, and for thus obtaining more quantitative measures of the trends visible in bin plots of such distributions.

I showed that radial slices of the mass, porosity or simply residence time distribution of the charge in a tumbling mill could be used to quantify the local density features in the charge- potentially a powerful tool for the investigation of segregation of the charge by size, density and so on.

I also showed that the tangential velocity distributions in the charge- at least along the radial slice through the centre of the mill and the CoC- are quadratic in shape, laying to rest the common assumption that charge in the rising region is in, or is close to, solid body motion. I discussed this finding in terms of functions fitted to radial slices of the tangential velocity through the centre of the mill and the CoC, and of their derivatives- the shear rate- and also of the shear rate distributions obtained by radial bin selection through the centre of the mill or the CoC.

I found, from these shear rate distributions that there is a band of maximum shear rate, corresponding to a band of minimum inter-layer mixing, passing through both the centre of the mill and through the CoC of the charge; another in the toe region; and that almost the whole active region is such a high-shear region irrespective of whether the charge is considered to be rotating about the centre of the mill, or its CoC.

Chapter 8

Conclusions

8.1 What has been done

8.1.1 Analysis routines

The main thrust of my work has been to develop a suite of computational routines that can be used to analyse PEPT data in general, and tumbling mill data in particular. The routines that I have produced are batched, and are called from a single driver routine that allows the user to tailor- using a system of flags, variables and settings files- the subset of analyses to be performed on a user-specified selection of experiments, and resulting in a user-specified range of outputs and stored output formats. This suite of analysis routines can be divided into the categories below.

Pre-analysis

The data produced by a PEPT camera takes the form of a series of detected events, labelled by the coordinates of the two detectors in which the end points of the line of responses (LoRs) were detected in coincidence. The location of the tracer particle at each time step is obtained from the triangulation of these LoRs, as described in Section 2.3.2.

As mentioned in Section 2.3.3, however, the triangulation procedure must be optimised for each new system under investigation. In appendix E I offer an example of such an optimisation to illustrate the extensive routines and heuristics that I have developed for this purpose. What is not mentioned elsewhere in this work is that I have also modified the triangulation program written by Prof. D.J. Parker at the University of Birmingham, to operate in batch mode, to provide the raw data for my optimisation routines in a more efficient way.

Once the raw data has been triangulated in an optimal way, it is useful to translate it into the most convenient reference frame for the geometry of the system under investigation. For tumbling mills, this is a cylindrical reference frame with a horizontal $\hat{z}$-axis. In this work, the position of the tumbling mill under investigation in the field of view of the PEPT camera is obtained from a series of location markers- tracer particles affixed at several axial points along the shell of the rotating mill. Fitting 3D circles rotated in space to the trajectories traced out by these location markers allows the position and orientation of the axis of the mill to be recovered. From this, the axis of the mill can be translated and rotated into a cylindrical reference frame along the $\hat{z}$-axis of the field of view.

For this- and future- work, I optimally triangulated and translated into the above cylindrical reference frame all of the experiments listed in appendix D.

Kinematics from trajectories

The velocity and acceleration of the tracer particle in each direction- $\hat{x}$, $\hat{y}$ and $\hat{z}$- can be calculated from the triangulated trajectory data by interpolation, as described in Section 5.2.2 and appendix G. These, and the compound kinematic data- such as angular kinematics, power draw and so on- calculated from them, can be used in the simple binning procedure to produce kinematic distributions. In appendix I, however, I show that the simple binning procedure is inferior to the residence time binning one. Since residence time binning relies on interpolation, it is computationally cheaper to calculate the kinematics at the time of binning, so the kinematics calculated as above are only used to produce variation plots as shown in Figure 6.9, for instance.

To facilitate future work, I have written out text files of all of the optimally triangulated, centred and aligned location data mentioned above, as well as the basic kinematic data mentioned here, for all of the experiments listed in appendix D.

Simple binning

In appendix I, I show that the simple binning procedure is inferior to the residence time binning one. The main use of the simply binned data has been as a standard of comparison to prove that this is the case.

Notwithstanding, I have produced 3D simply binned probability, $\hat{x}$-, $\hat{y}$- and $\hat{z}$-velocity, and $\hat{x}$-, $\hat{y}$- and $\hat{z}$-acceleration distributions, as well as distributions of their uncertainties[1], for all of the data listed in appendix D. I have done this for bin sizes of $1 \times 1 \times 1mm^3$ to $5 \times 5 \times 5mm^3$ in steps of $1mm$.

Residence time binning

I have binned the same data by the residence time binning method, producing 3D distributions of the probability, $\hat{x}$-, $\hat{y}$- and $\hat{z}$-velocity, and $\hat{x}$-, $\hat{y}$- and $\hat{z}$-acceleration distributions, as well as distributions of their uncertainties, as for the simple binning case.

In addition to these general purpose, 3D binned distributions, I have used the region selection procedures mentioned in Section 5.3.7 to exclude the end-effects introduced by the end-faces of the tumbling mills, as well as spurious outliers, and produced transaxial projections of the remaining data for both the simple and residence time binning distributions.

As well as the abovementioned distribution data saved both as text files and matrices, I have produced bin plots in a range of formats of the following transaxial distributions with the geometry of the mill superimposed upon them:

- probability distributions and their uncertainties
- mass, density, solidicity and porosity distributions and their uncertainties
- velocity distributions and their uncertainties
  - $\hat{x}$-, $\hat{y}$- and $\hat{z}$ velocities

[1] Except for the probability distribution for which no uncertainty estimate exists in the simple binning case.

  - transaxial velocity magnitudes
  - radial and tangential velocities about the centre of the mill and the CoC
  - angular velocities about the centre of the mill and the CoC
- acceleration distributions and their uncertainties
  - $\hat{x}$-, $\hat{y}$- and $\hat{z}$ accelerations
  - transaxial acceleration magnitudes
  - radial and tangential accelerations about the centre of the mill and the CoC
  - angular accelerations about the centre of the mill and the CoC
- power draw distributions[2] and their uncertainties
- shear rate distributions

Residence time versus simple binning

In appendix I, I compare the results obtained from the simple and residence time binning of artificial and real trajectory data.

I show that residence time binning reproduces well-known artificial data much more precisely and accurately than does simple binning, but that the performance of simple binning can be greatly improved by interpolating and re-sampling the trajectory of the tracer particle- albeit at a significant computational cost.

I investigate, though, the interpolating halo effect introduced into a residence time binned distribution, which is the cost of its ability to smooth out added Gaussian noise and to 'fill in' infrequently sampled trajectories. I show, though, that this effect is not significant at the sampling frequencies and noise-level typical of real PEPT data.

Using real data, I show that the simple binning method suffers terribly from the non-spatially uniform trajectory sampling that occurs in real data because of the inhomogeneous attenuating environment of the tumbling mill system, but that this effect can be drastically limited by interpolation and re-sampling at almost any sampling frequency.

Finally, using both real and artificial data, I show that while the simple binning method is highly sensitive to bin resolution, the residence time binning method is only sensitive to resolutions greater than $3 \times 3 \times 3mm^3$ below a far from realistic sampling frequency. Despite the extremely low sampling frequency at which residence time binning is susceptible to resolution effects, I still settle on an optimal bin resolution of $3 \times 3 \times 3mm^3$, for the sake of caution.

Charge features and regions

In Sections 5.5.2 and 5.5.3 I built on Powell and McBride's definitions of charge features, given in appendix A, and the detailed kinematic data available from a PEPT experiment to define my the charge features and regions in a tumbling mill. They are summarised in Figure 8.1.

Of these, the most important to mention here are the bulk and charge free surfaces, which allow the charge to be divided into the bulk and disperse regions and the in-flight and empty regions respectively; the equilibrium surface, which divides the bulk into the rising and active region; and the CoC of the charge.

[2]Based on the models given in Sections 3.3.5 and 5.5.4.

I have motivated the CoC as- by virtue of the way it is calculated[3]- a single-point measure of both the position and motion of the charge, as a privileged point- by virtue of the fact that the charge circulates about it and so mass must be conserved along any line passing through it- through which to sample data, and as a centre about which to calculate angular measures such as angular velocity and acceleration, shear rate, and the circulation rate of the charge[4].

Radial bin sampling

In Section 5.4.4 I describe my procedure for selecting radial slices through the 2D distributions of data. This allows local variations in the probability and kinematic distributions to be made rigorous.

I have used radial bin sampling to produce polar bin plots of the sort described in Section 5.4.3, and used these to produce convex shapes for the edge detection of the bulk and charge free surfaces, as well as of the boundaries of the cascading and cataracting charge in the in-flight region[5].

I have also used radial bin sampling to provide radial lines along which to calculate shear rates and shear rate distributions as described in Sections 5.5.6 and 7.3.4.

A quick summary

In summary, I have produced the following routines that are generally applicable to PEPT data, and are thus available for future work on any system:

- a procedure and set of heuristics for optimising the triangulation of PEPT data,
- a new binning algorithm- the residence time binning procedure- and proof of its superiority over the old one,
- a set of routines for the selection of regions of interest- or exclusion of unwanted regions- from binned data in 3D space, and for the centring and aligning of such data based on know circles, planes or cubes,
- a set of routines for the re-sampling and binning of such 3D distributions in polar, and cylindrical reference frames,
- a procedure for calculating angular velocity and acceleration distributions about an arbitrary line- given by two points- or point in space,
- a set of routines for the sectioning and projection of 3D distributions into an arbitrary plane defined by its normal, and
- extensive plotting and visualisation routines.

In addition, I have, from the data listed in appendix D, produced the following

- a set of text files containing triangulated and pre-processed trajectory, velocity and acceleration for all of the tumbling mill PEPT experiments performed at the University of Birmingham from 2005 - 2010,
- a complete set of all of the mentioned tumbling mill data binned at a range of binning resolutions in 3D space,
- transaxial projections of all of this data,

[3]See Section 5.5.3.
[4]See Section 5.5.5.
[5]See Section 5.5.2.

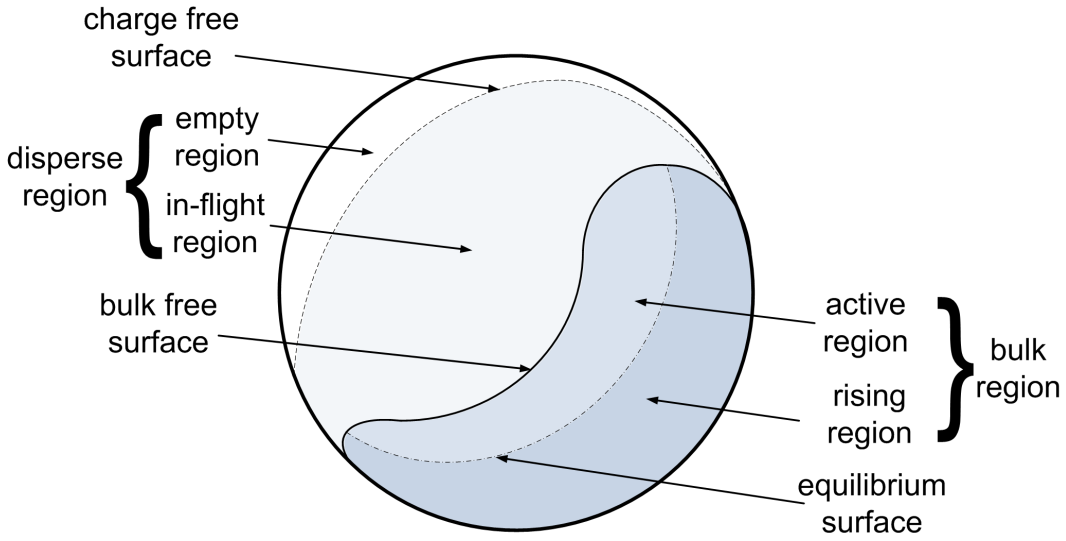

(a) Charge regions.

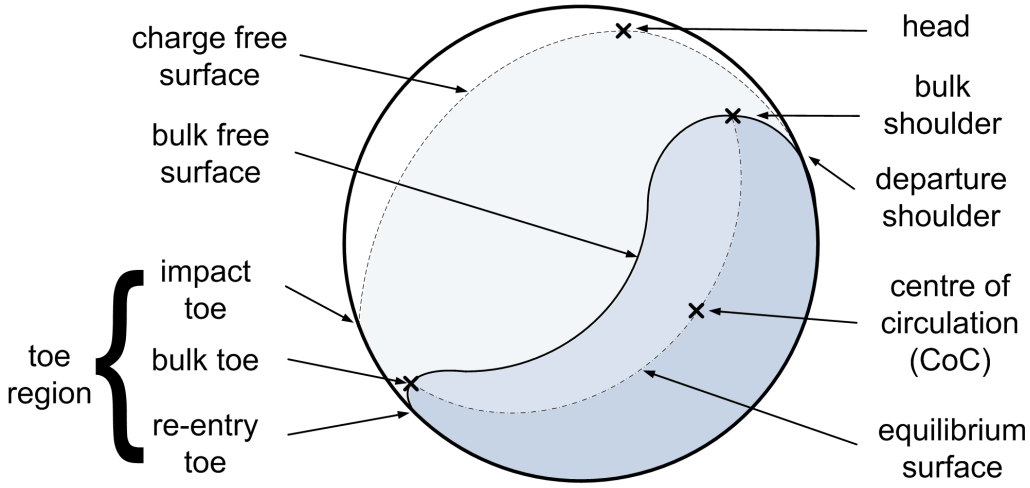

(b) Charge features.

Figure 8.1: Schematics of the transverse section of a tumbling mill showing the regions (top) and features (bottom) of the charge in motion

- radial slices of all of this data, and
- various plots of the data as mentioned above,

all of which will simplify and expedite future work on this data.

8.1.2 Results

In order to demonstrate the use of the analysis routines mentioned in the last section, I performed a 'basic' and then a 'more complete' analysis on only 4 of the hundreds of experiments listed in appendix D- those performed on a monosize distribution of glass beads in the 'old' $300mm$ diameter mill. I summarise the results of these analyses here.

Anatomy of a tumbling mill

Figure 8.1a shows a schematic of a typical charge divided into regions of distinct motion.

The first, and most obvious division of the charge is into the bulk and disperse regions by the bulk free surface, as described in Section 5.5.2 and demonstrated in Section 7.1.1. This bulk free surface is easily identifiable by eye in plots such as those shown in Figure 8.2a, but are obtained in practice by edge-detection applied to polar bin plots of the same data, as described in Section 5.5.2.

The region above the bulk free surface is the disperse region. The disperse region, in turn, is divided into two regions- the empty and in-flight regions- by the charge free surface, which is also obtained by edge-detection of a polar bin plot. The empty region is, of course, the least interesting region of the mill- it is the region of the mill into which charge never enters. However, the highest point of the charge free surface is the head of the charge, which is related to the maximum amount of energy available for impact breakage, and the intersection between the charge free surface and the mill shell is the impact toe.

The position of the impact toe is of interest because it is below the charge- that is, if the in-flight charge lands on the face of the bulk charge- this affects the behaviour of the charge in the bulk region, and if it is above the charge, it has an affect on the wear of the mill liner.

The in-flight region can be divided into two further regions or streams- the cascading and the cataracting charge. The cataracting charge is the more dilute and dispersed part of the in-flight charge, consisting of material in almost free fall. The cascading charge is slightly more dense, and forms more of a narrow stream than does the cataracting charge. The distinction between these two streams is only just visible in the RTDs shown in Figure 8.2a.

The uncertainty in the RTD in a particular bin is a measure of the spread of transit times of the tracer particle through that bin. A high uncertainty could be due to a number of factors, as described in Section 6.1.4, one of which is that it is a more dilute charge region. This is because densely-packed charge has fewer degrees of freedom than does more dilute charge. The uncertainty in the RTD is thus a complimentary measure of density.

Figure 8.2b shows the uncertainties in the RTDs shown in Figure 8.2a, with a ceiling such that the cascading stream is clearly visible. The cascading region is commonly considered to be a boundary layer that develops above the surface of the bulk of the charge, somewhat like a highly-fluidised and spread-out transition layer. Figure 8.2b demonstrates that this is not the case, and that the cascading charge is best considered to be a stream within the cataracting charge that makes up the rest of the in-flight region.

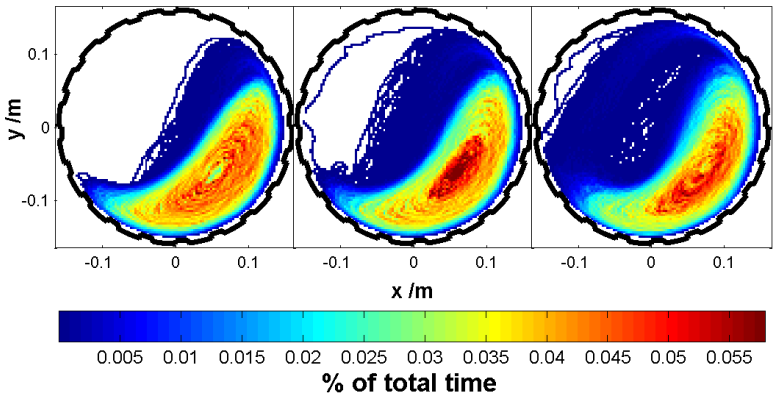

(a) RTDs

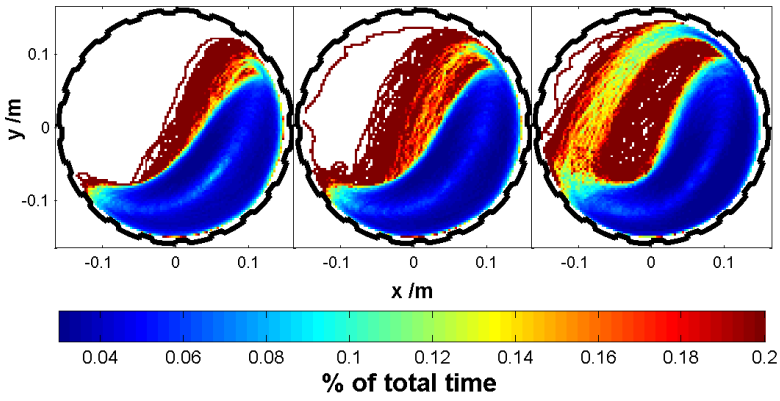

(b) Uncertainty in the RTDs

Figure 8.2: The residence time distributions (top) and their uncertainties (bottom) of a $5mm$ tracer particle in the 'old' $300mm$ mill filled to 31.25% and rotated at 50% (left), 60% (middle) and 75% (right) of its critical speed.

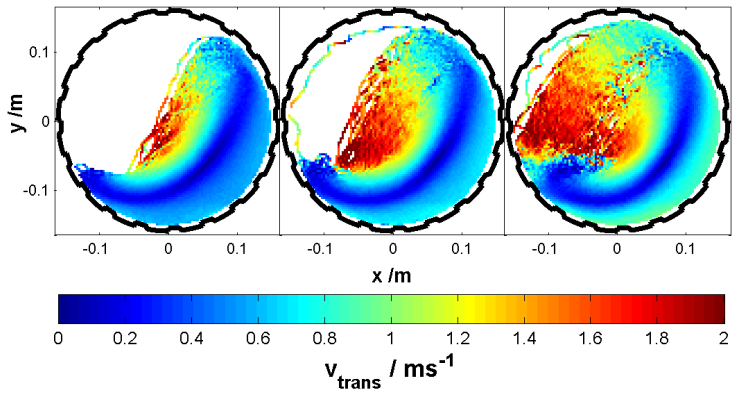

Figure 8.3: Time-weighted transverse velocity distributions of a $5mm$ tracer particle in the 'old' $300mm$ mill filled to 31.25% and rotated at 50% (left), 60% (middle) and 75% (right) of its critical speed.

Figure 8.3 shows the transverse velocity magnitude distributions of the same experiments as shown in Figure 8.2. In this figure, particularly at high mill speeds, the cascading stream is (barely) visible

as a slightly faster streak in the in-flight region, as is its effect on the motion of the charge in the bulk region.

The region below the bulk free surface is the bulk region. It consists of more densely-packed charge[6] moving in a more constrained manner than does the charge in the in-flight region. For this reason, it appears as a larger probability region in the RTD, and as a smaller fluctuation region in the distribution of the uncertainties in the RTD. The two exceptions to this latter observation are along the equilibrium surface where the charge motion has a large curvature, and in the toe region where it's behaviour is chaotic[7].

The bulk region of the charge can be further subdivided into two regions- the rising and active- or falling- regions. As their names suggest, these regions consist of charge moving up and with the mill, and down along the charge, respectively. Thus, by continuity, they must be divided by a surface of zero transverse velocity- the equilibrium surface, as defined in Section 5.5.2 and obtained in Section 7.1.1.

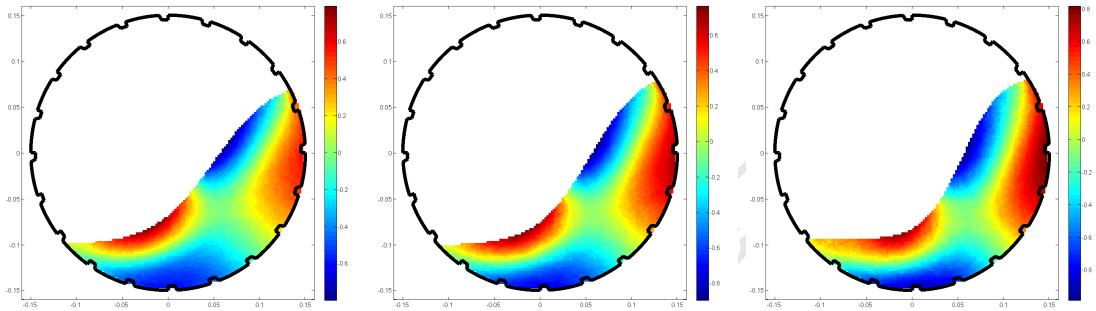

Figure 8.4: Radial velocity distributions of a $5mm$ tracer particle about the centre of the 'old' $300mm$ mill filled to 31.25% and rotated at 50% (left), 60% (middle) and 75% (right) of its critical speed.

The rising region of the charge is often assumed to be in solid body rotational motion about the centre of the mill. In fact, it is not even in solid body motion about the CoC of the charge[8], as illustrated in Figure 8.4, which shows radial velocity distributions in the charge. In this figure, though, are visible bands of low radial velocity around the line passing through the centre of the mill and through the CoC- that region in which the tangential velocity about the CoC roughly conforms to that about the centre of the mill- in which the assumption is less invalid. This solid body-like motion assumption is also lent credence by the wedge of centripetal acceleration in this region, as shown in Figure 8.5.

However, despite these observations, radial samples of the tangential velocity along a line through both the centre of the mill and the CoC of the charge clearly show that there is significant slippage between the layers of the charge in this area, particularly in the rising region. This is illustrated in Figure 8.6, and discussed in Section 7.3.2.

That part of the bulk region above the equilibrium surface- the active region- is so-called because it has been assumed to be the region of highest shear in the charge, and thus an important site of abrasion and attrition breakage. Figure 8.7 shows that this is true for the shear rate calculated both about the CoC of the charge, and the centre of the mill. Figure 8.3 also shows that it contains the region of highest transverse velocity approaching the transition layer and bulk free surface of the charge.

Thus to summarise, I have shown here and in Chapters 6 and 7 that the charge can be divided

[6] Between 70% and 90% of the maximum packing density of spheres- $\frac{\pi}{\sqrt{18}}$.
[7] See Section 6.1.4.
[8] See Section 7.3.4.

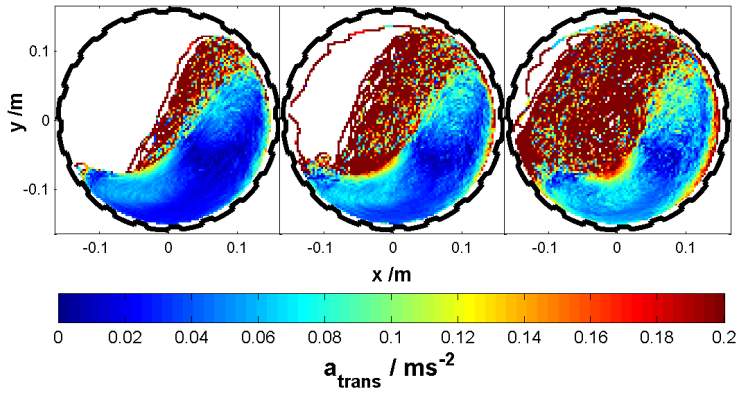

Figure 8.5: The time-weighted transverse acceleration distributions of a $5mm$ tracer particle in the 'old' $300mm$ mill filled to 31.25% and rotated at 50% (left), 60% (middle) and 75% (right) of its critical speed.

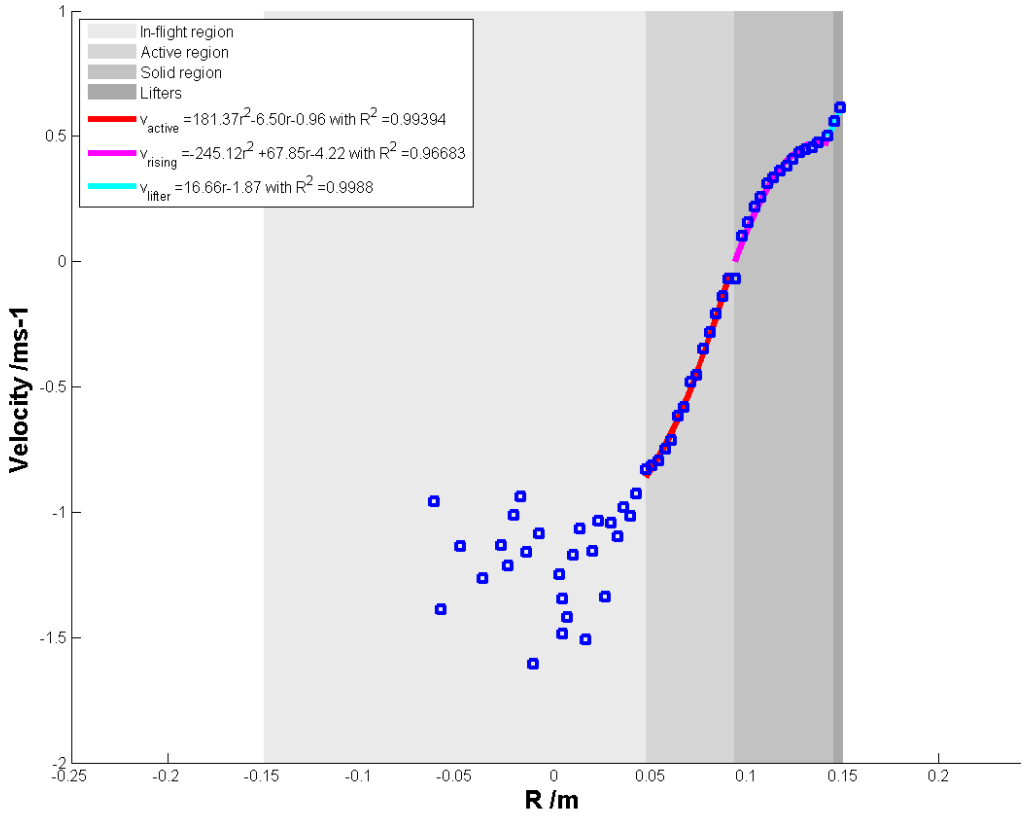

Figure 8.6: A radial sample through the CoC of the tangential velocity distribution of a $5mm$ tracer particle in the 'old' $300mm$ mill filled to 31.25% and rotated at 60% of its critical speed.

into three important regions- the rising, active and in-flight regions, that the cascading layer in the in-flight region is more of a stream, that the active region- sometimes called the solid region- does not undergo solid body rotation, and that the active region is, indeed, the site of the highest shear rates in the bulk charge.

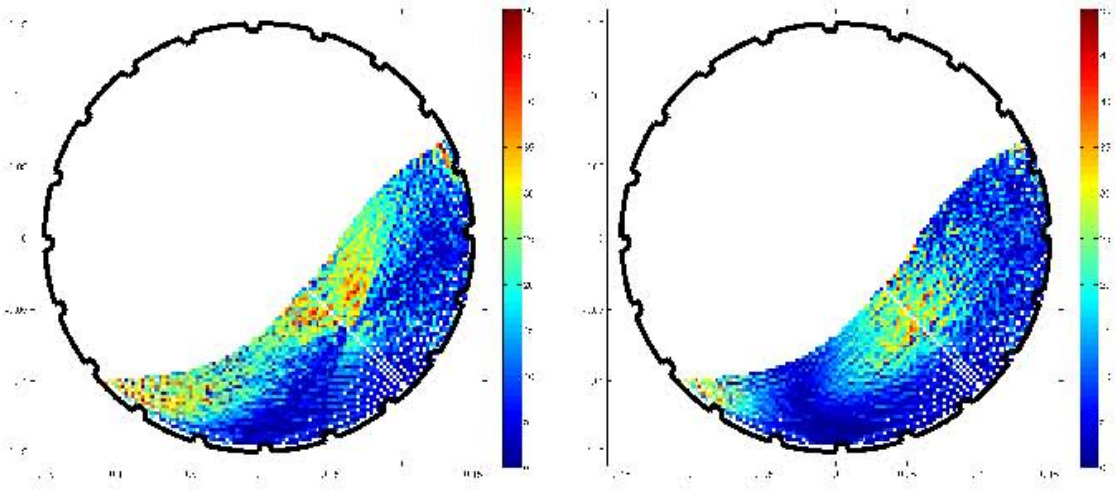

(a) $50\%v_{crit}$

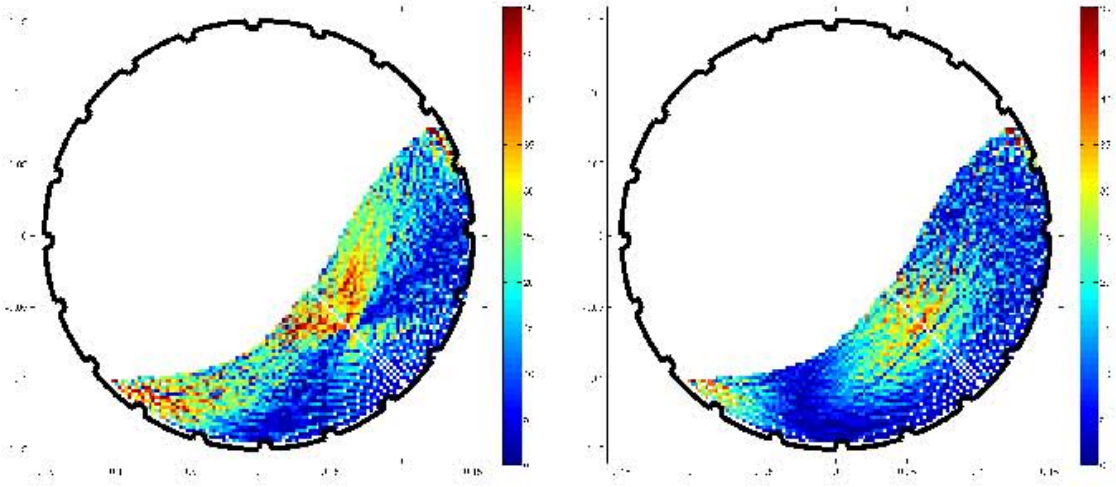

(b) $60\%v_{crit}$

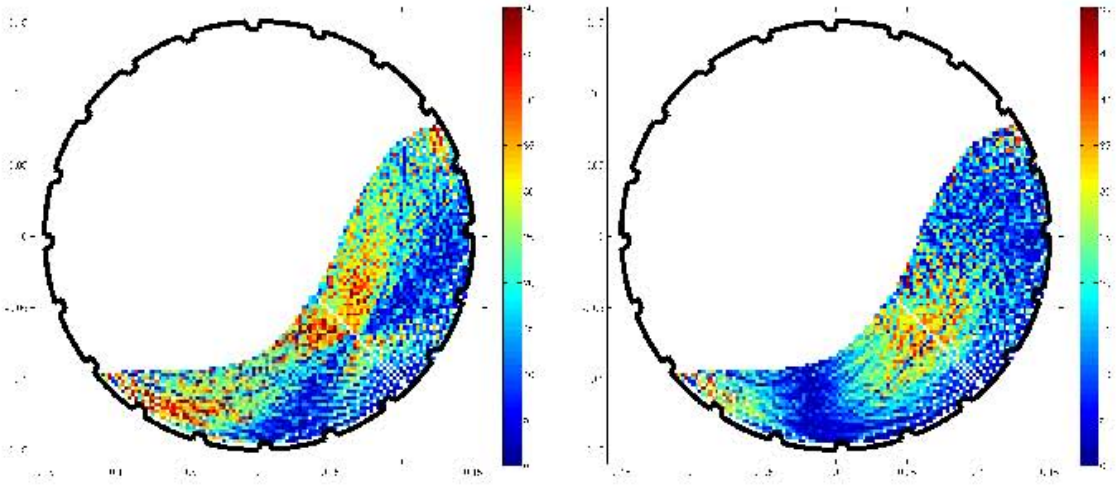

(c) $75\%v_{crit}$

Figure 8.7: Shear rate distributions calculated about the CoC (left) and centre of the mill (right).

The evolution of motion in a tumbling mill with mill speed

The experiments I analysed in Chapters 6 and 7 cover a very narrow range of mill speeds- 50% to 75%- chosen because they span the range of speeds typical in the mining industry[9]. These mill

[9]Although starting at an unusually-low 50%.

speeds are those at which the charge is in cascading or the low end of the cataracting motion; too high for rolling motion, and too low for centrifuging motion[10].

Section 8.2.1 contains a brief look at a more complete speed range. However, even from the limited experiments considered in Chapters 6 and 7, some regularities can be discerned.

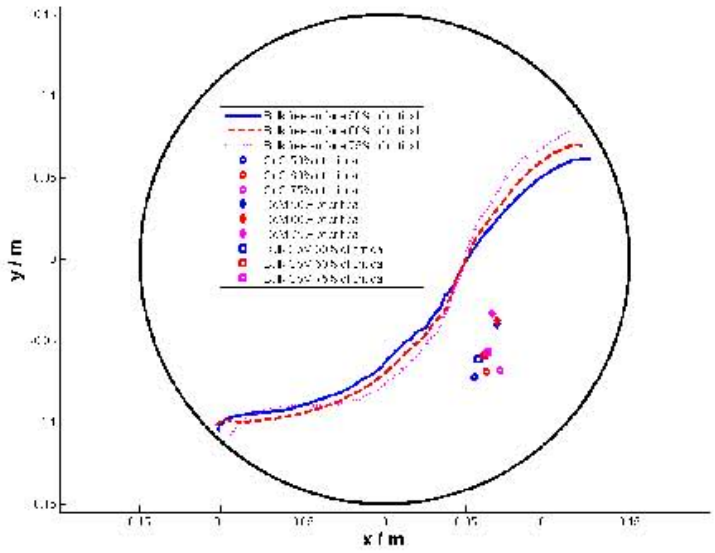

Figure 8.8: A summary of the features of a charge of $5mm$ tracer particles in the 'old' $300mm$ mill filled to 31.25% and rotated at 50%, 60% and 75% of its critical speed.

Figure 8.8 shows a summary of the charge features in the 'old' $300mm$ mill rotated at three mill speeds, as discussed in detail in Chapter 7.

The most important trends visible in this plot are that the bulk and departure shoulders of the charge move up in the mill shell at increasing speed; that its bulk and re-entry toes, in compensation, move down less quickly, leading to a flattening of the bulk charge against the mill shell; that this flattening disproportionately affects the rising region- a fact captured most sensitively in the movement of the CoC towards the shell at increasing speed; and that its bulk free surface becomes more and more S-shaped at increasing speed.

What is not visible in this plot, but is discussed in Chapter 7, is that at higher mill speeds more and more charge enters the in-flight region, attaining a higher and higher head, and reducing the extent of the empty region. Also at higher mill speeds, the effective circulation rate of the charge decreases, as it tends towards the circulation rate of the mill shell when the charge begins centrifuging; but that the range of circulation rates within the charge increases as more and more charge enters larger diameter, in-flight trajectories. Most importantly for the grinding efficacy of the mill, as the mill speed increases, a cascading stream of charge develops, whose impact toe moves further and further down the face of the charge at increasing mill speed.

Grinding regions

The combination of the increasing head and impact toe of the in-flight charge, and particularly those of the more dense cascading stream, increases the energy available for impact breakage- increasing both the likelihood[11] and efficacy of impact breakage at each interaction. Compounding

[10] Because of the lifters in the laboratory-scale mills used in this work, neither slipping, slumping nor surging motion is possible in these mills at any rotational speed.

[11] Given the threshold specific energy necessary for compressive breakage to occur.

this trend is the increasing mean circulation rate of the charge, which increases the frequency of candidate collisions for impact breakage.

Increasing the mill speed, however, does not improve the chances of impact breakage indefinitely. The specific energy available in a collision between a particle from the in-flight region and one in the bed depends on the initial speed with which the first particle entered the in-flight region[12], and the distance it falls before coming into contact with the bed. This falling distance initially increases as the increase in head is matched with a lower impact point as the impact toe moves down the face of the charge. Once the impact toe moves beyond the toe region, however, it begins to move up the side of the shell, both reducing the falling distance and contributing to the undesirable wear of lifters and liners[13]. Thus there exists an optimal speed for impact breakage.

Figure 8.7 shows shear rate distributions in the bulk region of the charge at increasing mill speed, normalised to the same maximum shear rate. From these plots, it is clear that the highest shear rates occur in the active region of the charge, and that they increase with increasing mill speed. However, as the speed of the mill increases, the volume density of the active region decreases[14], reducing the surface area of contact between shearing layers. The exact relationship between the density of a granular material, the shear rates within it, and the amount of abrasion and attrition grinding that occurs is not known precisely. It seems reasonable, however, to posit that grinding efficiency decreases with density at a constant shear rate. Assuming that this is the case, there exists a mill speed at which the tension between high shear rates and dilated charge results in optimal abrasion and attrition grinding.

8.2 What remains to be done

8.2.1 With existing data

Appendix D contains a list of all of the PEPT experiments performed on laboratory-scale tumbling mill by the UCT Centre for Minerals Research (CMR) from 2006 to 2009. They consist of experiments performed on three different mills, of two different diameters; filled with glass, plastic and bluestone charges of a range of volumes; with and without an interstitial fluid of various viscosities; and rotated at a range of speeds. I summarise all of these variables in Section 4.4.

In this work, for simplicity and because of time constraints, I have limited my analysis to a dry, monosize charge of a single volume in just one of the mills, rotated at a narrow range of speeds. This leaves a lot of scope for future work on this data. I will mention just some future opportunities that I would have liked to explore here, but haven't been able to.

Multi-component experiments

In fact, in this work I have analysed all of the monosize distribution experiments conducted by the CMR at the University of Birmingham. *All* of the remaining experiments were performed on polydisperse charges, and some of those performed on the $140mm$ diameter mill are not only bidisperse, but consist of materials with significantly different densities and material properties.

It would be of interest to investigate the effect of different material properties on the shape and motion of the charge in a tumbling mill- perhaps, though, a research program best undertaken in

[12] Of course higher at higher mill speeds.

[13] Not only are lifters and liners expensive to replace, but once the impact toe is on the shell, each collision involves only one-rather than two or more- particles, further reducing grinding efficacy.

[14] See Section 7.1.3.

computational space using DEM, and validated with the experiments mentioned here.

Of particular interest would be to compare the shape and motion of real, bluestone charge to that of the discrete Rosin-Rammler distribution of glass beads that we have, since 2007, used to approximate it. A challenge to be overcome in deciding on how well the glass beads approximate the real charge is the fact that only a selection of real charge particles were tracked; certainly not enough to be representative of the complex shapes, sizes and, potentially, densities that constitute this real charge. Notwithstanding, it would be of interest to compare the shape of the bulk free surfaces, positions of the CoCs, and shear rate distributions of the real and approximate charges- perhaps by comparing the mean and geometric mean-sized particles of each charge.

An interpretation of the results of this comparison would have to take into account the effects of material properties and density distributions obtained from the $140mm$ diameter mill and suggested DEM experiments mentioned above. DEM experiments could also be used to isolate the effects of particle shape on the motion of the charge.

Performing a detailed comparison of these sets of experiments would go some way to improving the predictive power and industrial acceptance of the results obtained in the rest of this extensive data set.

Segregation

An important emergent property of granular flows is its segregation behaviour. Granular material is known to segregate by size, density and shape- sometimes interpreted in terms of effective surface friction- and tumbling mills are certainly not immune to this phenomena.

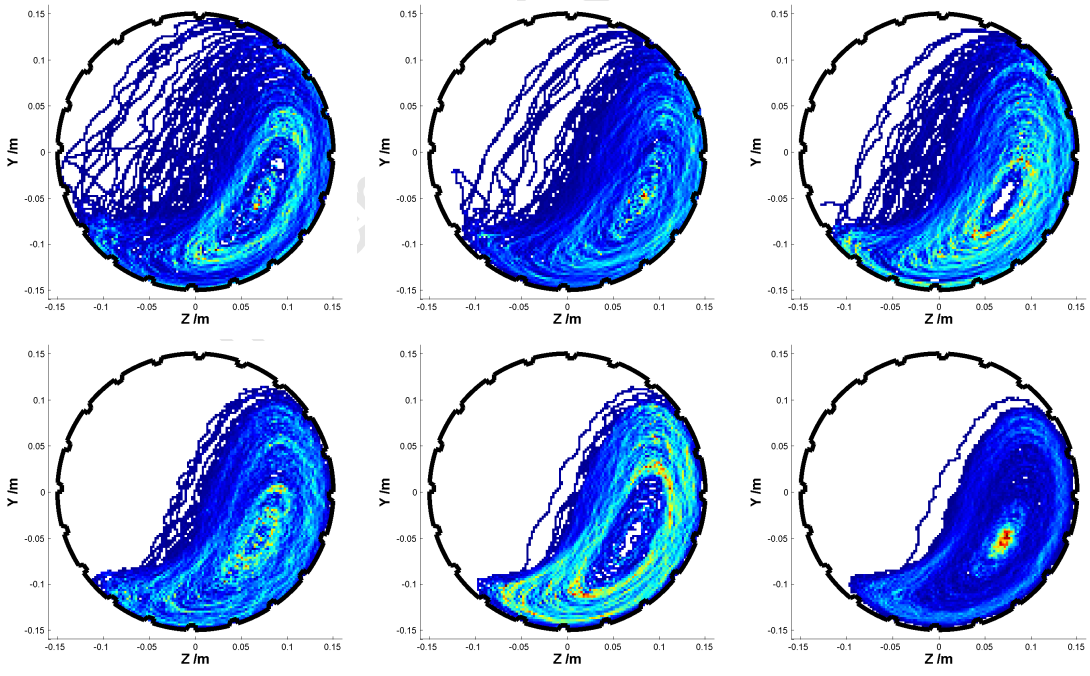

Figure 8.9: Residence time distributions of a tracer particle from each of the constituent size classes of a polydisperse charge filling the 'old' $300mm$ mill to 37.25% of its volume, and rotated at 75% of the critical speed of the mill. The charge consists of a discrete Rosin-Rammler distribution of glass beads of sizes $2mm$, $3mm$ and $4mm$ (top, l-r), and $5mm$, $6mm$ and $8mm$ (bottom, l-r).

Figure 8.9 shows the RTDs of the tracer particles representing the six different size classes used to approximate the discrete Rosin-Rammler size distribution described in Section 4.3.2. This figure shows a clear density maximum in the region around the CoC for the largest size particles, and a

more or less dilute region there for the other sizes. The banded structure of these RTDs are a clear sign that segregation by size is occurring here. This effect could be quantified using the radial bin selection technique described in Section 5.5.6 and demonstrated in Section 7.3.2.

Section 7.3.2, however, also shows some feature in the RTDs of even the monosize distribution considered there. Some thought will have to be applied in separating the self-organising effects that rely on size (or density, or shape) differences, and those that don't.

Combining multi-component experiments

The PEPT technique relies on the ergodic assumption treated in Section 5.3.1. Employing this assumption, allows us to interpret the time-averaged behaviour of a tracer particle as the ensemble-average behaviour of all of the particles in the bulk that it represents. In a system which contains particles of various sizes, densities and shapes, the ergodic assumption allows us to track a representative of each class of particle separately and to re-combine such experiments *a posteriori* to recover the ensemble behaviour of the bulk. There are at least two ways that these sub-experiments can be recombined to yield the over-all flow field of the bulk- equally or proportionally.

Treating each sub-experiment equally is the simplest approach to recombination. It consists of normalising each sub-experiment to the time over which it was run- so that the RTD sums to unity- and then simply averaging them. This might seem reasonable when the bulk consists of equal proportions, by mass or volume, of its constituents, but less so when this is not the case. Even when this is the case, it may not be meaningful to average RTDs, and this averaging procedure may only be acceptable for calculating mass, porosity or density distributions- distributions which take into account the physical differences between the tracer particles.

As an aside, I already use simple averaging to combine sub-experiments performed with the same tracer particle or with a tracer particle from the same class, and to combine sub-experiments created by the tracer particle going out of the field of view of the PEPT camera during a single run.

Weighting each sub-experiment according to the proportion of the bulk made up by the class represented by its tracer particle, is certainly easier to defend. Even in this case, however, it may not be meaningful to calculate the weighted average of RTDs. It seems likely to me, that the RTD can only be interpreted meaningfully as a probability distribution when considering the tracer particle from which it was calculated and that, in a multi-component experiment, the RTD can only be used as a step towards a combined distribution, not as a constituent of one.

If we accept the necessity of combining experiments by weighted averaging, the question still remains of how to calculate the proportional contribution from each class. For mass and solidicity distributions, it might be obvious to use the proportion by mass or volume, but which to use for calculating velocity distributions? Might the RTD make a comeback in this case as the probabilty that a particle of a particular class would be in a given voxel and travelling with a particular velocity?

Testing the first hypothesis- that the mass and solidicity distributions must be calculated proportionally by mass and volume- is easily done. If the solidicity distributions thus calculated are unphysical- greater than a polydisperse tight-packing, for instance- this method can be excluded for solidicity. If the total mass calculated from the distribution is greater than the measured mass in the mill, it can be excluded for the mass distribution. Of course, that they are consistent won't mean that they are necessarily correct. In that case, how much an effect does equal versus mass-weighting versus some other weighting affect the result?

Settling on a meaningful way to combine kinematics would be less straightforward for lack of an independent comparison. In such a case, we may have to retreat to considering power draw, already shown in this work to be a poor test of veracity because of the dissipated energy not captured by a PEPT calculation.

Deciding this last question may come down to a combination of artificial data and information gained using an independent method such as PIV, laser Doppler interferometry and so on.

The effect of interstitial fluids

A number of the experiments listed in appendix D contain not only a charge of rock or glass beads, but also an interstitial fluid- either water or a platinum slurry of a range of viscosities.

Some work has been done by the CMR to quantify the effect of slurry rheology on the shear rate in the charge along the line through both the centre of the mill and the CoC of the charge. Using the shear rate routine described in Section 5.5.6 and demonstrated in Section 7.3.4, this analysis could be taken much further.

No work has yet been done on the effect of interstitial fluid on the shape of the bulk free surface, or on other indicators of the type of mode of bed motion occurring in the mill[15]. This could easily be done using the routines developed in this work.

Internal structure of the mill

Another important driver of charge motion in a tumbling mill is the internal structure of the mill, including its inlet and outlet, and lifter and liner arrangements.

All of the experiments listed in appendix D were performed on conditioned charge, which does not undergo breakage. Thus there was no reason to remove or replenish charge, and the mills were operated in batch mode. In the wet and slurry experiments, however, fluid was introduced into and discharged from the mill through a grate[16]. The effect of flow rates and of the open area of the discharge grate could be investigated using this data[17].

The laboratory-scale tumbling mills used in this work were fitted with interchangeable lifter bars of varying height and face angle[18]. Although a CMR project to investigate the effect of lifters on charge motion is already underway using data obtained at PEPT Cape Town[19], I believe that the routines presented in this work could be used on the data listed in appendix D, as well as on the newly-collected data, to make this analysis more quantitative.

A larger range of mill speeds and fills

In Chapters 6 and 7, I demonstrated the analysis routines that I wrote for this work using experiments representing a very narrow range of mill speeds, and only one filling. The summaries of experiments conducted given in Section 4.4, however, demonstrate that this is only a very small part of the data that I have analysed- there is enormous scope for more detailed questions to be asked of this data.

[15] See Section 3.2.3.
[16] See Section 1.
[17] A project is already underway through the CMR to investigate slurry flow through a tumbling mill both mathematically and using computational fluid dynamics (CFD).
[18] See Section 1.
[19] `www.pept.uct.ac.za`

Figure 8.10 shows a 31.25% by volume, multi-component glass bead charge rotated at a range of speeds from 60% to 90% of the critical speed of the mill. At this wider range of speeds, the increasing S-shape of the bulk free surface is more pronounced than it was for the monosized charge, even achieving the hollowing out of the active region described in Section 3.2.3.

Also evident from this figure is the fact that different sized particles can move in different modes *in the same bulk*. In particular, even at the highest mill speeds, the largest- and thus heaviest-particles are still in cascading motion, while the smallest particles are in extreme cataracting motion and have even begun centrifuging.

Figure 8.11 shows a range of multi-component, glass bead charges, between 12.5% and 37.5% by volume of the mill, rotated at 70% of the critical speed of the mill. From this figure, it seems that increasing the mill load retards the development of more aggressive charge motions- the $2mm$ bead in the 12.5% load, for instance, is in advanced cataracting motion, whereas that in the 37.5% load is still in rolling motion.

These observations could be made rigorous with the bulk free and equilibrium surface routines I describe in Section 5.5.2, and with the charge region routines I demonstrate in Section 7.1.3.

Both Figures 8.10 and 8.11 suggest that the phenomenon of size segregation is influenced by the rolling mode of the charge, which is in turn influenced by the load and rotational speed of the mill. This insight could be interrogated using the radial bin selection routines I describe in Section 5.4.4.

Finally, since it appears that material of different sizes are segregated into different regions according to the load and rotational speed of the mill, it would be interesting to correlate these with high shear regions in the charge as a means of ensuring that large particles- those which benefit most from impact breakage- are segregated into the outer part of the charge, and smaller particles- those more resistant to impact breakage and susceptible to abrasion and attrition- are segregated into the high shear region around the CoC of the charge.

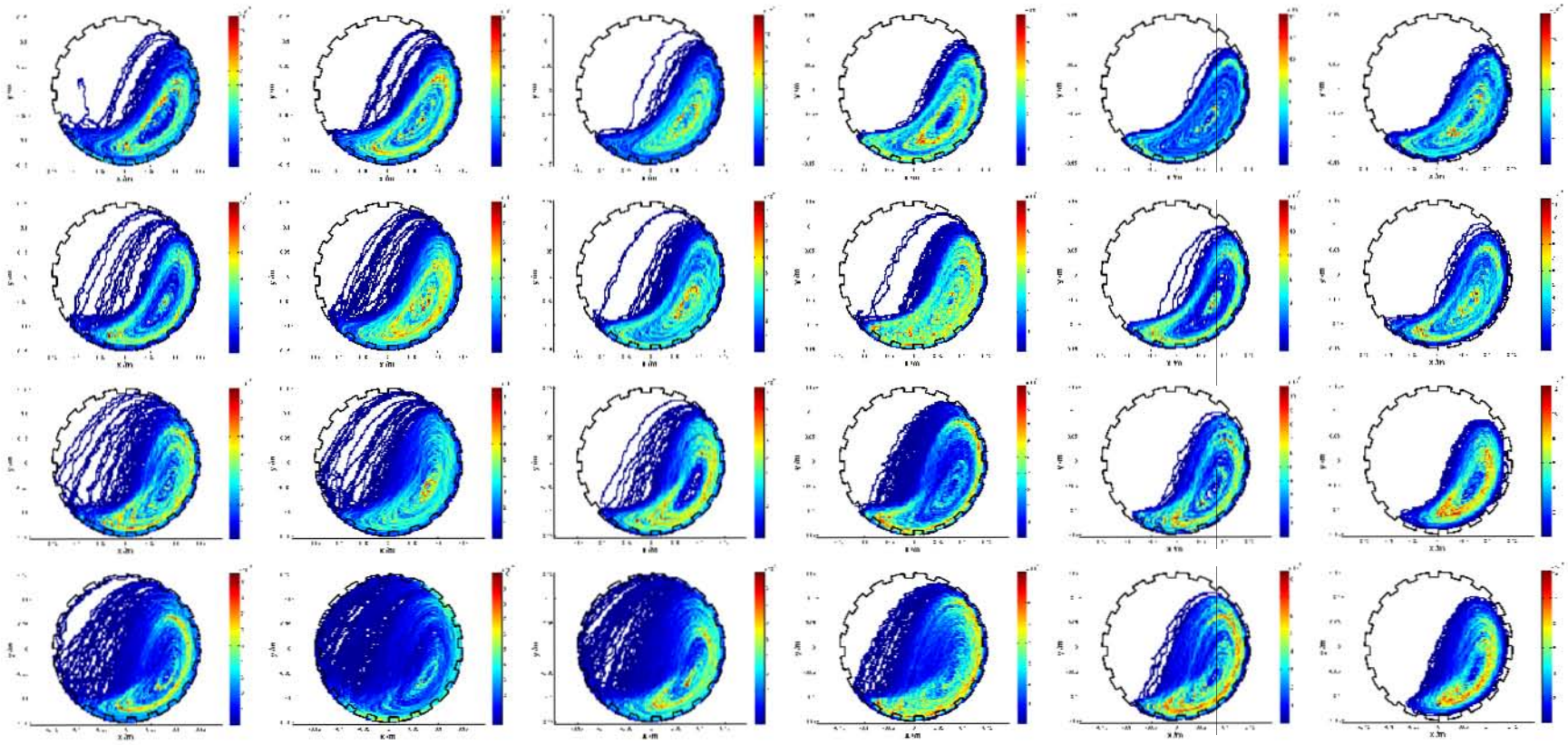

Figure 8.10: Residence time distributions of tracer particles representing each of the size classes (increasing in size from left to right) in a 31.25% load rotated at 60%, 70%, 80% and 90% of the critical speed of the mill (top to bottom).

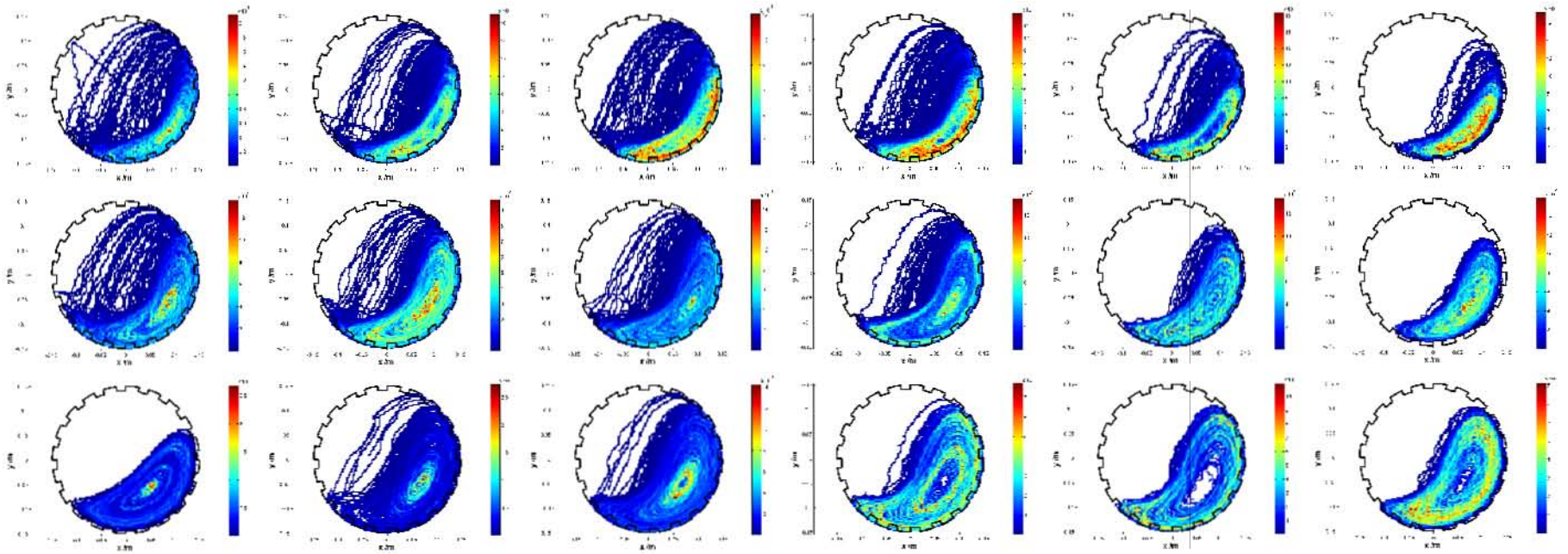

Figure 8.11: Residence time distributions of tracer particles representing each of the size classes (increasing in size from left to right) in a mill rotated at 70% of its critical speed and filled to 12.5%, 25%, and 37.5% of its volume (top to bottom).

Scale-up

The experiments listed in appendix D were performed on three different laboratory-scale tumbling mills, of two different diameters. In all cases, attempts were made to non-dimensionalise the operating parameters- the loads were described in terms of a fraction of the mill volume, and the mills' rotational speed in terms of its critical speed[20]- and the shape of the charge- charge features, for instance, are labelled by their angular position.

Much more work should be done, however, to determine whether the non-dimensionalised results can be made independent of the mill diameter and, if so, to probe the limits of this scalability. Performing scaling tests of this sort will go a long way towards defining the limits of applicability of models based on PEPT data to the industrial context.

8.2.2 Additional experiments

In order to properly perform the scalability tests mentioned in the last section, it would be helpful to perform PEPT experiments on a series of tumbling mills with a larger range of diameters. This is likely to happen in the near future as a $500mm$ diameter mill has been built to compliment the existing $300mm$ and $140mm$ diameter mills.

It would also be interesting to perform PEPT experiments on less realistic mills- ones without the inlet trunnions, end-windows and discharge grates that complicate the internal structure of the mill, affecting the motion of its charge in unknown ways- and on mills of varying lengths.

This latter program might be better tackled with the more flexible and less expensive DEM. In fact, I think that it is very important to increase the use of DEM software to replicate and extend the experimental program described in this work, if for no other reason than that it has access to particle-level information and time resolutions that are impossible to achieve with PEPT.

I also think that other complimentary measurement techniques should be considered as a way of capturing time-dependent phenomena such as surging, that are not visible to PEPT because of the time-averaging necessary to take advantage of the ergodic assumption.

Finally, I believe that the next step in the understanding of tumbling mills is the use of PEPT and other data to inform the building of mathematical models of the motion of granular media inside such equipment. I also believe that this is an incremental process that will require an incremental approach to system complexity. I do not think that considering smooth ended rotating drums will be a simple enough first step. Rather, I think that PEPT experiments on the behaviour of granular media down simple, varying gradient and more complex slopes; on the behaviour of granular material in chutes and channels of various shapes and gradients; on the behaviour of granular material in vibratory trays of various shapes and motions; and on the behaviour of granular materials in various confined and free-surface flows, are called for.

I hope that this dissertation has provided some of the tools, and even insights, that will prove useful in this future work.

[20] See Section 3.2.2.

Part IV

Appendices

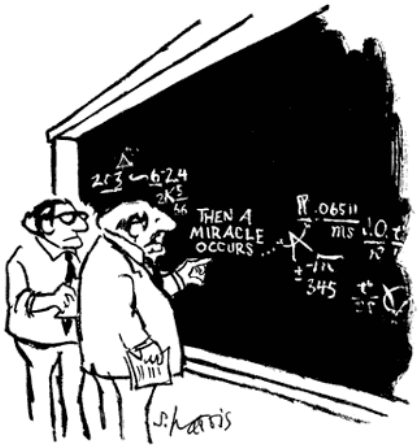

"I think you should be more explicit here in step two."

http://www.sciencecartoonsplus.com

Appendix A

Powell and McBride's summary of charge features in a tumbling mill

For some discussion of these charge features, see Section 3.2.4. For my redefinitions and extensions see Section 5.5.3.

References

[1] Powell, M.S. and McBride A.T. (2004). A three-dimensional analysis of media motion and grinding regions in mills. *Minerals Engineering*,17:1099-1109.

Table A.1: Powell and McBride's summary of charge features

Feature	Description	Analytic	Mathematical derivation
En masse	Bulk region of the charge moving in an upward direction	Region between equilibrium surface and mill shell moving in an upward direction	$R_{particle>R_{equil.surface}}$
Equilibrium surface	Surface separating the rising en masse charge from the descending charge	Defined by the turning point of the charge trajectories	Joining the horizontal and vertical equilibrium surfaces to form a continuous surface
Horizontal/vertical equilibrium surfaces		Surface defined by linking the maxima of the flow in the stated direction derived from a series of parallel flow control surfaces that intersect the charge	Maximum flow along a control line forms a point on the surface. The points from a family of parallel control surfaces are joined to form the equilibrium surface
Centre of circulation (CoC)	Axis about which all charge in the mill circulates	Region of zero velocity of particles	Intersection of horizontal and vertical equilibrium surfaces
Centre of mass (CoM)	Equivalent point to which all the mass of the charge can be condensed	Total charge mass placed here exerts the same torque on about the centre of the mill as the full tumbling charge	$X_{CoM} = \frac{\Sigma_{i=1}^{N} x_i}{N} \equiv \bar{x}$ and $X_{CoM} = \frac{\Sigma_{i=1}^{N} y_i}{N} \equiv \bar{y}$ for identical mass balls
Angle of repose	Cascade angle of the charge	Angular position of the CoC	
Rate of circulation (RoC)	Number of circulations of the mill a particle makes per mill revolution	Each particle is tracked from a given angular position relative to the CoC until it returns to that position to complete a full circuit of the CoC	$RoC = \frac{t(1circulation)}{T(1millrevolution)}$
Shoulder	Uppermost point at which material leaves the mill shell	Seek the point at which all material has lost contact with the mill shell	Incidence of $R_{part} \geq (R_{mill} - r_{part}(1+\Delta))$, where R_{part} = radial distance to centre of particle, R_{mill} = inside mill shell, r_{part} = radius of particle, Δ = small fraction of r_{part} to allow for slight fluctuations of motion
Head	Highest point of the charge trajectory	Maximum y coordinate of all particles	y_{max}
Bulk toe	Point of intersection of tumbling charge motion with mill shell	The intersection of the equilibrium surface with the mill shell, when all direct impact events are excluded	Find y_{min} of horizontal equilibrium surface. Extend horizontally to intersect with shell
Impact toe	The region where cataracting charge impacts on the mill shell	Highest point at which cataracting material strikes the mill shell	Point at which horizontal equil. surface intersects the mill shell

Appendix B

Morrell's power draw model

Figure B.1 show's Morrell's approximation to the shape of the charge in a tumbling mill. It consists of a crescent of charge delineated by the mill shell, an inner radius approximating the equilibrium surface of the charge, and radial lines to the toe and shoulder of the charge.

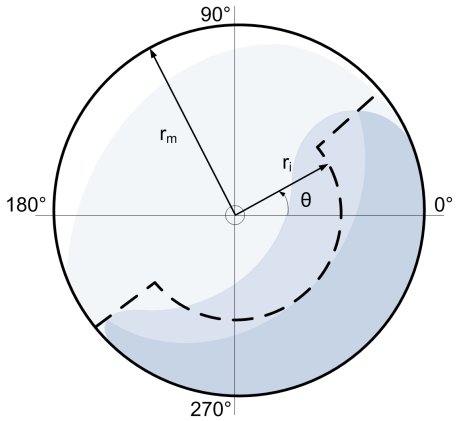

Figure B.1: Morrell's approximation to the shape of the charge in a tumbling mill.

Morrell models the variation in the angular position of the toe with mill rotational speed, ϕ, as a fraction of critical speed, ϕ_c, and of mill load, J_t, as

$$\theta_T = A\left(1 - \exp^{-B(\phi_c - \phi)}\right) + \frac{\pi}{2} \tag{B.1}$$

where A and B are functions of the mill load determined by experimental fits, as is the critical speed is expressed as

$$\phi_c = C + DJ_t \tag{B.2}$$

where C and D are constants.

To ensure that at critical speed the angular positions of the toe and shoulder of the charge converge to $\frac{\pi}{2}$ radians, the shoulder angle is expressed as

$$\theta_S = \frac{\pi}{2} - \left(\theta_T - \frac{\pi}{2}\right)(E + FJ_t) \tag{B.3}$$

where E and F are functions of the fractional mill speed ϕ, again fitted to data obtained from end-window experiments on a laboratory-scale tumbling mill.

Morrell obtains functional forms for the velocity of layers of charge in the mill from streak photo-

graphs of the end-window, which he expresses in terms of radial positions and tangential velocities normalised to those of the mill shell, thus

$$\begin{aligned} R_n &= \frac{r}{r_m} \\ V_n &= \frac{V_r}{V_m} \end{aligned} \tag{B.4}$$

where r is the radial position of the layer, V_r its tangential velocity, and r_m and V_m those of the mill shell.

In his experiments, Morrell found that the shear rates of charge in the rising region of the charge modelled by his crescent shape were linear but not equal to 1. That is, there was slip between the layers. He captures this slip with a parameter $z = (1 - J_t)^G$, where G is obtained from experimental fits. He uses z to relate the velocity of layers to that of the mill shell, thus:

$$V_r = \frac{r - zr_i}{r_m - zr_i} V_m \tag{B.5}$$

where r_i is the inner diameter of the crescent as shown in Figure B.1.

Morrell's power draw model considers the rate at which gravitational potential and kinetic energy are imparted to the charge by the mill. He does this by considering a radial section through the mill of length L. He divides this plane into strips of thickness dr, so that the cross-sectional area of each strip is Ldr.

If dr is considered to be the thickness of one layer in the charge, each strip can have a mass flow rate $V_r \rho L dr$ associated with it. This mass flow rate can then be used to calculate the rate of potential and kinetic energy transferred to charge in that layer.

Assuming that charge does not move between layers in the rising region, the rate of gravitational potential energy transfer to a given layer is

$$\begin{aligned} \Delta E_p &= V_r \rho L dr g h \\ &= V_r \rho L dr g r \left(\sin\theta_S - \sin\theta_T\right) \end{aligned} \tag{B.6}$$

and the rate of kinetic energy transfer is

$$\Delta E_k = \frac{V_r^3 \rho L dr}{2} \tag{B.7}$$

and so the total energy transfer rate to a given layer is

$$\Delta E_{tot} = V_r \rho L dr g r \left(\sin\theta_S - \sin\theta_T\right) + \frac{V_r^3 \rho L dr}{2} \tag{B.8}$$

The total energy transfer rate to the whole charge, interpreted as the power drawn by the charge, is therefore

$$\begin{aligned} P &= \int_{r_i}^{r_m} \left(V_r \rho L g r \left(\sin\theta_S - \sin\theta_T\right) + \frac{V_r^3 \rho L}{2} \right) dr \\ &= \frac{V_m \rho L g}{r_m - zr_i} \left(\sin\theta_S - \sin\theta_T\right) \int_{r_i}^{r_m} r\left(r - zr_i\right) dr + \frac{V_m^3 \rho L}{2\left(r_m - zr_i\right)^3} \int_{r_i}^{r_m} \left(r - zr_i\right)^3 dr \end{aligned} \tag{B.9}$$

which can be solved analytically, thus

$$P = \left[\frac{V_m \rho L g}{6\left(r_m - z r_i\right)}\left(\sin\theta_S - \sin\theta_T\right) r^2 \left(2r - 3 z r_i\right) + \frac{V_m^3 \rho L}{8\left(r_m - z r_i\right)^3}\left(z r_i - r\right)^4\right]_{r_i}^{r_m} \tag{B.10}$$

$$= \frac{V_m \rho L g}{6\left(r_m - z r_i\right)}\left(\sin\theta_S - \sin\theta_T\right)\left[r_m^2\left(2r_m - 3 z r_i\right) - r_i^3\left(2 - 3z\right)\right] + \frac{V_m^3 \rho L}{8\left(r_m - z r_i\right)^3}\left[\left(z r_i - r_m\right)^4 - \left(z-1\right)^4 r_i^4\right]$$

which can be solved for different speeds and loads using the correlations given in equations B.1 - B.3.

References

[1] Morrell, S. (1992). Prediction of grinding-mill power. *Transactions of the Institution of Mining and Metallurgy Section C: mineral Processing Extraction and Metallurgy*, 101:C25-C32.

[2] Wills, B.A. (2001). *Minerals Processing Technology*. Butterworth Heinemann, 6th edition.

Appendix C

Technical drawings of the $300mm$ diameter tumbling mills

C.1 The old $300mm$ mill

C.1.1 Profile

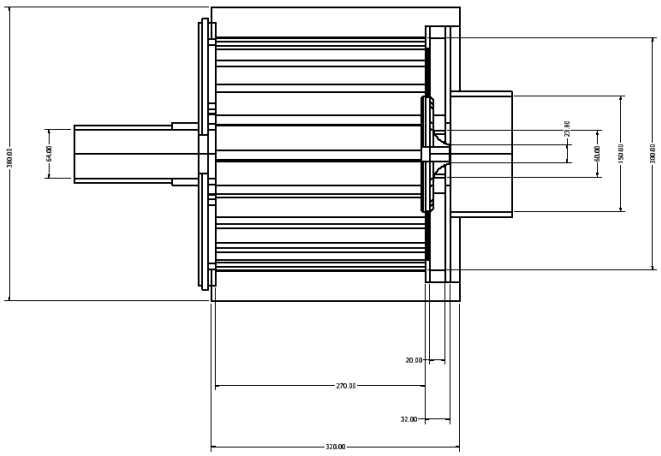

Figure C.1: A profile of the old 300mm mill with dimensions.

C.1.2 Pulp chamber

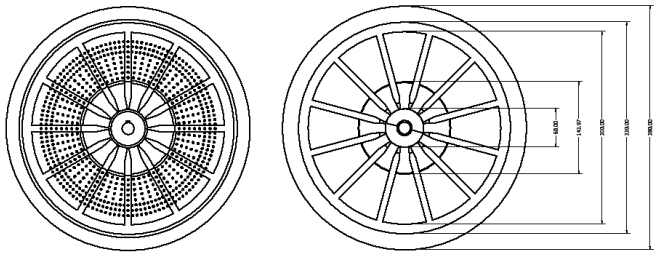

Figure C.2: The pulp chamber of the old 300mm mill with dimensions.

C.2 The new $300mm$ mill

C.2.1 Profile

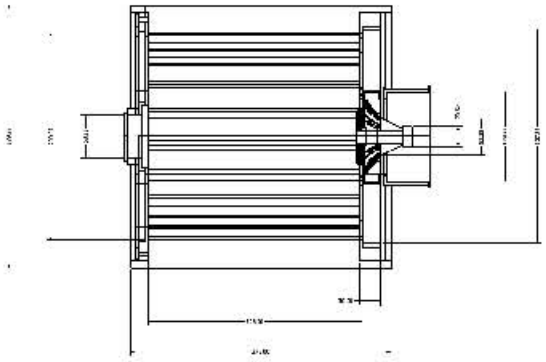

Figure C.3: A profile of the new 300mm mill with dimensions.

C.2.2 Pulp chamber

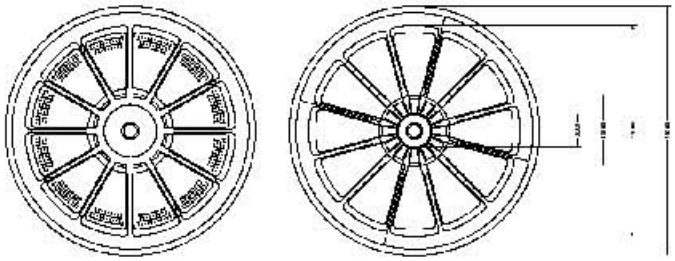

Figure C.4: The pulp chamber of the new 300mm mill with dimensions.

Appendix D

Laboratory-scale tumbling mill experiments

D.1 A complete list of experiments by trip

D.1.1 uct01: September 2006

These experiments were performed on the 14th and 15th of September 2006. They were performed on the now so-called 'old 300 mm mill', containing a *Rosin-Rammler* size distribution[1] of dry, conditioned blue stone. It was the first set of PEPT experiments performed by the UCT CMR at the University of Birmingham's Positron Imaging Centre. No experimental information was recorded for the first 25 of these runs because they were spent becoming familiar with the technique and equipment. Details of the remaining experiments are given in Table D.1.

Experimenters

These experiments were performed by Prof. Malcolm Powell, now at the Julius Kruttschnitt Mineral Research Centre at the University of Queensland, Drs. Indresan Govender and Aubrey Mainza, and Mr. Andre van der Westhuizen of the UCT CMR, Rajiv Chandramohan, now of the JKMRC and Ausenco, and Percy Condori, now of Rio Tinto.

Notes

This was the first set of PEPT experiments performed by the UCT CMR, so there was a fair amount of trial and error initially. In particular, the details of runs $001 - 025$ were not even recorded.

The charge in these experiments consisted of a *Rosin-Rammler* size distribution of dry, conditioned[2] blue stone.

Two representative tracer particles were chosen for these experiments- a roughly rectangular cuboid of length $6mm$ and with a square $2mm \times 2mm$ face, and a roughly spherical particle of diameter $5mm$.

[1] See Section 4.3.2.
[2] Previously tumbled to reduce the chances of breakage in these experiments.

Table D.1: Old 300 mm mill experiments

Run	Lifter		Load	Speed	Tracer		Locations	Comments
	Face angle/°	Height /mm	/%	/% v_{crit}	Material	Diameter /mm		
001-025	xxx	xxx	xxx	xxx	xxx	xxx	xxx	No records kept for these runs.
026-028	xxx	xxx	xxx	xxx	xxx	xxx	xxx	Location markers 1.1
029	60	19	24.63	80	bluestone	6x2 (rect)	1.1	
030	60	19	24.63	75	bluestone	6x2 (rect)	1.1	
031	60	19	24.63	65	bluestone	6x2 (rect)	1.1	
032	90	19	24.63	95	bluestone	6x2 (rect)	1.1	Reversed rotation direction.
033	90	19	24.63	90	bluestone	6x2 (rect)	1.1	
034	90	19	24.63	85	bluestone	6x2 (rect)	1.1	
035	90	19	24.63	80	bluestone	6x2 (rect)	1.1	
036	90	19	24.63	75	bluestone	6x2 (rect)	1.1	
037	90	19	24.63	65	bluestone	6x2 (rect)	1.1	
038	90	19	30.00	95	bluestone	6x2 (rect)	1.1	
039	90	19	30.00	90	bluestone	6x2 (rect)	1.1	
040	90	19	30.00	85	bluestone	6x2 (rect)	1.1	
041	90	19	30.00	80	bluestone	6x2 (rect)	1.1	
042	90	19	30.00	75	bluestone	6x2 (rect)	1.1	Torque reading failed.
043	90	19	30.00	75	bluestone	6x2 (rect)	1.1	
044	90	19	30.00	65	bluestone	6x2 (rect)	1.1	
045	60	19	30.00	95	bluestone	6x2 (rect)	1.1	Reversed rotation direction.
046	60	19	30.00	90	bluestone	6x2 (rect)	1.1	
047	60	19	30.00	85	bluestone	6x2 (rect)	1.1	
048	60	19	30.00	80	bluestone	6x2 (rect)	1.1	
049	60	19	30.00	75	bluestone	6x2 (rect)	1.1	

Continued on next page...

Table D.1 – Continued

Run	Lifter		Load	Speed	Tracer		Locations	Comments
	Face angle/°	Height /mm	/%	/% v_{crit}	Material	Diameter /mm		
050	60	19	30.00	65	bluestone	6x2 (rect)	1.1	
051	60	19	35.00	95	bluestone	6x2 (rect)	1.1	
052	60	19	35.00	90	bluestone	6x2 (rect)	1.1	
053	60	19	35.00	85	bluestone	6x2 (rect)	1.1	
054	60	19	35.00	80	bluestone	6x2 (rect)	1.1	
055	60	19	35.00	75	bluestone	6x2 (rect)	1.1	
056	60	19	35.00	65	bluestone	6x2 (rect)	1.1	
057	90	19	35.00	95	bluestone	6x2 (rect)	1.1	Reversed rotation direction.
058	90	19	35.00	90	bluestone	6x2 (rect)	1.1	
059	90	19	35.00	85	bluestone	6x2 (rect)	1.1	
060	90	19	35.00	80	bluestone	6x2 (rect)	1.1	
061	90	19	35.00	75	bluestone	6x2 (rect)	1.1	
062	90	19	35.00	65	bluestone	6x2 (rect)	1.1	
063	90	19	40.00	95	bluestone	6x2 (rect)	1.1	
064	90	19	40.00	90	bluestone	6x2 (rect)	1.1	
065	90	19	40.00	85	bluestone	6x2 (rect)	1.1	
066	90	19	40.00	80	bluestone	6x2 (rect)	1.1	
067	90	19	40.00	75	bluestone	6x2 (rect)	1.1	
068	90	19	40.00	65	bluestone	6x2 (rect)	1.1	
069	60	19	40.00	95	bluestone	6x2 (rect)	1.1	Reversed rotation direction.
070	60	19	40.00	90	bluestone	6x2 (rect)	1.1	
071	60	19	40.00	85	bluestone	6x2 (rect)	1.1	
072	60	19	40.00	80	bluestone	6x2 (rect)	1.1	
073	60	19	40.00	75	bluestone	6x2 (rect)	1.1	

Continued on next page...

Table D.1 – Continued

Run	Lifter		Load	Speed	Tracer		Locations	Comments
	Face angle/°	Height /mm	/%	/% v_{crit}	Material	Diameter /mm		
074	60	19	40.00	65	bluestone	6x2 (rect)	1.1	
075-077	xxx	xxx	xxx	xxx	xxx	xxx	xxx	Location markers 1.2
078	60	19	15.00	95	bluestone	5	1.2	New lifter height?
079	xxx	xxx	xxx	xxx	xxx	xxx	xxx	Not recorded.
080	60	19	15.00	90	bluestone	5	1.2	
081	60	19	15.00	85	bluestone	5	1.2	
082	60	19	15.00	80	bluestone	5	1.2	
083	60	19	15.00	75	bluestone	5	1.2	
084	60	19	15.00	65	bluestone	5	1.2	
085	90	19	15.00	95	bluestone	5	1.2	Reversed rotation direction.
086	90	19	15.00	90	bluestone	5	1.2	
087	90	19	15.00	85	bluestone	5	1.2	
088	90	19	15.00	80	bluestone	5	1.2	
089	90	19	15.00	75	bluestone	5	1.2	
090	90	19	15.00	65	bluestone	5	1.2	
091	90	19	23.60	95	bluestone	5	1.2	
092	90	19	23.60	90	bluestone	5	1.2	
093	90	19	35.00	95	bluestone	5	1.2	
094	90	19	35.00	90	bluestone	5	1.2	
095	90	19	35.00	85	bluestone	5	1.2	
096	90	19	35.00	80	bluestone	5	1.2	
097	90	19	35.00	75	bluestone	5	1.2	
098	90	19	35.00	65	bluestone	5	1.2	

Continued on next page...

Table D.1 – Continued

Run	Lifter		Load	Speed	Tracer		Locations	Comments
	Face angle/°	Height /mm	/%	/% v_{crit}	Material	Diameter /mm		
099	60	19	35.00	95	bluestone	5	1.2	Reversed rotation direction.
100	60	19	35.00	90	bluestone	5	1.2	
101	60	19	35.00	85	bluestone	5	1.2	
102	60	19	35.00	80	bluestone	5	1.2	
103	60	19	35.00	75	bluestone	5	1.2	
104	60	19	35.00	65	bluestone	5	1.2	
105	60	19	40.00	95	bluestone	5	1.2	
106	60	19	40.00	90	bluestone	5	1.2	
107	60	19	40.00	85	bluestone	5	1.2	
108	60	19	40.00	80	bluestone	5	1.2	
109	60	19	40.00	75	bluestone	5	1.2	
110	60	19	40.00	65	bluestone	5	1.2	
111	90	19	40.00	95	bluestone	5	1.2	Reversed rotation direction.
112	90	19	40.00	90	bluestone	5	1.2	
113	90	19	40.00	85	bluestone	5	1.2	
114	90	19	40.00	80	bluestone	5	1.2	
115	90	19	40.00	75	bluestone	5	1.2	
116	90	19	40.00	65	bluestone	5	1.2	

D.1.2 uct02: September 2006

These experiments were performed on the 18th of September 2006. They were performed on the 'old 300 mm mill', containing a *Rosin-Rammler* size distribution of conditioned blue stone. Some of the runs were dry, and others contained an additional 30% solids fraction slurry. Details of the experiments are given in Table D.2.

Experimenters

These experiments were performed by Prof. Malcolm Powell, now at the Julius Kruttschnitt Mineral Research Centre at the University of Queensland, Drs. Indresan Govender and Aubrey Mainza, and Mr. Andre van der Westhuizen of the UCT CMR, Rajiv Chandramohan, now of the JKMRC and Ausenco, and Percy Condori, now of Rio Tinto.

Notes

In this set of experiments, an attempt was made to recirculate a 30% solids concentration platinum slurry through the mill, and to both track the motion of the charge and of a neutrally-buoyant 'fluid' tracer particle. Runs $040 - 054$ were hit-and-miss slurry experiments.

Table D.2: Old 300 mm mill experiments

Run	Lifter		Fill	Load	Speed	Tracer		Locations	Comments
	Face angle/°	Height /mm	Wet/dry	/%	/% v_{crit}	Material	Diameter/mm		
001-003	xxx	xxx	xxx	xxx	xxx	xxx	xxx	xxx	Location markers 2.1
004	90	5	dry	15	95	bluestone	2	2.1	
005	90	5	dry	15	90	bluestone	2	2.1	
006	90	5	dry	15	85	bluestone	2	2.1	
007	90	5	dry	15	80	bluestone	2	2.1	
008	90	5	dry	15	75	bluestone	2	2.1	
009	90	5	dry	15	65	bluestone	2	2.1	
010	60	5	dry	15	95	bluestone	2	2.1	Reversed rotation direction.
011	60	5	dry	15	90	bluestone	2	2.1	
012	60	5	dry	15	85	bluestone	2	2.1	
013	60	5	dry	15	80	bluestone	2	2.1	
014	60	5	dry	15	75	bluestone	2	2.1	
015	60	5	dry	15	65	bluestone	2	2.1	
016	60	5	dry	35	95	bluestone	2	2.1	
017	60	5	dry	35	90	bluestone	2	2.1	
018	60	5	dry	35	85	bluestone	2	2.1	
019	60	5	dry	35	80	bluestone	2	2.1	
020	60	5	dry	35	75	bluestone	2	2.1	
021	60	5	dry	35	65	bluestone	2	2.1	
022	90	5	dry	35	95	bluestone	2	2.1	Reversed rotation direction.
023	90	5	dry	35	90	bluestone	2	2.1	
024	90	5	dry	35	85	bluestone	2	2.1	
025	90	5	dry	35	80	bluestone	2	2.1	

Continued on next page...

Table D.2 – Continued

Run	Lifter		Fill	Load	Speed	Tracer		Locations	Comments
	Face angle/°	Height /mm	Wet/dry	/%	/% v_{crit}	Material	Diameter/mm		
026	90	5	dry	35	75	bluestone	2	2.1	
027	90	5	dry	35	65	bluestone	2	2.1	
028	90	5	dry	40	95	bluestone	2	2.1	
029	90	5	dry	40	90	bluestone	2	2.1	
030	90	5	dry	40	85	bluestone	2	2.1	
031	90	5	dry	40	80	bluestone	2	2.1	
032	90	5	dry	40	75	bluestone	2	2.1	
033	90	5	dry	40	65	bluestone	2	2.1	
034	60	5	dry	40	95	bluestone	2	2.1	Reversed rotation direction.
035	60	5	dry	40	90	bluestone	2	2.1	
036	60	5	dry	40	85	bluestone	2	2.1	
037	60	5	dry	40	80	bluestone	2	2.1	
038	60	5	dry	40	75	bluestone	2	2.1	
039	60	5	dry	40	65	bluestone	2	2.1	
040-054	xxx	xxx	xxx	xxx	xxx	xxx	xxx	xxx	Hit and miss attempts with slurry.
055	90	5	30% slurry	40	95	bluestone	1	2.1	Reversed rotation direction.
056	90	5	30% slurry	40	90	bluestone	1	2.1	
057	90	5	30% slurry	40	85	bluestone	1	2.1	
058	90	5	30% slurry	40	80	bluestone	1	2.1	
059	90	5	30% slurry	40	75	bluestone	1	2.1	
060	90	5	30% slurry	40	65	bluestone	1	2.1	

D.1.3 uct03: October 2006

These experiments were performed on the 5th and 6th of October 2006. They were performed on the 'old 300 mm mill', containing a *Rosin-Rammler* size distribution of conditioned blue stone and a 30% solids fraction slurry. Details of the experiments are given in Table D.3.

Experimenters

These experiments were performed by Prof. Malcolm Powell, now at the Julius Kruttschnitt Mineral Research Centre at the University of Queensland, Drs. Indresan Govender and Aubrey Mainza, and Mr. Andre van der Westhuizen of the UCT CMR, Rajiv Chandramohan, now of the JKMRC and Ausenco, and Percy Condori, now of Rio Tinto.

Notes

This set of experiments consisted of attempts to track a neutrally-buoyant 'fluid' tracer particle in a Rosin-Rammler distribution of conditioned bluestone.

Table D.3: Old 300 mm mill experiments

Run	Lifter		Load	Speed	Tracer		Locations	Comments
	Face angle/°	Height /mm	/%	/% v_{crit}	Material	Diameter /mm		
001-003	xxx	xxx	xxx	xxx	xxx	xxx	xxx	Location markers 3.1
004	90	5	40	75	bluestone	1	3.1	
005	90	5	40	75	bluestone	1	3.1	
006	90	5	40	75	bluestone	1	3.1	
007	90	5	40	75	bluestone	1	3.1	
008	xxx	xxx	xxx	xxx	xxx	xxx	xxx	Not performed.
009	90	5	40	85	copper	1	3.1	
010	90	5	40	75	copper	1	3.1	
011	90	5	40	75	copper	1	3.1	Bad run
012	90	5	40	75	copper	1	3.1	
013	90	5	40	65	bluestone	1	3.1	
014-016	xxx	xxx	xxx	xxx	xxx	xxx	xxx	Location markers 3.2
017	90	5	40	100	bluestone	1	3.2	Particle left mill.
018	90	5	40	95	bluestone	1	3.2	Slight leak.
019	90	5	40	55	bluestone	1	3.2	
020	90	5	40	65	bluestone	1	3.2	Particle left mill.
021	90	5	40	70	bluestone	1	3.2	
022	90	5	40	75	bluestone	1	3.2	
023	90	5	40	80	bluestone	1	3.2	
024	90	5	40	85	bluestone	1	3.2	
025	90	5	40	90	bluestone	1	3.2	

D.1.4 uct04: April 2007

These experiments were performed from the 20th to the 23rd of April 2007. They were performed on the 'old 300 mm mill', containing a *Rosin-Rammler* size distribution of glass beads. Details of the experiments are given in Table D.4.

Experimenters

These experiments were performed by Drs. Indresan Govender and Aubrey Mainza, and Mr. Andre van der Westhuizen of the UCT CMR.

Notes

This set of experiments was a first attempt to approximate the bluestone charge used in series *uct01* to *uct03* with a discrete Rosin-Rammler size distribution of dry glass beads.

Table D.4: Old 300 mm mill experiments

Run	Lifter		Load	Speed	Tracer		Locations	Comments
	Face angle/°	Height /mm	/%	/% v_{crit}	Material	Diameter /mm		
001-003	xxx	xxx	xxx	xxx	xxx	xxx	xxx	Location markers 4.1
004	90	5	12.50	90	glass	4	4.1	
005	90	5	12.50	80	glass	4	4.1	
006	90	5	12.50	75	glass	4	4.1	Using wet air to reduce static.
007	90	5	12.50	70	glass	4	4.1	
008	90	5	12.50	60	glass	4	4.1	
009	90	5	25.00	90	glass	4	4.2	
010	90	5	25.00	80	glass	4	4.2	
011	90	5	25.00	75	glass	4	4.2	
012	90	5	25.00	70	glass	4	4.2	
013	90	5	25.00	60	glass	4	4.2	
014	90	5	31.25	90	glass	4	4.2	
015	90	5	31.25	80	glass	4	4.2	
016	90	5	31.25	75	glass	4	4.2	
017	90	5	31.25	70	glass	4	4.2	
018	xxx	xxx	xxx	xxx	xxx	xxx	xxx	Error.
019	90	5	31.25	60	glass	4	4.2	
020	90	5	37.50	90	glass	4	4.2	
021	90	5	37.50	80	glass	4	4.2	
022	90	5	37.50	75	glass	4	4.2	
023	90	5	37.50	70	glass	4	4.2	
024	90	5	37.50	60	glass	4	4.2	

Continued on next page...

Table D.4 – Continued

Run	Lifter		Load	Speed	Tracer		Locations	Comments
	Face angle/°	Height /mm	/%	/% v_{crit}	Material	Diameter /mm		
025	90	5	50.00	90	glass	4	4.2	
026	90	5	50.00	80	glass	4	4.2	
027	90	5	50.00	75	glass	4	4.2	
028	90	5	50.00	70	glass	4	4.2	
029	90	5	50.00	60	glass	4	4.2	Covered grate with masking tape.
030	xxx	xxx	xxx	xxx	xxx	xxx	xxx	Location markers 4.2
031	90	5	12.50	90	glass	3	4.2	
032	90	5	12.50	80	glass	3	4.2	
033	90	5	12.50	75	glass	3	4.2	
034	90	5	12.50	70	glass	3	4.2	
035	90	5	12.50	60	glass	3	4.2	
036	90	5	25.00	90	glass	3	4.2	
037	90	5	25.00	80	glass	3	4.2	
038	90	5	25.00	75	glass	3	4.2	
039	90	5	25.00	70	glass	3	4.2	
040	90	5	25.00	60	glass	3	4.2	
041	90	5	31.25	90	glass	3	4.2	
042	90	5	31.25	80	glass	3	4.2	
043	90	5	31.25	75	glass	3	4.2	
044	90	5	31.25	70	glass	3	4.2	
045	90	5	31.25	60	glass	3	4.2	
046	90	5	37.50	90	glass	3	4.2	
047	90	5	37.50	80	glass	3	4.2	

Continued on next page...

Table D.4 – Continued

Run	Lifter		Load	Speed	Tracer		Locations	Comments
	Face angle/°	Height /mm	/%	/% v_{crit}	Material	Diameter /mm		
048	90	5	37.50	75	glass	3	4.2	
049	90	5	37.50	70	glass	3	4.2	
050	90	5	37.50	60	glass	3	4.2	
051	90	5	50.00	90	glass	3	4.2	
052	90	5	50.00	80	glass	3	4.2	
053	90	5	50.00	75	glass	3	4.2	
054	90	5	50.00	70	glass	3	4.2	
055	90	5	50.00	60	glass	3	4.2	Could be a bad run.
056 - 059	xxx	xxx	xxx	xxx	xxx	xxx	xxx	Location markers 4.3
060	90	5	12.50	90	glass	5	4.3	
061	90	5	12.50	80	glass	5	4.3	
062	90	5	12.50	75	glass	5	4.3	
063	90	5	12.50	70	glass	5	4.3	
064	90	5	12.50	60	glass	5	4.3	
065	90	5	12.50	85	glass	5	4.3	
066	90	5	25.00	90	glass	5	4.3	
067	90	5	25.00	80	glass	5	4.3	
068	90	5	25.00	75	glass	5	4.3	
069	90	5	25.00	70	glass	5	4.3	
070	90	5	25.00	60	glass	5	4.3	
071	90	5	31.25	90	glass	5	4.3	
072	90	5	31.25	80	glass	5	4.3	
073	xxx	xxx	xxx	xxx	xxx	xxx	xxx	Redone as 075.

Continued on next page...

Table D.4 – Continued

Run	Lifter		Load	Speed	Tracer		Locations	Comments
	Face angle/°	Height /mm	/%	/% v_{crit}	Material	Diameter /mm		
074	90	5	31.25	75	glass	5	4.3	
075	90	5	31.25	70	glass	5	4.3	
076	90	5	31.25	60	glass	5	4.3	
077	90	5	37.50	90	glass	5	4.3	
078	90	5	37.50	80	glass	5	4.3	
079	90	5	37.50	75	glass	5	4.3	
080	90	5	37.50	70	glass	5	4.3	
081	90	5	37.50	60	glass	5	4.3	
082	90	5	50.00	90	glass	5	4.3	
083	90	5	50.00	80	glass	5	4.3	
084	90	5	50.00	75	glass	5	4.3	
085	90	5	50.00	70	glass	5	4.3	
086	90	5	50.00	60	glass	5	4.3	
087	xxx	xxx	xxx	xxx	xxx	xxx	xxx	Beads fell off.
088-089	xxx	xxx	xxx	xxx	xxx	xxx	xxx	Location markers 4.4
090	90	5	12.50	90	glass	6	4.4	
091	90	5	12.50	80	glass	6	4.4	
092	90	5	12.50	75	glass	6	4.4	
093	xxx	xxx	xxx	xxx	xxx	xxx	xxx	Error.
094	90	5	12.50	70	glass	6	4.4	
095	90	5	12.50	60	glass	6	4.4	
096	90	5	25.00	90	glass	6	4.4	
097	90	5	25.00	80	glass	6	4.4	

Continued on next page...

Table D.4 – Continued

Run	Lifter		Load	Speed	Tracer		Locations	Comments
	Face angle/°	Height /mm	/%	/% v_{crit}	Material	Diameter /mm		
098	90	5	25.00	75	glass	6	4.4	
099	90	5	25.00	70	glass	6	4.4	
100	90	5	25.00	60	glass	6	4.4	
101	90	5	31.25	90	glass	6	4.4	
102	90	5	31.25	80	glass	6	4.4	
103	90	5	31.25	75	glass	6	4.4	
104	90	5	31.25	70	glass	6	4.4	
105	90	5	31.25	60	glass	6	4.4	
106	90	5	37.50	90	glass	6	4.4	
107	90	5	37.50	80	glass	6	4.4	
108	90	5	37.50	75	glass	6	4.4	
109	90	5	37.50	70	glass	6	4.4	
110	90	5	37.50	60	glass	6	4.4	
111	90	5	50.00	90	glass	6	4.4	
112	90	5	50.00	80	glass	6	4.4	
113	90	5	50.00	75	glass	6	4.4	
114	90	5	50.00	70	glass	6	4.4	
115	90	5	50.00	60	glass	6	4.4	
116	90	5	50.00	50	glass	6	4.4	
117	90	5	50.00	100	glass	6	4.4	
118	90	5	50.00	120	glass	6	4.4	
119	90	5	50.00	40	glass	6	4.4	
120	90	5	50.00	30	glass	6	4.4	

Continued on next page...

Table D.4 – Continued

Run	Lifter		Load	Speed	Tracer		Locations	Comments
	Face angle/°	Height /mm	/%	/% v_{crit}	Material	Diameter /mm		
121 - 123	xxx	xxx	xxx	xxx	xxx	xxx	xxx	Location markers 4.5
124	90	5	12.50	90	glass	8	4.5	
125	90	5	12.50	80	glass	8	4.5	
126	90	5	12.50	75	glass	8	4.5	
127	90	5	12.50	70	glass	8	4.5	
128	90	5	12.50	60	glass	8	4.5	
129	90	5	25.00	90	glass	8	4.5	
130	90	5	25.00	80	glass	8	4.5	
131	90	5	25.00	75	glass	8	4.5	
132	90	5	25.00	70	glass	8	4.5	
133	90	5	25.00	60	glass	8	4.5	
134	90	5	31.25	90	glass	8	4.5	
135	90	5	31.25	80	glass	8	4.5	
136	90	5	31.25	75	glass	8	4.5	
137	90	5	31.25	70	glass	8	4.5	
138	90	5	31.25	60	glass	8	4.5	
139	90	5	37.50	90	glass	8	4.5	
140	90	5	37.50	80	glass	8	4.5	
141	90	5	37.50	75	glass	8	4.5	
142	90	5	37.50	70	glass	8	4.5	
143	90	5	37.50	60	glass	8	4.5	
144	90	5	50.00	90	glass	8	4.5	
145	90	5	50.00	80	glass	8	4.5	

Continued on next page...

Table D.4 – Continued

Run	Lifter		Load	Speed	Tracer		Locations	Comments
	Face angle/°	Height /mm	/%	/% v_{crit}	Material	Diameter /mm		
146	90	5	50.00	75	glass	8	4.5	
147	90	5	50.00	70	glass	8	4.5	
148	90	5	50.00	60	glass	8	4.5	
149	90	5	50.00	40	glass	8	4.5	
150	90	5	50.00	30	glass	8	4.5	
151	90	5	50.00	50	glass	8	4.5	
152	90	5	50.00	100	glass	8	4.5	
153	90	5	50.00	120	glass	8	4.5	
154 - 156	xxx	xxx	xxx	xxx	xxx	xxx	xxx	Location markers 4.6
157	90	5	12.50	90	glass	2	4.6	
158	90	5	12.50	80	glass	2	4.6	
159	90	5	12.50	75	glass	2	4.6	
160	90	5	12.50	70	glass	2	4.6	
161	90	5	12.50	60	glass	2	4.6	
162	90	5	25.00	90	glass	2	4.6	
163	90	5	25.00	80	glass	2	4.6	
164	90	5	25.00	75	glass	2	4.6	
165	90	5	25.00	70	glass	2	4.6	
166	90	5	25.00	60	glass	2	4.6	
167	90	5	31.25	90	glass	2	4.6	
168	90	5	31.25	80	glass	2	4.6	
169	90	5	31.25	75	glass	2	4.6	
170	90	5	31.25	70	glass	2	4.6	

Continued on next page...

Table D.4 – Continued

Run	Lifter		Load	Speed	Tracer		Locations	Comments
	Face angle/°	Height /mm	/%	/% v_{crit}	Material	Diameter /mm		
171	90	5	31.25	60	glass	2	4.6	
172	90	5	37.50	90	glass	2	4.6	
173	90	5	37.50	80	glass	2	4.6	
174	90	5	37.50	75	glass	2	4.6	
175	90	5	37.50	70	glass	2	4.6	
176	90	5	37.50	60	glass	2	4.6	
177	90	5	37.50	40	glass	2	4.6	
178	90	5	37.50	50	glass	2	4.6	
179	90	5	37.50	100	glass	2	4.6	
180	90	5	37.50	120	glass	2	4.6	Mill stopped during run.
181	90	5	43.75	90	glass	2	4.6	
182	90	5	43.75	80	glass	2	4.6	
183	90	5	43.75	75	glass	2	4.6	
184	90	5	43.75	70	glass	2	4.6	
185	90	5	43.75	60	glass	2	4.6	
186	90	5	50.00	90	glass	2	4.6	
187	90	5	50.00	80	glass	2	4.6	
188	90	5	50.00	75	glass	2	4.6	
189	90	5	50.00	70	glass	2	4.6	
190	90	5	50.00	60	glass	2	4.6	

D.1.5 uct05: February 2008

These experiments were performed from the 11th to the 22nd of February 2008. They were performed on the 140 mm diameter 'x-ray' mill, containing a *Rosin-Rammler* size distribution of glass beads, and binary distributions of plastic, and glass and plastic beads. Details of the experiments are given in Table D.5.

Experimenters

These experiments were performed by Drs. Indresan Govender and Aubrey Mainza, Mr Trevor Volkwyn, and Mr. Andre van der Westhuizen of the UCT CMR.

Table D.5: 140mm x-ray mill experiments

Run	Fill			Load	Speed	Tracer		Locations	Comments
	Distribution	Material	Diameter /mm	/%	/% v_{crit}	Material	Diameter /mm		
001	binary	plastic/glass	3,5	10.00	40	plastic	3	5.1	
002	binary	plastic/glass	3,5	10.00	60	plastic	3	5.1	
003	binary	plastic/glass	3,5	10.00	70	plastic	3	5.1	
004	binary	plastic/glass	3,5	10.00	80	plastic	3	5.1	
005	binary	plastic/glass	3,5	10.00	100	plastic	3	5.1	
006	binary	plastic/glass	3,5	10.00	110	plastic	3	5.1	
007	binary	plastic/glass	3,5	10.00	90	plastic	3	5.1	
008	binary	plastic/glass	3,5	20.00	40	plastic	3	5.1	
009	binary	plastic/glass	3,5	20.00	60	plastic	3	5.1	
010	binary	plastic/glass	3,5	20.00	70	plastic	3	5.1	
011	binary	plastic/glass	3,5	20.00	80	plastic	3	5.1	
012	binary	plastic/glass	3,5	20.00	90	plastic	3	5.1	
013	binary	plastic/glass	3,5	20.00	100	plastic	3	5.1	
014	binary	plastic/glass	3,5	20.00	110	plastic	3	5.1	
015	binary	plastic/glass	3,5	30.00	40	plastic	3	5.1	
016	binary	plastic/glass	3,5	30.00	60	plastic	3	5.1	
017	binary	plastic/glass	3,5	30.00	70	plastic	3	5.1	
018	binary	plastic/glass	3,5	30.00	80	plastic	3	5.1	
019	binary	plastic/glass	3,5	30.00	90	plastic	3	5.1	
020	binary	plastic/glass	3,5	30.00	100	plastic	3	5.1	
021	binary	plastic/glass	3,5	30.00	110	plastic	3	5.1	
022	binary	plastic/glass	3,5	40.00	40	plastic	3	5.1	
023	binary	plastic/glass	3,5	40.00	60	plastic	3	5.1	

Continued on next page...

Table D.5 – Continued

Run	Fill			Load	Speed	Tracer		Locations	Comments
	Distribution	Material	Diameter /mm	/%	/% v_{crit}	Material	Diameter /mm		
024	binary	plastic/glass	3,5	40.00	70	plastic	3	5.1	
025	binary	plastic/glass	3,5	40.00	80	plastic	3	5.1	
026	binary	plastic/glass	3,5	40.00	90	plastic	3	5.1	
027	binary	plastic/glass	3,5	40.00	100	plastic	3	5.1	
028	binary	plastic/glass	3,5	40.00	110	plastic	3	5.1	
029	binary	plastic/glass	3,5	10.00	40	plastic	5	5.1	
030	binary	plastic/glass	3,5	10.00	60	plastic	5	5.1	
031	binary	plastic/glass	3,5	10.00	70	plastic	5	5.1	
032	binary	plastic/glass	3,5	10.00	80	plastic	5	5.1	
033	binary	plastic/glass	3,5	10.00	90	plastic	5	5.1	
034	binary	plastic/glass	3,5	10.00	100	plastic	5	5.1	
035	binary	plastic/glass	3,5	10.00	110	plastic	5	5.1	
036	binary	plastic/glass	3,5	20.00	40	plastic	5	5.1	
037	binary	plastic/glass	3,5	20.00	60	plastic	5	5.1	
038	binary	plastic/glass	3,5	20.00	70	plastic	5	5.1	
039	binary	plastic/glass	3,5	20.00	80	plastic	5	5.1	
040	binary	plastic/glass	3,5	20.00	90	plastic	5	5.1	
041	binary	plastic/glass	3,5	20.00	100	plastic	5	5.1	
042	binary	plastic/glass	3,5	20.00	110	plastic	5	5.1	
043	binary	plastic/glass	3,5	30.00	40	plastic	5	5.1	
044	binary	plastic/glass	3,5	30.00	60	plastic	5	5.1	
045	binary	plastic/glass	3,5	30.00	70	plastic	5	5.1	
046	binary	plastic/glass	3,5	30.00	80	plastic	5	5.1	
047	binary	plastic/glass	3,5	30.00	90	plastic	5	5.1	

Continued on next page...

Table D.5 – Continued

Run	Fill			Load	Speed	Tracer		Locations	Comments
	Distribution	Material	Diameter /mm	/%	/% v_{crit}	Material	Diameter /mm		
048	binary	plastic/glass	3,5	30.00	100	plastic	5	5.1	
049	binary	plastic/glass	3,5	30.00	110	plastic	5	5.1	
050	binary	plastic/glass	3,5	40.00	40	plastic	5	5.1	
051	binary	plastic/glass	3,5	40.00	60	plastic	5	5.1	
052	binary	plastic/glass	3,5	40.00	70	plastic	5	5.1	
053	binary	plastic/glass	3,5	40.00	80	plastic	5	5.1	
054	binary	plastic/glass	3,5	40.00	90	plastic	5	5.1	
055	binary	plastic/glass	3,5	40.00	100	plastic	5	5.1	
056	binary	plastic/glass	3,5	40.00	110	plastic	5	5.1	
057-060	xxx	xxx	xxx	xxx	xxx	xxx	xxx	xxx	Loc 5.1
061	R-R	glass	2-8	12.50	40	glass	3	5.2	
062	R-R	glass	2-8	12.50	50	glass	3	5.2	
063	R-R	glass	2-8	12.50	60	glass	3	5.2	
064	R-R	glass	2-8	12.50	70	glass	3	5.2	
065	R-R	glass	2-8	12.50	80	glass	3	5.2	
066	R-R	glass	2-8	12.50	90	glass	3	5.2	
067	R-R	glass	2-8	12.50	100	glass	3	5.2	
068	R-R	glass	2-8	12.50	110	glass	3	5.2	
069	R-R	glass	2-8	25.00	40	glass	3	5.2	
070	R-R	glass	2-8	25.00	50	glass	3	5.2	
071	R-R	glass	2-8	25.00	60	glass	3	5.2	
072	R-R	glass	2-8	25.00	70	glass	3	5.2	
073	R-R	glass	2-8	25.00	80	glass	3	5.2	
074	R-R	glass	2-8	25.00	90	glass	3	5.2	

Continued on next page...

Table D.5 – Continued

Run	Fill			Load	Speed	Tracer		Locations	Comments
	Distribution	Material	Diameter /mm	/%	/% v_{crit}	Material	Diameter /mm		
075	R-R	glass	2-8	25.00	100	glass	3	5.2	
076	R-R	glass	2-8	25.00	110	glass	3	5.2	
077	R-R	glass	2-8	37.50	40	glass	3	5.2	
078	R-R	glass	2-8	37.50	50	glass	3	5.2	
079	R-R	glass	2-8	37.50	60	glass	3	5.2	
080	R-R	glass	2-8	37.50	70	glass	3	5.2	
081	R-R	glass	2-8	37.50	80	glass	3	5.2	
082	R-R	glass	2-8	37.50	90	glass	3	5.2	
083	R-R	glass	2-8	37.50	100	glass	3	5.2	
084	R-R	glass	2-8	37.50	110	glass	3	5.2	
085	R-R	glass	2-8	50.00	40	glass	3	5.2	
086	R-R	glass	2-8	50.00	50	glass	3	5.2	
087	R-R	glass	2-8	50.00	60	glass	3	5.2	
088	R-R	glass	2-8	50.00	70	glass	3	5.2	
089	R-R	glass	2-8	50.00	80	glass	3	5.2	
090	R-R	glass	2-8	50.00	90	glass	3	5.2	
091	R-R	glass	2-8	50.00	100	glass	3	5.2	
092	R-R	glass	2-8	50.00	110	glass	3	5.2	
093	R-R	glass	2-8	12.50	40	glass	4	5.2	
094	R-R	glass	2-8	12.50	50	glass	4	5.2	
095	R-R	glass	2-8	12.50	60	glass	4	5.2	
096	R-R	glass	2-8	12.50	70	glass	4	5.2	
097	R-R	glass	2-8	12.50	80	glass	4	5.2	
098	R-R	glass	2-8	12.50	90	glass	4	5.2	

Continued on next page...

Table D.5 – Continued

Run	Fill			Load	Speed	Tracer		Locations	Comments
	Distribution	Material	Diameter /mm	/%	/% v_{crit}	Material	Diameter /mm		
099	R-R	glass	2-8	12.50	100	glass	4	5.2	
100	R-R	glass	2-8	12.50	110	glass	4	5.2	
101	R-R	glass	2-8	25.00	40	glass	4	5.2	
102	R-R	glass	2-8	25.00	50	glass	4	5.2	
103	R-R	glass	2-8	25.00	60	glass	4	5.2	
104	R-R	glass	2-8	25.00	70	glass	4	5.2	
105	R-R	glass	2-8	25.00	80	glass	4	5.2	
106	R-R	glass	2-8	25.00	90	glass	4	5.2	
107	R-R	glass	2-8	25.00	100	glass	4	5.2	
108	R-R	glass	2-8	25.00	110	glass	4	5.2	
109	R-R	glass	2-8	37.50	40	glass	4	5.2	
110	R-R	glass	2-8	37.50	50	glass	4	5.2	
111	R-R	glass	2-8	37.50	60	glass	4	5.2	
112	R-R	glass	2-8	37.50	70	glass	4	5.2	
113	R-R	glass	2-8	37.50	80	glass	4	5.2	
114	R-R	glass	2-8	37.50	90	glass	4	5.2	
115	R-R	glass	2-8	37.50	100	glass	4	5.2	
116	R-R	glass	2-8	37.50	110	glass	4	5.2	
117	R-R	glass	2-8	50.00	40	glass	4	5.2	
118	R-R	glass	2-8	50.00	50	glass	4	5.2	
119	R-R	glass	2-8	50.00	60	glass	4	5.2	
120	R-R	glass	2-8	50.00	70	glass	4	5.2	
121	R-R	glass	2-8	50.00	80	glass	4	5.2	
122	R-R	glass	2-8	50.00	90	glass	4	5.2	

Continued on next page...

Table D.5 – Continued

Run	Fill			Load	Speed	Tracer		Locations	Comments
	Distribution	Material	Diameter /mm	/%	/% v_{crit}	Material	Diameter /mm		
123	R-R	glass	2-8	50.00	100	glass	4	5.2	
124	R-R	glass	2-8	50.00	110	glass	4	5.2	
125-128	xxx	xxx	xxx	xxx	xxx	xxx	xxx	xxx	Loc 5.2
129	R-R	glass	2-8	12.50	40	glass	5	5.3	
130	R-R	glass	2-8	12.50	50	glass	5	5.3	
131	R-R	glass	2-8	12.50	60	glass	5	5.3	
132	R-R	glass	2-8	12.50	70	glass	5	5.3	
133	R-R	glass	2-8	12.50	80	glass	5	5.3	
134	R-R	glass	2-8	12.50	90	glass	5	5.3	
135	R-R	glass	2-8	12.50	100	glass	5	5.3	
136	R-R	glass	2-8	12.50	110	glass	5	5.3	
137	R-R	glass	2-8	25.00	40	glass	5	5.3	
138	R-R	glass	2-8	25.00	50	glass	5	5.3	
139	R-R	glass	2-8	25.00	60	glass	5	5.3	
140	R-R	glass	2-8	25.00	70	glass	5	5.3	
141	R-R	glass	2-8	25.00	80	glass	5	5.3	
142	R-R	glass	2-8	25.00	90	glass	5	5.3	
143	R-R	glass	2-8	25.00	100	glass	5	5.3	
144	R-R	glass	2-8	25.00	110	glass	5	5.3	
145	R-R	glass	2-8	37.50	40	glass	5	5.3	
146	R-R	glass	2-8	37.50	50	glass	5	5.3	
147	R-R	glass	2-8	37.50	60	glass	5	5.3	
148	R-R	glass	2-8	37.50	70	glass	5	5.3	
149	R-R	glass	2-8	37.50	80	glass	5	5.3	

Continued on next page...

Table D.5 – Continued

Run	Fill			Load	Speed	Tracer		Locations	Comments
	Distribution	Material	Diameter /mm	/%	/% v_{crit}	Material	Diameter /mm		
150	R-R	glass	2-8	37.50	90	glass	5	5.3	
151	R-R	glass	2-8	37.50	100	glass	5	5.3	
152	R-R	glass	2-8	37.50	110	glass	5	5.3	
153	R-R	glass	2-8	50.00	40	glass	5	5.3	
154	R-R	glass	2-8	50.00	50	glass	5	5.3	
155	R-R	glass	2-8	50.00	60	glass	5	5.3	
156	R-R	glass	2-8	50.00	70	glass	5	5.3	
157	R-R	glass	2-8	50.00	80	glass	5	5.3	
158	R-R	glass	2-8	50.00	90	glass	5	5.3	
159	R-R	glass	2-8	50.00	100	glass	5	5.3	
160	R-R	glass	2-8	50.00	110	glass	5	5.3	
161	binary	plastic/glass	3,5	20.00	60	glass	5	5.3	
162	binary	plastic/glass	3,5	20.00	70	glass	5	5.3	
163	binary	plastic/glass	3,5	20.00	80	glass	5	5.3	
164	binary	plastic/glass	3,5	20.00	90	glass	5	5.3	
165	binary	plastic/glass	3,5	30.00	60	glass	5	5.3	
166	binary	plastic/glass	3,5	30.00	70	glass	5	5.3	
167	binary	plastic/glass	3,5	30.00	80	glass	5	5.3	
168	binary	plastic/glass	3,5	30.00	90	glass	5	5.3	
169	binary	plastic/glass	3,5	40.00	60	glass	5	5.3	
170	binary	plastic/glass	3,5	40.00	70	glass	5	5.3	
171	binary	plastic/glass	3,5	40.00	80	glass	5	5.3	
172	binary	plastic/glass	3,5	40.00	90	glass	5	5.3	

Continued on next page...

Table D.5 – Continued

Run	Fill			Load	Speed	Tracer		Locations	Comments
	Distribution	Material	Diameter /mm	/%	/% v_{crit}	Material	Diameter /mm		
173	R-R	glass	2-8	12.50	40	glass	6	5.3	
174	R-R	glass	2-8	12.50	50	glass	6	5.3	
175	R-R	glass	2-8	12.50	60	glass	6	5.3	
176	R-R	glass	2-8	12.50	70	glass	6	5.3	
177	R-R	glass	2-8	12.50	80	glass	6	5.3	
178	R-R	glass	2-8	12.50	90	glass	6	5.3	
179	R-R	glass	2-8	12.50	100	glass	6	5.3	
180	R-R	glass	2-8	12.50	110	glass	6	5.3	
181	R-R	glass	2-8	25.00	40	glass	6	5.3	
182	R-R	glass	2-8	25.00	50	glass	6	5.3	
183	R-R	glass	2-8	25.00	60	glass	6	5.3	
184	R-R	glass	2-8	25.00	70	glass	6	5.3	
185	R-R	glass	2-8	25.00	80	glass	6	5.3	
186	R-R	glass	2-8	25.00	90	glass	6	5.3	
187	R-R	glass	2-8	25.00	100	glass	6	5.3	
188	R-R	glass	2-8	25.00	110	glass	6	5.3	
189	R-R	glass	2-8	37.50	40	glass	6	5.3	
190	R-R	glass	2-8	37.50	50	glass	6	5.3	
191	R-R	glass	2-8	37.50	60	glass	6	5.3	
192	R-R	glass	2-8	37.50	70	glass	6	5.3	
193	R-R	glass	2-8	37.50	80	glass	6	5.3	
194	R-R	glass	2-8	37.50	90	glass	6	5.3	
195	R-R	glass	2-8	37.50	100	glass	6	5.3	

Continued on next page...

Table D.5 – Continued

Run	Fill			Load	Speed	Tracer		Locations	Comments
	Distribution	Material	Diameter /mm	/%	/% v_{crit}	Material	Diameter /mm		
196	R-R	glass	2-8	37.50	110	glass	6	5.3	
197	R-R	glass	2-8	50.00	40	glass	6	5.3	
198	R-R	glass	2-8	50.00	50	glass	6	5.3	
199	R-R	glass	2-8	50.00	60	glass	6	5.3	
200	R-R	glass	2-8	50.00	70	glass	6	5.3	
201	R-R	glass	2-8	50.00	80	glass	6	5.3	
202	R-R	glass	2-8	50.00	90	glass	6	5.3	
203	R-R	glass	2-8	50.00	100	glass	6	5.3	
204	R-R	glass	2-8	50.00	110	glass	6	5.3	
205-208	xxx	xxx	xxx	xxx	xxx	xxx	xxx	xxx	Loc 5.3
209	R-R	glass	2-8	25.00	40	glass	2	5.4	
210	R-R	glass	2-8	25.00	50	glass	2	5.4	
211	R-R	glass	2-8	25.00	60	glass	2	5.4	
212	R-R	glass	2-8	25.00	70	glass	2	5.4	
213	R-R	glass	2-8	25.00	80	glass	2	5.4	
214	R-R	glass	2-8	25.00	90	glass	2	5.4	
215	R-R	glass	2-8	25.00	100	glass	2	5.4	
216	R-R	glass	2-8	25.00	110	glass	2	5.4	
217	R-R	glass	2-8	37.50	40	glass	2	5.4	
218	R-R	glass	2-8	37.50	50	glass	2	5.4	
219	R-R	glass	2-8	37.50	60	glass	2	5.4	
220	R-R	glass	2-8	37.50	70	glass	2	5.4	
221	R-R	glass	2-8	37.50	80	glass	2	5.4	
222	R-R	glass	2-8	37.50	90	glass	2	5.4	

Continued on next page...

Table D.5 – Continued

Run	Fill			Load	Speed	Tracer		Locations	Comments
	Distribution	Material	Diameter /mm	/%	/% v_{crit}	Material	Diameter /mm		
223	R-R	glass	2-8	37.50	100	glass	2	5.4	
224	R-R	glass	2-8	37.50	110	glass	2	5.4	
225	R-R	glass	2-8	37.50	70	glass	2	5.4	Long run.
226	R-R	glass	2-8	50.00	40	glass	2	5.4	
227	R-R	glass	2-8	50.00	50	glass	2	5.4	
228	R-R	glass	2-8	50.00	60	glass	2	5.4	
229	R-R	glass	2-8	50.00	70	glass	2	5.4	
230	R-R	glass	2-8	50.00	80	glass	2	5.4	
231	R-R	glass	2-8	50.00	90	glass	2	5.4	
232	R-R	glass	2-8	50.00	100	glass	2	5.4	
233	R-R	glass	2-8	50.00	110	glass	2	5.4	
241	binary	plastic/glass	3,5	20.00	60	glass	3	5.4	
242	binary	plastic/glass	3,5	20.00	70	glass	3	5.4	
243	binary	plastic/glass	3,5	20.00	80	glass	3	5.4	
244	binary	plastic/glass	3,5	20.00	90	glass	3	5.4	
245	binary	plastic/glass	3,5	30.00	60	glass	3	5.4	
246	binary	plastic/glass	3,5	30.00	70	glass	3	5.4	
247	binary	plastic/glass	3,5	30.00	80	glass	3	5.4	
248	binary	plastic/glass	3,5	30.00	90	glass	3	5.4	
249	binary	plastic/glass	3,5	40.00	60	glass	3	5.4	
250	binary	plastic/glass	3,5	40.00	70	glass	3	5.4	
251	binary	plastic/glass	3,5	40.00	80	glass	3	5.4	
252	binary	plastic/glass	3,5	40.00	90	glass	3	5.4	

Continued on next page...

Table D.5 – Continued

Run	Fill			Load	Speed	Tracer		Locations	Comments
	Distribution	Material	Diameter /mm	/%	/% v_{crit}	Material	Diameter /mm		
268	R-R	glass	2-8	25.00	40	glass	8	5.4	
269	R-R	glass	2-8	25.00	50	glass	8	5.4	
270	R-R	glass	2-8	25.00	60	glass	8	5.4	
271	R-R	glass	2-8	25.00	70	glass	8	5.4	
272	R-R	glass	2-8	25.00	80	glass	8	5.4	
273	R-R	glass	2-8	25.00	90	glass	8	5.4	
274	R-R	glass	2-8	25.00	100	glass	8	5.4	
275	R-R	glass	2-8	25.00	110	glass	8	5.4	
276	R-R	glass	2-8	37.50	40	glass	8	5.4	
277	R-R	glass	2-8	37.50	50	glass	8	5.4	
278	R-R	glass	2-8	37.50	60	glass	8	5.4	
279	R-R	glass	2-8	37.50	70	glass	8	5.4	
280	R-R	glass	2-8	37.50	80	glass	8	5.4	
281	R-R	glass	2-8	37.50	90	glass	8	5.4	
282	R-R	glass	2-8	37.50	100	glass	8	5.4	
283	R-R	glass	2-8	37.50	110	glass	8	5.4	
284	R-R	glass	2-8	50.00	40	glass	8	5.4	
285	R-R	glass	2-8	50.00	50	glass	8	5.4	
286	R-R	glass	2-8	50.00	60	glass	8	5.4	
287	R-R	glass	2-8	50.00	70	glass	8	5.4	
288	R-R	glass	2-8	50.00	80	glass	8	5.4	
289	R-R	glass	2-8	50.00	90	glass	8	5.4	
290	R-R	glass	2-8	50.00	100	glass	8	5.4	
291	R-R	glass	2-8	50.00	110	glass	8	5.4	

Continued on next page...

Table D.5 – Continued

Run	Fill			Load	Speed	Tracer		Locations	Comments
	Distribution	Material	Diameter /mm	/%	/% v_{crit}	Material	Diameter /mm		
292	R-R	glass	2-8	50.00	65	glass	8	5.4	
293	R-R	glass	2-8	50.00	75	glass	8	5.4	
294	R-R	glass	2-8	50.00	85	glass	8	5.4	
295-298	xxx	xxx	xxx	xxx	xxx	xxx	xxx	xxx	Loc 5.4
299	binary	plastic	3,5	20.00	60	plastic	3	5.5	
300	binary	plastic	3,5	20.00	70	plastic	3	5.5	
301	binary	plastic	3,5	20.00	80	plastic	3	5.5	
302	binary	plastic	3,5	20.00	90	plastic	3	5.5	
303	binary	plastic	3,5	30.00	60	plastic	3	5.5	
304	binary	plastic	3,5	30.00	70	plastic	3	5.5	
305	binary	plastic	3,5	30.00	80	plastic	3	5.5	
306	binary	plastic	3,5	30.00	90	plastic	3	5.5	
307	binary	plastic	3,5	40.00	60	plastic	3	5.5	
308	binary	plastic	3,5	40.00	70	plastic	3	5.5	
309	binary	plastic	3,5	40.00	80	plastic	3	5.5	
310	binary	plastic	3,5	40.00	90	plastic	3	5.5	
311	binary	plastic	3,5	20.00	60	plastic	5	5.5	
312	binary	plastic	3,5	20.00	70	plastic	5	5.5	
313	binary	plastic	3,5	20.00	80	plastic	5	5.5	
314	binary	plastic	3,5	20.00	90	plastic	5	5.5	
315	binary	plastic	3,5	30.00	60	plastic	5	5.5	
316	binary	plastic	3,5	30.00	70	plastic	5	5.5	
317	binary	plastic	3,5	30.00	80	plastic	5	5.5	

Continued on next page...

Table D.5 – Continued

Run	Fill			Load	Speed	Tracer		Locations	Comments
	Distribution	Material	Diameter /mm	/%	/% v_{crit}	Material	Diameter /mm		
318	binary	plastic	3,5	30.00	90	plastic	5	5.5	
319	binary	plastic	3,5	40.00	60	plastic	5	5.5	
320	binary	plastic	3,5	40.00	70	plastic	5	5.5	
321	binary	plastic	3,5	40.00	80	plastic	5	5.5	
322	binary	plastic	3,5	40.00	90	plastic	5	5.5	
352-355	xxx	xxx	xxx	xxx	xxx	xxx	xxx	xxx	Loc 5.5

D.1.6 uct07: June and July 2009

These experiments were performed from the 17th of June to the 13th of July 2009. They were performed on the 140 mm diameter 'x-ray' mill, the 'old 300 mm mill' and the 'new 300 mm mill'. Details of the various experiments are given in Table D.6.

Experimenters

These experiments were performed by Drs. Indresan Govender and Aubrey Mainza, MrAngus Morrison, Mr Lawrence Bbosa, and Mr. Andre van der Westhuizen of the UCT CMR.

Notes

d is the diameter of the particle. The height of the lifters of all 3 mills were $5mm$.

Table D.6: Experiments on various mills

Run	Mill	Lifter	Fill			Load	Speed	Tracer		Locations	Comments
		Angle/°	Distr	Wet/dry	d /mm	/%	/% v_{crit}	Mat.	d /mm		
001	X-ray	45	binary	dry	3,5	30.00	80	plastic	5	xxx	Failed due to disk space.
002	X-ray	45	binary	dry	3,5	30.00	80	plastic	5	xxx	Speed error
003	X-ray	45	binary	dry	3,5	30.00	80	plastic	5	7.1	
004	X-ray	45	binary	dry	3,5	30.00	60	plastic	5	xxx	Failed
005	X-ray	45	binary	dry	3,5	30.00	60	plastic	5	7.1	
006-009	X-ray	xxx	xxx	xxx	xxx	xxx	xxx	xxx	xxx	xxx	Location markers 7.1
010-013	X-ray	xxx	xxx	xxx	xxx	xxx	xxx	xxx	xxx	xxx	Shell stationaries
014-016	X-ray	xxx	xxx	xxx	xxx	xxx	xxx	xxx	xxx	xxx	Charge stationaries
017	X-ray	45	binary	dry	3,5	30.00	80	plastic	3	7.1	
018	X-ray	xxx	xxx	xxx	xxx	xxx	xxx	xxx	xxx	xxx	Charge stationary
019	X-ray	45	binary	dry	3,5	30.00	60	plastic	3	7.1	
020	X-ray	xxx	xxx	xxx	xxx	xxx	xxx	xxx	xxx	xxx	Charge stationary
021	X-ray	45	binary	dry	3,5	30.00	70	plastic	3	7.1	
022	X-ray	xxx	xxx	xxx	xxx	xxx	xxx	xxx	xxx	xxx	Charge stationary
023	X-ray	45	binary	dry	3,5	30.00	70	plastic	5	7.1	
024-028	X-ray	xxx	xxx	xxx	xxx	xxx	xxx	xxx	xxx	xxx	Charge stationaries
029	Old	xxx	xxx	xxx	xxx	xxx	xxx	xxx	xxx	xxx	Charge stationary
030	Old	60	R-R	dry	2-8	31.25	75	glass	2	7.2	
031	Old	xxx	xxx	xxx	xxx	xxx	xxx	xxx	xxx	xxx	Charge stationary
032	Old	60	R-R	dry	2-8	31.25	60	glass	2	xxx	Stopped to fit antistatic hose
033	Old	60	R-R	dry	2-8	31.25	60	glass	2	7.2	

Continued on next page...

Table D.6 – Continued

Run	Mill	Lifter	Fill			Load	Speed	Tracer		Locations	Comments
		Angle/°	Distr	Wet/dry	d /mm	/%	/% v_{crit}	Mat.	d /mm		
034-035	Old	xxx	xxx	xxx	xxx	xxx	xxx	xxx	xxx	xxx	Charge stationary
036	Old	60	R-R	dry	2-8	31.25	75	glass	3	xxx	Mill stopped before run.
037	Old	60	R-R	dry	2-8	31.25	60	glass	3	7.2	Same as 44
038	Old	xxx	xxx	xxx	xxx	xxx	xxx	xxx	xxx	xxx	Charge stationary
039-042	Old	xxx	xxx	xxx	xxx	xxx	xxx	xxx	xxx	xxx	Location markers 7.2
043	Old	60	R-R	dry	2-8	31.25	75	glass	3	7.2	
044	Old	60	R-R	dry	2-8	31.25	60	glass	3	7.2	Same as 37
045	Old	60	R-R	dry	2-8	31.25	75	glass	4	7.2	
046	Old	60	R-R	dry	2-8	31.25	60	glass	4	7.2	
047	Old	60	R-R	dry	2-8	31.25	60	glass	5	7.2	
048	Old	60	R-R	dry	2-8	31.25	75	glass	5	7.2	
049-051	Old	xxx	xxx	xxx	xxx	xxx	xxx	xxx	xxx	xxx	Charge stationaries
52	Old	60	R-R	dry	2-8	31.25	75	glass	6	xxx	Run stopped
53	Old	60	R-R	dry	2-8	31.25	75	glass	6	7.2	
54	Old	xxx	xxx	xxx	xxx	xxx	xxx	xxx	xxx	xxx	Charge stationary
55	Old	60	R-R	dry	2-8	31.25	60	glass	6	7.2	
56	Old	60	R-R	dry	2-8	31.25	75	glass	8	7.2	
57	Old	xxx	xxx	xxx	xxx	xxx	xxx	xxx	xxx	xxx	Charge stationary
58	Old	60	R-R	dry	2-8	31.25	60	glass	8	7.2	
59	Old	xxx	xxx	xxx	xxx	xxx	xxx	xxx	xxx	xxx	Charge stationary
060-101	IsaMill	xxx	xxx	xxx	xxx	xxx	xxx	xxx	xxx	xxx	
102	Old	60	mono	dry	3	31.25	75	glass	3	7.2	

Continued on next page...

Table D.6 – Continued

Run	Mill	Lifter	Fill			Load	Speed	Tracer		Locations	Comments
		Angle/°	Distr	Wet/dry	d /mm	/%	/% v_{crit}	Mat.	d /mm		
103	Old	60	mono	dry	3	31.25	60	glass	3	7.2	
104-106	Old	xxx	xxx	xxx	xxx	xxx	xxx	xxx	xxx	xxx	Charge stationary
107-110	Old	xxx	xxx	xxx	xxx	xxx	xxx	xxx	xxx	xxx	Location markers 7.3
111	Old	60	mono	dry	5	31.25	75	glass	5	7.3	
112	Old	60	mono	dry	5	31.25	60	glass	5	7.3	
113	Old	60	mono	dry	5	31.25	50	glass	5	7.3	
114-116	Old	xxx	xxx	xxx	xxx	xxx	xxx	xxx	xxx	xxx	Charge stationaries
117	New	60	mono	dry	3	31.25	75	glass	3	7.4	
118	New	60	mono	dry	3	31.25	60	glass	3	7.4	
119-122	New	xxx	xxx	xxx	xxx	xxx	xxx	xxx	xxx	xxx	Charge stationaries
123-125	New	xxx	xxx	xxx	xxx	xxx	xxx	xxx	xxx	xxx	Location markers 7.4
126	New	60	mono	dry	5	31.25	75	glass	5	7.4	
127	New	60	mono	dry	5	31.25	60	glass	5	7.4	
128	New	60	mono	dry	5	31.25	31	glass	5	7.4	
129-131	New	xxx	xxx	xxx	xxx	xxx	xxx	xxx	xxx	xxx	Charge stationaries
132-155	IsaMill	xxx	xxx	xxx	xxx	xxx	xxx	xxx	xxx	xxx	
156	New	60	mono	wet	3	31.25	75	glass	3	xxx	Stopped for activity
157	New	60	mono	wet	3	31.25	75	glass	3	7.5	
158-160	New	xxx	xxx	xxx	xxx	xxx	xxx	xxx	xxx	xxx	Charge stationaries
161	New	60	mono	wet	5	31.25	75	glass	5	xxx	Pump problems
162	New	60	mono	wet	5	31.25	75	glass	5	xxx	Stopped
163	New	60	mono	wet	5	31.25	75	glass	5	7.5	

Continued on next page...

Table D.6 – Continued

Run	Mill	Lifter	Fill			Load	Speed	Tracer		Locations	Comments
		Angle/°	Distr	Wet/dry	d /mm	/%	/% v_{crit}	Mat.	d /mm		
164	New	60	mono	wet	5	31.25	75	resin	0.5	xxx	Particle stuck in inlet
165	New	60	mono	wet	5	31.25	75	resin	0.5	xxx	Lost particle, pump blew
166	New	60	mono	wet	5	31.25	75	resin	0.5	xxx	Lost particle
167	New	60	mono	wet	5	31.25	75	resin	0.5	7.5	Recirculated by hand
168	New	60	mono	wet	5	31.25	75	resin	0.5	7.5	Recirculated by hand
169	New	60	mono	20% slurry	5	31.25	75	glass	5	7.5	
170	New	60	mono	20% slurry	5	31.25	60	glass	5	7.5	
171	New	60	mono	30% slurry	5	31.25	75	glass	5	7.5	
172	New	xxx	xxx	xxx	xxx	xxx	xxx	xxx	xxx	xxx	Not recorded
173	New	60	Monosize	30% slurry	5	31.25	60	glass	5	xxx	Losing slurry
174-176	New	xxx	xxx	xxx	xxx	xxx	xxx	xxx	xxx	xxx	Location markers 7.5
177	New	60	mono	30% slurry	5	31.25	60	glass	5	7.5	
178	New	60	mono	40% slurry	5	31.25	75	glass	5	7.5	
179-181	New	xxx	xxx	xxx	xxx	xxx	xxx	xxx	xxx	xxx	Charge stationaries
182	New	60	mono	40% slurry	5	31.25	60	glass	5	7.5	
183	New	60	mono	20% slurry	5	31.25	75	resin	0.5	7.5	
184	New	60	mono	40% slurry	5	31.25	60	stone	1	7.5	
185	New	60	mono	40% slurry	5	31.25	75	stone	1	7.5	
186-188	New	xxx	xxx	xxx	xxx	xxx	xxx	xxx	xxx	xxx	Charge stationaries
189	New	60	mono	20% slurry	5	31.25	75	stone	1	xxx	Particle stuck
190	New	60	mono	20% slurry	5	31.25	75	stone	1	7.5	
191	New	60	mono	20% slurry	5	31.25	60	stone	1	xxx	Particle stuck
192	New	60	mono	20% slurry	5	31.25	60	stone	1	7.5	

Continued on next page...

Table D.6 – Continued

Run	Mill	Lifter	Fill			Load	Speed	Tracer		Locations	Comments
		Angle/°	Distr	Wet/dry	d /mm	/%	/% v_{crit}	Mat.	d /mm		
193	New	xxx	xxx	xxx	xxx	xxx	xxx	xxx	xxx	xxx	Error-moving mill
194-196	New	xxx	xxx	xxx	xxx	xxx	xxx	xxx	xxx	xxx	Charge stationaries
197	New	60	mono	30% slurry	5	31.25	60	stone	1	xxx	Particle lost
198	New	60	mono	30% slurry	5	31.25	60	stone	1	7.5	Low activity
199	New	60	mono	30% slurry	5	31.25	75	stone	1	xxx	Particle stuck
200	New	60	mono	30% slurry	5	31.25	75	stone	1	xxx	Pump problems
201	New	60	mono	30% slurry	5	31.25	75	stone	1	7.5	
202	New	60	mono	30% slurry	5	31.25	75	stone	1	7.5	
203	New	60	mono	30% slurry	5	31.25	60	stone	1	7.5	
204	New	60	mono	30% slurry	5	31.25	60	stone	1	7.5	
205	New	60	mono	30% slurry	5	31.25	60	stone	1	7.5	
206-208	New	xxx	xxx	xxx	xxx	xxx	xxx	xxx	xxx	xxx	Charge stationaries
209-211	New	xxx	xxx	xxx	xxx	xxx	xxx	xxx	xxx	xxx	Location markers 7.6
212	New	60	mono	wet	5	31.25	60	glass	5	7.6	
213-215	New	xxx	xxx	xxx	xxx	xxx	xxx	xxx	xxx	xxx	Charge stationaries
216	New	60	mono	wet	5	31.25	31	glass	5	xxx	Pump problems
217	New	60	mono	wet	5	31.25	31	glass	5	7.6	
218	New	60	mono	wet	5	31.25	60	glass	5	7.6	
219	New	60	mono	wet	5	31.25	50	glass	5	7.6	
220-222	New	xxx	xxx	xxx	xxx	xxx	xxx	xxx	xxx	xxx	Charge stationaries

D.2 A complete list of experiments by mill

D.2.1 The old 300mm mill

All of the experiments performed on the 'old 300 mm mill' at the University of Birmingham's Positron Imaging Centre between 2006 and 2009 are given in Table D.7.

Notes

d is the diameter of the particle, and h is the height of the lifters. $R-R$ stands for Rosin-Rammler, and *stone* is short for *bluestone*.

Table D.7: Old 300 mm mill experiments

Series	Run	Lifter		Fill				Load	Speed	Tracer		Locations	Comments
		Angle/°	h /mm	Distr	Wet/dry	Material	d /mm	/%	/% v_{crit}	Material	Size /mm		
uct01	026-028	xxx	xxx	xxx	xxx	xxx	xxx	xxx	xxx	xxx	xxx	xxx	Loc 1.1
uct01	029	60	19	R-R	dry	stone	2-8	24.63	80	stone	6x2 (rect)	1.1	
uct01	030	60	19	R-R	dry	stone	2-8	24.63	75	stone	6x2 (rect)	1.1	
uct01	031	60	19	R-R	dry	stone	2-8	24.63	65	stone	6x2 (rect)	1.1	
uct01	032	90	19	R-R	dry	stone	2-8	24.63	95	stone	6x2 (rect)	1.1	
uct01	033	90	19	R-R	dry	stone	2-8	24.63	90	stone	6x2 (rect)	1.1	
uct01	034	90	19	R-R	dry	stone	2-8	24.63	85	stone	6x2 (rect)	1.1	
uct01	035	90	19	R-R	dry	stone	2-8	24.63	80	stone	6x2 (rect)	1.1	
uct01	036	90	19	R-R	dry	stone	2-8	24.63	75	stone	6x2 (rect)	1.1	
uct01	037	90	19	R-R	dry	stone	2-8	24.63	65	stone	6x2 (rect)	1.1	
uct01	038	90	19	R-R	dry	stone	2-8	30.00	95	stone	6x2 (rect)	1.1	
uct01	039	90	19	R-R	dry	stone	2-8	30.00	90	stone	6x2 (rect)	1.1	
uct01	040	90	19	R-R	dry	stone	2-8	30.00	85	stone	6x2 (rect)	1.1	
uct01	041	90	19	R-R	dry	stone	2-8	30.00	80	stone	6x2 (rect)	1.1	
uct01	043	90	19	R-R	dry	stone	2-8	30.00	75	stone	6x2 (rect)	1.1	
uct01	044	90	19	R-R	dry	stone	2-8	30.00	65	stone	6x2 (rect)	1.1	
uct01	045	60	19	R-R	dry	stone	2-8	30.00	95	stone	6x2 (rect)	1.1	
uct01	046	60	19	R-R	dry	stone	2-8	30.00	90	stone	6x2 (rect)	1.1	
uct01	047	60	19	R-R	dry	stone	2-8	30.00	85	stone	6x2 (rect)	1.1	
uct01	048	60	19	R-R	dry	stone	2-8	30.00	80	stone	6x2 (rect)	1.1	
uct01	049	60	19	R-R	dry	stone	2-8	30.00	75	stone	6x2 (rect)	1.1	
uct01	050	60	19	R-R	dry	stone	2-8	30.00	65	stone	6x2 (rect)	1.1	
uct01	051	60	19	R-R	dry	stone	2-8	35.00	95	stone	6x2 (rect)	1.1	

Continued on next page...

Table D.7 – Continued

Series	Run	Lifter		Fill				Load	Speed	Tracer		Locations	Comments
		Angle/°	h /mm	Distr	Wet/dry	Material	d /mm	/%	/% v_{crit}	Material	Size /mm		
uct01	052	60	19	R-R	dry	stone	2-8	35.00	90	stone	6x2 (rect)	1.1	
uct01	053	60	19	R-R	dry	stone	2-8	35.00	85	stone	6x2 (rect)	1.1	
uct01	054	60	19	R-R	dry	stone	2-8	35.00	80	stone	6x2 (rect)	1.1	
uct01	055	60	19	R-R	dry	stone	2-8	35.00	75	stone	6x2 (rect)	1.1	
uct01	056	60	19	R-R	dry	stone	2-8	35.00	65	stone	6x2 (rect)	1.1	
uct01	057	90	19	R-R	dry	stone	2-8	35.00	95	stone	6x2 (rect)	1.1	
uct01	058	90	19	R-R	dry	stone	2-8	35.00	90	stone	6x2 (rect)	1.1	
uct01	059	90	19	R-R	dry	stone	2-8	35.00	85	stone	6x2 (rect)	1.1	
uct01	060	90	19	R-R	dry	stone	2-8	35.00	80	stone	6x2 (rect)	1.1	
uct01	061	90	19	R-R	dry	stone	2-8	35.00	75	stone	6x2 (rect)	1.1	
uct01	062	90	19	R-R	dry	stone	2-8	35.00	65	stone	6x2 (rect)	1.1	
uct01	063	90	19	R-R	dry	stone	2-8	40.00	95	stone	6x2 (rect)	1.1	
uct01	064	90	19	R-R	dry	stone	2-8	40.00	90	stone	6x2 (rect)	1.1	
uct01	065	90	19	R-R	dry	stone	2-8	40.00	85	stone	6x2 (rect)	1.1	
uct01	066	90	19	R-R	dry	stone	2-8	40.00	80	stone	6x2 (rect)	1.1	
uct01	067	90	19	R-R	dry	stone	2-8	40.00	75	stone	6x2 (rect)	1.1	
uct01	068	90	19	R-R	dry	stone	2-8	40.00	65	stone	6x2 (rect)	1.1	
uct01	069	60	19	R-R	dry	stone	2-8	40.00	95	stone	6x2 (rect)	1.1	
uct01	070	60	19	R-R	dry	stone	2-8	40.00	90	stone	6x2 (rect)	1.1	
uct01	071	60	19	R-R	dry	stone	2-8	40.00	85	stone	6x2 (rect)	1.1	
uct01	072	60	19	R-R	dry	stone	2-8	40.00	80	stone	6x2 (rect)	1.1	
uct01	073	60	19	R-R	dry	stone	2-8	40.00	75	stone	6x2 (rect)	1.1	
uct01	074	60	19	R-R	dry	stone	2-8	40.00	65	stone	6x2 (rect)	1.1	

Continued on next page...

Table D.7 – Continued

Series	Run	Lifter		Fill				Load	Speed	Tracer		Locations	Comments
		Angle/°	h /mm	Distr	Wet/dry	Material	d /mm	/%	/% v_{crit}	Material	Size /mm		
uct01	075-077	xxx	xxx	xxx	xxx	xxx	xxx	xxx	xxx	xxx	xxx	xxx	Loc 1.2
uct01	078	60	19	R-R	dry	stone	2-8	15.00	95	stone	5	1.2	
uct01	080	60	19	R-R	dry	stone	2-8	15.00	90	stone	5	1.2	
uct01	081	60	19	R-R	dry	stone	2-8	15.00	85	stone	5	1.2	
uct01	082	60	19	R-R	dry	stone	2-8	15.00	80	stone	5	1.2	
uct01	083	60	19	R-R	dry	stone	2-8	15.00	75	stone	5	1.2	
uct01	084	60	19	R-R	dry	stone	2-8	15.00	65	stone	5	1.2	
uct01	085	90	19	R-R	dry	stone	2-8	15.00	95	stone	5	1.2	
uct01	086	90	19	R-R	dry	stone	2-8	15.00	90	stone	5	1.2	
uct01	087	90	19	R-R	dry	stone	2-8	15.00	85	stone	5	1.2	
uct01	088	90	19	R-R	dry	stone	2-8	15.00	80	stone	5	1.2	
uct01	089	90	19	R-R	dry	stone	2-8	15.00	75	stone	5	1.2	
uct01	090	90	19	R-R	dry	stone	2-8	15.00	65	stone	5	1.2	
uct01	091	90	19	R-R	dry	stone	2-8	23.60	95	stone	5	1.2	
uct01	092	90	19	R-R	dry	stone	2-8	23.60	90	stone	5	1.2	
uct01	093	90	19	R-R	dry	stone	2-8	35.00	95	stone	5	1.2	
uct01	094	90	19	R-R	dry	stone	2-8	35.00	90	stone	5	1.2	
uct01	095	90	19	R-R	dry	stone	2-8	35.00	85	stone	5	1.2	
uct01	096	90	19	R-R	dry	stone	2-8	35.00	80	stone	5	1.2	
uct01	097	90	19	R-R	dry	stone	2-8	35.00	75	stone	5	1.2	
uct01	098	90	19	R-R	dry	stone	2-8	35.00	65	stone	5	1.2	
uct01	099	60	19	R-R	dry	stone	2-8	35.00	95	stone	5	1.2	
uct01	100	60	19	R-R	dry	stone	2-8	35.00	90	stone	5	1.2	

Continued on next page...

Table D.7 – Continued

Series	Run	Lifter		Fill				Load	Speed	Tracer		Locations	Comments
		Angle/°	h /mm	Distr	Wet/dry	Material	d /mm	/%	/% v_{crit}	Material	Size /mm		
uct01	101	60	19	R-R	dry	stone	2-8	35.00	85	stone	5	1.2	
uct01	102	60	19	R-R	dry	stone	2-8	35.00	80	stone	5	1.2	
uct01	103	60	19	R-R	dry	stone	2-8	35.00	75	stone	5	1.2	
uct01	104	60	19	R-R	dry	stone	2-8	35.00	65	stone	5	1.2	
uct01	105	60	19	R-R	dry	stone	2-8	40.00	95	stone	5	1.2	
uct01	106	60	19	R-R	dry	stone	2-8	40.00	90	stone	5	1.2	
uct01	107	60	19	R-R	dry	stone	2-8	40.00	85	stone	5	1.2	
uct01	108	60	19	R-R	dry	stone	2-8	40.00	80	stone	5	1.2	
uct01	109	60	19	R-R	dry	stone	2-8	40.00	75	stone	5	1.2	
uct01	110	60	19	R-R	dry	stone	2-8	40.00	65	stone	5	1.2	
uct01	111	90	19	R-R	dry	stone	2-8	40.00	95	stone	5	1.2	
uct01	112	90	19	R-R	dry	stone	2-8	40.00	90	stone	5	1.2	
uct01	113	90	19	R-R	dry	stone	2-8	40.00	85	stone	5	1.2	
uct01	114	90	19	R-R	dry	stone	2-8	40.00	80	stone	5	1.2	
uct01	115	90	19	R-R	dry	stone	2-8	40.00	75	stone	5	1.2	
uct01	116	90	19	R-R	dry	stone	2-8	40.00	65	stone	5	1.2	
uct02	001-003	xxx	xxx	xxx	xxx	xxx	xxx	xxx	xxx	xxx	xxx	xxx	Loc 2.1
uct02	004	90	5	R-R	dry	stone	2-8	15.00	95	stone	2	2.1	
uct02	005	90	5	R-R	dry	stone	2-8	15.00	90	stone	2	2.1	
uct02	006	90	5	R-R	dry	stone	2-8	15.00	85	stone	2	2.1	
uct02	007	90	5	R-R	dry	stone	2-8	15.00	80	stone	2	2.1	
uct02	008	90	5	R-R	dry	stone	2-8	15.00	75	stone	2	2.1	
uct02	009	90	5	R-R	dry	stone	2-8	15.00	65	stone	2	2.1	

Continued on next page...

Table D.7 – Continued

Series	Run	Lifter		Fill				Load	Speed	Tracer		Locations	Comments
		Angle/°	h /mm	Distr	Wet/dry	Material	d /mm	/%	/% v_{crit}	Material	Size /mm		
uct02	010	60	5	R-R	dry	stone	2-8	15.00	95	stone	2	2.1	
uct02	011	60	5	R-R	dry	stone	2-8	15.00	90	stone	2	2.1	
uct02	012	60	5	R-R	dry	stone	2-8	15.00	85	stone	2	2.1	
uct02	013	60	5	R-R	dry	stone	2-8	15.00	80	stone	2	2.1	
uct02	014	60	5	R-R	dry	stone	2-8	15.00	75	stone	2	2.1	
uct02	015	60	5	R-R	dry	stone	2-8	15.00	65	stone	2	2.1	
uct02	016	60	5	R-R	dry	stone	2-8	35.00	95	stone	2	2.1	
uct02	017	60	5	R-R	dry	stone	2-8	35.00	90	stone	2	2.1	
uct02	018	60	5	R-R	dry	stone	2-8	35.00	85	stone	2	2.1	
uct02	019	60	5	R-R	dry	stone	2-8	35.00	80	stone	2	2.1	
uct02	020	60	5	R-R	dry	stone	2-8	35.00	75	stone	2	2.1	
uct02	021	60	5	R-R	dry	stone	2-8	35.00	65	stone	2	2.1	
uct02	022	90	5	R-R	dry	stone	2-8	35.00	95	stone	2	2.1	
uct02	023	90	5	R-R	dry	stone	2-8	35.00	90	stone	2	2.1	
uct02	024	90	5	R-R	dry	stone	2-8	35.00	85	stone	2	2.1	
uct02	025	90	5	R-R	dry	stone	2-8	35.00	80	stone	2	2.1	
uct02	026	90	5	R-R	dry	stone	2-8	35.00	75	stone	2	2.1	
uct02	027	90	5	R-R	dry	stone	2-8	35.00	65	stone	2	2.1	
uct02	028	90	5	R-R	dry	stone	2-8	40.00	95	stone	2	2.1	
uct02	029	90	5	R-R	dry	stone	2-8	40.00	90	stone	2	2.1	
uct02	030	90	5	R-R	dry	stone	2-8	40.00	85	stone	2	2.1	
uct02	031	90	5	R-R	dry	stone	2-8	40.00	80	stone	2	2.1	
uct02	032	90	5	R-R	dry	stone	2-8	40.00	75	stone	2	2.1	

Continued on next page...

Table D.7 – Continued

Series	Run	Lifter		Fill				Load	Speed	Tracer		Locations	Comments
		Angle/°	h /mm	Distr	Wet/dry	Material	d /mm	/%	/% v_{crit}	Material	Size /mm		
uct02	033	90	5	R-R	dry	stone	2-8	40.00	65	stone	2	2.1	
uct02	034	60	5	R-R	dry	stone	2-8	40.00	95	stone	2	2.1	
uct02	035	60	5	R-R	dry	stone	2-8	40.00	90	stone	2	2.1	
uct02	036	60	5	R-R	dry	stone	2-8	40.00	85	stone	2	2.1	
uct02	037	60	5	R-R	dry	stone	2-8	40.00	80	stone	2	2.1	
uct02	038	60	5	R-R	dry	stone	2-8	40.00	75	stone	2	2.1	
uct02	039	60	5	R-R	dry	stone	2-8	40.00	65	stone	2	2.1	
uct02	055	90	5	R-R	30% slurry	stone	2-8	40.00	95	stone	1	2.1	
uct02	056	90	5	R-R	30% slurry	stone	2-8	40.00	90	stone	1	2.1	
uct02	057	90	5	R-R	30% slurry	stone	2-8	40.00	85	stone	1	2.1	
uct02	058	90	5	R-R	30% slurry	stone	2-8	40.00	80	stone	1	2.1	
uct02	059	90	5	R-R	30% slurry	stone	2-8	40.00	75	stone	1	2.1	
uct02	060	90	5	R-R	30% slurry	stone	2-8	40.00	65	stone	1	2.1	
uct03	001-003	xxx	xxx	xxx	xxx	xxx	xxx	xxx	xxx	xxx	xxx	xxx	Loc 3.1
uct03	004	90	5	R-R	30% slurry	stone	2-8	40.00	75	stone	1	3.1	
uct03	005	90	5	R-R	30% slurry	stone	2-8	40.00	75	stone	1	3.1	
uct03	006	90	5	R-R	30% slurry	stone	2-8	40.00	75	stone	1	3.1	
uct03	007	90	5	R-R	30% slurry	stone	2-8	40.00	75	stone	1	3.1	
uct03	009	90	5	R-R	30% slurry	stone	2-8	40.00	85	copper	1	3.1	
uct03	010	90	5	R-R	30% slurry	stone	2-8	40.00	75	copper	1	3.1	
uct03	012	90	5	R-R	30% slurry	stone	2-8	40.00	75	copper	1	3.1	
uct03	013	90	5	R-R	30% slurry	stone	2-8	40.00	65	stone	1	3.1	
uct03	014-016	xxx	xxx	xxx	xxx	xxx	xxx	xxx	xxx	xxx	xxx	xxx	Loc 3.2

Continued on next page...

Table D.7 – Continued

Series	Run	Lifter		Fill				Load	Speed	Tracer		Locations	Comments
		Angle/°	h /mm	Distr	Wet/dry	Material	d /mm	/%	/% v_{crit}	Material	Size /mm		
uct03	017	90	5	R-R	30% slurry	stone	2-8	40.00	100	stone	1	3.2	
uct03	018	90	5	R-R	30% slurry	stone	2-8	40.00	95	stone	1	3.2	
uct03	019	90	5	R-R	30% slurry	stone	2-8	40.00	55	stone	1	3.2	
uct03	020	90	5	R-R	30% slurry	stone	2-8	40.00	65	stone	1	3.2	
uct03	021	90	5	R-R	30% slurry	stone	2-8	40.00	70	stone	1	3.2	
uct03	022	90	5	R-R	30% slurry	stone	2-8	40.00	75	stone	1	3.2	
uct03	023	90	5	R-R	30% slurry	stone	2-8	40.00	80	stone	1	3.2	
uct03	024	90	5	R-R	30% slurry	stone	2-8	40.00	85	stone	1	3.2	
uct03	025	90	5	R-R	30% slurry	stone	2-8	40.00	90	stone	1	3.2	
uct04	001-003	xxx	xxx	xxx	xxx	xxx	xxx	xxx	xxx	xxx	xxx	xxx	Loc 4.1
uct04	004	90	5	R-R	dry	glass	2-8	12.50	90	glass	4	4.1	
uct04	005	90	5	R-R	dry	glass	2-8	12.50	80	glass	4	4.1	
uct04	006	90	5	R-R	dry	glass	2-8	12.50	75	glass	4	4.1	
uct04	007	90	5	R-R	dry	glass	2-8	12.50	70	glass	4	4.1	
uct04	008	90	5	R-R	dry	glass	2-8	12.50	60	glass	4	4.1	
uct04	009	90	5	R-R	dry	glass	2-8	25.00	90	glass	4	4.2	
uct04	010	90	5	R-R	dry	glass	2-8	25.00	80	glass	4	4.2	
uct04	011	90	5	R-R	dry	glass	2-8	25.00	75	glass	4	4.2	
uct04	012	90	5	R-R	dry	glass	2-8	25.00	70	glass	4	4.2	
uct04	013	90	5	R-R	dry	glass	2-8	25.00	60	glass	4	4.2	
uct04	014	90	5	R-R	dry	glass	2-8	31.25	90	glass	4	4.2	
uct04	015	90	5	R-R	dry	glass	2-8	31.25	80	glass	4	4.2	
uct04	016	90	5	R-R	dry	glass	2-8	31.25	75	glass	4	4.2	

Continued on next page...

Table D.7 – Continued

Series	Run	Lifter		Fill				Load	Speed	Tracer		Locations	Comments
		Angle/°	h /mm	Distr	Wet/dry	Material	d /mm	/%	/% v_{crit}	Material	Size /mm		
uct04	017	90	5	R-R	dry	glass	2-8	31.25	70	glass	4	4.2	
uct04	019	90	5	R-R	dry	glass	2-8	31.25	60	glass	4	4.2	
uct04	020	90	5	R-R	dry	glass	2-8	37.50	90	glass	4	4.2	
uct04	021	90	5	R-R	dry	glass	2-8	37.50	80	glass	4	4.2	
uct04	022	90	5	R-R	dry	glass	2-8	37.50	75	glass	4	4.2	
uct04	023	90	5	R-R	dry	glass	2-8	37.50	70	glass	4	4.2	
uct04	024	90	5	R-R	dry	glass	2-8	37.50	60	glass	4	4.2	
uct04	025	90	5	R-R	dry	glass	2-8	50.00	90	glass	4	4.2	
uct04	026	90	5	R-R	dry	glass	2-8	50.00	80	glass	4	4.2	
uct04	027	90	5	R-R	dry	glass	2-8	50.00	75	glass	4	4.2	
uct04	028	90	5	R-R	dry	glass	2-8	50.00	70	glass	4	4.2	
uct04	029	90	5	R-R	dry	glass	2-8	50.00	60	glass	4	4.2	
uct04	030	xxx	xxx	xxx	xxx	xxx	xxx	xxx	xxx	xxx	xxx	xxx	Loc 4.2
uct04	031	90	5	R-R	dry	glass	2-8	12.50	90	glass	3	4.2	
uct04	032	90	5	R-R	dry	glass	2-8	12.50	80	glass	3	4.2	
uct04	033	90	5	R-R	dry	glass	2-8	12.50	75	glass	3	4.2	
uct04	034	90	5	R-R	dry	glass	2-8	12.50	70	glass	3	4.2	
uct04	035	90	5	R-R	dry	glass	2-8	12.50	60	glass	3	4.2	
uct04	036	90	5	R-R	dry	glass	2-8	25.00	90	glass	3	4.2	
uct04	037	90	5	R-R	dry	glass	2-8	25.00	80	glass	3	4.2	
uct04	038	90	5	R-R	dry	glass	2-8	25.00	75	glass	3	4.2	
uct04	039	90	5	R-R	dry	glass	2-8	25.00	70	glass	3	4.2	
uct04	040	90	5	R-R	dry	glass	2-8	25.00	60	glass	3	4.2	

Continued on next page...

Table D.7 – Continued

Series	Run	Lifter		Fill				Load	Speed	Tracer		Locations	Comments
		Angle/°	h /mm	Distr	Wet/dry	Material	d /mm	/%	/% v_{crit}	Material	Size /mm		
uct04	041	90	5	R-R	dry	glass	2-8	31.25	90	glass	3	4.2	
uct04	042	90	5	R-R	dry	glass	2-8	31.25	80	glass	3	4.2	
uct04	043	90	5	R-R	dry	glass	2-8	31.25	75	glass	3	4.2	
uct04	044	90	5	R-R	dry	glass	2-8	31.25	70	glass	3	4.2	
uct04	045	90	5	R-R	dry	glass	2-8	31.25	60	glass	3	4.2	
uct04	046	90	5	R-R	dry	glass	2-8	37.50	90	glass	3	4.2	
uct04	047	90	5	R-R	dry	glass	2-8	37.50	80	glass	3	4.2	
uct04	048	90	5	R-R	dry	glass	2-8	37.50	75	glass	3	4.2	
uct04	049	90	5	R-R	dry	glass	2-8	37.50	70	glass	3	4.2	
uct04	050	90	5	R-R	dry	glass	2-8	37.50	60	glass	3	4.2	
uct04	051	90	5	R-R	dry	glass	2-8	50.00	90	glass	3	4.2	
uct04	052	90	5	R-R	dry	glass	2-8	50.00	80	glass	3	4.2	
uct04	053	90	5	R-R	dry	glass	2-8	50.00	75	glass	3	4.2	
uct04	054	90	5	R-R	dry	glass	2-8	50.00	70	glass	3	4.2	
uct04	055	90	5	R-R	dry	glass	2-8	50.00	60	glass	3	4.2	
uct04	056 - 059	xxx	xxx	xxx	xxx	xxx	xxx	xxx	xxx	xxx	xxx	xxx	Loc 4.3
uct04	060	90	5	R-R	dry	glass	2-8	12.50	90	glass	5	4.3	
uct04	061	90	5	R-R	dry	glass	2-8	12.50	80	glass	5	4.3	
uct04	062	90	5	R-R	dry	glass	2-8	12.50	75	glass	5	4.3	
uct04	063	90	5	R-R	dry	glass	2-8	12.50	70	glass	5	4.3	
uct04	064	90	5	R-R	dry	glass	2-8	12.50	60	glass	5	4.3	
uct04	065	90	5	R-R	dry	glass	2-8	12.50	85	glass	5	4.3	
uct04	066	90	5	R-R	dry	glass	2-8	25.00	90	glass	5	4.3	

Continued on next page...

Table D.7 – Continued

Series	Run	Lifter		Fill				Load	Speed	Tracer		Locations	Comments
		Angle/°	h /mm	Distr	Wet/dry	Material	d /mm	/%	/% v_{crit}	Material	Size /mm		
uct04	067	90	5	R-R	dry	glass	2-8	25.00	80	glass	5	4.3	
uct04	068	90	5	R-R	dry	glass	2-8	25.00	75	glass	5	4.3	
uct04	069	90	5	R-R	dry	glass	2-8	25.00	70	glass	5	4.3	
uct04	070	90	5	R-R	dry	glass	2-8	25.00	60	glass	5	4.3	
uct04	071	90	5	R-R	dry	glass	2-8	31.25	90	glass	5	4.3	
uct04	072	90	5	R-R	dry	glass	2-8	31.25	80	glass	5	4.3	
uct04	074	90	5	R-R	dry	glass	2-8	31.25	75	glass	5	4.3	
uct04	075	90	5	R-R	dry	glass	2-8	31.25	70	glass	5	4.3	
uct04	076	90	5	R-R	dry	glass	2-8	31.25	60	glass	5	4.3	
uct04	077	90	5	R-R	dry	glass	2-8	37.50	90	glass	5	4.3	
uct04	078	90	5	R-R	dry	glass	2-8	37.50	80	glass	5	4.3	
uct04	079	90	5	R-R	dry	glass	2-8	37.50	75	glass	5	4.3	
uct04	080	90	5	R-R	dry	glass	2-8	37.50	70	glass	5	4.3	
uct04	081	90	5	R-R	dry	glass	2-8	37.50	60	glass	5	4.3	
uct04	082	90	5	R-R	dry	glass	2-8	50.00	90	glass	5	4.3	
uct04	083	90	5	R-R	dry	glass	2-8	50.00	80	glass	5	4.3	
uct04	084	90	5	R-R	dry	glass	2-8	50.00	75	glass	5	4.3	
uct04	085	90	5	R-R	dry	glass	2-8	50.00	70	glass	5	4.3	
uct04	086	90	5	R-R	dry	glass	2-8	50.00	60	glass	5	4.3	
uct04	088-089	xxx	xxx	xxx	xxx	xxx	xxx	xxx	xxx	xxx	xxx	xxx	Loc 4.4
uct04	090	90	5	R-R	dry	glass	2-8	12.50	90	glass	6	4.4	
uct04	091	90	5	R-R	dry	glass	2-8	12.50	80	glass	6	4.4	
uct04	092	90	5	R-R	dry	glass	2-8	12.50	75	glass	6	4.4	

Continued on next page...

Table D.7 – Continued

Series	Run	Lifter		Fill				Load	Speed	Tracer		Locations	Comments
		Angle/°	h /mm	Distr	Wet/dry	Material	d /mm	/%	/% v_{crit}	Material	Size /mm		
uct04	094	90	5	R-R	dry	glass	2-8	12.50	70	glass	6	4.4	
uct04	095	90	5	R-R	dry	glass	2-8	12.50	60	glass	6	4.4	
uct04	096	90	5	R-R	dry	glass	2-8	25.00	90	glass	6	4.4	
uct04	097	90	5	R-R	dry	glass	2-8	25.00	80	glass	6	4.4	
uct04	098	90	5	R-R	dry	glass	2-8	25.00	75	glass	6	4.4	
uct04	099	90	5	R-R	dry	glass	2-8	25.00	70	glass	6	4.4	
uct04	100	90	5	R-R	dry	glass	2-8	25.00	60	glass	6	4.4	
uct04	101	90	5	R-R	dry	glass	2-8	31.25	90	glass	6	4.4	
uct04	102	90	5	R-R	dry	glass	2-8	31.25	80	glass	6	4.4	
uct04	103	90	5	R-R	dry	glass	2-8	31.25	75	glass	6	4.4	
uct04	104	90	5	R-R	dry	glass	2-8	31.25	70	glass	6	4.4	
uct04	105	90	5	R-R	dry	glass	2-8	31.25	60	glass	6	4.4	
uct04	106	90	5	R-R	dry	glass	2-8	37.50	90	glass	6	4.4	
uct04	107	90	5	R-R	dry	glass	2-8	37.50	80	glass	6	4.4	
uct04	108	90	5	R-R	dry	glass	2-8	37.50	75	glass	6	4.4	
uct04	109	90	5	R-R	dry	glass	2-8	37.50	70	glass	6	4.4	
uct04	110	90	5	R-R	dry	glass	2-8	37.50	60	glass	6	4.4	
uct04	111	90	5	R-R	dry	glass	2-8	50.00	90	glass	6	4.4	
uct04	112	90	5	R-R	dry	glass	2-8	50.00	80	glass	6	4.4	
uct04	113	90	5	R-R	dry	glass	2-8	50.00	75	glass	6	4.4	
uct04	114	90	5	R-R	dry	glass	2-8	50.00	70	glass	6	4.4	
uct04	115	90	5	R-R	dry	glass	2-8	50.00	60	glass	6	4.4	
uct04	116	90	5	R-R	dry	glass	2-8	50.00	50	glass	6	4.4	
uct04	117	90	5	R-R	dry	glass	2-8	50.00	100	glass	6	4.4	

Continued on next page...

Table D.7 – Continued

Series	Run	Lifter		Fill				Load	Speed	Tracer		Locations	Comments
		Angle/°	h /mm	Distr	Wet/dry	Material	d /mm	/%	/% v_{crit}	Material	Size /mm		
uct04	118	90	5	R-R	dry	glass	2-8	50.00	120	glass	6	4.4	
uct04	119	90	5	R-R	dry	glass	2-8	50.00	40	glass	6	4.4	
uct04	120	90	5	R-R	dry	glass	2-8	50.00	30	glass	6	4.4	
uct04	121 - 123	xxx	xxx	xxx	xxx	xxx	xxx	xxx	xxx	xxx	xxx	xxx	Loc 4.5
uct04	124	90	5	R-R	dry	glass	2-8	12.50	90	glass	8	4.5	
uct04	125	90	5	R-R	dry	glass	2-8	12.50	80	glass	8	4.5	
uct04	126	90	5	R-R	dry	glass	2-8	12.50	75	glass	8	4.5	
uct04	127	90	5	R-R	dry	glass	2-8	12.50	70	glass	8	4.5	
uct04	128	90	5	R-R	dry	glass	2-8	12.50	60	glass	8	4.5	
uct04	129	90	5	R-R	dry	glass	2-8	25.00	90	glass	8	4.5	
uct04	130	90	5	R-R	dry	glass	2-8	25.00	80	glass	8	4.5	
uct04	131	90	5	R-R	dry	glass	2-8	25.00	75	glass	8	4.5	
uct04	132	90	5	R-R	dry	glass	2-8	25.00	70	glass	8	4.5	
uct04	133	90	5	R-R	dry	glass	2-8	25.00	60	glass	8	4.5	
uct04	134	90	5	R-R	dry	glass	2-8	31.25	90	glass	8	4.5	
uct04	135	90	5	R-R	dry	glass	2-8	31.25	80	glass	8	4.5	
uct04	136	90	5	R-R	dry	glass	2-8	31.25	75	glass	8	4.5	
uct04	137	90	5	R-R	dry	glass	2-8	31.25	70	glass	8	4.5	
uct04	138	90	5	R-R	dry	glass	2-8	31.25	60	glass	8	4.5	
uct04	139	90	5	R-R	dry	glass	2-8	37.50	90	glass	8	4.5	
uct04	140	90	5	R-R	dry	glass	2-8	37.50	80	glass	8	4.5	
uct04	141	90	5	R-R	dry	glass	2-8	37.50	75	glass	8	4.5	
uct04	142	90	5	R-R	dry	glass	2-8	37.50	70	glass	8	4.5	

Continued on next page...

Table D.7 – Continued

Series	Run	Lifter		Fill				Load	Speed	Tracer		Locations	Comments
		Angle/°	h /mm	Distr	Wet/dry	Material	d /mm	/%	/% v_{crit}	Material	Size /mm		
uct04	143	90	5	R-R	dry	glass	2-8	37.50	60	glass	8	4.5	
uct04	144	90	5	R-R	dry	glass	2-8	50.00	90	glass	8	4.5	
uct04	145	90	5	R-R	dry	glass	2-8	50.00	80	glass	8	4.5	
uct04	146	90	5	R-R	dry	glass	2-8	50.00	75	glass	8	4.5	
uct04	147	90	5	R-R	dry	glass	2-8	50.00	70	glass	8	4.5	
uct04	148	90	5	R-R	dry	glass	2-8	50.00	60	glass	8	4.5	
uct04	149	90	5	R-R	dry	glass	2-8	50.00	40	glass	8	4.5	
uct04	150	90	5	R-R	dry	glass	2-8	50.00	30	glass	8	4.5	
uct04	151	90	5	R-R	dry	glass	2-8	50.00	50	glass	8	4.5	
uct04	152	90	5	R-R	dry	glass	2-8	50.00	100	glass	8	4.5	
uct04	153	90	5	R-R	dry	glass	2-8	50.00	120	glass	8	4.5	
uct04	154 - 156	xxx	xxx	xxx	xxx	xxx	xxx	xxx	xxx	xxx	xxx	xxx	Loc 4.6
uct04	157	90	5	R-R	dry	glass	2-8	12.50	90	glass	2	4.6	
uct04	158	90	5	R-R	dry	glass	2-8	12.50	80	glass	2	4.6	
uct04	159	90	5	R-R	dry	glass	2-8	12.50	75	glass	2	4.6	
uct04	160	90	5	R-R	dry	glass	2-8	12.50	70	glass	2	4.6	
uct04	161	90	5	R-R	dry	glass	2-8	12.50	60	glass	2	4.6	
uct04	162	90	5	R-R	dry	glass	2-8	25.00	90	glass	2	4.6	
uct04	163	90	5	R-R	dry	glass	2-8	25.00	80	glass	2	4.6	
uct04	164	90	5	R-R	dry	glass	2-8	25.00	75	glass	2	4.6	
uct04	165	90	5	R-R	dry	glass	2-8	25.00	70	glass	2	4.6	
uct04	166	90	5	R-R	dry	glass	2-8	25.00	60	glass	2	4.6	
uct04	167	90	5	R-R	dry	glass	2-8	31.25	90	glass	2	4.6	

Continued on next page...

Table D.7 – Continued

Series	Run	Lifter		Fill				Load	Speed	Tracer		Locations	Comments
		Angle/°	h /mm	Distr	Wet/dry	Material	d /mm	/%	/% v_{crit}	Material	Size /mm		
uct04	168	90	5	R-R	dry	glass	2-8	31.25	80	glass	2	4.6	
uct04	169	90	5	R-R	dry	glass	2-8	31.25	75	glass	2	4.6	
uct04	170	90	5	R-R	dry	glass	2-8	31.25	70	glass	2	4.6	
uct04	171	90	5	R-R	dry	glass	2-8	31.25	60	glass	2	4.6	
uct04	172	90	5	R-R	dry	glass	2-8	37.50	90	glass	2	4.6	
uct04	173	90	5	R-R	dry	glass	2-8	37.50	80	glass	2	4.6	
uct04	174	90	5	R-R	dry	glass	2-8	37.50	75	glass	2	4.6	
uct04	175	90	5	R-R	dry	glass	2-8	37.50	70	glass	2	4.6	
uct04	176	90	5	R-R	dry	glass	2-8	37.50	60	glass	2	4.6	
uct04	177	90	5	R-R	dry	glass	2-8	37.50	40	glass	2	4.6	
uct04	178	90	5	R-R	dry	glass	2-8	37.50	50	glass	2	4.6	
uct04	179	90	5	R-R	dry	glass	2-8	37.50	100	glass	2	4.6	
uct04	180	90	5	R-R	dry	glass	2-8	37.50	120	glass	2	4.6	
uct04	181	90	5	R-R	dry	glass	2-8	43.75	90	glass	2	4.6	
uct04	182	90	5	R-R	dry	glass	2-8	43.75	80	glass	2	4.6	
uct04	183	90	5	R-R	dry	glass	2-8	43.75	75	glass	2	4.6	
uct04	184	90	5	R-R	dry	glass	2-8	43.75	70	glass	2	4.6	
uct04	185	90	5	R-R	dry	glass	2-8	43.75	60	glass	2	4.6	
uct04	186	90	5	R-R	dry	glass	2-8	50.00	90	glass	2	4.6	
uct04	187	90	5	R-R	dry	glass	2-8	50.00	80	glass	2	4.6	
uct04	188	90	5	R-R	dry	glass	2-8	50.00	75	glass	2	4.6	
uct04	189	90	5	R-R	dry	glass	2-8	50.00	70	glass	2	4.6	
uct04	190	90	5	R-R	dry	glass	2-8	50.00	60	glass	2	4.6	
uct07	030	60	5	R-R	dry	glass	2-8	31.25	75	glass	2	7.2	

Continued on next page...

Table D.7 – Continued

Series	Run	Lifter		Fill				Load	Speed	Tracer		Locations	Comments
		Angle/°	h /mm	Distr	Wet/dry	Material	d /mm	/%	/% v_{crit}	Material	Size /mm		
uct07	033	60	5	R-R	dry	glass	2-8	31.25	60	glass	2	7.2	
uct07	037	60	5	R-R	dry	glass	2-8	31.25	60	glass	3	7.2	See 44
uct07	039-042	xxx	xxx	xxx	xxx	xxx	xxx	xxx	xxx	xxx	xxx	xxx	Loc 7.2
uct07	043	60	5	R-R	dry	glass	2-8	31.25	75	glass	3	7.2	
uct07	044	60	5	R-R	dry	glass	2-8	31.25	60	glass	3	7.2	See 37
uct07	045	60	5	R-R	dry	glass	2-8	31.25	75	glass	4	7.2	
uct07	046	60	5	R-R	dry	glass	2-8	31.25	60	glass	4	7.2	
uct07	047	60	5	R-R	dry	glass	2-8	31.25	60	glass	5	7.2	
uct07	048	60	5	R-R	dry	glass	2-8	31.25	75	glass	5	7.2	
uct07	53	60	5	R-R	dry	glass	2-8	31.25	75	glass	6	7.2	
uct07	55	60	5	R-R	dry	glass	2-8	31.25	60	glass	6	7.2	
uct07	56	60	5	R-R	dry	glass	2-8	31.25	75	glass	8	7.2	
uct07	58	60	5	R-R	dry	glass	2-8	31.25	60	glass	8	7.2	
uct07	102	60	5	mono	dry	glass	3	31.25	75	glass	3	7.2	
uct07	103	60	5	mono	dry	glass	3	31.25	60	glass	3	7.2	
uct07	107-110	xxx	xxx	xxx	xxx	xxx	xxx	xxx	xxx	xxx	xxx	xxx	Loc 7.3
uct07	111	60	5	mono	dry	glass	5	31.25	75	glass	5	7.3	
uct07	112	60	5	mono	dry	glass	5	31.25	60	glass	5	7.3	
uct07	113	60	5	mono	dry	glass	5	31.25	50	glass	5	7.3	

D.2.2 The 140mm mill

All of the experiments performed on the 140 mm-diameter 'x-ray' mill at the University of Birmingham's Positron Imaging Centre between 2006 and 2009 are given in Table D.8.

Notes

All of the runs performed in the 'x-ray' mill were dry. d is the diameter of the particle, and $R-R$ stands for Rosin-Rammler.

Table D.8: 140 mm x-ray mill experiments

Series	Run	Fill			Load	Speed	Tracer		Loc.	Comment
		Distr.	Mat.	d /mm	/%	/% v_{crit}	Mat.	d /mm		
uct05	001	binary	p/g	3,5	10.0	40	plastic	3	5.1	
uct05	002	binary	p/g	3,5	10.0	60	plastic	3	5.1	
uct05	003	binary	p/g	3,5	10.0	70	plastic	3	5.1	
uct05	004	binary	p/g	3,5	10.0	80	plastic	3	5.1	
uct05	005	binary	p/g	3,5	10.0	100	plastic	3	5.1	
uct05	006	binary	p/g	3,5	10.0	110	plastic	3	5.1	
uct05	007	binary	p/g	3,5	10.0	90	plastic	3	5.1	
uct05	008	binary	p/g	3,5	20.0	40	plastic	3	5.1	
uct05	009	binary	p/g	3,5	20.0	60	plastic	3	5.1	
uct05	010	binary	p/g	3,5	20.0	70	plastic	3	5.1	
uct05	011	binary	p/g	3,5	20.0	80	plastic	3	5.1	
uct05	012	binary	p/g	3,5	20.0	90	plastic	3	5.1	
uct05	013	binary	p/g	3,5	20.0	100	plastic	3	5.1	
uct05	014	binary	p/g	3,5	20.0	110	plastic	3	5.1	
uct05	015	binary	p/g	3,5	30.0	40	plastic	3	5.1	
uct05	016	binary	p/g	3,5	30.0	60	plastic	3	5.1	
uct05	017	binary	p/g	3,5	30.0	70	plastic	3	5.1	
uct05	018	binary	p/g	3,5	30.0	80	plastic	3	5.1	
uct05	019	binary	p/g	3,5	30.0	90	plastic	3	5.1	
uct05	020	binary	p/g	3,5	30.0	100	plastic	3	5.1	
uct05	021	binary	p/g	3,5	30.0	110	plastic	3	5.1	
uct05	022	binary	p/g	3,5	40.0	40	plastic	3	5.1	
uct05	023	binary	p/g	3,5	40.0	60	plastic	3	5.1	
uct05	024	binary	p/g	3,5	40.0	70	plastic	3	5.1	
uct05	025	binary	p/g	3,5	40.0	80	plastic	3	5.1	
uct05	026	binary	p/g	3,5	40.0	90	plastic	3	5.1	
uct05	027	binary	p/g	3,5	40.0	100	plastic	3	5.1	
uct05	028	binary	p/g	3,5	40.0	110	plastic	3	5.1	
uct05	029	binary	p/g	3,5	10.0	40	plastic	5	5.1	
uct05	030	binary	p/g	3,5	10.0	60	plastic	5	5.1	
uct05	031	binary	p/g	3,5	10.0	70	plastic	5	5.1	
uct05	032	binary	p/g	3,5	10.0	80	plastic	5	5.1	
uct05	033	binary	p/g	3,5	10.0	90	plastic	5	5.1	
uct05	034	binary	p/g	3,5	10.0	100	plastic	5	5.1	

Continued on next page...

Table D.8 – Continued

Series	Run	Fill			Load	Speed	Tracer		Loc.	Comment
		Distr.	Mat.	d /mm	/%	/% v_{crit}	Mat.	d /mm		
uct05	035	binary	p/g	3,5	10.0	110	plastic	5	5.1	
uct05	036	binary	p/g	3,5	20.0	40	plastic	5	5.1	
uct05	037	binary	p/g	3,5	20.0	60	plastic	5	5.1	
uct05	038	binary	p/g	3,5	20.0	70	plastic	5	5.1	
uct05	039	binary	p/g	3,5	20.0	80	plastic	5	5.1	
uct05	040	binary	p/g	3,5	20.0	90	plastic	5	5.1	
uct05	041	binary	p/g	3,5	20.0	100	plastic	5	5.1	
uct05	042	binary	p/g	3,5	20.0	110	plastic	5	5.1	
uct05	043	binary	p/g	3,5	30.0	40	plastic	5	5.1	
uct05	044	binary	p/g	3,5	30.0	60	plastic	5	5.1	
uct05	045	binary	p/g	3,5	30.0	70	plastic	5	5.1	
uct05	046	binary	p/g	3,5	30.0	80	plastic	5	5.1	
uct05	047	binary	p/g	3,5	30.0	90	plastic	5	5.1	
uct05	048	binary	p/g	3,5	30.0	100	plastic	5	5.1	
uct05	049	binary	p/g	3,5	30.0	110	plastic	5	5.1	
uct05	050	binary	p/g	3,5	40.0	40	plastic	5	5.1	
uct05	051	binary	p/g	3,5	40.0	60	plastic	5	5.1	
uct05	052	binary	p/g	3,5	40.0	70	plastic	5	5.1	
uct05	053	binary	p/g	3,5	40.0	80	plastic	5	5.1	
uct05	054	binary	p/g	3,5	40.0	90	plastic	5	5.1	
uct05	055	binary	p/g	3,5	40.0	100	plastic	5	5.1	
uct05	056	binary	p/g	3,5	40.0	110	plastic	5	5.1	
uct05	057-060	xxx	xxx	xxx	xxx	xxx	xxx	xxx	xxx	Loc 5.1
uct05	061	R-R	glass	2-8	12.5	40	glass	3	5.2	
uct05	062	R-R	glass	2-8	12.5	50	glass	3	5.2	
uct05	063	R-R	glass	2-8	12.5	60	glass	3	5.2	
uct05	064	R-R	glass	2-8	12.5	70	glass	3	5.2	
uct05	065	R-R	glass	2-8	12.5	80	glass	3	5.2	
uct05	066	R-R	glass	2-8	12.5	90	glass	3	5.2	
uct05	067	R-R	glass	2-8	12.5	100	glass	3	5.2	
uct05	068	R-R	glass	2-8	12.5	110	glass	3	5.2	
uct05	069	R-R	glass	2-8	25.0	40	glass	3	5.2	
uct05	070	R-R	glass	2-8	25.0	50	glass	3	5.2	
uct05	071	R-R	glass	2-8	25.0	60	glass	3	5.2	
uct05	072	R-R	glass	2-8	25.0	70	glass	3	5.2	
uct05	073	R-R	glass	2-8	25.0	80	glass	3	5.2	
uct05	074	R-R	glass	2-8	25.0	90	glass	3	5.2	
uct05	075	R-R	glass	2-8	25.0	100	glass	3	5.2	
uct05	076	R-R	glass	2-8	25.0	110	glass	3	5.2	
uct05	077	R-R	glass	2-8	37.5	40	glass	3	5.2	
uct05	078	R-R	glass	2-8	37.5	50	glass	3	5.2	
uct05	079	R-R	glass	2-8	37.5	60	glass	3	5.2	
uct05	080	R-R	glass	2-8	37.5	70	glass	3	5.2	

Continued on next page...

Table D.8 – Continued

Series	Run	Fill			Load	Speed	Tracer		Loc.	Comment
		Distr.	Mat.	d /mm	/%	/% v_{crit}	Mat.	d /mm		
uct05	081	R-R	glass	2-8	37.5	80	glass	3	5.2	
uct05	082	R-R	glass	2-8	37.5	90	glass	3	5.2	
uct05	083	R-R	glass	2-8	37.5	100	glass	3	5.2	
uct05	084	R-R	glass	2-8	37.5	110	glass	3	5.2	
uct05	085	R-R	glass	2-8	50.0	40	glass	3	5.2	
uct05	086	R-R	glass	2-8	50.0	50	glass	3	5.2	
uct05	087	R-R	glass	2-8	50.0	60	glass	3	5.2	
uct05	088	R-R	glass	2-8	50.0	70	glass	3	5.2	
uct05	089	R-R	glass	2-8	50.0	80	glass	3	5.2	
uct05	090	R-R	glass	2-8	50.0	90	glass	3	5.2	
uct05	091	R-R	glass	2-8	50.0	100	glass	3	5.2	
uct05	092	R-R	glass	2-8	50.0	110	glass	3	5.2	
uct05	093	R-R	glass	2-8	12.5	40	glass	4	5.2	
uct05	094	R-R	glass	2-8	12.5	50	glass	4	5.2	
uct05	095	R-R	glass	2-8	12.5	60	glass	4	5.2	
uct05	096	R-R	glass	2-8	12.5	70	glass	4	5.2	
uct05	097	R-R	glass	2-8	12.5	80	glass	4	5.2	
uct05	098	R-R	glass	2-8	12.5	90	glass	4	5.2	
uct05	099	R-R	glass	2-8	12.5	100	glass	4	5.2	
uct05	100	R-R	glass	2-8	12.5	110	glass	4	5.2	
uct05	101	R-R	glass	2-8	25.0	40	glass	4	5.2	
uct05	102	R-R	glass	2-8	25.0	50	glass	4	5.2	
uct05	103	R-R	glass	2-8	25.0	60	glass	4	5.2	
uct05	104	R-R	glass	2-8	25.0	70	glass	4	5.2	
uct05	105	R-R	glass	2-8	25.0	80	glass	4	5.2	
uct05	106	R-R	glass	2-8	25.0	90	glass	4	5.2	
uct05	107	R-R	glass	2-8	25.0	100	glass	4	5.2	
uct05	108	R-R	glass	2-8	25.0	110	glass	4	5.2	
uct05	109	R-R	glass	2-8	37.5	40	glass	4	5.2	
uct05	110	R-R	glass	2-8	37.5	50	glass	4	5.2	
uct05	111	R-R	glass	2-8	37.5	60	glass	4	5.2	
uct05	112	R-R	glass	2-8	37.5	70	glass	4	5.2	
uct05	113	R-R	glass	2-8	37.5	80	glass	4	5.2	
uct05	114	R-R	glass	2-8	37.5	90	glass	4	5.2	
uct05	115	R-R	glass	2-8	37.5	100	glass	4	5.2	
uct05	116	R-R	glass	2-8	37.5	110	glass	4	5.2	
uct05	117	R-R	glass	2-8	50.0	40	glass	4	5.2	
uct05	118	R-R	glass	2-8	50.0	50	glass	4	5.2	
uct05	119	R-R	glass	2-8	50.0	60	glass	4	5.2	
uct05	120	R-R	glass	2-8	50.0	70	glass	4	5.2	
uct05	121	R-R	glass	2-8	50.0	80	glass	4	5.2	
uct05	122	R-R	glass	2-8	50.0	90	glass	4	5.2	
uct05	123	R-R	glass	2-8	50.0	100	glass	4	5.2	

Continued on next page...

Table D.8 – Continued

Series	Run	Fill			Load	Speed	Tracer		Loc.	Comment
		Distr.	Mat.	d /mm	/%	/% v_{crit}	Mat.	d /mm		
uct05	124	R-R	glass	2-8	50.0	110	glass	4	5.2	
uct05	125-128	xxx	xxx	xxx	xxx	xxx	xxx	xxx	xxx	Loc 5.2
uct05	129	R-R	glass	2-8	12.5	40	glass	5	5.3	
uct05	130	R-R	glass	2-8	12.5	50	glass	5	5.3	
uct05	131	R-R	glass	2-8	12.5	60	glass	5	5.3	
uct05	132	R-R	glass	2-8	12.5	70	glass	5	5.3	
uct05	133	R-R	glass	2-8	12.5	80	glass	5	5.3	
uct05	134	R-R	glass	2-8	12.5	90	glass	5	5.3	
uct05	135	R-R	glass	2-8	12.5	100	glass	5	5.3	
uct05	136	R-R	glass	2-8	12.5	110	glass	5	5.3	
uct05	137	R-R	glass	2-8	25.0	40	glass	5	5.3	
uct05	138	R-R	glass	2-8	25.0	50	glass	5	5.3	
uct05	139	R-R	glass	2-8	25.0	60	glass	5	5.3	
uct05	140	R-R	glass	2-8	25.0	70	glass	5	5.3	
uct05	141	R-R	glass	2-8	25.0	80	glass	5	5.3	
uct05	142	R-R	glass	2-8	25.0	90	glass	5	5.3	
uct05	143	R-R	glass	2-8	25.0	100	glass	5	5.3	
uct05	144	R-R	glass	2-8	25.0	110	glass	5	5.3	
uct05	145	R-R	glass	2-8	37.5	40	glass	5	5.3	
uct05	146	R-R	glass	2-8	37.5	50	glass	5	5.3	
uct05	147	R-R	glass	2-8	37.5	60	glass	5	5.3	
uct05	148	R-R	glass	2-8	37.5	70	glass	5	5.3	
uct05	149	R-R	glass	2-8	37.5	80	glass	5	5.3	
uct05	150	R-R	glass	2-8	37.5	90	glass	5	5.3	
uct05	151	R-R	glass	2-8	37.5	100	glass	5	5.3	
uct05	152	R-R	glass	2-8	37.5	110	glass	5	5.3	
uct05	153	R-R	glass	2-8	50.0	40	glass	5	5.3	
uct05	154	R-R	glass	2-8	50.0	50	glass	5	5.3	
uct05	155	R-R	glass	2-8	50.0	60	glass	5	5.3	
uct05	156	R-R	glass	2-8	50.0	70	glass	5	5.3	
uct05	157	R-R	glass	2-8	50.0	80	glass	5	5.3	
uct05	158	R-R	glass	2-8	50.0	90	glass	5	5.3	
uct05	159	R-R	glass	2-8	50.0	100	glass	5	5.3	
uct05	160	R-R	glass	2-8	50.0	110	glass	5	5.3	
uct05	161	binary	p/g	3,5	20.0	60	glass	5	5.3	
uct05	162	binary	p/g	3,5	20.0	70	glass	5	5.3	
uct05	163	binary	p/g	3,5	20.0	80	glass	5	5.3	
uct05	164	binary	p/g	3,5	20.0	90	glass	5	5.3	
uct05	165	binary	p/g	3,5	30.0	60	glass	5	5.3	
uct05	166	binary	p/g	3,5	30.0	70	glass	5	5.3	
uct05	167	binary	p/g	3,5	30.0	80	glass	5	5.3	
uct05	168	binary	p/g	3,5	30.0	90	glass	5	5.3	
uct05	169	binary	p/g	3,5	40.0	60	glass	5	5.3	

Continued on next page...

Table D.8 – Continued

Series	Run	Fill			Load	Speed	Tracer		Loc.	Comment
		Distr.	Mat.	d /mm	/%	/% v_{crit}	Mat.	d /mm		
uct05	170	binary	p/g	3,5	40.0	70	glass	5	5.3	
uct05	171	binary	p/g	3,5	40.0	80	glass	5	5.3	
uct05	172	binary	p/g	3,5	40.0	90	glass	5	5.3	
uct05	173	R-R	glass	2-8	12.5	40	glass	6	5.3	
uct05	174	R-R	glass	2-8	12.5	50	glass	6	5.3	
uct05	175	R-R	glass	2-8	12.5	60	glass	6	5.3	
uct05	176	R-R	glass	2-8	12.5	70	glass	6	5.3	
uct05	177	R-R	glass	2-8	12.5	80	glass	6	5.3	
uct05	178	R-R	glass	2-8	12.5	90	glass	6	5.3	
uct05	179	R-R	glass	2-8	12.5	100	glass	6	5.3	
uct05	180	R-R	glass	2-8	12.5	110	glass	6	5.3	
uct05	181	R-R	glass	2-8	25.0	40	glass	6	5.3	
uct05	182	R-R	glass	2-8	25.0	50	glass	6	5.3	
uct05	183	R-R	glass	2-8	25.0	60	glass	6	5.3	
uct05	184	R-R	glass	2-8	25.0	70	glass	6	5.3	
uct05	185	R-R	glass	2-8	25.0	80	glass	6	5.3	
uct05	186	R-R	glass	2-8	25.0	90	glass	6	5.3	
uct05	187	R-R	glass	2-8	25.0	100	glass	6	5.3	
uct05	188	R-R	glass	2-8	25.0	110	glass	6	5.3	
uct05	189	R-R	glass	2-8	37.5	40	glass	6	5.3	
uct05	190	R-R	glass	2-8	37.5	50	glass	6	5.3	
uct05	191	R-R	glass	2-8	37.5	60	glass	6	5.3	
uct05	192	R-R	glass	2-8	37.5	70	glass	6	5.3	
uct05	193	R-R	glass	2-8	37.5	80	glass	6	5.3	
uct05	194	R-R	glass	2-8	37.5	90	glass	6	5.3	
uct05	195	R-R	glass	2-8	37.5	100	glass	6	5.3	
uct05	196	R-R	glass	2-8	37.5	110	glass	6	5.3	
uct05	197	R-R	glass	2-8	50.0	40	glass	6	5.3	
uct05	198	R-R	glass	2-8	50.0	50	glass	6	5.3	
uct05	199	R-R	glass	2-8	50.0	60	glass	6	5.3	
uct05	200	R-R	glass	2-8	50.0	70	glass	6	5.3	
uct05	201	R-R	glass	2-8	50.0	80	glass	6	5.3	
uct05	202	R-R	glass	2-8	50.0	90	glass	6	5.3	
uct05	203	R-R	glass	2-8	50.0	100	glass	6	5.3	
uct05	204	R-R	glass	2-8	50.0	110	glass	6	5.3	
uct05	205-208	xxx	xxx	xxx	xxx	xxx	xxx	xxx	xxx	Loc 5.3
uct05	209	R-R	glass	2-8	25.0	40	glass	2	5.4	
uct05	210	R-R	glass	2-8	25.0	50	glass	2	5.4	
uct05	211	R-R	glass	2-8	25.0	60	glass	2	5.4	
uct05	212	R-R	glass	2-8	25.0	70	glass	2	5.4	
uct05	213	R-R	glass	2-8	25.0	80	glass	2	5.4	
uct05	214	R-R	glass	2-8	25.0	90	glass	2	5.4	
uct05	215	R-R	glass	2-8	25.0	100	glass	2	5.4	

Continued on next page...

Table D.8 – Continued

Series	Run	Fill			Load	Speed	Tracer		Loc.	Comment
		Distr.	Mat.	d /mm	/%	/% v_{crit}	Mat.	d /mm		
uct05	216	R-R	glass	2-8	25.0	110	glass	2	5.4	
uct05	217	R-R	glass	2-8	37.5	40	glass	2	5.4	
uct05	218	R-R	glass	2-8	37.5	50	glass	2	5.4	
uct05	219	R-R	glass	2-8	37.5	60	glass	2	5.4	
uct05	220	R-R	glass	2-8	37.5	70	glass	2	5.4	
uct05	221	R-R	glass	2-8	37.5	80	glass	2	5.4	
uct05	222	R-R	glass	2-8	37.5	90	glass	2	5.4	
uct05	223	R-R	glass	2-8	37.5	100	glass	2	5.4	
uct05	224	R-R	glass	2-8	37.5	110	glass	2	5.4	
uct05	225	R-R	glass	2-8	37.5	70	glass	2	5.4	Long run
uct05	226	R-R	glass	2-8	50.0	40	glass	2	5.4	
uct05	227	R-R	glass	2-8	50.0	50	glass	2	5.4	
uct05	228	R-R	glass	2-8	50.0	60	glass	2	5.4	
uct05	229	R-R	glass	2-8	50.0	70	glass	2	5.4	
uct05	230	R-R	glass	2-8	50.0	80	glass	2	5.4	
uct05	231	R-R	glass	2-8	50.0	90	glass	2	5.4	
uct05	232	R-R	glass	2-8	50.0	100	glass	2	5.4	
uct05	233	R-R	glass	2-8	50.0	110	glass	2	5.4	
uct05	241	binary	p/g	3,5	20.0	60	glass	3	5.4	
uct05	242	binary	p/g	3,5	20.0	70	glass	3	5.4	
uct05	243	binary	p/g	3,5	20.0	80	glass	3	5.4	
uct05	244	binary	p/g	3,5	20.0	90	glass	3	5.4	
uct05	245	binary	p/g	3,5	30.0	60	glass	3	5.4	
uct05	246	binary	p/g	3,5	30.0	70	glass	3	5.4	
uct05	247	binary	p/g	3,5	30.0	80	glass	3	5.4	
uct05	248	binary	p/g	3,5	30.0	90	glass	3	5.4	
uct05	249	binary	p/g	3,5	40.0	60	glass	3	5.4	
uct05	250	binary	p/g	3,5	40.0	70	glass	3	5.4	
uct05	251	binary	p/g	3,5	40.0	80	glass	3	5.4	
uct05	252	binary	p/g	3,5	40.0	90	glass	3	5.4	
uct05	268	R-R	glass	2-8	25.0	40	glass	8	5.4	
uct05	269	R-R	glass	2-8	25.0	50	glass	8	5.4	
uct05	270	R-R	glass	2-8	25.0	60	glass	8	5.4	
uct05	271	R-R	glass	2-8	25.0	70	glass	8	5.4	
uct05	272	R-R	glass	2-8	25.0	80	glass	8	5.4	
uct05	273	R-R	glass	2-8	25.0	90	glass	8	5.4	
uct05	274	R-R	glass	2-8	25.0	100	glass	8	5.4	
uct05	275	R-R	glass	2-8	25.0	110	glass	8	5.4	
uct05	276	R-R	glass	2-8	37.5	40	glass	8	5.4	
uct05	277	R-R	glass	2-8	37.5	50	glass	8	5.4	
uct05	278	R-R	glass	2-8	37.5	60	glass	8	5.4	
uct05	279	R-R	glass	2-8	37.5	70	glass	8	5.4	
uct05	280	R-R	glass	2-8	37.5	80	glass	8	5.4	

Continued on next page...

Table D.8 – Continued

Series	Run	Fill			Load	Speed	Tracer		Loc.	Comment
		Distr.	Mat.	d /mm	/%	/% v_{crit}	Mat.	d /mm		
uct05	281	R-R	glass	2-8	37.5	90	glass	8	5.4	
uct05	282	R-R	glass	2-8	37.5	100	glass	8	5.4	
uct05	283	R-R	glass	2-8	37.5	110	glass	8	5.4	
uct05	284	R-R	glass	2-8	50.0	40	glass	8	5.4	
uct05	285	R-R	glass	2-8	50.0	50	glass	8	5.4	
uct05	286	R-R	glass	2-8	50.0	60	glass	8	5.4	
uct05	287	R-R	glass	2-8	50.0	70	glass	8	5.4	
uct05	288	R-R	glass	2-8	50.0	80	glass	8	5.4	
uct05	289	R-R	glass	2-8	50.0	90	glass	8	5.4	
uct05	290	R-R	glass	2-8	50.0	100	glass	8	5.4	
uct05	291	R-R	glass	2-8	50.0	110	glass	8	5.4	
uct05	292	R-R	glass	2-8	50.0	65	glass	8	5.4	
uct05	293	R-R	glass	2-8	50.0	75	glass	8	5.4	
uct05	294	R-R	glass	2-8	50.0	85	glass	8	5.4	
uct05	295-298	xxx	xxx	xxx	xxx	xxx	xxx	xxx	xxx	Loc 5.4
uct05	299	binary	plastic	3,5	20.0	60	plastic	3	5.5	
uct05	300	binary	plastic	3,5	20.0	70	plastic	3	5.5	
uct05	301	binary	plastic	3,5	20.0	80	plastic	3	5.5	
uct05	302	binary	plastic	3,5	20.0	90	plastic	3	5.5	
uct05	303	binary	plastic	3,5	30.0	60	plastic	3	5.5	
uct05	304	binary	plastic	3,5	30.0	70	plastic	3	5.5	
uct05	305	binary	plastic	3,5	30.0	80	plastic	3	5.5	
uct05	306	binary	plastic	3,5	30.0	90	plastic	3	5.5	
uct05	307	binary	plastic	3,5	40.0	60	plastic	3	5.5	
uct05	308	binary	plastic	3,5	40.0	70	plastic	3	5.5	
uct05	309	binary	plastic	3,5	40.0	80	plastic	3	5.5	
uct05	310	binary	plastic	3,5	40.0	90	plastic	3	5.5	
uct05	311	binary	plastic	3,5	20.0	60	plastic	5	5.5	
uct05	312	binary	plastic	3,5	20.0	70	plastic	5	5.5	
uct05	313	binary	plastic	3,5	20.0	80	plastic	5	5.5	
uct05	314	binary	plastic	3,5	20.0	90	plastic	5	5.5	
uct05	315	binary	plastic	3,5	30.0	60	plastic	5	5.5	
uct05	316	binary	plastic	3,5	30.0	70	plastic	5	5.5	
uct05	317	binary	plastic	3,5	30.0	80	plastic	5	5.5	
uct05	318	binary	plastic	3,5	30.0	90	plastic	5	5.5	
uct05	319	binary	plastic	3,5	40.0	60	plastic	5	5.5	
uct05	320	binary	plastic	3,5	40.0	70	plastic	5	5.5	
uct05	321	binary	plastic	3,5	40.0	80	plastic	5	5.5	
uct05	322	binary	plastic	3,5	40.0	90	plastic	5	5.5	
uct05	352-355	xxx	xxx	xxx	xxx	xxx	xxx	xxx	xxx	Loc 5.5
uct07	003	binary	plastic	3,5	30.0	80	plastic	5	7.1	
uct07	005	binary	plastic	3,5	30.0	60	plastic	5	7.1	

Continued on next page...

Table D.8 – Continued

Series	Run	Fill			Load	Speed	Tracer		Loc.	Comment
		Distr.	Mat.	d /mm	/%	/% v_{crit}	Mat.	d /mm		
uct07	006-009	xxx	xxx	xxx	xxx	xxx	xxx	xxx	xxx	Loc 7.1
uct07	017	binary	plastic	3,5	30.0	80	plastic	3	7.1	
uct07	019	binary	plastic	3,5	30.0	60	plastic	3	7.1	
uct07	021	binary	plastic	3,5	30.0	70	plastic	3	7.1	
uct07	023	binary	plastic	3,5	30.0	70	plastic	5	7.1	

D.2.3 The new 300mm mill

All of the experiments performed on the 'new 300 mm mill' at the University of Birmingham's Positron Imaging Centre between 2006 and 2009 are given in Table D.9.

Notes

Only monosize distribution charges were investigated for the 'new 300 mm mill'.

Table D.9: New 300 mm mill experiments

Series	Run	Fill		Load	Speed	Tracer		Loc.	Comment
		Wet/dry	d/mm	/%	/% v_{crit}	Mat.	d /mm		
uct07	117	dry	3	31.25	75	glass	3	7.4	
uct07	118	dry	3	31.25	60	glass	3	7.4	
uct07	123-125	xxx	xxx	xxx	xxx	xxx	xxx	xxx	Loc 7.4
uct07	126	dry	5	31.25	75	glass	5	7.4	
uct07	127	dry	5	31.25	60	glass	5	7.4	
uct07	128	dry	5	31.25	31	glass	5	7.4	
uct07	157	wet	3	31.25	75	glass	3	7.5	
uct07	163	wet	5	31.25	75	glass	5	7.5	
uct07	167	wet	5	31.25	75	resin	0.5	7.5	
uct07	168	wet	5	31.25	75	resin	0.5	7.5	
uct07	169	20% slurry	5	31.25	75	glass	5	7.5	
uct07	170	20% slurry	5	31.25	60	glass	5	7.5	
uct07	171	30% slurry	5	31.25	75	glass	5	7.5	
uct07	174-176	xxx	xxx	xxx	xxx	xxx	xxx	xxx	Loc 7.5
uct07	177	30% slurry	5	31.25	60	glass	5	7.5	
uct07	178	40% slurry	5	31.25	75	glass	5	7.5	
uct07	182	40% slurry	5	31.25	60	glass	5	7.5	
uct07	183	20% slurry	5	31.25	75	resin	0.5	7.5	
uct07	184	40% slurry	5	31.25	60	stone	1	7.5	
uct07	185	40% slurry	5	31.25	75	stone	1	7.5	
uct07	190	20% slurry	5	31.25	75	stone	1	7.5	
uct07	192	20% slurry	5	31.25	60	stone	1	7.5	
uct07	198	30% slurry	5	31.25	60	stone	1	7.5	
uct07	201	30% slurry	5	31.25	75	stone	1	7.5	

Continued on next page...

Table D.9 – Continued

Series	Run	Fill		Load	Speed	Tracer		Loc.	Comment
		Wet/dry	d/mm	/%	/% v_{crit}	Mat.	d /mm		
uct07	202	30% slurry	5	31.25	75	stone	1	7.5	
uct07	203	30% slurry	5	31.25	60	stone	1	7.5	
uct07	204	30% slurry	5	31.25	60	stone	1	7.5	
uct07	205	30% slurry	5	31.25	60	stone	1	7.5	
uct07	209-211	xxx	xxx	xxx	xxx	xxx	xxx	xxx	Loc 7.6
uct07	212	wet	5	31.25	60	glass	5	7.6	
uct07	217	wet	5	31.25	31	glass	5	7.6	
uct07	218	wet	5	31.25	60	glass	5	7.6	
uct07	219	wet	5	31.25	50	glass	5	7.6	

D.3 Other runs

D.3.1 Location marker runs

As part of the pre-processing procedure[3], tracers are attached to a slowly rotating mill shell to obtain the position and orientation of the mill. These location markers are given in Table D.10.

Table D.10: Mill locations

Series	Locations		Mill	Runs
	Number	Runs		
uct01	1.1	026-028	Old 300mm	029-074
uct01	1.2	075-077	Old 300mm	078-116
uct02	2.1	001-003	Old 300mm	004-060
uct03	3.1	001-003	Old 300mm	004-013
uct03	3.2	014-016	Old 300mm	017-025
uct04	4.1	001-003	Old 300mm	004-008
uct04	4.2	030	Old 300mm	009-055
uct04	4.3	056 - 059	Old 300mm	060-087
uct04	4.4	088-089	Old 300mm	090-120
uct04	4.5	121 - 123	Old 300mm	124-153
uct04	4.6	154 - 156	Old 300mm	157-190
uct05	5.1	057-060	X-ray	001-056
uct05	5.2	125-128	X-ray	61-124
uct05	5.3	205-208	X-ray	129-204
uct05	5.4	295-298	X-ray	209-294
uct05	5.5	352-355	X-ray	299-322
uct07	7.1	006-009	X-ray	001-023
uct07	7.2	039-042	Old 300mm	030-103
uct07	7.3	107-110	Old 300mm	111-113
uct07	7.4	123-125	New 300mm	126-128
uct07	7.5	174-176	New 300mm	157-205
uct07	7.6	209-211	New 300mm	212-219

[3]See Section 4.5

D.3.2 Stationary particle runs

As part of the pre-processing procedure[4], runs are performed with the mill stationary to investigate the attenuating environment of the experiment. These stationary runs are given in Table D.11.

Table D.11: Stationary runs

Series	Mill	Runs
uct07	X-ray	010-013, 014-016, 018, 020, 022, 024-028
uct07	Old 300mm	029, 031, 034, 035, 038, 049-051, 054, 057, 059, 104-106, 114-116
uct07	New 300mm	119-122, 129-131, 158-160, 179-181, 186-188, 194-196, 206-208, 213-215, 220-222

[4]See Section 4.5

Appendix E

Optimisation of triangulation parameters

In this appendix I will step through the process of choosing the optimal number, N_{events}, of detected LoRs from which to begin the iterative triangulation procedure, and the optimum fraction, f_{opt}, of these events with which to triangulate the tracer particle's position after the final iteration. This appendix should be read in conjunction with Section 2.3.2.

For the purpose of illustration, I will optimise the triangulation procedure for just one run- the 'old' $300mm$ diameter mill filled to 31.25% of its volume with a mono-sized charge of $5mm$ glass beads, and operated at 60% of critical speed.

Figure E.1 shows this experiment triangulated with a range of values of f_{opt} and N_{events}. The top left subfigure shows a triangulation with $f_{opt} = 5\%$ and $N_{events} = 100$. The N_{events} used in each triangulation increases in steps of 25 left to right in the figure, and the f_{opt} increases in steps of 5% top to bottom. Thus the bottom right subfigure shows a triangulation with $f_{opt} = 30\%$ and $N_{events} = 300$.

From Figure E.1 it is clear that some combinations of f_{opt} and N_{events} result in fewer outliers than others. In particular, it seems that there are more outliers for smaller N_{events} and larger f_{opt}, and that these outliers are most pronounced in the chaotic toe region.

What isn't clear from Figure E.1 is the quality of the non-outlier data in the body of the mill. Figures E.2 and E.3 show the variations of the tracer particle's position, velocity and acceleration over a $30s$ in each direction for three illustrative combinations of f_{opt} and N_{events}.

The $\hat{x}$-direction is axial with the mill, and so only slight, stochastic variation in this direction occur. The tracer particle is circulating in the $\hat{y}$- and $\hat{z}$-directions, giving rise to a sinusoidal variation with time. Although the overall trends in the variation of tracer particle position are the same for all of these combinations, there are some differences in the very short term variations, and large differences in the kinematic quantities derived from them. In particular, it seems that larger N_{events} result in smoother data all the way up to the second derivative, especially for larger f_{opt}.

Although qualitative assessments of the type entered into above are extremely important- in fact, indispensable- in the optimisation procedure, it is computationally-expensive to produce and plot all of the figures shown above, and time-consuming to visually inspect them. In the following sections I will discuss methods of reducing the range of values of f_{opt} and N_{events} to so investigate, and in Section E.3 I will return to a more quantitative analysis of the triangulated data shown in Figures E.1, E.2 and E.3.

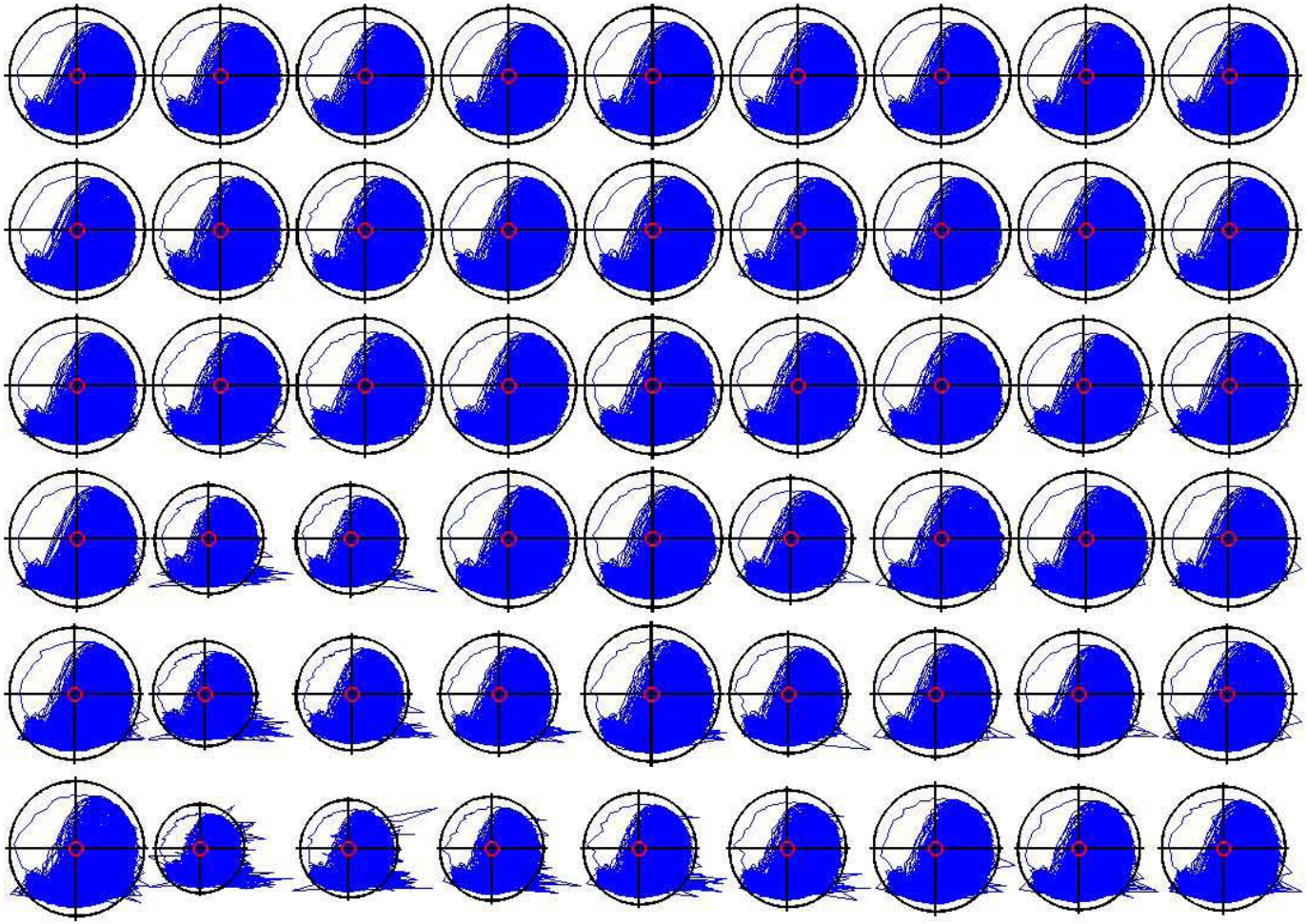

Figure E.1: 2D projections of a typical PEPT tumbling mill experiment triangulated with f_{opt} from 5% to 30% (top to bottom) and N_{events} from 100 to 300 (left to right).

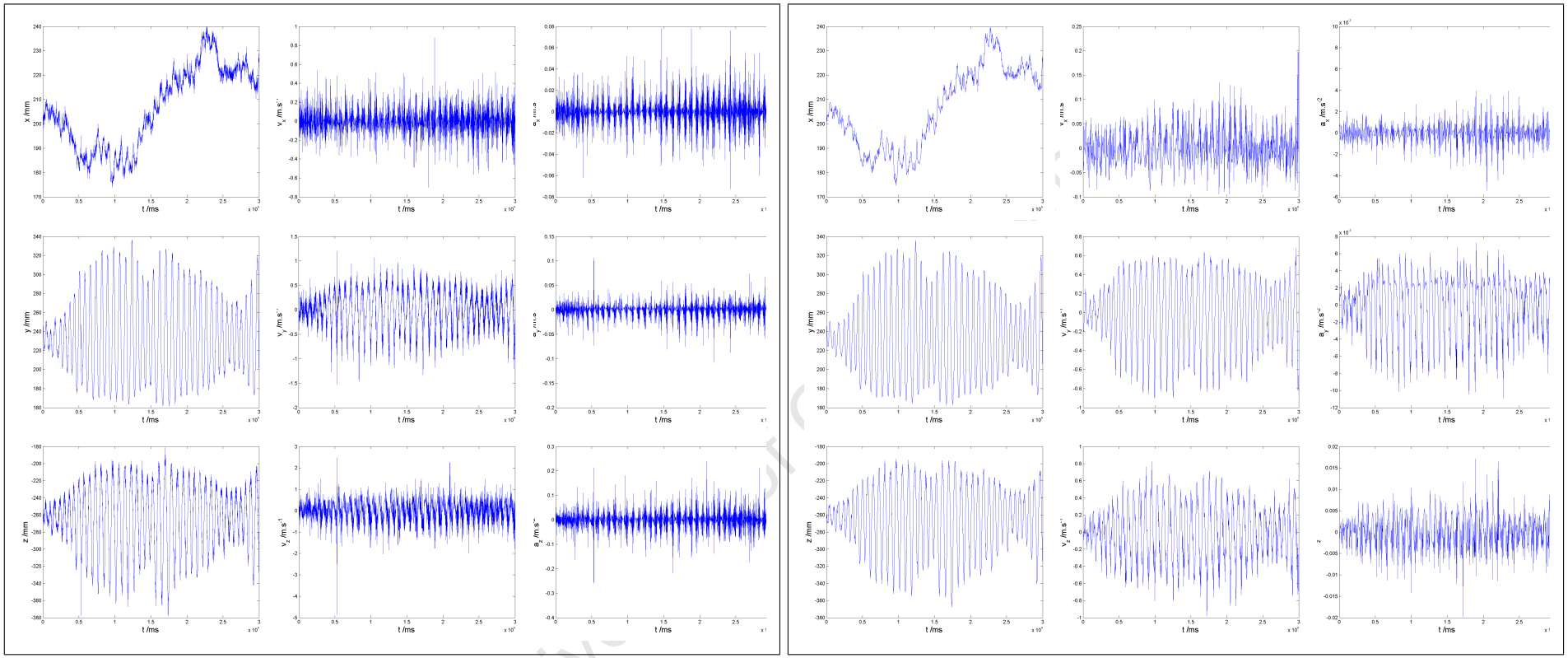

(a) $f_{opt} = 5\%$ and $N_{events} = 100$

(b) $f_{opt} = 5\%$ and $N_{events} = 300$

Figure E.2: Variations of $\hat{x}$-, $\hat{y}$- and $\hat{z}$- (top to bottom in each subfigure) location, velocity and acceleration (left to right in each subfigure) for data triangulated with $f_{opt} = 5\%$ and two different N_{events}.

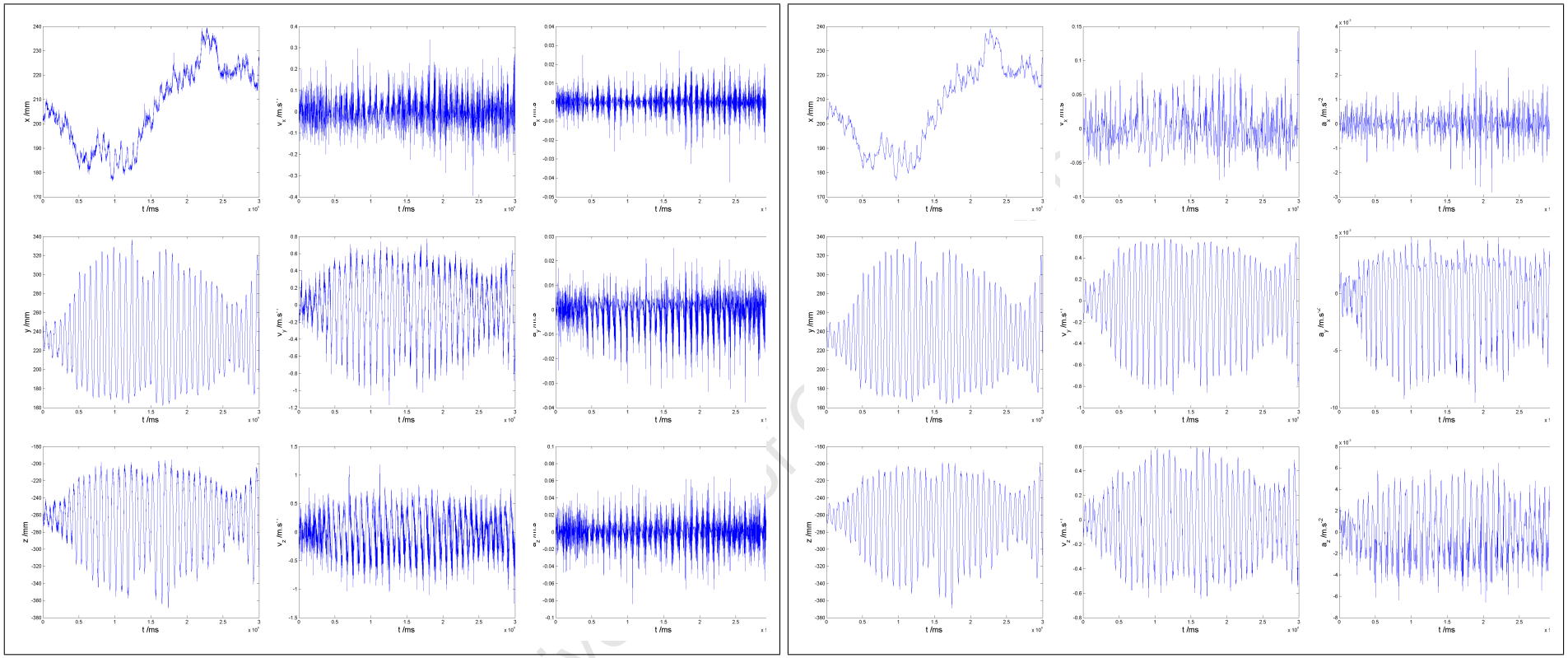

(a) $f_{opt} = 30\%$ and $N_{events} = 100$

(b) $f_{opt} = 30\%$ and $N_{events} = 300$

Figure E.3: Variations of $\hat{x}$-, $\hat{y}$- and $\hat{z}$- (top to bottom in each subfigure) location, velocity and acceleration (left to right in each subfigure) for data triangulated with $f_{opt} = 30\%$ and two different N_{events}.

E.1 Stationary particle runs

Figure E.4 shows the locations of the tracer particle for three stationary runs performed on the mill and charge described above. These three positions were obtained by abruptly stopping the mill, running an experiment once the charge had completely settled down, restarting, restopping and repeating.

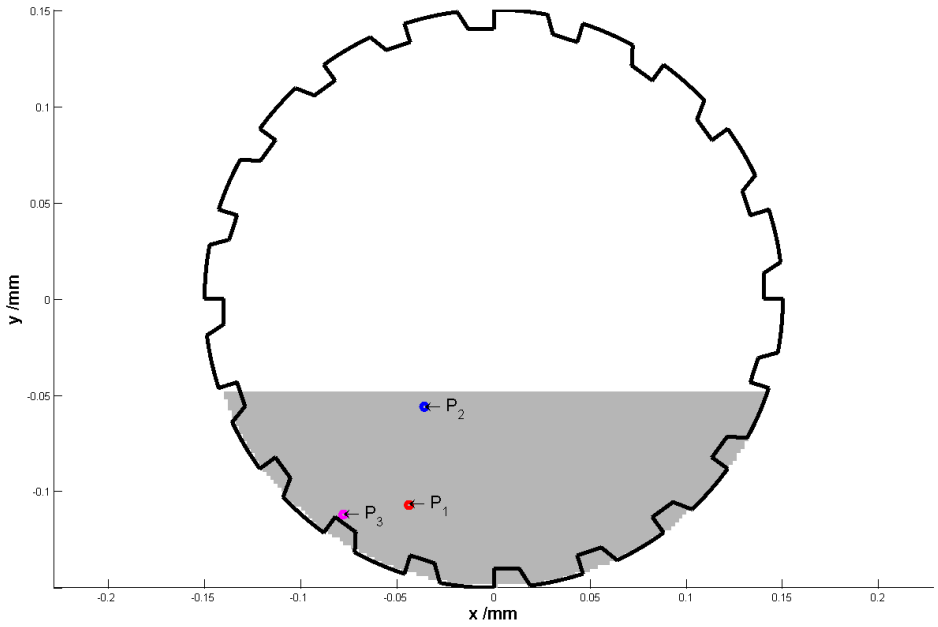

Figure E.4: The locations of three stationary particles in a representative bulk.

The mill is roughly central in the field of view of the camera, and these runs were chosen because the $z-$coordinates of all three positions are roughly the same, and roughly in the centre of the axial plane of the cameras. Thus the amount of attenuating material through which the LoRs must pass depends on the position of the tracer between, rather than along, the detectors.

Figure E.5 shows the point spread functions of one of the points, P_1, in directions perpendicular and parallel to the plane of the detectors. To these point spread functions are fitted Gaussian curves, all with adjusted R^2 values of approximately 0.9- see the legends of each plot. For legibility, these plots are not normalised to the same values and are thus not comparable. However, figures to show the variation of the spread, modelled as the normalised standard deviation of the Gaussian- $\frac{\sigma}{N_{events}}$- for each of the points shown in Figure E.4.

Figures E.6, E.7 and E.8 show no clear optimum N_{events} based on the thickness of the point spread function. From this figure it is clear, though, that sharper points are obtainable starting from larger N_{events} and retaining a bigger fraction, f_{opt}, of these in the triangulation. It is also clear that, under these conditions, the points are much sharper in the directions parallel to the plates of the detectors than in the direction perpendicular to them- in this case the $\hat{z}$-direction.

Figures E.9, E.10 and E.11 show the thickness of the triangulated point spread functions as a function of f_{opt}. In this case, the thickness of the points seems to fall off more quickly than it did in the N_{events} case, and there is a suggestion of a weak optimum around $f_{opt} = 25\%$. This 'optimum' is most obvious in the more deeply-embedded P_1 and P_2. It is possible that a more pronounced optimum would be visible in a tracer embedded in an even more attenuating environment, such as one containing a slurry or more steel structure.

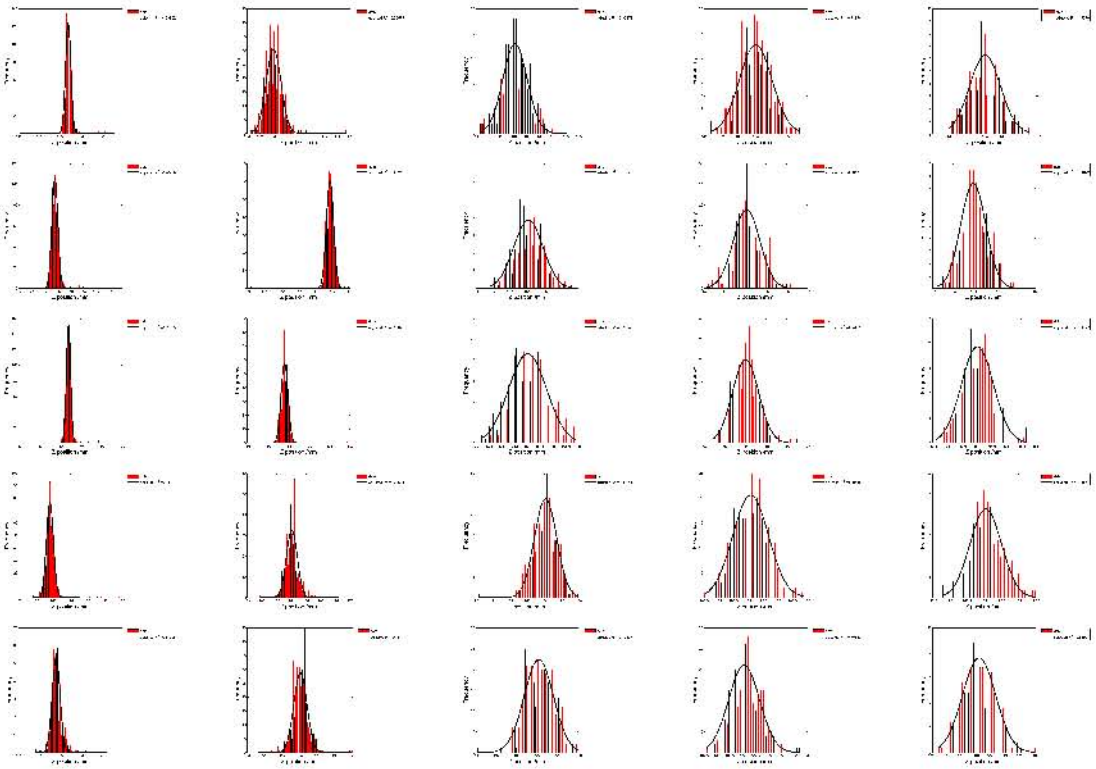

(a) Perpendicular to the cameras

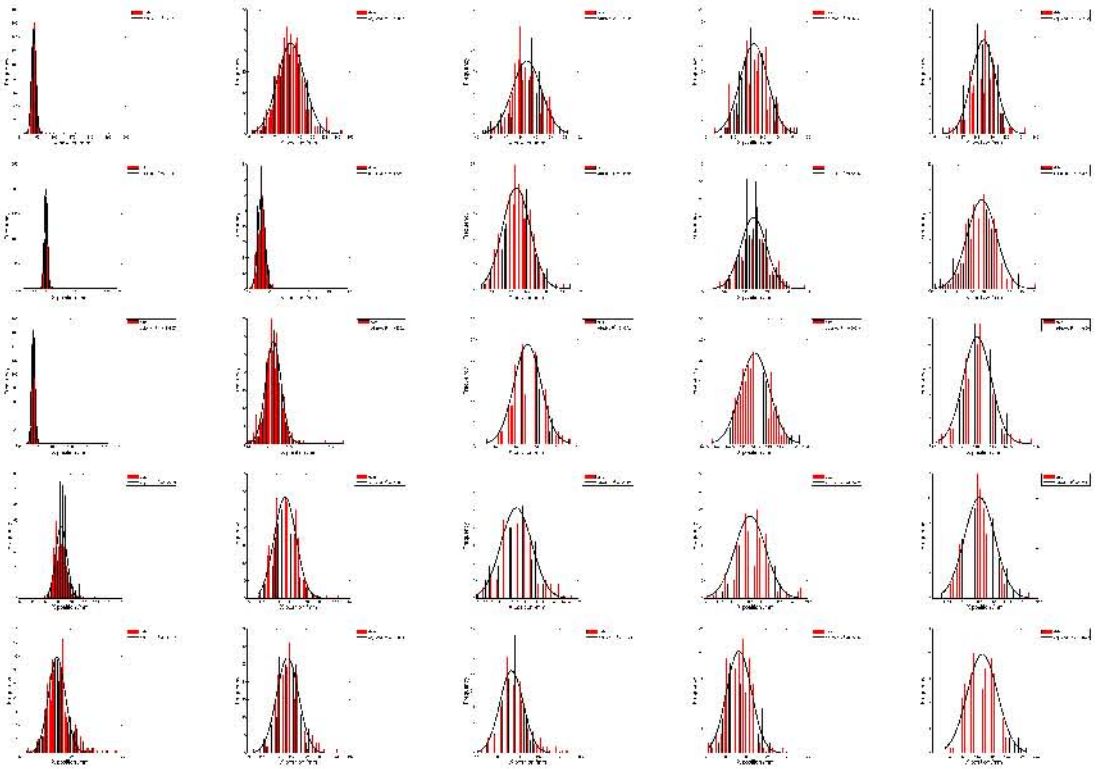

(b) Parallel to the cameras

Figure E.5: Point spread functions of point P_1 in the directions perpendicular (top) and parallel (bottom) to the plane of the detectors. These are produced with increasing f_{opt} from 5% to 25% left to right in each subplot, and increasing N_{events} from 100 to 300 top to bottom in each subplot.

In this case too, the figure shows that retaining a larger fraction, f_{opt}, of a larger starting number of events, N_{events}, results in a more *precise* triangulation. However, in order to know whether the triangulations are *accurate* as well as *precise*, it is necessary to know the actual position of the tracer.

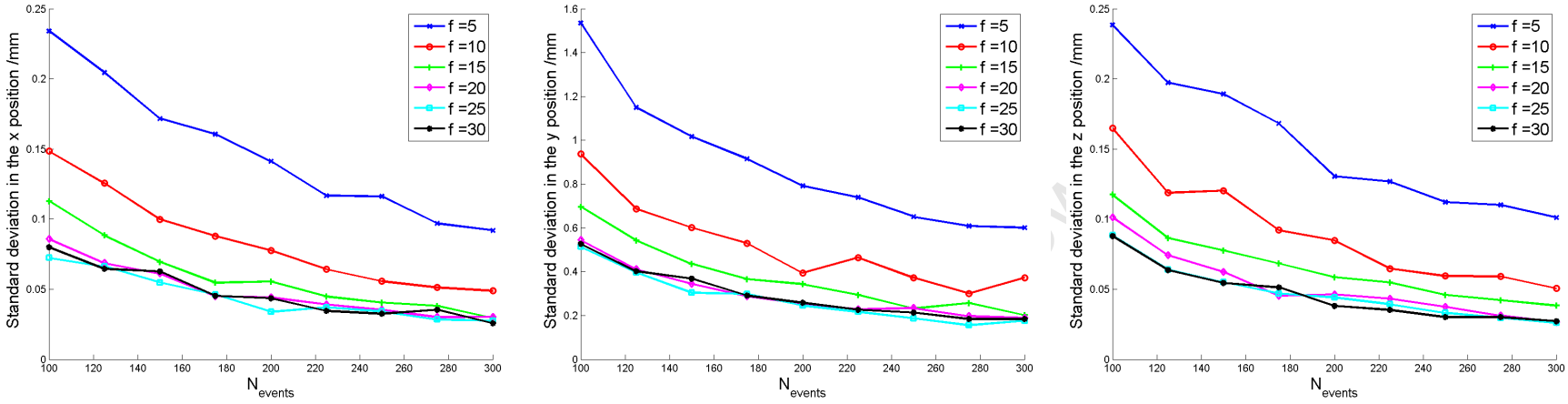

(a) $\hat{x}$-direction **(b)** $\hat{y}$-direction **(c)** $\hat{z}$-direction

Figure E.6: The variation in spread for point P_1 in directions parallel with (left and centre) and perpendicular to (right) the plates of the detectors, as a function of N_{events} for a range of values of f_{opt}.

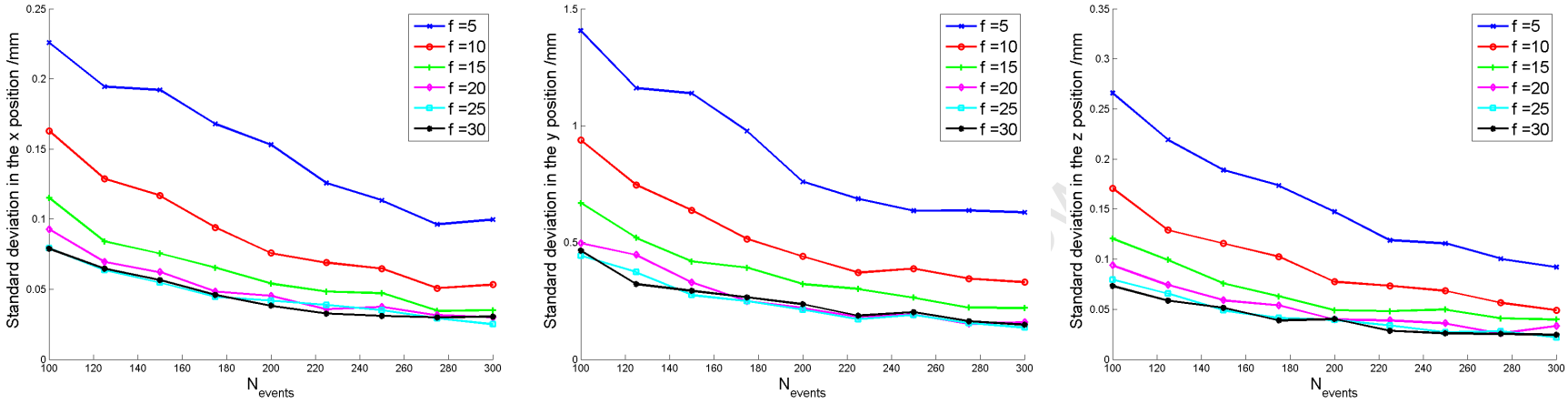

(a) $\hat{x}$-direction **(b)** $\hat{y}$-direction **(c)** $\hat{z}$-direction

Figure E.7: The variation in spread for point P_2 in directions parallel with (left and centre) and perpendicular to (right) the plates of the detectors, as a function of N_{events} for a range of values of f_{opt}.

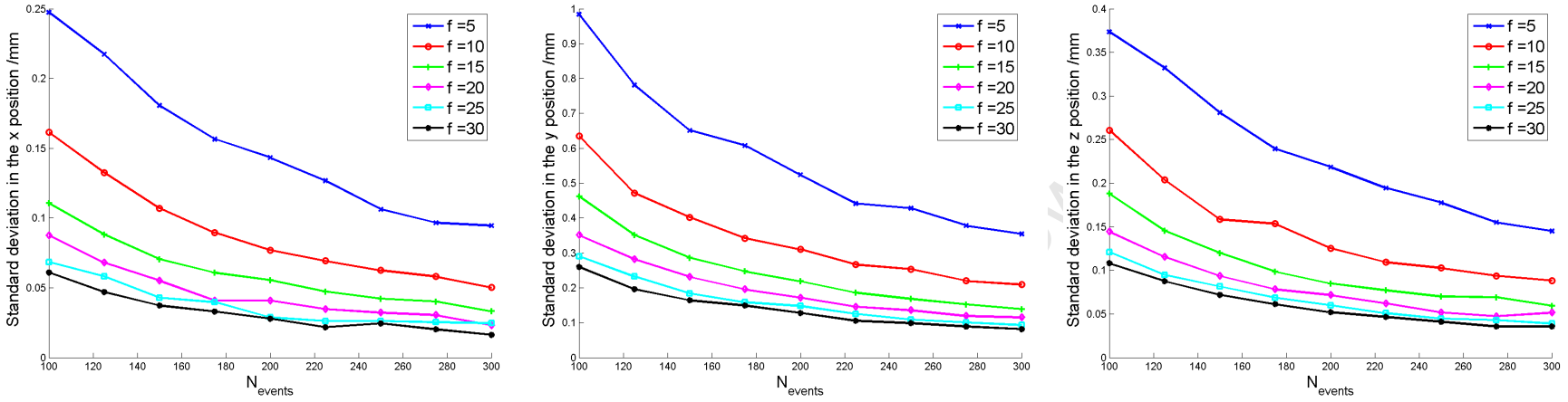

(a) $\hat{x}$-direction **(b)** $\hat{y}$-direction **(c)** $\hat{z}$-direction

Figure E.8: The variation in spread for point P_3 in directions parallel with (left and centre) and perpendicular to (right) the plates of the detectors, as a function of N_{events} for a range of values of f_{opt}.

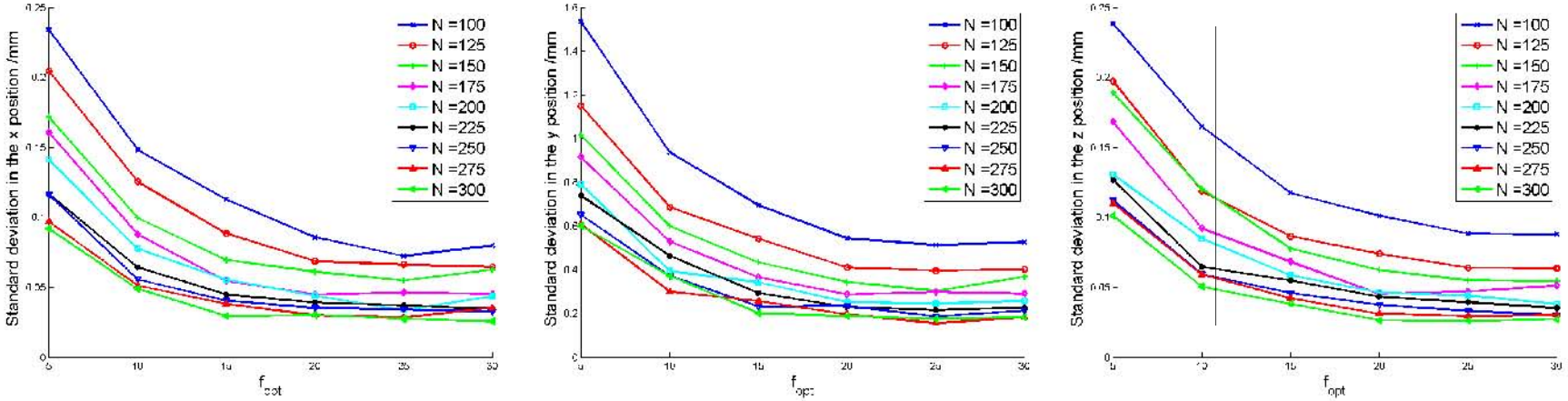

(a) $\hat{x}$-direction **(b)** $\hat{y}$-direction **(c)** $\hat{z}$-direction

Figure E.9: The variation in spread for point P_1 in directions parallel with (left and centre) and perpendicular to (right) the plates of the detectors, as a function of f_{opt} for a range of values of N_{events}.

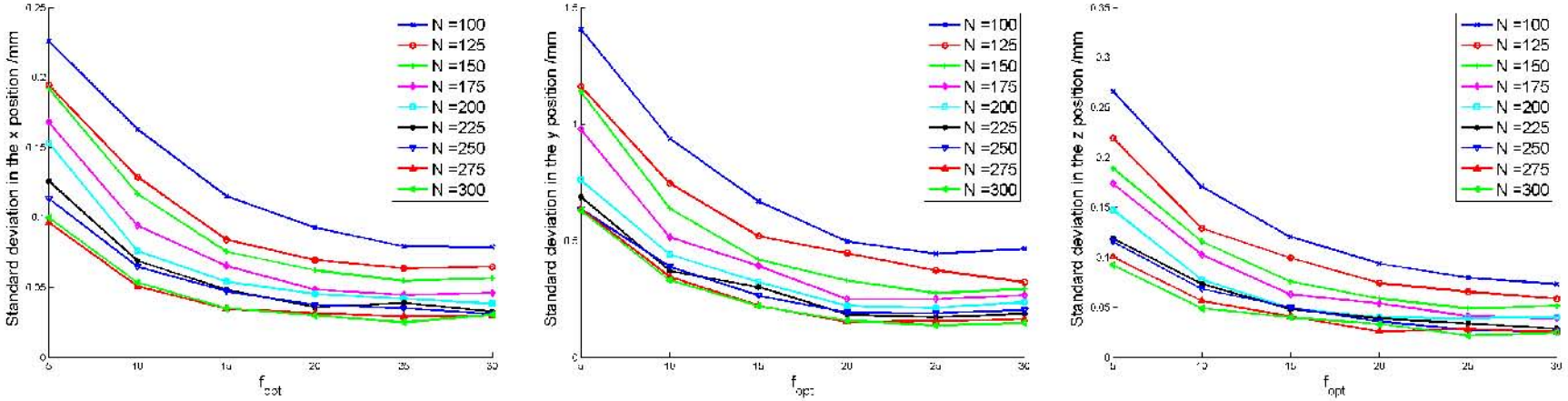

(a) $\hat{x}$-direction **(b)** $\hat{y}$-direction **(c)** $\hat{z}$-direction

Figure E.10: The variation in spread for point P_2 in directions parallel with (left and centre) and perpendicular to (right) the plates of the detectors, as a function of f_{opt} for a range of values of N_{events}.

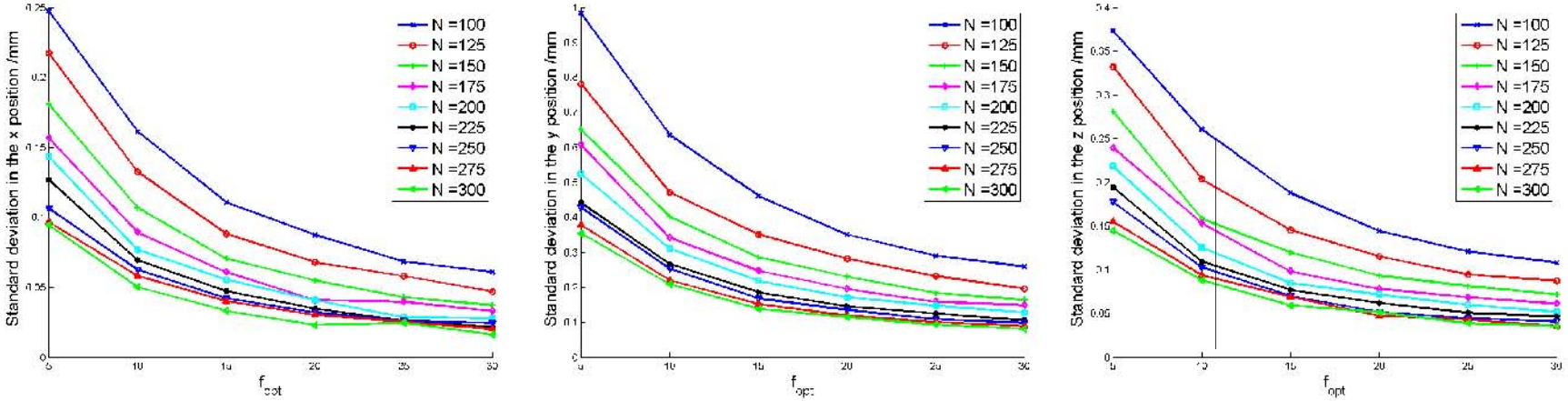

(a) $\hat{x}$-direction **(b)** $\hat{y}$-direction **(c)** $\hat{z}$-direction

Figure E.11: The variation in spread for point P_3 in directions parallel with (left and centre) and perpendicular to (right) the plates of the detectors, as a function of f_{opt} for a range of values of N_{events}.

E.2 Location markers

In Sections 4.5 and 5.5.1, and in Appendix F, I describe the process of centring and aligning the mill based on a series of location markers- tracer particles attached to the outside of a rotating mill shell to trace out a circle of known radius. These location markers can also be used to optimise the triangulation parameters by providing a well-known trajectory with which to compare the triangulated one.

Figure E.12 shows a location marker experiment triangulated with various combinations of f_{opt} and N_{events}. The top left subplot is triangulated with $f_{opt} = 5\%$ and $N_{events} = 100$. The f_{opt} used in each triangulation increases by 5% for each row, and the N_{events} increase by 100 for each column. Thus the bottom right subplot was triangulated with $f_{opt} = 30\%$ and $N_{events} = 300$.

From Figure E.12 it is clear that there is a good deal of deviation from the expected circular at some combinations of parameters, and that this is especially pronounced on the edges of the circles closest to the detectors. This could be due to the reduced solid angle of receptivity close to one detector[1], or to the fact that one half of each LoR must pass through the mill- through much more attenuating material- than the other. This effect seems less pronounced at larger f_{opt} and N_{events}, although the reduced sampling frequency effects the angular distribution of detections for large N_{events}.

Figure E.13 illustrates this uneven angular distribution of triangulated locations for a range of f_{opt} and N_{events}.

Figure E.14 shows histogrammed differences between the radial coordinate of the triangulated tracer particle and the known actual radius of its motion. From this figure it is clear that for increasingly large N_{events}- during which time the tracer particle may have moved an appreciable distance- the triangulated radii become smaller and smaller, leading to a skewed distribution. This corresponds to the averaging out of the curvature of the tracer particle's path for large N_{events}. This is particularly pronounced in the low statistics regions closest to the detectors.

Figure E.15 shows the increased deviation from the expected radius at angular positions closest to the detectors. Qualitatively, the plots in Figure E.15 are the inverse of those in Figure E.13. The combination of these two effects is to produce significantly worse data near the detectors than in the centre of the field of view- the opposite of the case for the stationary particles in which the uncertainty was dominated by the attenuating environment.

E.2.1 Circular measures

Since we know *a priori* that the tracer particle in a location marker run moves in a circular orbit of well-known radius, we can use this fact to assess the accuracy of the triangulation- at least for the circular 'toy' case.

The trends in deviation from the known radius shown in Figures E.14 and E.15 can be made more quantitative by considering the variation of mean and standard deviations as a function of f_{opt} and N_{events}, as shown in figure.

Figure E.16 shows that the standard deviation from the known radius drops off quickly for both increasing f_{opt} and N_{events}. There is a similar drop in the mean deviation from the known radius with increasing N_{events}, as was also obvious in Figure E.12. More interesting, however, is the appearance of an optimum f_{opt} at about 15%[2].

[1] See Section 2.3.2.

[2] cf. the apparent optimum at $f_{opt} \approx 20\%$ suggested by Figures E.9, E.10 and E.11.

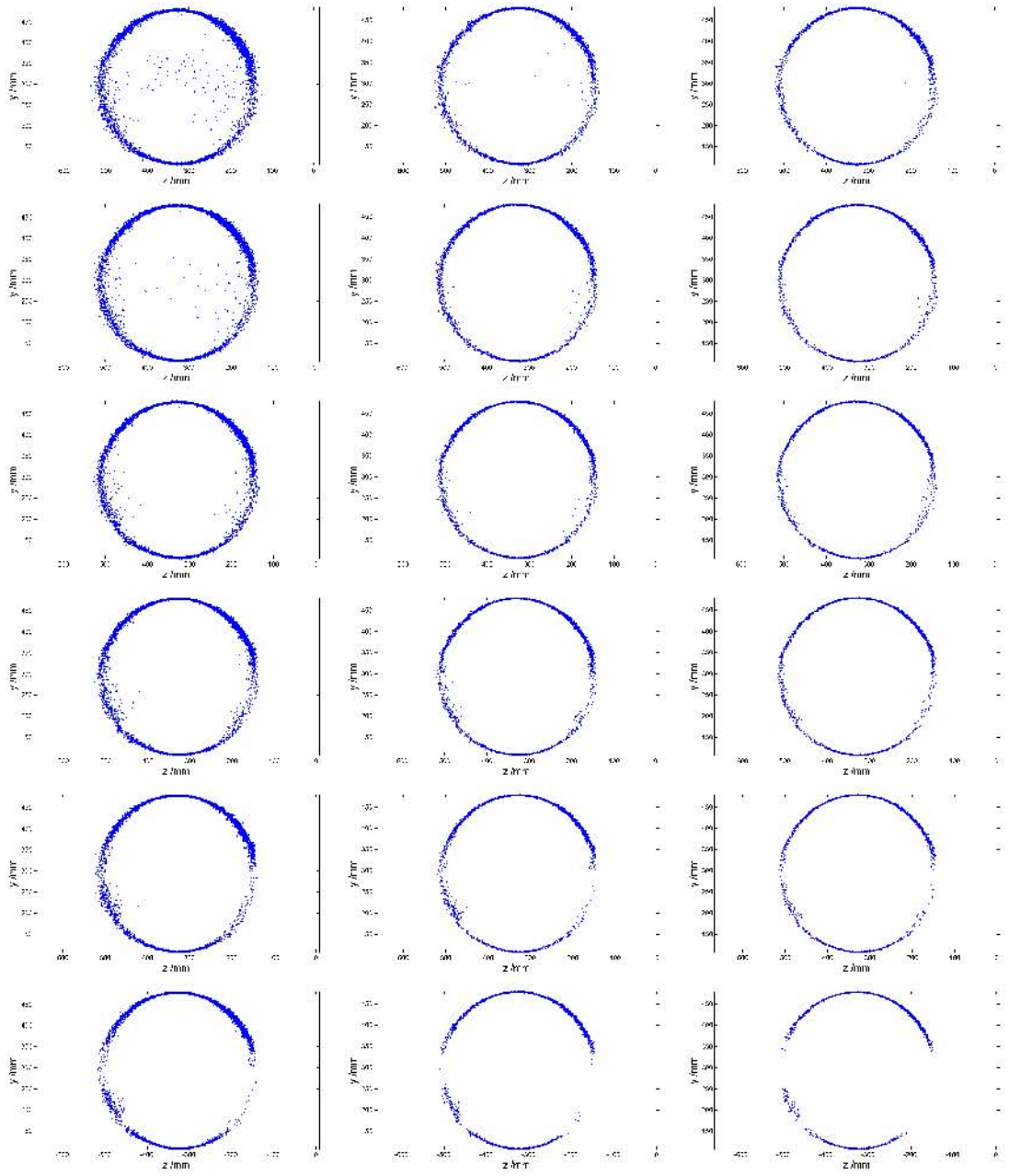

Figure E.12: 2D transaxial projections of a location marker run triangulated with increasing f_{opt} (top to bottom) and N_{events} (left to right).

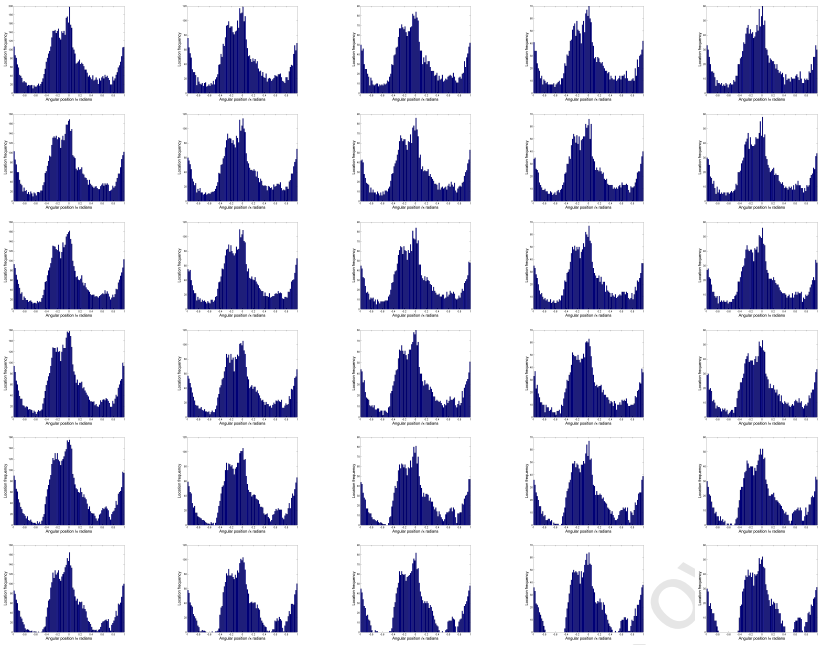

Figure E.13: The angular distribution of locations for a run triangulated with increasing f_{opt} (top to bottom) and N_{events} (left to right).

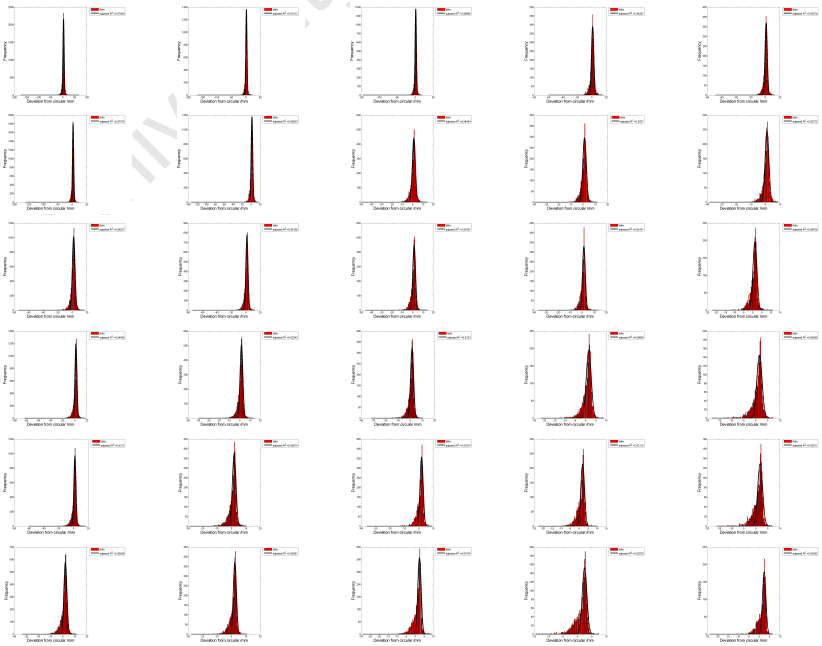

Figure E.14: Deviation of the triangulated radial position from the expected one for a run triangulated with increasing f_{opt} (top to bottom) and N_{events} (left to right).

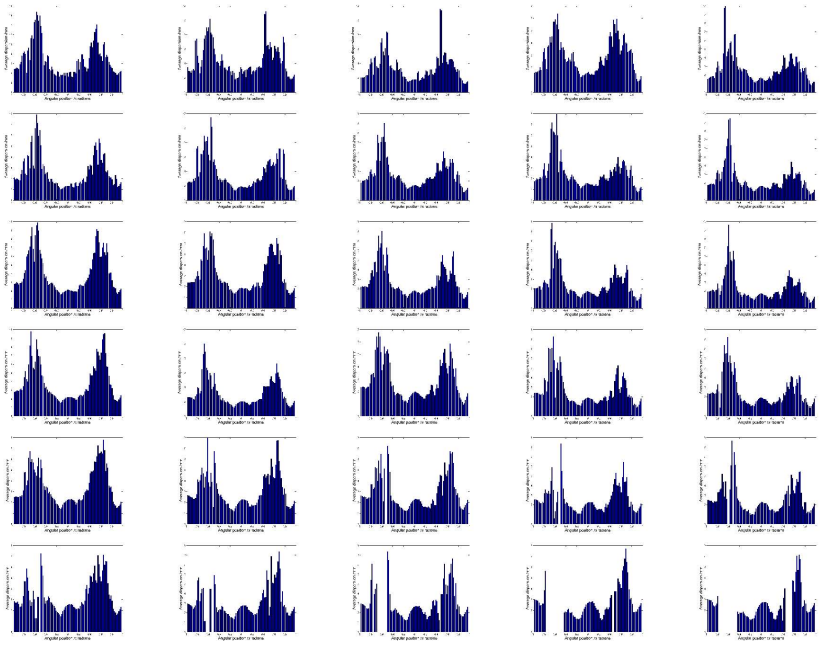

Figure E.15: Deviation of the triangulated radial position from the expected one for a run triangulated with increasing f_{opt} (top to bottom) and N_{events} (left to right), as a function of the angular position of the tracer particle.

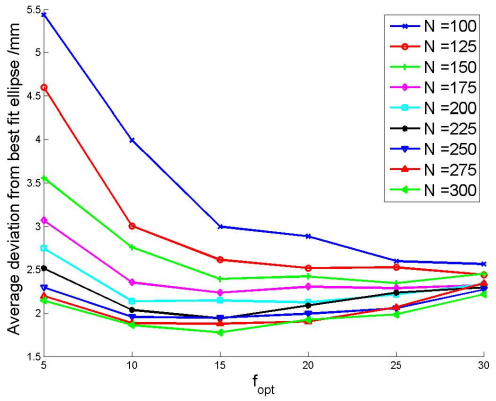

(a) Mean deviation as a function of f_{opt}

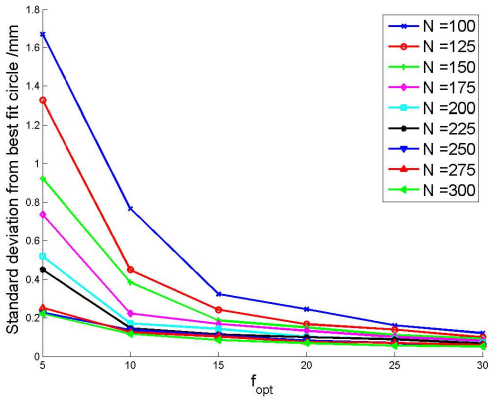

(b) Standard deviation as a function of f_{opt}

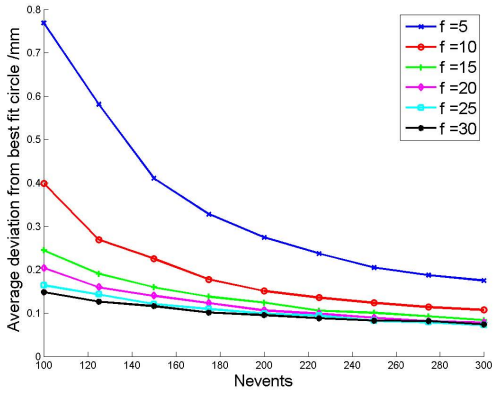

(c) Mean deviation as a function of N_{events}

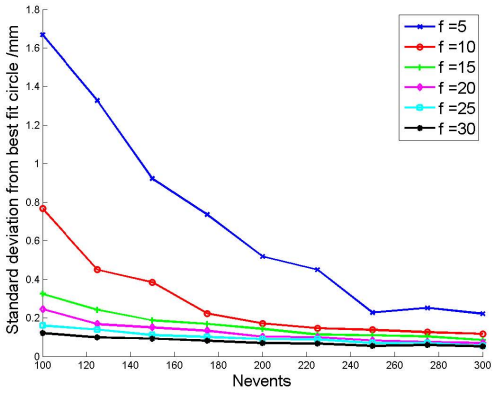

(d) Standard deviation as a function of N_{events}

Figure E.16: The mean (left) and standard (right) deviation from the known path radius of the motion of a tracer particle as a function of f_{opt} (top) and N_{events} (bottom).

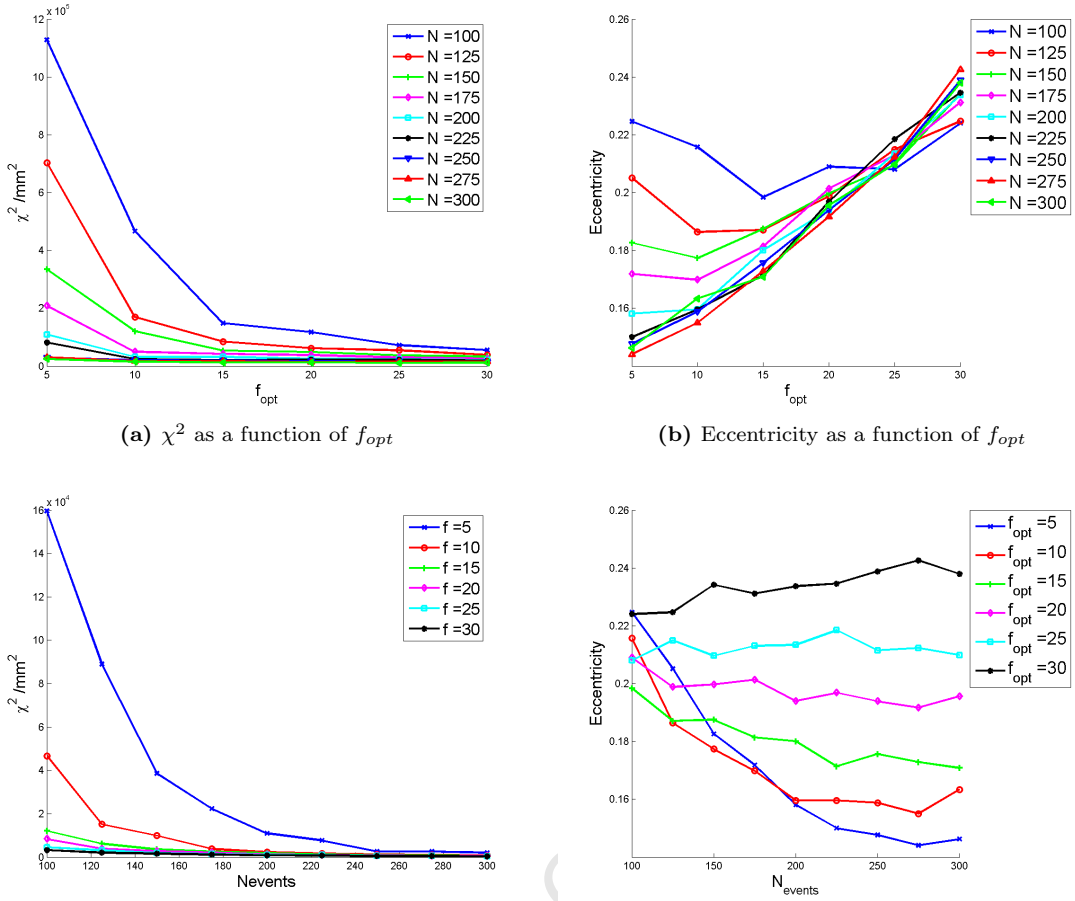

(a) χ^2 as a function of f_{opt}

(b) Eccentricity as a function of f_{opt}

(c) χ^2 as a function of N_{events}

(d) Eccentricity as a function of N_{events}

Figure E.17: The χ^2 (left) and eccentricity (right) of the ellipse of best fit to the triangulated positions of a location marker as a function of f_{opt} (top) and N_{events} (bottom).

This still does not capture the loss of statistics shown in Figure E.12. To make this more quantitative, I fit an ellipse to the data and investigate its properties. Figure E.17 shows the χ^2 of the fit, and the eccentricity- that is, the ratio of the semi-major and -minor axes of the fitted ellipses- as a function of f_{opt} and N_{events}.

From Figure E.17 it is clear that better fits are obtainable from datasets triangulated with larger f_{opt} and N_{events}. However, larger f_{opt} lead to greater deviation from circular- higher eccentricity- and larger N_{events} only lead to greater circularity for smaller f_{opt}. This suggests that there is an optimum number of remaining events $f_{opt}N_{events}$ that should be used in the final iteration.

E.3 Location error in the real system

The traditional method of optimising the triangulation parameters is to minimise the mean, normalised location error for a given run. Figure shows the location error as a function of f_{opt} and N_{events}.

From Figure E.18, it is clear that average location error increases with increasing f_{opt} and decreases with increasing N_{events}. It is unclear, however, how best to interpret this result since we don't know the true motion of the particle or the intrinsic error in its location.

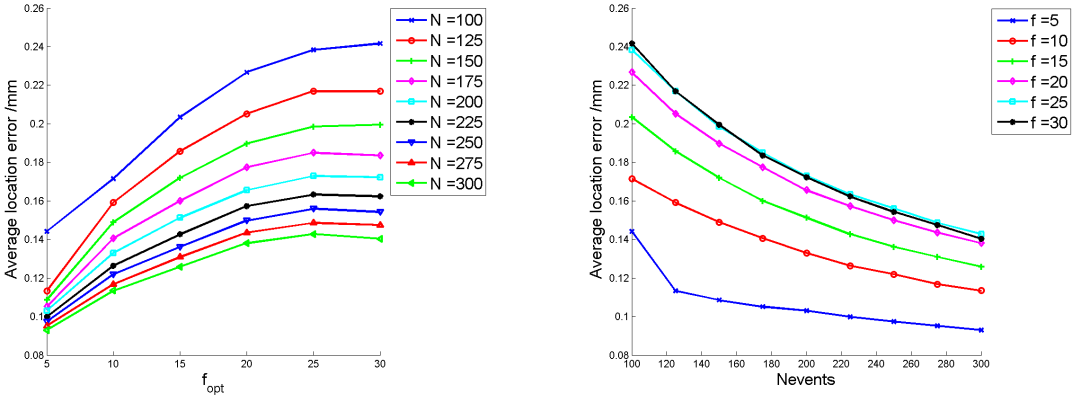

(a) Location error as a function of f_{opt}

(b) location error as a function of N_{events}

Figure E.18: Average location error as a function of f_{opt} (left) and N_{events} (right).

E.4 A quick summary

From a consideration of 2D plots of tracer particle locations in the mill- see Figure E.1- it seems that a smaller f_{opt} produces fewer very serious outliers. The point spread functions- see Figures E.9, E.10 and E.11- of several stationary particles, however, show that larger f_{opt}s produce more precise locations. These point spread functions also suggest that there may be an optimum at around $f_{opt} \approx 15 - 20\%$. A similar trend appears in the accuracy of location as measured by a deviation from a known circular path- see Figure E.16- with greater accuracies at higher f_{opt} and an optimum at $f_{opt} \approx 15\%$.

A quick look at the variation of tracer particle location, velocity and acceleration with time- see Figures E.2 and E.3- seems to suggest that a larger N_{events} produces smoother data. Larger N_{events} also produce more precise stationary particle locations- see Figures E.6, E.7 and E.8- as well as more accurate ones- see Figure E.16. Using too many events in each triangulation, leads to losses of statistics- an effect exacerbated by the geometry of this camera[3]- which can lead to poor accuracy of the sort not captured in the above, but shown in Figure E.17.

Thus, so far, an f_{opt} of between 15% and 25% is indicated with high, but not too high, N_{events}- perhaps the value suggested by equation 2.21.

Equation 2.21 provides an estimate for an optimal N_{events} thus

$$N \approx \left(\frac{\sigma R}{v\sqrt{f_{opt}}} \right)^{\frac{2}{3}} \tag{E.1}$$

where σ is the value of the point spread function to which the measured one asymptotes along the optimum $f_{opt} = 20\%$ curve in Figure E.9.

In this case, $f_{opt} = 20\%$, $\sigma \approx 0.05$, $R = 2.57kHz$[4], and the tangential speed of the mill shell is $v \approx 0.728ms^{-1}$, thus $N \approx 250$.

It is important to note, though, that I chose to interpret σ as the asymptotic value of the point spread function because it gives such a compelling estimate of N_{events}- any other, larger estimate results in very large optimum N_{events}. for instance, a σ of 0.1 yields an $N_{events} \approx 400$, which is patently too large.

[3] See Figures E.12, E.13 and E.15.

[4] Averaged over the 20 minute run.

E.5 The full list of measures used for my optimisation

In this example I have employed a range of measures to decide on the optimum triangulation parameters for each run or family of runs. In my work, however, I have considered all of the following:

- Visual inspection
  - 3D locations
  - 2D projections in the xy-, zy- and xz-directions
  - Variations with time of location, velocity and acceleration in each direction
- Aggregate measures
  - Average and standard deviation of the location error
  - Average and standard deviation of all of the locations in each dimension
  - Measured and calculated detection rates
  - Measured particle activity
  - Mean and maximum time steps
  - Mean and maximum x, y and z steps
- Circular measures
  - Mean and standard deviation from expected radius
  - χ^2 of the ellipse and circles of best fit
  - Radius, semi-major and semi-minor axes of circle or ellipse of best fit
  - Eccentricity, aspect ratio and flattening of the best fit ellipse
  - Centres and focal points of the circles and ellipses of best fit
  - Mean and standard deviation of the particle locations in each direction
  - Fourier analyses of variations in particle position
  - Angular location frequency
  - Angular dispersion- mean, standard deviation and range
- Point spread function
  - Point spread functions
  - Average and standard deviation of the particle locations in each direction

Despite- or because of- this, optimisation remains a subjective and labour-intensive undertaking.

Appendix F

Triangulation, optimisation and pre-processing of PEPT data

F.1 Centring and aligning the mill

F.1.1 The equation of a circle rotated in 3D space

A circle in 3D space is the intersection of a plane and a sphere, as shown in Figure F.1a. Thus the orientation of such a circle is given by the orientation of the plane, which itself is given by the normal to the plane, as shown in Figure F.1b.

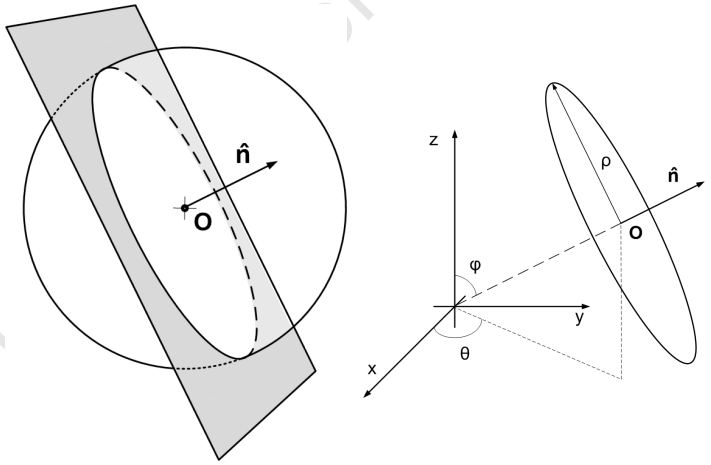

(a) The intersection of a sphere and a plane

(b) A circle in 3D space

Figure F.1: A circle in 3D space as the intersection between a sphere and a plane (left), and showing its orientation in terms of the unit vector to the plane (right).

The equation of a sphere of radius ρ centred at $\vec{O} = (x_0, y_0, z_0)$ is

$$\begin{aligned} (\vec{O} - \vec{x}_0) \cdot (\vec{O} - \vec{x}_0) - \rho^2 &= 0 \\ (x - x_0)^2 + (y - y_0)^2 + (z - z_0)^2 - \rho^2 &= 0 \end{aligned} \tag{F.1}$$

where $\vec{x}_0$ is some point on the sphere.

The equation of a plane passing through the centre of the sphere $\vec{O} = (x_0, y_0, z_0)$ can be written

in terms of its unit normal $\hat{n}$, as

$$\begin{aligned} \hat{n} \cdot (\vec{x}_0 - \vec{O}) &= 0 \\ n_x(x - x_0) + n_y(y - y_0) + n_z(z - z_0) &= 0 \end{aligned} \tag{F.2}$$

where

$$\begin{aligned} n_x &= \cos\theta \sin\phi \\ n_y &= \sin\theta \sin\phi \\ n_z &= \cos\phi \end{aligned}$$

as per Figure F.1b.

Thus the equation of this circle can be obtained by equating equations F.1 and F.2, thus

$$\begin{aligned} (\vec{O} - \vec{x}_0) \cdot (\vec{O} - \vec{x}_0) - \rho^2 &= \hat{n} \cdot (\vec{x}_0 - \vec{O}) \\ \Rightarrow (x - x_0)^2 - n_x(x - x_0) + (y - y_0)^2 - n_y(y - y_0) + (z - z_0)^2 - n_z(z - z_0) - \rho^2 &= 0 \qquad \text{(F.3)} \\ \Rightarrow (x - x_0 - \frac{n_x}{2})^2 - \frac{n_x^2}{4} + (y - y_0 - \frac{n_y}{2})^2 - \frac{n_y^2}{4} + (z - z_0 - \frac{n_z}{2})^2 - \frac{n_z^2}{4} - \rho^2 &= 0 \\ \because (r - r_0)^2 - n_r(r - r_0) + \frac{n_r^2}{4} &= ((r - r_0) - \frac{n_r}{2})^2 \\ \Rightarrow (x - x_0 - \frac{n_x}{2})^2 + (y - y_0 - \frac{n_y}{2})^2 + (z - z_0 - \frac{n_z}{2})^2 - \frac{1}{4} - \rho^2 &= 0 \\ \because n_x^2 + n_y^2 + n_z^2 &= 1 \end{aligned}$$

and so, the equation of a circle in 3D space, in terms of its centre $\vec{O} = (x_0, y_0, z_0)$, radius ρ, and two angles of orientation θ and ϕ, can be written as a ternary quadratic polynomial with no cross-terms, thus

$$\begin{aligned} f(x, y, z) &= (x - x_0 - \frac{n_x}{2})^2 + (y - y_0 - \frac{n_y}{2})^2 + (z - z_0 - \frac{n_z}{2})^2 - \frac{1}{4} - \rho^2 \qquad \text{(F.4)} \\ &= (x - x_0 - \frac{1}{2}\cos\theta \sin\phi)^2 + (y - y_0 - \frac{1}{2}\sin\theta \sin\phi)^2 + (z - z_0 - \frac{1}{2}\cos\phi)^2 - \frac{1}{4} - \rho^2 \\ &= x^2 + \xi_1 x + y^2 + \xi_2 y + z^2 + \xi_3 z - \xi_4 \end{aligned}$$

where

$$\begin{aligned} \xi_1 &= -(2x_0 + \cos\theta \sin\phi) \\ \xi_2 &= -(2y_0 + \sin\theta \sin\phi) \\ \xi_3 &= -(2z_0 + \cos\phi) \\ \xi_4 &= \rho^2 - (x_0^2 + \cos\theta \sin\phi x_0) - (y_0^2 + \sin\theta \sin\phi y_0) - (z_0^2 + \cos\phi z_0) \end{aligned}$$

F.1.2 Fitting a 3D circle to location markers using an iterative least squares method

Given the equation of a circle in 3D space, equation F.4, and a series of N locations x_N, it is possible to obtain the centre, radius and orientation of the circle of best fit to these locations by solving the resultant system of ternary quadratic equations.

Consider the general case of solving the equation

$$a_1x^2 + a_2y^2 + a_3z^2 + a_4xy + a_5xz + a_6yz + a_7x + a_8y + a_9z + a_{10} = 0 \tag{F.5}$$

which can be written more compactly in matrix form as

$$\begin{aligned} 0 &= xAx^T \\ &= \begin{pmatrix} x & y & z & 1 \end{pmatrix} \begin{pmatrix} A_{11} & A_{12} & A_{13} & A_{14} \\ A_{21} & A_{22} & A_{23} & A_{24} \\ A_{31} & A_{32} & A_{33} & A_{34} \\ A_{41} & A_{42} & A_{43} & A_{44} \end{pmatrix} \begin{pmatrix} x \\ y \\ z \\ 1 \end{pmatrix} \end{aligned} \tag{F.6}$$

thus the coefficients in equation F.5 are

$$\begin{aligned} a_1 &= A_{11} \\ a_2 &= A_{22} \\ a_3 &= A_{33} \\ a_4 &= (A_{12} + A_{21}) = 2A_{12} = 2A_{21} \\ a_5 &= (A_{13} + A_{31}) = 2A_{13} = 2A_{31} \\ a_6 &= (A_{23} + A_{32}) = 2A_{23} = 2A_{32} \\ a_7 &= (A_{14} + A_{41}) = 2A_{14} = 2A_{41} \\ a_8 &= (A_{24} + A_{42}) = 2A_{24} = 2A_{42} \\ a_9 &= (A_{34} + A_{43}) = 2A_{34} = 2A_{43} \\ a_{10} &= A_{44} \end{aligned} \tag{F.7}$$

for a symmetric coefficient matrix, A, because

$$A_{11}x^2+A_{22}y^2+A_{33}z^2+(A_{12}+A_{21})xy+(A_{13}+A_{31})xz+(A_{23}+A_{32})yz+(A_{14}+A_{41})x+(A_{24}+A_{42})y+(A_{34}+A_{43})z+A_{44} = 0$$

For the case the case of the 3D circle described by equation F.4, and for a series of N locations x_N, matrix equation F.6 can be written as

$$\begin{pmatrix} 0 \\ \vdots \\ \vdots \\ 0 \end{pmatrix} = \begin{pmatrix} x_1 & y_1 & z_1 & 1 \\ \vdots & \ddots & & \vdots \\ \vdots & & \ddots & \vdots \\ x_N & y_N & z_N & 1 \end{pmatrix} \begin{pmatrix} 1 & 0 & 0 & \frac{1}{2}\xi_1 \\ 0 & 1 & 0 & \frac{1}{2}\xi_2 \\ 0 & 0 & 1 & \frac{1}{2}\xi_3 \\ \frac{1}{2}\xi_1 & \frac{1}{2}\xi_2 & \frac{1}{2}\xi_3 & \xi_4 \end{pmatrix} \begin{pmatrix} x_1 & \cdots & x_N \\ y_1 & \cdots & y_N \\ z_1 & \cdots & z_N \\ 1 & \cdots & N \end{pmatrix} \tag{F.8}$$

Equation F.8 is overdetermined- it consists of $N >> 4$ equations in 4 unknowns. It is thus appropriate to solve equation F.8 for coefficient matrix A by an iterative least squares method, discarding the points with the largest residual errors at each step. The resultant entries of A can then be used to obtain the centre $\vec{O} = (x_0, y_0, z_0)$ of the fitted circle, its radius ρ, and its two angles of orientation, θ and ϕ, via equation F.4.

F.1.3 A quick method of obtaining the orientation of a plane using Singular Value Decomposition

The singular value decomposition is a method of factorising a real or complex matrix in terms of two orthogonal and one diagonal matrices. It has many applications in statistics, signals processing and least-squares fitting. As a result, there are many effecient numerical schemes to obtain the singular value decomposition of a given matrix.

The singular value decomposition of a matrix X is given by

$$X = USV^T \tag{F.9}$$

where $U \in \mathbb{R}^{m\times m}$ and $V \in \mathbb{R}^{n\times n}$ are orthogonal matrices, and $S \in \mathbb{R}^{m\times n}$ is a diagonal matrix containing the singular values $\sigma_1 \geqslant \sigma_2 \geqslant \ldots \geqslant \sigma_r \geqslant 0, r = min(m, n)$.

Inge Söderkvist at the LuleåUniversity of Technology in Sweden offers the following algorithm for obtaining both the normal to a best-fit plane, and the vectors spanning it.

1. Let p_i be the point to which to fit the plane.
2. Let $c = \frac{1}{n}\Sigma_{1=1}^{n} p_i$ be the 'centre' of these points.
3. $X = [p_1 - c, \ldots, p_n - c]$
4. $X = USV^T$
5. $\hat{n} = U(:, 3)$ is the normal to the plane and the remaining two columns of U span the plane.

F.1.4 Rotating and translating the data

Once the centre, radius, and two angles of orientation of the mill have been obtained by the preceding procedure, the mill can be centred in the Eulerian reference frame of the system by translating all of the points in the Lagrangian reference frame of the tracked particle to the fitted centre $\vec{O} = (x_0, y_0, z_0)$, and by rotating them about that centre in the following way.

Referring for orientation to Figure F.1b, the system must be rotated by $-\theta$ about the $\hat{z}$-axis, and $-\phi$ about the $\hat{y}$-axis to align with the $\hat{z}$-axis. This means an effective rotation matrix of

$$\begin{aligned} R_{eff} &= R_z R_y \\ &= \begin{pmatrix} \cos\theta & \sin\theta & 0 \\ -\sin\theta & \cos\theta & 0 \\ 0 & 0 & 1 \end{pmatrix} \begin{pmatrix} \cos\phi & 0 & -\sin\phi \\ 0 & 1 & 0 \\ \sin\phi & 0 & \cos\phi \end{pmatrix} \\ &= \begin{pmatrix} \cos\theta\cos\phi & \sin\theta & -\cos\theta\sin\phi \\ -\sin\theta\cos\phi & \cos\theta & \sin\theta\sin\phi \\ \sin\phi & 0 & \cos\phi \end{pmatrix} \end{aligned} \tag{F.10}$$

Appendix G

Some technical aspects of interpolation

G.1 Polynomial interpolation

Given a set of $(n+1)$ data points $(s_i, t_i)_{0\leq i\leq n}$, the *values of interpolation* $(s_i)_{0\leq i\leq n}$ are related to the *points of interpolation* $(t_i)_{0\leq i\leq n}$ by the *interpolant* $f(t_i)$ such that

$$s_i = f(t_i)\ \forall i = 0\dots n. \tag{G.1}$$

If the interpolant is a polynomial of degree n, $P_n(t_i)$, such that

$$P_n(t_i) = f(t_i)\ \forall i = 0\dots n, \tag{G.2}$$

then this polynomial is unique.

G.1.1 Proof of uniqueness

Lemma 1 (Fundamental Theorem of Algebra)**.** *Every non-zero, single-variable polynomial with complex coefficients has exactly as many (possible degenerate) complex roots as its degree.*
Theorem 1. *For any set of data points (s_i, t_i) the interpolating polynomial of least degree is unique.*

Proof. Consider two polynomials $\{P_n, Q_n\} \in \mathcal{P}_n$, which both satisfy condition G.2. Let $R_n = (P_n - Q_n) \in \mathcal{P}_n$. The polynomial R_n has $(n+1)$ roots, which are exactly the points of interpolation $(t_i)_{0\leq i\leq n}$ since

$$R_n(t_i) = P_n(t_i) - Q_n(t_i) = f(t_i) - f(t_i) = 0\ \forall i = 0\dots n. \tag{G.3}$$

Therefore R_n has $(n+1)$ roots and can be written in the form

$$R_n(t) = \prod_i (t - t_i)\ \forall i = 0\dots n, \tag{G.4}$$

but $R_n \in \mathcal{P}_n$ and so, by Lemma 1, can only have n roots if it is non-zero. R_n must therefore be zero, and

$$R_n = 0 \Rightarrow P_n = Q_n; \tag{G.5}$$

the interpolating polynomial is unique. □

G.1.2 Interpolation error

The uniqueness of the interpolating polynomial of least degree means that the choice of interpolant can be made based on the facility of its implementation. However, the accuracy of the result is still a consideration when choosing the order of the interpolating polynomial to use.

I give here, without proof, an expression for the interpolation error for a polynomial of degree n. Let $f \in \mathbb{C}^{n+1}$ be the function to be interpolated and $t \in [t_{min}, t_{max}]$ the range over which it is to be interpolated. Let I be the smallest closed set containing both t, an arbitrary point, and $t_i, \forall i$, the sample points. The error in the interpolated data is given by

Theorem 2.

$$\forall t \in [t_{min}, t_{max}],\ \exists \xi \in I : f(t) - L_n(t) = \frac{f^{n+1}(\xi)}{(n+1)!} \prod_{i=0}^{n} (t - t_i) \tag{G.6}$$

This says that the interpolation error goes like the product $\mid \prod_{i=0}^{n}(t - t_i) \mid$. For equally-spaced times, such that $t_i = t_{i-1} + \Delta t$, the interpolation error would be proportional to $\mathcal{O}(\Delta t^n)$. Thus, unsurprisingly, the interpolation error is smallest when the sampling frequency is greatest, and increases exponentially with the order of the interpolating polynomial.

Furthermore, high-degree polynomial interpolation may suffer from spurious oscillation, especially at the end-points of the interpolating interval- an occurrence called *Runge's phenomenon*. The usual way of dealing with this is to choose special sampling points, such as *Chebyshev nodes*, which counteract it. Obviously, in this case that is not possible. This sort of phenomenon can only be mitigated here by interpolating in a piece-wise fashion using lower-degree polynomials. Since the datasets produced by Lagrangian particle tracking techniques are generally so large, it is infeasible to construct an interpolant for the whole dataset, and the data must be interpolated in a piece-wise way anyway. We are free to choose, with justification, the order of these interpolants.

G.2 Explicit forms of the Lagrange interpolating polynomial

The explicit form of a 2nd order Lagrange interpolant over data points $(s_j, t_j),\ j \in [i-1, i, i+1]$ can be written as:

$$s(t) = s_{i-1}\frac{(t-t_i)(t-t_{i+1})}{(t_{i-1}-t_i)(t_{i-1}-t_{i+1})} + s_i\frac{(t-t_{i-1})(t-t_{i+1})}{(t_i-t_{i-1})(t_i-t_{i+1})} + s_{i+1}\frac{(t-t_{i-1})(t-t_i)}{(t_{i+1}-t_{i-1})(t_{i+1}-t_i)} = pt^2 - qt + r \tag{G.7}$$

where

$$\begin{aligned} p &= \frac{s_{i-1}}{a} + \frac{s_i}{b} + \frac{s_{i+1}}{c} \\ q &= \frac{s_{i-1}}{a}(t_i + t_{i+1}) + \frac{s_i}{b}(t_{i-1} + t_{i+1}) + \frac{s_{i+1}}{c}(t_{i-1} + t_i) \\ r &= \frac{s_{i-1}}{a} t_i t_{i+1} + \frac{s_i}{b} t_{i-1} t_{i+1} + \frac{s_{i+1}}{c} t_{i-1} t_i \end{aligned}$$

and

$$\begin{aligned} a &= (t_{i-1} - t_i)(t_{i-1} - t_{i+1}) \\ b &= (t_i - t_{i-1})(t_i - t_{i+1}) \\ c &= (t_{i+1} - t_{i-1})(t_{i+1} - t_i). \end{aligned}$$

Of course, a quadratic can be easily inverted to yield

$$t(s) = \frac{q \pm \sqrt{q^2 + 4p(s-r)}}{2p}, \tag{G.8}$$

which is used for the residence time binning in Section 5.3.5.

The explicit form of a 3rd order Lagrange interpolant, as well as its inverse, could similarly be written, but would be less clear for illustrative purposes. A 3rd order solution is implemented in my code, though.

Appendix H

Residence time binning: Program listing


```
% ajm 20110708.1201
%
% This is a generalisation of my earlier residence time distribution code
% tmResidenceTime, which is optimised for cylindrical symmetry and only
% bins in a plane, assumed to be in the transaxial direction.
%
% This version takes as input the trajectory (t,x,y,z) the ranges over
% which to bin the data xrange = [x lower limit, x upper limit] etc., and
% the number of bins to divide each dimension into. To bin a projection in
% the XY direction, for instance, set zbins = 1 and squeeze the resultant
% matrices.
%
% It returns the coordinates of the lines separating bins in each
% dimension— xVals, yVals and zVals— and 4 xbins x ybins x zbins x N arrays
% of binned data. grdRes contains residence time—weighted binned measures,
% and grdCnt contains simple binned measures. N = 7 for grdRes and N = 3
% for grdCnt (see below). Below are listed the contents of these matrices:
%
% grdRes(1,:,:,:) the residence time distribution
% grdRes(2,:,:,:) time—weighted x—velocity distribution
% grdRes(3,:,:,:) time—weighted y—velocity distribution
% grdRes(4,:,:,:) time—weighted z—velocity distribution
% grdRes(5,:,:,:) time—weighted x—acceleration distribution
% grdRes(6,:,:,:) time—weighted y—acceleration distribution
% grdRes(7,:,:,:) time—weighted z—acceleration distribution
%
% grdCnt(1,:,:,:) simple binning
% grdCnt(2,:,:,:) simple averaged velocity magnitude
% grdCnt(3,:,:,:) simple averaged acceleration magnitude
%
% grdResErr and grdCntErr contain the corresponding standard deviations in
% the binned measures mentioned above, except that grdCntErr(1,:,:,:) is a
% xbins x ybins x zbins zero matrix included just for indexing consistency.
%
% angus.morrison@uct.ac.za

function [xVals yVals zVals grdRes grdResErr grdCnt grdCntErr] = ...
    residenceTime(t,x,y,z,xrange,yrange,zrange,xbins,ybins,zbins)

    % the grid end points
```

```
xVals = linspace(xrange(1),xrange(2),xbins+1);
yVals = linspace(yrange(1),yrange(2),ybins+1);
zVals = linspace(zrange(1),zrange(2),zbins+1);

% initialising the grids
gridCnt = zeros(xbins,ybins,zbins);    % traditional bin count
gridRes = zeros(xbins,ybins,zbins);    % residence time distribution
gridErr = zeros(xbins,ybins,zbins);    % std dev of the rtd

gridVel = zeros(xbins,ybins,zbins);    % unweighted
gridVelErr = zeros(xbins,ybins,zbins);
gridVx = zeros(xbins,ybins,zbins);  % residence time-weighted
gridVxErr = zeros(xbins,ybins,zbins);    % std dev of the time-weighted velocity
gridVy = zeros(xbins,ybins,zbins);
gridVyErr = zeros(xbins,ybins,zbins);
gridVz = zeros(xbins,ybins,zbins);
gridVzErr = zeros(xbins,ybins,zbins);

gridAcc = zeros(xbins,ybins,zbins);    % unweighted
gridAccErr = zeros(xbins,ybins,zbins);
gridAx = zeros(xbins,ybins,zbins);  % residence time-weighted
gridAxErr = zeros(xbins,ybins,zbins);
gridAy = zeros(xbins,ybins,zbins);
gridAyErr = zeros(xbins,ybins,zbins);
gridAz = zeros(xbins,ybins,zbins);
gridAzErr = zeros(xbins,ybins,zbins);

% a counter to keep track of the number of points lying outside the
% binning limits supplied
outliers = 0;

% stepping through the location arrays from the second to the second
% last elements in steps of 2 elements to avoid overlapping the
% interpolating 2nd order Lagrange polynomials (which require 3 points)
for i = 2:2:length(t)-1
    times = []; % initialising time array on each pass

    % finding the grid elements in which the end points of the
    % interpolated function are found, and then adding them to the
    % times array for later sorting.

    % grid element in which the start point is found
    indxl = x(i-1) < xVals;
    xl = find(indxl,1,'first') - 1;

    % grid element in which the end point is found
    indxh = x(i+1) < xVals;
    xh = find(indxh,1,'first') - 1;

    indyl = y(i-1) < yVals;
    yl = find(indyl,1,'first') - 1;

    indyh = y(i+1) < yVals;
    yh = find(indyh,1,'first') - 1;

    indzl = z(i-1) < zVals;
    zl = find(indzl,1,'first') - 1;

    indzh = z(i+1) < zVals;
    zh = find(indzh,1,'first') - 1;
```

```
        % if the start or endpoints are not in the grid,
        % increment the outlier counter and continue
        if isempty(xl) || isempty(xh) || isempty(yl) ||...
                isempty(yh) || isempty(zl) || isempty(zh)
            outliers = outliers + 1;
            continue;
        end

        % adding the time and grid elements of the start and end points of
        % the interpolating polynomial to the time matrix
        times = [times; [t(i-1),xl,yl,zl]];
        times = [times; [t(i+1),xh,yh,zh]];

        % constructing the interpolating polynomial x(t) = pt^2 -qt + r

        a = (t(i-1) - t(i))*(t(i-1) - t(i+1));
        b = (t(i) - t(i-1))*(t(i) - t(i+1));
        c = (t(i+1) - t(i-1))*(t(i+1) - t(i));

        p1x = (x(i-1)/a);
        p2x = (x(i)/b);
        p3x = (x(i+1)/c);

        px = p1x + p2x + p3x;
        qx = p1x*(t(i) + t(i+1)) + p2x*(t(i-1) + t(i+1)) + p3x*(t(i-1) + t(i));
        rx = p1x*t(i)*t(i+1) + p2x*t(i-1)*t(i+1) + p3x*t(i-1)*t(i);

        % stepping through each of the grid elements bounded by the xVal
        % vertical lines
        for q = 1:length(xVals)-1
            % solving the quadratic interpolating polynomial to determine
            % at what times it crosses the vertical voxel boundary j
            t1 = (qx + (qx^2 + 4*px*(xVals(q) - rx))^0.5)/(2*px);
            t2 = (qx - (qx^2 + 4*px*(xVals(q) - rx))^0.5)/(2*px);

            % if the solutions are real and lie between the start and end
            % times of the interpolating polynomial, add the crossing times
            % and index j of the vertical voxel limit to the times array
            if isreal(t1)
                if t(i-1) < t1 && t(i+1) > t1
                    times = [times;[t1,q,0,0]];
                end
            end

            if isreal(t2)
                if t(i-1) < t2 && t(i+1) > t2
                    times = [times;[t2,q,0,0]];
                end
            end
        end

        % constructing the interpolating polynomial y(t) = pt^2 -qt + r
        p1y = (y(i-1)/a);
        p2y = (y(i)/b);
        p3y = (y(i+1)/c);

        py = p1y + p2y + p3y;
        qy = p1y*(t(i) + t(i+1)) + p2y*(t(i-1) + t(i+1)) + p3y*(t(i-1) + t(i));
        ry = p1y*t(i)*t(i+1) + p2y*t(i-1)*t(i+1) + p3y*t(i-1)*t(i);

        % stepping through each of the grid elements bounded by the yVal
```

```
% horizontal lines
for r = 1:length(yVals)-1
    % solving the quadratic interpolating polynomial to determine
    % at what times it crosses the horizontal voxel boundary r
    t1 = (qy + (qy^2 + 4*py*(yVals(r) - ry))^0.5)/(2*py);
    t2 = (qy - (qy^2 + 4*py*(yVals(r) - ry))^0.5)/(2*py);

    % if the solutions are real and lie between the start and end
    % times of the interpolating polynomial, add the crossing times
    % and index r of the horizontal voxel limit to the times array
    if isreal(t1)
        if t(i-1) < t1 && t(i+1) > t1
            times = [times;[t1,0,r,0]];
        end
    end

    if isreal(t2)
        if t(i-1) < t2 && t(i+1) > t2
            times = [times;[t2,0,r,0]];
        end
    end
end

% constructing the interpolating polynomial z(t) = pt^2 -qt + r

p1z = (z(i-1)/a);
p2z = (z(i)/b);
p3z = (z(i+1)/c);

pz = p1z + p2z + p3z;
qz = p1z*(t(i) + t(i+1)) + p2z*(t(i-1) + t(i+1)) + p3z*(t(i-1) + t(i));
rz = p1z*t(i)*t(i+1) + p2z*t(i-1)*t(i+1) + p3z*t(i-1)*t(i);
% stepping through each of the grid elements bounded by the zVal
% horizontal lines
for s = 1:length(zVals)-1
    % solving the quadratic interpolating polynomial to determine
    % at what times it crosses the horizontal voxel boundary s
    t1 = (qz + (qz^2 + 4*pz*(zVals(s) - rz))^0.5)/(2*pz);
    t2 = (qz - (qz^2 + 4*pz*(zVals(s) - rz))^0.5)/(2*pz);

    % if the solutions are real and lie between the start and end
    % times of the interpolating polynomial, add the crossing times
    % and index s of the horizontal voxel limit to the times array
    if isreal(t1)
        if t(i-1) < t1 && t(i+1) > t1
            times = [times;[t1,0,0,s]];
        end
    end

    if isreal(t2)
        if t(i-1) < t2 && t(i+1) > t2
            times = [times;[t2,0,0,s]];
        end
    end
end

% sorting the times array by time so that it contains a list of
% voxel crossing times and the indices of the corresponding voxel
% boundaries
times = sortrows(times);
```

```
% stepping through the sorted times array from the first to the
% last boundary crossing (recall that the first and last elements
% contain the endpoint times and voxels)
for l = 2:length(times(:,1))-1
    % if the particle has crossed a z boundary, then neither x nor
    % y indices should be non-zero since they have not changed.
    % They can be populated with the values in the preceding row
    if ~(times(l,2)||times(l,3))
        times(l,2) = times(l-1,2);
        times(l,3) = times(l-1,3);

        % if the particle's previous z index is the same as the
        % crossed boundary index, then the particle is moving in
        % the negative z direction, and has moved into the voxel
        % immediately before the crossing boundary rather than
        % after it
        if times(l,4) == times(l-1,4)
            times(l,4) = times(l,4) - 1;
        end
    end

    % if the particle has crossed a y boundary, then neither the x
    % nor the z crossing boundary indices will be non-zero
    if ~(times(l,2)||times(l,4))
        times(l,2) = times(l-1,2);
        times(l,4) = times(l-1,4);

        % if the particle is moving in the negative y direction
        if times(l,3) == times(l-1,3)
            times(l,3) = times(l,3) - 1;
        end
    end

    % if the particle has crossed an x boundary, then neither the y
    % nor the z crossing boundary indices will be non-zero
    if ~(times(l,3)||times(l,4))
        times(l,3) = times(l-1,3);
        times(l,4) = times(l-1,4);

        % if the particle is moving in the negative y direction
        if times(l,2) == times(l-1,2)
            times(l,2) = times(l,2) - 1;
        end
    end
end

% the weights matrix now contains the time spent in the voxel
% specified by the corresponding indices. The final entry can be
% ignored because the particle enters but does not leave the last
% element.
weights = [diff(times(:,1)) times(1:end-1,2) times(1:end-1,3) times(1:end-1,4)];

% performing the binning
for s = 1:length(weights(:,1))
    % if the index is less than 1, it is spurious, go on to the
    % next iteration
    if weights(s,2) < 1 || weights(s,3) < 1 || weights(s,4) < 1
        continue;
    end
    % adding the residence time to each voxel
    gridRes(weights(s,2),weights(s,3),weights(s,4)) = ...
```

```
285                 gridRes(weights(s,2),weights(s,3),weights(s,4)) + weights(s,1);
            gridErr(weights(s,2),weights(s,3),weights(s,4)) = ...
                gridErr(weights(s,2),weights(s,3),weights(s,4)) + weights(s,1)^2;

            % counting each time the particle passes through a voxel
290         gridCnt(weights(s,2),weights(s,3),weights(s,4)) = ...
                gridCnt(weights(s,2),weights(s,3),weights(s,4)) + 1;

            % calculating the time-weighted average velocity contribution
            % (integral(dr/dt)dt)/(integral dt)*delta t
295         % = (integral(2pt - q)/(delta t)*delta t
            % = p*(t_f^2 - t_i^2) - q*(t_f - t_i)
            % = r_f - r_i
            Vx = px*(times(s+1,1)^2 - times(s,1)^2) - qx*(times(s+1,1) - times(s,1));
            Vy = py*(times(s+1,1)^2 - times(s,1)^2) - qy*(times(s+1,1) - times(s,1));
300         Vz = pz*(times(s+1,1)^2 - times(s,1)^2) - qz*(times(s+1,1) - times(s,1));

            % transverse speed
            V = sqrt(Vx^2 + Vy^2 + Vz^2);

305         % unweighted average velocity
            gridVel(weights(s,2),weights(s,3),weights(s,4)) = ...
                gridVel(weights(s,2),weights(s,3),weights(s,4)) +...
                V/(times(s+1,1) - times(s,1));
            gridVelErr(weights(s,2),weights(s,3),weights(s,4)) = ...
310             gridVelErr(weights(s,2),weights(s,3),weights(s,4)) +...
                (V/(times(s+1,1) - times(s,1)))^2;

            % adding x, y and z dispacements contributions to each voxel
            gridVx(weights(s,2),weights(s,3),weights(s,4)) = ...
315             gridVx(weights(s,2),weights(s,3),weights(s,4)) + Vx;
            gridVxErr(weights(s,2),weights(s,3),weights(s,4)) = ...
                gridVxErr(weights(s,2),weights(s,3),weights(s,4)) + Vx^2;
            gridVy(weights(s,2),weights(s,3),weights(s,4)) = ...
                gridVy(weights(s,2),weights(s,3),weights(s,4)) + Vy;
320         gridVyErr(weights(s,2),weights(s,3),weights(s,4)) = ...
                gridVyErr(weights(s,2),weights(s,3),weights(s,4)) + Vy^2;
            gridVz(weights(s,2),weights(s,3),weights(s,4)) = ...
                gridVz(weights(s,2),weights(s,3),weights(s,4)) + Vz;
            gridVzErr(weights(s,2),weights(s,3),weights(s,4)) = ...
325             gridVzErr(weights(s,2),weights(s,3),weights(s,4)) + Vz^2;

            % calculating the time-weighted average acceleration
            % contribution
            % (integral(d^2r/dt^2)dt)/(integral dt)*delta t
330         % = integral(2p dt) / (delta t)*delta t
            % = 2p*(t_f - t_i)
            Ax = 2*px*(times(s+1,1) - times(s,1));
            Ay = 2*py*(times(s+1,1) - times(s,1));
            Az = 2*pz*(times(s+1,1) - times(s,1));
335
            A = sqrt(Ax^2 + Ay^2 + Az^2);

            % unweighted average acceleration
            gridAcc(weights(s,2),weights(s,3),weights(s,4)) =...
340             gridAcc(weights(s,2),weights(s,3),weights(s,4)) +...
                A/(times(s+1,1) - times(s,1));
            gridAccErr(weights(s,2),weights(s,3),weights(s,4)) =...
                gridAccErr(weights(s,2),weights(s,3),weights(s,4)) +...
                (A/(times(s+1,1) - times(s,1)))^2;
345
```

```
            % adding time-weighted average acceleration contributions to each voxel
            gridAx(weights(s,2),weights(s,3),weights(s,4)) =...
                gridAx(weights(s,2),weights(s,3),weights(s,4)) + Ax;
            gridAxErr(weights(s,2),weights(s,3),weights(s,4)) =...
                gridAxErr(weights(s,2),weights(s,3),weights(s,4)) + Ax^2;
            gridAy(weights(s,2),weights(s,3),weights(s,4)) =...
                gridAy(weights(s,2),weights(s,3),weights(s,4)) + Ay;
            gridAyErr(weights(s,2),weights(s,3),weights(s,4)) =...
                gridAyErr(weights(s,2),weights(s,3),weights(s,4)) + Ay^2;
            gridAz(weights(s,2),weights(s,3),weights(s,4)) =...
                gridAz(weights(s,2),weights(s,3),weights(s,4)) + Az;
            gridAzErr(weights(s,2),weights(s,3),weights(s,4)) =...
                gridAzErr(weights(s,2),weights(s,3),weights(s,4)) + Az^2;
        end

    end

    fprintf('%2.2f %% of all supplied data points lie outside the limits of the grid.\n',...
        1e2*outliers/length(t));

    % normalising the binned matrices
    gridVel = gridVel./gridCnt;
    gridVelErr = gridVelErr./gridCnt;
    gridAcc = gridAcc./gridCnt;
    gridAccErr = gridAccErr./gridCnt;
    gridCnt = gridCnt/sum(sum(sum(gridCnt)));

    % normalising the velocity to the total time spent in each voxel (hence
    % the weighted average of the velocity)
    gridVx = gridVx./gridRes;
    gridVxErr = gridVxErr./(gridRes.^2);
    gridVy = gridVy./gridRes;
    gridVyErr = gridVyErr./(gridRes.^2);
    gridVz = gridVz./gridRes;
    gridVzErr = gridVzErr./(gridRes.^2);

    % normalising the acceleration as above and expressing the acceleration
    % in SI units
    gridAx = gridAx./gridRes;
    gridAxErr = gridAxErr./(gridRes.^2);
    gridAy = gridAy./gridRes;
    gridAyErr = gridAyErr./(gridRes.^2);
    gridAz = gridAz./gridRes;
    gridAzErr = gridAzErr./(gridRes.^2);

    % normalising the residence time to the total time of the experiment
    T = sum(sum(sum(gridRes)));
    gridRes = gridRes/T;
    gridErr = gridErr/T;

    % completing the standard deviation calculation for the errors
    gridErr = sqrt(abs(gridErr - gridRes.^2));

    gridVelErr = sqrt(abs(gridVelErr - gridVel.^2));
    gridVxErr = sqrt(abs(gridVxErr - gridVx.^2));
    gridVyErr = sqrt(abs(gridVyErr - gridVy.^2));
    gridVzErr = sqrt(abs(gridVzErr - gridVz.^2));

    gridAccErr = sqrt(abs(gridAccErr - gridAcc.^2));
    gridAxErr = sqrt(abs(gridAxErr -gridAx.^2));
    gridAyErr = sqrt(abs(gridAyErr -gridAy.^2));
```

```
        gridAzErr = sqrt(abs(gridAzErr -gridAz.^2));

        % putting all of the time-weighted data into a single array
        grdRes(1,:,:,:) = gridRes;
        grdRes(2,:,:,:) = gridVx;
        grdRes(3,:,:,:) = gridVy;
        grdRes(4,:,:,:) = gridVz;
        grdRes(5,:,:,:) = gridAx;
        grdRes(6,:,:,:) = gridAy;
        grdRes(7,:,:,:) = gridAz;

        % putting all of the time-weighted error data into a single array
        grdResErr(1,:,:,:) = gridErr;
        grdResErr(2,:,:,:) = gridVxErr;
        grdResErr(3,:,:,:) = gridVyErr;
        grdResErr(4,:,:,:) = gridVzErr;
        grdResErr(5,:,:,:) = gridAxErr;
        grdResErr(6,:,:,:) = gridAyErr;
        grdResErr(7,:,:,:) = gridAzErr;

        % putting all of the simple-binning data into a single array
        grdCnt(1,:,:,:) = gridCnt;
        grdCnt(2,:,:,:) = gridVel;
        grdCnt(3,:,:,:) = gridAcc;

        % putting all of the simple-binning error data into a single array
        grdCntErr(1,:,:,:) = zeros(size(gridVelErr));
        grdCntErr(2,:,:,:) = gridVelErr;
        grdCntErr(3,:,:,:) = gridAccErr;

        % replacing NaNs and infs with zeros for plotting later
        for s = 1:7
            for m = 1:xbins
                for n = 1:ybins
                    for p = 1:zbins
                        if ~isfinite(grdRes(s,m,n,p))
                            grdRes(s,m,n,p) = 0;
                            grdResErr(s,m,n,p) = 0;
                        end

                        if s < 4
                            if ~isfinite(grdCnt(s,m,n,p))
                                grdCnt(s,m,n,p) = 0;
                                grdCntErr(s,m,n,p) = 0;
                            end
                        end
                    end
                end
            end
        end
    end
```

Appendix I

The optimal binning procedure

I.1 Artificial data

In order to test the simple and residence time binning methods, I generated artificial data of various levels of complexity. I first used a simple harmonic oscillator in two dimensions to produce a circular motion of well-known kinematics, and then added a small, velocity-dependent damping force to produce an equally-well defined logarithmic spiral motion.

I simply binned and residence time binned each of these trajectories sampled at various even and uneven frequencies, with various bin sizes to investigate the sensitivity of these two binning methods to sampling rate. I repeated these tests with and without added Gaussian noise to probe the smoothing properties of the two binning methods.

I was content to compare the reconstructed binned trajectories with a plot of the actual trajectory, but the binned kinematics required a more detailed comparison. I obtained such a comparison by inverting the definitions given in equations I.1 and I.2 to obtain the time, if any, at which the 'tracer' would have been at the centre of each bin. I then used this time to estimate the particle's true velocity or acceleration in that bin.

I.1.1 Circular motion

I define my simple harmonic oscillators by the steady-state solutions

$$\begin{aligned} q(t) &= A\cos(\omega t - \phi) \\ \dot{q}(t) &= -A\omega\sin(\omega t - \phi) \\ \ddot{q}(t) &= -A\omega^2\cos(\omega t - \phi) \end{aligned} \tag{I.1}$$

where A is the amplitude of the motion, $\phi = 0$ is its phase shift, $\omega = 2\pi f$ is its angular frequency, and t is the time in seconds.

Figure I.1 shows such a particle motion with amplitude 0.150 m and angular frequency 10 Hz, sampled at a range of time intervals between 10 and 25 ms.

The top row of Figure I.2 shows the same plots as in Figure I.1, but with sequential sample points joined by straight lines. As the sampling frequency decreases, therefore, the 'thickness' of the circle appears to increase as the straight lines joining each sample point approximate a circle less and less well.

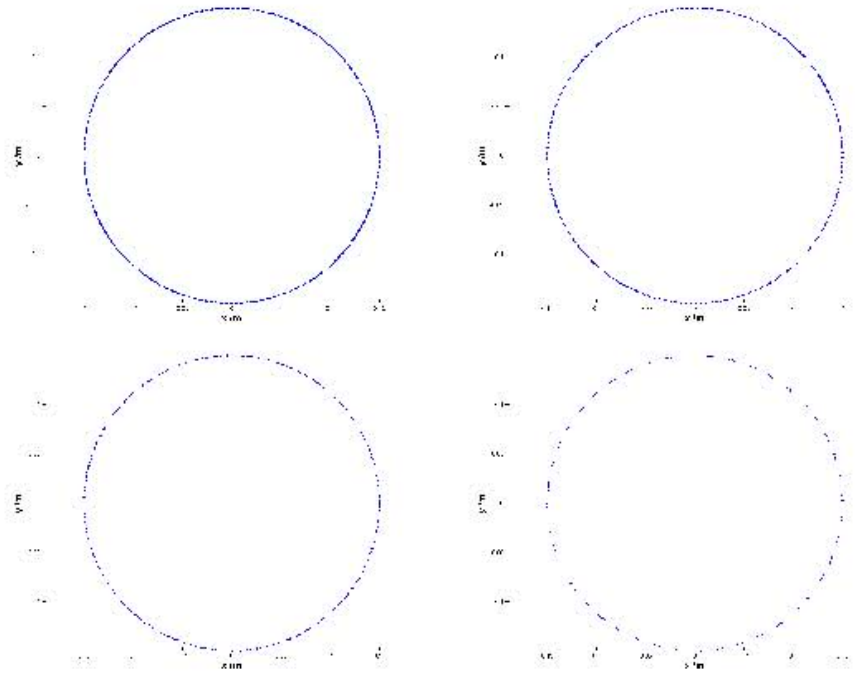

Figure I.1: Circular motion, of amplitude 0.150 m and angular frequency 10 Hz, sampled every $10, 25, 50$ and 100 ms (clockwise from top left).

The second row of Figure I.2 shows a simple binning of the data shown in Figure I.1, with a grid size of $3 \times 3mm^2$. In this, the simple binning case, the thickness of the recovered particle trajectory is limited only by the resolution of the grid. While the sampling rate does not affect the overall shape of the trajectory, it is clear that it does affect its continuity. This effect is even more pronounced in smaller (higher resolution) grids.

The third row of Figure I.2 shows the same data, residence time binned at the same resolution. Since residence time binning entails interpolating the data[1], trajectories binned in this way suffer from the 'thickening' of the sort shown in Figure I.2d. However, since the interpolants used in residence time binning are polynomials, they have some curvature, and the 'thickening' effect is less pronounced. Moreover, although the trajectory is artificially thickened, a high probability thread is visible along the true trajectory. The data shown in Figure I.1 is 15s worth of the particle's trajectory. If it was longer- and thus the particle circulated more often- the true trajectory would be further enhanced at the expense of the interpolating thickness.

[1]See Section 5.3.5.

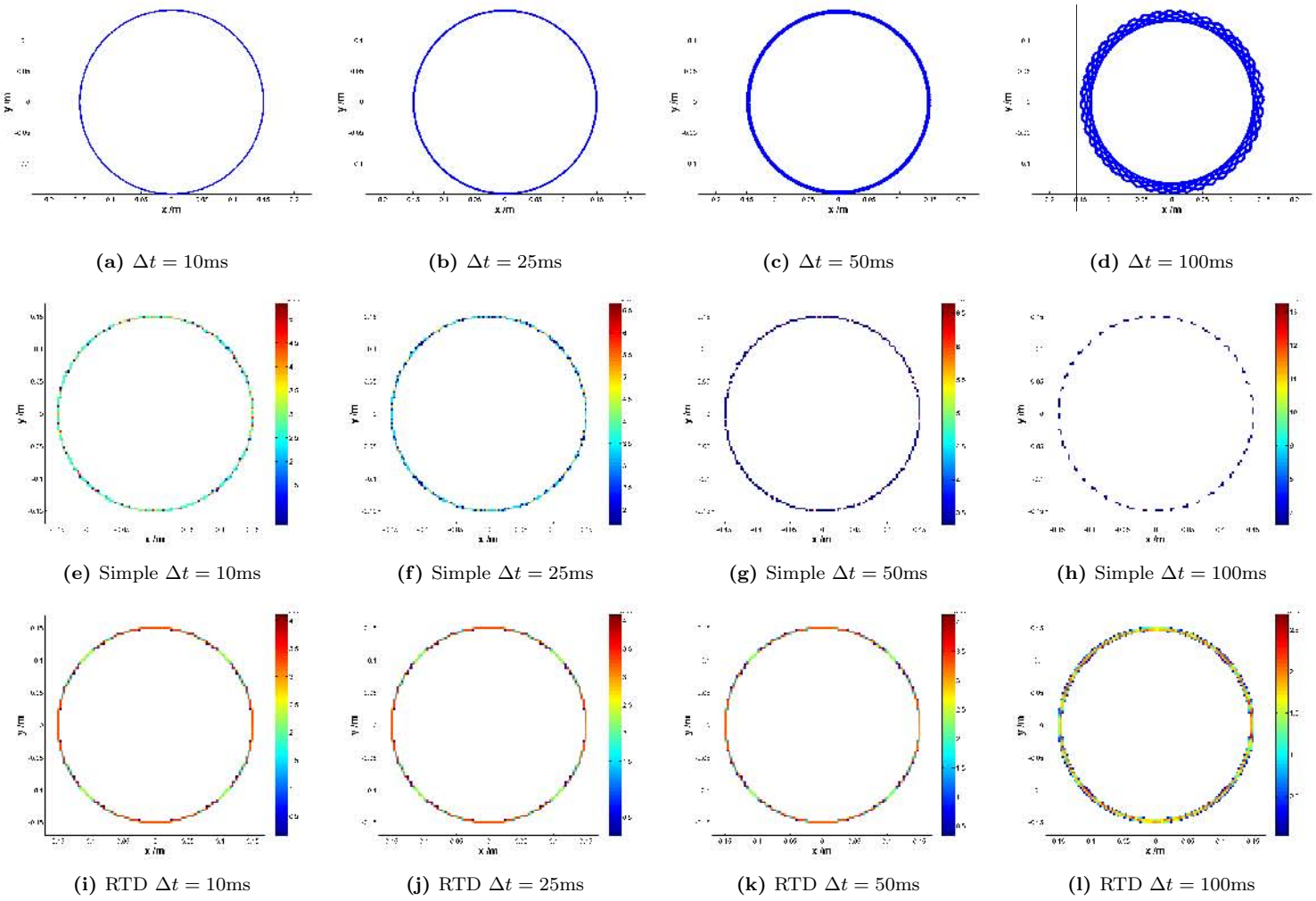

(a) $\Delta t = 10$ms **(b)** $\Delta t = 25$ms **(c)** $\Delta t = 50$ms **(d)** $\Delta t = 100$ms

(e) Simple $\Delta t = 10$ms **(f)** Simple $\Delta t = 25$ms **(g)** Simple $\Delta t = 50$ms **(h)** Simple $\Delta t = 100$ms

(i) RTD $\Delta t = 10$ms **(j)** RTD $\Delta t = 25$ms **(k)** RTD $\Delta t = 50$ms **(l)** RTD $\Delta t = 100$ms

Figure I.2: Artificial data sampled at decreasing frequency (top, left to right), binned by the simple binning (middle) and residence time (bottom) methods.

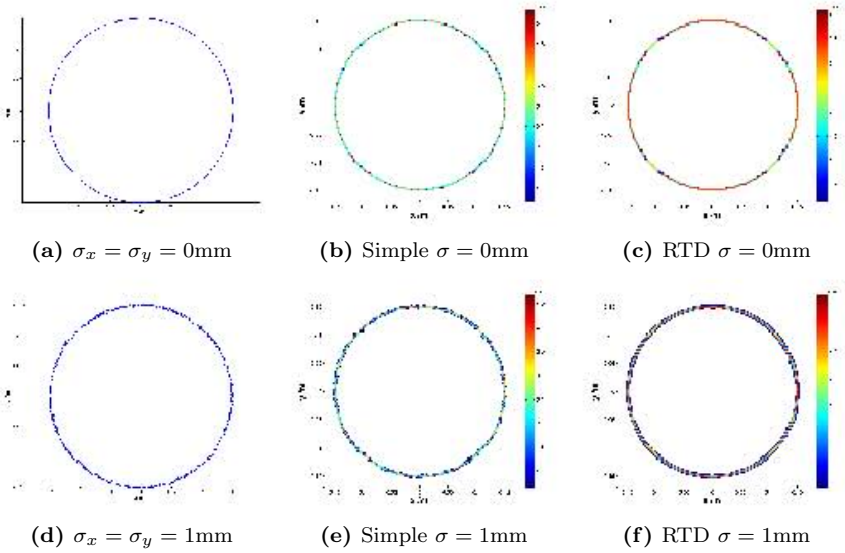

(a) $\sigma_x = \sigma_y = 0$mm **(b)** Simple $\sigma = 0$mm **(c)** RTD $\sigma = 0$mm

(d) $\sigma_x = \sigma_y = 1$mm **(e)** Simple $\sigma = 1$mm **(f)** RTD $\sigma = 1$mm

Figure I.3: Artificial data (left) with (bottom) and without (top) 1mm of Gaussian noise sampled at intervals of 10ms, and binned by the simple binning (middle) and residence time (right) methods.

Of course, in reality, PEPT data is not perfectly triangulated[2]. Figure I.3 shows the same data as before, sampled at intervals of $\Delta t = 10$ms, but now with Gaussian noise of amplitude 1mm added in the x and y coordinates. Figure I.3f shows the same high probability thread as was visible in the residence time binning of low-frequency sampled data in Figure I.2, a feature absent in the randomly thickened simply binned case. Residence time binning is thus capable of picking out the true trajectory from mildly noisy data- an advantage over simple binning.

More on this with a slightly more complicated trajectory later, first, though, a discussion of the recovered kinematics in the simple and residence time binning cases.

In the case of simple circular motion, the tangential speed of the particle is constant, and its $\hat{x}$- and $\hat{y}$- velocities can simply be calculated from the angular position of each bin. Similarly, its centripetal acceleration is constant and its $\hat{x}$- and $\hat{y}$- accelerations can be calculated as for its velocities, making comparisons very easy to perform.

Figure I.4 shows the theoretical data with which to compare the kinematics of the artificial data as produced in by the simple and residence time binning methods. These theoretical values are calculated from knowledge of the particle's true angular velocity and the radial position of the *centre* of the bin to which each value is assigned. Note the centripetal acceleration.

Subtracting theoretical values from calculated ones gives a measure of how well each binning method reproduces the real data. Figure I.5 shows a series of histograms of the deviations from the theoretical kinematics of a particle whose trajectory is sampled at intervals of $\Delta t = 25$ms.

Two things are notable from this figure. The first is that although particles are more likely to deviate from the theoretical than not, the histogrammed probability distribution is symmetric about the zero deviation- the binned data is as likely to over- as under-predict the kinematics. Secondly, the simple binning seems to produce both a thinner distribution and relatively more particles in the zero deviation bin. This is because more off-true trajectory data is created by the residence time binning method due to interpolation.

Although useful to consider qualitatively, trends in the deviations from theoretical emerge best in collated data. Figure I.6 shows the mean magnitude deviations of the binned artificial data from its theoretical values. Figures I.6a and I.6b show that increasing the sampling interval strongly

[2]See Section 2.3.4.

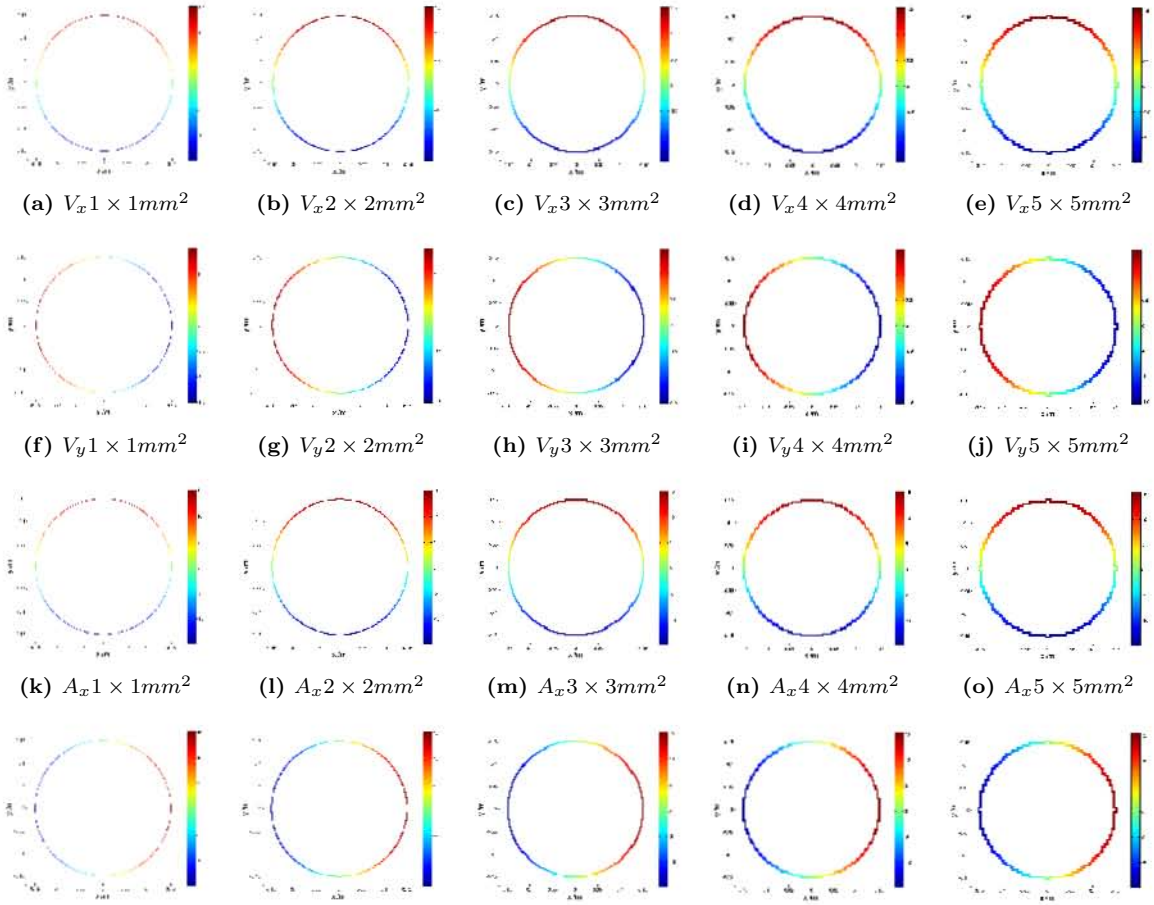

(a) $V_x1 \times 1mm^2$ **(b)** $V_x2 \times 2mm^2$ **(c)** $V_x3 \times 3mm^2$ **(d)** $V_x4 \times 4mm^2$ **(e)** $V_x5 \times 5mm^2$

(f) $V_y1 \times 1mm^2$ **(g)** $V_y2 \times 2mm^2$ **(h)** $V_y3 \times 3mm^2$ **(i)** $V_y4 \times 4mm^2$ **(j)** $V_y5 \times 5mm^2$

(k) $A_x1 \times 1mm^2$ **(l)** $A_x2 \times 2mm^2$ **(m)** $A_x3 \times 3mm^2$ **(n)** $A_x4 \times 4mm^2$ **(o)** $A_x5 \times 5mm^2$

(p) $A_y1 \times 1mm^2$ **(q)** $A_y2 \times 2mm^2$ **(r)** $A_y3 \times 3mm^2$ **(s)** $A_y4 \times 4mm^2$ **(t)** $A_y5 \times 5mm^2$

Figure I.4: Theoretical velocities and accelerations in grids of decreasing resolution (left to right).

increases the mean deviation of the velocity and acceleration from the theoretical at all grid sizes. This is born out in Figure I.8. Furthermore, because of the smoothing effect of larger grid sizes (lower resolution grids), mean deviations decrease with increasing grid size.

Figure I.6 shows that the residence time binning method produces mean deviations significantly closer to zero than does the simple binning method, for all sampling rates. Figures I.6c and I.6d, however, show that this advantage is reduced for noisy data[3].

Also from this figure, it is clear that the binned velocities are much closer to the theoretical ones than are the binned accelerations, but that their variations with bin size are very nearly identical, especially for the case without noise. This is not unexpected because the velocities and accelerations are not measured independently, but rather calculated from the underlying trajectory of the particle.

Figure I.7 shows that the standard deviations of the binned from the theoretical kinematics follow less pronounced trends than do their means. This is true for all cases except the residence time binned data sampled at 50ms intervals, whose standard deviation suddenly drops at a grid size of $3 \times 3mm^2$.

This is interesting because it suggests that there is an optimum resolution for a given sampling frequency. Figures I.7a and I.7b suggest that the spread of deviations for residence time binned data is greatest for low sampling rates and high resolutions. It is tempting to accept this as an optimum, but I will show that this spread is not necessarily a good indicator of the accuracy- as

[3]Here sampled at 25ms intervals.

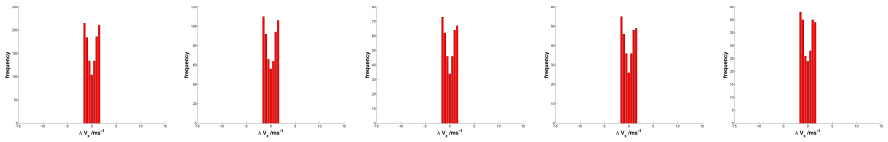

(a) Simple V_x

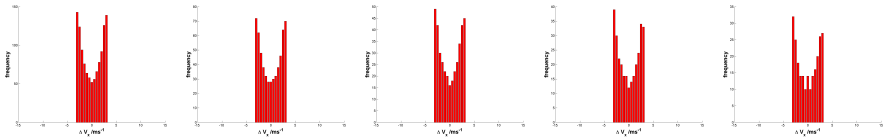

(b) RTD V_x

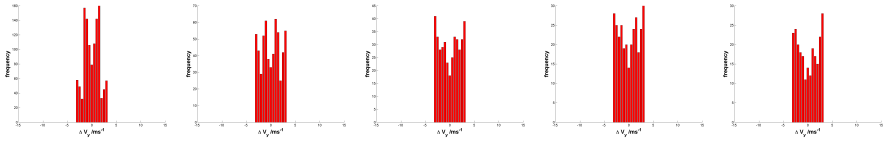

(c) Simple V_y

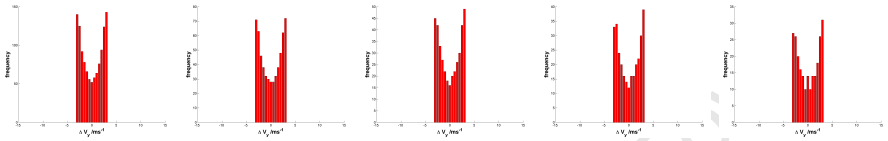

(d) RTD V_y

Figure I.5: Histogrammed deviations from theoretical velocities simply and residence time binned at increasing grid size (left to right).

opposed to the precision- of the data[4].

PEPT data is not only noisy, it is also non-uniformly sampled in time. The leftmost column in Figure I.9 shows artificial data sampled at intervals of $\Delta t = 100 \pm 50$ms with increasing levels of Gaussian noise. As in Figure I.3, sample points are connected sequentially with straight lines, leading to the 'thickening' effect as before. However, in this case the non-uniform sampling and scatter in the sample points both increases the apparent 'thickness' of the circle, and destroys its geometric appearance.

The residence time binning of this data results, again, in a less-pronounced 'thickness' than did the straight lines, with a clearly visible high-probability thread corresponding to the true, underlying trajectory. This effect is not apparent in the simple binning case, once again affirming residence time binning's advantage over simple binning with respect to smoothing out noise at the expense of introducing an 'interpolating halo'.

Figures I.10 and I.11 show plots of the differences between theoretical and binned values of the transverse velocity and acceleration of the artificial data, respectively. The colour scales of these plots are different, but a clear, blue thread of zero deviation is seen in the residence time binned data in all cases. A similar blue thread is seen in the simple binning cases, but here blue is strongly negative, signifying a large under-prediction in the binned case. This could be due to the poor sampling frequency as much as anything.

Figure I.12 shows the mean and standard deviations from theoretical transverse velocities and accelerations of the binned data as a function of bin size. Here, the residence time binned velocities and accelerations show the smallest mean deviation from theoretical, but the largest standard deviations. That is, while the residence time binning method produces more accurate results, it produces a greater number of less precise results. The opposite is true of the simple binning

[4]Notwithstanding, it will turn out that this is the optimum grid resolution for this sort of data, but this can only be confirmed after further investigation in the following sections.

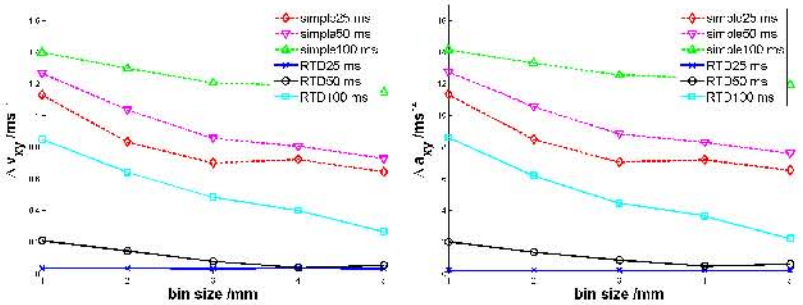

(a) Transverse velocity without noise

(b) Transverse acceleration without noise

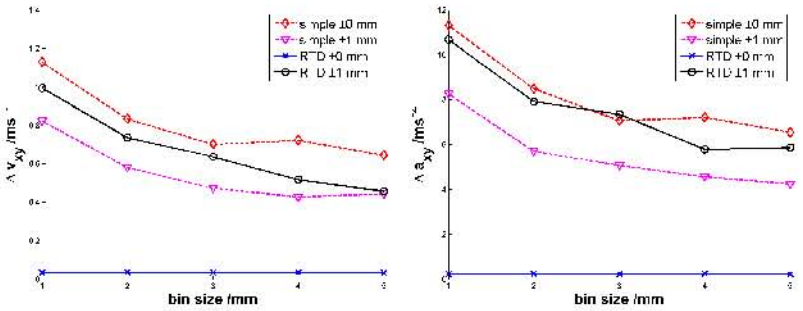

(c) Transverse velocity with noise

(d) Transverse acceleration with noise

Figure I.6: Mean deviations from theoretical velocity (left) and acceleration (right), of binned data with (bottom) and without (top) noise, as a function of bin size.

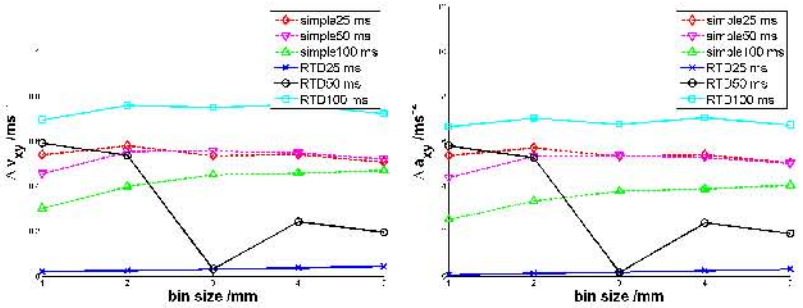

(a) Transverse velocity without noise

(b) Transverse acceleration without noise

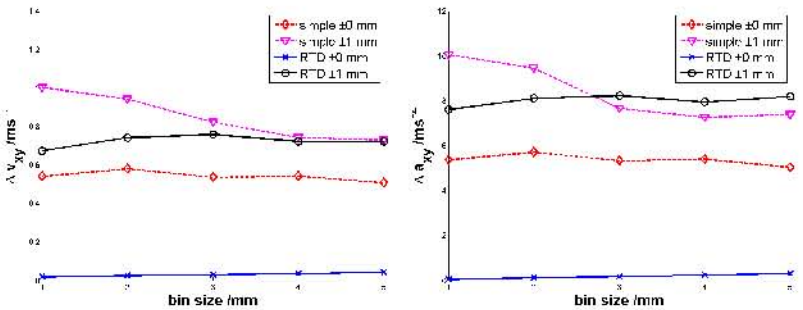

(c) Transverse velocity with noise

(d) Transverse acceleration with noise

Figure I.7: Standard deviations from theoretical velocity (left) and acceleration (right), of binned data with (bottom) and without (top) noise, as a function of bin size.

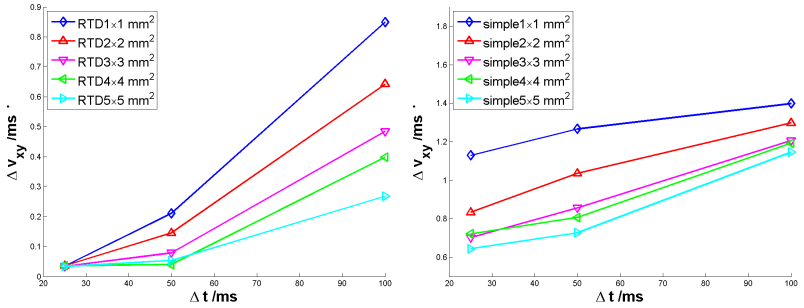

(a) RTD transverse velocity **(b)** Simple transverse velocity

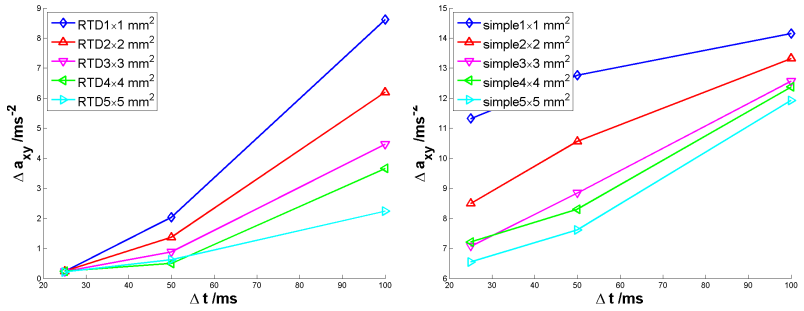

(c) RTD transverse acceleration **(d)** Simple transverse acceleration

Figure I.8: Mean deviations from theoretical velocity (top) and acceleration (bottom) of residence time (bottom) and simply (top) binned data.

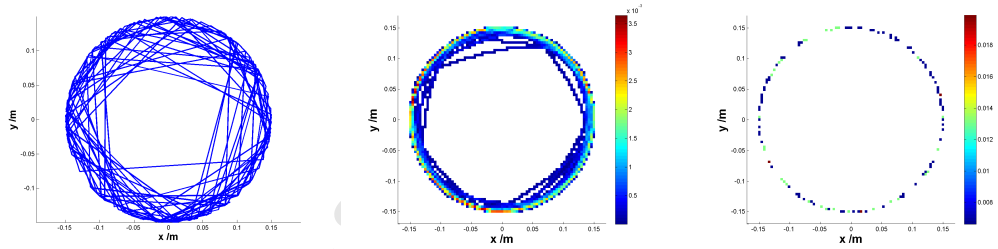

(a) $\sigma_x = \sigma_y = 0$mm

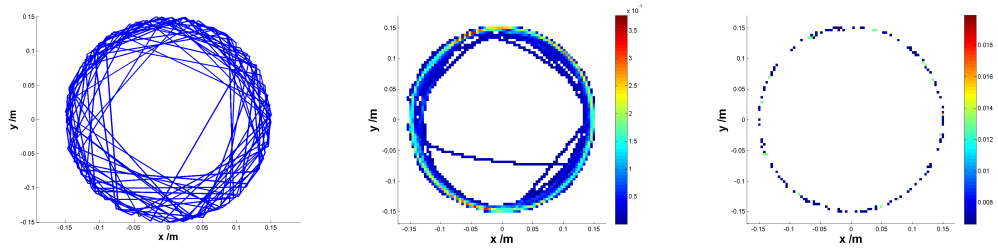

(b) $\sigma_x = \sigma_y = 1$mm

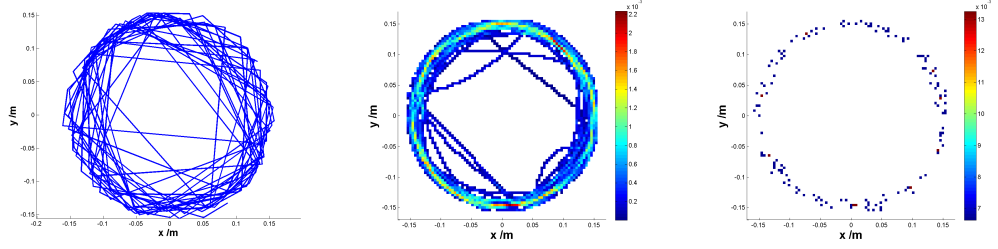

(c) $\sigma_x = \sigma_y = 5$mm

Figure I.9: Artificial data sampled at intervals of $\Delta t = 100 \pm 50$ms, with increasing Gaussian noise (top to bottom), binned by the residence time (middle) and simple (right) methods at a resolution of 4mm.

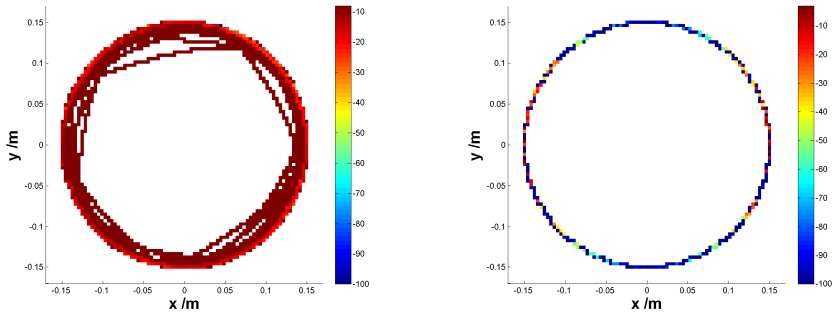

(a) RTD $\sigma = 0$mm

(b) Simple $\sigma = 0$mm

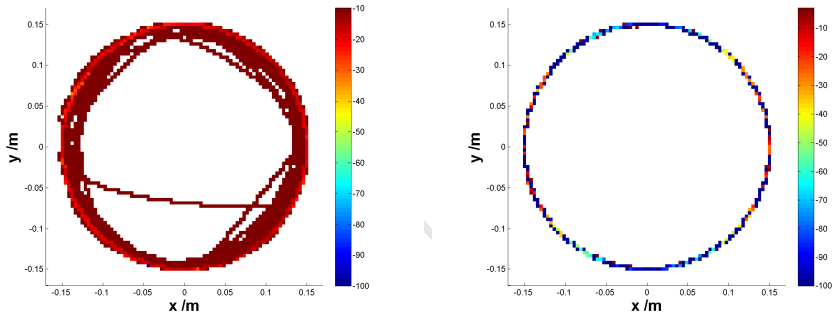

(c) RTD $\sigma = 1$mm

(d) Simple $\sigma = 1$mm

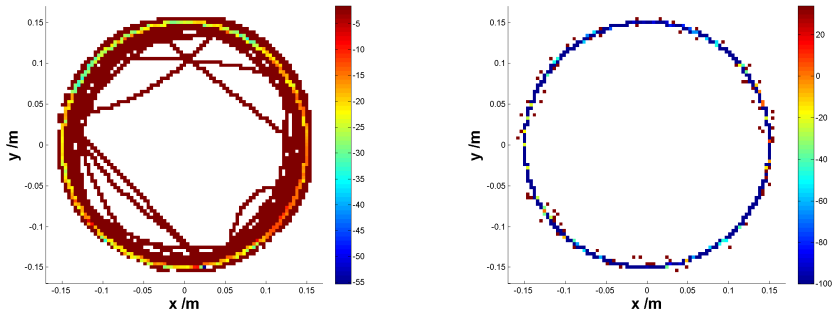

(e) RTD $\sigma = 5$mm

(f) Simple $\sigma = 5$mm

Figure I.10: Difference plots between theoretical and transverse velocities binned by the residence time (left) and simple (right) binning methods, sampled at intervals of $\Delta t = 100 \pm 50$ms and with increasing Gaussian noise (top to bottom).

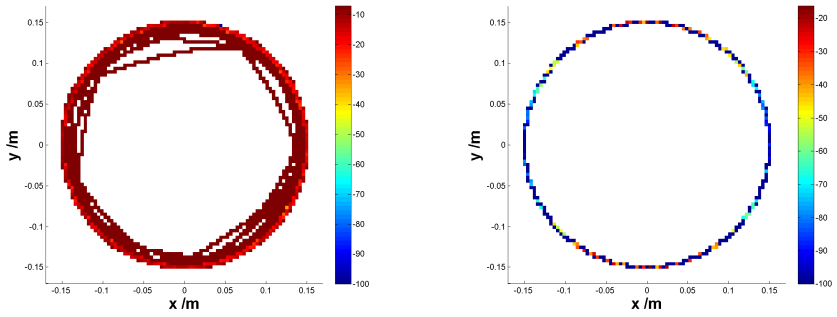

(a) RTD $\sigma = 0$mm

(b) Simple $\sigma = 0$mm

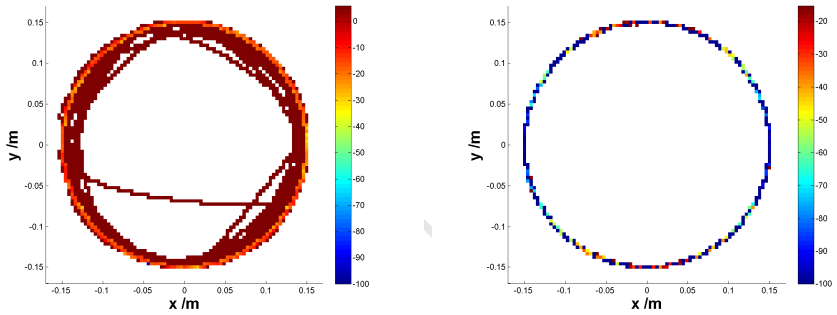

(c) RTD $\sigma = 1$mm

(d) Simple $\sigma = 1$mm

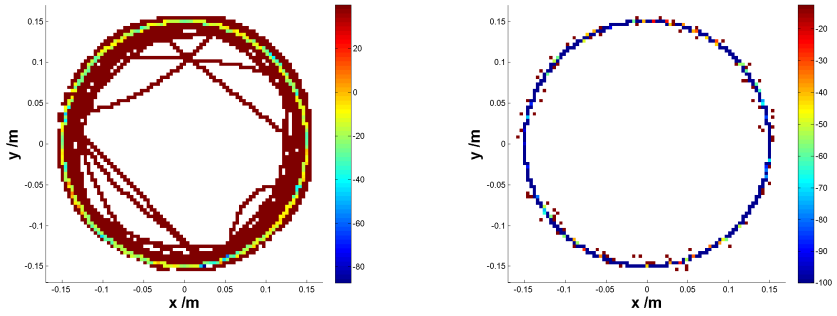

(e) RTD $\sigma = 5$mm

(f) Simple $\sigma = 5$mm

Figure I.11: Difference plots between theoretical and transverse accelerations binned by the residence time (left) and simple (right) binning methods, sampled at intervals of $\Delta t = 100 \pm 50$ms and with increasing Gaussian noise (top to bottom).

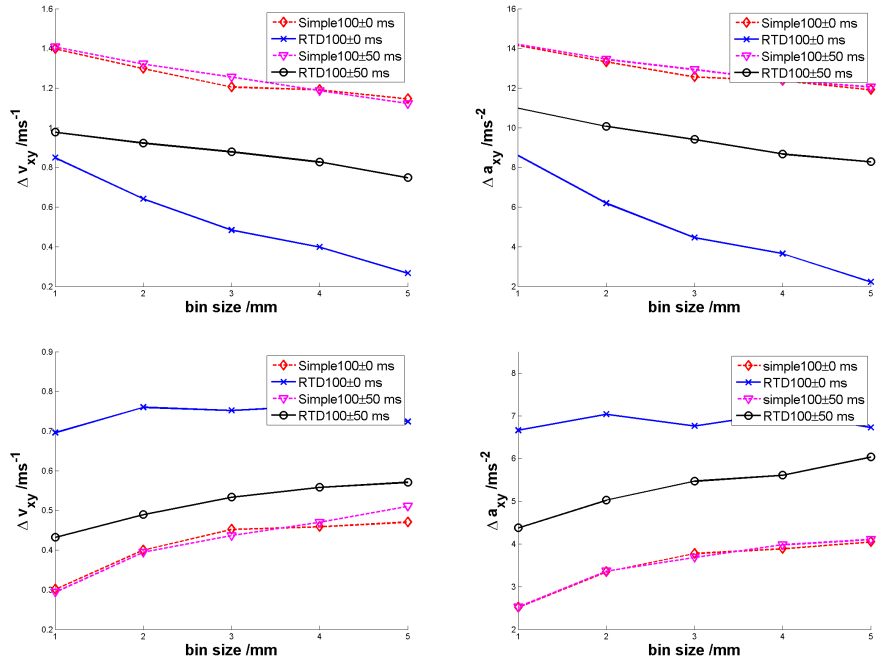

Figure I.12: Mean (top) and standard (bottom) deviations from theoretical velocity (left) and acceleration (right), of binned data sampled at intervals of 100 ± 50ms.

method.

Interestingly- while an uneven sampling frequency not only affects the accuracy and precision of the residence time binned data, but also reduces the smoothing effect of larger bin sizes- it has almost no effect on simply binned data. Clearly, then, these measures have nothing to say about the important loss of statistics that results from simple binning.

It is important to note, by the way, that the data considered in Figure I.9 is the worst case scenario for PEPT data. Typical PEPT data has an uncertainty of the order of a few millimetres and a sampling frequency of about 25 ± 10ms. Figure I.13 contrasts a realistic sampling rate with the exaggerated one considered above, both with a realistic location uncertainty. Clearly, more realistic data does not suffer from the interpolating halo effect nearly as much as might have been suggested.

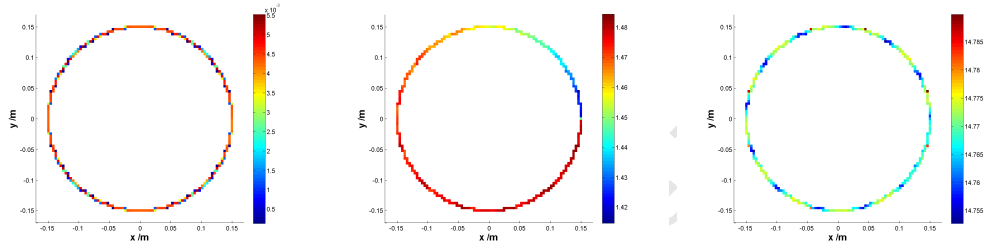

(a) $\Delta t = 25 \pm 10$ms, $\sigma = 1$mm

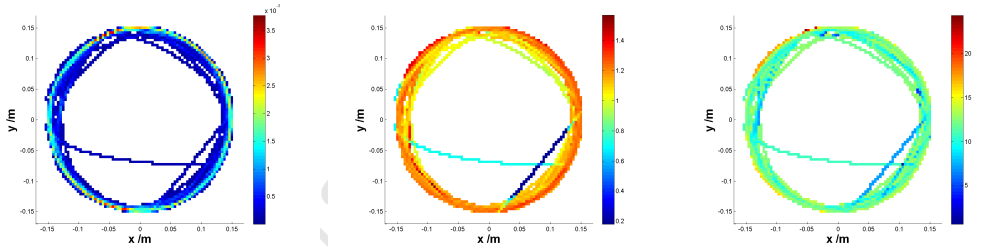

(b) $\Delta t = 100 \pm 50$ms, $\sigma = 1$mm

Figure I.13: Artificial tracer location (left), speed (middle) and acceleration (right in each row), binned by the residence time method, and sampled at a realistic, high frequency (top), and a less realistic low frequency (bottom).

I.1.2 Spiral motion

In order to further explore the limits of the accuracy and precision of the simple and residence time binning procedures, I here introduce a slightly more complicated particle motion- that of a logarithmic spiral.

It is important to note at the outset that whereas in the circular motion case above, the true trajectory passed through each point roughly 24 times[5], the radius of the spiral defined by equation I.2 diminishes with each revolution, and so the particle never passes through the same point twice. Thus, this example not only provides insight into the effect of curvature on accuracy and precision, but also an indication of how close a single pass- rather than the average of several passes- comes to the underlying data for each binning method.

To produce the logarithmic spiral motion, I use a small, velocity-dependent damping force, $F_d = c\dot{q}$, where c is a constant. I chose the value of c such that the damping constant, γ, is less than its critical value[6]. This motion is described as

$$\begin{aligned} q_d(t) &= e^{-\gamma t} A\cos(\omega t) \\ \dot{q}_d(t) &= -Ae^{-\gamma t}(\omega\sin(\omega t) + \gamma\cos(\omega t)) \\ \ddot{q}_d(t) &= Ae^{-\gamma t}\left(2\gamma\omega\sin(\omega t) + \left(\gamma^2 - \omega^2\right)\cos(\omega t)\right) \end{aligned} \tag{I.2}$$

where the symbols are as for the simple harmonic motion case with $\phi = 0$.

These equations result in a spiral motion of the sort shown in Figure I.14. The trajectories shown in this figure are sampled at uniform intervals of $\Delta t = 25$ ms, with added Gaussian noise of amplitude $0, 1$ or 5 mm. As before, sequential sample points are joined with straight lines, resulting in a more and more jumbled trajectory with more and more Gaussian noise. Also of note is that the 'jumble' gets more pronounced at smaller radii when the particle is slower and the curvature of its path greater.

Figure I.15 shows a comparison of the simple and residence time binning methods for the data shown in Figure I.14, binned at a resolution of $3 \times 3mm^2$. It is clear that at this level of smoothing, the effect of Gaussian noise on the residence time binned data only appears at $\sigma_x = \sigma_y = 5$mm, particularly near the centre of the motion, which develops into an indistinct region rather than a trajectory.

It is hard to make any sort of qualitative assessment of the simple binning case at any resolution, but it is of interest to consider residence time binning at different resolutions. Figure I.16 shows the residence time binning of a spiral trajectory sampled at various intervals, with large amplitude Gaussian noise added to it to exaggerate the sampling frequency effects. Here, it is clear that lower sampling frequencies have more of a smoothing effect on the data than do lower resolution grids.

Figure I.17 shows the residence time binning of this same data, sampled at non-uniform time intervals- at a realistic 25 ± 10ms and extreme 100 ± 50ms. Both of these trajectories appear smooth at all grid resolutions, but the lower sampling frequency case is clearly less accurate than the higher frequency one. It is thus not necessarily a good tactic to reduce sampling frequencies as a smoothing tactic.

As before, the accuracy- as opposed to the smoothness- of the data can be further investigated using the kinematics of the particle's trajectory.

[5] The particle's angular frequency was $\omega = 10$ Hz, and thus its period was $T = \frac{2\pi}{\omega} \approx 0.6s$. The data was for the first 15s: nearly 24 periods.

[6] That is $\gamma = \frac{c}{2m} < \gamma_{critical}$.

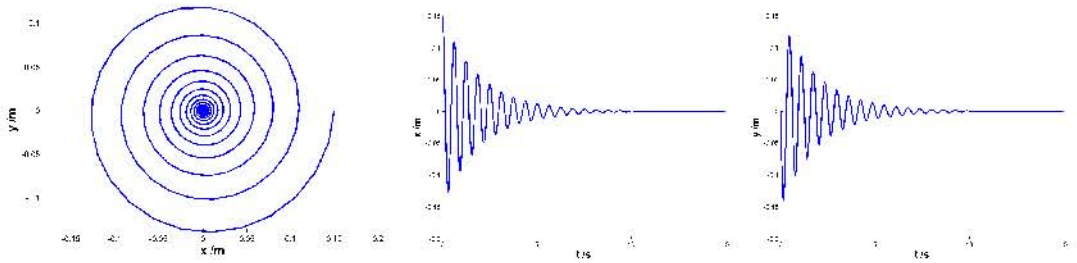

(a) $\sigma = 0$mm

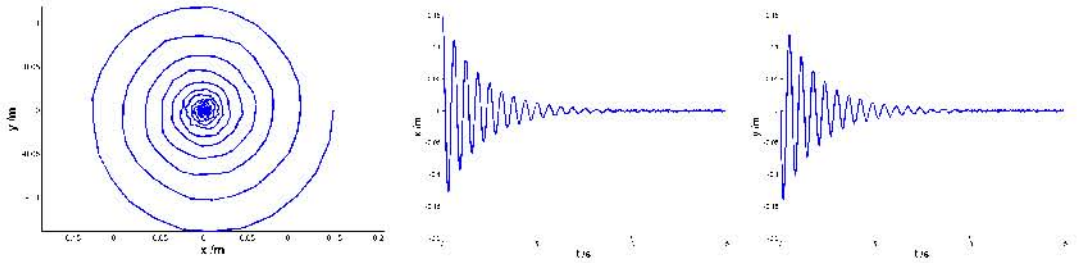

(b) $\sigma = 1$mm

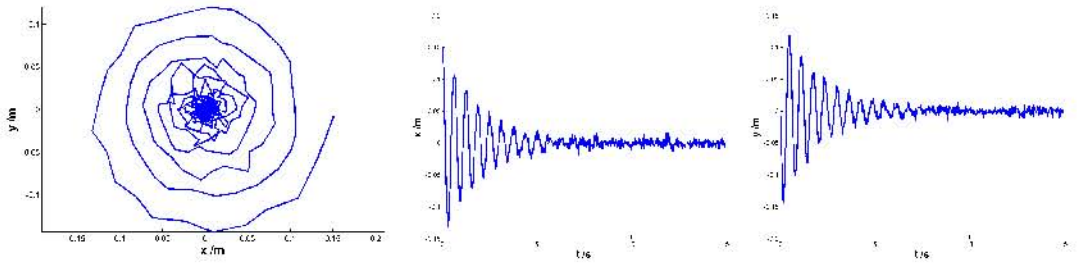

(c) $\sigma = 5$mm

Figure I.14: Spiral motion, of initial amplitude 0.150 m, angular frequency 10 Hz and damping constant 0.5 Hz, sampled every 25 ms with increasing Gaussian noise (top to bottom), shown here in the xy-plane (left) and varying in the $\hat{x}$- (middle) and $\hat{y}$-directions (right) with time.

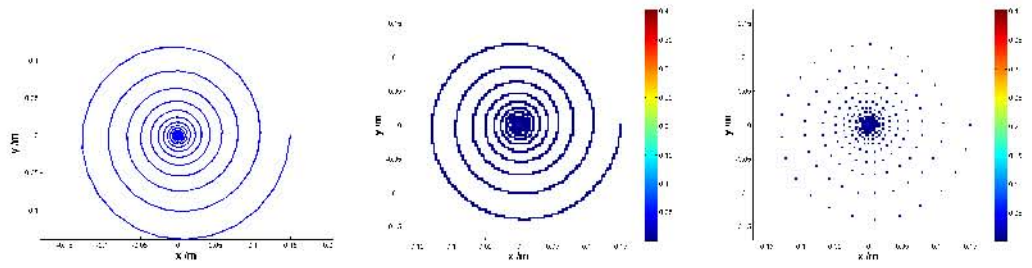

(a) $\sigma = 0$mm

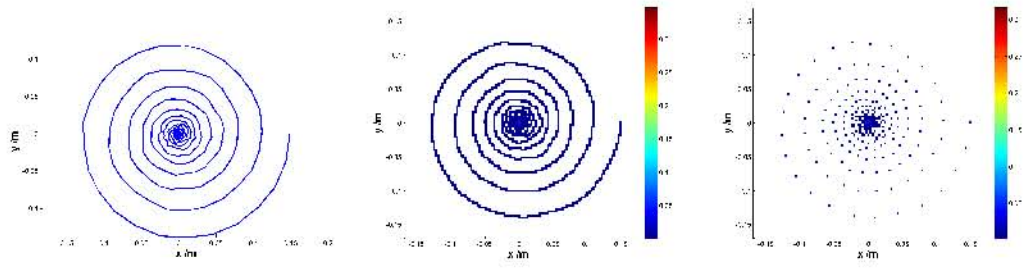

(b) $\sigma = 1$mm

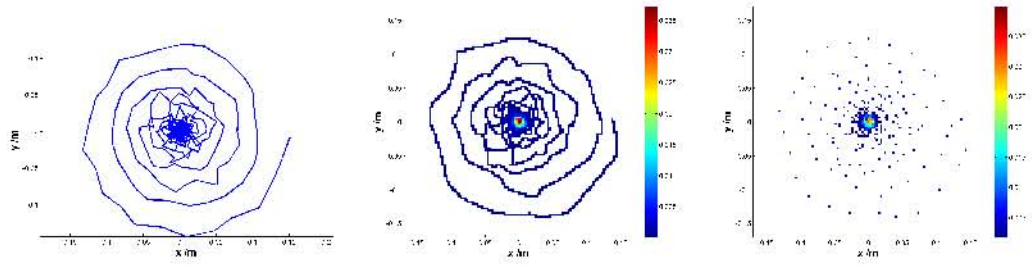

(c) $\sigma = 5$mm

Figure I.15: Spiral motion, of initial amplitude 0.150 m, angular frequency 10 Hz and damping constant 0.5 Hz, sampled every 25 ms with increasing Gaussian noise (top to bottom), shown here binned by the residence time (middle) and simple (right) binning methods.

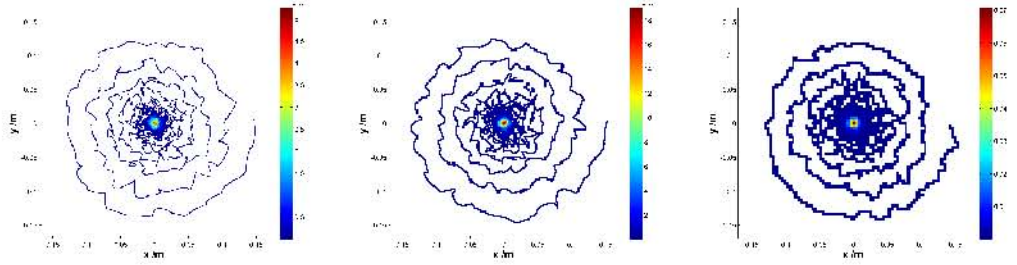

(a) $\Delta t = 10$ms

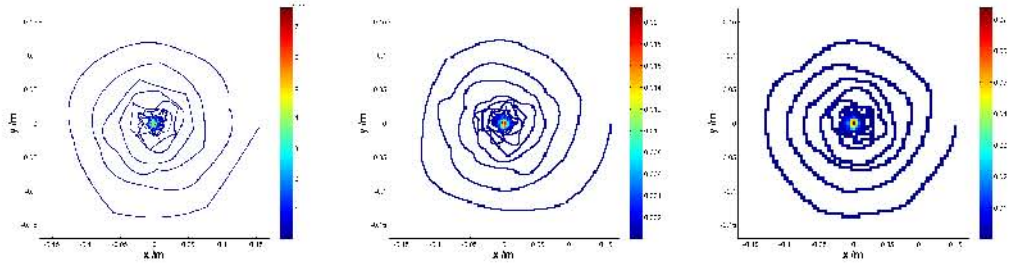

(b) $\Delta t = 50$ms

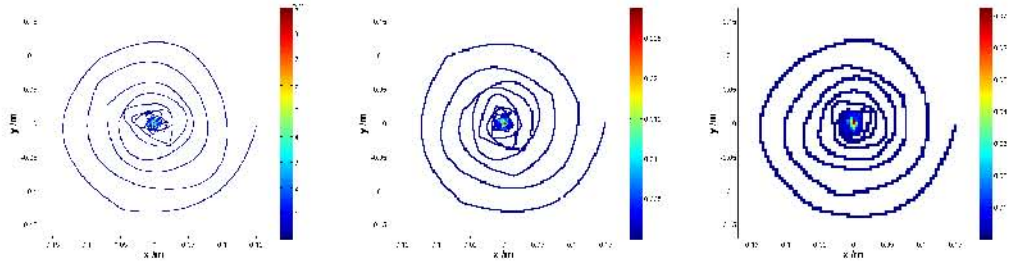

(c) $\Delta t = 100$ms

Figure I.16: Residence time binning of a spiral trajectory with $\sigma = 5$mm sampled at intervals of $10, 50$ and 100 ms (top to bottom), for grid resolutions of $1, 2$ and 4mm (left to right).

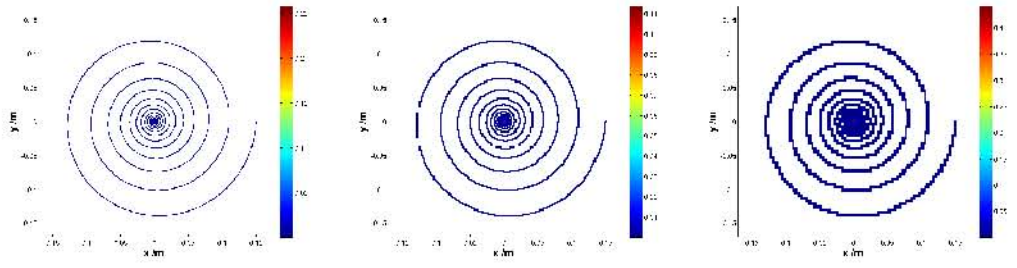

(a) $\Delta t = 25 \pm 10$ms

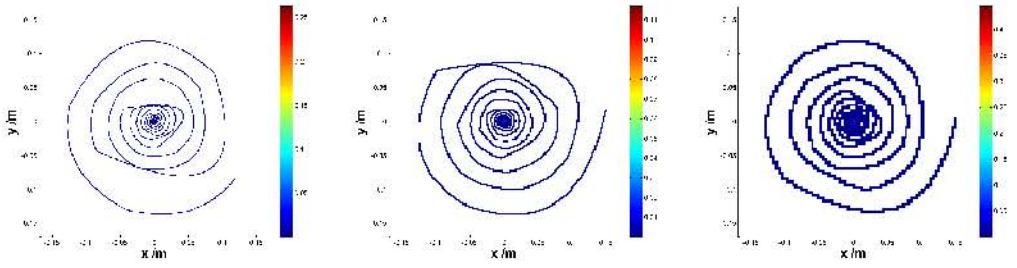

(b) $\Delta t = 100 \pm 50$ms

Figure I.17: Residence time binning of a spiral trajectory with $\sigma = 0$mm sampled at intervals of 25 ± 10ms (top) and 100 ± 50ms (bottom), for grid resolutions of $1, 2$ and 4mm (left to right).

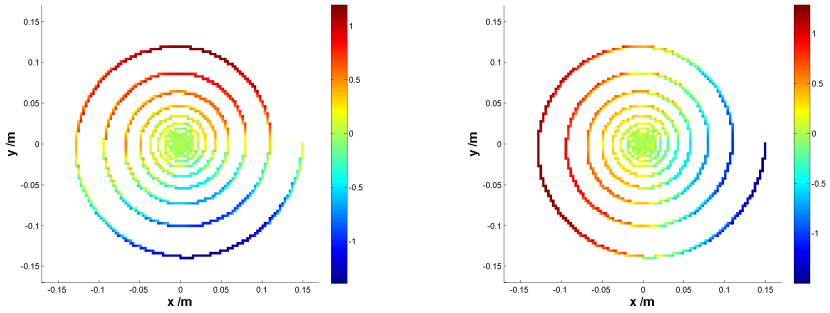

(a) Velocity

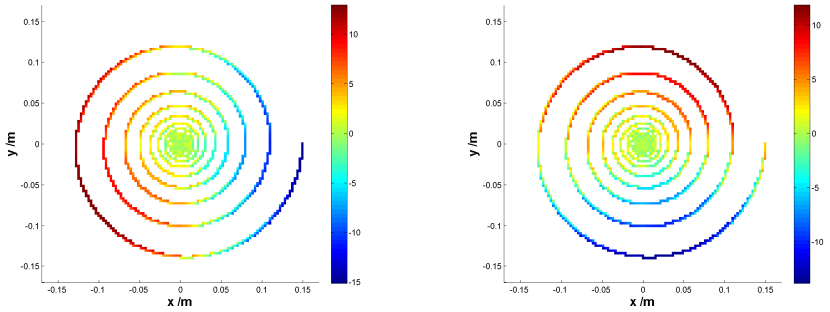

(b) Acceleration

Figure I.18: Theoretical values of the particle's velocity (top) and acceleration (bottom) in the $\hat{x}$- and $\hat{y}$-directions (left and right, respectively), along its spiral path.

From equation I.2, the time at which a particle would be at radial position r, would be

$$t = \frac{-1}{\gamma} \ln\left(\frac{r}{A}\right) \tag{I.3}$$

The particle's velocity and acceleration in each direction are then calculable from the coordinates of each bin and the time at which the particle is in it according to equation I.3. This provides the binned standard of comparison for the spiral motion case as shown in Figure I.18.

Figure I.19 shows histogrammed deviations of binned velocity data from the theoretical values given in Figure I.18, for a range of grid sizes. Unlike the circular motion case, these deviations conform well[7] to normal distributions. The subplots in Figure I.19 all include best fit Gaussian curves with their goodness of fit in the legend.

The mean and standard deviation of these best-fit Gaussians can be used[8] as a measure of how accurate and how precise are the binned results, respectively.

An extremely important note: In the spiral motion case, as in the case of circular motion, absolute- rather than normalised or percentage- deviations from theoretical are used. This is because the theoretical values are only defined along the actual motion of the particle, but the binned data contains noise and, in the case of residence time binning, the interpolating halo.

For constant circular motion, absolute and percentage deviations differ only by a multiplicative constant, and so talking about either is basically equivalent. For spiral motion of the sort considered here, though, both the particle's velocity and acceleration decrease over time, that is, at smaller radial positions. This means that smaller proportional errors in larger absolute numbers- at larger

[7] Adjusted $R^2 > 0.9$ in most cases.

[8] As were the simple mean and standard deviation in the circular motion case, despite a more complicated underlying distribution.

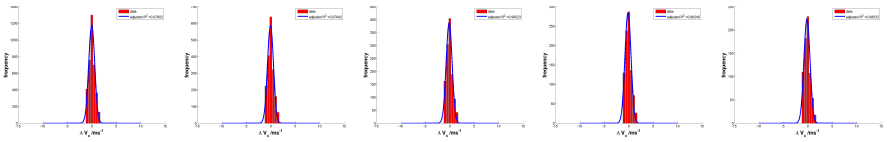

(a) Simple V_x

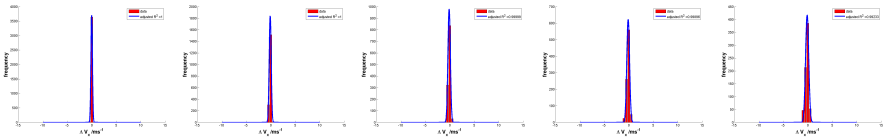

(b) RTD V_x

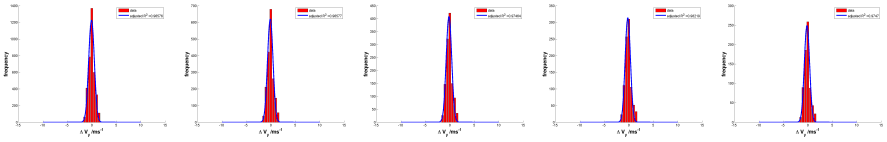

(c) Simple V_y

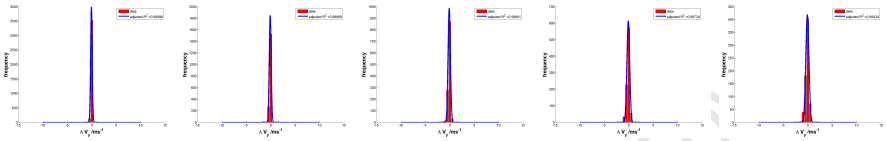

(d) RTD V_y

Figure I.19: Histogrammed deviations from theoretical velocities simply and residence time binned at increasing grid size (left to right).

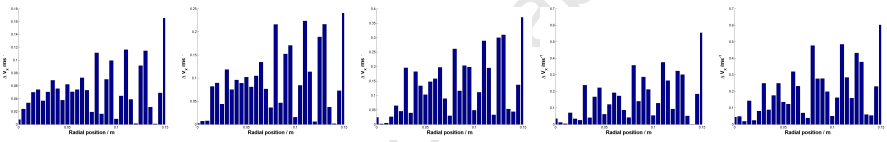

(a) V_x

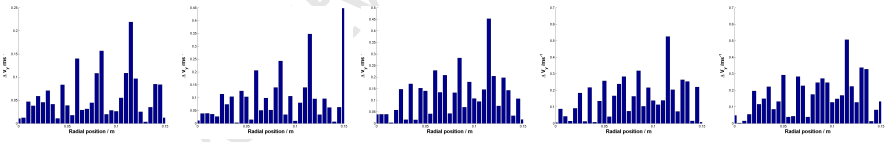

(b) V_y

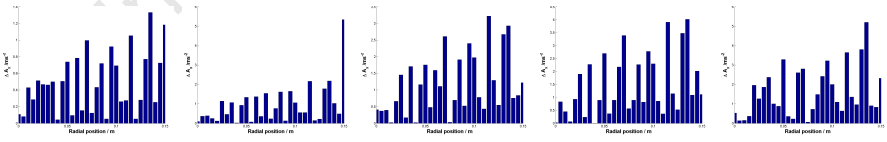

(c) A_x

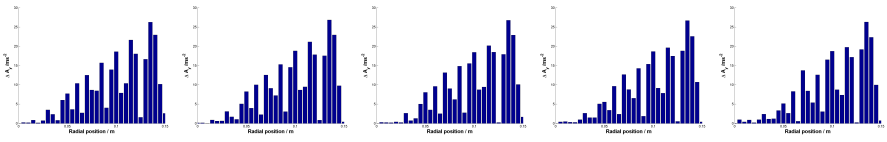

(d) A_y

Figure I.20: Mean deviations from theoretical velocities (top) and accelerations (bottom) residence time binned at increasing grid size (left to right), as a function of radial position.

radii- are disproportionately represented in the calculation of mean and standard deviations. This leads to counter-intuitive results such as those shown in Figures I.20 and I.21, which show mean deviations increasing with radial position, despite what Figure I.15 seems to suggest.

In particular, Figure I.20 shows a gradual increase in deviation with radial position, while Figure

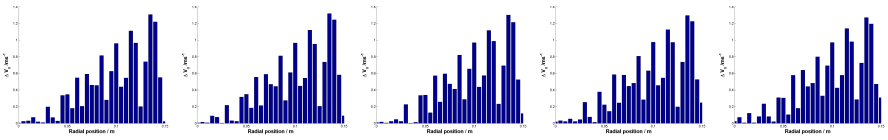

(a) V_x

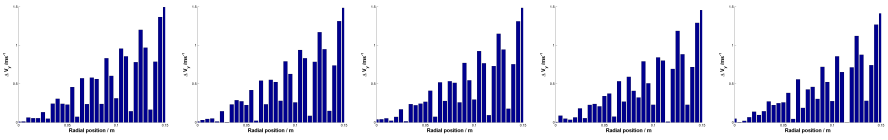

(b) V_y

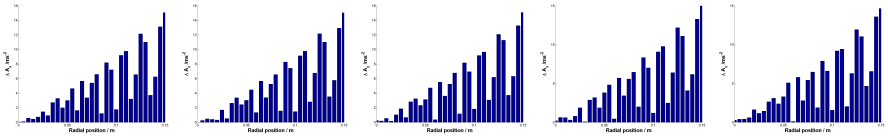

(c) A_x

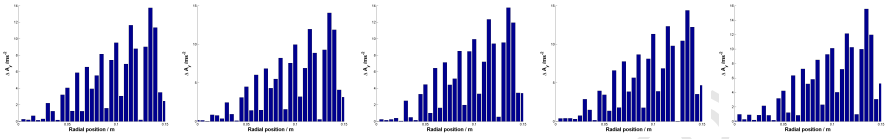

(d) A_y

Figure I.21: Mean deviations from theoretical velocities (top) and accelerations (bottom) simply binned at increasing grid size (left to right), as a function of radial position.

I.21 shows a sharp increase. This is because the effect of sampling frequency on the simple binning is greatest in the fast-moving, large radius outer revolutions. In Figure I.21 in particular, the spaces between orbits are visible as dips in the otherwise climbing deviation. If the data consisted of concentric circles rather than a single path of gradually-decreasing radius, this effect would be more pronounced.

Figures I.22 and I.23 show the mean deviations from theoretical velocities and accelerations as a function of angular position.

The starting point- and thus farthest radial position- of the particle on its spiral trajectory is at an angle of 0 radians. This angular position, and its antipode, correspond to a maximum deviation in the $\hat{x}$-velocities and $\hat{y}$-accelerations a minimum in the $\hat{y}$-velocities and $\hat{x}$-accelerations. This is because the velocities in this motion are always tangential, and the accelerations are almost centripetal[9].

The deviations in the transverse velocities have a slightly bimodal distribution both maximum and, oddly, minimum at 0 radians. The velocity of a particle in a logarithmic spiral motion is related to the magnitude of its tangential velocity, which depends on how long the particle has been subjected to the damping force. That deviations from theoretical peak at 0 radians, decline in a negative angular direction- the direction of decreasing maximum radial position- and approach a minimum again towards 0 radians suggests that structure is washed out by the larger contributions from this much faster point.

The deviations in the transverse accelerations have a more complicated, periodic shape, especially in the residence time binning case. They seem to alternate peaks and troughs at intervals of $\frac{\pi}{4}$, beginning with a trough at 0 radians. It is interesting that this structure should develop in the acceleration and not in the velocity, perhaps explicable by the greater symmetry of the $\hat{x}$- and

[9]With some contribution from the damping force.

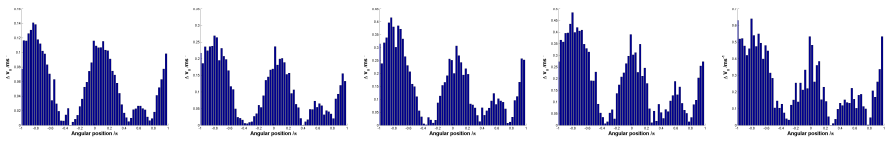

(a) V_x

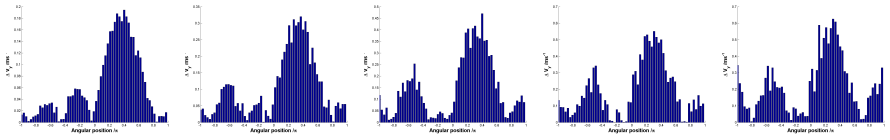

(b) V_y

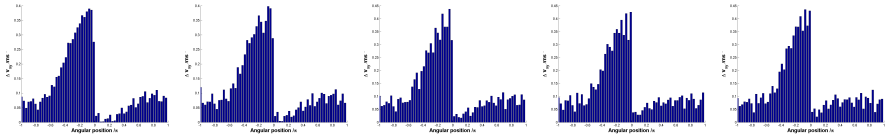

(c) V_{xy}

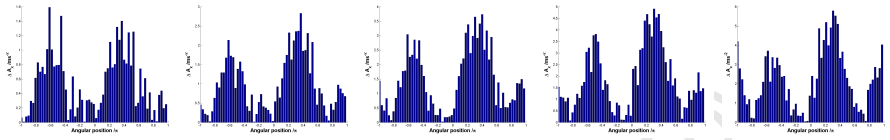

(d) A_x

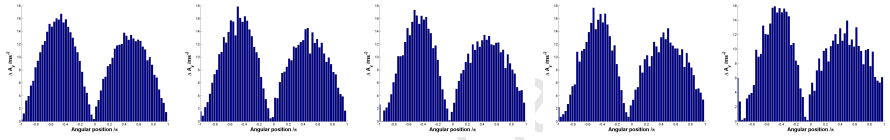

(e) A_y

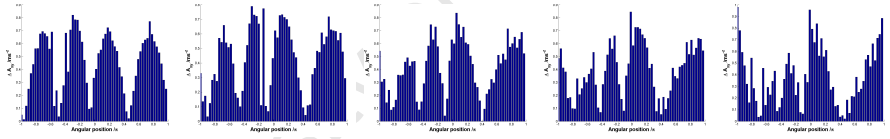

(f) A_{xy}

Figure I.22: Mean deviations from theoretical velocities (top) and accelerations (bottom) residence time binned at increasing grid size (left to right), as a function of angular position.

$\hat{y}$-accelerations compared to the velocities.

This caveat in mind, however, it is still interesting to consider the variations in the mean and standard deviations from theoretical obtained from the- now somewhat surprisingly good- best-fit Gaussians of Figure I.19. Figure I.24 shows these variations as a function of bin size.

Figures I.24a and I.24b shows the variation in mean and standard deviation, respectively, from theoretical transverse velocity for the residence time (left) and simple (right) binning cases.

In the high- and medium-frequency residence time binning case, the mean deviation is high and broadly increasing with decreasing grid resolution, and the standard deviation is low and unchanging with resolution. In the low frequency case, the mean deviation starts off roughly the same as for the medium-frequency but drops significantly at a grid resolution of $3 \times 3mm^2$. Similarly, the standard deviation in the low-frequency case starts off high, drops at a grid resolution of $3 \times 3mm^2$ and then remains constant.

It is interesting to compare this with the circular motion case shown in Figures I.6 and I.7. In the circular motion case, the mean deviation does not show this sudden minimum at a grid resolution of $3 \times 3mm^2$ because it is the average of the number of passes that the tracer makes through

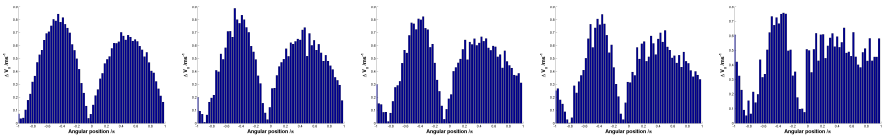

(a) V_x

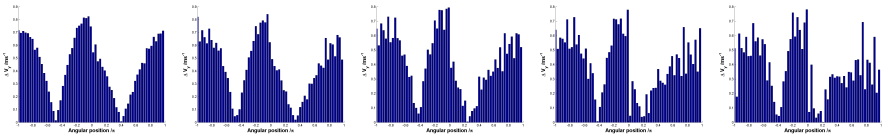

(b) V_y

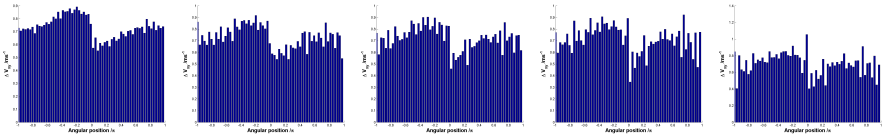

(c) V_{xy}

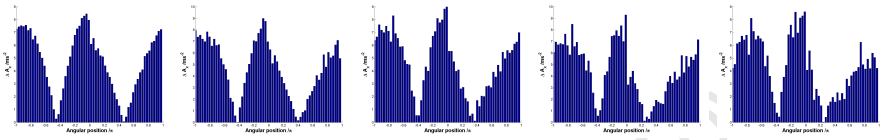

(d) A_x

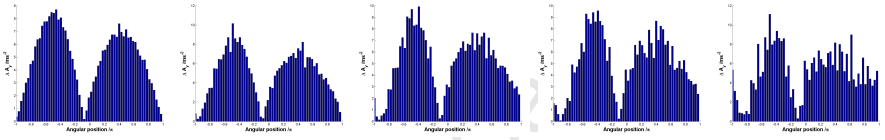

(e) A_y

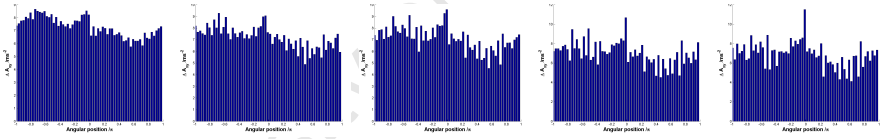

(f) A_{xy}

Figure I.23: Mean deviations from theoretical velocities (top) and accelerations (bottom) simply binned at increasing grid size (left to right), as a function of angular position.

each bin. The standard deviation in the circular case does, however, show this minimum because it captures the deviations of each pass. This is born out by the fact that the magnitudes of the standard deviations in the circular and spiral case are roughly the same[10], but the mean deviations in the spiral case are twice or more those of the circular case. This is again due to the smoothing available from multiple passes in the circular case. In the spiral case, the only smoothing available is from low sampling frequencies- see Figure I.16- which accounts for the opposite trends in Figure I.25 and Figure I.8, the circular case.

The simply binned mean deviation from theoretical transverse velocity, also shown in Figure I.24a, present much clearer trends with grid resolution, with low and medium sampling frequency data benefiting from decreasing resolution, and the opposite for high sampling frequency data. This is because high frequency data conforms most well to the shape of the true data- as is clear from the standard deviations in Figure I.24b. The mean deviations are much larger for the simple than the residence time binning case, in part because of the incomplete coverage afforded by simple binning, despite the interpolating halo of residence time binning.

[10]Except for the very high standard deviation at low sampling frequency and high resolution in the spiral case.

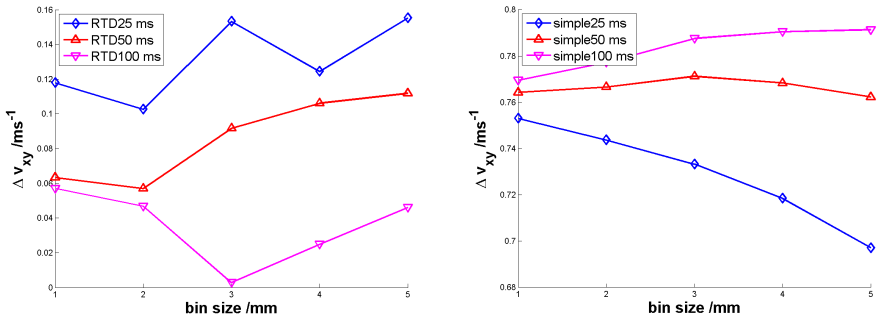

(a) Mean deviation in the transverse velocity

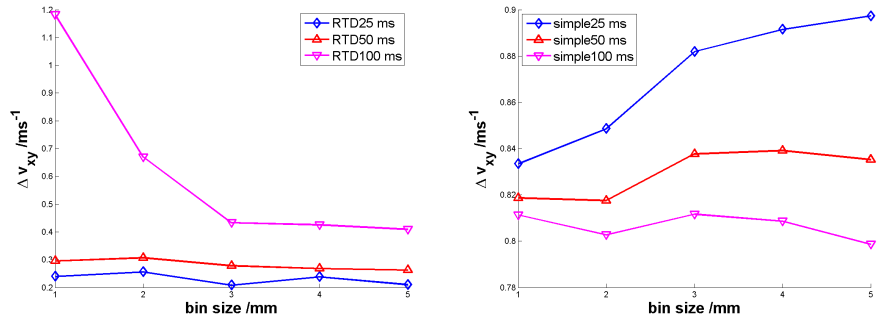

(b) Standard deviation in the transverse velocity

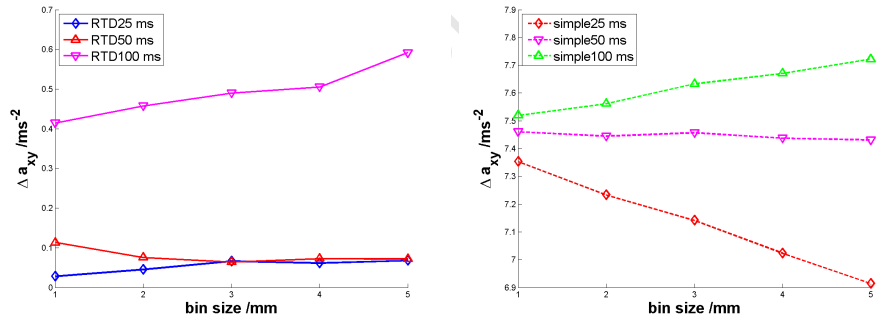

(c) Mean deviation in the transverse acceleration

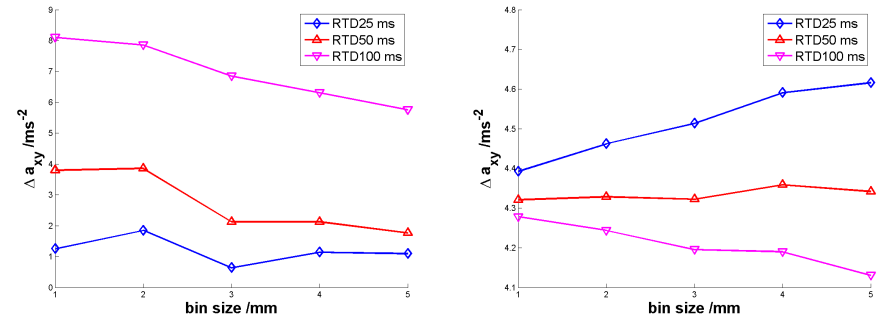

(d) Standard deviation in the transverse acceleration

Figure I.24: Mean and standard deviations from theoretical kinematics for residence time (left) and simply (right) binned data, as a function of grid size.

These magnitude differences are also visible in the acceleration deviations shown in Figures I.24c and I.24d.

The deviations from theoretical of the simply binned accelerations show much the same trends with grid resolution as do the simply binned velocities- the accuracy of high sampling frequency data benefits, while its precision suffers, from lower resolution; the opposite for low sampling frequency data; and almost no variation in medium sampling frequency data with grid resolution.

The mean and standard deviations from theoretical acceleration in the residence time binning case shows much less variation with grid resolution than did its deviations from theoretical velocity. This is particularly the case for the low sampling frequency case that showed such a marked change in behaviour at a grid resolution of $3 \times 3mm^2$. This low sampling frequency data does, though, show both much worse accuracy and precision than do the medium and high frequency data, as shown in Figures I.24c and I.24d.

The mean deviations in the simply binned velocities and accelerations increase with decreasing sampling frequency as they did in the case of circular motion[11] because of the susceptibility of simple binning to sampling error. The standard deviations from theoretical velocity and acceleration in the spiral case decrease with decreasing sampling frequency, unlike in the circular case, because the particle is only likely to pass through a given bin once in the high velocity and acceleration outer regions of the spiral motion, so most of this standard deviation comes from the dense, but low velocity and acceleration, inner region shown in Figures I.15 and I.16, for instance.

Non-uniform sampling intervals don't seem to have much effect on simply binned data, as shown in Figure I.26, but clearly decrease the accuracy and precision of the residence time binned data by forcing higher-order interpolants, thus increasing the interpolating halo. It is important to note here, too, that the data shown in Figure I.26 is very much an extreme and exaggerated example, unlikely to occur- at least in a sustained way- in PEPT data.

Adding Gaussian noise to the data, as in Figure I.27, obviously decreases both the accuracy and precision of both the simply and residence time binned data. This effect is most pronounced where the amplitude of the noise is the same or larger than the grid resolution. This is why the $\sigma = 5$ mm data is so distinct from both the $\sigma = 1$ mm and $\sigma = 0$ mm data, and why there are large jumps in the $\sigma = 1$ mm data from grid resolutions of $1 \times 1mm^2$ to $2 \times 2mm^2$. Other than these effects, the trends with grid resolution remain the same for data with and without Gaussian noise, with the same important increase in both accuracy and precision in the residence time binning over the simple binning case.

[11] See Figure I.6.

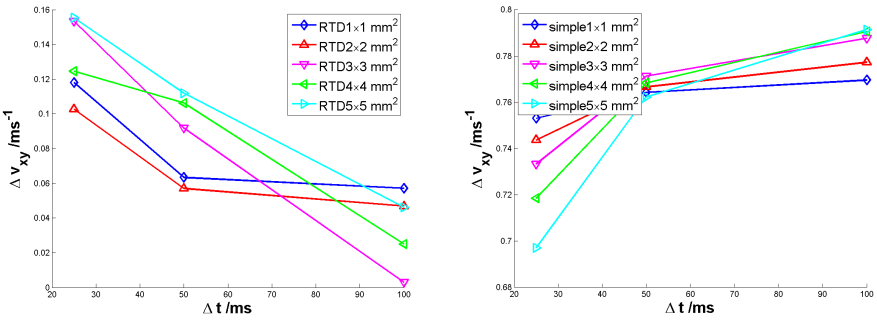

(a) Mean deviation in the transverse velocity

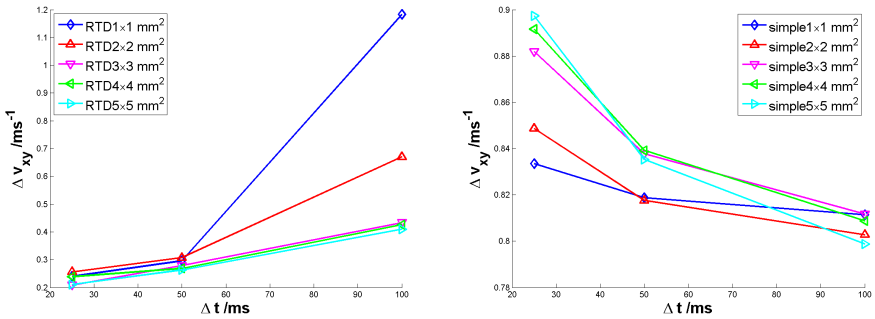

(b) Standard deviation in the transverse velocity

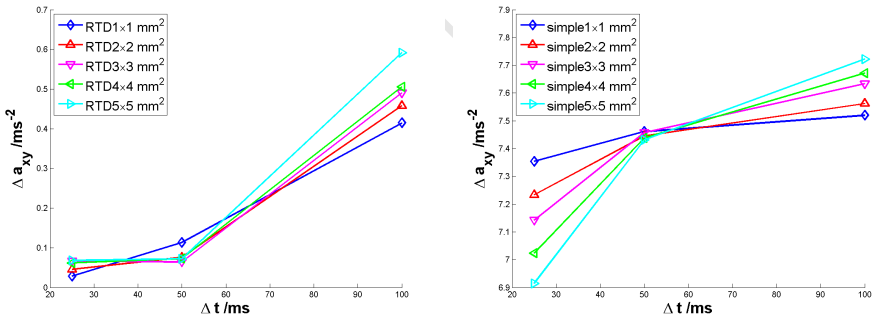

(c) Mean deviation in the transverse acceleration

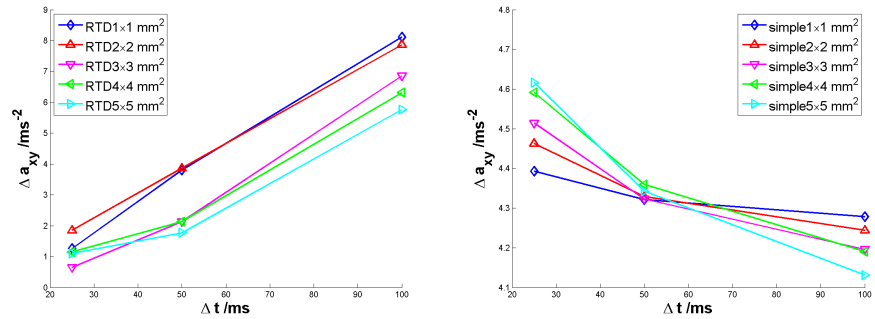

(d) Standard deviation in the transverse acceleration

Figure I.25: Mean and standard deviations from theoretical kinematics for residence time (left) and simply (right) binned data, as a function of sampling interval.

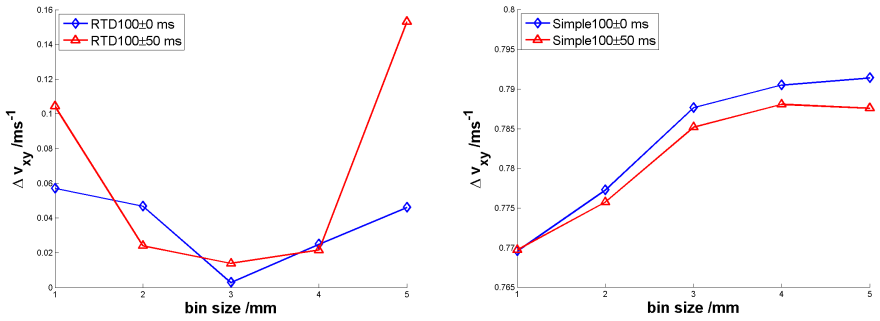

(a) Mean deviation in the transverse velocity

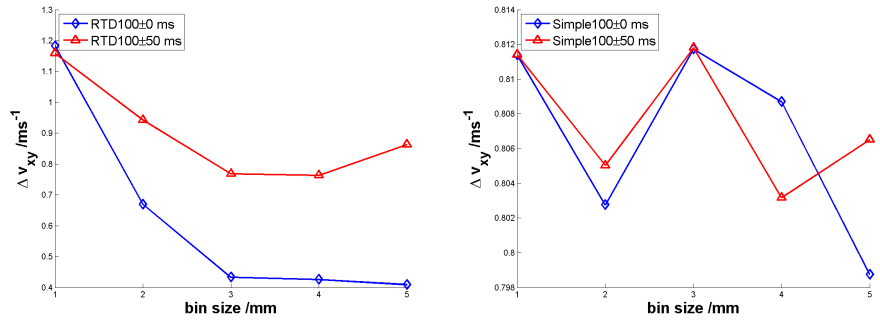

(b) Standard deviation in the transverse velocity

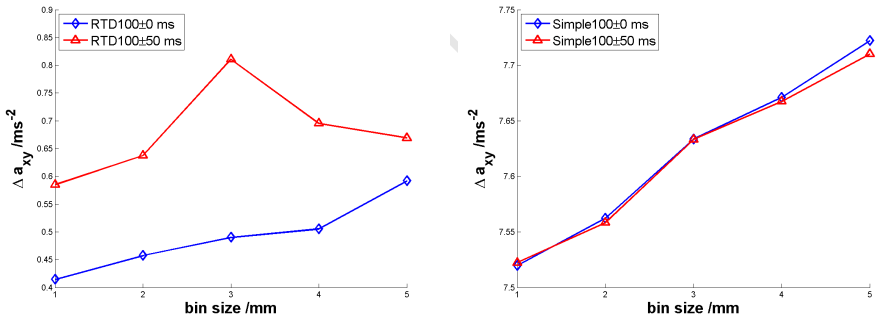

(c) Mean deviation in the transverse acceleration

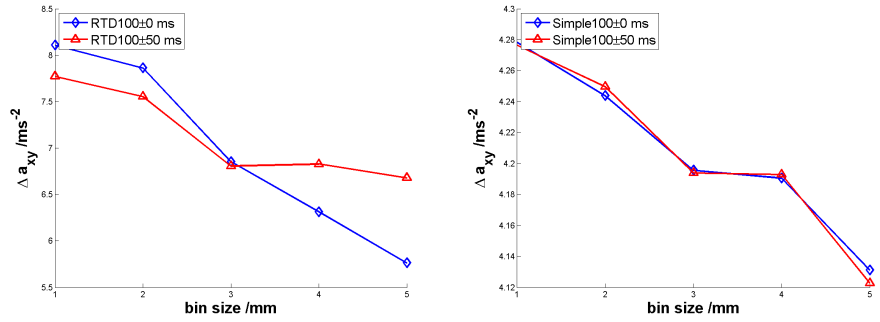

(d) Standard deviation in the transverse acceleration

Figure I.26: Mean and standard deviations from theoretical kinematics for uniform and non-uniformly sampled data binned by the residence time (left) and simple (right) binning methods, as a function of grid size.

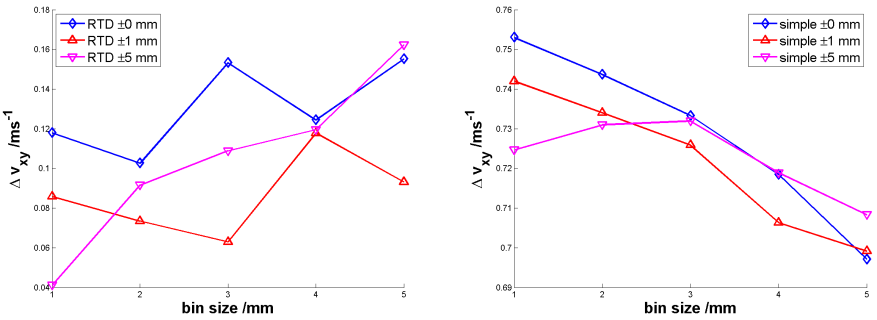

(a) Mean deviation in the transverse velocity

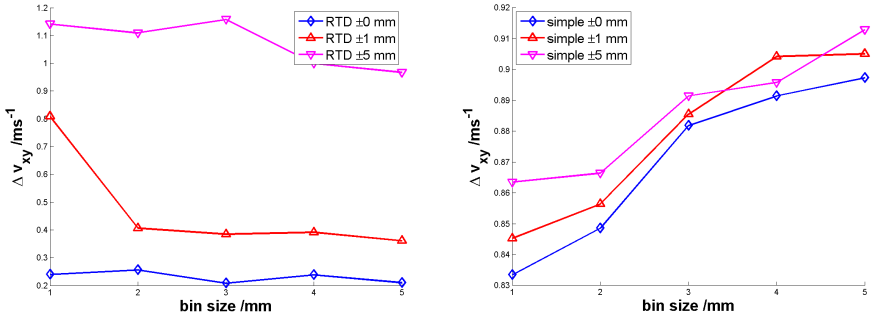

(b) Standard deviation in the transverse velocity

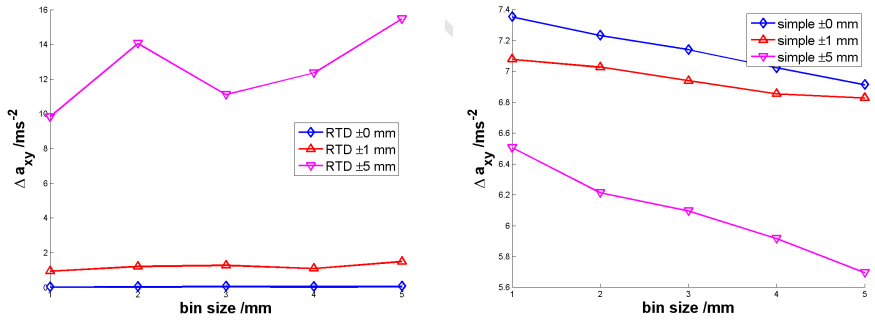

(c) Mean deviation in the transverse acceleration

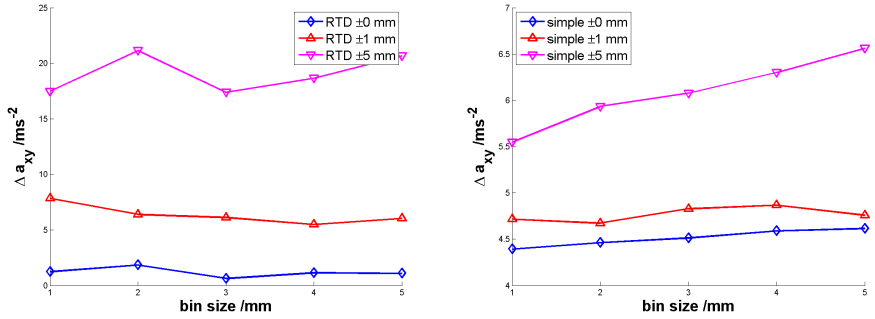

(d) Standard deviation in the transverse acceleration

Figure I.27: Mean and standard deviations from theoretical kinematics of data with and without Gaussian noise binned by the residence time (left) and simple (right) binning methods, as a function of grid size.

I.1.3 A summary of the lessons learnt from the binning of artificial data

I used two sets of artificial data to compare the simple and residence time binning methods. My main consideration in choosing the form of this artificial data was to ensure that their kinematics were well-known. This was to facilitate the comparison between the known kinematics of the artificial data at each time and position, and those produced by the two binning methods. By subtracting the distributions of known kinematics from those produced by the two binning methods, mean and standard deviations of the differences between them could be calculated. I interpreted the mean differences as indicative of the accuracy of the binning method, and the standard deviation of the differences as its precision.

The first artificial data set I used was a circular path arising from simple harmonic motion of amplitude 0.150 m and angular frequency 10 Hz, in two dimensions. The second was this same simple harmonic motion with an exponential damping force of damping constant 0.5 Hz in each dimension, resulting in a logarithmic spiral motion. Whereas the circular motion was of constant angular velocity and radial position, both the angular velocity and radial position of the particle in spiral motion reduced over time under the action of the damping force. Both of these artificial motions were sampled over the first 15s of their motion. This was roughly 24 periods of the circular motion, and the time taken for the spiral motion to asymptote to within 10^{-5} m of zero displacement.

Thus the circular motion provides a means of testing the two binning methods for not only a fixed angular velocity and curvature but, importantly, for multiple-pass data. That is, data that passes through each bin along its path many times over the course of the experiment. This allows an averaged- or time-averaged in the residence time case- value of the particle's velocity or acceleration, and so on, to be assigned to each bin. By adding Gaussian noise to the true motion, and by varying its sampling rate, uncertainty and errors can be introduced into the motion, and the ability of each binning method to deal with such errors evaluated.

The spiral motion, on the other hand, provides a means of testing the two binning methods for single-pass data. At first glance, it might seem that a spiral motion could also be used to assess the two methods for various angular speeds and curvatures, but, as mentioned above, this is not the case. This is because the true kinematics of the artificial data are only defined in bins through which the true trajectory passes, thus a value in a non-true bin would represent an infinite percentage deviation- clearly unphysical. For the constant tangential velocity, centripetal acceleration, and so on, of the circular motion, considering absolute rather than proportional deviations from true is not significant. However, in the non-constant spiral case, small proportional deviations from larger kinematic quantities at larger radial distances over-contribute to mean differences, and the poorly-resolved inner region of the motion over-contributes to their standard deviations. Thus only overall measures are meaningful, and angular and radial trends must be investigated with series of concentric circles[12].

These two sets of artificial data were binned by both methods for various grid resolutions, with various amounts of Gaussian noise, and at various sampling frequencies. From this, it was possible to show that the residence time binning method is both more accurate and more precise than the the simple binning method under almost all conditions, like-for-like. That is, for data sampled at the same frequency, with the same amount of Gaussian noise, and binned at the same resolution, residence time binned data shows both a lower mean and standard deviation from the known kinematics of the artificial data than does simply binned data. There are two exceptions to this.

The first is that above a certain sampling interval- here 50 ms- and below a threshold grid resolution-

[12]Note done here.

here $3 \times 3mm^2$, the simply binned data is more precise than the same data residence time binned. The second is that above a certain level of Gaussian noise- here $\sigma = 5$ mm- and below the same threshold grid resolution, the residence time binned data is again less precise than that simply binned. The accuracy of the residence time binned data in these cases, however, remains better than the simply binned data. Both of these losses of precision are due to the residence time binning interpolating halo effect.

Decreasing the sampling frequency of the data decreases both the accuracy and precision of both binning methods for multiple-pass data, in which some smoothing can occur, but 'improves' precision in single-pass data for obvious reasons. The accuracy of residence time binned, single-pass data seems to improve with decreasing sampling frequency due to the smoothing effect shown in Figure I.16. This effect is even more pronounced for noisy data. An uneven sampling interval has no effect on simply binned data, but affects the residence time binning data through increased demands made on the interpolant.

Within binning methods, decreasing the resolution- by increasing the bin size- has a smoothing effect on the multiple-pass data, slightly increasing both the accuracy and precision of binned data. Decreasing the binning resolution, by exacerbating the interpolating halo effect, decreases the precision of residence time binned single-pass data, but has no effect on its accuracy[13]. Decreasing the resolution has exactly the opposite effect on the precision of simply binned single-pass data. By assigning data to bigger bins it reduces the unsampled space, thus reducing the number effectively zero-value bins. This reduces the accuracy of the simply binned data, though, especially in the non-constant spiral motion case.

In summary, the residence time binning method suffers from the interpolating halo effect, although this seems negligible at realistic PEPT sampling rates and uncertainties. The same interpolation scheme that gives rise to this interpolating halo, however, allows residence time binning to recover the true and continuous trajectory from even noisy and infrequently sampled multiple-pass data. It also leads to more accurate results from residence time binning than from simple binning, and to more precise results above a threshold sampling rate and grid resolution.

I.2 Real data

The foregone discussion suggests that the residence time binning method produces more accurate and, in most cases, more precise results than does the simple binning method- at least for artificial data. In this subsection I will use these two methods to bin real PEPT data obtained from a tumbling mill.

The data I will use was obtained from the 'old' 300 mm mill operated at 60% of its critical speed- an angular velocity of about 8 Hz- and filled to 31.25% of its volume with a 3 mm mono-size charge of glass beads. Although the motion of the tracer particle in this mill will not be constrained to a well known path as was the 'particle' in the artificial data case, its maximum radial position will be the same as for the artificial data, and its maximum angular velocity comparable.

[13]Both of these, though with the exception of the threshold effect mentioned before.

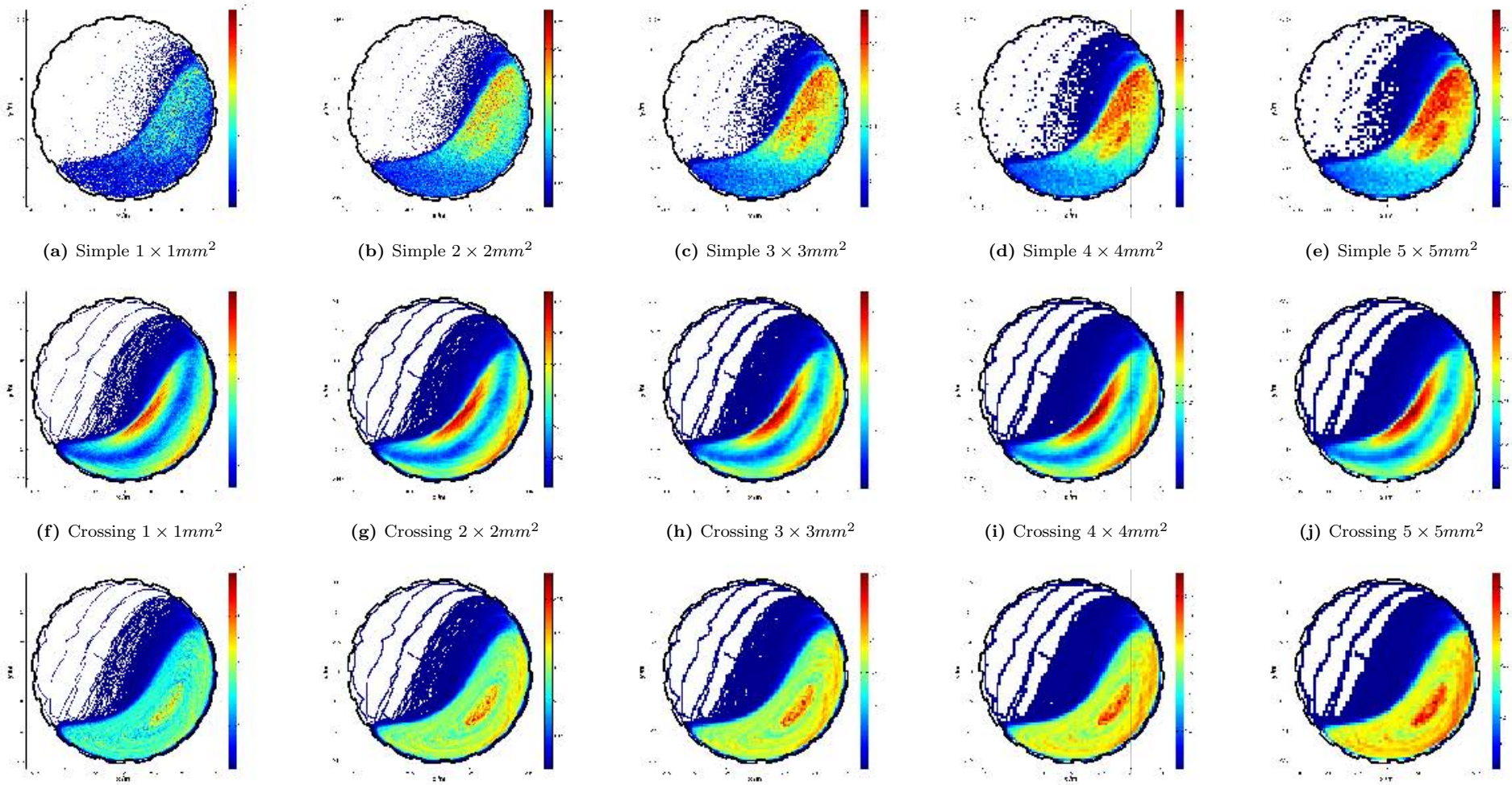

(a) Simple $1 \times 1mm^2$ **(b)** Simple $2 \times 2mm^2$ **(c)** Simple $3 \times 3mm^2$ **(d)** Simple $4 \times 4mm^2$ **(e)** Simple $5 \times 5mm^2$

(f) Crossing $1 \times 1mm^2$ **(g)** Crossing $2 \times 2mm^2$ **(h)** Crossing $3 \times 3mm^2$ **(i)** Crossing $4 \times 4mm^2$ **(j)** Crossing $5 \times 5mm^2$

(k) RTD $1 \times 1mm^2$ **(l)** RTD $2 \times 2mm^2$ **(m)** RTD $3 \times 3mm^2$ **(n)** RTD $4 \times 4mm^2$ **(o)** RTD $5 \times 5mm^2$

Figure I.28: Simple (top), bin-crossing (middle) and residence time (bottom) binning of the motion of a $3mm$ tracer particle in the 'old' $300mm$ mill filled to 31.25% with mono-sized charge and rotated at 60% of its critical speed.

I begin by binning the data by three different methods, as shown in Figure I.28. As well as the familiar simple binning (top row) and residence time binning methods (bottom row) I also include a third method- a variant on the residence time binning method called the bin-crossing method.

Whereas in the residence time binning method the cumulative time spent by the tracer particle in a given bin- or the time-weighted average value of its kinematics on each pass- is assigned to that bin, in the bin-crossing method only the number of times that the tracer particle has passed through a given bin- or the simple average of its kinematics on each pass- is so assigned. The bin-crossing method is thus the limiting case of a trajectory sampled perfectly uniformly in space. The residence time binning method is the limiting case of a trajectory sampled perfectly uniformly in time.

The residence time binning method, however, relies on calculating the cumulative time spent by a tracer particle in each bin over the course of an experiment. The first step in doing so is determining which bins were crossed by the tracer particle, and the second is determining how long it spent in each bin. Plots produced by the bin-crossing method, are thus a measure of the statistics available for residence time binning- high crossing density regions contribute more passes to the residence time binning calculation and thus benefit most from the smoothing effect seen in the multiple-pass artificial data above. The simply-binned RTD is a direct measure of the statistics available in that case.

The first thing to notice in Figure I.28 is that the bulk free surface of the charge seems to be the same for all three binning methods. However, the local variations in the RTD within the charge in these three cases are very different.

Figures I.28a to I.28e show the RTDs obtained by the simple binning method for various grid resolutions. It is clear here that the most detections occur in the top part of the bulk region of the charge. This data is sampled at intervals of 25.1 ± 13.1 ms, so its sampling frequency is well within the high range of the artificial data, and not tremendously non-uniform. In fact, a comparison between Figures I.15 and I.17 shows that there is no appreciable effect on the recovered data- simply or residence time binned- at this sort of sampling rate[14]. since there is a significant difference between the simply and residence time binned RTDs in Figure I.28, there must be some other effect at play here.

It turns out that the geometry of the camera, and the distribution of attenuating material affects the sampling frequency *spatially*- that is, LoRs originating in certain regions of the system of interest are more likely to reach the detectors than others[15]. This effect can be ameliorated by re-sampling the trajectory at uniform intervals.

Unlike in the artificial data case, I do not, here, have access to the true underlying trajectory, and so this re-sampling can only occur by interpolation. Since the residence time binning method relies on interpolation of the same data, re-sampling by interpolation will have no effect on its outcome, but a potentially large effect on the outcome of simple binning.

[14] A sampling rate of 25 ± 10 ms in these figures.
[15] For more on this, see Section 2.3.4.

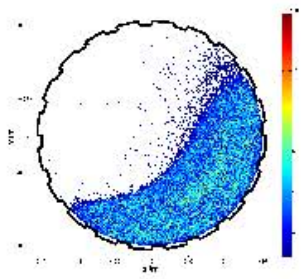

(a) Sampled at $\Delta t = 25 \pm 0$ms, binned at $1 \times 1mm^2$

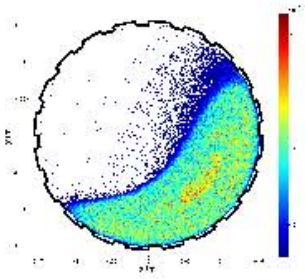

(b) Sampled at $\Delta t = 25 \pm 0$ms, binned at $2 \times 2mm^2$

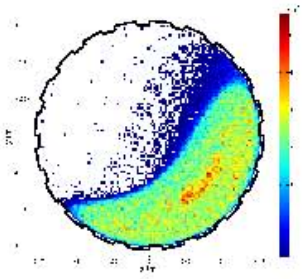

(c) Sampled at $\Delta t = 25 \pm 0$ms, binned at $3 \times 3mm^2$

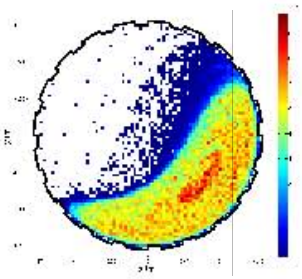

(d) Sampled at $\Delta t = 25 \pm 0$ms, binned at $4 \times 4mm^2$

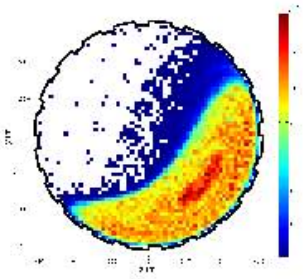

(e) Sampled at $\Delta t = 25 \pm 0$ms, binned at $5 \times 5mm^2$

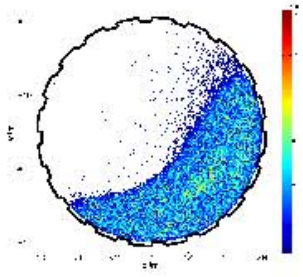

(f) Sampled at $\Delta t = 25 \pm 10$ms, binned at $1 \times 1mm^2$

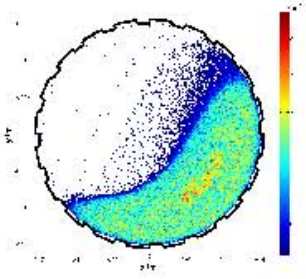

(g) Sampled at $\Delta t = 25 \pm 10$ms, binned at $2 \times 2mm^2$

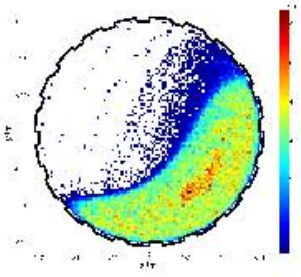

(h) Sampled at $\Delta t = 25 \pm 10$ms, binned at $3 \times 3mm^2$

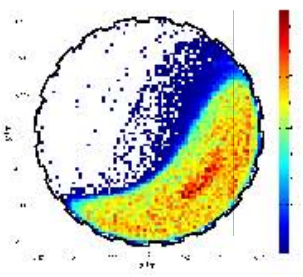

(i) Sampled at $\Delta t = 25 \pm 10$ms, binned at $4 \times 4mm^2$

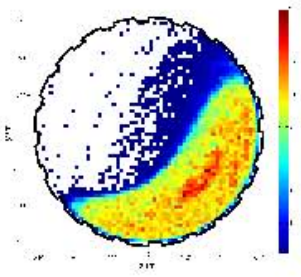

(j) Sampled at $\Delta t = 25 \pm 10$ms, binned at $5 \times 5mm^2$

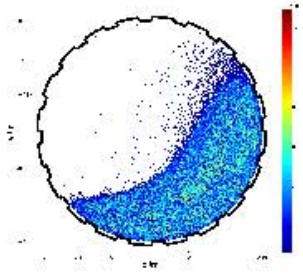

(k) Sampled at $\Delta t = 25 \pm 20$ms, binned at $1 \times 1mm^2$

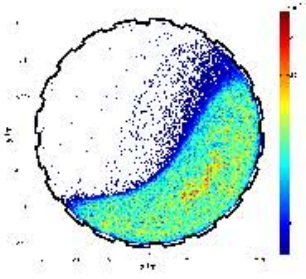

(l) Sampled at $\Delta t = 25 \pm 20$ms, binned at $2 \times 2mm^2$

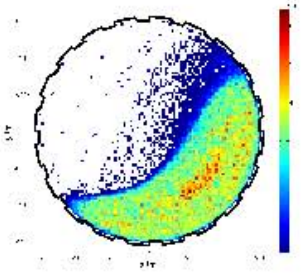

(m) Sampled at $\Delta t = 25 \pm 20$ms, binned at $3 \times 3mm^2$

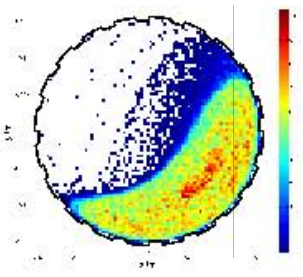

(n) Sampled at $\Delta t = 25 \pm 20$ms, binned at $4 \times 4mm^2$

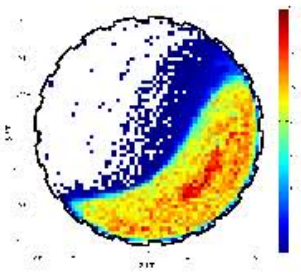

(o) Sampled at $\Delta t = 25 \pm 20$ms, binned at $5 \times 5mm^2$

Figure I.29: Simple binning of the motion of a $3mm$ tracer particle in the 'old' $300mm$ mill filled to 31.25% with mono-sized charge and rotated at 60% of its critical speed, re-sampled at 25 ms intervals.

Figure I.29 shows the simple binning of the trajectory data interpolated and re-sampled at $25 \pm \sigma_t$ ms, for a range of σ_t. For all values of σ_t, the simple binning of the re-sampled trajectory no longer shows the bias of Figures I.28a to I.28e. The simple binning of the re-sampled trajectory, in fact, now much more closely resembles the residence time binning shown in Figures I.28k to I.28o.

Furthermore, while increased sampling intervals decreases the resolution of local features in the RTD, as shown in Figure I.30, merely re-sampling more or less evenly in space completely eliminates the camera and environmental artefacts seen in the simple binning of raw data. That the uniformity of the time intervals make less of a difference- within reason- than do these environmental effects, is further reinforced by the only very small variation introduced into the RTDs of data uniformly spatially sampled, but non-uniformly time sampled, as shown in Figure I.31.

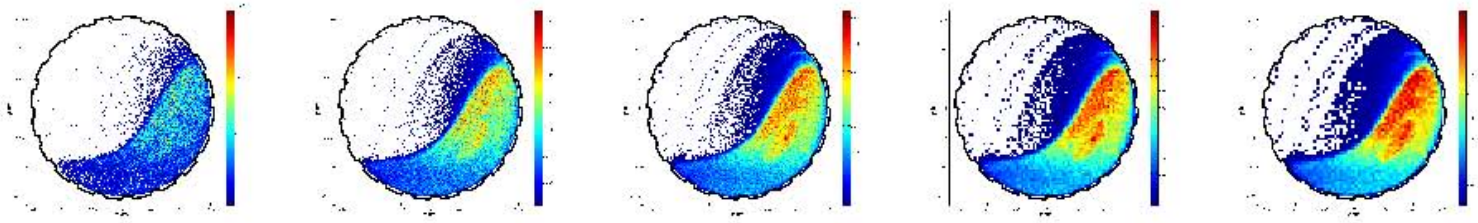

(a) Raw

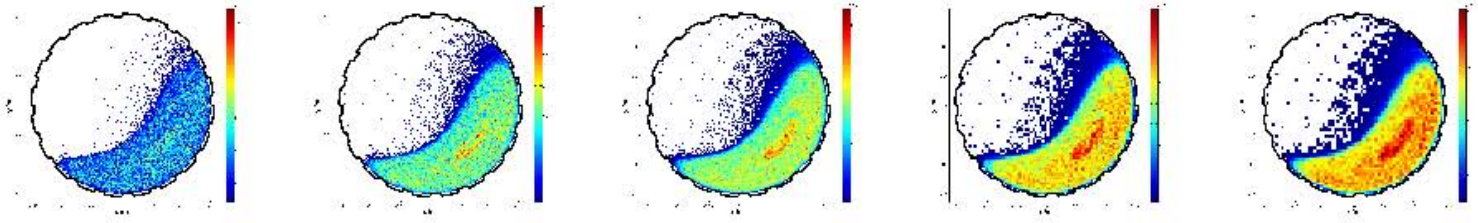

(b) Sampled at $\Delta t = 25 \pm 0$ms

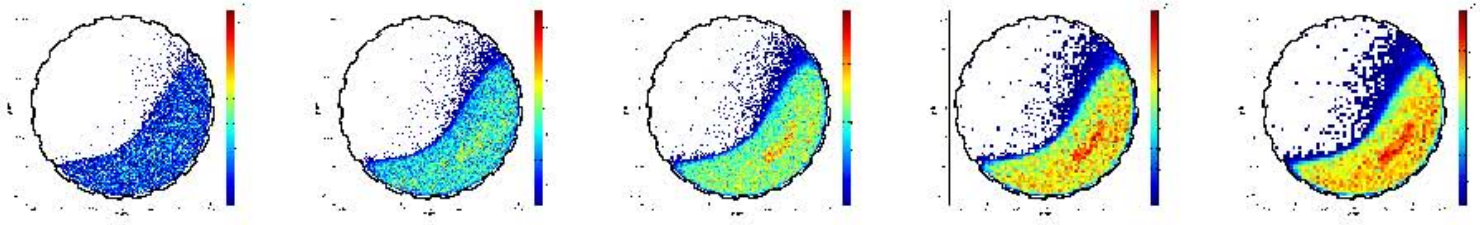

(c) Sampled at $\Delta t = 50 \pm 0$ms

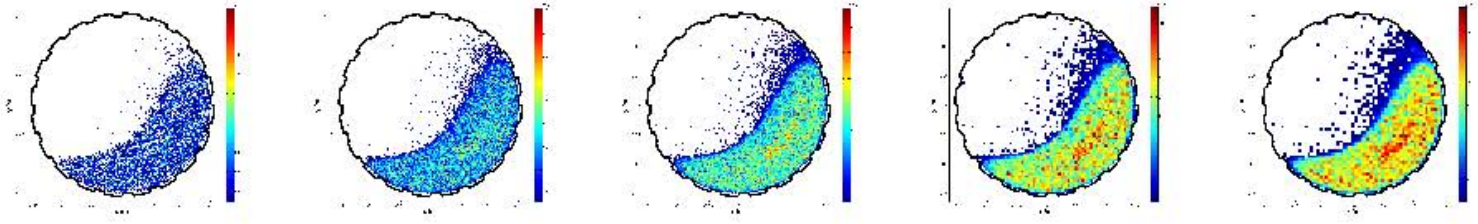

(d) Sampled at $\Delta t = 100 \pm 0$ms

Figure I.30: Simple binning of the motion of a $3mm$ tracer particle in the 'old' $300mm$ mill filled to 31.25% with mono-sized charge and rotated at 60% of its critical speed, re-sampled at various intervals and binned at increasing grid sizes (left to right).

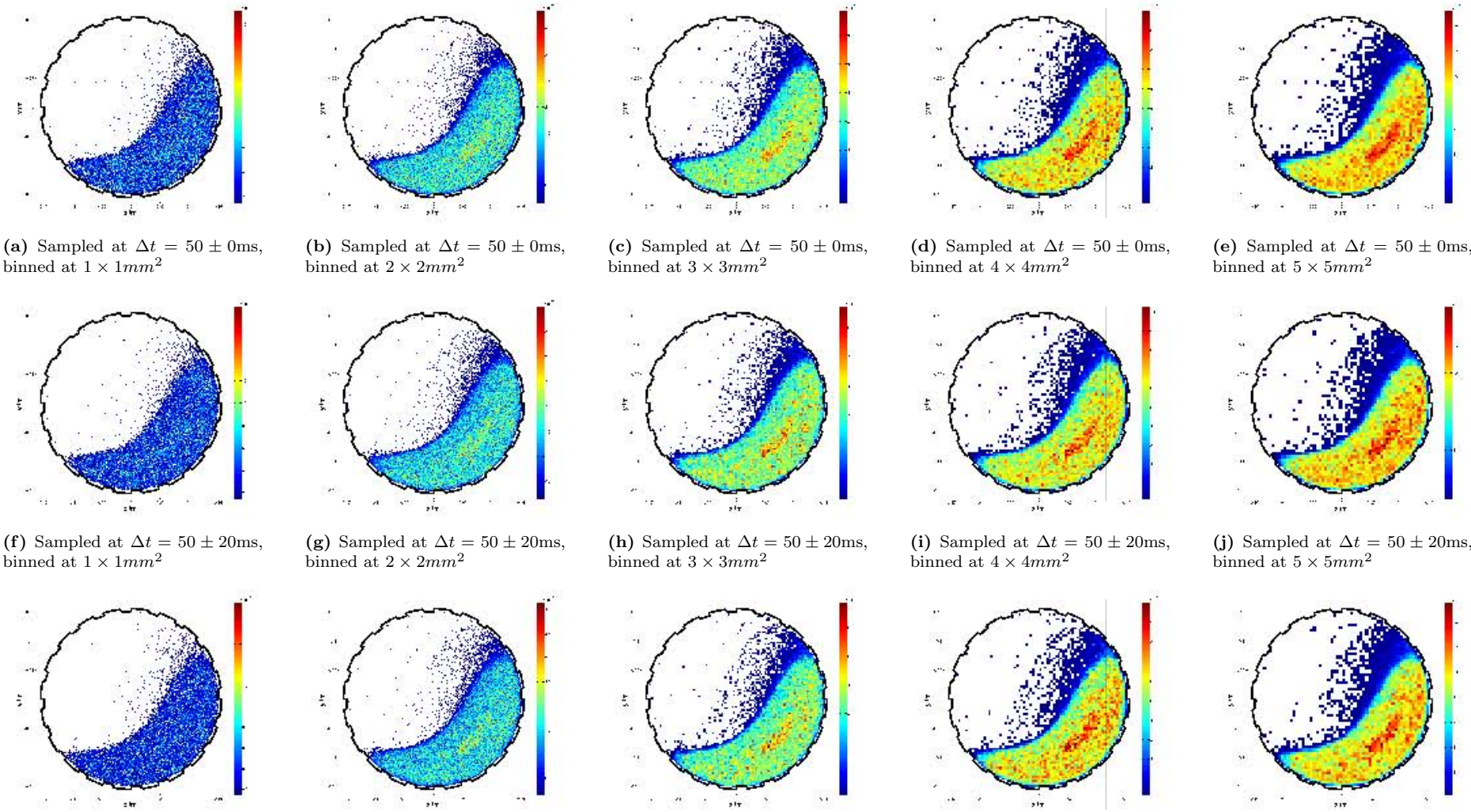

(a) Sampled at $\Delta t = 50 \pm 0$ms, binned at $1 \times 1mm^2$

(b) Sampled at $\Delta t = 50 \pm 0$ms, binned at $2 \times 2mm^2$

(c) Sampled at $\Delta t = 50 \pm 0$ms, binned at $3 \times 3mm^2$

(d) Sampled at $\Delta t = 50 \pm 0$ms, binned at $4 \times 4mm^2$

(e) Sampled at $\Delta t = 50 \pm 0$ms, binned at $5 \times 5mm^2$

(f) Sampled at $\Delta t = 50 \pm 20$ms, binned at $1 \times 1mm^2$

(g) Sampled at $\Delta t = 50 \pm 20$ms, binned at $2 \times 2mm^2$

(h) Sampled at $\Delta t = 50 \pm 20$ms, binned at $3 \times 3mm^2$

(i) Sampled at $\Delta t = 50 \pm 20$ms, binned at $4 \times 4mm^2$

(j) Sampled at $\Delta t = 50 \pm 20$ms, binned at $5 \times 5mm^2$

(k) Sampled at $\Delta t = 50 \pm 40$ms, binned at $1 \times 1mm^2$

(l) Sampled at $\Delta t = 50 \pm 40$ms, binned at $2 \times 2mm^2$

(m) Sampled at $\Delta t = 50 \pm 40$ms, binned at $3 \times 3mm^2$

(n) Sampled at $\Delta t = 50 \pm 40$ms, binned at $4 \times 4mm^2$

(o) Sampled at $\Delta t = 50 \pm 40$ms, binned at $5 \times 5mm^2$

Figure I.31: Simple binning of the motion of a $3mm$ tracer particle in the 'old' $300mm$ mill filled to 31.25% with mono-sized charge and rotated at 60% of its critical speed, re-sampled at 50 ms intervals.

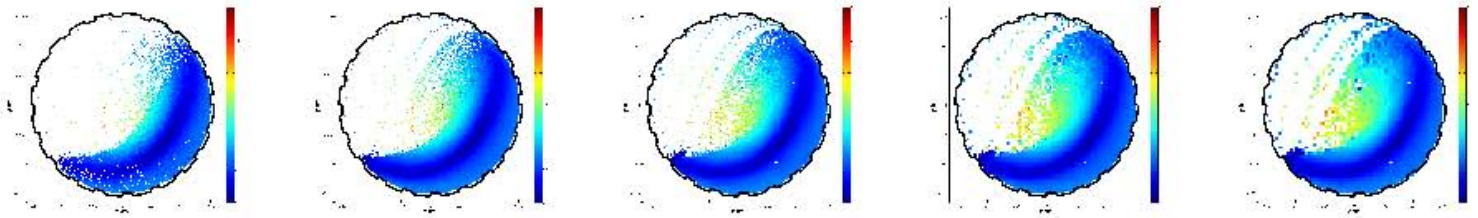

(a) Simply binned raw data

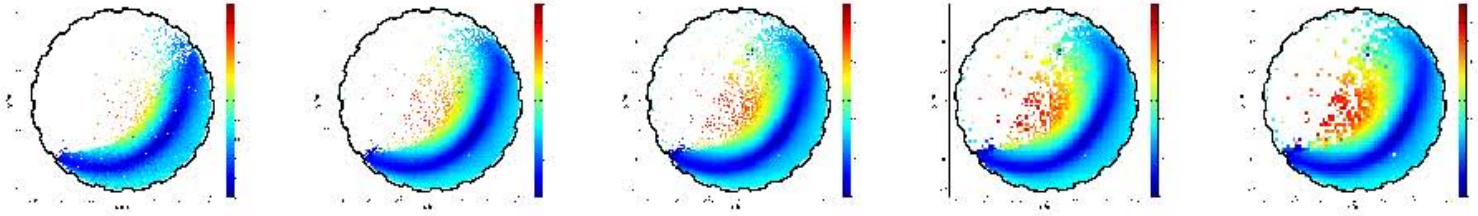

(b) Simply binned data re-sampled at 25 ms intervals

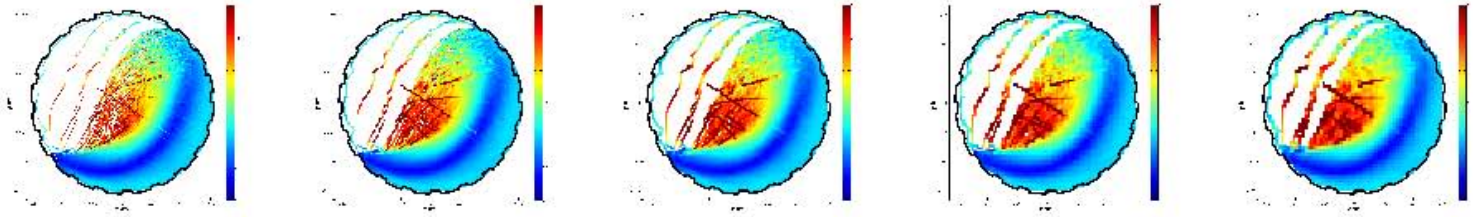

(c) Bin-crossing

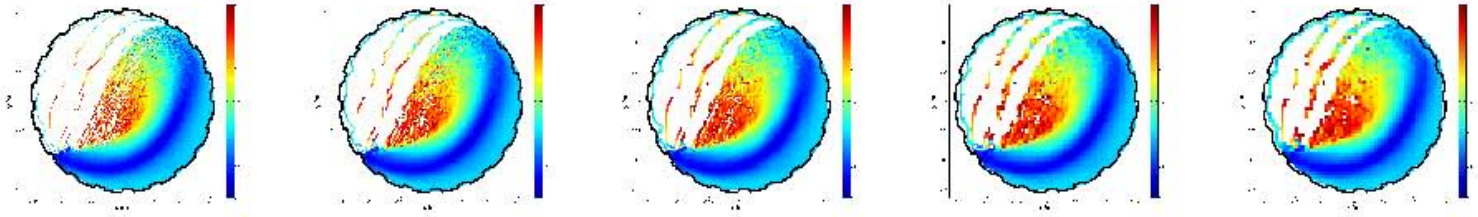

(d) RTD

Figure I.32: Simple (top, upper middle), bin-crossing (lower middle) and residence time (bottom) binning of the transverse velocity of a $3mm$ tracer particle in the 'old' $300mm$ mill filled to 31.25% with mono-sized charge and rotated at 60% of its critical speed.

Figure I.32 shows the experimental data binned by the simple binning method- raw and re-sampled- by the bin-crossing method and by the residence time binning method for various bin sizes. Unlike in the case of the RTD, the colour scales here- as they are also in Figures I.33 and I.34- are normalised to the same value. Thus the distributions can be compared simply between plots.

In all three velocity figures- Figure I.32 of the transverse velocity, Figure I.33 of the $\hat{x}$-velocity and Figure I.34 of the $\hat{y}$-velocity- the residence time bin plots show greater contrast and range than do the simply binned ones. However, the structure of the velocity distributions in all of these figures are similar, suggesting that even the simple binning of raw data does a reasonable job of capturing these features.

Re-sampling the trajectory has the effect of increasing the effective resolution of the simply binned distribution, making more pronounced the velocity gradient towards the equilibrium surface of the charge, and filling more of the in-flight region.

The velocity distributions produced by the bin-crossing method are simple averages of the velocities in each bin, rather than time-averages in the residence time binning case. The distributions produced by the residence time binning and bin-crossing methods are very similar, especially in the dense bulk region. They differ most strongly in the shoulder and in-flight regions where the charge becomes more dilute and its motion less smooth. The interpolating halo effect is also clearly visible in the bin-crossing method, but is smoothed out in the residence time binning case- an important advantage.

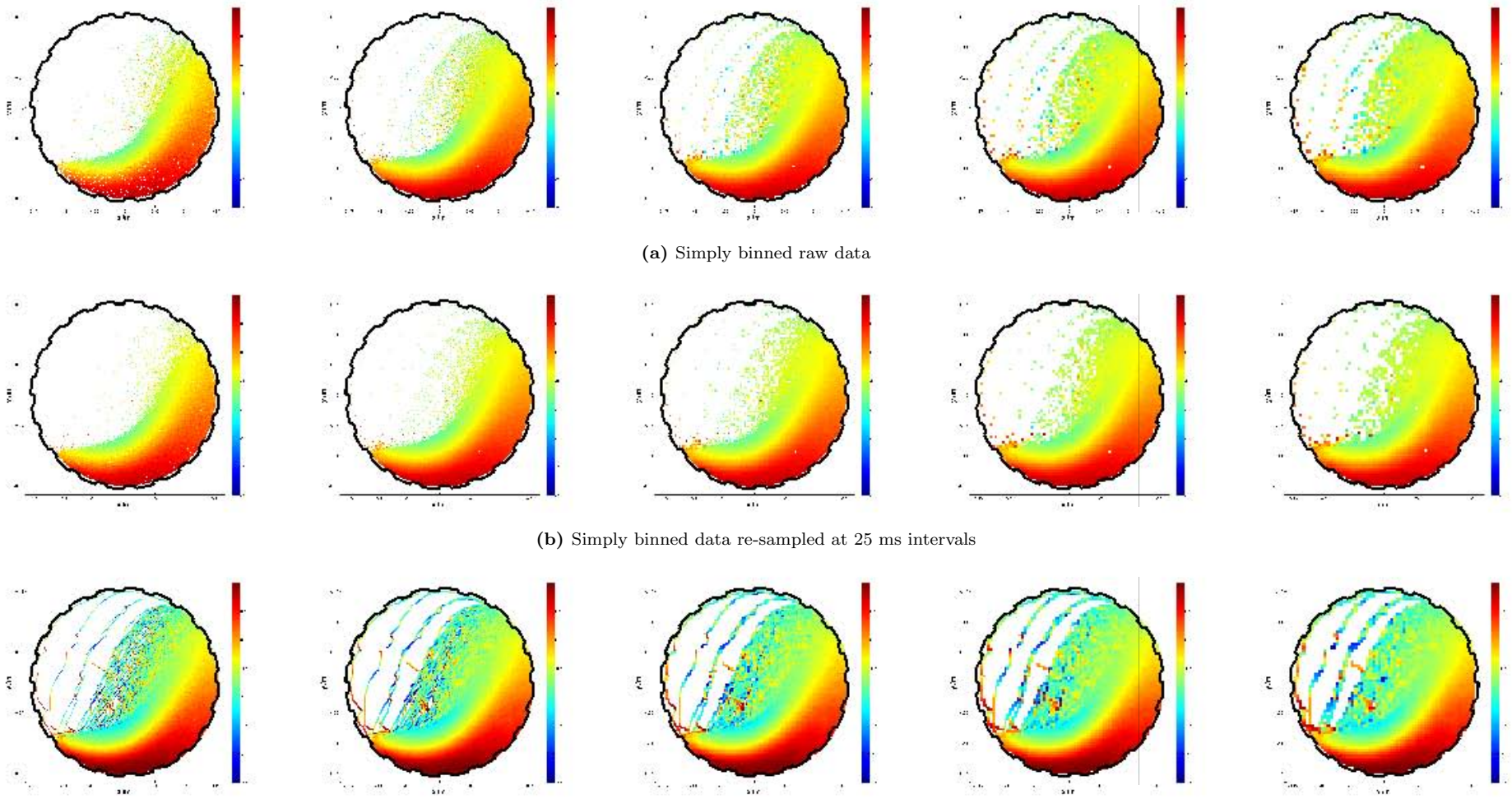

(a) Simply binned raw data

(b) Simply binned data re-sampled at 25 ms intervals

(c) RTD

Figure I.33: Simple (top, middle) and residence time (bottom) binning of the $\hat{x}$-velocity of a $3mm$ tracer particle in the 'old' $300mm$ mill filled to 31.25% with mono-sized charge and rotated at 60% of its critical speed.

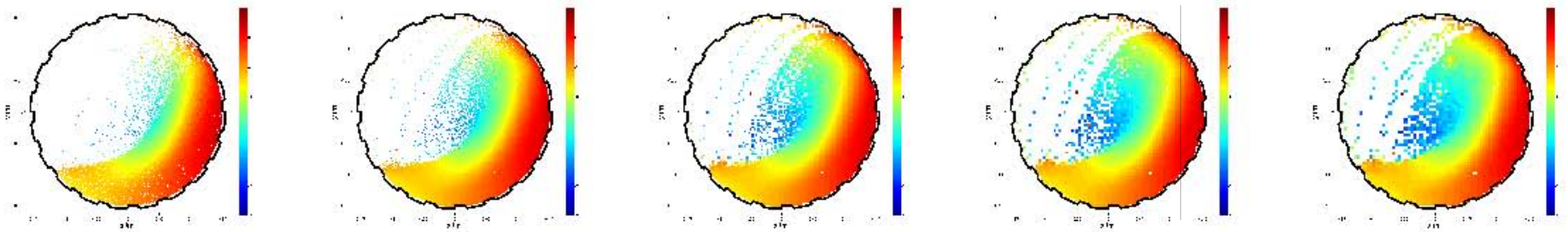

(a) Simply binned raw data

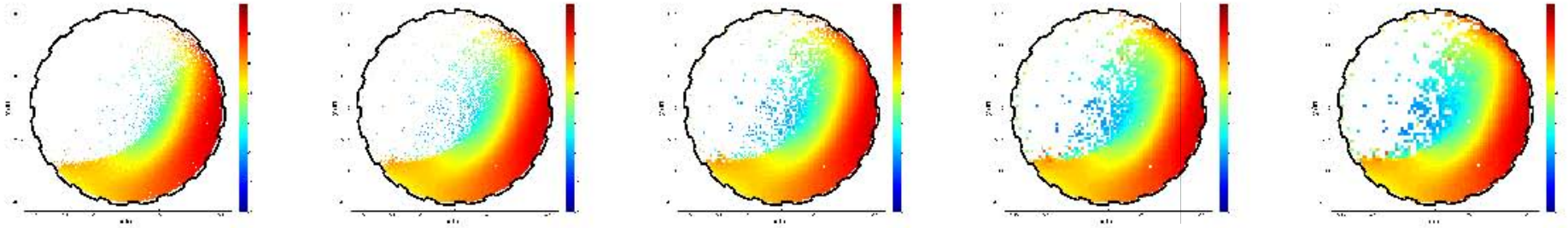

(b) Simply binned data re-sampled at 25 ms intervals

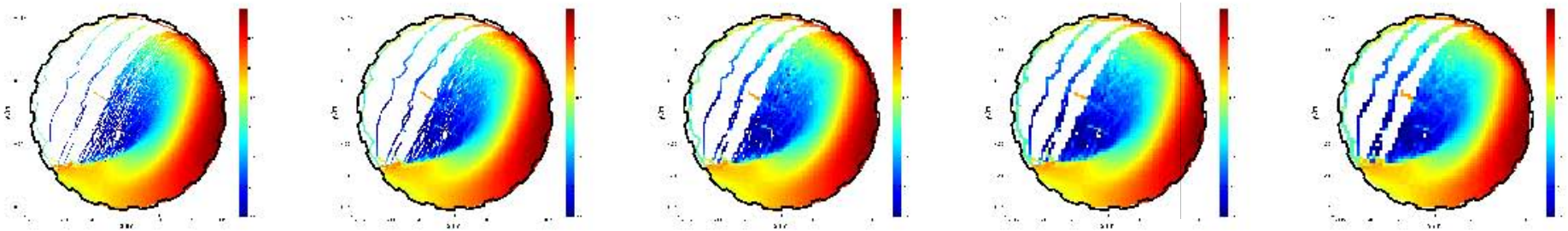

(c) RTD

Figure I.34: Simple (top, middle) and residence time (bottom) binning of the $\hat{y}$-velocity of a $3mm$ tracer particle in the 'old' $300mm$ mill filled to 31.25% with mono-sized charge and rotated at 60% of its critical speed.

Importantly, as is clear from Figures I.32, I.33 and I.34, there are magnitude differences between the velocity distributions calculated by the simple and residence time binning methods. Unfortunately, we do not have access to the true velocity distribution as we did in the artificial data case and so can not directly chose between the methods. However, there is a way to do so indirectly.

I.2.1 Power draw

As part of our experimental program, we used a torque sensor and tachometer to log the torque, τ, on the drive shaft between the motor and the mill, and the angular speed, ω, of the mill, respectively[16]. From this we can calculate the power, P, drawn by the mill, since $P = \tau \cdot \omega$. This is an external measurement, completely independent of the rest of the PEPT experiment, and so is an important comparator.

Also, we can calculate the power drawn by the laboratory-scale tumbling mill from the motion and distribution of the charge inside it- information available from a PEPT experiment. There are several ways to do this, but I will use the '(gravitational) torque per bin' approach given in Section 5.5.4. It can be summarised as

$$\begin{aligned} P_{ijk} &= \tau_{ijk} \cdot \omega_{ijk} = (r_{ij} \times F_{ijk}) \cdot \omega_{ijk} \\ \Rightarrow |P_{ijk}| &= m_{ijk} g \omega_{ijk} r_{ij} \cos\theta_{ij} = m_{ijk} g \omega_{ijk} x_i \end{aligned} \tag{I.4}$$

where the indices i, j and k label each bin in the $\hat{x}, \hat{y}$ and $\hat{z}$ directions, respectively.

This results in power draw distributions of the sort shown in Figure I.35. Here, again, the raw simply binned distribution is skewed towards the shoulder of the charge, an effect counteracted somewhat by re-sampling the trajectory. It is clear, though, that there is a good deal more structure in the residence time binned distributions at all grid resolutions. This, however, still says nothing about the veracity or otherwise of the distributions produced by these two methods.

[16] See Section 4.2.3.

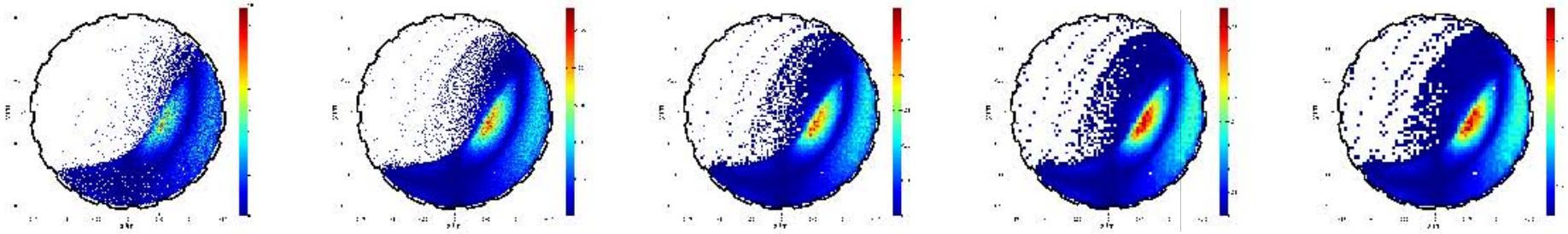

(a) Simply binned raw data

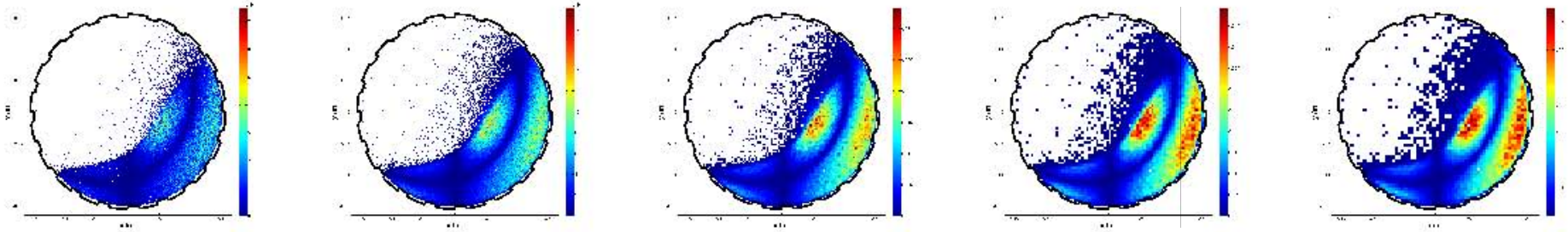

(b) Simply binned data re-sampled at 25 ms intervals

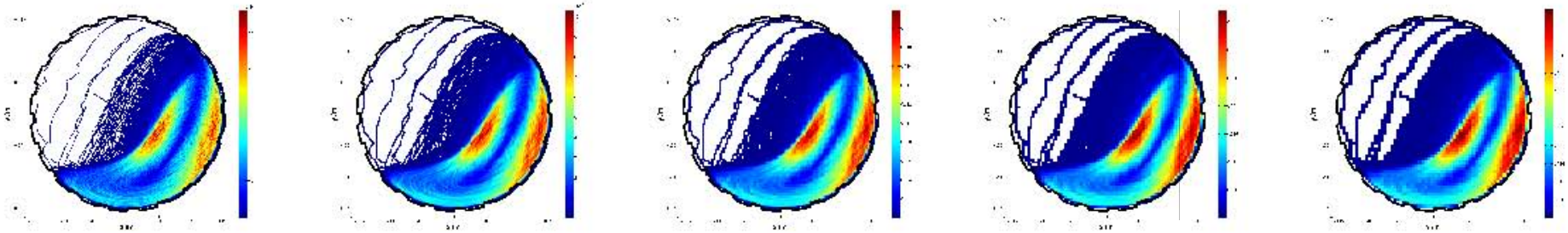

(c) RTD

Figure I.35: Simple (top, middle) and residence time (bottom) binning of the power drawn by a mono-size charge of $3mm$ glass beads in the 'old' $300mm$ mill filled to 31.25% and rotated at 60% of its critical speed.

Summing the contributions to the total power draw due to the gravitational torque and angular velocity in each bin, however, yields an estimate that can be compared with the measured power draw. While it is true that the calculated and measured powers should not match perfectly, because of the energy dissipated in inelastic impacts, frictional interactions, and so on, it is still instructive to compare the power draw calculated by the two binning methods under various conditions.

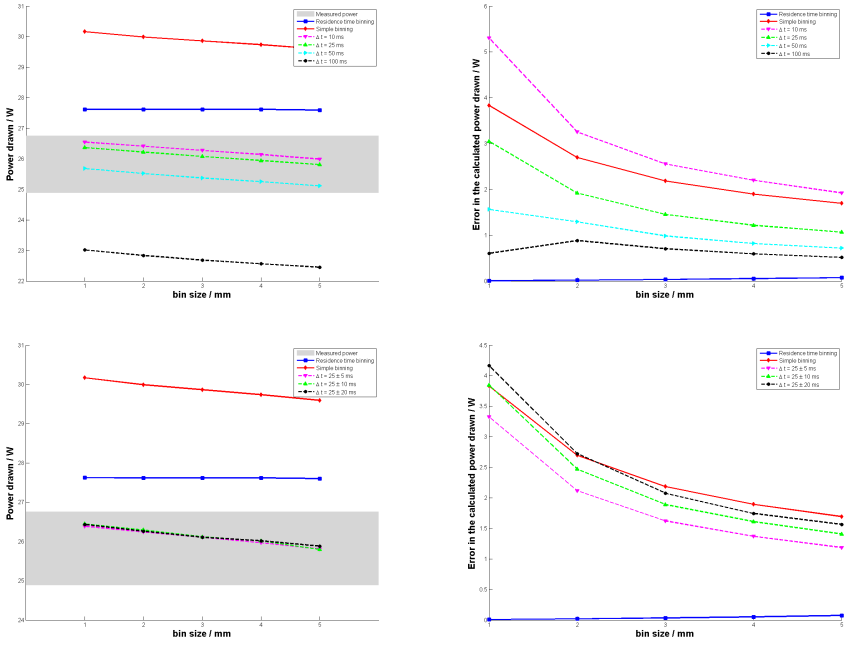

Figure I.36: Calculated power draw (left) and its uncertainty (right) as a function of grid resolution for residence time binned data and simply binned data raw and re-sampled uniformly (top) and non-uniformly (bottom). **Note**: The grey bands are the $\sim 68\%$ confidence interval on the measured power draw.

Figure I.36 shows the calculated power draw and uncertainty as a function of grid resolution for residence time and simply binned data. In the calculated power draw plots, the grey bands are the $\sim 68\%$ confidence interval on the measured power draw.

From these plots, it is clear that the power draw calculated from simply binned raw data over-predicts the measured power draw, and that it does this more so than does the the residence time binned calculation. However, re-sampling the data at greater and greater frequencies lowers the predicted power draw, even below the lower bound of the measured value. This could be due to the loss of resolution at lower sampling frequencies. This loss of resolution disproportionately affects high particle speed regions; regions likely to dominate the power draw calculation. This is what reduces contrast between and range of values in Figure I.35.

Figure I.35 shows, though, that there is almost no effect on the power draw predicted from simple binning of non-uniformly sampled data.

From Figure I.35 it seems that decreasing the grid resolution has little or no effect on the power draw calculated by the residence time binning method, but that it lowers the power draw predicted by the simple binning method. This could be because the resolution of simply binned data is much more effected by bin size than is residence time binned data- tracer particle locations that only just make it into a bin are treated the same as those in the centre; there is no time-weighting as in residence time binning.

This time-weighting offers a measure of uncertainty in the RTD that is not available for simple binning. Thus there is no way for simply binned data to reflect decrease in certainty from increased statistics. This is why the uncertainty in residence time binned power calculations are much lower

than simply binned ones. The apparent drop in uncertainty with decreasing grid resolution for simply binned power calculations is not, therefore, due to improved statistics in each bin, but rather to the fewer number of bins for which an estimate can be made.

I.2.2 Ergodicity and power draw

The shortcomings of the simple binning method with respect to its susceptibility to sampling effects can be probed by considering the variation of calculated power draw with time, as shown in Figure I.37, for a grid resolution of $3 \times 3mm^2$.

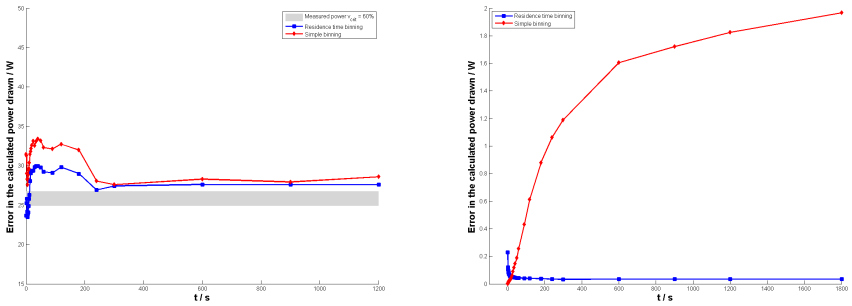

Figure I.37: The variation of calculated power draw (left) and its uncertainty (right) with time for residence time binned data and simply binned data. **Note**: The grey band is the $\sim$ 68% confidence interval on the measured power draw.

While the power draw calculated by the simple binning method is further from the measured than is that calculated by the residence time binning method, the two converge to their final values after about 5 minutes. After an hour, the power draw calculated from these two binning methods differ by only about 3 W.

That the power converges to a pseudo-constant value at all means that the system can be said to be ergodic.

On the other hand, as more and more data is collected, the uncertainty in the residence time binned calculation decreases very quickly to a steady, low number. The uncertainty in the simply binned calculation, however, asymptotes to a large number[17], and is still growing even after half an hour of data collection.

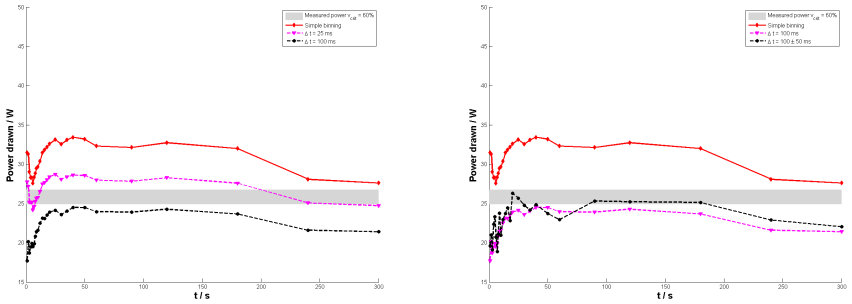

Figure I.38: The variation of power draw calculated from simply binned uniformly (left) and non-uniformly (right) re-sampled trajectories.

Figure I.38 shows predicted power draws obtained from simple binning. The leftmost plot shows the lowering of predicted power draw due to the sampling bias mentioned above, and the rightmost

[17] Of the order of 2 W.

one shows the increased variation in the calculated power draw for non-uniform sampling rates- an effect which does not emerge in plots such as Figure I.38, for instance.

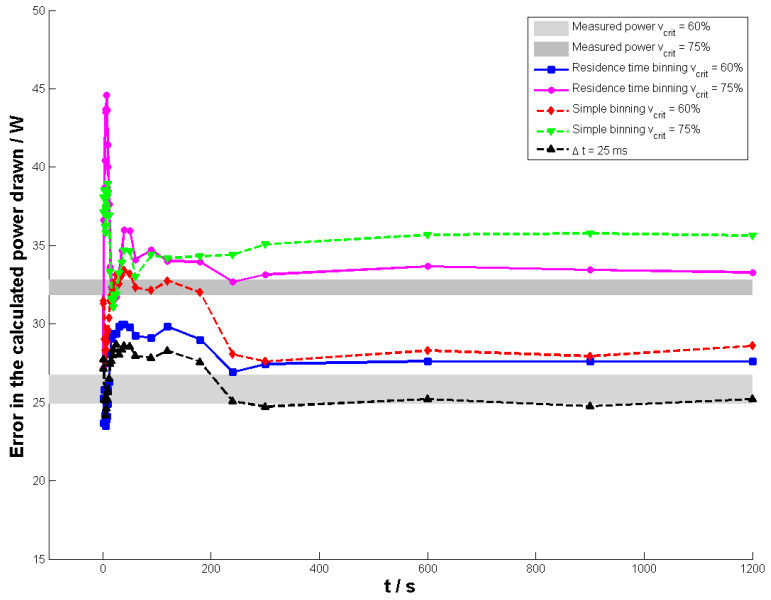

Figure I.39: A combined plot of the variations in calculated power draw for two different mill speeds.

Finally, Figure I.39 shows the variation in power draw calculated with simple, re-sampled simple and residence time binning for two mill speeds- 60% and 75% of critical speed. From this plot, it is clear that residence time binning data settles down quicker than even re-sampled simple binning data, and better predicts the measured power draw for both mill speeds, but especially for the higher speed for which the sampling bias is more pronounced.

Some discussion of how to interpret the magnitudes of the predicted powers, especially in relation to the measured ones, is given in Chapter 7.

I.3 Summary

A full summary of the results of binning artificial data is given in Section I.1.3.

In Section I.1, though, I investigated the effect of sampling rate, Gaussian noise and grid resolution on the ability of the two binning methods to reproduce the well-known kinematics of artificial data. I found that residence time binning has the effect of picking the true, underlying trajectory out of even noisy and infrequently sampled data, but that it did so at the expense of introducing an interpolating halo. I found that simple binning could approach the performance of residence time binning for high sampling frequencies, that it is less badly affected by non-uniform sampling intervals, and that- because it does not suffer from an interpolating halo- simply binned data can be more precise than residence time binned data above a certain sampling frequency and grid resolution. I found this threshold sampling frequency to be much lower than can be expected for PEPT data, and the threshold grid resolution- for this data- to be about $3 \times 3mm^2$. This suggests an optimum binning resolution.

In Section I.2, I investigated the efficacy of simple and residence time binning for real data. I found that although the real data was- in the limiting case- similar to the artificial data I had just considered, and although it was sampled at a relatively high frequency, there were unexpectedly

large differences between the RTDs obtained by the simple and residence time binning cases. I showed that this was as a result of non-uniform spatial sampling due to the geometry of the gamma camera and the attenuating environment, and that this could be overcome by re-sampling the data before simply binning it. I also found, though, that the shape of the charge and the structure of the kinematics in it were largely unaffected[18] by the choice of binning method.

I found, though, differences in the magnitudes, spreads and spatial contrast of the kinematic distributions obtained from each binning method, and tried- unsuccessfully- to choose between them using power draw considerations. I was able to show, however, that the power draw calculated by the residence time binning method settles down sooner to a more constant steady-state value than does that calculated by the simple binning method, but that both revealed the ergodicity of the system.

Finally, I showed that although the simple binning method is affected by grid resolution (bin size), the residence time binning method is not sensitive to it, beyond the resolution limit so imposed. Having decided that, for reasons already discussed at length, the residence time binning method is the superior one, I settled on the optimum bin size- $3 \times 3mm^2$ suggested by the artificial data.

[18]Beyond the obvious loss of statistics in the simple binning case.

A complete set of references

[Anger, 1957] Anger, H. (1957). A new instrument for mapping gamma ray emitters. *University of California Radiation Laboratory*, 3653:xxx–xxx.

[Anger, 1963] Anger, H. (1963). Positron scintillation camera. *Nuclear Medicine*, 4:326–330.

[Bailey et al., 2005] Bailey, D. L., Townsend, D. W., Valk, P. E., and Maisey, M. N., editors (2005). *Positron Emission Tomography*. Springer-Verlag London Ltd.

[Bbosa et al., 2011] Bbosa, L., Govender, I., Mainza, A., and Powell, M. (2011). Power draw estimations in experimental tumbling mills using pept. *Minerals Engineering*, 24:319–324.

[Bemrose et al., 1988] Bemrose, C., Fowles, P., Hawkesworth, M., and O'Dwyer, M. (1988). Application of positron emission tomography to particulate flow measurement in chemical engineering processes. *Nuclear Instruments and Methods in Physics Research A*, 273:874–880. Unread.

[Berger and Hubbell, 1987] Berger, M. and Hubbell, J. (1987). Xcom: Photon cross sections database. Technical report, National Institute of Standards and Technology.

[Boateng and Barr, 1996] Boateng, A. and Barr, P. (1996). Modelling of particle mixing and segregation in the transverse plane of a rotary kiln. *Chemical Engineering Science*, 51:4167–4181.

[Boateng and Barr, 1997] Boateng, A. and Barr, P. (1997). Granular flow behaviour in the transverse plane of a partially filled rotating cylinder. *Journal of Fluid Mechanics*, 330:233–249.

[Bond, 1961] Bond, F. (1961). Crushing and grinding calculations part i and ii. *British Chemical Engineering*, 6(6):xxx.

[Buffler et al., 2011] Buffler, A., Govender, I., Cilliers, J., Parker, D., Franzidis, J.-P., Mainza, A., Newman, R., Powell, M., and van der Westhuizen, A. (2011). Pept cape town: a new positron emission particle tracking facility at ithemba labs. *Minerals Engineering*, 24:261–266.

[Canny, 1986] Canny, J. (1986). A computational approach to edge detection. *IEEE Transactions on Pattern Analysis and Machine Intelligence*, PAMI-8:679–698.

[Cassen et al., 1950] Cassen, B., Curtis, L., and Reed, C. (1950). A sensitive directional gamma-ray detector. *Nucleonics*, 2:78–81.

[Chou, 2007] Chou, C.-W. (2007). Application of pept to track a single labelled red blood cell in vitro. Master's thesis, University of Birmingham.

[Cleary, 1998] Cleary, P. (1998). Predicting charge motion, power draw, segregation, wear and particle breakage in ball mills using discrete element methods. *Minerals Engineering*, 11:1061–1080.

[Cleary, 2001] Cleary, P. (2001). Charge behaviour and power consumption in ball mills: Sensitivity to mill operating conditions, liner geometry and charge composition. *International Journal of Mineral Processing*, 63:79–114.

[Cleary et al., 2003] Cleary, P. W., Morrison, R., and Morrell, S. (2003). Comparison of dem and experiment for a scale model sag mill. *International Journal of Mineral Processing*, 68:129–165.

[Curie and Joliot, 1934] Curie, I. and Joliot, F. (1934). Artificial production of a new kind of radioactive element. *Nature*, 133:201.

[Ding et al., 2002] Ding, Y., Forster, R., Seville, J., and Parker, D. (2002). Granular motion in rotating drums: bed turnover time and slumpingrolling transition. *Powder Technology*, 124:18 27.

[Ding et al., 2001a] Ding, Y. L., Forster, R. N., Seville, J. P. K., and Parker, D. J. (2001a). Scaling relationships for rotating drums. *Chemical Engineering Science*, 56:37373750.

[Ding et al., 2001b] Ding, Y. L., Seville, J. P. K., Forster, R., and Parker, D. J. (2001b). Solids motion in rolling mode rotating drums operated at low to medium rotational speeds. *Chemical Engineering Science*, 56:1769–1780.

[Dong and Moys, 2003] Dong, H. and Moys, M. (2003). Load behavior and mill power. *International Journal of Mineral Processing*, 69:11–28.

[Dury et al., 1998] Dury, C., Ristow, G., Moss, J., and Nakagawa, M. (1998). Boundary effects on the angle of repose in rotating cylinders. *Physical Review E*, 57(4):4491–4497.

[El-Rahman et al., 2001] El-Rahman, M. A., Mishra, B., and Rajamani, R. (2001). Industrial tumbling mill power prediction using the discrete element method. *Minerals Engineering*, 14:1321–1328.

[Elperin and Vikhansky, 2000] Elperin, T. and Vikhansky, A. (2000). Granular flow in a three-dimensional rotating cylinder. *Physical Review E*, 62(3):4446–4449.

[Fan et al., 2006a] Fan, X., Parker, D., and Smith, M. (2006a). Enhancing 18f uptake in a single particle for positron emission particle tracking through modification of solid surface chemistry. *Nuclear Instruments and Methods in Physics Research A*, 558:542546.

[Fan et al., 2006b] Fan, X., Parker, D., and Smith, M. (2006b). Labelling a single particle for positron emission particle tracking using direct activation and ion-exchange techniques. *Nuclear Instruments and Methods in Physics Research A*, 562:345350.

[Fan et al., 2009] Fan, X., Waters, K. E., Rowson, N. A., and Parker, D. J. (2009). Modification of ilmenite surface chemistry for enhancing surfactants adsorption and bubble attachment. *Journal of Colloid and Interface Science*, 329:167172.

[Govender et al., 2011a] Govender, I., Mangesana, N., Mainza, A., and Franzidis, J.-P. (2011a). Measurement of shear rates in a laboratory tumbling mill. *Minerals Engineering*, 24:225–229.

[Govender and Powell, 2006] Govender, I. and Powell, M. (2006). An empirical power model derived from 3d particle tracking experiments. *Minerals Engineering*, 19:1005–1012.

[Govender et al., 2001] Govender, I., Powell, M., and Nurick, G. (2001). 3d particle tracking: A rigorous technique for verifying dem. *Minerals Engineering*, 14(10):1329–1340.

[Govender et al., 2011b] Govender, I., Tupper, G., and Mainza, A. (2011b). Towards a mechanistic model for slurry transport in tumbling mills. *Minerals Engineering*, 24:230–235.

[Harris et al., 1985] Harris, C., Schnock, E., and Arbiter, N. (1985). Grinding mill power consumption. *Mineral Processing and Extractive Metallurgy Review*, 1:297–345.

[Hawkesworth et al., 1986] Hawkesworth, M., O'Dwyer, M., Walker, J., Fowles, P., Heritage, J., Stewart, P., Witcomb, R., Bateman, J., Connolly, J., and Stephenson., R. (1986). A positron camera for industrial application. *Nuclear Instruments and Methods in Physics Research A*, 253:145–157.

[Henein et al., 1983] Henein, H., Brimacombe, J., and Watson, A. (1983). Experimental study of transverse bed motion in rotary kilns. *Metallurgical and materials transactions B*, 14(2):191–205.

[Hogg et al., 1972] Hogg, R., , and Fuerstenau, D. (1972). Power relationships for tumbling mills. *Transaction of SME/AIME*, 252:418–423.

[Ingram et al., 2005] Ingram, A., Seville, J., Parker, D., Fan, X., and Forster, R. (2005). Axial and radial dispersion in rolling mode rotating drums. *Powder Technology*, 158:76–91.

[Jain et al., 2002] Jain, N., Ottino, J., and Lueptow, R. (2002). An experimental study of the flowing granular layer in a rotating tumbler. *Physics of fluids*, 14:572–582.

[Kallon et al., 2011] Kallon, D., Govender, I., and Mainza, A. (2011). Circulation rate modelling of charge using positron emission particle tracking. *Minerals Engineering*, 24:282–289.

[Krane, 1988] Krane, K. S. (1988). *Introductory Nuclear Physics*. Wiley.

[Kuhl and Edwards, 1968] Kuhl, D. and Edwards, R. (1968). Reorganizing data from transverse section scans using digital processing. *Radiology*, 91:975–983.

[Leadbeater, 2009] Leadbeater, T. W. (2009). *The Development of Positron Imaging Systems for Applications in Industrial Process Tomography*. PhD thesis, University of Birmingham.

[Leung, 1987] Leung, K. (1987). *An energy-based, ore-specific model for autogeneous and semi-autogeneous grinding*. PhD thesis, University of Queensland.

[Levin and Hoffman, 1999] Levin, C. S. and Hoffman, E. J. (1999). Calculation of positron range and its effect on the fundamental limit of positron emission tomography system spatial resolution. *Phys. Med. Biol.*, 44:781–799.

[Lidell and Moys, 1988] Lidell, K. and Moys, M. (1988). The effects of mill speed and filling on the behaviour of the load in a rotary grinding mill. *Journal of the South African Institute of Mining and Metallurgy*, 88:49–57.

[Lim et al., 2003] Lim, S.-Y., Davidson, J., Forster, R., Parker, D., Scott, D., and Seville, J. (2003). Avalanching of granular material in a horizontal slowly rotating cylinder: Pept studies. *Powder Technology*, 138:25–30.

[McBride et al., 2004] McBride, A., Govender, I., Powell, M., and Cloete, T. (2004). Contributions to the experimental validation of the discrete element method applied to tumbling mills. *Engineering Computations*, 21:119–136.

[Mellmann, 2001] Mellmann, J. (2001). The transvers motion of solids in rotating cylinders- forms of motion and transition behaviour. *Powder Technology*, 118:251–270.

[Mishra and Rajamani, 1994] Mishra, B. and Rajamani, R. (1994). Simulation of charge motion in ball mills: Part 1. experimental verifications. *International Journal of Mineral Processing*, 40:171–186.

[Morell, 1992] Morell, S. (1992). Prediction of grinding-mill power. *Transactions of the Institution of Mining and Metallurgy Section C: Mineral Processing Extraction and Metallurgy*, 101:C25–C32.

[Nakagawa et al., 1993] Nakagawa, M., Altobelli, S., Caprihan, A., Fukushima, E., and Jeong, E. (1993). Non-invasive measurements of granular flows by magnetic resonance imaging. *Experiments in Fluids*, 16(1):54–60.

[Napier-Munn et al., 2005] Napier-Munn, T., Morrell, S., Morrison, R., and Kojovic, T. (2005). *Mineral Comminution Circuits*. The Julis Kruttscnitt Mineral Research Centre.

[Parker et al., 1993] Parker, D., Broadbent, C., Fowles, P., Hawkesworth, M., and McNeil, P. (1993). Positron emission particle tracking - a technique for studying flow within engineering equipment. *Nuclear Instruments and Methods in Physics Research A*, 326:592. Unread.

[Parker et al., 2002] Parker, D., Forster, R., Fowles, P., and Takhar, P. (2002). Positron emission particle trackingusingthe new birmingham positron camera. *Nuclear Instruments and Methods in Physics Research A*, 477:540545.

[Parker et al., 2008] Parker, D., Leadbeater, T., Fan, X., Hausard, M., Ingram, A., and Yang, Z. (2008). Positron imaging techniques for process engineering: recent developments at birmingham. *Measurement Science and Technology*, 19:xxx–xxx.

[Parker et al., 1997] Parker, D. J., Allen, D., Benton, D., Fowles, P., McNeil, P., Tan, M., and Beynona, T. (1997). Developments in particle tracking using the birmingham positron camera. *Nuclear Instruments and Methods in Physics Research A*, 392:421–426.

[Phelps et al., 1975] Phelps, M., Hoffman, E., and Mullani, M. (1975). Application of annihilation coincidence detection to transaxial reconstruction tomography. *Journal of Nuclear Medecine*, 16:210–224.

[Powell and McBride, 2004] Powell, M. and McBride, A. (2004). A three-dimensional analysis of media motion and grinding regions in mills. *Minerals Engineering*, 17:1099–1109.

[Powell and Nurick, 1996a] Powell, M. and Nurick, G. (1996a). A study of charge motion in rotary mills part 1- extension of the theory. *Minerals Engineering*, 9:259–268.

[Powell and Nurick, 1996b] Powell, M. and Nurick, G. (1996b). A study of charge motion in rotary mills part 2- experimental work. *Minerals Engineering*, 9:343–350.

[Powell and Nurick, 1996c] Powell, M. and Nurick, G. (1996c). A study of charge motion in rotary mills part 3- analysis of results. *Minerals Engineering*, 9:399–418.

[Rajchenbach, 1990] Rajchenbach, J. (1990). Flow in powders: From discrete avalanches to continuous regime. *Physical Review Letters*, 65(18):2221–2224.

[Reivich et al., 1979] Reivich, M., Kuhl, D., and Wolf, A. (1979). The [18f]fluoro-deoxyglucose method for the measurement of local cerebral glucose utilization in man. *Circulation Research*, 44:127–137.

[Rogovin and Herbst, 1989] Rogovin, Z. and Herbst, J. (1989). Charge motion in a semi-autogeneous grinding mill. *Minerals and Metallurgical Processing*, 6:18–23.

[Rose and Sullivan, 1957] Rose, H. and Sullivan, R. (1957). *A treatise on the Internal Mechanics of Ball, Tube and Rod mills*. Constable, London.

[Sadrmomtaz et al., 2007] Sadrmomtaz, A., Parker, D., and Byars, L. (2007). Modification of a medical pet scanner for pept studies. *Nuclear Instruments and Methods in Physics Research A*, 573:9194.

[Santomaso et al., 2003] Santomaso, A., Ding, Y., Lickiss, J., and York, D. (2003). Investigation of the granular behaviour in a rotating drum operated over a wide range of rotational speed. *Transactions of the Institute of Chemical Engineers*, 81:936–945.

[Sichalwe et al., 2011] Sichalwe, K., Govender, I., and Mainza, A. (2011). Characterising porosity of multi-component mixtures in rotary mills. *Minerals Engineering*, 24:276–281.

[Taberlet et al., 2006] Taberlet, N., Richard, P., and hinch, E. J. (2006). S shape of a granular pile in a rotating drum. *Physical Review E*, 73:050301–1–4.

[Ter-Pogossian et al., 1975] Ter-Pogossian, M., Phelps, M., and Hoffman, E. (1975). A positron-emission transaxial tomograph for nuclear imaging (pett). *Radiology*, 114:89–98.

[Tordesillas and Arber, 2005] Tordesillas, A. and Arber, D. (2005). Capturing the s in segregation: A simple model of flowing granular mixtures in rotating drums. *International Journal of Mathematical Education in Science and Technology*, 36(8):861–877.

[Wagner, 1998] Wagner, H. N. (1998). A brief history of positron emission tomography (pet). *Seminars in Nuclear Medicine*, Vol XXVIII, No 3:213–220.

[Watanabe, 1999] Watanabe, H. (1999). Critical rotation speed for ball-milling. *Powder Technology*, 104:95–99.

[Wills, 2001] Wills, B. A. (2001). *Mineral Processing Technology*. Butterworth Heinemann, 6 edition.

[Yang et al., 2007] Yang, Z., Fryer, P., Bakalis, S., Fan, X., Parker, D., and Seville, J. (2007). An improved algorithm for tracking multiple, freely moving particles in a positron emission particle tracking system. *Nuclear Instruments and Methods in Physics Research A*, 577:585594.

[Zik et al., 1994] Zik, O., Levine, D., Lipson, S., Shtrikman, S., and Stavans, J. (1994). Rotationally induced segregation of granular materials. *Physical Review Letters*, 73(5):644–647.

Glossary

abrasion a surface grinding mechanism in which two particles are worn down by rubbing against each other. 3, 28, 35, 45, 49, 50, 52, 53, 157, 168, 172, 176, 340

active region the portion of the charge in the bulk region of a tumbling mill above the equilibrium surface that flows down over the rising charge under the influence of gravity. 32–38, 41, 52–56, 102, 103, 119, 139, 143, 144, 151, 154–157, 159, 160, 163, 168, 169, 172, 176, 338, 340, 344

agitated system a class of cylindrically symmetric systems consisting of a cylinder either rotated about its centre or driven by some 1D forcing function. 94, 95

angle of repose the maximum angle that a slopes of a pile of granular material can make with the horizontal before slipping. Strictly, the *critical* angle of repose. 34, 35, 37, 55, 104, 344

associated event this is a spurious event that is due to the detection of two gamma rays that were not both created in the same positronium annihilation. The associated gamma ray could be from the decay of an excited daughter nucleus or from background radiation. 15, 16, 22

attrition a surface grinding mechanism in which a particle is worn down by being rubbed between two other, generally larger, particles. 3, 35, 45, 49, 50, 52, 53, 157, 168, 172, 176

autogenous mill a ball mill containing only charge and no grinding media. 43, 44, 337, 342, 346

axis of circulation the not necessarily linear curve about which charge rotates in a tumbling mill. 103, 107

ball mill a class of tumbling mill containing steel balls as grinding media. The term ball mill is usually reserved for such mills whose length to diameter ratio is between 1.5 and 2, and which contain between 20% and 40% steel balls by volume. See tube mill, semi-autogenous mill and autogenous mill. 45, 46, 337, 341, 342, 344, 346

basis a set of linearly independent vectors that in linear combination can represent any vector in a co-ordinate system. They define that co-ordinate system. 78, 338

bed turnover rate see circulation rate. 107, 339

bin-crossing method a variant of the residence time binning method in which each bin contains not how long the tracer particle has spent in it on cumulative passes, but rather how many times the tracer particle has passed through it during the experiment- how many times each bin has been crossed by the tracer particle. 317, 323

binning the procedure of dividing a region of space into small sampling voxels, or bins, for the purposes of representing in the Eulerian reference frame data collected in the Lagrangian reference frame. 80, 98, 101, 108, 343, 344

biplanar x-ray imaging a Lagrangian optical particle tracking technique based on the 3D reconstruction of a field of view using photogrammetric techniques. For a more complete treatement, see Section . 41, 54, 63, 77, 83

bivariate a function of only two variables, one usually the dependent and one the independent. 85, 341

blasting the use of explosives to break up mineral-bearing ores (usually while still underground) to facilitate handling and treatment. 43, 342, 344

bulk departure shoulder the point at which the trajectory of an element of the outermost layer of the charge in the bulk region begins to deviate from that of a rigid pody rotating about the centre of the mill. cf departure shoulder. 106, 339

bulk free surface the surface dividing the bulk region and disperse region of the charge in a tumbling mill. 35, 36, 38–41, 52, 55, 56, 101, 102, 105, 106, 116, 127, 130, 132–134, 136, 139–141, 148, 150, 151, 154, 158, 166, 168, 171, 173, 175, 176, 317, 338–340

bulk region that part of the charge below the bulk free surface consisting of granular material of sufficient density that its constituents are in contact with each other at all times. It is divided by the bulk free surface into the rising region and active region. 32, 33, 35, 36, 38, 41, 48, 52, 54, 56, 101–103, 106, 116, 118, 119, 122, 130, 132–134, 136, 139, 144–146, 148, 151, 166, 168, 172, 317, 323, 337, 338, 340, 344, 345

bulk shoulder the turning point at which the outermost layer of the charge in the rising region enters the active region. 106, 140, 338, 344

bulk toe the turning point at which the outermost layer of the charge in the active region re-enters the rising region. 42, 105, 106, 140, 345

Cartesian co-ordinates the usual, rectangular co-ordinate reference frame defined by the basis made up of unit vectors $\hat{\imath}$,$\hat{\jmath}$ and $\hat{k}$. 78

cascading a mode of charge motion in which there is significant fluidisation of the charge as it enters the disperse region, leading to the characteristic S-shape of its bulk free surface. cf rolling, cataracting. 32, 38, 39, 116, 118, 119, 127, 166, 167, 169, 171, 176, 338, 344

cataracting a mode of charge motion in which the head and bulk shoulder of the charge begin to deviate significantly, and the bulk free surface begins to lose its S-shape as a significant proportion of the charge leaving the rising region enters the in-flight region. cf cascading. 38, 40, 42, 57, 114, 116, 119, 166, 171, 176, 338

centre of circulation the point about which all of the charge in a tumbling mill circulates. 1, 28, 41, 101, 103, 347

centre of mass the weighted mean position of all of the mass in a system. 41, 104, 347

centrifuging a mode of charge motion in which most or all of the charge has begun to move with the mill shell for a complete revolution. 38, 55, 113, 114, 139, 171, 176, 339

centroid in this sense, the point that minimises the sum of perpendicular distances to a collection of LoRs. 16–18

charge the material inside a mill. In an industrial mill, the charge consists of coarse ore, slurry and grinding media. 1, 3, 4, 28–30, 32, 38, 41, 43–49, 52–57, 63, 65, 71–73, 76, 99–101, 103, 106–108, 112, 114, 116, 118, 119, 122, 124, 127–130, 132–134, 138–148, 150, 151, 154–160,

edge detection an image analysis technique used to simplify an image by picking out only its outlines, or edges. 101

empty region the portion of the charge in the disperse region of a tumbling mill above the charge free surface that is effectively devoid of in-flight charge for all time. 101, 106, 130, 163, 166, 171, 339

end effect the deviation of the motion of the charge in a tumbling mill due to the fact that it is not an infinitely long cylinder, but has at least frictional, and potentially geometrically complicated end walls. 103

equilibrium surface the surface dividing the rising region and active region in the bulk region of a tumbling mill. 1, 33, 35–37, 41, 42, 52, 56, 103, 106, 118, 119, 122, 123, 127, 128, 136, 138–140, 150, 151, 154–158, 163, 168, 176, 183, 323, 337, 344

ergodic could refer to either the ergodic assumption of mathematics, or the ergodic hypothesis of statistical physics. 79, 329

ergodic assumption in mathematics, the assumption is that the time-average behaviour of a system is the same as its ensemble average. 1, 2, 79, 80, 106, 107, 116, 174, 179, 340

ergodic hypothesis in statistical physics, the hypothesis that the time spent by a particle in some region of the phase space of microstates corresponding to a fixed macrostate of some system is proportional to the volume of that region, and thus the probability of those microstates' existence. 13, 79, 81–83, 85, 87, 89, 91, 92, 94, 105–107, 114, 340, 343

Eulerian reference frame that reference frame in which the flow field is sampled at fixed points in space. The Eulerian reference frame is the stationary reference frame of the total system, rather than of single particles in it. cf. the Lagrangian reference frame. 1, 2, 4, 77, 82, 85, 96, 98–100, 107–109, 115, 122, 276, 337, 342

feed the material added to the mill, usually consisting of a mix of ore and water. 44–46

fill level See load. 30

finite difference method a class of numerical schemes for solving differential and partial differential equations by approximating them with finite, as opposed to continuous, difference equations. 77

fluidised bed a bed of granular material that has taken on fluid-like properties by being either vibrated or dilated with a pressurised liquid or gas. 94, 345

free surface can refer to either the bulk free surface or charge free surface . 28, 55, 106, 114, 127

Froude number a dimensionless number based on the speed to length ratio. In rotating drums, it is usually given as $Fr = \frac{\omega^2 R}{g}$. 30, 31

gangue the commercially worthless material in which a mineral is embedded or disseminated in an ore. 339

grinding in mineral processing, the procedure of reducing the size of particles by a combination of impact and abrasion. Grinding mills usually operate by the movement of charge in a vessel, promoting stochastic collisions and contacts between the ore and the freely-moving grinding media. Cf. crushing. 43–46, 339, 342, 345

grinding media additional material added to a mill to aid grinding. The media could be steel rods in a rod mill, balls in a ball mill or ceramic beads in a fine grinding stirred mill such as an IsaMill^{TM}. 43–46, 48, 337, 341, 343, 344

grinding region a high-shear or high impact stress region in a grinding mill. 99

half-space Euclidean space, that is the usual 3D rectilinear space, can be divided by any infinite plane into two half spaces, one of which extends in the direction of the normal to the plane and the other in the opposite direction. 92, 93

half-value layer the thickness of a given material which reduces the intensity of a beam of radiation passing through it by half. That is, the thickness of material through which a beam of particles can pass before half of its constituents have interacted in the material. cf mean free path. 15, 342, 347

head the highest point attained by the outermost layer of in-flight charge in a tumbling mill. 38, 42, 53, 105, 106, 133, 134, 140, 158, 166, 171, 172, 338

hydrocyclone a broadly conical device used in the mining industry to separate particles by density using counter-rotating vortices and the centrifugal force. 94

impact toe the highest point at which in-flight charge strikes the mill shell. 1, 36, 42, 105, 106, 124, 127, 128, 133, 134, 140, 158, 166, 171, 172, 345

in-flight region the portion of the charge in the disperse region of a tumbling mill below the charge free surface containing charge in free fall. 33–36, 38, 52–56, 103, 105, 106, 118, 124, 127, 130, 133, 136, 140, 142–144, 146, 148, 150, 151, 154, 158–160, 164, 166, 168, 169, 171, 172, 323, 338, 339, 345

interpolant see interpolating function. 78, 84, 85, 87

interpolating function a function that passes through all of the discrete, bivariate sample points in a data set, evaluated between the sample points in the process of interpolation. 77, 85, 88, 89, 341

interpolating halo data introduced around the true trajectory being interpolated in order to satisfy the condition that distinguishes interpolation from curve fitting- that the interpolant must pass through all of the sample points. 163, 293, 298, 304, 308, 310, 315, 323, 330

interpolating polynomial an interpolating function that has the form of a polynomial rather than say a trigonometric function.. 77, 78, 87–89, 91, 93

interpolation the process of extracting new data points between discrete sample points by obtaining a function that passes through all of those points, see below. 85, 341

IsaMill^{TM} a stirred mill developed by Xtrata Technology, consisting of a stationary horizontal shell containing charge and grinding media driven by a series of spinning disks concentric with the shell. 43, 94, 95, 341, 345

kinematics a branch of classical mechanics dealing only with the motion of particles and not with the causes of that motion. I use the word kinematics to mean the particle's position, velocity and acceleration (all in rectilinear or curvilinear coordinates) at a given time or times. 77, 85, 95

Lagrangian reference frame that reference frame in which the flow field is sampled along the trajectory of a tracked particle. The Lagrangian reference frame is the stationary reference frame of a single tracked particle in a system, rather than of the entire system. cf.the Eulerian reference frame. 1, 2, 77, 82, 95, 100, 109, 115, 122, 276, 337, 340

least squares a standard approach to approximate a solution to an overdetermined system of equations by minimising the sum of the squares of the residual errors for each equation. 275

line of response a line through space defined by points of detection of the two back-to-back γs produced in a positron annihilation event. The fact that the point of annihilation must be along such a line of response is used in both positron emission tomography (PET) and PEPT reconstruction. 12, 161, 347

linear combination an expression of the form $\vec{r} = a\vec{x}_1 + b\vec{x}_2,\ (a, b) \in (C)$ is a linear combination of of the vectors $\vec{x}_i$. 337

load the material inside a mill, synonymous with charge, or that fraction of the mill volume taken up by the charge. 28, 30, 33, 44, 45, 55–57, 72, 183, 340

macrostate defined here in analogy with the macrostate of thermodynamics- the macrostate of a mechanical system is the combination of bulk properties such as total energy, velocity field etc., that it can have as a result of the microstates of its constituents. 79, 340, 342, 345

mean free path the average distance that a particle can travel through a given medium before interacting in a way which will change either its energy or momentum. cf half-value layer (HVL) . 15, 341

microstate defined here in analogy with the microstate of thermodynamics- the microstate of an element in a mechanical system is the combination of position and momentum (and thus energy and other derivative properties) that it can have, with some probabilty, due to the macrostate of the system. 79, 340, 342, 343, 345

mill in mineral processing, either the entire comminution circuit, consisting of blasting, crushing and grinding, or a single grinding unit such as a rod mill, ball mill, tube mill, semi-autogenous mill or autogenous mill. 43, 44, 46, 345

milling the process of size reduction of mineral-bearing ores. See comminution. 43, 44

normal stress the force per unit area applied to a material in the direction normal to the surface of the material. 345

open area that fraction of the area of the discharge grate through which slurry and fines can flow. 49

overdetermined a system of equations is said to be overdetermined when it consists of more equations than unknowns. 275, 342

particle image velocimetry a Lagrangian optical particle tracking technique used to calculate instantaneous velocity fields in fluids or granular material by comparing the positions of tracer particles in a series of images. 29, 77, 347

pebble mill an autogenous mill with the ratio of its top and bulk sizes increased by pre-screening and crushing, or the addition of large preconditioned rocks. 44

periodic self-repeating in time. 79

phase space if each degree of freedom available to a system is represented as one of a set of orthogonal axes in multidimensional space, this space is called the phase space. All possible microstates of the system correspond to a unique point in phase space. 79, 340

pin mill a stirred mill consisting of a stationary vertical shell containing charge and grinding media driven by a rotor series of rods, or pins, attached to central, rotating shaft. 43

porosity the fraction of empty space per unit volume. See solidicity. 92, 101, 116, 127, 345

positron the antiparticle of an electron, with which it annihilates by the electroweak interaction. 1, 2, 7–9, 11, 12, 14, 15, 20, 21, 25, 343

positron emission particle tracking a Lagrangian nuclear imaging technique based on the detection of the decay products of positron annihilation. For a more complete treatment, see Chapter 2. 1, 2, 11, 12, 30, 63, 77, 347

positron emission tomography a medical imaging technique in which the density distribution of a positron-emitting radioisotope is obtained by the back-projection of detected LoRs defined by the back-to-back γs produced by positron annihilation. 11, 29, 342, 347

positronium a short-lived exotic atom similar in structure to a hydrogen atom, but with a positron rather than a proton as a 'nucleus'. 8, 9, 20, 21, 337

probability distribution by the ergodic hypothesis, the time spent by a particle in some microstate is proportional to the likelihood of that microstate's existence. Thus, the time spent by a particle in some region of space (in a steady state system), normalised by the total time of the experiment, is proportional to its likelihood of being there at any given moment. The distribution of the normalised residence times in space is interpreted as a probability distribution. 81, 82, 85–87, 90, 91, 95, 127, 344

pulp a mixture of slurry and small rocks or fines, discharged from a tumbling mill. 49, 64

pulp chamber the portion of a tumbling mill just before the discharge trunnion, separated from the body of the mill by a discharge grate. 48, 49, 63, 64, 339

quadratic a polynomial of order 2. 345

radial binning a method of binning perfectly cylindrically symmetric data by summing over 2π radians for each binned radial position. 94, 95

random event this is a spurious event that is due to the detection of gamma rays not originating from the same radioactive decay. 13, 14, 16

re-entry toe the point at which the charge in the toe region of a tumbling mill is re-inducted into the rising region. 41, 106, 133, 134, 140, 158, 171, 345

rectilinear in a straight line. 78, 341

reduction ratio the ration between the sizes of the rocks supplied to and produced by a comminution device. 43

residence time binning a method of binning in which the time spent by a tracked particle in each bin is calculated by determining the intercepts with the bin boundaries of the interpolant to the sample points of the particle's trajectory. 1, 2, 4, 83, 87–91, 93, 98, 115, 122, 127, 162–164, 288, 289, 291–293, 300, 304, 306–308, 310, 314, 315, 317, 319, 323, 326, 328–331, 337

residence time distribution a probability distribution calculated by binning data based on the time spent in each bin. 1, 2, 81, 91, 347

residual error the difference between a theoretical or predicted value and the measured or actual value. 275, 342

rising region the portion of the charge in the bulk region of a tumbling mill below the equilibrium surface that moves in a quasi-rigid body way with the mill shell. 32–37, 40–42, 52–56, 102, 103, 118, 119, 127, 128, 138–140, 143, 151, 155, 156, 159, 160, 168, 171, 184, 338, 340, 343

rocked system a class of cylindrically symmetric systems consisting of a cylinder that is moved in any way other than rotation about its central axis. 95

rod mill a class of tumbling mill containing steel rods as grinding media. 46, 341, 342, 346

rolling a mode of charge motion in which some charge avalanches down the rising bulk, forming for the first time an equilibrium surface and active region as the charge begins to circulate about its CoC. cf cascading. 37, 38, 40, 171, 176, 338

rotated system a class of cylindrically symmetric systems consisting of a cylinder that is rotated about its central axis. 95

run of mine the coarse rock and ore produced in the mine by blasting and before primary crushing. 3, 43, 344, 347

run of mine ball mill an autogenous mill used to treat run of mine (RoM) charge. 43

scattered event this is a spurious event that is due to the detection of two gamma rays that originated from the same radioactive decay but at least one of which has experienced Compton scattering. 14, 16

semi-autogenous mill a ball mill containing less than 15% steel balls by volume. 3, 44, 45, 337, 342, 346

shear rate the rate application of shear stress to a material. An important quantity in fluid and granular dynamics. 1, 3, 4, 33, 35–38, 53, 55, 56, 108, 139, 154–157, 160, 164, 168, 169, 172, 173, 175, 184

shear stress the force per unit area applied to a material perpendicular to a normal to the surface of the material. 28, 108, 344, 345

shoulder can refer to either the bulk shoulder or departure shoulder . 28, 29, 33, 35, 40–42, 48, 54–56, 105, 106, 114, 116, 118, 127, 132, 133, 142, 150, 183, 323, 326

simple binning a method of binning in which the sample points are assumed to be uniformly distributed in time so that the RTD can be approximated by simply counting the number of sample points falling in each bin. 1, 4, 81, 84, 85, 87, 89–91, 162, 163, 289, 291–293, 298, 300, 306, 308, 310, 314, 315, 317, 319, 323, 328–331

slipping a mode of charge motion in which there is significant slippage between the body of the charge and the mill shell. As such, the charge moves up the side of the mill to a stable point and stays there as the mill rotates beneath it. cf surging. 37, 40, 47, 171, 344, 345

slumping a mode of charge motion in which the charge moves sufficiently above its equilibrium point that some fraction of it is above the angle of repose of the material. This unstable fraction then avalanches down the rest of the charge to its toe region. The now-lower charge is then lifted again above its equilibrium point and the process repeats itself. cf slipping,surging. 37, 171

solidicity the fraction of filled space per unit volume. It is the complement of the porosity. 92, 116, 127, 343

spurious a detection or a LoR can be described as spurious if it is due to the detection of two gamma rays at least one of which has changed direction or energy in transit. cf true event. 13, 15, 16, 18, 22, 337, 343–345

steady state globally invariant with time. That is, although the microstate of a system element may vary over time, the macrostate of the system remains the same. 28, 29, 46, 55, 79, 81, 343

stirred mill a grinding mill whose shell is generally stationary, but which contains a moving agitator or rotor which drives the charge. An example is the IsaMill^{TM}. 43, 50

stirred system a class of cylindrically symmetric systems consisting of a stationary vessel containing material that is driven periodically by an impeller or, in the case of vertical fluidised beds, by gas or liquid. 94, 95

stress the sum of the shear stress and normal stress. 108

surging a mode of charge motion in which there is significant slippage between the body of the charge and the mill shell. As such, the charge cyclically moves up the side of the mill slightly above its stable point and slides back down again. cf slipping. 37, 40, 47, 171, 179, 344

ternary quadratic a quadratic polynomial in 3 variables. 274

toe can refer to either the bulk toe, impact toe, re-entry toe, or the toe region. 28, 33, 40–42, 45, 54–57, 106, 132, 142, 183

toe region the complex region of the charge between the impact toe where the in-flight charge lands, and the re-entry toe where it is re-inducted into the rising charge. 28, 36, 42, 48, 53, 101, 103, 106, 118, 119, 127, 132, 133, 136, 139, 140, 156–158, 168, 172, 253, 343–345

torque arm approach an approach to calculating the power drawn by a tumbling mill by considering the charge to experience a gravitational torque at its CoM and to rotate about some centre with some angular frequency. 107

torque per bin approach an approach to calculating the power drawn by a tumbling mill by calculating the gravitational torque experienced by each bin rotating about some centre with some angular frequency. 107

tracer particle the representative particle that has been radio-labelled for tracking in the bulk. 1, 2, 13, 18–25, 112–119, 122, 127, 136, 138, 139, 147, 148, 151, 161–163, 166, 173, 174, 253, 266, 271, 315, 317, 328, 337

transition layer the layer of intermediate density between the bulk region and in-flight region of the charge. 103, 116, 119, 130, 132, 140, 166, 168

transport region a high pressure drop region in a grinding mill through which sufficiently small particles can be pumped out of the mill. 99

trommel a slightly-inclined, rotating cylinder whose shell is made of progressively coarser mesh from the feed to the discharge ends, used to separate material by size. 99

true event a detection or a LoR can be described as a true event if it is due to the detection of two gamma rays, initiating from the same radioactive decay, and that have not changed direction or energy in transit. cf spurious. 13, 14, 16, 19, 345

trunnion one of a pair of cylindrical supports permitting rotation of the supported body. In this work, it refers to the feed and discharge trunnions of a tumbling mill, which are hollow and permit charge to be introduced into or removed from the mill through them. 49, 63

tube mill a ball mill whose length to diameter ratio is between 3 and 5. 45, 337, 342, 346

tumbling mill a piece of machinery- common in the mineral processing, pharmaceutical, food processing and other chemical processing industries- used to reduce the size or increase the surface area to volume ratio of particulate material. See rod mill, ball mill, tube mill, semi-autogenous mill and autogenous mill. 1–4, 25, 29–31, 38, 41–50, 52, 53, 55, 57, 62, 71, 72, 76, 91, 94, 95, 99–101, 103, 105–109, 112, 116, 129, 133, 142, 144, 148, 156, 160–164, 172, 173, 175, 179, 183, 326, 337–341, 343, 344, 346

values in mineral processing, the commercially valuable minerals contained in an ore body. 48, 339

washing out the loss of information about the fine detail of a tracked particle's trajectory and kinematics by the aggregating effect of the binning procedure. 82, 84, 91

Acronyms

CMR UCT Centre for Minerals Research. 1, 3, 172, 175

CoC centre of circulation. 1, 28, 29, 33, 34, 36, 37, 41, 42, 53–56, 101–108, 116, 124, 127, 128, 138–140, 142, 145–147, 150, 151, 154, 156, 157, 160, 163, 164, 168, 171, 173, 175, 176, 339, 344

CoM centre of mass. 41, 56, 57, 104–107, 132, 134, 138, 140, 145, 147, 160, 345

DEM discrete element method. 30, 41, 42, 54, 55, 73, 103, 173, 179

HDPE high-density polyethylene. 62–64

HVL half-value layer. 15, 342

JKMRC The Julius Kruttschnitt Mineral Research Centre. 42

LoR line of response. 12–19, 21–23, 161, 253, 257, 266, 317, 338, 343, 345

NIST National Institute of Standards and Technology. 14

PEPT positron emission particle tracking. 1–4, 11–13, 19–25, 30, 41, 42, 54, 63, 69, 71, 76–78, 83, 101, 103, 107, 112, 113, 115, 127, 144, 148, 158, 161, 163, 164, 172, 174, 175, 179, 291, 293, 298, 310, 315, 326, 330, 342

PET positron emission tomography. 11–13, 21, 22, 29, 342

PIV particle image velocimetry. 29, 77, 175

RoM run of mine. 3, 43, 44, 344

RTD residence time distribution. 1, 2, 81, 84–86, 89–93, 95, 98, 101, 105, 107, 108, 115, 116, 127, 129, 130, 139, 160, 166, 168, 173, 174, 317, 319, 323, 328, 331, 344

Index